Highly Luminescent Platinum Complexes for Light Emitting Devices and Bio-Imaging

MURPHY, LISA

HIGHLY LUMINESCENT PLATINUM COMPLEXES FOR LIGHT EMITTING DEVICES AND BIO-IMAGING

Lisa Murphy

A thesis submitted in partial fulfilment of the requirements for the degree of Ph.D.

Department of Chemistry

University of Durham

2010

Abstract

Intensely luminescent cyclometallated platinum(II) complexes have been prepared containing N^C^N-coordinating ligands, based on 1,3-dipyridylbenzene. Exceptionally high quantum yields ($\leq$ 0.85, degassed DCM, 298 K) are rationalised in terms of the particularly short Pt-C bond, which raises the energy of the normally deactivating d-d* state. Terdentate ligand functionalisation has been employed to obtain complexes with tuneable emission. Fluorination at the 3,5-aryl positions and/or placing electron-releasing substituents at the 4-pyridyl position gave complexes with blue-shifted emission, whilst retaining a high quantum yield. Substitution of the chloride ancillary ligand for cyanide led to further blue-shifts.

In general, these complexes undergo intermolecular interactions in solutions of higher concentration to form excimers. The excimers are emissive in their own right, and display broad, structureless emission bands at lower energy than the isolated molecules (monomers). The influence of substituents in the terdentate ligand and the identity of the coligand on the energy and relative intensity of excimer emission has been elucidated.

Some complexes have been used as phosphorescent dopants in the fabrication of high efficiency organic light emitting devices (OLED)s. The colour of a device depends on the monomer-to-excimer emission ratio, which is controlled by varying the dopant concentration. At intermediate concentrations, white OLEDs, with properties approaching pure white light, have been obtained.

Preliminary investigations into the utility of the complexes as bio-imaging agents in live cells are reported. The complexes which contain small substituents on the terdentate ligand enter cells rapidly, retaining their phosphorescence. These Pt(II) complexes appear to localise simultaneously in both the nucleus and mitochondria of cells, where their emission characteristics differ: the application of appropriate filter sets allows separate visualisation of the two organelles. A selection of iridium(III) complexes were also investigated as bio-imaging agents. These complexes localise in cytoplasm-based organelles, and do not appear to enter the nucleus. Both classes of organometallic complexes are shown to be suitable candidates for time resolved emission imaging microscopy (TREM).

DECLARATION

The research described herein was undertaken at the Department of Chemistry at Durham University between October 2006 and December 2009. All of the work is my own, except where specifically stated otherwise. No part of it has previously been submitted for a degree at this or any other university.

STATEMENT OF COPYRIGHT

Acknowledgements

I have thoroughly enjoyed researching for my PhD here in Durham, and have made many good friends along the way. Before getting into the science, I would like to say thank you to all those who have helped me over the past three years:

Firstly, my most sincere thanks go to my supervisor, Dr Gareth Williams for all the support, guidance and encouragement given throughout my PhD studies. I would also like to thank all members of the Williams group, past and present: Louise Parkes, Pierpaolo Brulatti, Stéphanie Develay, Victoria Whittle, Will Tarran, Gemma Freeman, Jonathan Barnard and all of the 4th year project students. Thank you for your friendship, and making our lab such a fun place to work – it has been a pleasure to work with you all. Thank you to the University of Durham and the Department of Chemistry for my Doctoral Fellowship and financial support.

Special thanks go to Dr Aileen Congreve for help with the flow cytometry, and continued encouragement during the writing of this thesis, to Dr Lars-Olaf Palsson for all his help with the time resolved emission imaging studies, to Professor David Parker for allowing me the use of the Parker group fluorescence microscope and various other cell studies related equipment, to Dr Hazel Sparkes for the numerous crystal structure determinations, and to Liz New for all of the help and advice she gave me with regards to working with cells, and for her continued friendship.

Thank you also to Dr Alan Kenwright, Catherine Heffernan and Ian McKeag for all the high resolution NMR spectroscopy and advice regarding NMR, to Dr Mike Jones, Dr Jackie Moseley, Lara Turner, David Parker and Peter Stokes for the mass spectrometry service, Jarka Dorstal and Judith Magee for the elemental analysis results, to Peter Coyne and Malcolm Richardson for fixing the numerous pieces of glassware that I broke over the years, and to everyone working at the chemistry stores.

Finally I would like to thank my family and friends for all the support and encouragement they have given. In particular, I would like to thank my parents and Alisdair Wallis, who have been brilliant throughout, and always knew how to make me smile.

Abbreviations

Acac	Acetylacetone
AgOTf	Silver triflate
AlQ_3	Tris(8-hydroxyquinolate)aluminium
ASAP	Atmospheric solids analysis probe
ATP	Adenosine triphosphate
B_2pin_2	Bis(pinacolato)diboron
Bipy	2,2'bipyridine
br	Broad
BSA	Bovine serum albumin
CBP	4,4'-(N,N'-dicarbazole)biphenyl
CCD	Charge-coupled device
cd	Candela
CIE	Comission Internationale de L'Eclairage
CHO	An adherent cultured cell line derived from transformed Chinese hamster ovary cells
cm^{-1}	Wavenumbers
C^N^C	A terdentate ligand with coordination pattern carbon, nitrogen, carbon
COD	1,5-Cyclooctadiene
COSY	Correlation spectroscopy
Cp	Cyclopentadiene
CRI	Colour rendering index
DCM	Dichloromethane
dctb	Trans-2-[3,4-tert-butylphenyl]-2-methyl-2-propenylidene]malonitrile
DFT	Density functional theory
DMAE	2-(dimethylamino)ethanol
DMAP	4-N,N-dimethylaminopyridine
DME	Dimethoxyethane
DMEM	Dulbecco's modified Eagle medium
DMF	Dimethylformamide
DMSO	Dimethylsulfoxide
DNA	Deoxyribonucleic acid
dpm	Dipivaloylmethane
dppf	1,1'-bis(diphenylphosphino)ferrocene
dpyb	1,3-di(2-pyridyl)benzene
dppy	1,3-diphenylpyridine

E	Energy
ε	Extinction coefficient (L mol^{-1} cm^{-1})
E.D.G	Electron donating group
E_{em}	Energy of emission
EI	Electron impact ionisation
em	Emission
EPA	Diethyl ether:isopropane:ethanol (2:2:1 v/v)
E_p^{ox}	Peak potential of irreversible oxidation process
E_p^{red}	Peak potential of irreversible reduction process
Equiv.	Equivalents
ES^+	Positive ion electrospray ionisation
ET	Electron transfer
E.W.G	Electron withdrawing group
ex	excitation
Fc	Ferrocene
FITC	Fluorescein isothiocyanate
h	Hour
HeLa	An adherent cultured cell line derived from human cervical carcinoma cells
HOMO	Highest occupied molecular orbital
HPLC	High pressure liquid chromatography
HRMS	High resolution mass spectrometry
HSQC	Heteronuclear single quantum correlation
Hz	Hertz
IC	Internal conversion
IC_{50}	Half-maximal inhibitory concentration
ILCT	Intraligand charge transfer
ISC	Intersystem crossing
ITO	Indium tin oxide
k_0	Self-quenching rate constant at infinite dilution
k_{nr}	Rate constant of non-radiative decay
k_r	Rate constant of radiative decay
k_{sq}	Quenching rate constant
λ_{em}	Emission wavelength
λ_{ex}	Excitation wavelength
λ_{max}	Wavelength at which an absorption/emission band maximum occurs
L	Some derivatised 1,3-di(2-pyridyl)benzene N^C^N ligand
LC	Ligand-centred
LCD	Liquid crystal display

Ln^{3+}	Lanthanide
lp	Long pass
LTR	LysoTracker Red™
LUMO	Lowest unoccupied molecular orbital
MALDI	Matrix assisted laser desorption ionisation
MC	Metal centred
MLCT	Metal-to-ligand charge transfer
MMLCT	Meta-metal-to-ligand charge transfer
m-MTDATA	4,4',4''-tris(N-(3-methylphenyl)-N-phenylamino)triphenylamine
MO	Molecular orbital
MS	Mass spectrometry
MTR	MitoTracker Red™
MTT	3-(4,5-dimethylthiazol-2-yl)-2,5-diphenyltetrazolium bromide
μ-dppm	Bis(diphenylphosphino)methane
N^C	A bidentate ligand coordinating via one nitrogen and one carbon atom
N^C^N	A terdentate ligand with coordination pattern nitrogen, carbon, nitrogen
NIH 3T3	An adherent cultured cell line derived from transformed mouse embryonic fibroblast cells
NIR	Near-infra red
nm	Nanometers
NMR	Nuclear magnetic resonance
N^N	A bidentate ligand coordinating via two nitrogens
N^N^C	A terdentate ligand with coordination pattern nitrogen, nitrogen, carbon
N^N^N	A terdentate ligand coordinating via three nitrogens
OLED	Organic light emitting device/diode
ORTEP	Oak Ridge thermal ellipsoid plot
PBS	Phosphate-buffered saline
PC	Bisphenol-A-polycarbonate
phbpy	6-phenyl-2,2'-bipyridine
PI	Propidium iodide
ppm	Parts per million
ppy	2-phenylpyridine
PtOEP	Platinum (II) octaethylporphyrin
py	Pyridine
φ	Quantum yield
Qdot	Quantum dot
R_f	Retention function
RNA	Ribonucleic acid

rpm	Revolutions per minute
R.T.	Room temperature
S_0	Singlet ground state
S_n	nth excited singlet state
SD	Standard deviation
sh	Shoulder
SOC	Spin orbit coupling
τ	Lifetime
τ_{obs}	Observed lifetime
τ_0	Lifetime at infinite dilution
TAZ	3-phenyl-4-(1'-naphthyl)-5-phenyl-1,2,4-triazole
TBAF	Tetrabutylammonium fluoride
TCTA	4,4,4"-tris(*N*-carbazolyl-triphenylamine)
TDDFT	Time-dependent density functional theory
TFA	Trifluoroacetic acid
THF	Tetrahydrofuran
tlc	Thin layer chromatography
TMEDA	Tetramethylethylene diamine
TPD	N,N'-bis(m-tolyl)-1,1'-biphenyl-4,4'-diamine
trpy	2,2':6,2"-terpyridine
UV	Ultra violet
v/v	Volume ratio between two solutions
WOLED	White organic light emitting device
w.r.t	With respect to
ZFS	Zero field splitting

Table of Contents

CHAPTER TWO: SYNTHESIS AND CHARACTERISATION

CHAPTER THREE: ELECTRONIC PROPERTIES OF THE COMPLEXES

CHAPTER ONE:

Introduction

1.1 Overview

Since the realisation of the photochemical properties of $[Ru(bipy)_3]^{2+}$ in 1959,[1] interest in luminescent organometallics involving polypyridyl ligands has increased dramatically.[2,3,4] Of particular interest are such complexes involving the platinum-group metals. These 2nd and 3rd row transition metals possess high spin-orbit coupling (SOC) constants, which dramatically increases the rate of intersystem crossing (ISC), so that, upon excitation, the lowest energy triplet state is populated almost instantaneously (see Figure 1). As a consequence, the photophysics of these complexes is usually dominated by triplet states.[2] Fast ISC and high yields of triplet formation are, of course, also possible in certain purely organic compounds, aryl ketones being good examples.[5] Where heavy metal complexes really differ is in the extent to which the high SOC can relax the spin selection rule ($\Delta S = 0$), promoting the rate of radiative decay of the triplet state and allowing phosphorescence to compete with the non-radiative decay pathways, that would normally predominate at room temperature.[6] Since the $T_1 \rightarrow S_0$ transition is still only partially allowed, the lifetime of phosphorescence of such metal complexes is typically significantly longer than fluorescence lifetimes, often being of the order of a microsecond rather than a nanosecond.[7]

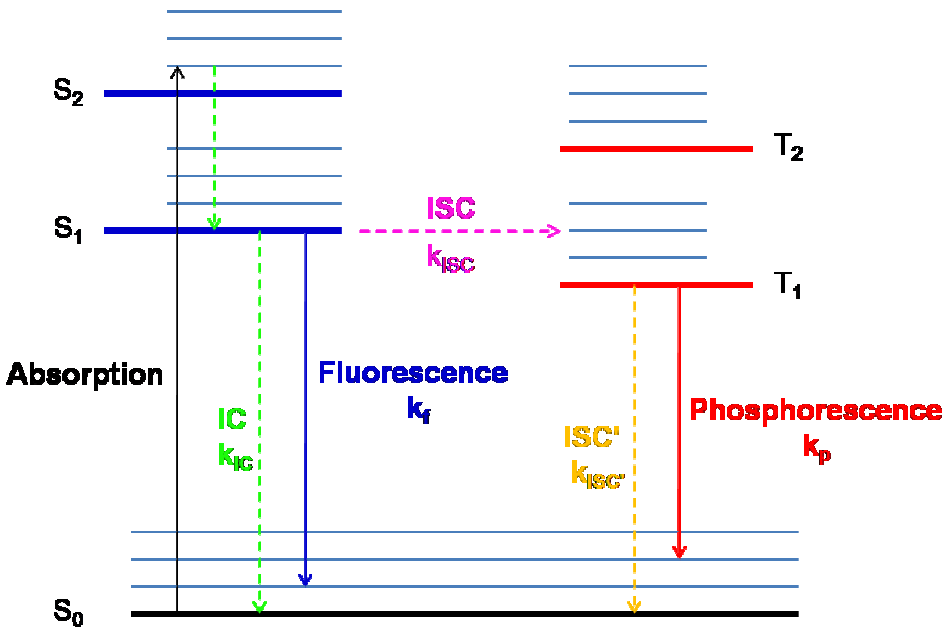

Figure 1: A typical Jablonski diagram. IC represents internal conversion followed by vibrational relaxation, ISC and ISC' represent intersystem crossing followed by vibrational relaxation. Solid coloured arrows represent radiative transitions, and broken arrows represent non-radiative transitions.

Luminescent organometallic complexes find use in organic light emitting devices (OLEDs)[8,9] sensors, light-energy conversion[10] and more recently bio-imaging.[11,12,13] A big draw for such research at present is the advancement of OLED technology, in which triplet-emitting organometallic complexes find use as phosphors, and their triplet-harvesting ability offers a significant efficiency advantage over organic fluorophores.

Interest initially focused around d^6 metal complexes such as those of Ru^{2+}, Ir^{3+} and Os^{2+}, and investigations into luminescent d^8 metal (e.g. Pt(II), Pd(II)) complexes only really took off in the late eighties. The delayed interest in luminescent d^8 complexes can be attributed in part to the geometry of such species – whereas d^6 complexes are generally octahedral, d^8 complexes tend to be square planar, as a consequence of ligand field stabilisation. The more open geometry of a square planar complex lends itself to intermolecular interactions, and the complexes have a tendency to undergo inner sphere interactions with other molecules (including the solvent), generating multimolecular species such as aggregates, excimers and exciplexes.[5,14] Formation of such species 'quenches' the emission of the isolated molecules (monomeric emission) of the complex: an undesirable property of a luminescent species. Hence such complexes were initially less attractive than the co-ordinately saturated d^6 analogues.

However, in some cases these multimolecular species are emissive in their own right, where emission typically occurs at lower energy than the monomeric species.[15,16,17,18,19] The overall colour of light emitted then depends on the ratio of the intensity of monomer-to-multimolecular emission. This effect can be exploited in OLEDs, as a facile way to obtain white light emitting devices using a single phosphor material.

1.2 Electronic Transitions

Emission will normally occur from the lowest-energy electronic excited state. For organometallic species, to a first approximation, this state is usually classified as one of four possible electronic states, according to the predominant character of the orbitals involved. If some of these orbitals lie at similar energy, a degree of mixing may occur. As a consequence, the emission of such complexes may stem from an excited state containing an admixture of the various electronic transitions:

1. Metal centred (MC) d-d states. When a ligand binds to a transition metal, the five metal d-orbitals become non-degenerate in a manner determined by the symmetry. MC transitions occur between d-orbitals, which are localised on the metal.

2. Metal-to-ligand-charge transfer (MLCT) states. Here the molecule becomes excited from a metal-centred orbital into a ligand-centred π*-antibonding orbital (also known as d-π*).

3. Intraligand (IL) transitions. The molecule becomes promoted from a ligand centred π-bonding orbital (or non-bonding orbital) to a higher energy π*-antibonding orbital (π-π*). The metal may sometimes have relatively little effect in such cases.

4. Ligand-to-metal-charge-transfer (LMCT) states. In this case, the molecule is promoted from a ligand π-orbital to a metal-centred d orbital.

The relative energies of the above states may vary greatly depending on the nature of the ligand(s), the identity of the metal and its charge, and the geometry of the complex.[20] There are therefore more possible available ways to tune the emission, compared with typical fluorescent organics.

1.3 A Brief History of Luminescent Platinum(II) Poylpyridyl Complexes

Many of the early d^8 platinum(II) complexes prepared for luminescence studies were based on pyridine and polypyridine ligands, similar to those that had been successfully incorporated into the earlier luminescent d^6 systems. Unfortunately, these Pt(II) complexes proved to be scarcely emissive in solution at room temperature because rapid non-radiative decay of the excited state occurs. For example, $[Pt(bipy)_2]^{2+}$ (the Pt analogue of $[Ru(bipy)_3]^{2+}$)[21,1] is practically non-emissive at room temperature, as is $[Pt(bipy)Cl_2]$.[16,22] It has been suggested that the non-emissive decay is associated with the structure of such complexes. Square planar Pt(II) complexes involving monodentate and/or bidentate ligands are prone to D_{2d} distortions. Such distortions involve twisting out of the square plane, to form an approximate tetrahedral geometry. As a rule of

thumb, radiative emission is most likely when there is minimal distortion between the ground state and excited state. Figure 2 a) exemplifies this - in potential energy surface terms, a distorted excited state will be displaced relative to the ground state. If the minimum of the excited state lies at similar energy to one of the vibrational levels of the ground state, intersystem crossing and non-radiative relaxation will result.

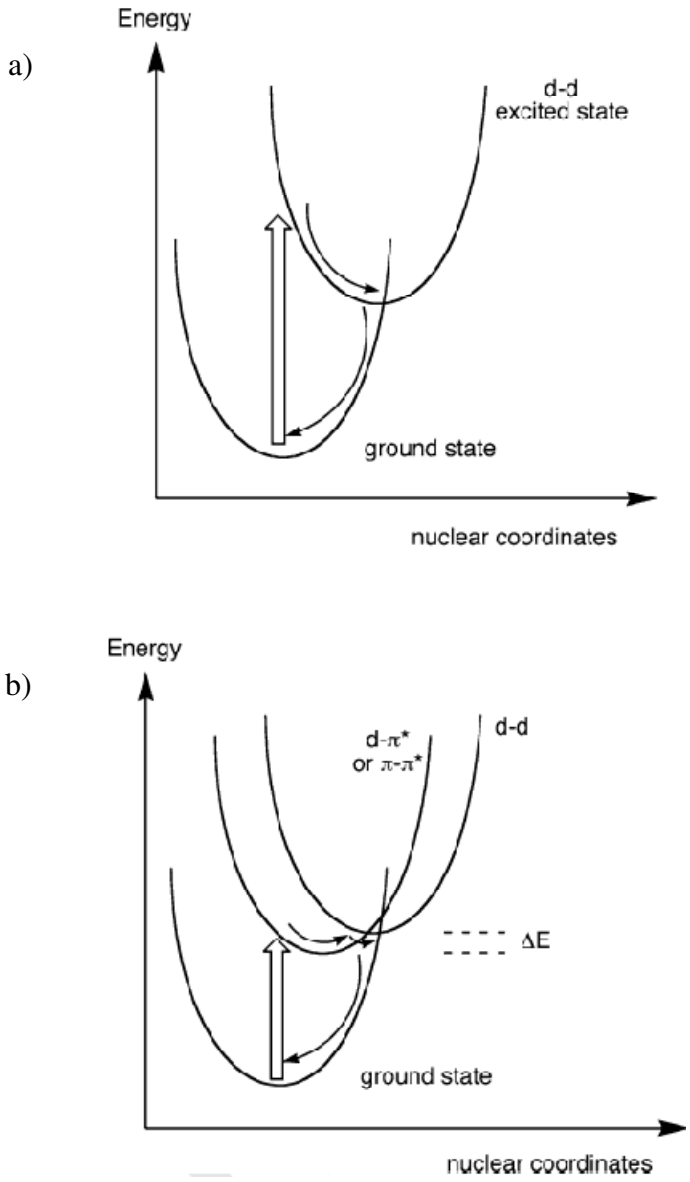

Figure 2: a) represents the energy minimum displacement of the excited state relative to the ground state, on population of the dx^2-y^2 orbital of a square planar d^8 complex (also applies to other excited states that are significantly distorted relative to the ground state). b) represents excitation to an emissive state (e.g. MLCT or ILCT), followed by thermal conversion to a low lying metal-centred state and non-radiative decay. For simplicity, the effects of anharmonicity on the form of the potential energy curves is ignored.[23]

$[Pt(trpy)Cl]^+$ incorporates a tridentate terpyridyl ligand, 2,2':6,2''-terpyridine – such a ligand enforces rigidity in the system. D_{2d} distortions are not possible here, so one might expect the complex to display room temperature luminescence. Unfortunately this

complex is also non-emissive in solution at ambient temperature, but for different reasons.[18,24] There is significant strain within this molecule due to a less than optimum bite angle around platinum, enforced by the rigidity of the system.[18] As a consequence, the ligand field splitting energy is relatively small and the π* orbital is of similar energy to the strongly antibonding d_{x2-y2} orbital (d-d* state). At room temperature, thermal promotion from the excited state to this antibonding orbital occurs, accompanied by intersystem crossing and a non-radiative return to the ground state (Figure 2 b)).

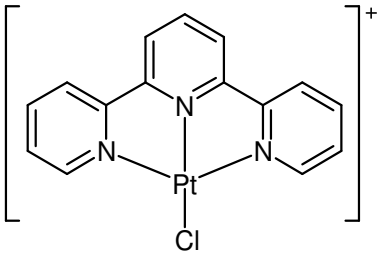

Figure 3: The structure of $[Pt(trpy)Cl]^+$.

For such complexes to be luminescent at room temperature, one can envisage that either the emissive excited state must be of sufficiently low energy that thermal population of d_{x2-y2} becomes unfeasible, or that the d_{x2-y2} state is raised in energy, which can be achieved by increasing the ligand field strength.

1.4 N^N^N Complexes of Pt(II) Displaying Room Temperature Luminescence

Structural modification of the polypyridine ligands can influence the energy of the lowest excited charge-transfer state (here a MLCT state) relative to the deactivating d-d* states.[25,26] D. R. McMillin et al. found that by placing a substituent in the para-position of the central pyridyl ring of a trpy system, one could lower the energy of the emissive excited state, thus increasing the gap between it and the deactivating d-d* state.[25] Surprisingly, both electron withdrawing and electron releasing substituents were found to have this effect, though for different reasons. With electron withdrawing substituents, the energy of the MLCT state drops by a larger amount than the d-d* state, meaning that the energy difference is greater and thermal population of the deactivating d-d* state is unlikely. When electron releasing substituents are involved, mixing between the MLCT state and an ILCT state of similar energy occurs, again resulting in a

larger energy difference between the lowest excited state and the d-d* state (see Figure 4).

Placing aromatic substituents in the 4-position was found to increases the lifetime of the emissive state.[27] However, as the fused ring system becomes larger and easier to ionise, although the lifetime increases, the energy of the emission decreases. The latter effect is attributed to a greater orbital mixing of the emissive MLCT state with an ILCT state.

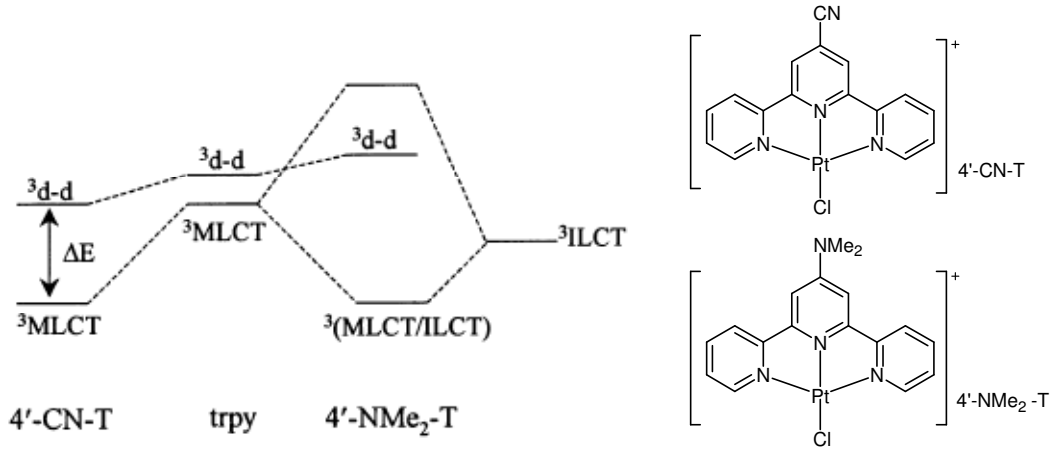

Figure 4: Excited state energies of various $[Pt(4\text{-}X\text{-}terpy)Cl]^+$ complexes, compared to the unsubstituted $[Pt(trpy)Cl]^+$ complex. The left side of the diagram represents the case where X is electron withdrawing (here, CN), and the right side shows what happens when X is electron releasing (here, NMe_2).[27]

N^N^N complexes involving more favourable bite angles around platinum have been prepared, and such complexes have recently been shown to exhibit room temperature luminescence with quantum yields as high as 4%.[28,29] The complexes are based on 2,6-di(8-quinolyl)pyridine and 2-(8'-quinolinyl)-1,10-phenanthroline ligands (e.g. complexes **1** and **2** respectively), and involve 6-membered chelating rings as opposed to the typical 5-membered chelating rings in the previously discussed terpyridine coordinating ligands (see Figure 5). Crystal structures and DFT results indicate that ring strain is significantly reduced in such systems. For example, the crystal structure of **2** revealed a N^Pt^N bond angle of 93.0˚ within the 6-membered chelating ring, and a N^Pt^N bond angle of 82.2˚ in the 5-membered chelating ring[29] (note, $[Pt(trpy)Cl]^+$ chelating rings have N^Pt^N angles of 82˚),[18] whilst DFT calculations on complex **1** suggest a lateral N-Pt-N bond angle of approximately 180˚ (the $[Pt(trpy)Cl]^+$ lateral N^Pt^N angle is 163.5˚).[28] The more favourable bite angle that such 6-membered chelating ligands offer results in a stronger ligand field, shifting the deactivating d-d* state to higher energy, and reducing the likelihood of population of this non-radiative state via thermal promotion.

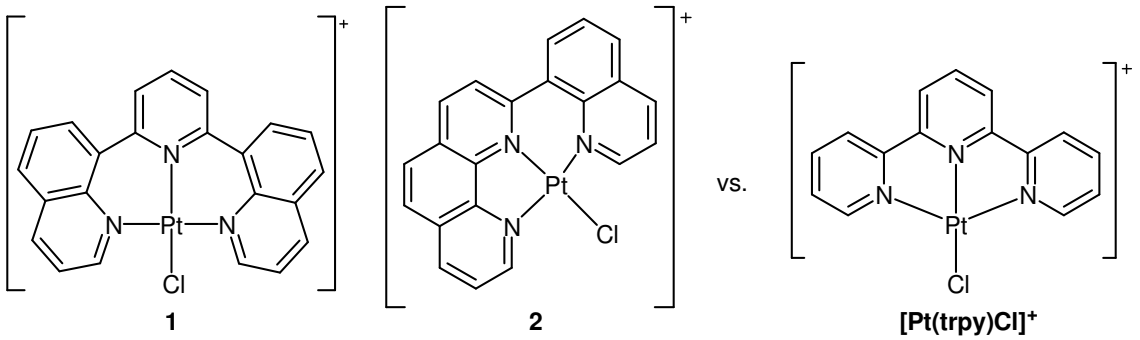

Figure 5: Structures of complexes 1 (left)[28] and 2 (middle)[29], which contain 6-membered chelating rings. Such complexes possess more favourable bite angles around platinum than 5-membered chelating ligands such as $[Pt(trpy)Cl]^+$, and are luminescent at 298 K.

A third route to obtaining room temperature luminescence is to replace the ancillary ligand (typically chloride) with a strong field ligand, a ligand that occurs higher in the spectrochemical series, such as an acetylide or cyanide.[2,30,31,32,33,34,35,36,37] This increases the ligand field splitting, and shifts the deactivating d-d* state to higher energy, reducing its effect. This strategy has also been employed with complexes of derivatised bipyridines and other N^N ligands, affording N^N complexes with room temperature emission.[38,39,40,41,42,43,44]

The fourth strategy involves the replacement of one of the donor nitrogens in the terdentate (or bidentate) polypyridyl system with a cyclometallating carbon – such systems are the focus of this review and the work described in subsequent chapters. Cyclometallated carbons induce strong ligand fields that may raise the energy of the metal-centred d-d* states sufficiently to reduce their deactivating ability.[20,19,45] The remainder of this review will mainly consider various types of cyclometallated platinum(II) complexes involving aromatic chelating ligands based on combinations of pyridyl and phenyl rings. Particular consideration will be given as to how the luminescent properties can be altered by changing the intrinsic structure of the cyclometallating ligand, or by altering the functional groups attached.

1.5 Pt(II) Complexes Containing Bidentate Cyclometallated Ligands

The first cyclometallated Pt(II) complexes studied involved bidentate N^C type ligands (examples of structures are given in Figure 6).[46,47] These complexes can be classified as homoleptic, which contain two identical N^C ligands simultaneously bound to platinum, i.e. $[Pt(N^C)_2]$,[46] or heteroleptic,[48,49,50,51] which contain one N^C ligand and

either a second bidentate ligand, L (e.g. bipyridine, acetylacetonate, ethylenediamine, etc.), or two monodentate ligands X and Y (e.g. halides, acetylides, etc.). Homoleptic complexes always form as the cis isomer, i.e. with carbon trans to nitrogen, due to the large trans effect of the cyclometallating carbon. The literature contains more examples of heteroleptic complexes, as these are generally easier to synthesise. Syntheses of homoleptic complexes typically require use of lithiated ligands, a route that is intolerable to many functional groups. On the contrary, reaction of K_2PtCl_4 with one equivalent of an N^C ligand forms a chloro-bridged dimer which can be cleaved under relatively mild conditions by a variety of monodentate or bidentate ligands, thus forming a heteroleptic complex.[50,51,52] The nature of these "ancillary" ligands can significantly influence the photophysical properties of a heteroleptic complex.[49,50,53] For example, $[Pt(N^C)Cl_2]^-$ (where N^C = 2-phenylpyridine) does not emit from solution at room temperature – the chloride ancillary ligands occur low down the spectrochemical series, and do not confer a large ligand field splitting. As a consequence, the deactivating d-d* states are relatively close in energy to the excited charge transfer state, and thermal population is possible, leading to non-radiative decay. The complex does emit at low temperature (77 K), where this thermal promotion is prohibited.

Ancillary ligands higher up the spectrochemical series such as acetylides, cyanide, bipyridine (bipy), acetylacetonate (acac), isocyanides, etc. lead to larger ligand field splittings.[48,53,54] The deactivating d-d* states are moved to higher energy so that the probability of non-radiative deactivation (via thermal population of this state) is greatly reduced, and such complexes are often emissive at room temperature. The emission of luminescent N^C-type Pt(II) complexes based on phenyl pyridine (see Figure 6 for example structures) is typically red-shifted relative to the free N^CH ligand phosphorescence, with lifetimes on the microsecond timescale. Their emission has been assigned to emanate from a mixed ^{3}LC-^{3}MLCT excited state.[48]

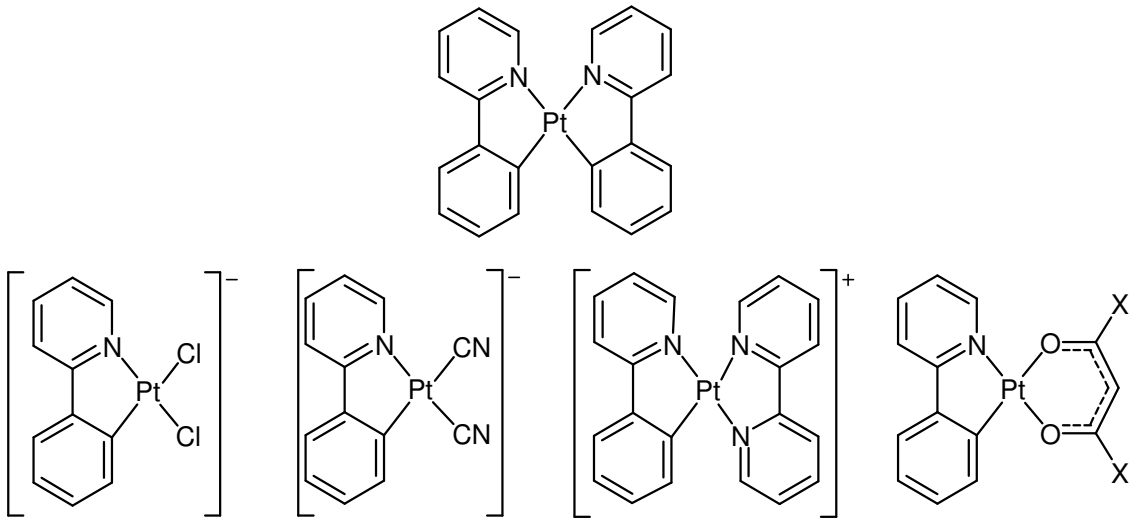

Figure 6: Homoleptic complex [Pt(ppy)$_2$] (top), and a selection of heteroleptic complexes involving ppy (bottom).[46,48,53,54]

Functionalisation of the N^C ligand can alter the photophysical properties of such complexes,[55] and a key study has been performed by Thompson et al.[48] They considered a large selection of [Pt(N^C)(O^O)] complexes (Figure 7), where N^C was a derivatised aryl pyridine and O^O was either acetylacetonate (acac) or dipivaloylmethane (dpm). Beta-diketonate ligands such as acac are a popular ancillary ligand choice with heteroleptic N^C complexes, as they are easily incorporated and have minimal influence on the photophysics, allowing the N^C system to be studied directly. DFT calculations indicate that the HOMO is largely localised on the metal, the O^O ligand and the phenyl ring, whereas the LUMO is largely localised on the pyridine ring, with some phenyl contribution.

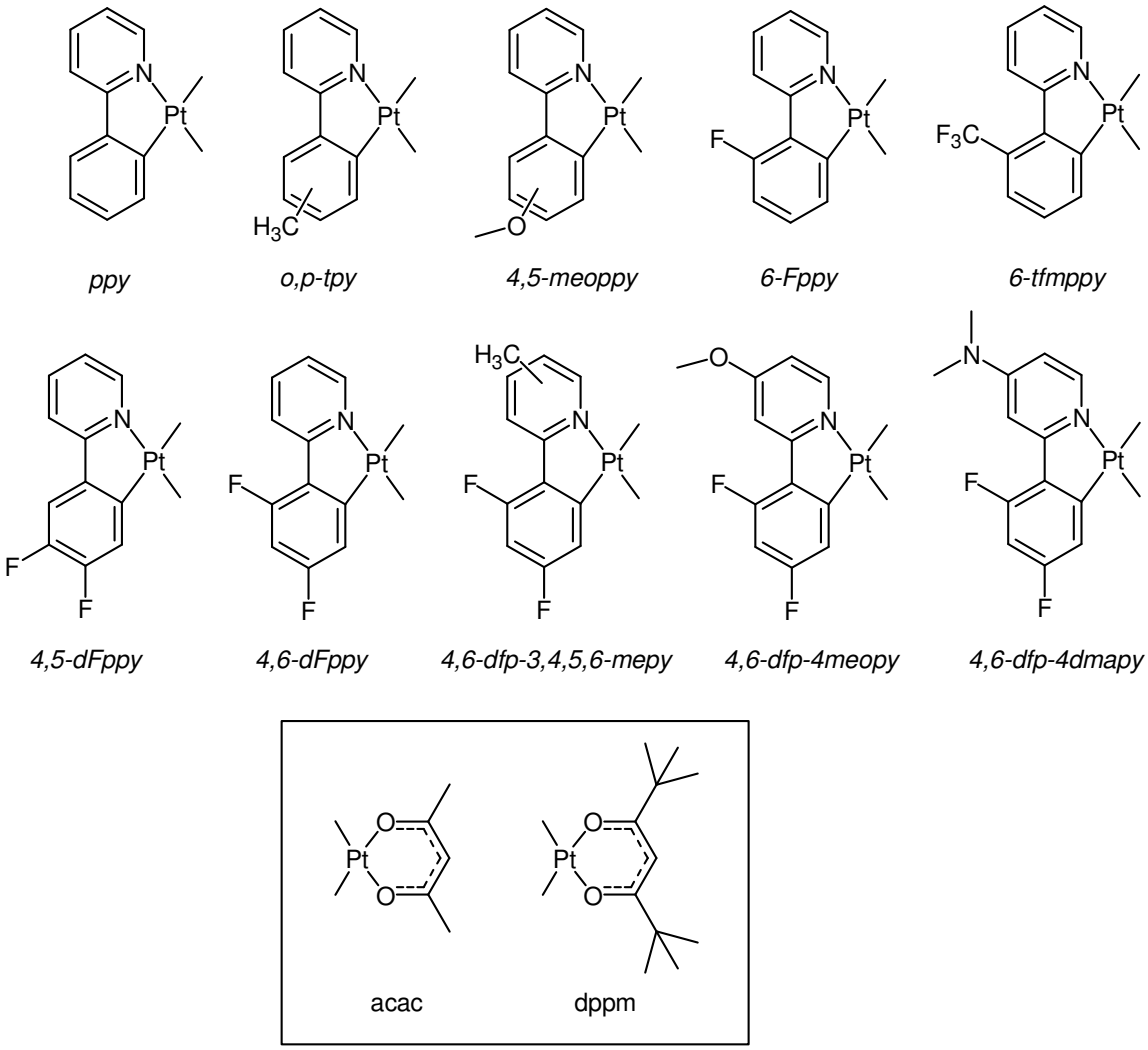

Figure 7: The large selection of Pt(II) complexes involving modified phenyl pyridine ligands, prepared by Thompson et al. in reference 48.

All complexes were found to emit at 77 K and some also emit at room temperature. The emission of the derivatised phenylpyridine complexes varied between 438 and 525 nm in a 2-methyltetrahydrofuran glass at 77 K. Incorporation of electron withdrawing fluorine atoms on the phenyl ring resulted in blue-shifted emission, and this effect was enhanced when electron releasing groups were introduced in to the pyridyl ring (particularly at the 4-position, the position para to nitrogen). Complexes ***4,6-dfp-4-meopy*** and ***4,6-dfp-4-dmapy*** gave the bluest emission (λ_{em} = 438 and 440 nm respectively, 77 K glass). On the face of it, these complexes represent some of the bluest emitting cyclometallated platinum(II) complexes reported to date. Unfortunately, the luminescent efficiency and lifetime were found to decrease with increasing emission energy (see Table 1), and the blue-emitters were practically non-emissive at room temperature.

Table 1: Emission properties of the C^NPt(O^O) complexes at room temperature (2-methyltetrahydrofuran solutions). This table was adapted from reference 48.

C^N	O^O	λ_{max} / nm	τ_{298K} / μs	Φ_{298K}
ppy	acac	486	2.6	0.15
p-tpy	acac	485	4.5	0.22
6-fppy	dpm	476	<1.0	0.06
4,5-dfppy	acac	484	3.0	0.22
4,6-dfppy	acac	466	<1.0	0.02
4,6-dfppy	dpm	466	<1.0	0.02
4,6-dfp-5-mepy	dpm	472	<1.0	0.05
4,6-dfp-4-meopy	dpm	456	<1.0	<0.001
4,6-dfp-4-dmapy	dpm	447	<1.0	<0.001
4-meoppy	dpm	490	7.4	0.20

In summary, cyclometallation in N^C systems successfully shifts the deactivating d-d state to higher energy compared to analogous N^N systems. Unfortunately complexes involving these bidentate ligands are still prone to D_{2d} distortions. As a consequence, the photophysical properties are often far from optimum, with quantum yields only really reaching 0.25 for the most luminescent of such systems. One may expect that increasing the rigidity of the cyclometallating system will lead to enhanced luminous yields.

1.6 Pt(II) Complexes Containing Terdentate Cyclometallated Ligands

Such complexes can be classified as N^N^C, N^C^N or C^N^C, and the luminescence behaviour is dependent on the coordination pattern. To date, most work has been done on the N^N^C and N^C^N complexes, and examples of C^N^C complexes, which involve two cyclometallating sites, are still quite rare. “Pseudocyclometallates” (where

the cyclometallating carbon is replaced by an anionic nitrogen, oxygen or sulphur) are also being developed.

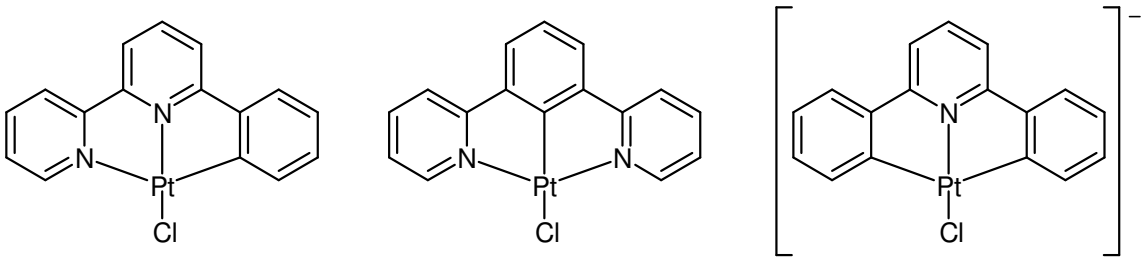

Figure 8: The "parent" complexes of the N^N^C (left), N^C^N (middle) and C^N^C (right) systems.

1.6.1 N^N^C Systems

In 1990, Constable showed that 6-phenyl-2,2'-bipyridine (phbpy-H) would bind to Pt(II) in a terdentate fashion.[56,57] Che and co-workers realised the photophysical properties of such complexes, and have since devoted much time to the development of such systems, for a variety of applications. Similar complexes, in which the terminal pyridyl has been replaced by a pyrazolyl ring have recently been used in bio-imaging of live cells by Che et al. and Lam et al. – this work will be covered in Chapter 5.

The unsubstituted parent complex, [Pt(phbpy)Cl] displays room temperature luminescence (λ_{em} = 565 nm, φ = 0.025, degassed DCM).[58] This is in contrast to $[Pt(trpy)Cl]^+$, which is non-emissive in solution at room temperature, demonstrating the effect of larger ligand field splitting induced by the cyclometallating carbon. The emission spectrum is broad and the complex exhibits a lifetime of 0.51 μs. A solvatochromic response is observed upon changing the solvent – the emission blue-shifts in the presence of more polar solvents (e.g. CH_3CN). Based upon such observations, Che assigned the emission to occur primarily from a ^{3}MLCT state. The lifetime was found to decrease with increasing concentration, suggesting self-quenching was occurring.

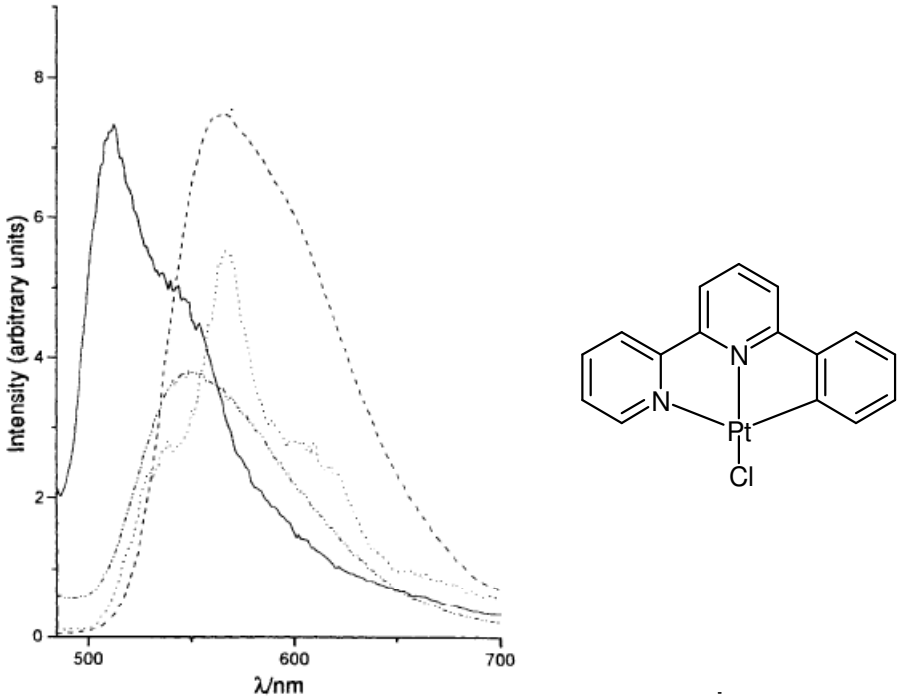

Figure 9: Emission spectra of [Pt(phbpy)Cl] in DCM (298 K) (- - -), CH_3CN (298 K) (-···-), DCM (77 K) (----) and CH_3CN (77 K) (····). the chart was taken from reference 58.

For structures of the type [Pt(N^N^C)X], varying the nature of the ancillary ligand X and/or the substituents of the core cyclometallating ligand allows the photophysical properties to be tuned.[59,60] Trends between substituents and the observed photochemical properties have been realised, and various groups are employing rational structure design to produce complexes with more desired characteristics. For example, an extensive study was undertaken by Che et al., who prepared a large series of [Pt(N^N^C)X] complexes based on a 6-aryl-2,2'-bipyridine tridentate system, incorporating a σ-alkynyl group as the ancillary ligand, X (see Figure 10).[61]

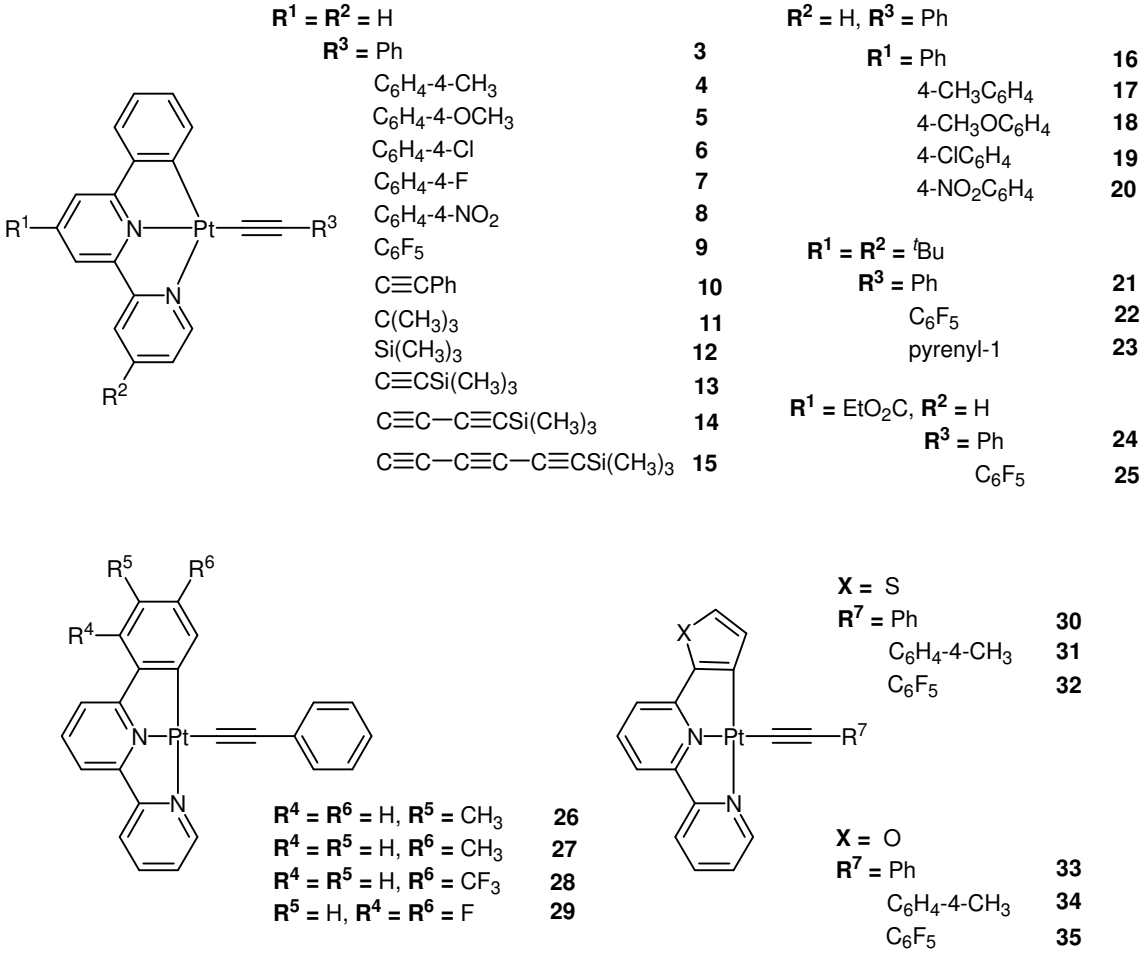

Figure 10: The extensive range of N^N^C complexes prepared by Che et al.[61]

Most of the complexes prepared here were emissive in solution at room temperature (φ = 0.001 – 0.08, τ = 0.1 – 1.1 μs, degassed DCM), giving featureless emission spectra and exhibiting emission colours ranging from green (560 nm) to red (644 nm). In analogy with [Pt(phbpy)Cl], the excited state was assigned to a ^{3}MLCT state for most complexes (for exceptions, see later). The electronic nature of the alkynyl substituent was found to influence the photochemical properties. For example, complexes **3-8** contain a 4-substituted phenyl attached to the alkynyl ligand (i.e. R^3). Substituents of electron releasing character were found to blue shift the emission and substituents of electron withdrawing character caused a red shift. Incorporation of a selection of substituents onto the terdentate ligand was also investigated. For example, incorporation of an electron withdrawing ethoxy-carbonyl group at R^1 led to a dramatic red-shift – complexes **24** and **25** emit at 620 and 593 nm respectively, whereas the parent complexes **3** and **9**, (in which R^1 = H) emit at 582 and 560 nm.

The group found that it was possible to significantly vary the nature of the emissive excited state, by incorporating σ-alkynyl ligands involving R-groups of higher conjugation. Complexes **15** and **23**, which incorporate an octatetraynyl or 1-ethynylpyrene ligand respectively, display highly structured, narrow-bandwidth emission spectra from solution at room temperature. The emissive excited state in these complexes is assigned to a $^3\pi$-π^* (alkynyl) state, that occurs at lower energy than the ^{3}MLCT state, as a consequence of the increased conjugation. Changing the structure of the "cyclometallating" group also caused a change in the origin of the emissive state. The thienyl and furyl-containing complexes **30-32** and **33-35**, show red-shifted, more structured emission compared to the related phenyl-containing complexes (**3, 4** and **7**). Based on the experimental findings, it was concluded that emission of the complexes **30-35** emanates from ^{3}IL excited states.

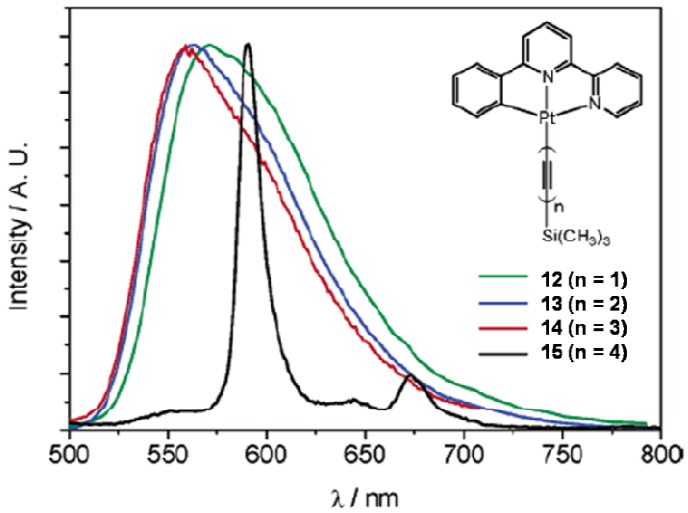

Figure 11: Emission spectra of complexes **12-15** in DCM at 298 K (λ_{ex} = 350 nm). Note the highly structured emission of the more conjugated complex, complex **15**.[61]

Sun et al. have prepared a series of highly luminescent N^N^C complexes, and have found that introduction of an alkoxyl substituent on the phenyl ring leads to an increase in solubility.[62] All complexes (see Figure 12) were luminescent in CH_3CN at room temperature, and complexes **37-39** have quantum yields of 0.15-0.21, which are relatively high for N^N^C complexes. All of the alkoxyl complexes prepared were found to emit around 580 nm, regardless of the ancillary ligand. The electron donating effect of the alkoxyl group was found to introduce a significant ILCT contribution to the low lying ^{3}MLCT and ^{3}LLCT states. As consequence of this, the alkoxyl complexes had longer luminescent lifetimes than alkoxyl-free analogues (460 – 570 ns vs. 40-100 ns respectively), and the emission maxima were less sensitive to solvent polarity.

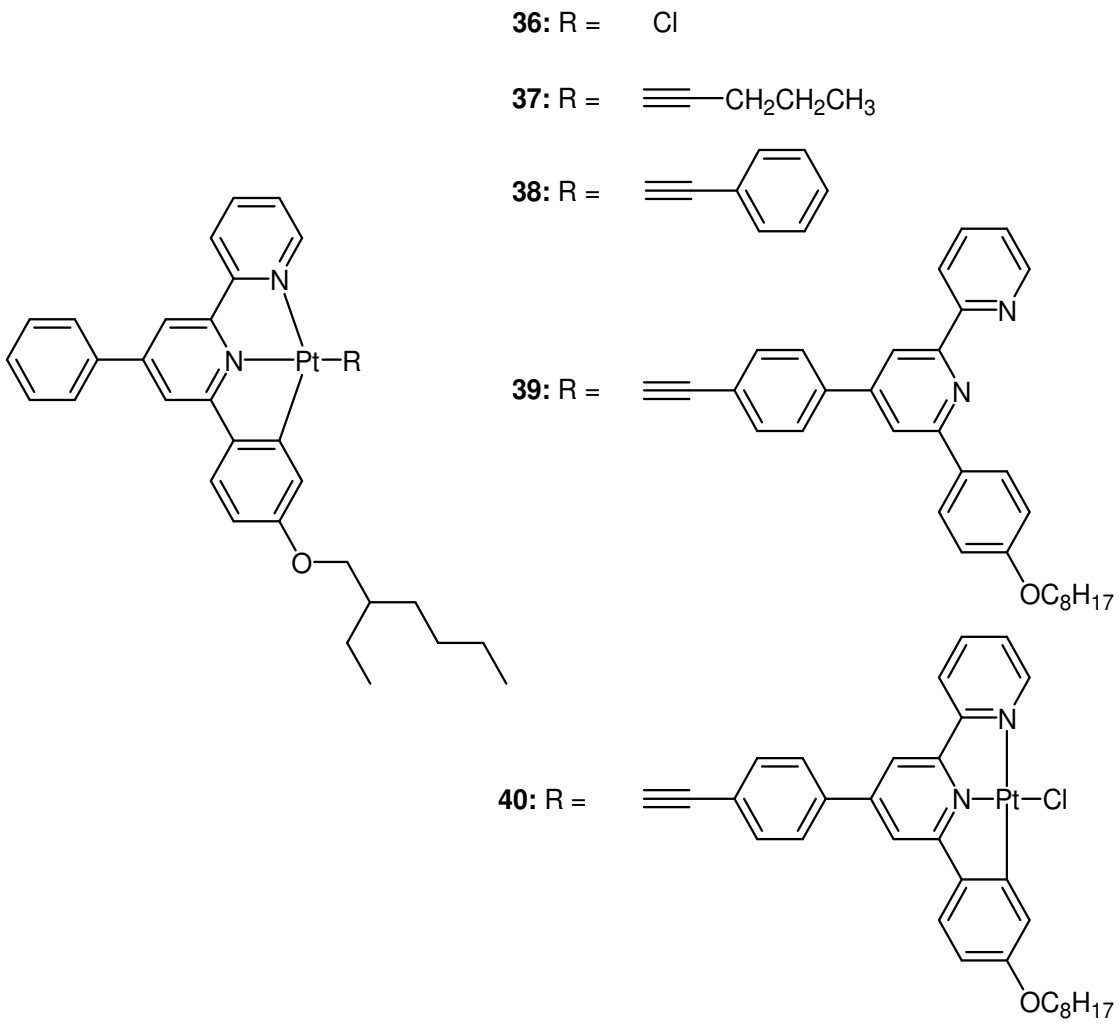

Figure 12: Structures of the alkoxyl complexes, **36 - 40**, prepared by Sun et al. in reference 62.

N^N^C systems where the terminal N-moiety is pyrazole have been prepared (Figure 13), and show blue-shifted emission relative to the 6-phenyl-2,2'-bipyridine platinum complexes. For example, complex **41** emits from DCM solution at 516 nm, whereas [Pt(phbpy)Cl] emits at 565 nm.[63] Pyrazine is a weaker π-acceptor than pyridine, so it is expected that such systems will have higher energy π* states (LUMOs), leading to greater HOMO-LUMO energy gaps. The pyrazine N^N^C complexes were found to exhibit acid/base sensitivity via the 1-pyrazolyl N-H. In the presence of base, complex **41** deprotonates, loses the ancillary chloride ion, and forms a bimetallic complex (**42**). Deprotonation of complex **43** does not result in formation of the bimetallic complex, but the photophysical properties are sensitive to pH. In this case, deprotonation of complex **43** with Et_3N led to an increase in the emission intensity, and the effect could be reversed with the addition of trifluoroacetic acid.

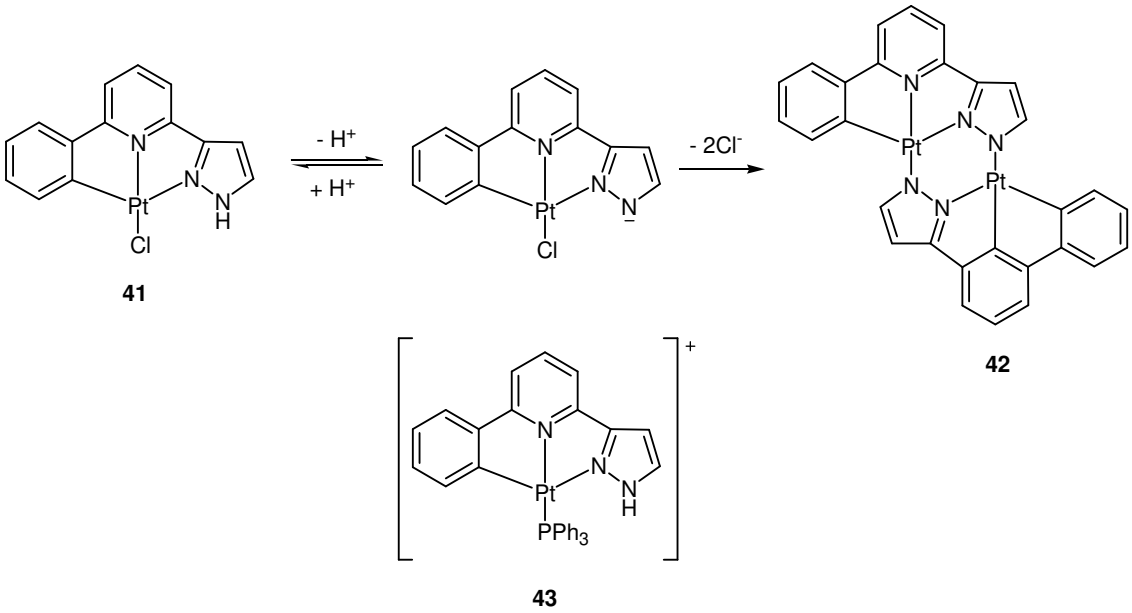

Figure 13: Top – the acid promoted conversion of complex **41** to the bimetallic complex, complex **42**, and bottom – structure of complex **43**.[62]

To sum things up, N^N^C complexes typically exhibit broad, featureless emission that emanates from a primarily ^{3}MLCT state. The extent of mixing of this state with other charge transfer states depends on the structure and properties of the ligands associated, and in some cases, the nature of the lowest excited state can even be altered. Most of the complexes are emissive in solution at room temperature, and the photophysical properties largely depend on the associated ligands. The best N^N^C complexes exhibit quantum yields of around 0.25, similar to the best N^C bidentate systems, so there is still plenty of room for improvement.[64]

1.6.2 N^C^N Systems

Of the three cyclometallated terdentate possibilities, N^C^N Pt(II) complexes typically exhibit the best room-temperature luminescence properties. 1,3-Di(2-pyridyl)benzene (dpyb) is a very good ligand for Pt(II) – the symmetrical arrangement of the cyclometallating phenyl ring and two pyridyl groups confers a large ligand field splitting within such systems. Complexes involving these ligands typically exhibit high quantum yields. For example, the unsubstituted [Pt(dpyb)Cl] complex is highly emissive in DCM solution at room temperature, with a quantum yield of 0.60, which is an order of magnitude greater than the quantum yield of its regioisomer, [Pt(phbpy)Cl]) (φ = 0.025).[19] In further contrast to analogous N^N^C systems, the emission spectra of

N^C^N complexes are usually highly structured (Figure 14), and the lifetimes are typically longer (several microseconds). The highest energy peak (v' = 0) generally has the greatest intensity – this indicates that there is little difference in geometry between the excited state and ground state, and is testament to the rigidity enforced by the terdentate system. Based on experimental observations (structured emission profile, small Stokes shift, weak solvatochromism, etc.) and theoretical results, the emission of such complexes has been assigned to occur from primarily $^3\pi$-π^* states, with significant ^{3}MLCT admixture.[45,65,66]

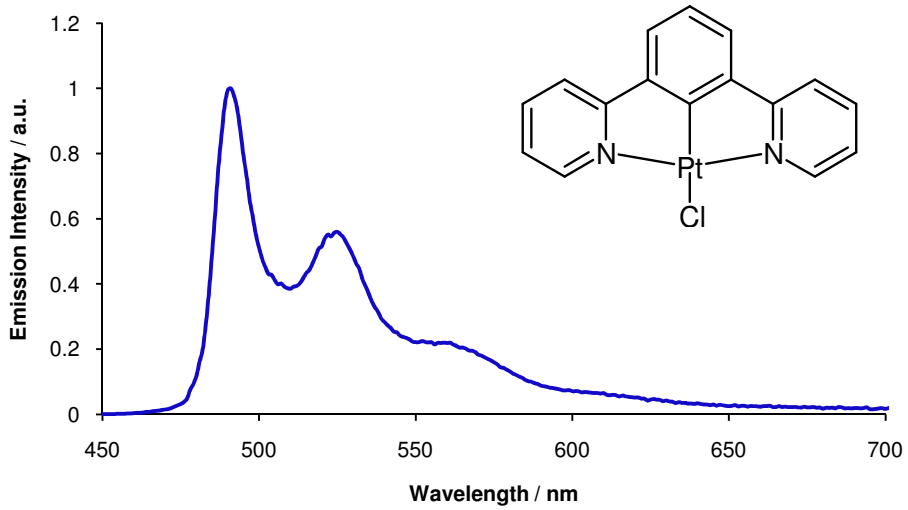

Figure 14: Emission spectrum of a dilute sample of [Pt(dpyb)Cl] in DCM at 298 K (λ_{ex} = 401 nm).

Williams et al. found that it is possible to tune the emission of [Pt(N^C^N)Cl] complexes by varying substituents at the 4-phenyl position (Figure 15).[67] The emission maxima varied (between 491 – 588 nm) with the electron donating ability of the substituent: electron donating groups red-shifted the emission, whereas electron withdrawing substituents led to a blue-shift (Note: complex **50** had slightly different excited state behaviour, but this will not be discussed here). All of the investigated complexes were highly luminescent (φ = 0.45 – 0.68, degassed DCM) and displayed lifetimes in the microsecond regime (7.9 – 20.5 µs).

a)

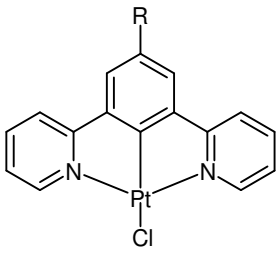

Complex =	44	[Pt(dpyb)Cl]	45	46	47	48	49	51
R =	–CO_2Me,	–H,	–Mesityl,	–2-pyridyl,	–4-tolyl,	–4-biphenyl,	–2-thienyl,	–4-amino

Increasing Energy of emission

b)

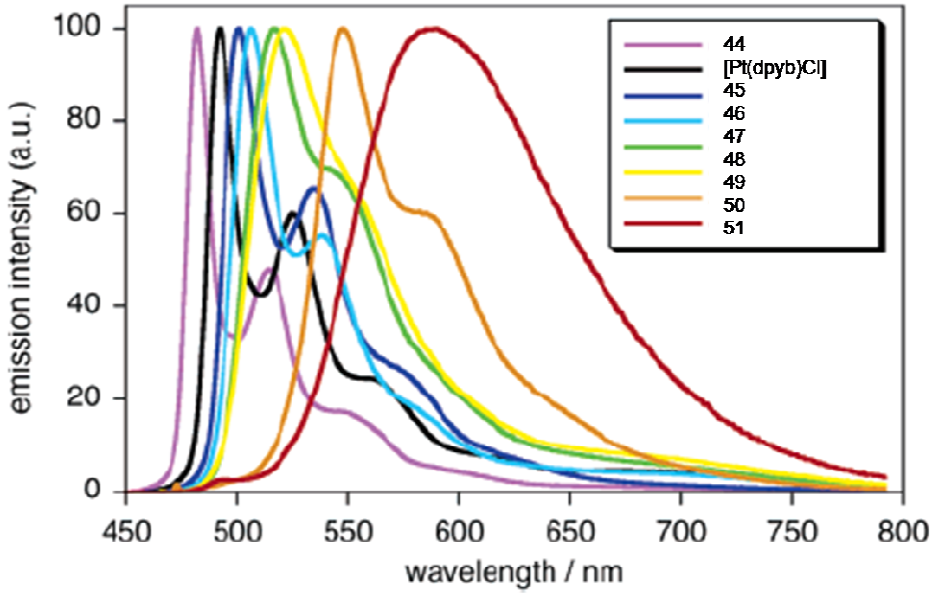

Figure 15: a) the structures of [Pt(N^C^N)Cl] prepared by Williams et al. and b) their emission spectra, recorded in DCM at 298 K (λ_{ex} = 400 nm). [67] From this, it is clear to see that emission energy can be tuned by varying the 4-phenyl substituent.

These results are consistent with DFT calculations, which predict that the phenyl ring makes a significant contribution to the HOMO energy.[45,66] DFT studies on the parent complex, [Pt(dpyb)Cl], indicate that the important HOMO-based orbitals are largely localised along the central axis of the molecule (involving the phenyl ring, the metal and the ancillary chloride), and the LUMO-based orbitals are largely localised on the side pyridyl rings. There is an increasing trend for researchers to look to theory to help rationalise experimental results, and predict structures of related molecules with desired characteristics.[45,65,68,69,70] For example, a theoretical study has been undertaken to determine why Pt(II) complexes of 1,3-di(2-pyridyl)benzene (N^C^N) exhibit superior luminescent properties to 6-phenyl-2,2'-bipyridine (N^N^C) and terpyridine (N^N^N) complexes, and to determine the effect of the presence and position of the aryl group in

such terdentate systems.[65] The ground and excited state geometries were calculated for each complex, and from a comparison of bond lengths, the trans influence of the platinum coordinating groups was assigned: aryl group > pyridyl group > chloride. The results indicated that the different coordinating geometries lead to different geometry relaxations. Of the cyclometallating systems, the N^C^N system was found to experience the smallest geometry change between the ground and excited states (least change in coordination bond lengths between the ground and excited state, and smallest bond-length alteration within the aromatic rings), and exhibited the largest spatial overlap between the transition orbitals. This is consistent with the experimentally observed trend, in which [Pt(N^C^N)Cl] systems exhibit the largest emission efficiency.

A kinetic study was performed by van Eldik et al. to determine the relative reactivity of the three systems towards substitution reactions of the fourth monodentate ligand.[71] The N^C^N system was found to display significantly higher reactivity than N^N^C – this is because the leaving group is trans to the cyclometallating carbon in the NCN system, and the trans influence is greater than the cis influence. The NCN was only slightly more reactive than the NNN system – the high reactivity of the NCN system stems from the trans-labilising effect of the C-Pt bond, whereas the high reactivity of the N^N^N system is due to the increased electrophilicity of the Pt centre, owing to the three π-accepting pyridine substituents of the terdentate frame.

The photophysical properties can be modified by replacing the pyridine rings with other heterocycles, such as quinolines,[72,28] pyrazoles[73] or azaindoles.[74] The bis-pyrazolyl analogue of [Pt(4-Me dpyb)Cl] (Figure 16) has been prepared (complex **51**), and shows emission that is significantly blue-shifted (λ_{em} = 455 nm, degassed DCM) relative to all previously reported bis-pyridyl systems (c.f. for [Pt(4-Me dpyb)Cl], λ_{max} = 505 nm).[73] The pyrazole unit is a poorer π-acceptor than pyridine, and as a consequence, the LUMO of such complexes lies at higher energy. Unfortunately, the quantum yield of **51** is significantly lower than the values typical of bispyridyl systems (φ = 0.02)

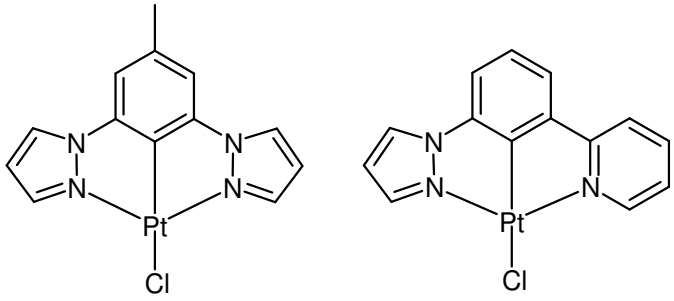

51 **52**

Figure 16: Structures of complex **51**, the bis-pyrazolyl analogue of [Pt(4-Me dpyb)Cl], and complex **52**, one of the unsymmetrical systems containing both a pyridyl and pyrazolyl heterocycle, reported in reference 73.

Asymmetric systems, involving both a pyrazine and pyridine ring (e.g. complex **52**) were also reported. These systems had higher quantum yields (φ = 0.32-0.64), and emitted around 500 nm, similar to the dpyb complexes. DFT studies indicated that the LUMO-based orbitals of the unsymmetrical complexes were localised on the pyridyl ring, which is more stable than the electron rich pyrazole.

Wada et al. have described a unique synthetic route to a different type of N^C^N system (see Figure 17).[75] The route involves oxidative cyclisation of 3,5-bis(anilinothiocarbonyl)toluene. The precursor ligand can itself bind to Pt(II) in a terdentate fashion, acting as an S^C^S pincer ligand.

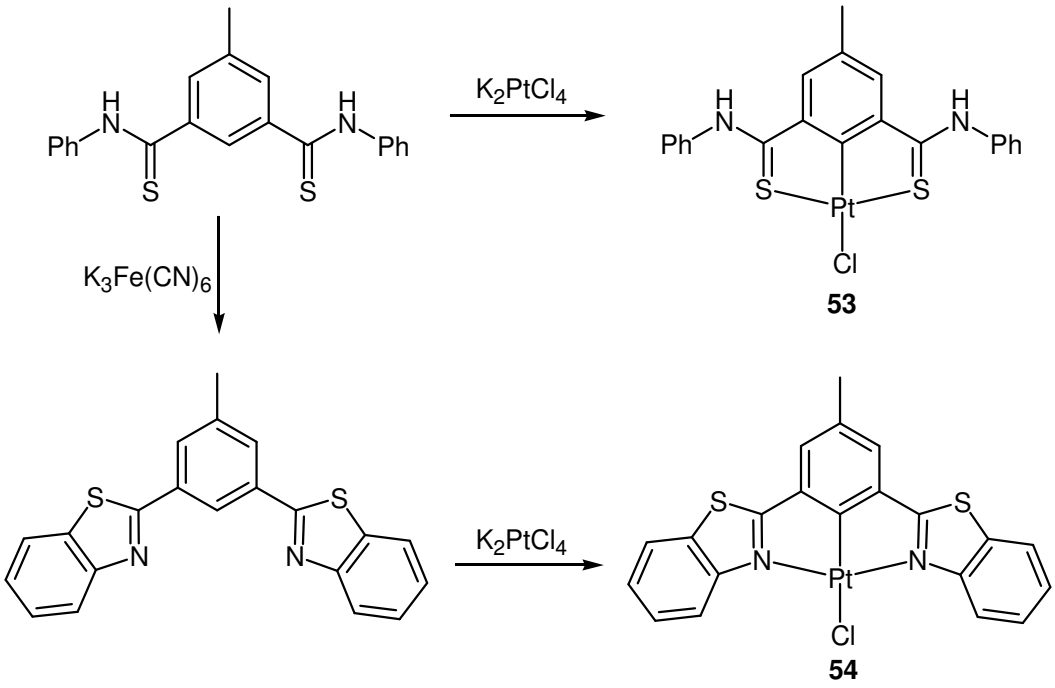

53

54

Figure 17: Synthetic scheme used by Wada et al.[75] to prepare complexes **53** and **54**.

Both complexes exhibit phosphorescence, but to varying degrees. The S^C^S complex, complex **53** exhibited no luminescence in solution at room temperature, but emitted from a frozen glassy state at 77 K and from the solid phase. A broad structureless band was observed in the emission spectrum of the frozen glass ($\lambda_{max} \approx 630$ nm), and a lifetime of 3.7 μs was recorded. Based on a similarity of the photophysical properties of this complex with previous tertiary thioamide-based pincer Pt(II) complexes, the emission was assigned to a ^{3}MLCT state. On the contrary, the emission of the N^C^N complex, complex **54** was assigned to a $^3\pi$-π^* state. The emission spectrum was highly structured ($\lambda_{max} = 530$ nm), and the lifetime was approximately three times greater than for **53** ($\tau = 9.4$ μs), indicating a smaller metal contribution to the excited state. This complex also emitted at room temperature, the spectrum being very similar to the 77 K spectrum.

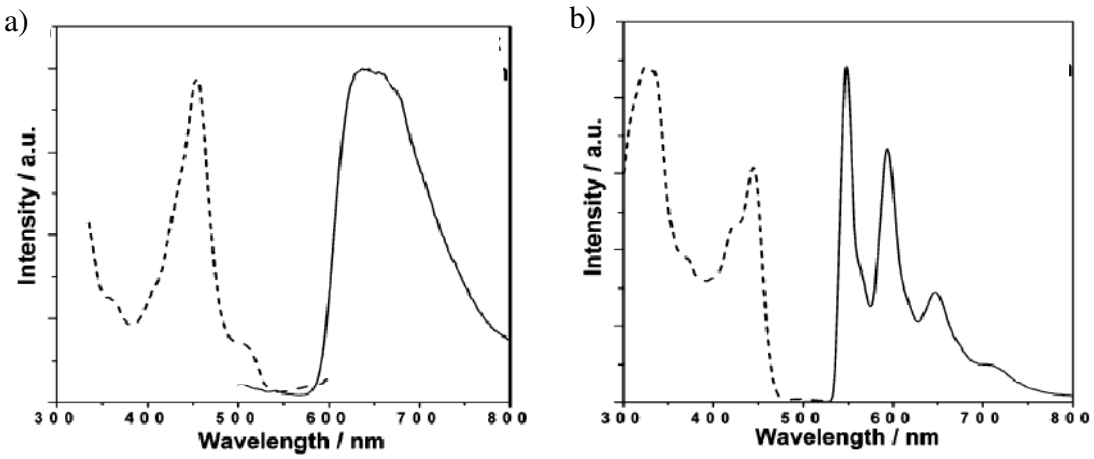

Figure 18: Excitation (- - -) and emission (——) spectra of a) **53** and b) **54**, in a frozen matrix of DCM/THF (3:2) at 77 K.[75]

1.6.3 C^N^C Systems

C^N^C complexes of platinum(II), incorporating 1,3-diphenylpyridine (dppy) as the terdentate ligand, were first reported by Von Zelewsky et al. back in 1991.[76] The group prepared a selection [Pt(dppy)L] complexes for which the identity of ancillary ligand, L, was varied (L = Et_2S, pyridine or pyrazine). The "cis" analogue of these complexes, [Pt(H-dppy)$_2$] (which involved two diphenylpyridine ligands bound bidentately), was prepared for structural and photophysical comparison (Figure 19). Crystal structures revealed that the C-Pt bonds are longer in the terdentately-bound trans complexes than

in the analogous cis complex (i.e. the bis-bidentate species), as a consequence of the mutually opposing trans influence in the former.

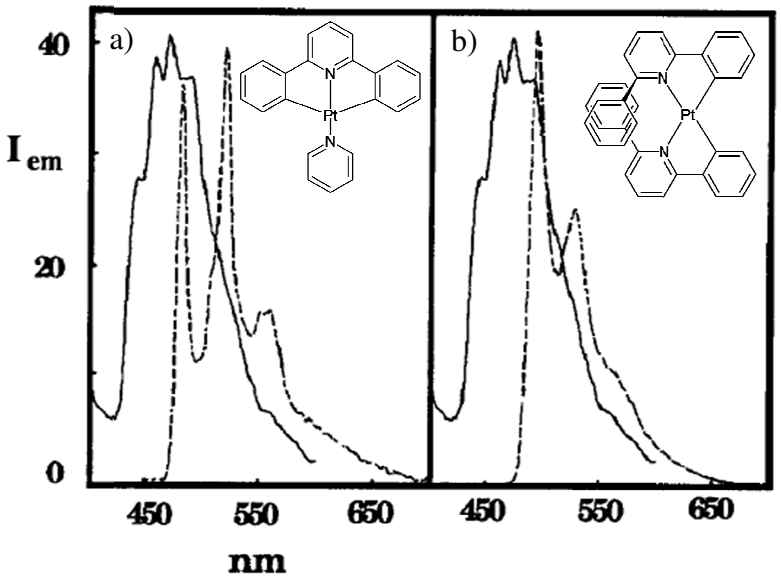

Figure 19: Emission spectra in MeOH/EtOH at 77 K of (——) the dppy free ligand and of (- - -): a) [Pt(dppy)py] and b) [Pt(H-dppy)$_2$].[76]

The complexes were either non-emissive at room temperature, or only weakly so, but all showed emission at 77 K. At 77 K, the luminescent lifetimes of the trans complexes were approximately double that of the cis complex (~20 μs and 11 μs, respectively). Secondly, the emission energies of the trans complexes were less red-shifted relative to the free ligand than the cis complex (Figure 19). Both observations confirm a smaller contribution of the metal to the excited states, and an increase in LC character in the terdentate systems compared to the bidentate analogue.

Since these initial studies, a large selection of Pt (C^N^C) complexes have been synthesised.[77,78,79,80] Most of this work has been pioneered by Che and colleagues. Unfortunately, however, most C^N^C complexes prepared to-date are non-emissive at room temperature, regardless of the ancillary ligand. In an attempt to understand why the C^N^C complexes are such poor emitters compared to N^C^N and N^N^C systems, despite the former possessing a stronger field ligand, Che et al. have performed a recent theoretical analysis.[68] The results indicate that C^N^C complexes undergo significant structural distortion upon going from the S_0 ground state to the T_1 excited state. This leads to a reduced S_0-T_1 energy gap, and a decreased d-d* splitting (smaller than for N^C^N and N^N^C), resulting in a larger k_{nr}. Also, the calculations indicate that the T_1 state in C^N^C systems contains a small admixture of the d-d* character (~ 3%),

providing a further non-radiative decay channel. On top of this, the closest singlet state with which the T_1 state can undergo significant SOC is the S_5 state, which lies at much higher energy (~ 13,500 cm^{-1}). This large energy gap imparts a small SOC effect, which results in a small k_r. It is thus the combination of a small k_r and large k_{nr} that results in these complexes being non-luminescent at room temperature.

In summary, most C^N^C complexes prepared to-date are non-emissive at room temperature, regardless of the ancillary ligand or substituents present on the terdentate framework. One may have expected that the luminescence properties would be greatly enhanced by having two cyclometallating sites held rigidly in a terdentate ligand. However, forcing the cyclometallating carbons trans to each other seems to disfavour luminescence. This effect is further emphasised by the strong tendency of bis N^C complexes to form the cis complex, where the cyclometallating carbon is always trans to the nitrogen donor of the other bidentate ligand.[81,82]

1.7 Multi-Molecular Interactions/Species

Figure 20 represents some of the possible fates of an excited species. The triplet excited state of phosphorescent organometallic species is typically quenched by triplet oxygen, which is why solution-based photochemistry is often performed on deaerated samples. In many cases, excited Pt(II) species can form inner sphere interactions with a ground state molecule, X, either forming an exciplex (excited electron donor-acceptor complex) when the ground state molecule is a different chemical species from the excited species (i.e. $X \neq M$) or an excimer (excited dimer) when the ground state molecule is of the same chemical species (i.e. $X = M$). Both are dissociative in the ground state. Formation of these excited multimolecular species results in depletion of M*, essentially quenching monomeric emission.[33,83,84] However, sometimes decay of these binuclear species is also accompanied by the emission of light.[37,40,48,67,77,85]

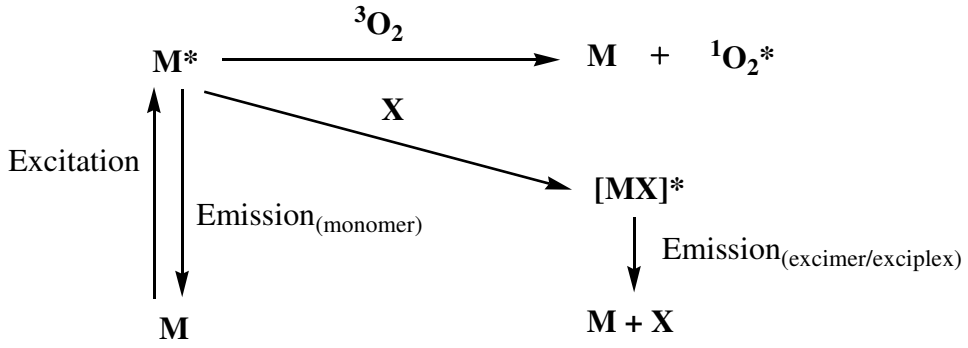

Figure 20: Possible fates of a triplet excited state.

Hence, intermolecular interactions can have a big impact on the photophysics of Pt(II) complexes[30,86,87] Under certain conditions, Pt(II) complexes may also participate in intermolecular interactions in the ground state, resulting in aggregate formation. An aggregate may also have different photophysics from the isolated molecule.

Pt(II) multimolecular species typically involve metal-metal (involving the vacant d_{z2} orbitals) and/or π-π interactions (when planar aromatic ligands are present).[16,88,89,90] Such interactions have been identified in the solid state of many Pt(II) complexes, and emission from the solid state is often perturbed relative to the emission from solution[18,91] In some cases, these intermolecular interactions lead to well ordered packing and the formation of extended structures, such as 1D chains[92] and 2D sheets[93,94] in the crystal structure. Introduction of larger, bulky groups to the ligand framework can reduce (or in some cases remove) the tendency to form such intermolecular interactions.[17,50,95,96] Similarly, for charged complexes, the nature of the counter ion can influence the formation of intermolecular interactions.[30,97]

We will now examine the distinct photophysical properties of aggregates and excimers. As mentioned, these multimolecular species can be emissive, although this is not always the case. For example, terdentate N^N^C systems undergo self-quenching, with self-quenching constants, k_{sq}, of the order of 10^9 M^{-1} s^{-1}, yet excimer emission is never observed.[61] Related N^C^N complexes also undergo self-quenching to a similar extent, but often display excimeric emission from solutions of higher concentration.[19,67] Emission due to an aggregate or excimer always occurs at lower energy than the monomeric emission, and the emission is typically broad and structureless. However, excimers and aggregates are distinctly different species, and their lower energy emissions arise for different reasons.

1.7.1 Aggregates

Aggregates are multi-molecular species that form in the ground state, and aggregation can occur in solution or in the solid phase.[30] Many square planar Pt(II) complexes have been observed to form aggregates under certain circumstances,[15,98,99,100,101,102] for example, altering the concentration, temperature and solvent polarity can influence the extent of aggregate formation. These aggregates often display different photophysical behaviour to the isolated molecules, with the absorption (and emission, for luminescent aggregates) of the aggregate typically occurring at lower energy. It is believed that such multimolecular species involve non-covalent Pt-Pt and/or π-π intermolecular interactions – such interactions are commonly noticed in the crystal structures of Pt(II) complexes. These favourable intermolecular interactions can influence the molecular packing, and the Pt(II) molecules often stack and form one-dimensional chains.[18,92,100,103]

Rundle and Miller used MO theory to account for the tendency of square planar Pt(II) complexes to form aggregates.[15,104,105] The stabilisation is attributable (in part) to overlap of $5d_{z2}$ and $6p_z$ orbitals of adjacent metal centres.[100] Figure 21 considers how these orbitals interact upon formation of a dimer (the simplest form of an aggregate).[15] The two $5d_{z2}$ atomic orbitals split to give a new antibonding and bonding molecular orbitals, and these orbitals have a_{2u} and a_{1g} symmetries respectively. The $6p_z$ orbitals also split into an antibonding and bonding molecular orbital, with a_{2u} and a_{1g} symmetries respectively. Each complex had two electrons in their d_{z2} orbital, so four electrons are to be accommodated in the new MOs. The electrons fill the two lowest energy MOs, one of which is a bonding MO, and the other is an antibonding MO. Such an electron configuration would normally result in no net bonding. However, configuration interaction with the $6p_z$ bonding and antibonding MOs (non-degenerate MOs of the same symmetry repel each other) results in stabilisation of the $5d_{z2}$ bonding and antibonding MOs, decreasing the total energy of the system, and leading to net favourable interactions.

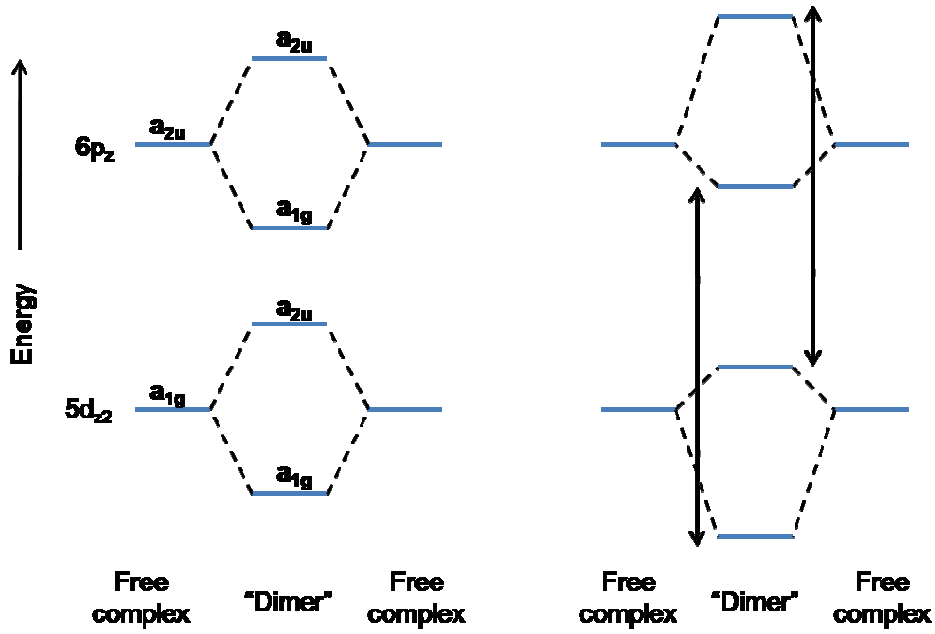

Figure 21: MO scheme for a "dimer" consisting of two planar complexes a) without and b) with configuration interaction (redrawn from reference 15). It is important to appreciate that the number of MOs is determined by the number of molecules that are interacting. When many molecules are involved in the aggregate, MO's with the same atomic orbital parentage will become very close in energy, effectively forming an energy continuum (or energy band).

The MO description presented above only considers orbitals localised on the Pt centre. The ligands will also introduce orbitals to the total MO description (e.g. π/π*), and the relative energies of all orbitals will depend on the identity of the complex. In the literature, the low energy transition that occurs in aggregates is often described as a metal-metal-to-ligand charge transfer state (MMLCT, dσ*-π*),[17,106] however, d-π* or π-π* states may equally account for such effects (see Figure 22).

Furthermore, the bonding interaction reduces the HOMO-LUMO energy gap, accounting for the red-shifted absorption and emission of aggregates relative to the isolated molecules. The extent of this red-shift depends on the strength of intermolecular interaction between molecules – it is possible to tune the low-energy emission by varying the steric bulk of surrounding ligands, or by varying the electronic nature of the ligands.[17,30,95,96,97]

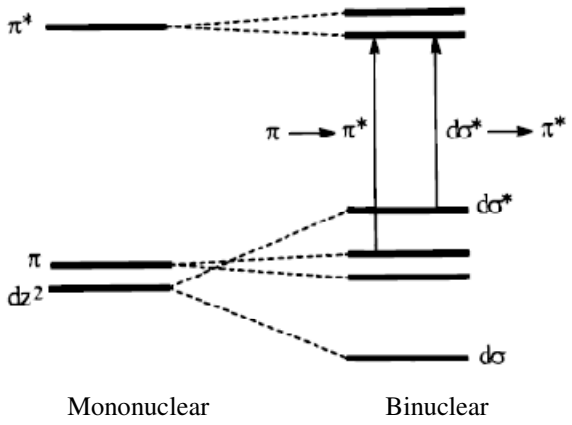

Figure 22: Schematic MO diagram illustrating d^8-d^8 and π-π interactions in binuclear Pt(II) polypyridine complexes (note: dσ*-π* can also be represented as MMLCT). This figure was taken from reference 107.

1.7.2 Excimers

An excimer forms when a molecule in the excited state interacts with a ground state molecule of the same chemical species.[108] Unlike aggregates, excimers exist only in the excited state.

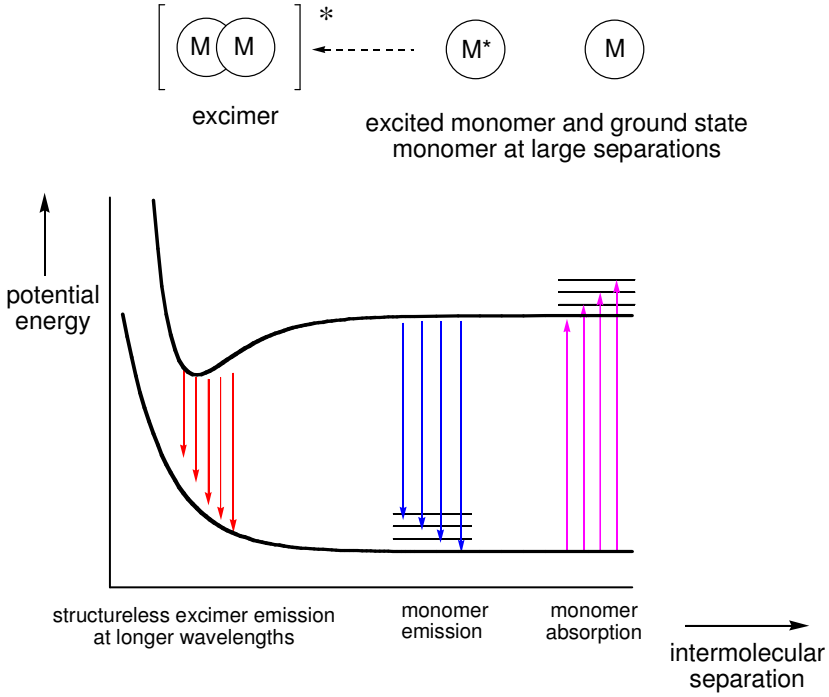

Figure 23: Potential energy surface interpretation of excimer emission (also applies to exciplex emission, where M and M* are different chemical species).

Formation of excimers is a diffusion controlled process, so the extent of excimer formation is greater in solutions of higher concentration.[83] But why do excited

molecules have such a tendency to form excimers? The answers come from a consideration of MO theory.[109] Upon excitation, one electron becomes promoted, creating an electrophilic half-filled HOMO and nucleophilic half-filled LUMO. Hence, the molecule in an electronically excited state possesses both a stronger electron affinity and lower ionization potential than a molecule in the ground state. These orbitals can participate in charge transfer interactions with other polar or polarisable species (such as a ground state molecule in excimer formation, or a completely different molecule in exciplex formation). Such charge transfer interactions result in a net stabilisation of the excited state (Figure 24).

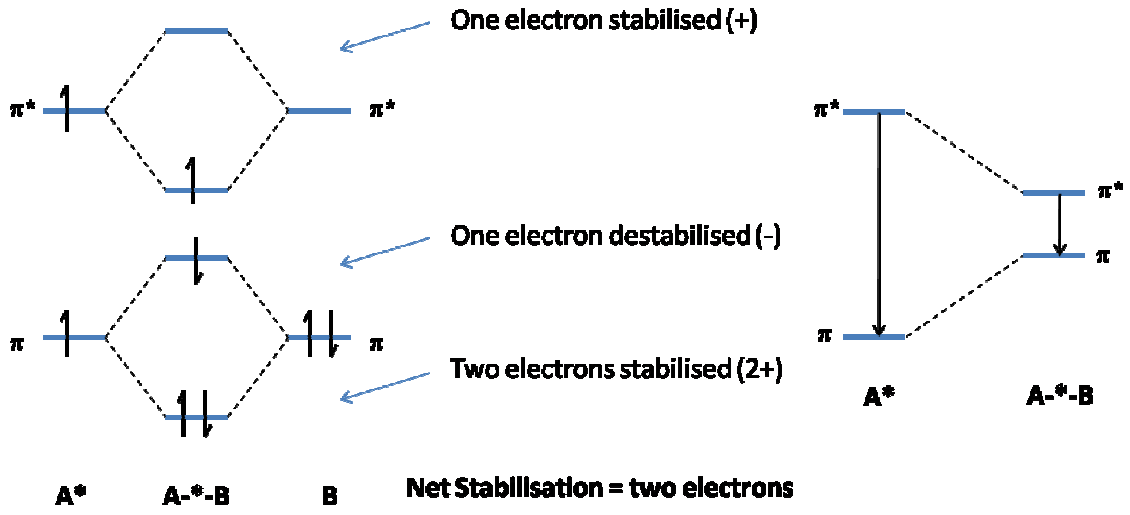

Figure 24: Orbital interactions of excimers (A = B) and exciplexes (A ≠ B) – redrawn from reference 109.

The interaction between a molecule in the excited state and a molecule in the ground state can be considered as a donor-acceptor (or acceptor-donor) interaction. As for aggregates, the interaction can involve Pt-Pt interactions between the vacant d_{z2} orbitals and/or π-π interactions when aromatic ligands are present. Upon return to the ground state, the dimeric species is unstable relative to isolated molecules, so it instantaneously dissociates. Again MO theory provides the answers – intermolecular interaction between two ground state molecules has no net stabilisation, as an equal number of electrons occupy bonding and antibonding orbitals (Figure 25). As antibonding effects are slightly greater than bonding, the interaction is unfavourable, accounting for the immediate dissociation upon emission. This dissociative ground state accounts for the broadness of the emission band (note: we previously described that aggregates are stable in the ground state. It is therefore anticipated that the relative orientation of, and/or

interactions between adjacent molecules in an excimer differ to those in an aggregate, and the factors that led to stabilisation of the aggregate must not apply here).[110]

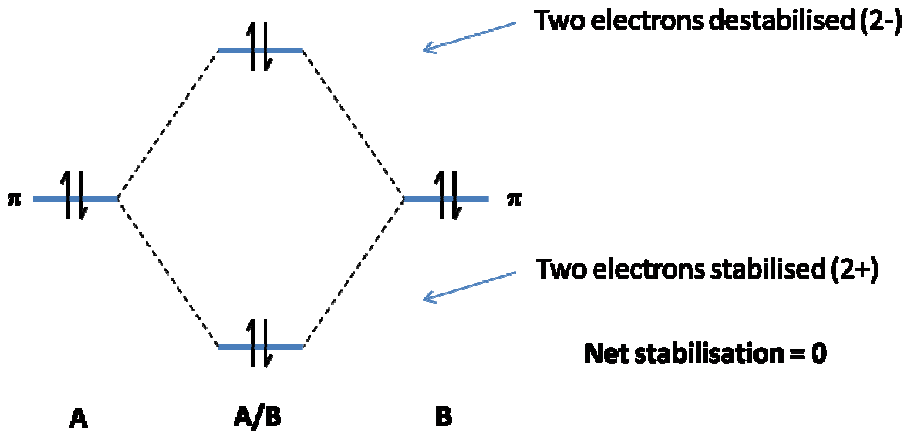

Figure 25: Orbital interactions of an A/B collision pair – redrawn from reference 109.

It is often possible to distinguish between excimers and aggregates by monitoring absorption. Because aggregates exist in the ground state, low energy bands due to such species are often observed in both the absorption and emission spectrum. As excimers only exist in the excited state, their occurrence will only affect the emission spectrum.[111] Comparing an excitation spectrum recorded at the monomer emission maximum with one recorded at the emission maximum of the low energy band can also be used to determine the origin of the multimolecular species.[112] If the multimolecular species is excimeric, then the excitation spectra will be identical, as the excimer originates from the same ground state species as the excited monomer. The excitation spectra should differ if an aggregate is present, as in this case, the high and low energy bands observed in the emission spectrum arise from different ground state species.

1.7.3 Examples of Pt Complexes Possessing Intermolecular Interactions

The [Pt(N^C^N)] systems involving 1,3-dipyridylbenzene ligands typically exhibit self-quenching by excimer formation in solutions at elevated concentration.[19,67] The excimers are usually emissive, and appear in the emission spectrum around 690 – 700 nm as a broad, structureless band (e.g. see Figure 26). This observation contrasts with the N^N^C systems – here, self-quenching is observed at elevated concentration, but the emission profile does not change, suggesting that the excimers are non-emissive.

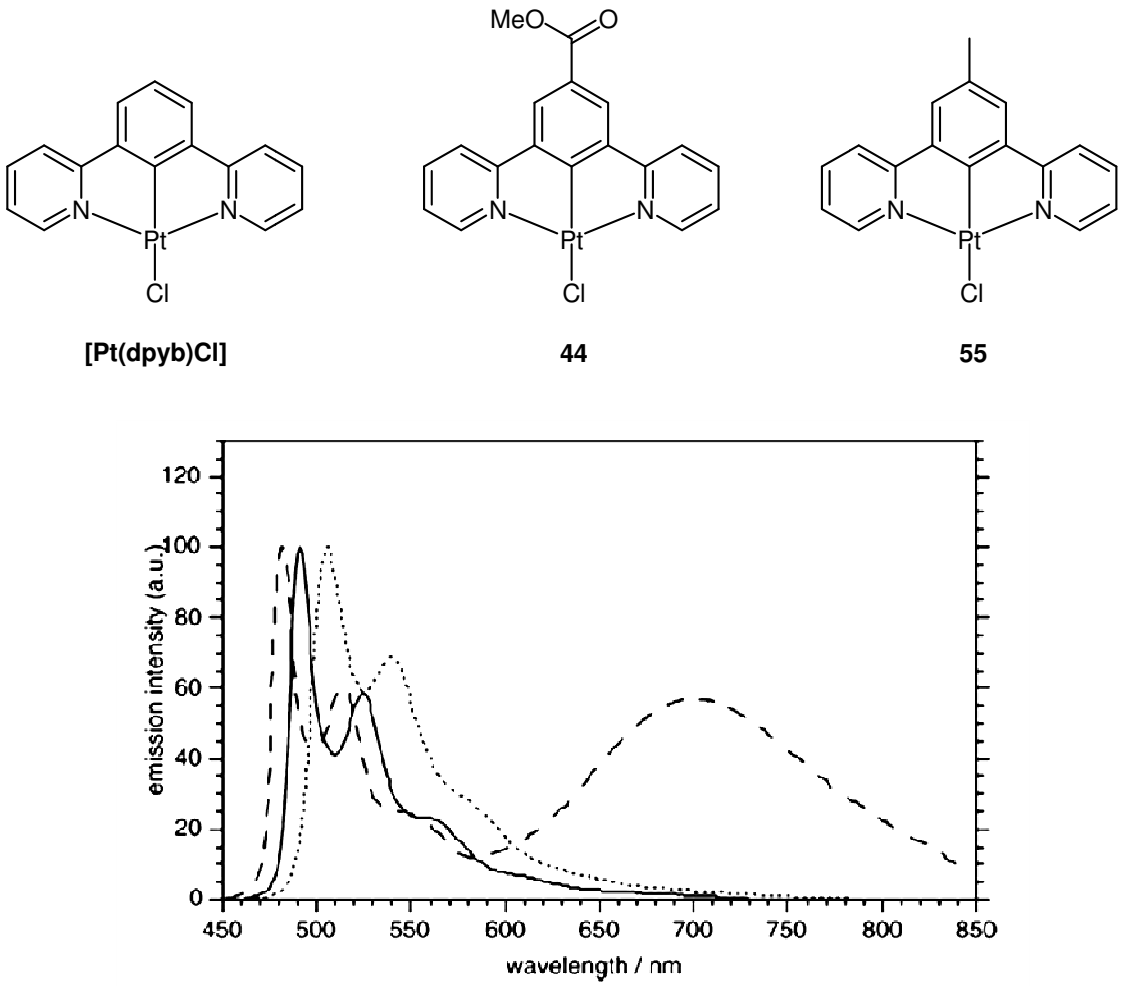

Figure 26: Top: The structure of the unsubstituted parent complex, [Pt(dpyb)Cl] an ester derivative (**44**) and a 4-methyl derivative (**55**), and Bottom: The emission spectra of these complexes from DCM solution at 298 K: (——) and (·····) represent the emission of dilute samples (2.5 x 10^{-6} M) of [Pt(dpyb)Cl] and **55**, respectively (λ_{ex} = 401 nm and 412 nm respectively), whereas (- - -) represents the emission of a concentrated sample of **44** (1.0 x 10^{-4} M).[19] The broad band around 700 nm in the spectrum of complex **44** is due to excimeric emission.

The unsymmetrical N^C^N complex, complex **52**, which contains one pyrazole and one pyridyl heterocycle, displays excimeric emission from solutions of higher concentration (Figure 27).[73] The excimeric emission of this complex is significantly blue-shifted relative to the excimeric emission of [Pt(dppy)Cl] (645 nm vs. 695 nm). In contrast, the monomeric emission of these two complexes occurs at similar energy (as discussed in Section 1.6.2). The presence of the more electron rich pyrazole in **52** destabilises the donor-acceptor interaction within the excimer, accounting for the observed blue-shift. **51**, the bis-pyrazolyl analogue of [Pt(dpyb)Cl], does not exhibit excimeric emission. Here, the presence of two pyrazolyl groups presumably destabilises the donor-acceptor interaction so much that the excimer does not form.

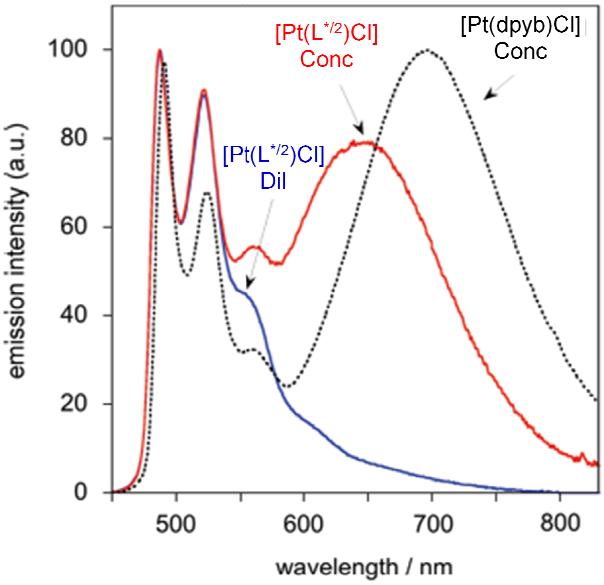

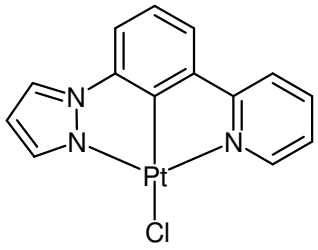

52

Figure 27: Influence of concentration on the emission spectrum of **52**. All spectra were recorded in degassed DCM at 298 K. The blue curve represents emission from a dilute (10^{-5} M) solution of **52** and the red curve represents emission from a concentrated solution (3 x 10^{-4} M). As the concentration is increased, the grow-in of an excimer band is observed around 650 nm. This band is blue-shifted relative to the excimer of [Pt(dpyb)Cl] (black).[73]

In many cases, the solid-state emission of Pt complexes has been found to occur at lower energy than the solution-based emission.[58,113] This phenomenon has been related to the occurrence of intermolecular interactions in the solid state. In an attempt to model these interactions, various groups have prepared multinuclear Pt complexes, in which two Pt units are connected via a bridging unit.[98,107,114,115,116,117] Che et al. found that such Pt N^N^C complexes involving a short bridging unit, bis(diphenylphosphino)methane, μ-dppm, exhibited lower energy emission in solution than their mononuclear analogues.[107] For example, the emission of complexes **56** and **57** (Figure 28) occurred at 562 and 654 nm respectively, from a degassed acetonitrile solution, and at 602 and 665 nm respectively from a microcrystalline solid phase, all recorded at ambient temperature. Short *intramolecular* Pt-Pt contacts were identified in the crystal structure of **57** and it was anticipated that these interactions would be maintained in solution. However, increasing the length of the bridging unit resulted in complexes which displayed similar emission to the mononuclear versions, indicating that the two Pt units were acting as discrete Pt(L) fragments.

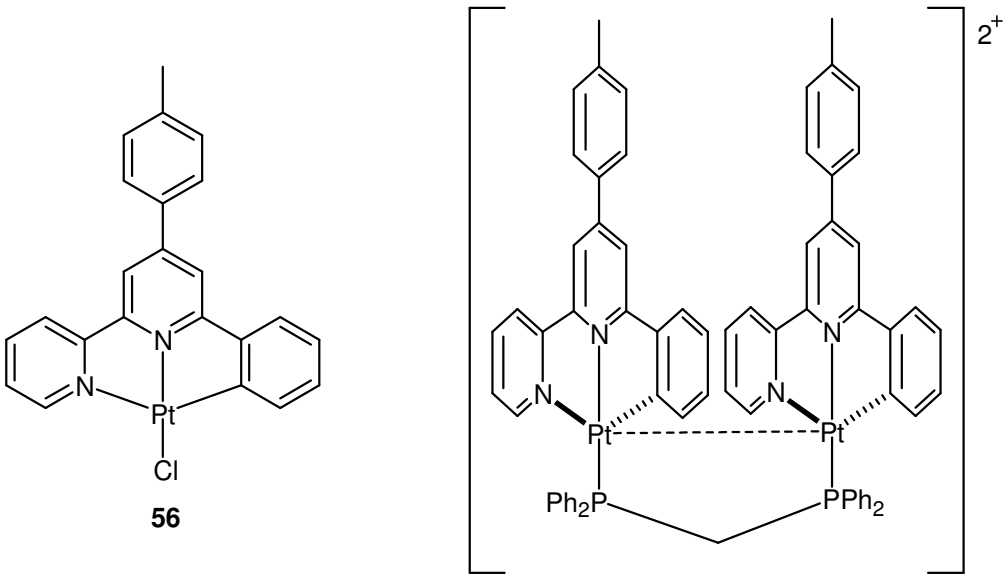

Figure 28: The structure of complex **56**, and its bimetallic analogue, complex **57**.[107]

A nice example of monomeric vs. excimeric emission has recently been demonstrated by Bruce et al.[118] Here, [Pt(N^C^N)X] systems which incorporate long alkyl chain groups on the 5-pyridyl position of the N^C^N backbone have demonstrated the ability to form a liquid crystalline state. Structural analysis revealed that the liquid crystalline phase was composed of a columnar phase of anti-parallel complexes which are independent of one another, and contain no intermolecular interactions. Contrary to this, the sample prepared by fast cooling from the isotropic phase consists of a high degree of isotropic grain boundaries, and the molecules are in close contact. As a result, emission from the liquid crystalline state was found to be purely monomeric, whereas emission from this second phase was purely excimeric.

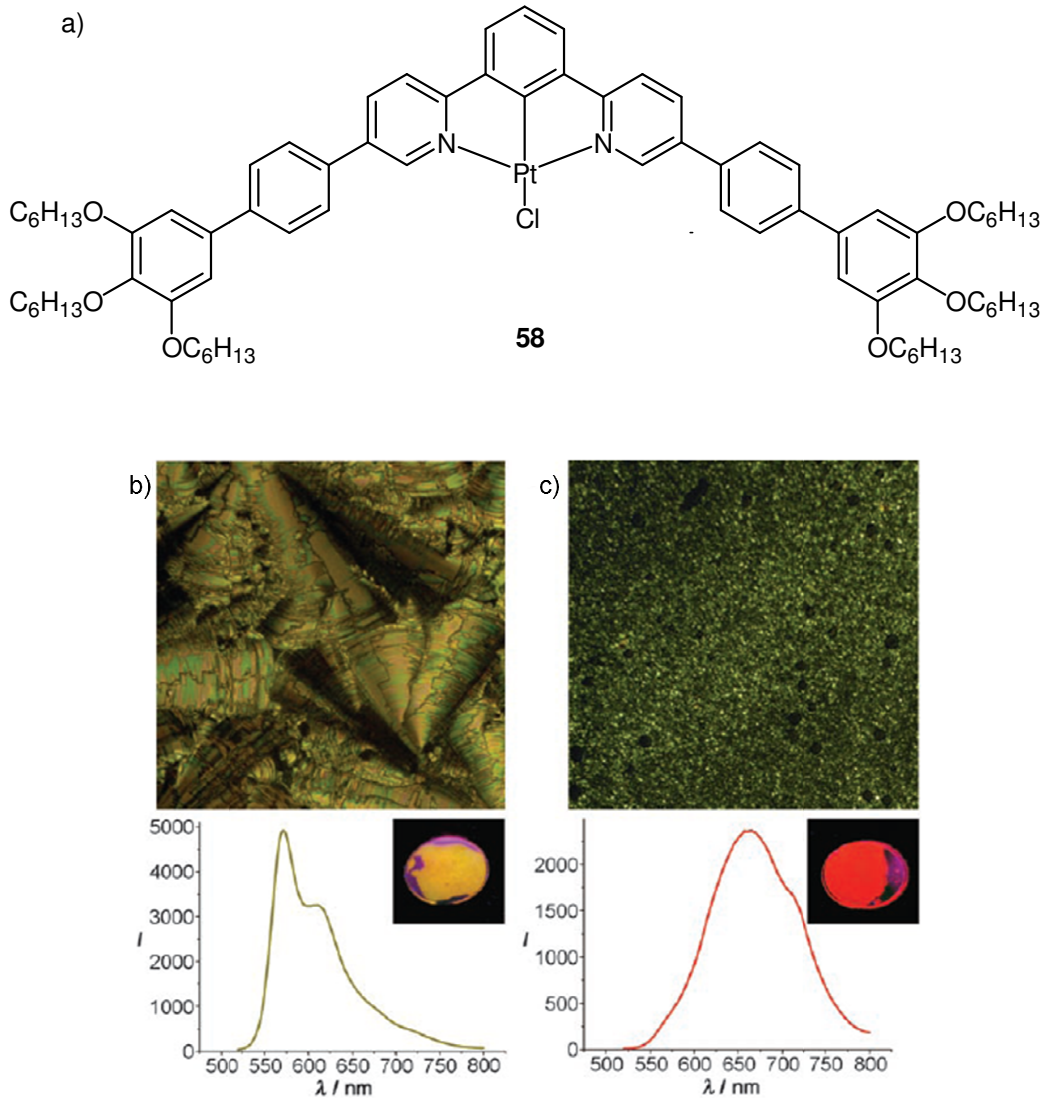

Figure 29: a) Structure of one of the complexes containing a N^C^N ligand appended with long alkyl chains, prepared by Bruce et al. , b) Photomicrograph (top) and emission spectrum (bottom, λ_{ex} = 420 nm) of a sample of **58** that has been fast cooled from the liquid crystal phase, and c) Photomicrograph (top) and emission spectrum (bottom, λ_{ex} = 420 nm) of a sample of **58** that has been fast cooled direct from the isotropic phase. Insets show photographs of real samples of pure films sandwiched between glass slides.[118]

1.8 Applications of Luminescent Platinum Complexes

1.8.1 Sensors

There is a high demand for species that are able to sense and react to their environment in a non-invasive way.[119] The open geometry of platinum(II) complexes can allow the formation of inner sphere interactions with other molecules (e.g. solvents), leading to sensory behaviour.[120] For some Pt(II) complexes, inter/intramolecular interactions are

sensitive to temperature, resulting in thermochromism,[121,122] or are sensitive to certain vapours, leading to vapochromism[54,86,123,124] In some cases, luminescent complexes have been appended with a binding group, where binding of the appropriate analyte alters the photophysical behaviour relative to the unbound complex.[125,126,127,128,129] Additionally, the triplet excited state of luminescent platinum complexes is usually sensitive to the presence of oxygen, and some complexes have been used in oxygen sensors.

1.8.1.1 Oxygen Sensors

The emission intensity of many phosphorescent complexes varies inversely with oxygen concentration. The potential of such complexes as oxygen sensors has been realised, and attempts have been made to produce organometallic complexes with optimum properties for this purpose.[130,131,132] $[Ru(bpy)_3]^{2+}$ has been used in previous oxygen sensors, but the charged species tend to have poor solubility in organic solvents. W. W. S. Lee et al. report on the use of neutral dicyanoplatinum(II) complexes, $[Pt(L)(CN)_2]$ (where L = 4,7-diphenyl-1,10-phenanthroline or 4,4'-di-tert-butyl-2,2'bipyridine) as optical sensors for measuring oxygen concentration.[130] These neutral complexes have greater solubility than $[Ru(bpy)_3]^{2+}$, and can be used to study microenvironments inside polymers. They are also less susceptible to interferents.

A colorimetric luminescent oxygen sensor involving two luminophores with both different oxygen sensitivities and different emission colours has been developed by Evans et al.[132] The first luminophore is a platinum octaethylporphyrin (PtOEP, complex **59**) (see Figure 30), which emits red light – this complex has a long phosphorescent lifetime, and in solution its emission was found to be very efficiently quenched by oxygen. The second luminophore, complex **60**, is a N^C^N Pt(II) complex of 1,3,5-tri-(2-pyridyl)benzene, and has a lower sensitivity to oxygen and emits in the green region of the visible spectrum. At low oxygen concentration, emission from the porphyrin dominates due to its larger molar extinction coefficient at the chosen excitation wavelength, and the overall emission appears red. As oxygen concentration increases, emission from the porphyrin becomes increasingly quenched, and eventually emission from **60** dominates. Physically, the oxygen sensor exhibits a "traffic light" response from red to green, as the oxygen concentration increases.

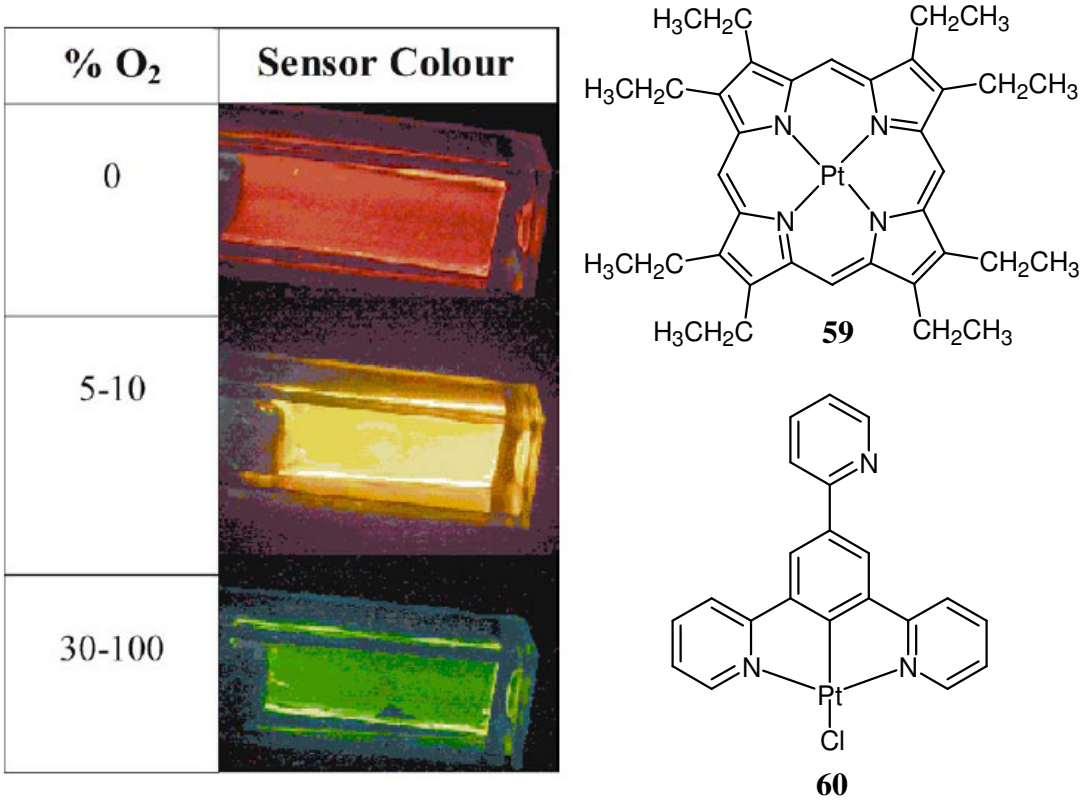

Figure 30: The colourimetric response of the oxygen sensor prepared by Evans et al., to different partial pressures of oxygen, and the two luminescent components used to prepare the device.[132]

1.8.1.2 Sensor Based On Oxidation

Some luminescent bis-cyclometallated Pt(II) complexes have been found to be highly reactive towards oxidative addition reactions.[46,133,134] In some cases, the Pt (IV) products are also luminescent, with a different emission energy (blue-shifted) compared to the parent complex (Figure 31). Swager et al. have exploited this property to design sensors for cyanogen halides, which are toxic agents that are commonly used in chemical weapons.[134] In the presence of a cyanogen halide, spontaneous oxidative addition occurs, resulting in a blue-shift in emission. Detailed structure-property investigations revealed that complexes that were twisted from the ideal square planar geometry, due to unfavourable sterics, reacted faster with CNBr than complexes with less distorted geometries. Additionally, these twisted Pt(II) complexes were generally non-luminescent in solution at room temperature, so oxidative addition resulted in a "switch-on" of emission.

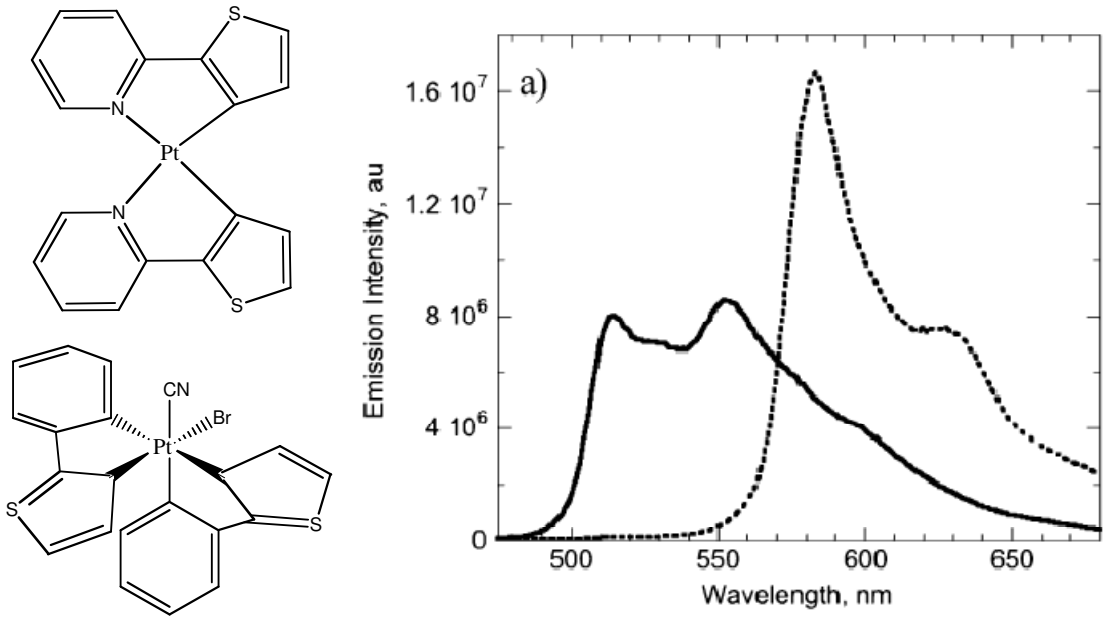

Figure 31: One of the bis-cyclometallated Pt(II) complexes synthesised (top left), its oxidative addition product with CNBr (bottom left), and its emission spectra (right) taken before (dotted line) and after (solid line) exposure to CNBr for 15 s, demonstrating the complex's capacity as a sensor for such molecules. Such oxidative addition reactions have been found to be stereospecific.[134]

1.8.1.3 Analyte Sensors

The sensor applicability of luminescent platinum(II) complexes covalently bound to analyte-binding groups has been investigated by several groups.[35,125,135,136] Binding of the analyte can alter the electronic or steric environment of the platinum complex, affecting its luminescence properties. Tung et al. have reported such a sensor, which incorporates a square planar Pt(II) centre with an N^N^C cyclometallating ligand and an ancillary acetylide ligand that is connected to an azacrown, which is capable of chelating to Mg^{2+} ions.[136] When no Mg^{2+} ions are present, the complex is non-emissive – a low energy LLCT excited state results in non-radiative decay back to the ground state. Binding to Mg^{2+} decreases the electron-donating ability of the acetylide ligand, which causes the LLCT excited state to shift to higher energy than an emissive MLCT state (Figure 32).

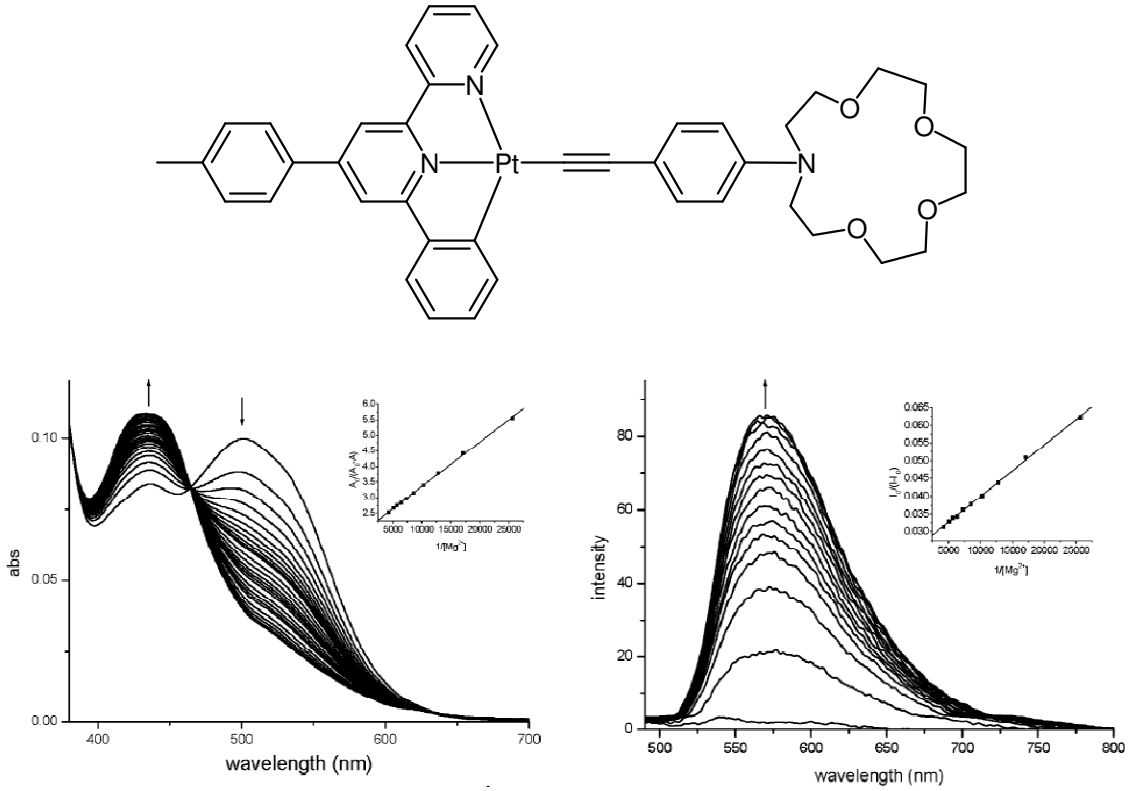

Figure 32: Top: structure of the cation sensor complex and Bottom: charts representing the effect of increasing concentrations of Mg^{2+} ions on the absorbance (left, inset = plot of $A_0/(A_0-A)$ vs. $[Mg^{2+}]^{-1}$) and b) the emission (right, inset = plot of $I_0/(I-I_0)$ vs. $[Mg^{2+}]^{-1}$) spectra. The emission spectra were obtained upon excitation at 465 nm.[136]

A similar example involving a N^N^C Pt(II) complex has been reported by Guerchais et al.[126] This complex involves a different azacrown, and is selective for Pb^{2+} cations. Binding of Pb^{2+} again affects both the absorption and emission spectra, but this time the emission intensity was found to decrease with increasing analyte concentration.

1.8.2 Organic Light Emitting Diodes (OLEDs)

OLEDs are light emitting devices that have a luminescent 'organic' molecule in an emissive layer.[137,138] Electricity is supplied to the device, and light is emitted at ambient temperature (electroluminescence).

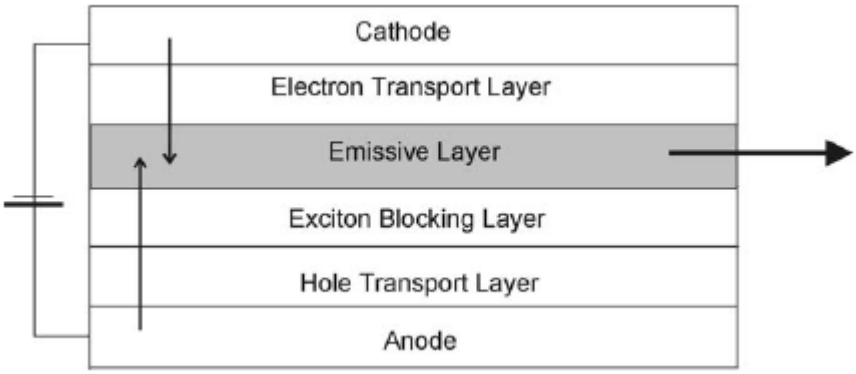

Figure 33: Schematic representation of a typical OLED structure.[137]

Standard OLEDs contain multiple layers, each of which performs a single function, that additively result in the electroluminescence (Figure 33). These multilayered devices typically consist of a series of organic layers sandwiched between two electrodes. Indium tin oxide is generally used as the anode, as this material is transparent and allows light generated to escape from the device. A low-work function metal, such as aluminium or magnesium, is generally incorporated as the cathode. The organic layers typically consist of a hole transporting layer, an electron transporting layer and the electroluminescent (emissive) layer. More sophisticated devices also contain an exciton blocking layer between the hole transporting and emissive layers, which confines charge recombination to the emissive layer, improving the maximum efficiency of the device.

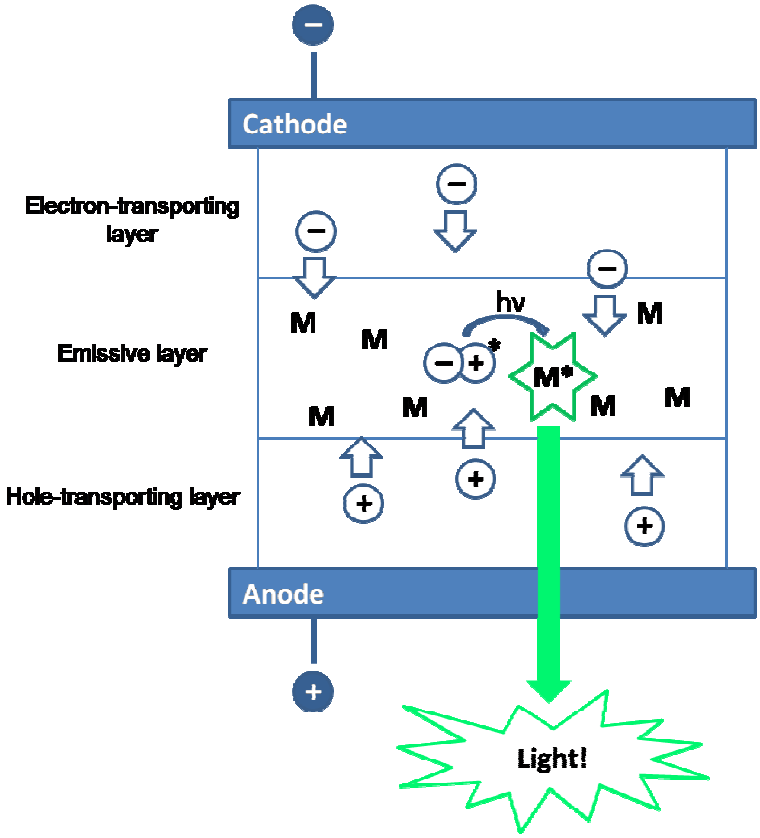

Figure 34: Basic working diagram of an OLED containing a luminescent dopant.

Figure 34 represents the working principles of an OLED. When an external voltage is applied across the device, holes get injected from the anode and electrons get injected from the cathode. The net charge separation across the device causes the electrons and holes to migrate towards the opposite electrode. If an electron and a hole end up in the same place, they will combine to form an exciton (a bound excited state consisting of the electron and the hole, with overall charge neutrality). Charge recombination occurs in the emissive layer, and the energy of the exciton is transferred to the luminescent dopant. The dopant becomes excited, and on the decay back to the ground state emits light over the known and desired wavelength range.

Organometallic species are taking over from typical organic fluorophores as luminescent dopants, due to the additional 'triplet harvesting' ability offered.[23,137] This refers to the fact that in a device, excitons are formed in particular spin-states. Spin statistics predicts that charge recombination in the emissive layer will form excitons in a singlet-to-triplet ratio of 1:3. Some researchers believe that this ratio is not strict, and that in some cases singlet states may be formed in greater than 25% contribution.[139] However, there will always be excess of triplet states over singlet states. The excitons pass on their excitation energy into the corresponding excited states of the luminescent

dopant. If we consider a typical organic fluorophore, decay from a triplet excited state to a singlet ground state is strictly forbidden. Hence in an OLED, the triplet energy is wasted as non-radiative decay to the ground state, limiting the efficiency of the OLED. Such non-radiative transitions release heat, which is also detrimental to the device. As already explained, luminescent organometallic species that involve a heavy metal atom such as platinum, iridium, ruthenium etc. involve significant spin-orbit coupling, resulting in faster intersystem crossing and faster decays from the triplet state. In OLEDs, such complexes can use both singlet and triplet excitons to produce light, meaning the maximum possible efficiency of such devices is 100%.

OLEDs hold many advantages over liquid crystal display (LCD) systems, and so may begin to compete in the display technology market. Advantages include:

- Self luminescence – this avoids the need for backlighting, allowing them to be thinner, lighter and more efficient
- Lower power consumption – 20-80% less than typical LCDs, because light is only emitted from the desired pixels compared to the whole panel
- Robustness – OLEDs can be deposited onto a wide variety of substrates, including flexible ones – it may be possible to produce roll-up TV screens
- Wider viewing angle and aesthetic superiority

So far, OLEDs have found wide usage in mobile phone screens, stereo faces and digital cameras, and it is expected that usage in larger applications such as TVs, computer screens and even ambient lighting will become increasingly popular, as the technology develops.

1.8.2.1 Parameters Used to Measure OLED Performance

Many parameters are used to describe the performance of an OLED.[140] Such parameters include:

- Internal Electroluminescence quantum efficiency, η_{int} – this is defined as the ratio of photons emitted to the number of electrons injected. This value can be of a similar order of magnitude to the photoluminescence quantum yield of the

dopant (i.e. the ratio of the number of photons emitted to the number of photons absorbed. However, this value also depends upon the charge-recombination efficiency. For example, if the dopant is a bright emitter, but charge recombination in the emissive layer is poor, the value of η_{int} will be much lower than the dopant quantum yield.

- External electroluminescence quantum efficiency, η_{ext} – this relates the number of photons *observed* externally to the number of electrons injected. Its value is typically lower than η_{int}, as not all photons produced will leave the device as a consequence of refraction. The two values are therefore related by

  $\eta_{int} = 2n^2\eta_{ext}$

  where n is the refractive index of the medium.

- The power efficiency, η_{pow} – this represents the ratio of output light power to input electric power, and is measured in W W^{-1}. This value is related to η_{ext} via

  $\eta_{pow} = \eta_{ext} - (E_p/V)$

  where E_p is the average energy of the emitted photons and V is the voltage applied across the device.

- The luminous efficiency η_{lum} is measured in lm W^{-1}. It takes into account that the human eye is more sensitive to green light than red or blue, and is effectively a "correction" of the power efficiency to what we actually observe. η_{lum} is obtained by multiplying η_{pow} with the appropriate value from the eye sensitivity curve, $S(\lambda)$, as determined by the Comission Internationale de L'Eclairage (CIE).

  $\eta_{pow} = \eta_{pow}S(\lambda)$

- CIE coordinates – The Commission Internationale de L'Eclairage (CIE) system of colourimetry provides a numerical description of colour (in terms of x and y colour coordinates), which is based on the eye's sensitivity to light across the visible region.[132]

- Colour rendering index (CRI) – this indicates the ability of the light produced by a device to reproduce the colours of various objects faithfully, when compared

with a reference illuminant. The value is typically a percentage. A high CRI indicates a similar performance to the reference. A low CRI indicates that the light produced distorts the true colours of objects relative to the reference. This is an especially important parameter in white OLED design.

- The OLED brightness – defined as the amount of light emitted per unit area (cd m^{-2}).

1.8.2.2 OLEDs Involving Luminescent Pt Complexes

The first reported OLED containing a phosphorescent platinum complex was reported in 1998.[141] The OLEDs involved a platinum porphyrin species, complex **59** (see Figure 30 for structure), doped into an tris(8-hydroxyquinolinato)aluminium (Alq_3) host, and were found to emit in the red region (λ_{max} = 650 nm). Studies revealed that over 90% of the energy was transferred from Alq_3, confirming that both singlet and triplet excitons were being utilised. A device displaying optimal characteristics was obtained when a molar ratio of 6% of **59** was employed in the emissive layer. For example, the device registered an external quantum efficiency of 4%. The characteristics of this device exceeded those of other saturated red-emitting devices reported at the time by an order of magnitude, demonstrating the efficiency improvements made possible by the additional participation of triplet excitons. However, the extremely long lifetime (~ 90 μs) of **59** results in severe triplet-triplet annihilation at high current or higher dosing concentrations (*Eqn.* 1), affecting the quantum efficiency. Other Pt porphyrin systems have since been incorporated into OLEDs to give red and near-red emitting devices.[142,143,144] Unfortunately, the quantum efficiencies of all devices suffer with increasing current, due to the long phosphorescent lifetimes of such complexes.

$$4(^3M^* + {}^3M^*) \rightarrow {}^1M^* + 3\,{}^3M^* + 4M \qquad \textit{Eqn.}\ 1$$

Since the pioneering work with complex **59**, many other luminescent platinum complexes have been investigated as phosphorescent dopants.[102,145,146,147,148,149,150,151] Apparently, the characteristic current (J_0) at which the external quantum efficiency falls to 50% of its peak value due to T-T annihilation is inversely proportional to the square of the lifetime, so devices incorporating dopants with shorter phosphorescent lifetimes often display enhanced performances.[152] For example, some of the [Pt(dpyb)Cl]

complexes shown in Figure 15 have been incorporated into OLEDs,[153] These complexes have lifetimes of approximately 8 μs, almost an order of magnitude less than the porphyrin systems. The devices exhibited impressive external quantum efficiencies and luminous efficiencies, ranging between 4-16% ph/e and 15-40 cd A^{-1} respectively. The concentration and nature of the R-substituent was used to tune the colour of the device emission.

A selection of the [Pt(N^N^C)X] (where X = a 2-functionalised acetylide) complexes that were discussed in Section 1.6.1 have been incorporated into OLEDs.[154] The molecular structures are those reported in Figure 10. The strong σ-donor effect of the acetylide significantly destabilises the HOMO which is largely localised on the metal, and the devices incorporating these complexes emit in the orange-red region of the spectrum (560 – 630 nm). Of particular interest is the device incorporating complex **31** (at 4% dopant concentration) in a CBP host matrix (λ_{max} = 612 nm). This OLED gave results that were comparable with the best red-light emitting OLEDs (the device gave CIE coordinates of x = 0.594, y = 0.341, a maximum luminance of 3100 cd m^{-2} at 12 V, and a maximum efficiency of 30 mA cm^{-2}).

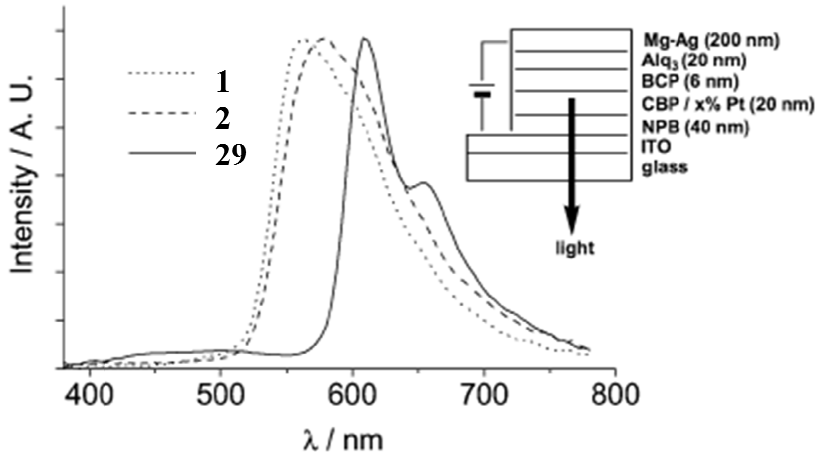

Figure 35: Normalised electroluminescence spectra of complexes **3**, **4** and **31**, at 4% doping level (inset: multi-layer configuration of the OLEDs). Image taken from reference 154.

The three additive primary colours are red, green and blue. Certain combinations of these three colours of light can be used to generate any other colour, so devices producing the primary colours are key to development of OLEDs in display technology. Whereas examples of green OLEDs are abundant, and red OLEDs are quite common, examples of blue OLEDs involving organometallic dopants are still quite rare.[155,156]

Good blue emitters are also relevant to the production of optimised white OLEDs, since white light requires coverage of the whole visible range.

1.8.2.3 White OLEDs

As well as being able to tune emission to give monochromatic emission with a desired wavelength, there is a strong desire to produce OLEDs with high efficiency white light output.[8,157,158,159] Such white organic light emitting diodes (WOLEDs) could be used for general lighting applications, and offer lower preparation costs and greater efficiencies than existing sources. Various different approaches to WOLED production exist:

- Preparing multilayer devices containing separate emitter layers, which include lumophores offering different colour emission (the lumophores collectively cover the visible spectrum, generating white emission)[160,161,162,163]

- Mixing red, green and blue emitters (in correct proportion) in a single layer[164,165,166]

- Use of a single dopant that emits from both monomer (blue) and excimer (red) states at the same time – the overall colour of light observed depends on the monomer: excimer emission ratio. The extent of excimer emission (relative to monomer emission) increases with concentration, hence the colour of a device can be controlled by simply varying the dopant concentration.

Some of the cyclometallated polypyridyl Pt(II) complexes form emissive excimers (see earlier sections), so the latter principle can be exploited to generate WOLEDs. However, examples of such WOLEDs are still quite scarce. This method has several advantages over the previous two traditional methods. For example, excimer:monomer based devices only require one emissive layer. Devices which involve several emissive layers containing different luminophores require more complicated device architectures and are more costly to produce. Secondly, devices which contain several different luminophores are prone to colour degradation over time, as certain components degrade faster than others.

Thompson et al. were the first to apply this strategy using phosphorescent emitters – structures of two of the first dopants examined for such behaviour are given in Figure

36 (note FPt1 is the same molecule as *4,6-dfppy* mentioned in Section 1.5).[167] Both complexes contain a (2-(4',6'-difluorophenyl)pyridinato-N, C^2) ligand, and exhibit monomeric emission in the blue region (~ 470 nm), and excimeric emission in the red region (~ 600 nm) of the visible spectrum. For devices incorporating FPt1, as dopant levels were increased, emission from the excimer rapidly appeared, and was found to dominate the spectrum at dopant levels of as low as 8%. White light emitting devices were prepared for dopant concentrations between 3 and 4%, but as emission from the host was not fully quenched at such low concentration, the device efficiencies were far from optimal. Doping concentrations of > 5% are typically required to efficiently quench host luminescence and achieve good carrier transport in phosphorescent OLEDs[168,169]

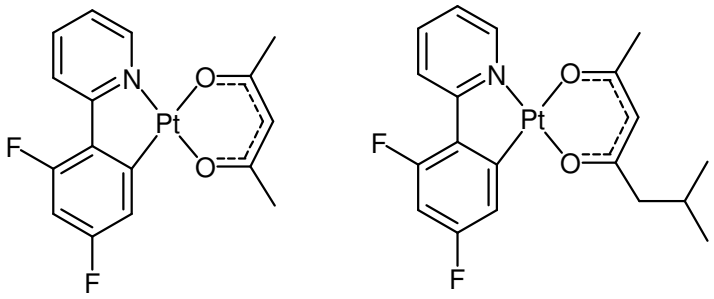

Figure 36: Two of the initial Pt complexes used as single dopants to prepare WOLEDs.

On the contrary, the additional isopentyl group on the O^O ligand of FPt2 confers an increase in steric bulk. As a consequence, FPt2 demonstrated a lower susceptibility to form excimers (smaller k_{sq}), and devices displaying balanced monomer/excimer emission could be prepared using dopant concentrations of 10-12% (Figure 37). These devices did not suffer significant contamination from residual host luminescence. Good white light characteristics were reported for an optimised device containing 10% dopant – the device displayed CIE coordinates of (x = 0.36, y = 0.44), which are similar to those of natural white light (x = 0.33, y = 0.33), and had a maximum quantum efficiency of 3.3 ± 0.3% (η_{lum} = 7.3 ± 0.7 lm W^{-1}) at 0.5 cd m^{-2}.[167,170,171]

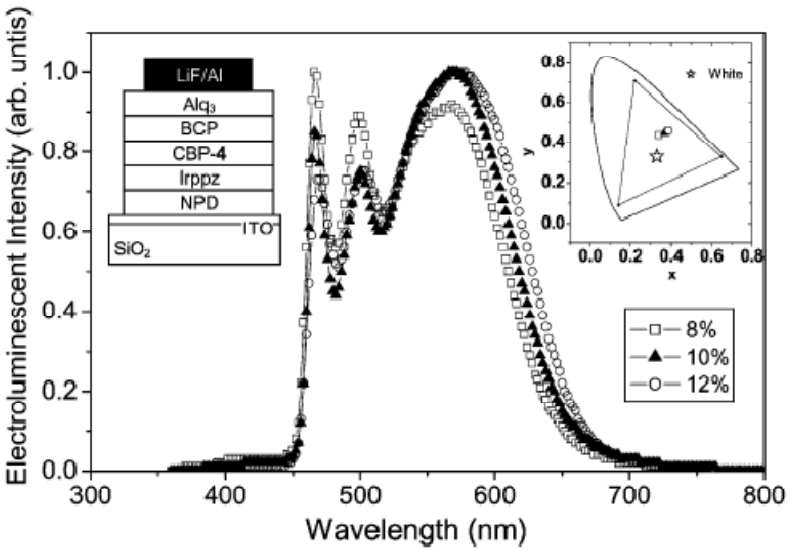

Figure 37: Electroluminescence spectra of devices containing FPt2 at 8, 10 and 12% dosage – notice the balanced monomeric/excimeric emission. Left inset: device structure, and right inset: Chromaticity diagram including the CIE coordinates of the devices and of pure white light.[170]

The highly luminescent [Pt(dpyb)Cl] complexes reported by Williams et al. (Figure 15) also display excimeric emission from solutions of increasing concentration, and some of these complexes have been examined as dopants for WOLEDs. For example, devices containing varying amounts of complex **44** have been reported,[153] and the emission of these devices spans the visible region of the spectrum (Figure 38). The device containing a dopant concentration of 15% gave emission that was closest to white light (CIE coordinates of x = 0.43, y = 0.43, note: CIE coordinates of an incandescent lamp ≈ x = 0.41, y = 0.41). This device displayed an impressive maximal efficiency of 15.5 ± 0.2% ph/e (14.2 ± 0.2 cd/A) at 10 cd/m^2.

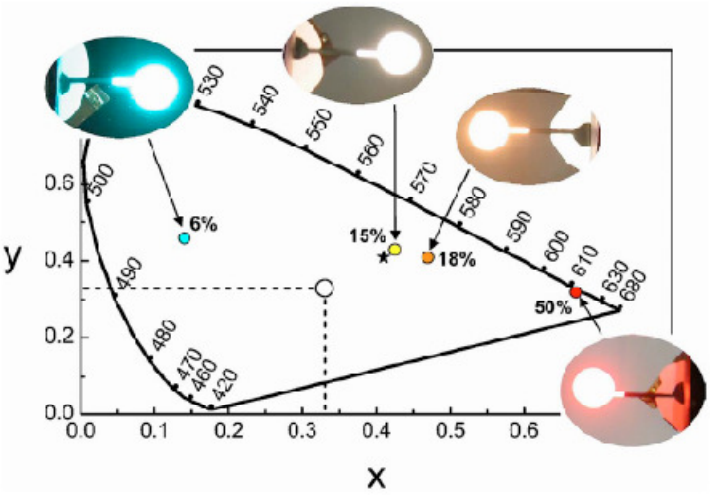

Figure 38: CIE Chromaticity diagram of OLEDs containing various dopant concentrations of complex **44** (image taken from reference 153).

The CRI of such WOLEDs did not exceed 75, due to the excessive distinctiveness of individual components in the structured emission spectrum. This stimulated the development of an OLED incorporating both a [Pt(N^C^N)Cl] complex, (platinum(methyl-3,5-di(2-pyridyl)benzoate) chloride, and 4,4',4''-tris(N-(3-methylphenyl)-N-phenylamino)triphenylamine (m-MTDATA) in the emissive layer.[172] m-MTDATA can act as an electron donor, and can form emissive exciplexes with the Pt species, that emit at an intermediate energy to the monomer and excimer emission bands. These OLEDs therefore have three emissive states contributing to the total emission: 1) monomeric emission, 2) excimeric 3) exciplex excited states. Greater coverage of the visible region was achieved, and an efficient WOLED displaying a remarkably high CRI value of 90 was obtained.

Alternatively, examples exist where the emission from the excimer is used exclusively. For example, M. Cocchi et al. have prepared OLED utilising the near-infra red emission from [Pt(N^C^N)Cl] excimers.[173] Whereas previous NIR devices suffered poor quantum efficiency and low power output, their devices were found to be highly efficient (>10% quantum efficiency). Such devices will have uses in biomedicine (for example, biological tissues only weakly absorb in the NIR region, allowing deeper penetration of the light source), and in the communication industry.[174,175]

1.8.3 Bio-Imaging

A relatively new application of luminescent platinum complexes involves their incorporation into living cells and tissue as luminescent probes. This will be discussed in greater detail at the start of Chapter 5.

1.9 Objectives

Pt(II) complexes involving 1,3-di(2-pyridyl)benzene terdentate ligands often posses many attractive photophysical properties, and are desirable as phosphorescent dopants in OLEDs. For example, such complexes tend to have much higher quantum yields than related N^N^C and C^N^C systems. One of the main aims of the work reported in this thesis was to develop 1,3-di(2-pyridyl)benzene-type Pt(II) complexes with tuneable photophysical properties, by functionalisation of the terdentate ligand and/or substitution of the ancillary chloride. In particular, complexes exhibiting blue emission have been targeted. A selection of groups has performed DFT calculations on the unsubstituted parent complex, 2,6-di(2-pyridyl)benzene Pt(II) chloride ([PtL^1Cl]).[45,65,66] The predicted orbital contour plots have been used as an initial guide to aid rational structure design.

Over the last few years, a small selection of groups has started to look at the applicability of luminescent organometallic complexes as bio-imaging agents.[11,12,13] For example, our group studied the behaviour of [PtL^1Cl] in cells – this complex enters the cell rapidly (within 5 min) and retains its emission.[11] Furthermore, the complex localises in a subcellular organelle (the nucleus), which can be visualised using fluorescence microscopy. Another key aim of the work reported in this thesis was to screen a large selection of luminescent cyclometallated Pt(II) and Ir (III) complexes for their behaviour as bio-markers, and to perform some preliminary studies into the elucidation of intracellular binding and uptake routes. Another aim was to study intracellular behaviour of complex using time resolved emission imaging (TREM) – these complexes have phosphorescent lifetimes of the order of a few microseconds, making them suitable candidates for such a technique.

1.10 References

1. J. P. Paris and W. W. Brandt, *J. Am. Chem. Soc.*, 1959, **81**, 5001

2. M. L. Muro, A. A. Rachford, X. Wang and F. N. Castellano, *Top. Organomet. Chem.*, 2010, **29**, 159-191

3. V. Balzani, "Topics in Current Chemistry; 280 Coordination Compounds. Photochemistry", 2007, Springer, Berlin

4. D. M. Roundhill, "Photochemistry and Photophysics of Metal Complexes", Plenum Press, New York, 1994

5. N. J. Turro, "Modern Molecular Photochemistry", The Benjamin/Cummings Publishing Co., Inc., California, 1978

6. A. Gilbert and J. Baggot, "Essentials of Molecular Photochemistry", Blackwell Scientific Publications, Oxford, 1991

7. P. Borrell, " Photochemistry: A Primer", Edward Arnold Ltd., London, 1973

8. E. Polikarpov and M. E. Thompson, *Mater. Matters*, 2007, **2(3)**, 21-23

9. J. A. G. Williams, *Chem. Soc. Rev.*, 2009, **38**, 1783-1801

10. A. Vlcek Jr., *Coord. Chem. Rev.*, 2000, **200-202**, 933-977

11. S. W. Botchway, M. Charnley, J. W. Haycock, A. W. Parker, D. L. Rochester, J. A. Weinstein and J. A. G. Williams, *PNAS*, 2008, **105 (42)**, 16071-16076

12. C-K. Koo, K-L. Wong, C. W-Y. Man, Y-W. Lam, L. K-Y. So, H-L. Tam, S-W. Tsao, K-W. Cheah, K-C. Lau, Y-Y. Yang, J-C. Chen and M. H-W. Lam, *Inorg. Chem.*, 2009, **48**, 872-878

13. V. Fernández-Moreira, F. L. Thorp-Greenwood and M. P. Coogan, *Chem. Commun.*, 2010, **46**, 186 - 202

14. A. Gilbert and J. Baggot, "Essentials of Molecular Photochemistry", 1991, Blackwell, Oxford

15. K. Krogmann, *Angew. Chem. Internat. Ed.*, 1969, **8**, 35 - 42

16. V. M. Miskowski and V. H. Houlding, *Inorg. Chem.*, 1989, **28**, 1529-1533

17. V. W. W. Yam, K. M. C. Wong and N. Zhu, *J. Am. Chem. Soc.*, 2002, **124**, 6506-6507

18. J. A. Bailey, M. G. Hill, R. E. Marsh, V. M. Miskowski, W. P. Schaefer and H. B. Gray, *Inorg. Chem.*, 1995, **34**, 4591-4599

19. J. A. G. Williams, A. Beeby, E. S. Davies, J. A. Weinstein and C. Wilson,

Inorg. Chem., 2003, **42**, 8609-8611

20. S. W. Lai, M. C. W. Chan, Y. Wang, H. W. Lam, S. M. Peng and C. M. Che, *J. Organometallic Chem.*, 2001, **617-618**, 133-140

21. F. H. Burstall, *J. Chem. Soc.*, 1939, 173

22. H. Yersin, W. Humbs and J. Strasser, *Coord. Chem. Rev.*, 1997, **159**, 325-359

23. J. A. G. Williams, *Topics Curr. Chem.*, 2007, **281**, 205 - 268.

24. R. Buchner, J. S. Field R. J. Haines, C. T. Cunningham and D. R. McMillin, *Inorg. Chem.*, 1997, **36**, 3952-3956

25. D. R. McMillin and J. J. Moore, *Coord. Chem. Rev.*, 2002, **229**, 113-121

26. J. F. Michalec, S. A. Bejune and D. R. McMillin, *Inorg. Chem.*, 2000, **39**, 2708-2709

27. J. F. Michalec, S. A. Bejune, D. G. Cuttell, G. S. Summerton, J. A. Gertenbach, J. S. Field, R. J. Haines and D. R. McMillin, *Inorg. Chem.*, 2001, **40**, 2193-2200

28. K. L. Garner, L. F. Parkes, J. D. Piper and J. A. G. Williams, *Inorg. Chem.*, 2010, **49**, 47-487

29. Y-Z. Hu, M. H. Wilson, R. Zong, C. Bonnefous, D. R. McMillin and R. P. Thummel, *Dalton Trans.*, 2005, 354 - 358

30. V. W-W. Yam, K. H-Y. Chan, K. M-C. Wong and N. Zhu, *Chem. Eur. J.*, 2005, **11**, 4535-4543

31. P. Shao, Y. Li and W. Sun, *Organometallics*, 2008, **27**, 2743-2749

32. T. K. Aldridge, E. M. Stacey and D. R. McMillin, *Inorg. Chem.*, 1994, **33**, 722

33. M. Hissler, W. B. Connick, D. K. Geiger, J. E. McGarrah, D. Lipa, R. J. Lachicotte and R. Eisenberg, *Inorg. Chem.*, 2000, **39**, 447-457

34. M. H. Wilson, L. P. Ledwaba, J. S. Field and D. R. McMillin, *Dalton Trans.*, 2005, 2754-2759

35. V. W-W. Yam, R. P-L. Tang, K. M-C. Wong and K-K. Cheung, *Organometallics*, 2001, **20**¸ 4476 - 4482

36. Q-Z. Yang, L-Z. Wu, Z-X. Wu, L-P. Zhang and C-H. Tung, *Inorg. Chem.*, 2002, **41**, 5653-5655

37. S-W. Lai, M. C. W. Chan, K-K. Cheung and C-M. Che, *Inorg. Chem.*, 1999, **38(19)**, 4262-4267

38. F. Hua, S. Kinayyigit, J. R. Cable and F. N. Castellano, *Inorg. Chem.* 2006, **45**,

4304-4306

39. C. W. Chan, L. K. Cheng and C. M. Che, *Coord. Chem. Rev.*, 1994, **132**, 87-97

40. M. Kato, Y. Shishido, Y. Ishida and S. Kishi, *Chem. Lett.*, 2008, **37(1)**¸16-17

41. C-M. Che, K-T. Wan, L-Y. He, C-K. Poon and V. W-W Yam, *J. Chem. Soc.*¸*Chem. Commun.*, 1989, 943-944

42. I. E. Pomestchenko, C. R. Luman, M. Hissler, R. Ziessel and F. N. Castellano, *Inorg. Chem.*, 2003, **42**, 1394-1396

43. F. Hua, S. Kinayyigit, J. R. Cable and F. N. Castellano, *Inorg. Chem.*, **44**, 471-473

44. C. E. Whittle, J. A. Weinstein, M. W. George and K. S. Schanze, *Inorg. Chem.*, 2001, **40**, 4053-4062

45. W. Sotoyama, T. Satoh, H. Sato, A. Matsuura and N. Sawatari, *J. Phys. Chem. A*, 2005, **109**, 9760-9766

46. L. Chassot, E. Müller and A. Von Zelewsky, *Inorg. Chem.*, 1984, **23**, 4249-4253

47. P. Jolliet, M. Gianini, A. Von Zelewsky, G. Bernardinelli and H. Stoeckli-Evans, *Inorg. Chem.*, 1996, **35**, 4883-4888

48. J. Brooks, Y. Babayan, S. Lamansky, P. I. Djurovich, I. Tsyba, R. Bau and M. E. Thompson, *Inorg. Chem.*, 2002, **41**, 3055-3066

49. K. P. Balashev, M. V. Puzyk, V. S. Kotlyar and M. V. Kulikova, *Coord. Chem. Rev.*, 1997, **159**, 109-120

50. M. M. Mdleleni, J. S. Bridgewater, R. J. Watts and P. C. Ford, *Inorg. Chem.*, 1995, **34**, 2334-2342

51. T. Yagyu, J-I. Ohashi and M. Maeda, *Organometallics*, 2007, **26**, 2383-2391

52. F. Niedermair, K. Waich, S. Kappaun, T. Mayr, G. Trimmel, K. Mereiter and C. Sluovc, *Inorganica Chimica Acta*, 2007, **360**, 2767-2777

53. P-I. Kvam, M. V. Puzyk, K. P. Balashev and J. Songstad, *Acta. Chem. Scand.*, 1995, **49**¸ 335-343

54. J. Forniés, S. Fuertes, J. A. López, A. Martín and V. Sicilia, *Inorg. Chem.*, 2008, **47**, 7166-7176

55. S-Y. Chang, Y-M. Cheng, Y. Chi, Y-C. Lin, C-M. Jiang, G-H. Lee and P-T. Chou, *Dalton Trans.*, 2008, 6901-6911

56. E. C. Constable, R. P. G. Henney, T. A. Leese and D. A. Tocher, *Chem.*

Commun., 1990, 513-515

57. E. C. Constable, R. P. G. Henney and T. A. Leese, *Dalton Trans.*, 1990, 443-450

58. T-C. Cheung, K-K. Cheung, S-M. Peng and C-M. Che, *Dalton Trans.*, 1996, 1645-1651

59. Q. Wang, F. Xiong, F. Morlet-Savary, S. Li, Y. Li, J-P. Fouassier and G. Yang, *J. Photochem. Photobiol A: Chem.*, 2008, **194**, 230-237

60. J. H. K. Yip, Suwarno and J. J. Vittal, *Inorg. Chem.*, 2000, **39**, 3537-3543

61. W. Lu, B-X. Mi, M. C. W. Chan, Z. Hui, C-M. Che, N. Zhu and S-T. Lee, *J. Am. Chem. Soc.*, 2004, **126**, 4958-4971

62. P. Shao, Y. Li, A. Azenkeng, M. R. Hoffmann and W. Sun, *Inorg. Chem.* 2009, **48(8)**, 2407 – 2419

63. C-K. Koo, Y-M. Ho, C-F. Chow, M. H-W. Lam, T-C. Lau and W-Y. Wong, *Inorg. Chem.*, 2007, **46**, 3603-3612

64. Z. Jun-Feng, G. Xin, F. Wen-Fu, H. Xu and L. Li, *Inorg. Chim. Acta*, 2010, **363**, 338-345

65. L. L. Shi, T. Li, S. S. Zhao and H. Li, *Theor. Chem. Acc.*, 2009, **124**, 29-36

66. D. L. Rochester, S. Develay, S. Záliš and J. A. G. Williams, *Dalton Trans.*, 2009, 1728-1741

67. S. J. Farley, D. L. Rochester, A. L. Thompson, J. A. K. Howard and J. A. G. Williams, *Inorg. Chem.*, 2005, **44**, 9690 – 9703

68. G. S-O. Tong and C-M. Che, *Chem. Eur. J.*, 2009, **15**, 7225-7237

69. X. Zhou, Q-J. Pan, B-H. Xia, M-X. Li, H-X. Zhang and A-C. Tung, *J. Phys. Chem. A*, 2007, **111**, 5465-5472

70. X-J. Liu, J-K. Feng, J. Meng, Q-J. Pan, A-M. REn, X. Zhou and H-X. Zhang, *Eur. J. Inorg. Chem.*, 2005, 1856-1866

71. A. Hofmann, L. Dahlenburg and R. van Eldik, *Inorg. Chem.*, 2003, **42**, 6528-6538

72. C. Baik, W-S. Han, Y. Kang, S. O. Kang and J. Ko, *J. Organometallic. Chem.*, 2006, **691**, 5900 - 5910

73. S. Develay and J. A. G. Williams, *Dalton Trans.*, 2008, 4562-4564

74. D. Song, Q. Wu, A. Hook, I. Kozin and S. Wang, *Organometallics*, 2001, **20**, 4683-4689

75. K. Okamoto, T. Kanbara, T. Yamamoto and A. Wada, *Organometallics*, 2006, **25**, 4026-4029

76. M. Maestri, C. Deuschel-Cornioley and A. Von Zelewsky, *Coord. Chem. Rev.*, 1991, **111**, 117-123

77. W. Lu, M. C. W. Chan, K. K. Cheung and C. M. Che, *Organometallics*, 2001, **20**, 2477-2486

78. A. Zucca, G. L. Petretto, S. Stoccoro,M. A. Cinellu and G. Minghetti, *Organometallics*, 2006, **25**, 2253-2265

79. C. P. Newman, G. W. V. Cave, M. Wong, W. Errington, N. W. Alcock and J. P. Rourke, *Dalton Trans.*, 2001, **18** 2678-2682

80. J. R. Berenguer, E. Lalinde and J. Torroba, *Inorg. Chem.*, 2007, **46(23)**, 9919-9930

81. G. W. V. Cave, F. P. Fanizzi, R. J. Deeth, W. Errington and J. P. Rourke, *Organometallics*, 2000, **19**, 1355-1364

82. G. W. V. Cave, N. W. Alcock and J. P. Rourke, *Organometallics*, 1999, **18**, 1801-1803

83. W. B. Connick, D. Geiger and R. Eisenberg, *Inorg. Chem.*, 1999, **38**, 3264-3265

84. M. Maestri, D. Sandrini, A. Von Zelewsky and C. Deuschel-Cornioley, *Inorg. Chem.*, 1991, **30**, 2476-2478

85. B. Ma, P. I. Djurovich and M. E. Thompson, *Coord. Chem. Rev.*, 2005, **249**, 1501-1510

86. L. J. Grove, J. M. Rennekamp, H. Jude and W. B. Connick, *J. Am. Chem. Soc.*, 2004, **126**, 1594-1595

87. H-K. Yip, L-K. Cheng, K-K. Cheung and C-M. Che, *Dalton Trans.*, 1993, 2933-2939

88. D. Kim and J-L. Brédas, *J. Am. Chem. Soc.*, 2009, **131**, 11371-11380

89. A. E. Stiegman, S. F. Rice H. B. Gray and V. M. Miskowski, *Inorg. Chem.*, 1987, **26(7)**¸ 1112-1117

90. V. H. Houlding and A. J. Frank, *Inorg. Chem.*, 1985, **24(22)**, 3664-3669

91. E. M. A. Ratilla, B. K. Scott, M. S. Moxness and N. M. Kostić, *Inorg. Chem.*, 1990, **29**, 918-926

92. V. M. Miskowski and V. H. Houlding, *Inorg. Chem.*, 1991, **30**, 4446-4452

93. T. Abe, K. Shinozaki, N. Ikeda and T. Suzuki, *Acta Cryst.*, 2007, **C63**, m456 – m458

94. Y. Chen, K. Li, W. Lu, S. S-Y. Chui, C-W. Ma and C-M. Che, *Angew. Chem. Int. Ed.*, 2009, **48**, 9909-9913

95. A. S. Ionkin, W. J. Marshall and Y. Wang, *Organometallics*, 2005, **24**, 619-627

96. J-I. Nishida, A. Maruyama, T. Iwata and Y. Yamashita, *Chem. Lett.*, 2005, **34(4)**, 592 - 593

97. Á. Díez, J. Forniés, S. Fuertes, E. Lalinde, C. Larraz, J. A. López, A. Martín, M. T. Moreno and V. Sicilia, *Organometallics*, 2009, **28**, 1705-1718

98. B. Ma, J. Li, I. Djurovich, M. Yousufuddin, R. Bau, M. E. Thompson, *J. Am. Chem.Soc.*, 2005, **127**, 28 – 29

99. W. Lu, C. W. Chan, N. Zhu, C-M. Che, C. Li and Z. Hui, *J. Am. Chem. Soc.*, 2004, **126**, 7639 – 7651

100. W. B. Connick, R. E. Marsh, W. P. Schaefer and H. B. Gray, *Inorg. Chem.*, 1997, **36**, 913 – 922

101. H. Yersin, D. Donges, W. Humbs, J. Strasser, R. Sitters and M. Glasbeek, *Inorg. Chem.*, 2002, **41**, 4915 – 4922

102. S-Y. Chang, J. Kavitha, S-W. Li, C-S. Hsu, Y. Chi, Y-S. Yeh, P-T. Chou, G-H. Lee, A. J. Carty, Y-T. Tao and C-H. Chien, *Inorg. Chem.*, 2006, **45**, 137-146

103. D. J. Cárdenas and A. M. Echavarren, *Organometallics*, 1999, **18**, 3337-3341

104. R. E. Rundle, *J. Phys. Chem.*, 1957, **61**, 45 – 50

105. J. R. Miller, *J. Chem. Soc.*, 1965, 713 – 720

106. S-W. Lai, H-W. Lam, W. Lu, K-K. Cheung and C-M. Che, *Organometallics*, 2002, **21**, 226-234

107. S-W. Lai, M. C-W. Chan, T-C. Cheung, S-M. Peng and C-M. Che, *Inorg. Chem.*, 1999, **38**, 4046-4055

108. T. Dienel, H. Proehl, T. Fritz and K. Leo, *J. Luminescence*, 2004, **110**, 253-257

109. N. J. Turro, V. Ramamurthy and J. C. Scaiano, "Modern Molecular Photophysics of Organic Molecules", University Science Books, California, 2010

110. E. A. Chandross, J. Ferguson and E. G. McRae, *J. Chem. Phys.*, 1966, **45(10)**, 3546 - 3553

111. J-I. Lee, V. Y. Lee and R. D. Miller, *ETRI Journal*, 2002, **24(6)**, 409-414

112. K-T. Wan, C-M. Che and K-C Cho, *Dalton Trans.*, 1991, 1077 - 1080

113. F. Neve, A. Crispini and S. Campagna, *Inorg. Chem.*, 1997, **36**, 6150-6156

114. M-Y. Yuen, V. A. L. Roy, W. Lu, S. C. F. Kui, G. S. M. Tong, M-H. So, S. S-Y. Chui, M. Muccini, J. Q. Ning, S. J. Xu and C-M. Che, *Angew. Chem. Unt. Ed.*, 2008, **47**, 9895-9899

115. W. Lu, N. Zhu and C-M. Che, *Chem. Commun.*, 2002, 900-902

116. W. Lu, M. C. W. Chan, N. Zhu, C-M. Che, C. Li and Z. Hui, *J. Am. Chem. Soc.*, 2004, **126**, 7639-7651

117. S. C. F. Kui, I. H. T. Sham, C. C. C. Cheung, C-W. Ma, B. Yan, N. Zhu, C-M. Che and W-F. Fu, *Chem. Eur. J.*, 2007, 417-435

118. V. N. Kozhevnikov, B. Donnio and D. W. Bruce, *Angew. Chem. Int. Ed.*, 2008, **47**, 1-5

119. J. N. Demas and B. A. DeGraff, *Coord. Chem. Rev.*, 2001, **211**, 317-351

120. M. Kato, *Bull. Chem. Soc. Jpn.*, 2007, **80(2)**, 287-294

121. A. A. Rachford and F. N. Castellano, *Inorg. Chem.*, 2009, 48, 10865-10867

122. J. Moussa, K. M-C. Wong, L-M. Chamoreau, H. Amouri and V. W-W. Yam, *Dalton Trans.*, 2007, 3526-3530

123. P. Du, J. Schneider, W. W. Brennessel and R. Eisenberg, *Inorg. Chem.*, 2008, **47(1)**, 69-77

124. S. C. F. Kui, S. S-Y. Chui, C-M. Che and N. Zhu, *J. Am. Chem. Soc.*, 2006, **128**¸ 8297-8309

125. S-W. Lai, Q. K-W. Chan, J. Han, Y-G. Zhi, N. Zhu and C-M. Che, *Organometallics*, 2009, **28**, 34-37

126. P-H. Lanoë, H. Le Bozec, J. A. G. Williams, J-L. Fillaut and V. Guerchais, *Dalton Trans.*, 2010, **39**, 707-710

127. Y. Kang, J. Lee, D. Song and S. Wang, *Dalton Trans*., 2003, 3493-3499

128. P. K. M. Siu, S-W. Lai, W. Lu, N. Zhu and C-M. Che, *Eur. J. Inorg. Chem.*, 2003, 2749-2752

129. K. M-C. Wong, W-S. Tang, X-X. Lu, N. Zhu and V. W-W Yam, *Inorg. Chem.*, 2005, **44**, 1492-1498

130. W. W. S. Lee, K. Y. Wong and X. M. Li, *Anal. Chem.* 1993, **65**, 255-258

131. R. C. Evans and P. Douglas, *Anal. Chem.*, 2006, **78**, 5645-5652

132. R. C. Evans, P. Douglas, D. L. Rochester and J. A. G. Williams, *J. Fluor.*, 2006, **16(2)**¸ 200 - 205

133. L. Chassot, A. Von Zelewsky, D. Sandrini, M. Maestri and V. Balzani, *J. Am. Chem. Soc.*, 1986, **108**¸ 6084-6085

134. S. W. Thomas III, K. Vankatesan, P. Muller and T. M. Swager, *J. Am. Chem. Soc.*, 2006, **128**, 16641-16648

135. V. W-W. Yam, R. P-L. Tang, K. M-C. Wong, C-C. Ko and K-K. Cheung, *Inorg. Chem.*, 2001, **40**, 571 - 574

136. Q-Z. Yang, L.Z. Wu, H. Zhang, B. Chen, Z-X Wu, L-P. Zhang and C-H. Tung, *Inorg. Chem.*, 2004, **43**, 5195-5197

137. R. C. Evans, P. Douglas and C. J. Winscom, *Coord. Chem. Rev.*, 2006, **250**, 2093-2126

138. L. S. Hung and C. H. Chen, *Materials Science and Engineering R*, 2002, **39**, 143 - 222

139. J. S. Wilson, A. S. Dhoot, A. J. A. B. Seeley, M. S. Khan, A. Köhler and R. H. Friend, *Nature*, 2001, **413**, 828 - 831

140. J. A. G. Williams, S. Develay, D. L. Rochester and L. Murphy, *Coord. Chem. Rev.*, 2008, **252**, 2596 – 2611

141. M. A. Baldo, D. F. O'Brien, Y. You, A. Shoustikov, S. Sibley, M. E. Thompson and S. R. Forrest, *Nature*, 1998, **395**, 151-154

142. R. C. Kwong, S. Sibley, T. Dubovoy, M. Baldo, S. R. Forrest and M. E. Thompson, *Chem. Mater.*, 1999, **11(12)**, 3709-3713

143. C. Borek, K. Hanson, P. I. Djurovich, M. E. Thompson, K. Aznavour, R. Bau, Y. Sun, S. R. Forrest, J. Brooks, L. Michalski and J. Brown, *Angew. Chem. Int. Ed.*, 2007, **46**, 1109-1112

144. D. U. Kim, S-H. Paik, S-H. Kim, Y-H. Tak, S-D. Kim, Y-S. Han, T-J. Kim, T-H. Ko., U-C. Yoon and P. S. Mariano, *Colloids and Surfaces AP Physicochem. Eng. Aspects*, 2008, **313-314**, 444-447

145. T. Tsuzuki, Y. Nakayama, J. Nakamura, T. Iwata and S. Tokito, *Appl. Phys. Lett.*, 2006, **88**, 243511

146. C-C. Kwok, H. M. Y. Ngai, S-C. Chan, I. H. T. Sham, C-M. Che and N. Zhu, *Inorg. Chem.*, 2005, **44**, 4442-4444

147. G-J. Zhou, X-Z Wang, W-Y. Wong, X-M Yu, H-S Kwok and Z. Lin, *J. Organometallic Chem*, 2007, **692**, 3461-3473

148. I. R. Laskar, S. H. Fsu and T. M. Chen, *Polyhedron*, 2005, **24**, 881-888

149. W-Y. Wong, Z. He, S-K. So, K-L Tong and Z. Lin, *Organometallics*, 2005, **24**, 4079-4082

150. Z. He, W. Y. Wong, X. Yu, H. S. Kwok and Z. Lin, *Inorg. Chem.*, 2006, **45**, 10922-10937

151. W. Sotoyama, T. Satoh, N. Sawatari and H. Inoue, *Appl. Phys. Lett.* 2005, **86**, 153505 - 153507

152. C Adachi, M. A. Baldo, S. R. Forrest, S. Lamansky and M. E. Thompson, *Appl. Phys. Letters*, 2001, **78(11)**, 1622 -1624

153. M. Cocchi, J. Kalinowski, D. Virgili, V. Fattori, S. Develay and J. A. G. Williams, *Appl. Phys. Lett.*, 2007, **90**, 163508

154. W. Lu, B-X. Mi, M. C. W. Chan, Z. Hui, N. Zhu, S-T. Lee and C-M. Che, *Chem. Commun.*, 2002, 206-207

155. U. S. Bhansali, E. Polikarpov, J. S. Swensen, W-H. Chen, H. Jia, D. J. Gaspar, B. E. Gnade, A. B. Padmaperuma and M. A. Omary, *Appl. Phys. Lett.*, 2009, **95**, 233304

156. S-Y. Chang, J-L. Chen, Y. Chi, Y-M. Cheng, G-H. Lee, C-M. Jiang and P-T. Chou, *Inorg. Chem.*, 2007, **46**, 11202 – 11212

157. C. W. Ko and Y. T. Tao, *Appl. Phys. Lett.*, 2001, **79(25)**, 4234-4236

158. X. Jiang, Z. Zhang, W. Zhao, W. Zhu, B. Zhang and S. Xu, *J. Phys. D: Appl. Phys*, 2000, **33**, 473-476

159. B. W. D'Andrade and S. R. Forrest, *Adv. Mater.*, 2004, **16(18)**¸ 1585 - 1595

160. Y. Sun, N. C. Giebink, H. Kanno, B. Ma, M. E. Thompson and S. R. Forrest, *Nature*, 2006, **440**, 908-912

161. P. Tyagi, R. Srivastava, A. Kumar, V. K. Rai, R. Grover and M. N. Kamalasanan, *Synthetic Metals*, 2010, **160**, 756-761

162. B. W. D'Andrade, M. E. Thompson and S. R. Forrest, *Adv. Mater.*, 2002, **14(2)**, 147-151

163. J. Kido, M. Kimura and K. Nagai, *Science*, 1995, **267**, 1332-1334

164. Y. Kawamura, S. Yanagida, S. R. Forrest, *J. Appl. Phys.*, 2002, **92(1)**, 87-93

165. S. Tasch, E. J. W. List, O. Ekström, W. Graupner, G. Leising, P. Schlichting, U. Rohr, Y. Geerts, U. Scherf and K. Müllen, *Appl. Phys. Lett.*, 1997, **71(20)**, 2883-2885

166. J. Kido, H. Shionoya and K. Nagai, *Appl. Phys. Lett.*, 1995, **67(16)**, 2281-2283

167. B. W. D'Andrade, J. Brooks, V. Adamovich, M. E. Thompson and S. R. Forrest, *Adv. Mater.*, 2002, **14(15)**, 1032-1036

168. D. F. O'Brien, M. A. Baldo and M. E. Thompson, *Appl. Phys. Lett.*,1999, **74(3)**, 442-444

169. S. Lamansky, P. Djurovich, D. Murphy, F. Abdel-Razzaq, H-E. Lee, C. Adachi, P. E. Burrows, S. R. Forrest and M. E. Thompson, *J. Am. Chem. Soc.*, 2001, **123**, 4304-4312

170. V. Adamovich, J. Brooks, A. Tamayo, A. M. Alexander, P. I. Djurovich, B. W. D'Andarade, C. Adachi, S. R. Forrest and M. E. Thompson, *New J. Chem.*, 2002, **26**, 1171-1178

171. P. T. Furuta, L. Deng, S. Garon, M. E. Thompson and J. M. J. Fréchet, *J. Am. Chem. Soc.*, 2004, **126**, 15388-15389

172. J. Kalinowski, M. Cocchi, D. Virgili, V. Fattori and J. A. G. Williams, *Adv. Mater.*, 2007, **19**¸ 4000-4005

173. M. Cocchi, D. Virgili, V. Fattori, J. A. G. Williams and J. Kalinowski, *Appl. Phys. Lett.*, 2007, **90**, 023506

174. http://www.science.edu/TechoftheYear/Finalists/UnivStAndrews/1%20Press%20Release.pdf

175. http://www.oled-info.com/lumicure

CHAPTER TWO:

Synthesis and Characterisation

2.1 Overview of the Synthesis of 1,3-Di(2-pyridyl)benzene Systems

The project involved the synthesis and characterisation of platinum complexes incorporating variously functionalised 1,3-di(2-pyridyl)benzene ligands. A number of synthetic strategies have previously been employed in the synthesis of such ligands, and the main strategies involve either a cyclotrimerisation, a condensation reaction or a cross-coupling reaction (Figure 1). Each strategy has its own merits and disadvantages, which will now be discussed in turn.

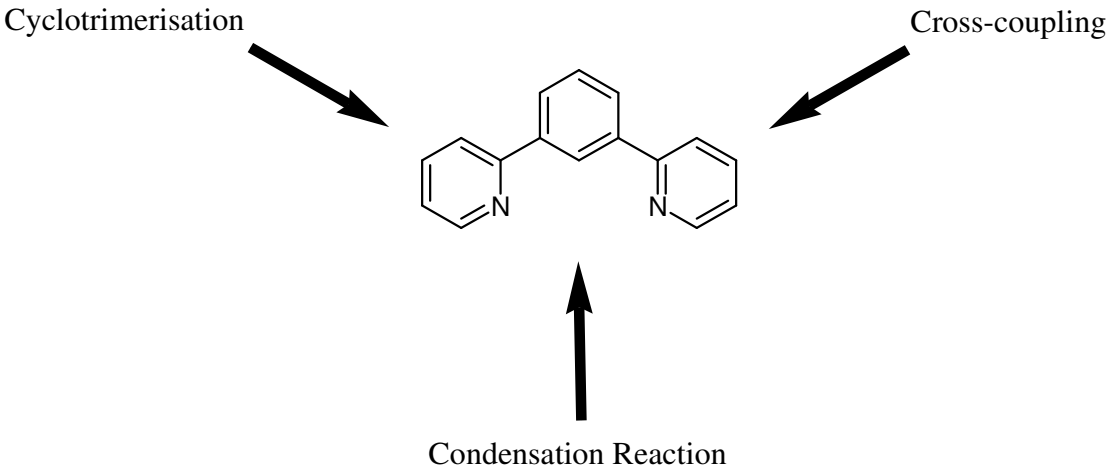

Figure 1: The three C's. Three routes that have been adopted to prepare 1,3-di(2-pyridyl)benzene systems.

2.1.1 Cyclotrimerisation

The synthesis of 1,3-di(2-pyridyl)benzene was first reported by Collin and Sauvage in 1991 – the group adopted a cyclotrimerisation reaction that had previously been used to prepare the 1,4-isomer.[1,2] The reaction involves 1,3-dicyanobenzene and acetylene precursors (Scheme 1), and proceeds under 10 atm pressure at 130˚C in the presence of a cobalt catalyst, Co(Cp)(COD) (Cp = cyclopentadiene, COD = 1,5-cyclooctadiene).

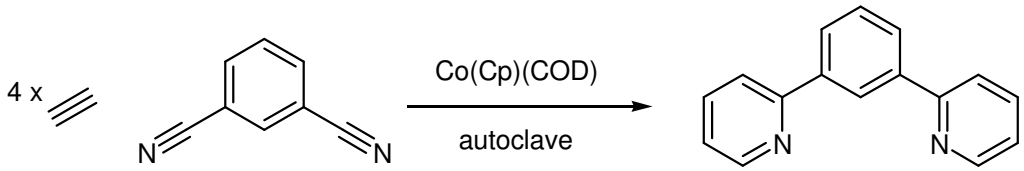

Scheme 1: Synthesis of 1,3-di(2-pyridyl)benzene via cyclotrimerisation

This reaction is high yielding (90%), but acetylene gas is potentially explosive under pressure, reducing the desirability of this methodology. Another downside is that it is difficult to introduce functionality into the terdentate system using this method, as functionalised precursors are not easy to obtain, and the use of asymmetrically substituted acetylenes will lead to several different regioisomers.

2.1.2 Condensation Reactions

Condensation reactions are often employed in the synthesis of bipyridine and terpyridine ligands, typically involving procedures based on Kröhnke annulations developed in the 1960s and 70s.[3,4,5] The reactions involve the condensation of α-pyridinium methyl ketone salts and proceed through a 2,3-ene-1,5-dione.[6] The methodology has been adopted by a few groups to prepare dipyridylbenzene systems (Scheme 2).[7,8] However, this route is infrequently used by other groups, as 1,3-diacetyl benzene compounds are relatively rare. Nevertheless, one of the ligands prepared in this project by cross-coupling, HL[7] (see Table 1), has also recently been prepared by a group in Japan using a Kröhnke synthesis (Scheme 2b).

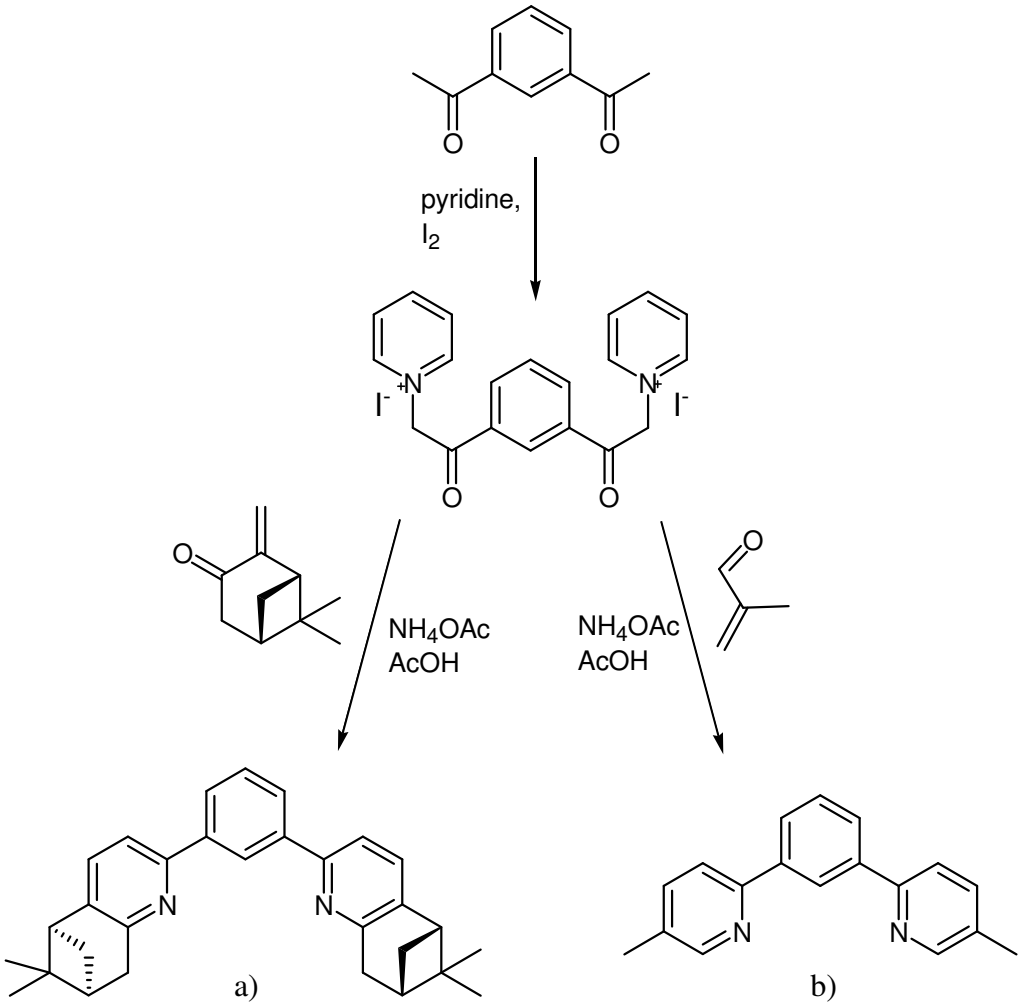

Scheme 2: Synthesis of a) chiral pinocarvone-appended N^C^N ligand[7] and b) 1,3-di(5-methyl-2-pyridyl)benzene, HL[7,8] via the condensation route.

In the late 90's Sauer developed a novel route for the synthesis of oligopyridines.[9,10,11,12] The method involves condensation of carboxamidrazones with 1,2-dicarbonyl compounds, giving a triazine intermediate. This species undergoes a [4+2] cycloaddition with a suitable electrophile (e.g. bicycle[221]hepta-2,5-diene or norborna-2,5-diene) followed by [4+2] cycloreversions of nitrogen and cyclopentadiene. Bruce et al. have adapted the method for the synthesis of dipyridylbenzene ligands containing substituents on the 5-pyridyl position (Scheme 3).[13] These reactions involve an initial condensation between benzene-1,3-dialdehyde and a hydrozone oxime precursor, which generates the triazine intermediate. The aryl triazine intermediate undergoes a cycloaddition with a suitable electrophile (e.g. 2,5-norbornene or 1-morpholinocyclopentene), generating the 1,3-dipyridylbenzene derivative with elimination of nitrogen.

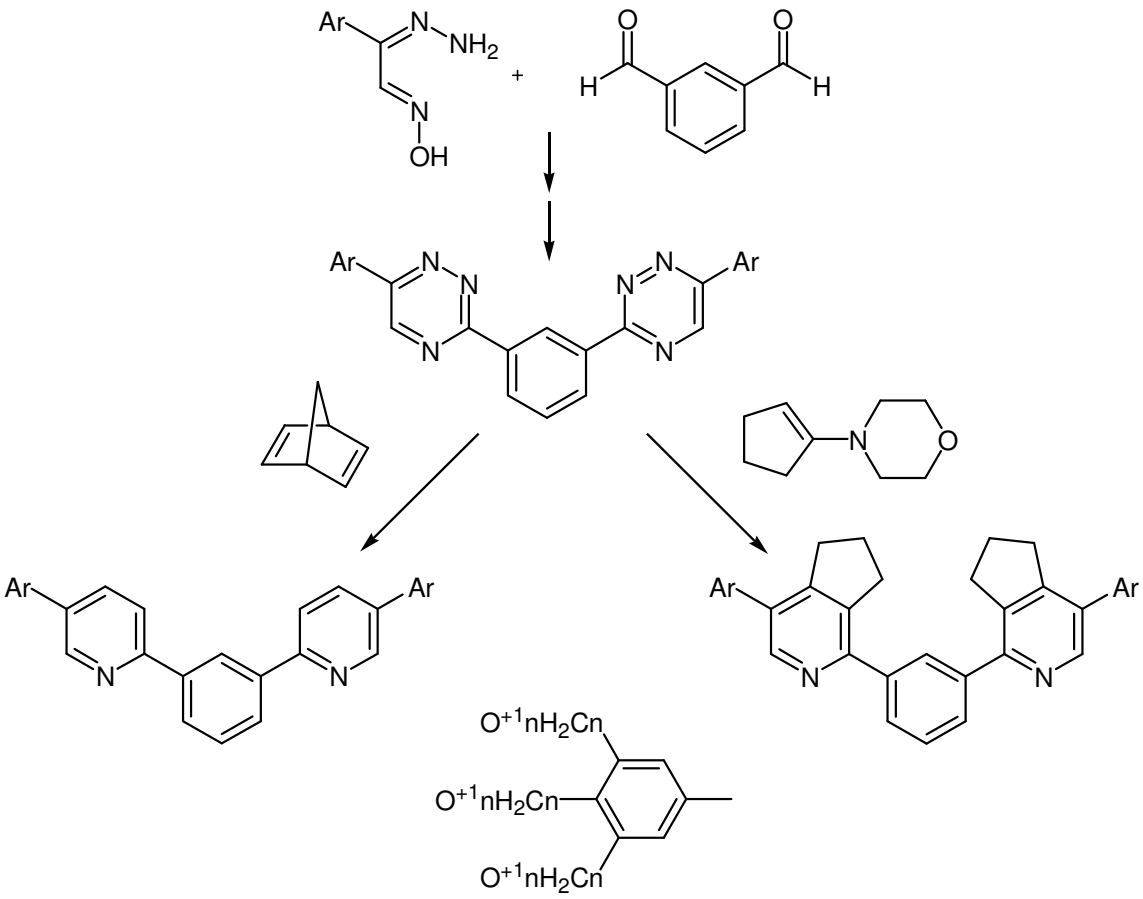

Scheme 3: Alternative condensation route employed by Bruce et al. to produce a selection of dipyridylbenzene ligands containing substituents on the 5-pyridyl position[13]

2.1.3 Cross-Coupling

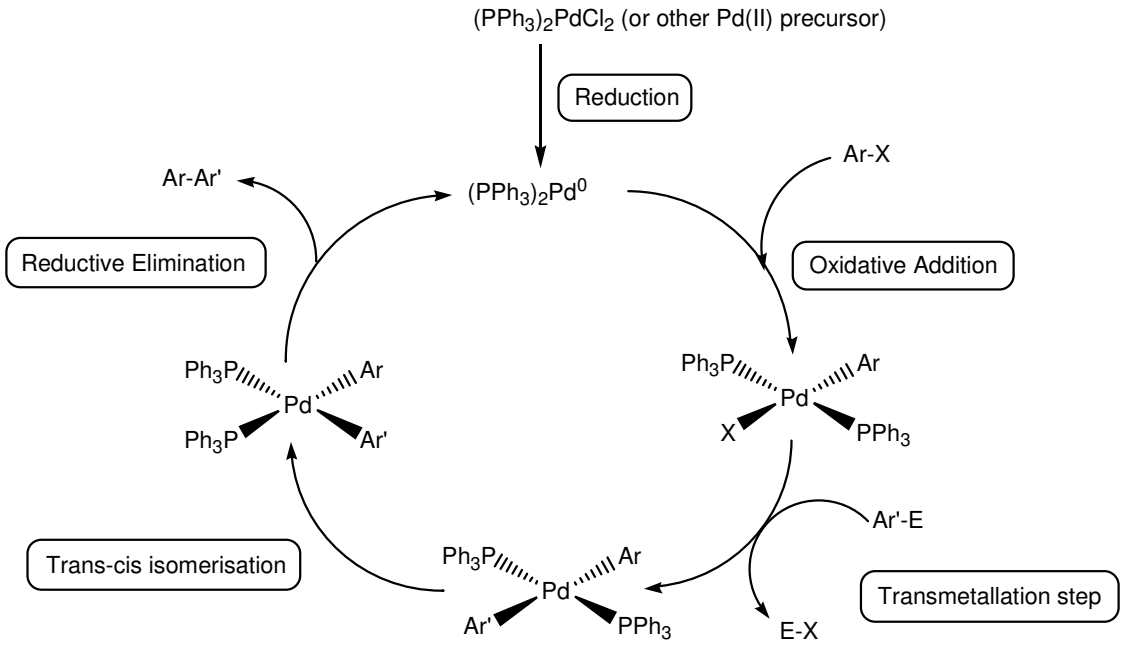

Figure 2: Proposed general catalytic cycle for cross-coupling reactions.[14,15] Here, Ar-X represents an aryl halide or triflate and E-Ar' represents the "metalloaryl" species.

Palladium catalysed cross-coupling reactions are most commonly used to produce 1,3-di(2-pyridyl)benzene ligands.[16,17,18,19] These methodologies are extremely versatile, and are becoming increasingly used in the synthesis of a vast array of ligands, pharmaceuticals and extended organic systems. The method offers a route to more functionalised ligands than those previously discussed, as many of the ligand precursors can be prepared within a few steps from commercially available starting materials. Such reactions typically occur between an aryl halide or triflate and a "metalloaryl" species, and result in the formation of an aryl-aryl bond. The mechanism of cross-coupling is determined by the nature of the "metalloaryl" species, which can be, for example, an aryl-stannane (Stille reaction), an aryl-zinc reagent (Negishi reaction) or an aryl-boronic acid/ester (Suzuki reaction – note that boron is considered an honorary metal here). A generalised catalytic cycle is shown in Figure 2. Cross-coupling reactions to produce dipyridylbenzene systems can proceed via one of two routes, as shown in Scheme 4.

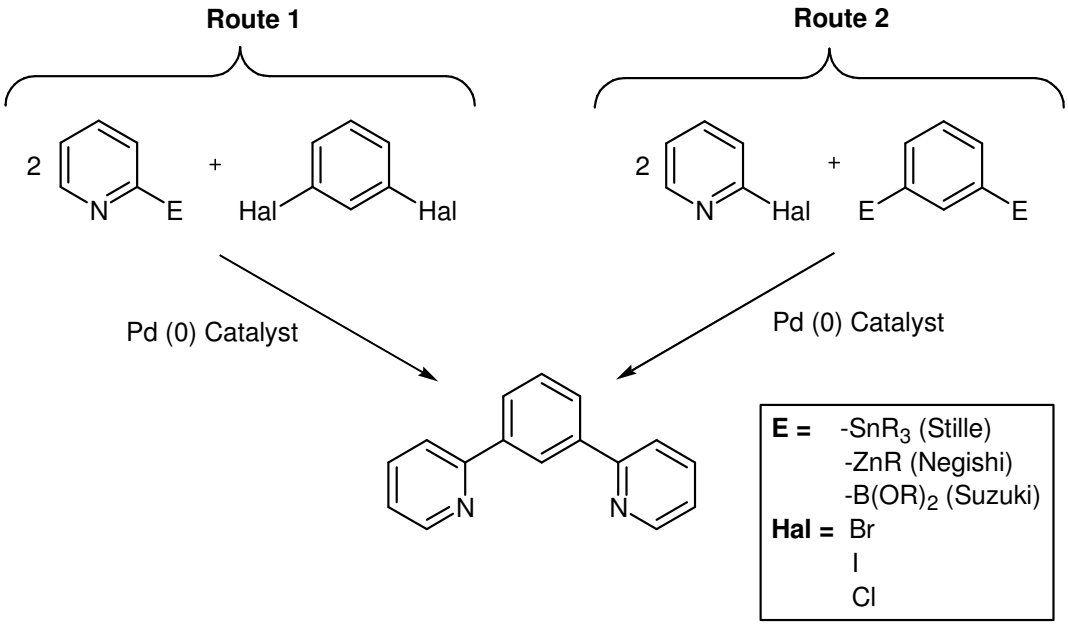

Scheme 4: The two possible cross-coupling routes to a 1,3-di(2-pyridyl)benzene

Route 1 involves reaction between a 1,3-dihalogenated aryl core (typically a dibromo- or diiodo-derivative) and a 2-"metallo" pyridine. 1,3-Dichloro aryls are relatively unreactive, and require more sophisticated caltalysts which can increase the cost dramatically. Hence 1,3-dibromo and 1,3-diiodo aryls are commonly used. The majority of ligands prepared via this route have involved Stille reactions utilising a 2-(trialkyl)stannyl pyridine, as such species can be readily prepared from the 2-bromo pyridine via an initial lithium-halogen exchange, followed by reaction with a tin electrophile (e.g. $SnBu_3Cl$).[16,18,19] The Stille cross-coupling reaction was initially proposed by Stille et al. in 1978.[20] Stille found that selective ketone synthesis would result from a cross-coupling reaction between an organo-tin compound and an acyl-chloride in the presence of a palladium catalyst. Since then, the Stille reaction has been greatly developed, and is widely used in organic synthesis of a vast array of compounds.[21,22] The reaction can be generalised as the formation of a carbon-carbon bond between an organotin species and an sp^2 hybridised organic halide, catalysed by palladium. The catalytic cycle shown in Figure 2 describes the general mechanism. However, differences in experimental observations between Stille reactions indicate that the precise mechanisms of individual reactions vary slightly, and are dependent on the reaction conditions employed (e.g. solvent polarity, the catalyst's ligands, nature of the coupling partners, etc.).[23]

In some cases, the addition of copper(I) salts can beneficially promote the Stille reaction, especially for sterically hindered systems and reactions involving

electronically disfavoured coupling reagents.[24,25,26,27] How the copper species achieves this is dependent on solvent – in ethereal solvents copper acts as a scavenger for free ligand released from the catalyst during/before the oxidative addition with R-X.[24,25] By mopping up the free ligand, copper reduces autoretardation of the associative transmetallation step. However in polar solvents, mechanistic evidence suggests that an additional transmetallation occurs between the organostannane and copper.[26,27] This produces an organocopper species that is more reactive towards transmetallation with the palladium catalyst, thereby facilitating the Stille reaction.

Tin species are highly toxic, so reactions involving such species are not ideal. Tin by-products are also notoriously difficult to remove from the desired product.[28] Suzuki-Miyaura reactions involve palladium catalysed C-C bond formations between an aryl (or vinyl) halide and an aryl (or vinyl) boronic acid/ester.[28,29,30,31] Unlike organo-stannanes, boronic acid derivatives are relatively non-toxic, they are easier to handle and are stable once formed. On top of this, the removal of boron containing by-products is much easier to achieve than stannyl by-products. However, unlike other cross-coupling reactions, Suzuki-Miyaura cross-couplings require the presence of a base (such as Na_2CO_3) to activate the aryl boronic acid/boronate and the catalyst.

Unfortunately, pyridyl-2-boronic acids are unstable to protodeboronation. These electron-deficient species undergo transmetallation at a much slower rate than protodeboronation under standard Suzuki conditions, leading to poor conversions. As a consequence, there are very few examples of syntheses utilising pyridyl-2-boronic acids. Recently however, several successful attempts have been made into the creation of more stable or activated 2-pyridyl boronate esters, that may find use in future syntheses of 1,3-di(2-pyridyl)benzene systems.[32,33,34] For example, Miyaura et al. have developed an air-stable 2-pyridyl triolborate that undergoes cross-coupling reactions with bromoarenes in dry DMF.[33] In 2008, Buchwald et al. reported on lithium triisopropyl 2-pyridylborates that were stable up to month after their preparation.[32] The borates were readily prepared in high yield from the respective 2-bromopyridine by lithium-halogen exchange, followed by immediate in-situ quenching of the anion with triisopropylborate. In the presence of a $[Pd_2(dba)_3]$ catalyst and suitable phosphate or phosphine oxide ligand, most 2-pyridyl borates underwent Suzuki-Miyaura cross-coupling reaction with aryl/heteroaryl iodides, bromides, and chlorides, resulting in high product yields. However, for highly electron-deficient boronates, the transmetallation step was very slow, and incomplete conversions were observed. Also, lithiation is an

essential step in the synthesis of the lithium triisopropyl 2-pyridylborates, which limits the functionality available on the heteroaromatic ring.

Burgey et al. have developed an efficient Suzuki-Miyaura cross-coupling methodology involving 2-pyridyl pinacol boronates, where addition of copper(I) chloride significantly increases the yield.[35] The pinacol boronates are more stable than the 2-pyridyl boronic acids and the synthesis tolerates a wider array of functional groups than lithium triisopropyl 2-pyridylborates. Mechanistic studies indicate that the copper salt facilitates transmetallation of the boronate to the palladium complex, by forming a more reactive organometal species in situ. High yields were obtained with both electron rich and electron deficient 2-pyridyl pinacol boronates.

A few groups have employed Negishi cross-coupling reactions to synthesise 1,3-dipyridylbenzene systems.[36,37] These reactions require initial preparation of a pyridylzinc chloride species, which is then cross-coupled with a 1,3-dibromobenzene in the presence of a palladium catalyst. Pyridylzinc chloride species are prepared via lithium-halogen exchange between 2-bromopyridine and nBuLi at -78˚C, followed by nucleophilic substitution with $ZnCl_2$. Previous group members tried to use this synthesis for 1,3-dipyridylbenzene ligands, but found the route to be very unreliable (low yields etc.), especially compared to the other cross-coupling methods.

Fagnou et al. have reported a direct arylation synthetic route as an alternative to cross-coupling, which avoids the need for such problematic "2-metallopyridines" altogether.[38] The reaction involves a pyridine N-oxide and an aryl bromide, which selectively couple via the pyridine N-oxide 2-position. The N-oxide is then removed under mild conditions. The direct arylation requires a palladium catalyst/ligand system {$Pd(OAc)_2$ and P^tBu_3-HBF_4 were used here}, and the reactions are insensitive to the presence of water. High yields are reported to be attainable (74 – 97%), regardless of the electronic nature of the pyridine N-oxide or aryl bromide. To our knowledge, no one has used this route to produce dipyridylbenzene systems – another member of our group has recently attempted this, but has so far been unsuccessful.

Route 2 involves reaction between a 2-halopyridine and a 1,3-diE-functionalised aryl core. Unlike the 1,3-dichloroaryl systems, 2-chloropyridines are sufficiently reactive to undergo cross-couplings with standard catalysts. The "dimetallate" species benzene-1,3-diboronic acid, and some of its derivatives have been employed in the preparation of

some 1,3-dipyridylbenzene systems.[19,39] Reactions involving boronic acid-based metalloaryls tend to go more cleanly than those involving tin-based metalloaryls, and it is often easier to isolate the pure product. However, very few functionalised benzene-1,3-diboronic acids have been reported to date, as the standard syntheses of such molecules typically involve harsh conditions that are incompatible with many substituents. This has limited the use of this route in preparation of the terdentate ligands. During the project, it was discovered that functionalised 1,3-dibromobenzenes (e.g. 1,3-dibromo-4,6-difluorobenzene, 1,3-dibromo-4,6-dimethylbenzene, etc.) could be converted into functionalised benzene-1,3-diboronic esters, that underwent Suzuki cross-coupling with 2-halopyridines (Section 2.2.2.1). This discovery has opened up new routes to highly functionalised dipyridylbenzene ligands, without the need for toxic tin species, examples of which will be discussed in subsequent sections of this chapter.

2.2 Ligand Synthesis

The dipyridylbenzene ligands prepared during the project were all made via cross-coupling reactions, which involved either Suzuki or Stille methodology (Table 1).

Table 1: The selection of terdentate ligands prepared herein, the reactive precursors, and the reaction conditions employed.

Ligand	Precursors	Synthetic Procedure	Solvent	Catalyst System	Yield / %
HL[1] 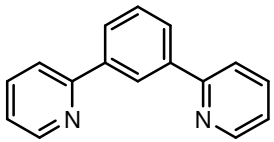	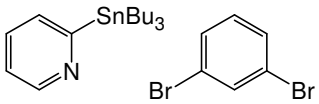	Stille	Toluene	$Pd(PPh_3)_2Cl_2$	87
HL[2] 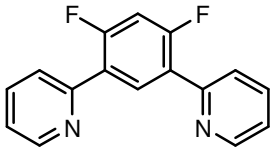	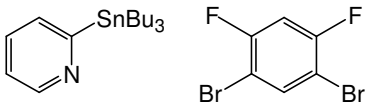	Stille	Toluene	$Pd(PPh_3)_2Cl_2$	53
HL[3] 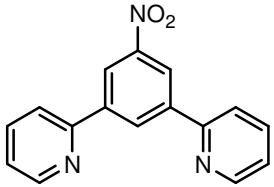	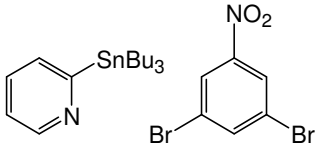	Stille	Toluene	$Pd(PPh_3)_2Cl_2$	55
HL[4] 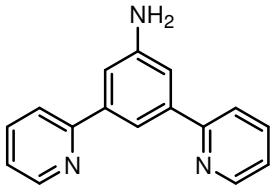	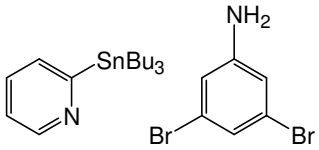	Stille	Toluene	$Pd(PPh_3)_2Cl_2$	31
HL[5] 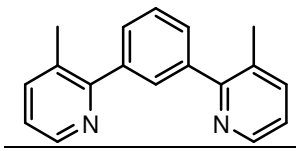	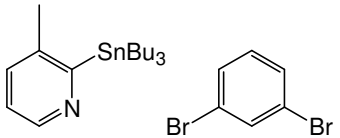	Stille	Toluene	$Pd(PPh_3)_2Cl_2$	43

Ligand	Precursors	Synthetic Procedure	Solvent	Catalyst System	Yield / %
HL[7] 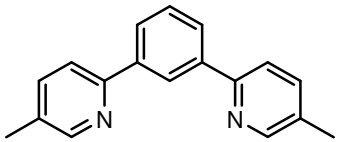	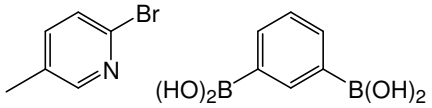	Suzuki	DME/H_2O (1:1)	$Pd(PPh_3)_4$	72
HL[8] 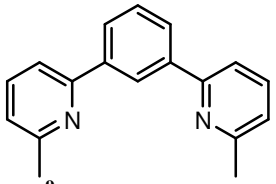	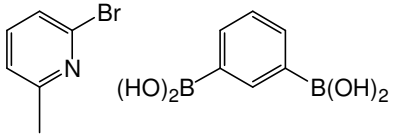	Suzuki	DME/H_2O (1:1)	$Pd(PPh_3)_4$	27
HL[9] 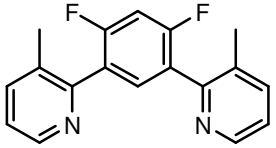	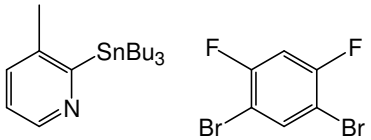	Stille	Toluene	$Pd(PPh_3)_2Cl_2$	27
HL[10] 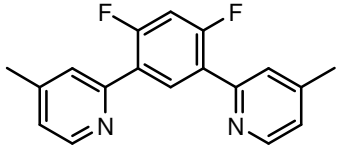	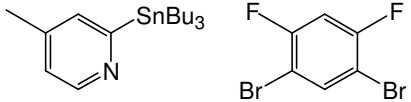	Stille	Xylene	$Pd(PPh_3)_2Cl_2 + PPh_3$	88
		Stille	Toluene	$Pd(PPh_3)_2Cl_2$	40
HL[11] 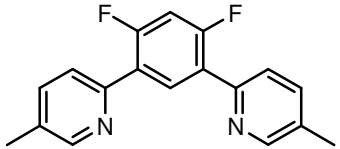	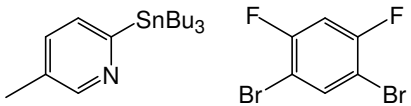	Stille	Toluene	$Pd(PPh_3)_2Cl_2$	39

Ligand	Precursors	Synthetic Procedure	Solvent	Catalyst System	Yield / %
HL[12] 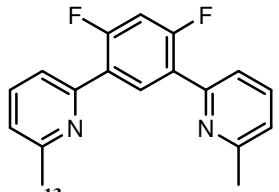	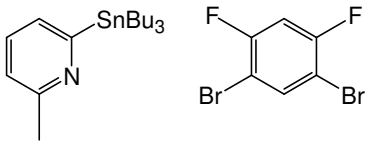	Stille	Toluene	$Pd(PPh_3)_2Cl_2$	58
HL[13] 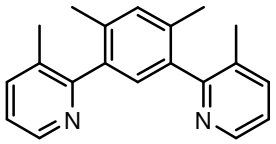	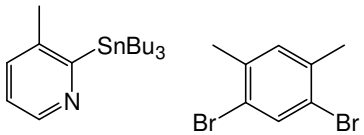	Stille	Toluene	$Pd(PPh_3)_2Cl_2$	9
	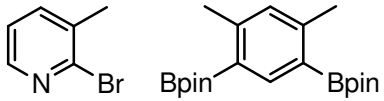	Suzuki	DME/H_2O (1:1)	$Pd(PPh_3)_4$	42
HL[14] 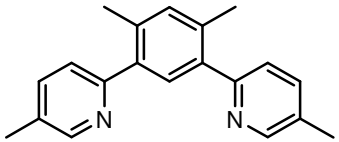	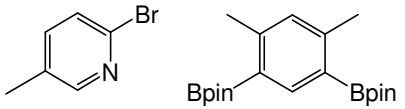	Suzuki	DME/H_2O (1:1)	$Pd(PPh_3)_4$	95
HL[15] 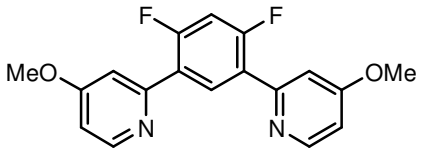	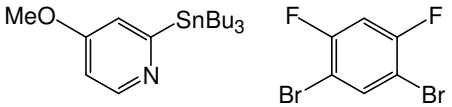	Stille	Toluene	$Pd(PPh_3)_2Cl_2$	31

Ligand	Precursors	Synthetic Procedure	Solvent	Catalyst System	Yield / %
HL[16] 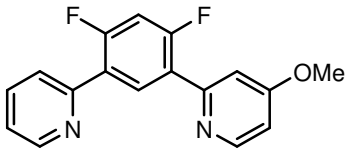	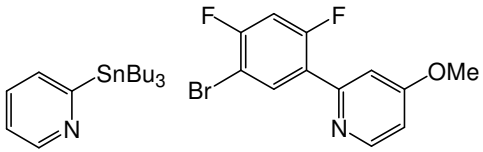	Stille	Toluene	$Pd(PPh_3)_2Cl_2$	32
HL[17] 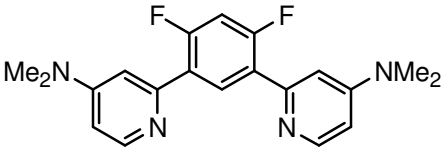	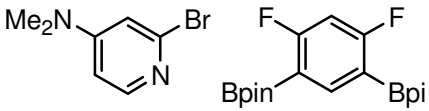	Suzuki	DME/H_2O (1:1)	$Pd(PPh_3)_4$	51
HL[18] 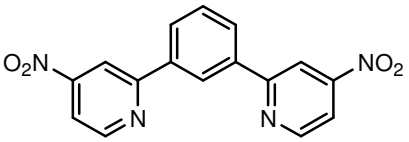	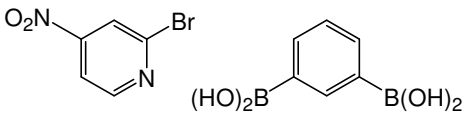	Suzuki	DME/H_2O (1:1)	$Pd(PPh_3)_4$	38
HL[19] 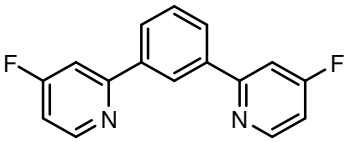	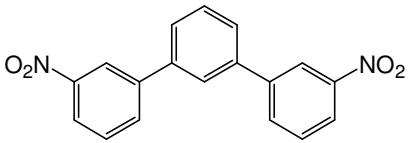	Fluorodenitration	DCM	----------	96
		Fluorodenitration	DMF	----------	72

Ligand	Precursors	Synthetic Procedure	Solvent	Catalyst System	Yield / %
HL[20] 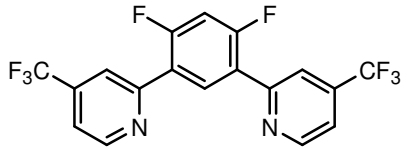	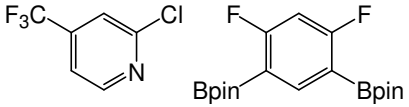	Suzuki	DME/H_2O (1:1)	$Pd(PPh_3)_4$	89
HL[21] 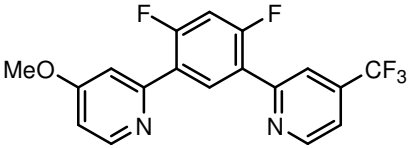	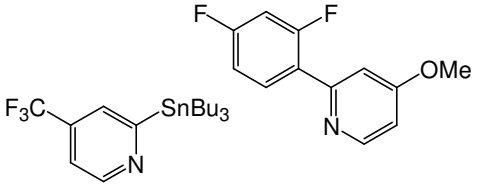	Stille	Toluene	$Pd(PPh_3)_2Cl_2$	55
HL[22] 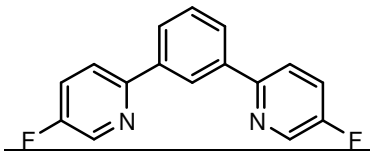	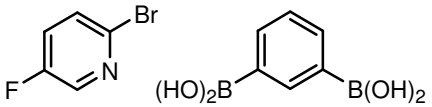	Suzuki	DME/H_2O (1:1)	$Pd(PPh_3)_4$	54

2.2.1 Ligands Prepared via Stille Cross-Coupling

Stille cross-coupling reactions utilised during the project involved a 2-tri-n-butylstannyl pyridine species and a 1,3-dibromo aryl species (Scheme 4, Route 1), and were performed in toluene or xylene. $Pd(PPh_3)_2Cl_2$ was added as catalyst. Reactants were degassed using freeze-pump-thaw methodology, and the reactions were heated at 120℃ under nitrogen for three days. An inert atmosphere was crucial to prevent oxidation (and deactivation) of the palladium catalyst and to minimise homo-coupling reactions between the stannanes, both of which would have a detrimental effect on the yield. LiCl was also added to increase the yield – the compound is thought to stabilise the intermediate complex formed after oxidative addition, accelerating the reaction.

The reactions were found to generate a significant amount of waste material, which was removed from the desired product by lengthy work-up followed by column chromatography. Stannyl by-products can be notoriously difficult to remove – they are insoluble in water so cannot be simply washed out. KF was added during the work-up to form insoluble tri-n-butyltin fluorides, which are subsequently filtered from the product. Sometimes, however, some tin residues remained after the full work-up and column; since the desired products were generally insoluble in hexane, several washings with this solvent were usually sufficient to remove the excess tin by-products.

The Stille reaction gave a wide range of yields (27 – 88%), but most ligands were formed in moderate (40-50%) yield. The presence of an ionisable or protonable group (e.g. NH_2, OH) on the central ring seemed to hinder the reaction, giving the low yields. Otherwise, there was no noticeable trend between yield and structure of the reactants.

2.2.1.1 Preparation of Precursors

1,3-Dibromobenzene and Derivatives

1,3-Dibromobenzene and 3,5-dibromophenol are commercially available and were used as bought in the Stille reactions. 1,3-Dibromo-4,6-difluorobenzene was prepared by brominating commercially available 1-bromo-2,5-difluorobenzene with bromine in the presence of iron filings (Scheme 5)[40,41] The bromine reacts with iron to form a Lewis

acid, $FeBr_3$, which in combination with Br_2 is an electrophilic source of bromine. This reacts with the aryl ring via electrophilic aromatic substitution. Bromination occurred selectively, despite using an excess of bromine, and a yield of 68% was obtained.

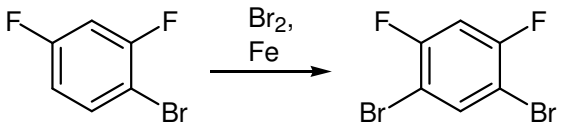

Scheme 5: Preparation of 1,3-dibromo-4,6-difluorobenzene.

1,3-Dibromo-5-nitrobenzene was prepared from 2,6-dibromo-4-nitroaniline. The reaction involves an initial nitrosation to give an aryl diazonium salt, followed by reductive deamination with H_3PO_2 (Scheme 6).[42,43] The overall reaction was relatively high yielding (70%). Some of the 1,3-dibromo-5-nitrobenzene was reduced with Sn/HCl to give 3,5-dibromoaniline.[44]

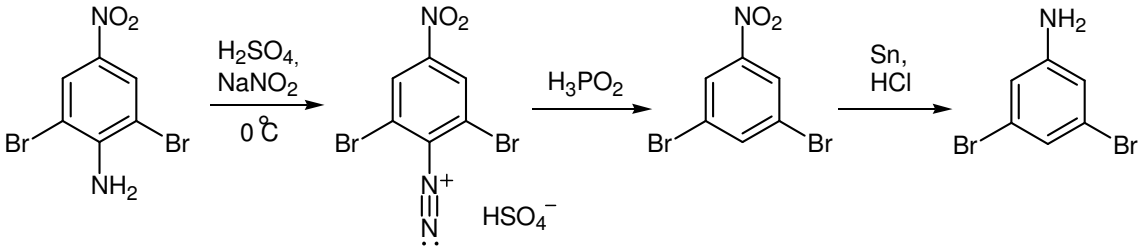

Scheme 6: Synthetic route to 1,3-dibromo-5-nitrobenzene and 3,5-dibromoaniline.

Pyridyl Stannane Precursors

Table 1 shows the selection of 2-pyridyl stannanes used. Their synthesis involved a two-step process: initial lithiation at the 2-pyridyl position, followed by nucleophilic substitution with a tin electrophile (Bu_3SnCl). The lithiation proceeded by one of two mechanisms, depending on the initial pyridyl starting material (Scheme 7). 2-Bromo pyridines were lithiated directly: mixing with n-butyllithium (n-BuLi) at 0˚C resulted in lithium-halogen exchange.[45]

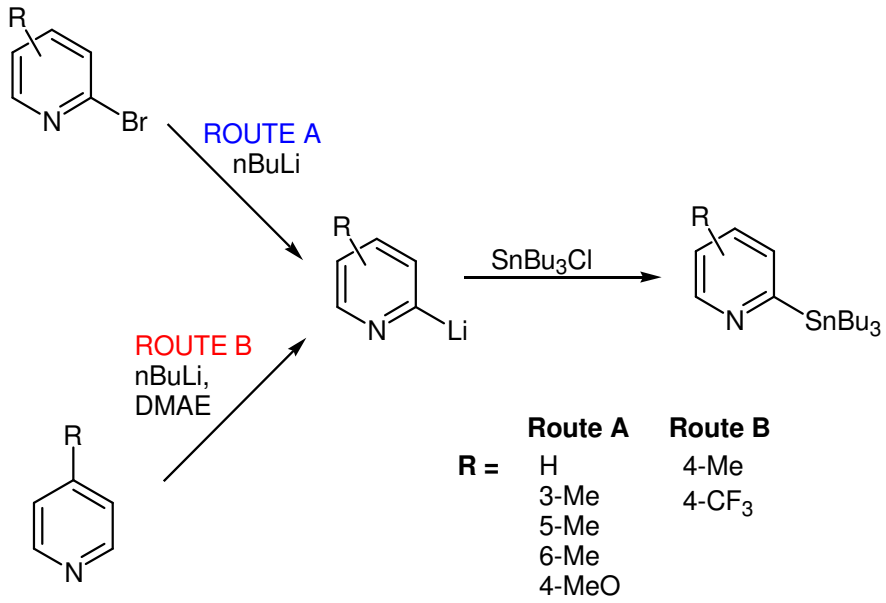

Scheme 7: Routes employed in the synthesis of 2-pyridyl stannanes.

Fort and Gros have reported an alternative route to 4-functionalised-2-pyridyl stannanes. Here, a 2-bromo substituent is not necessary to achieve selective lithiation, and simple 4-functionalised pyridines can be used directly (Scheme 7, Route B). Some of the 4-functionalised-2-pyridyl stannanes (functionality = Me, CF_3), were prepared via this route. In these reactions, n-BuLi was initially mixed with dimethylaminoethanol (DMAE), a coordinating molecule, in dry hexane.[46] When the 4-functionalised pyridine is added, a mixed lithium aggregate intermediate is initially formed (Figure 3), where induced proximity effects and an enhancement of the acidity of the proton ortho to nitrogen cumulatively result in selective lithiation at the C-2 position. This method is only reliable for use with some 4-substituted pyridines, as a mixture of isomers would result from reaction with other n-substituted pyridines (n = 3, 5 and 6).

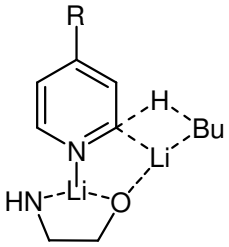

Figure 3: The mixed lithium aggregate intermediate in the ortho-directed lithiation/stannylation route.

The synthesis of 4-methoxy-2-tri-n-butylstannyl pyridine via ortho-directed lithiation and its subsequent Stille cross-coupling gave unsatisfactory yields of 4-methoxy-2-tri-n-butylstannyl pyridine. Hence, 2-bromo-4-methoxy pyridine was synthesised, in the

expectation that lithium-halogen exchange might prove more successful in providing access to the stannane. The synthesis of 2-bromo-4-methoxy pyridine was taken from reference 47, and involves four steps (Scheme 8): formation of the N-oxide of 2-bromopyridine, nitration of 2-bromopyridine N-oxide, N-oxide removal and substitution of NO_2 by MeO^-. In pyridine N-oxides, the lone pair of the oxygen is delocalised round the aromatic ring, increasing the susceptibility towards electrophilic substitution (especially at the 4-position). Hence NO_2^+ generated by mixing concentrated sulphuric acid with fuming nitric acid attacks the 4-position via electrophilic substitution. Removal of the oxide was achieved with a phosphorus based reductant, PBr_3. Phosphorus has an extremely high affinity for oxygen, forming a very stable P=O bond. Removal of the N-oxide removes the heightened nucleophilicity of the pyridine ring system, meaning the molecule is no longer susceptible to electrophilic aromatic substitutions (electronegative nitrogen would destabilise any cationic intermediate, and the free lone pair might attack an electrophile). The system has, however, become more susceptible to nucleophilic substitution. Dissolving sodium in methanol produces strongly basic/nucleophilic methoxide ions, which will attack at the electron deficient C-4 and displace the nitro group.

Lithiation of 2-bromo-4-methoxy pyridine via lithium-halogen exchange, followed by stannylation proved successful, and 2-tri-n-butylstannylpyridine underwent Stille cross-coupling to give the desired ligand, 1,3-di(4-methoxy-2-pyridyl)-4,6-difluorobenzene, HL^{15}, (31% yield). The mono-substituted molecule, 1-bromo-2,4-difluoro-5-(4-methoxy-2-pyridyl)-benzene was also isolated from this reaction (38%). Some of this was further reacted with 2-tri-n-butylstannylpyridine, and some with 2-tri-n-butylstannyl-4-trifluoromethylpyridine, to give two asymmetric ligands, HL^{16} and HL^{21} (Table 1).

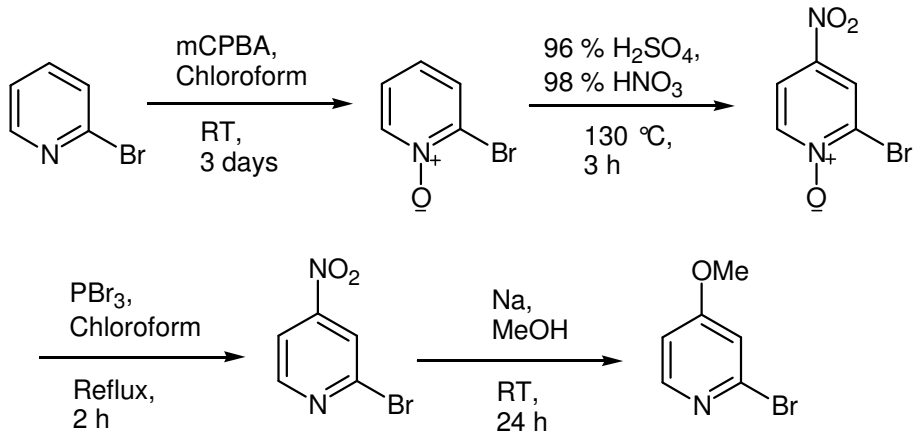

Scheme 8: Synthetic route to 2-bromo-4-methoxypyridine, taken from reference 47**.**

A previous group member found that stannylation of 4-dimethylamino pyridine via ortho-directed lithiation gave very unsatisfactory yields. The failure of ortho-directed lithiation with both 4-dimethylaminopyridine and 4-methoxypyridine indicates that pyridyl substituents of greater electron donating character have a detrimental effect on this route. 2-Bromo-4-dimethylamino pyridine has been prepared, but the stannylation/Stille reaction route was not followed with this precursor, due to development of an alternative route to synthesis of ligands incorporating functionalised central phenyl rings (Section 2.2.2.1).

It was found that the stannanes partly decompose during column chromatography, particularly when electron rich substituents are present, and are best used straight from the reaction work-up. An estimate of purity was gained from proton NMR, by comparing the integrals of the aromatic region with those of the aliphatic region.

2.2.2 Ligands Prepared via Suzuki-Miyaura Cross-Coupling

Ligands HL^7, HL^8, HL^{13}, HL^{14}, HL^{17}, HL^{18}, HL^{19}, HL^{20} and HL^{22} were all prepared via Suzuki-Miyaura cross-coupling. The most commonly used base in Suzuki-Miyaura cross-coupling is Na_2CO_3; which was used throughout the project. The reactions were performed in a mixed dimethoxyethane/water solvent system (1:1), in the presence of a $Pd(PPh_3)_4$ catalyst. The reactions were degassed (freeze-pump-thaw methodology) and heated under nitrogen at 85 ° C for two days. The $Pd(PPh_3)_4$ catalyst was added just before heating to prevent initial decomposition. Initially, Suzuki-Miyaura reactions were performed utilising a low water content (DME/water, 6:1)[19], but a previous group

member found that an increased water content (DME/water, 1:1) led to enhanced yields when using diboronic acids. This enhancement probably results from the increased solubilisation of benzene-1,3-diboronic acid, which creates a more homogeneous system. The yield varied significantly between reactions (27 – 95%), but with no apparent trend amongst reactants.

Benzene-1,3-diboronic acid is commercially available, and most ligands involving an unsubstituted central phenyl ring were prepared via Suzuki-Miyaura cross-coupling. There are very few examples of syntheses using benzene-1,3-diboronic acid in the literature (and even fewer involving functionalised benzene-1,3-diboronic acids)[39,48,49,50] During the project, a facile route to the formation of derivatized benzene-1,3-diboronate ester species was developed based on a transition-metal-catalysed cross-coupling initially proposed by Miyaura et al.[51] (see Section 2.2.2.1). In his initial paper on the subject, Miyaura reported that 1,3-dibromobenzene would form a diboronate species under Miyaura conditions, however to our knowledge, no one has ever used the methodology to create functionalised aryl-diboronate systems. These aryl diboronate esters were found to react well under the Suzuki conditions employed with benzene-1,3-diboronic acid, and were used to synthesise ligands HL^{13}, HL^{14}, HL^{17} and HL^{20} in moderate to excellent yields (42 – 95%). This was a big breakthrough, as the methodology has opened up a less toxic route to N^C^N units offering a greater extent of derivatisation.

2.2.2.1 Synthesis of Precursors

Aryl-1,3-diboronate esters

Literature procedures for the synthesis of benzene diboronic acids typically involve lithium-halogen exchange between the bromobenzene precursor and nBuLi, followed by transmetallation with a trialkoxy borane {e.g. $B(OPr^i)_3$, $B(OMe)_3$, etc}, and finally hydrolysis with concentrated acid.[39,52] Alternatively, boronic acids are produced via the addition of Grignard reagents to trialkoxy boranes at low temperature, again followed by hydrolysis[53,54,55] Both routes involve harsh conditions and are incompatible with many functional groups, limiting the synthetic diversity.

Some aryl-boronate esters (e.g. pinacol esters) have been found to react via Suzuki-Miyaura routes under similar conditions to aryl boronic acids, meaning acid hydrolysis is not always necessary. These compounds initially involved lithium-halogen exchange in their synthesis, so diversification was still difficult.[56] However in 1995, Miyaura et al. reported a direct one-step synthesis of aryl-boronate esters from the aryl bromide or iodide.[51] The mechanism involves a transition-metal-catalysed cross-coupling of a boron nucleophile with an aryl electrophile (Scheme 9), and is tolerant of a wider range of functionality on the aryl electrophile than previous lithiation routes.[57,58,59] Miyaura found that the catalyst Pd(dppf)Cl_2 generally gave the best results, and the reaction was favoured in polar solvents such as DMSO. Addition of a weak base was necessary to activate the catalyst; the highest yields and selectivities were obtained with KOAc.

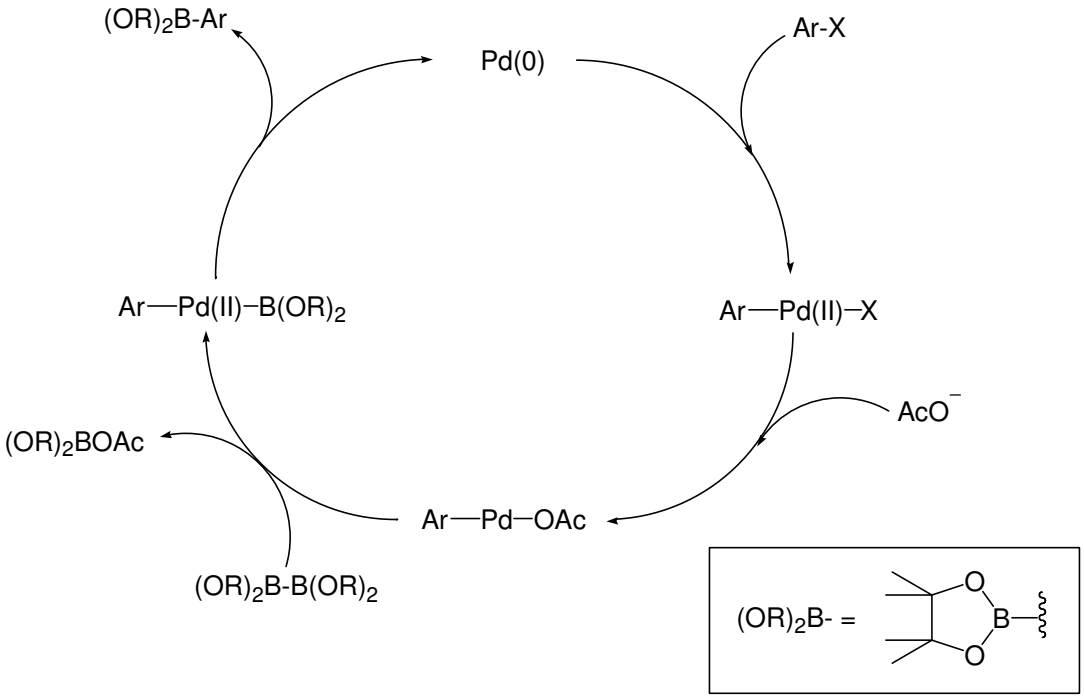

Scheme 9: Miyaura cross-coupling catalytic cycle for formation of aryl boronic esters.[51]

1,3-Dimethyl-4,6-(4,4,5,5-tetramethyl-1,3,2-dioxaborolan-2-yl)benzene (Me_2pin_2) and 1,3-difluoro-4,6-(4,4,5,5-tetramethyl-1,3,2-dioxaborolan-2-yl)benzene (F_2pin_2) were prepared from their dibromo-precursors and bispinacolatodiboron (B_2pin_2) using the Miyaura cross-coupling route. Pd(dppf)Cl_2 was used as catalyst, KOAc was added as the base and the solvent was dry DMSO. *Dry* DMSO was found to be essential – excessive homocoupling was observed when laboratory grade DMSO was initially used. Reactions were heated at 80˚C for 12 h under a nitrogen atmosphere.[60,61] The products

were purified via column chromatography and were obtained in high yield (69 – 86%). This method was tolerant of fluorine atoms on the aryl ring. The incorporation of this route into the total synthesis of the dipyridylbenzene ligands has led to increased chemical versatility and allowed greater functionalisation of such systems.

2-Bromo-4-dimethylaminopyridine

2-Bromo-4-dimethylaminopyridine was prepared via a two step process: ortho-directed lithiation of 4-dimethylamino pyridine, followed by reaction with CBr_4 and purification by column chromatography.[62] This was reacted with F_2pin_2 via Suzuki-Miyaura cross-coupling, to give 1,3-di(4-dimethylamino-2-pyridyl)-4,6-difluorobenzene, HL^{17}, in modest yield (51%). It has since been found that 2-bromo-4-methoxypyridine can also be prepared this way from 4-methoxypyridine, avoiding the initial lengthy synthesis of 2-bromo-4-methoxypyridine presented in Scheme 8.

2.2.3 Synthesis of a Tetradentate Ligand

For reasons that will be discussed in Chapter 5, it was of interest to prepare a dipyridylbenzene ligand appended with a fourth ligating group, to occupy the fourth coordination site of Pt (II). A phenolic appendage was proposed, and ligand HL^{23} was targeted. Selective ortho-lithiation of anisole was achieved by metallating in the presence of an ortho-directing group, tetramethylethylene diamine (TMEDA).[63,64] The substitution of an aryl-lithium species into the ortho-position of a pyridyl system is well represented in the literature,[65,66] for example, Che et al. have reported on the synthesis of a system related to the targeted molecule, that involves 2-lithioanisole coupling with C^6 of bipy (i.e. position next to the nitrogen).[67] This method was used successfully in the preparation of ligand HL^{23} (Scheme 10).

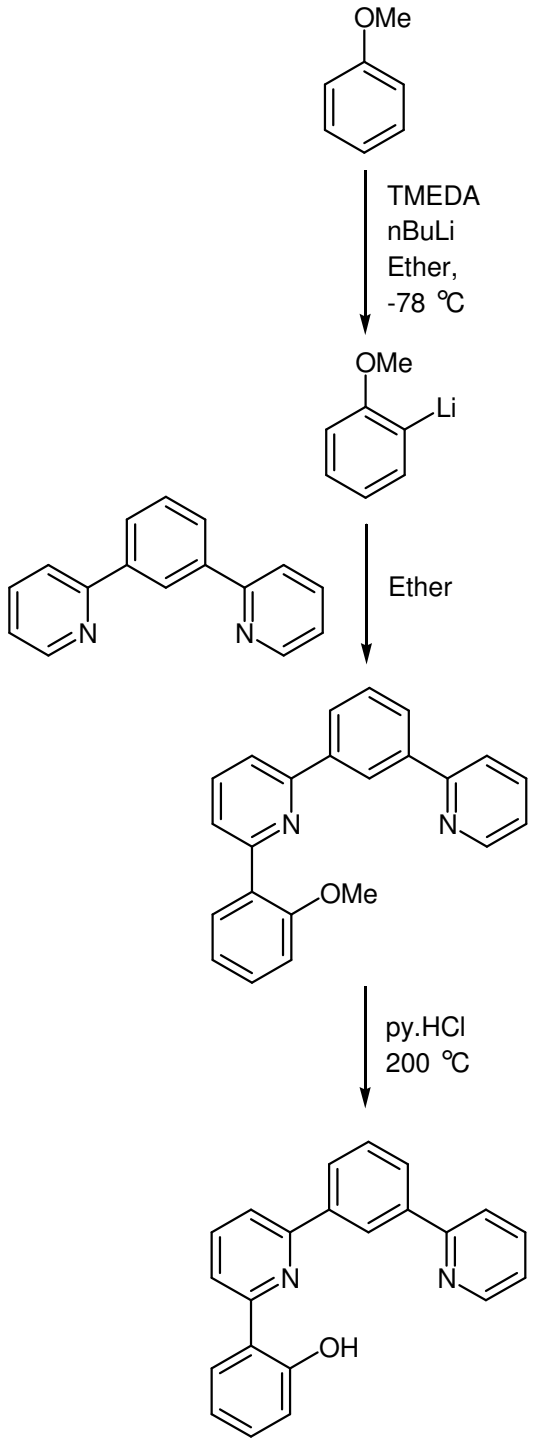

Scheme 10: The synthetic route to HL[23].

2.2.4 Fluorination at the 4-Pyridyl Position

The platinum(II) complex containing ligand HL[19] was a desirable target, for reasons discussed in Chapter 3. Unfortunately neither 4-fluoropyridine nor 2-bromo-4-fluoropyridine are commercially available. Only one article reporting the synthesis of 2-bromo-4-fluoropyridine could be found.[68] The method involved fluorodenitration of 2-

bromo-4-nitropyridine with tetrabutylammoniumfluoride (TBAF); the former had already been prepared as an intermediate used in the synthesis of HL[15]. This reaction was attempted twice, but the desired product was never isolated. On consultation with a fluorine expert, the authenticity of the reported reaction was brought into question – the expert suggested that a fluorine atom on C-4 of pyridine would make this position extremely electron deficient, and open to attack by the nucleophilic nitrogen of another 4-fluoropyridine. This process would continue, generating polypyridine species (Scheme 11). This is the reason why there are not very many 4-fluoropyridine based molecules in existence.

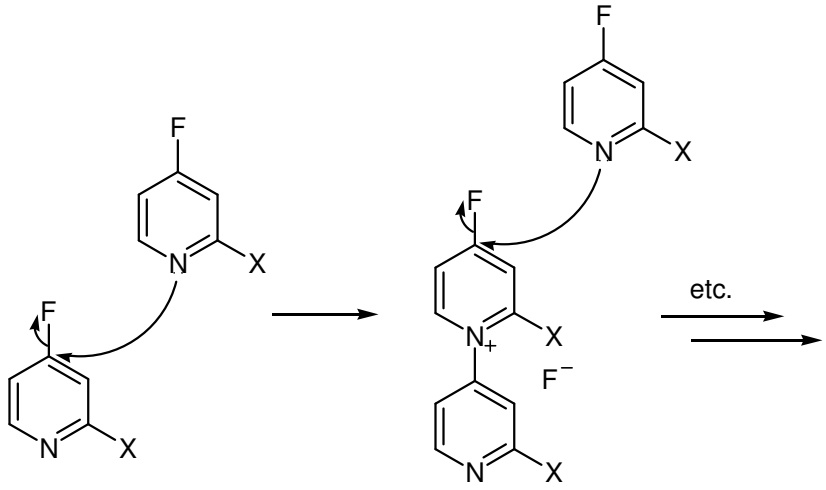

Scheme 11: Stipulated polymerisation reaction between the nucleophilic pyridine lone pair and the electropositive centre at C4.

The expert thought that fluorodenitration of 1,3-di(4-nitro-2-pyridyl)benzene, HL[18],would also lead to an intractable mixture of polymers. However, this synthesis was still attempted. Initially, HL[18] was stirred at room temperature with four equivalents of TBAF in DMF. The reaction did not go to completion – some of the monofluorinated product was detected by NMR. A larger excess of TBAF was required to enforce full conversion. Nevertheless, the ligand, HL[19] was prepared via the fluorodenitration method and was purified by column chromatography.

The reaction was also attempted in DCM. The paper from which the initial procedure was adapted (reference 68) reports DMF to be the solvent of choice, as hydroxydenitration, a competing process is suppressed. Unlike the DMF reaction, fluorodenitration of HL[18] in DCM did not occur at room temperature, however heating at reflux in DCM for 1.5 h gave the desired product without any trace of the side-product. As in the DMF reaction, a large excess of TBAF (~ 4 equiv.) was required to

drive the reaction to completion. The DMF based reaction was lower yielding, possibly due to the difficulty of extracting the product from the DMF layer.

2.3 Synthesis of Platinum Complexes

2.3.1 Complexation to Pt (II)

Two solvent systems are commonly used within the group for complexations of the terdentate ligands: 1) glacial acetic acid and 2) acetonitrile/water (3:1), and the general reaction scheme is presented in Scheme 12.[18,19] Both systems involve heating at 120˚C under nitrogen for 3 days, and give complexes in comparable yield. Where possible, ligands were complexed with K_2PtCl_4 in glacial acetic acid. The acetonitrile/water system requires the aqueous solution of K_2PtCl_4 to be degassed separately from the solution of ligand in acetonitrile. However, this solvent system proves invaluable when ligands containing acid sensitive groups required complexation, such as HL^{17}. During complexation, most complexes were observed to precipitate out of solution as bright yellow or orange solids; the process is further facilitated by cooling prior to the work-up. The complexes generally had low solubility, and the work-up involved a series of washings to remove any uncomplexed ligand and K_2PtCl_4.

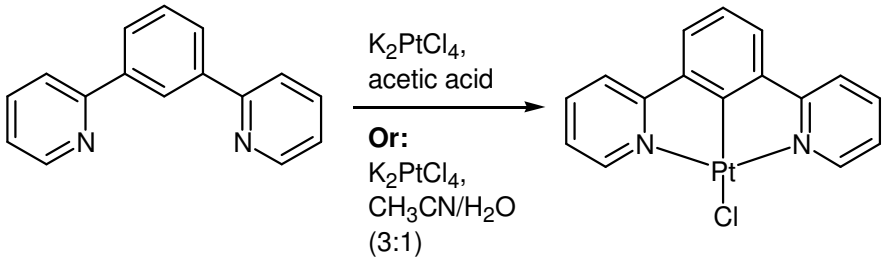

Scheme 12: Complexation of the terdentate ligand to Pt (II).

With the exception of ligands HL^4 and HL^{19}, complexation of the ligands via these routes succeeded, giving yields ranging from 32 to 81%, and mostly towards the higher end. Ligands HL^8, HL^{12} and HL^{13} underwent lower yielding complexations (32 – 44%) – these ligands generate complexes that possess unfavourable steric interactions (see Section 2.4.3.1), which must hinder the complexation process.

Complexation of HL^4 did not appear to work – an insoluble brown oil was obtained that could not be characterised. Complexation of HL^{19} led to a mixture of inseparable products – ^1H NMR indicated that a complexation had occurred, (^{195}Pt satellites were observed around some of the peaks), but the pyridyl proton J-values were much smaller than found in the ligand, indicating that the fluorine atoms had been replaced. Also, the molecular ion peak for the desired complex was absent from the ASAP mass spectrum, further suggesting decomposition of the ligand had occurred upon complexation. Complexation of this ligand failed with both solvent systems – this indicates that the fluorine-carbon bond must be relatively labile in HL^{19}.

Initially we thought that complexation of the potentially terdentate ligand HL^{23} in acetic acid would disfavour the necessary deprotonation of the OH group, so the complexation was performed in an acetonitrile/water solvent system. From this reaction we obtained a mixture of low solubility products that could not be separated or identified. The complexation was attempted in acetic acid – this time a complex was formed which was pure by NMR. There was some concern that the complex obtained involved the ligand bound terdentately with an ancillary chloride (Figure 4). Hence, the complex was mixed with silver triflate in acetone and stirred for 2 h (silver has a strong binding affinity for chloride). Isolation of the product revealed an NMR identical to the precursor, indicating that the non-chlorinated form was initially obtained from the complexation reaction.

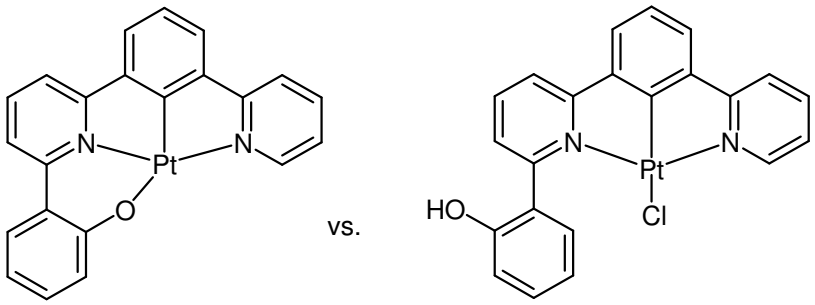

Figure 4: Possible binding modes of L^{23} to Pt (II).

2.3.2 Substitution of the Ancillary Chloride by Other Halides or Cyanide

These reactions proceeded via two steps: removal of the ancillary chloride followed by addition of the new ancillary ligand. Silver has a high affinity for chloride, so to remove the chloride, a slight excess of silver triflate was added to a suspension of appropriate

complex in acetone. The mixture was stirred at room temperature for 1-2 h, during which the acetone-ligated containing species dissolved and silver chloride precipitated. Upon removal of the silver chloride via centrifugation, a potassium salt of the new ancillary ligand was added to the acetone solution. Precipitation of the new complex was observed, and after 1-2 h stirring, the precipitate was isolated and washed accordingly.

Solubility of the complex was found to increase on substituting the chloride with a heavier halide ion. On the other hand, the cyanide complexes were much less soluble than their chloro-analogues. The substitution reactions were high yielding (71 – 85%), and the proton NMR indicated that full conversion had occurred.

2.3.3 Oxidation to Pt (IV)

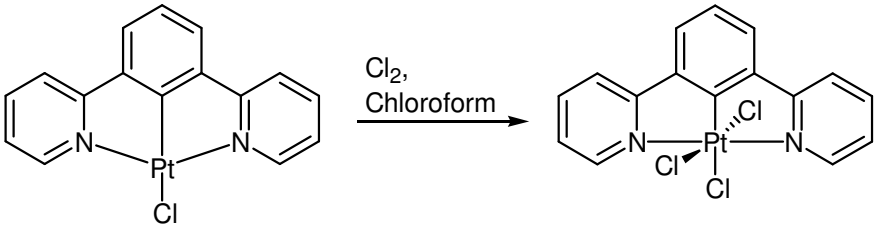

Scheme 13: Oxidation of [PtLCl] to [$PtLCl_3$].

A selection of the Pt (II) complexes ([PtL^2Cl], [PtL^7Cl], [PtL^9Cl], [$PtL^{10}Cl$], and [$PtL^{11}Cl$]) were oxidised to their Pt (IV) analogues, by bubbling chlorine gas through a chloroform solution containing the Pt (II) complex for 30 min – 1 h.[69] The colour of the solution appeared to lighten as soon as chlorine was added. 1H NMR and MS indicated that the oxidations were successful, and had gone to completion. However, photochemical analysis consistently revealed that trace amounts of the Pt (II) precursors still prevailed (Chapter 3, Section 3.5). The Pt (IV) complexes are charge-neutral and consist of the terdentate ligand and three chloride ligands.

2.4 Spectroscopic Characterisation

2.4.1 Characterisation of Ligands and Ligand Precursors

2.4.1.1 NMR

The aromatic region of the proton NMR of the symmetric terdentate ligands was generally straightforward to assign, due to the recurrence of certain trends. Figure 5 shows the generic numbering used for all symmetrical ligands prepared here – the pyridyl groups have been given priority over any substituent to aid comparison.

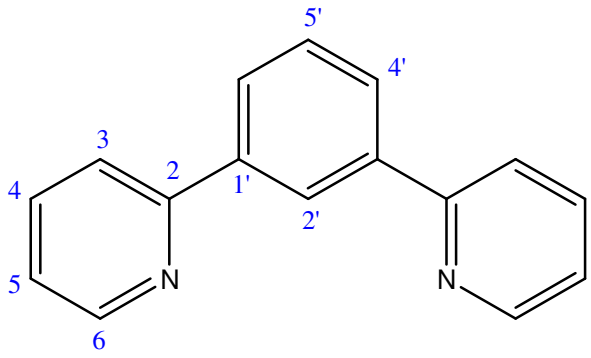

Figure 5: General numbering scheme of the symmetric terdentate ligands.

To describe the patterns observed in the proton NMR of such ligands, it is easiest to start by describing trends observed in the precursors. For example, the proton NMR of 1,3-dibromobenzene consists of two triplets and a doublet at intermediate chemical shift. The triplet of lowest shift corresponds to proton $H_{5'}$ and the triplet of highest shift to $H_{2'}$, which is confirmed by the relative magnitudes of the J-couplings. The doublet occurring at intermediate shift obviously corresponds to $H_{4'}$, with a relative intensity of two protons. In comparison, 1,3-dibromo-4,6-difluorobenzene contains two triplets at higher and lower field only, and again the triplet at lowest chemical shift corresponds to $H_{5'}$. In this molecule, $H_{4'}$ has been replaced by fluorine. These patterns are carried through to the respective terdentate ligands.

Larger ^{3}J- and ^{4}J-values are observed for $H_{5'}$ and $H_{2'}$ respectively when fluorine occupies the $C_{4'}$ positions. This is because fluorine-19 is also a spin-active nucleus (S = ½) and in these particular environments exhibit stronger coupling than protons.[70]

Between non-fluorinated and fluorinated analogues (e.g. HL^1 and HL^2), the ^3J value of $H_{5'}$ typically increases from approximately 9 to 11 Hz. The ^4J value of $H_{2'}$ increases by a greater extent, from about 2 to 9 Hz. The proton-decoupled carbon spectra also show coupling to fluorine – for example, the ^1J-coupling with $C_{4'}$, of approximately 250 Hz.

2-Tri-n-butylstannylpyridine and 2-bromopyridine proton NMR spectra show a consistent trend of peak ordering, regardless of any additional substituent. H_5 always occurs at the lowest shift, and H_6 always occurs at the highest shift, with H_3 and H_4 peaks occurring somewhere in-between. This trend was carried through to the ligand (Figure 6), where COSY spectra and the J-splitting pattern were used to check and confirm the assignments. In addition, the proton NMR of tri-n-butylstannyl pyridine species showed satellites around the H_3 signal. Tin has three spin ½ nuclei (^{115}Sn, ^{117}Sn and ^{119}Sn) hence the satellites arise through ^3J coupling to tin.

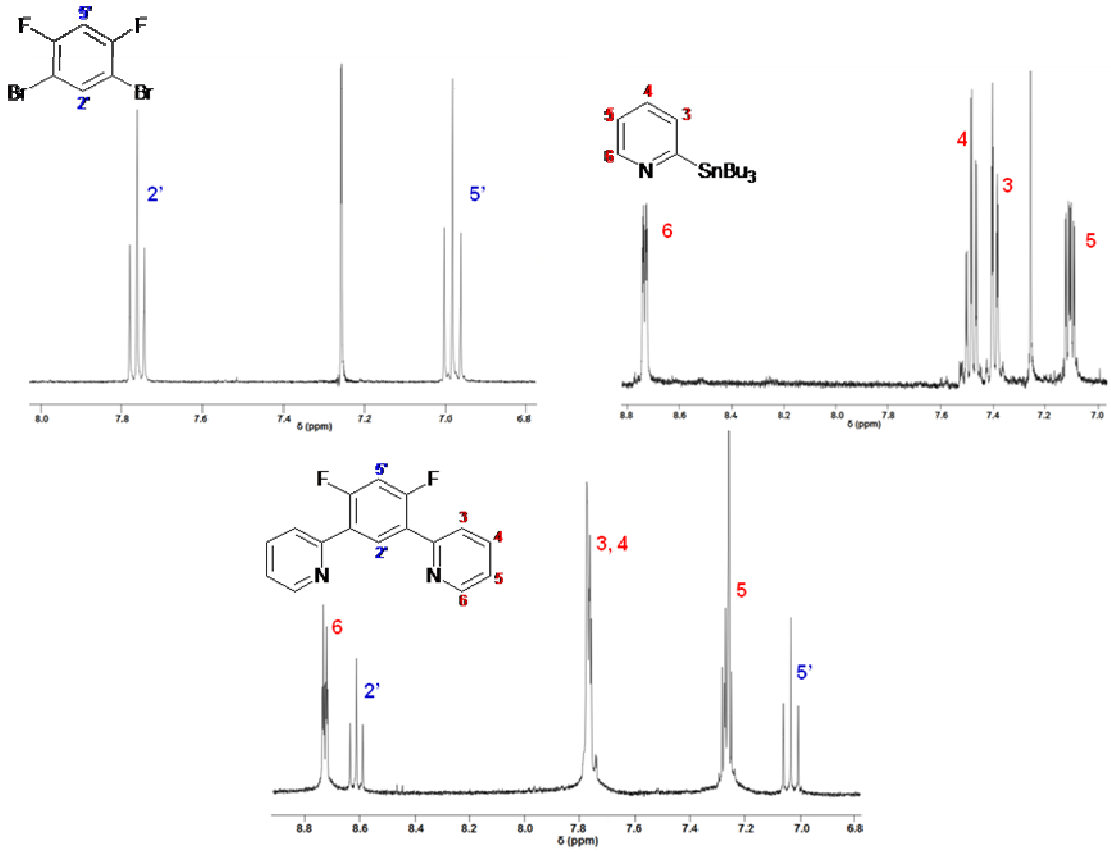

Figure 6: TOP: ^1H NMRs of ligand precursors, 1,3-dibromo-4,6-difluorobenzene (left), and 2-tri-n-butylstannyl pyridine (right), BOTTOM: ^1H NMR of the resultant terdentate ligand, 1,3-di(2-pyridyl)-4,6-difluorobenzene (spectra were acquired in $CDCl_3$ at 400 MHz).

For ligands containing a 3',5'-difluorinated central ring, a signal around −113 ppm occurred in the ^{19}F spectrum. The fluorine atoms couple to both $H_{2'}$ (^4J) and $H_{5'}$ (^3J), so strictly, the peak should be assigned as a doublet of doublets. However, the magnitude

of the ^{4}J and ^{3}J couplings are so similar, that this peak appeared as a triplet with a J-splitting of between 9 and 10 Hz, for all fluorinated ligands.

2.4.1.2 Mass Spectrometry

Electrospray-positive mass spectrometry was used to confirm the molecular weight of the ligands. Protonated and sodium-bound ions were typically observed in the mass spectra. This method is a relatively soft ionisation technique (compared to electron impact, EI, mass spectrometry for example), and as a consequence, fragmentation of the molecular ion was hardly ever observed. In most cases, the $[M+H^{+}]$ peak had an intensity of 100%.

2.4.2 Characterisation of Complexes

2.4.2.1 NMR

The numbering scheme used for the complexes is slightly different to that of the ligand (Figure 7). Here, the platinum-bound carbon is given the priority.

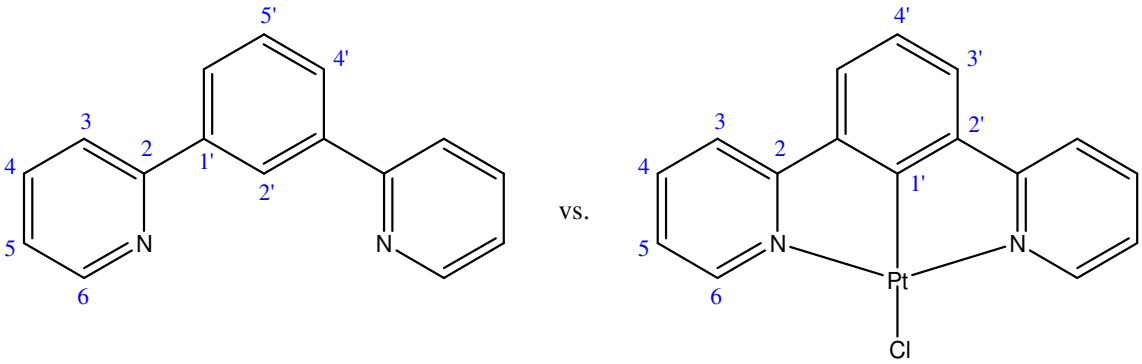

Figure 7: Comparison of the numbering schemes used with the ligands and the complexes.

Proton NMR spectra of the Pt (II) complexes display some significant differences (Figure 8) compared to the free ligand spectra. There is always one less signal in the aromatic region of a Pt (II) complex NMR – $H_{2'}$ of the ligand is lost upon cyclometallation. Secondly, well-resolved ^{195}Pt satellites are observed around the signal

of H_6 ($^3J \approx 40$ Hz). Other more subtle differences upon complexation include the signal due to H_6 moving to higher shift (by approximately 0.5 ppm), and the signal due to $H_{4'}$ (i.e. $H_{5'}$ in the ligand) moving to lower shift (by approximately 0.5 ppm). The latter effect is due to increased shielding within the phenyl ring, which is brought about by an increase in electron density upon cyclometallation, and is consistent with results reported for similar systems.[19] H_5 stays at approximately the same position, and H_3 and H_4 are sometimes observed to change their relative positions.

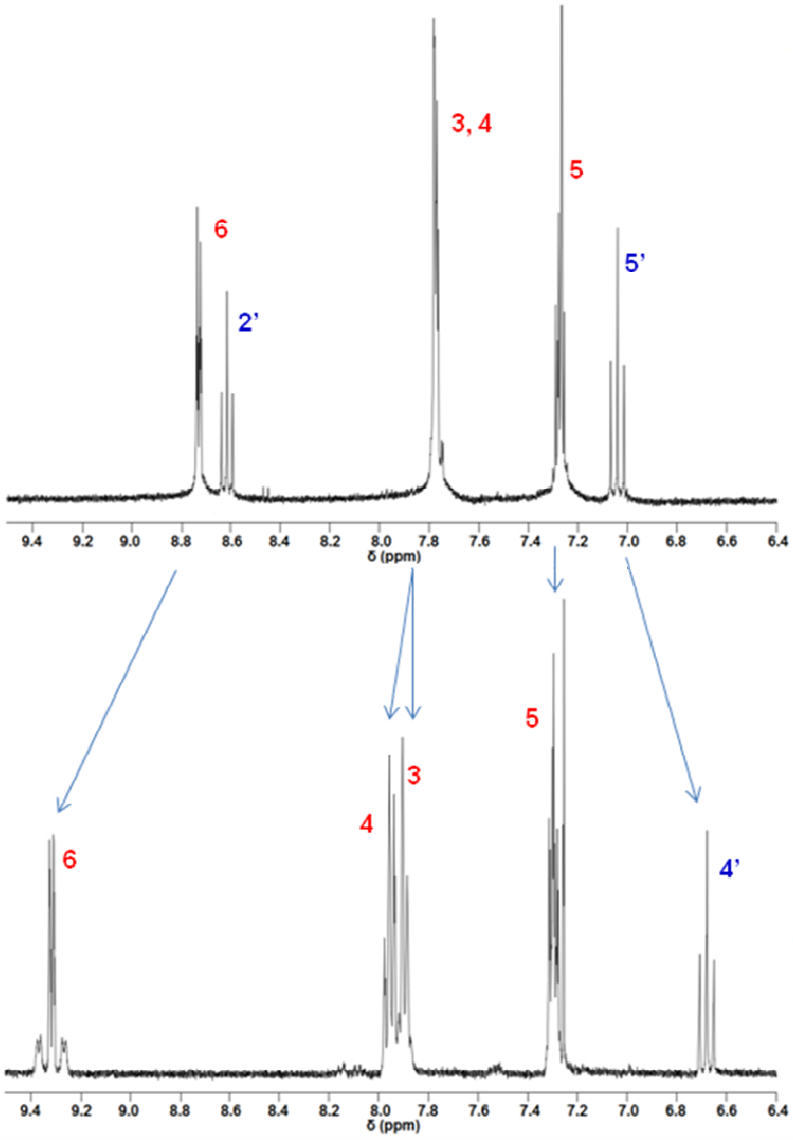

Figure 8: TOP: ^{1}H NMR of the ligand, 1,3-di(2-pyridyl)-4,6-difluorobenzene (HL^2) and BOTTOM: ^{1}H NMR of the corresponding complex, [PtL^2Cl]. The spectra are plotted on the same scale to aid visualisation of the relative shifts of peaks between ligand and complex. Notice the ^{195}Pt satellites observed around the peak corresponding to H_6 in the complex (spectra were acquired in $CDCl_3$ at 400 MHz).

The fluorine spectra also differ between complex and ligand – complexes containing a symmetrical ligand incorporating a 3,5-difluorinated phenyl ring show a doublet around

⁻110 ppm that is often accompanied by $^{4}J(^{195}Pt)$ satellites (Figure 9b). The doublet splitting corresponds to ^{3}J coupling of the ^{19}F atom with $H_{4'}$. The slight increase in chemical shift indicates that the fluorine atoms become more deshielded upon cyclometallation. The fluorine NMR spectrum of [PtL^{9}Cl] is vastly different from all other complexes (Figure 9c) – here, a broad multiplet is observed at much higher field (-92 ppm). In this complex, there is a steric interaction between the fluorine atoms and the methyl hydrogens. The close proximity of these atoms results in a non-bonding orbital overlap, which decreases the shielding around fluorine. Such through-space interactions are commonly observed in polycyclic arenes containing fluorine atoms and protons in close proximity.[71] The observed peak is broad because the fluorine experiences some coupling interaction with the methyl protons via the through space interaction. This was confirmed by performing a proton-decoupled ^{19}F NMR, which revealed only a singlet peak, accompanied by $^{4}J(^{195}Pt)$ satellites (Figure 9d).

a)

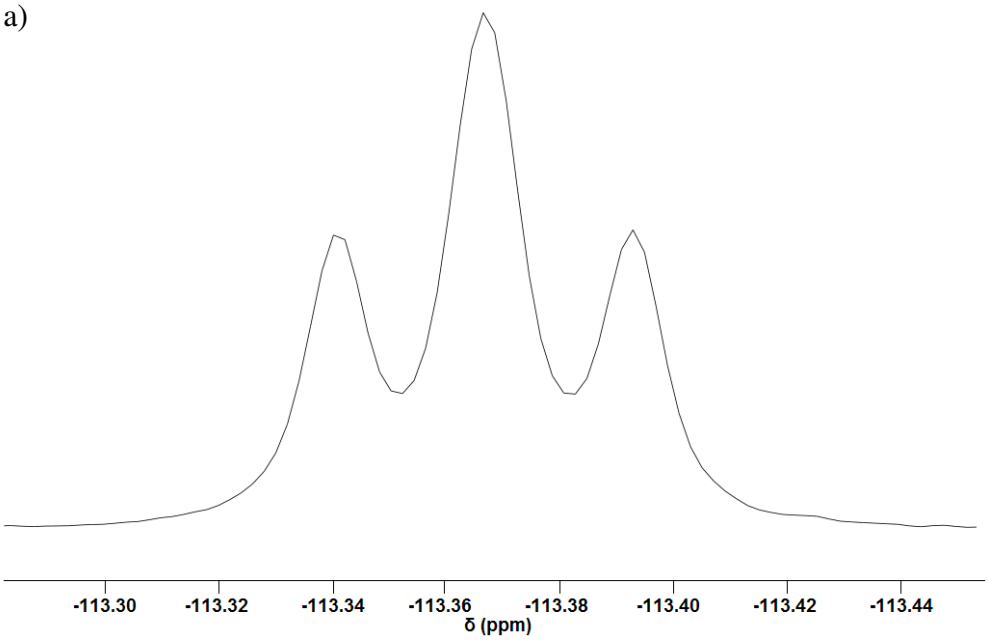
-113.30
-113.32
-113.34
-113.36
-113.38
-113.40
-113.42
-113.44
δ (ppm)

b)

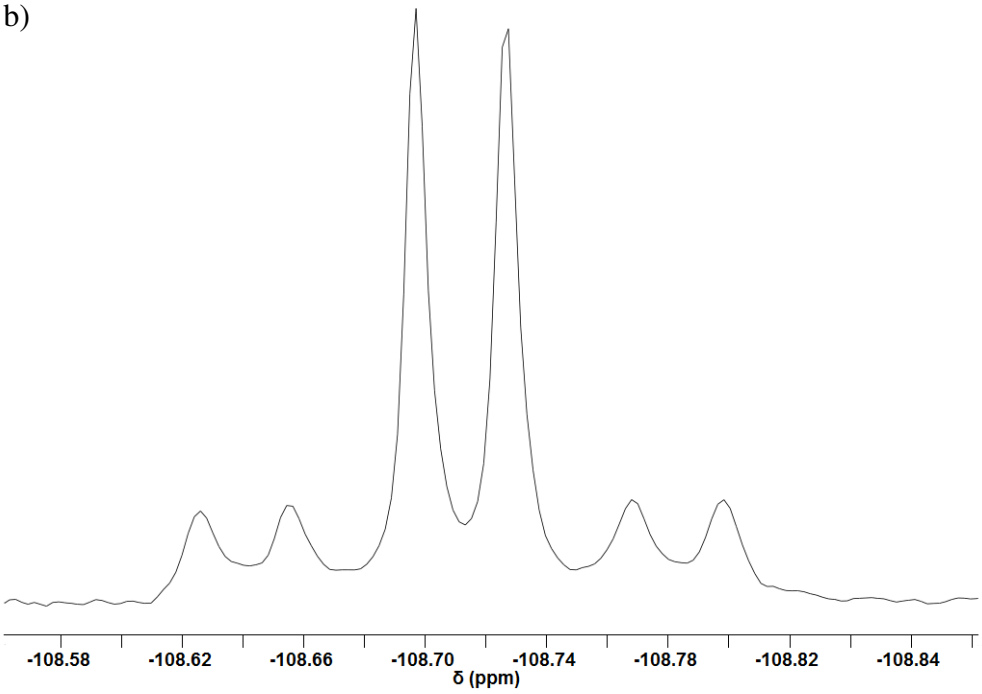
-108.58
-108.62
-108.66
-108.70
-108.74
-108.78
-108.82
-108.84
δ (ppm)

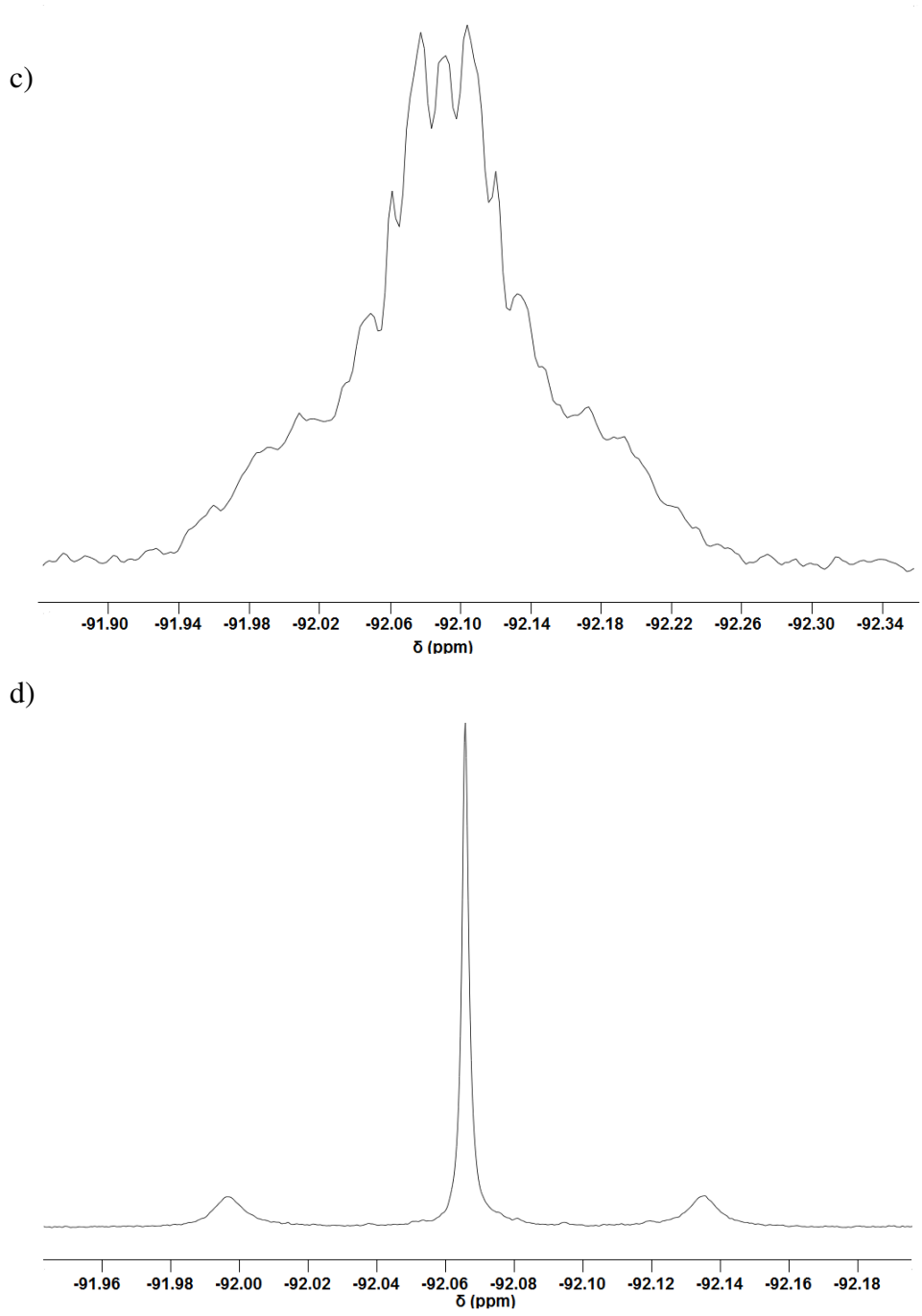

Figure 9: ^{19}F NMR spectra of some representative species. a) ^{19}F NMR spectrum of HL^2, b) ^{19}F spectrum of $[PtL^2Cl]$, c) ^{19}F spectrum of $[PtL^9Cl]$ and d) Proton-decoupled ^{19}F NMR spectrum of $[PtL^9Cl]$ (spectra a) and b) were acquired in $CDCl_3$ at 376 MHz, and spectra c) and d) were acquired in $CDCl_3$ at 470 MHz).

Changing the ancillary ligand led to subtle changes in the proton NMR. For example, substitution of the chloro ancillary ligand by cyanide results in a shift of all aromatic protons to lower chemical shift. This indicates that all aromatic protons are becoming increasingly shielded (cyanide is a better σ-donor than chloride).

For the halogenated series of [PtL^{1}X], the signal due to H_6 shifts to higher field as the size of the halogen increases (Figure 10). Otherwise, all other proton signals occur at very similar chemical shifts.

Complex:	[PtL^{1}I]	[PtL^{1}Br]	[PtL^{1}Cl]
δ of H_6 / ppm:	9.89	9.56	9.31

Increasing Chemical Shift

Figure 10: Chemical shifts of proton H_6 from the series [PtL^{1}X].

For the Pt (IV) complexes, all of the aromatic proton resonances of the ligand occurred at higher chemical shift than for the respective Pt (II) complexes. This is consistent with the increasing positive charge on platinum, reducing electron density on the ligand. The ^{195}Pt satellites around H_6 show smaller J-coupling (^{3}J ~ 20 – 25 Hz), indicative of a poorer overlap with the contracted orbitals of the Pt (IV) centre. For 3,5-difluorinated Pt (IV) complexes, the signals in the ^{19}F spectra occur at higher chemical shift than the Pt (II) analogues (approximately $^-$104 ppm) in line with the increasing positive charge. Analogous to [PtL^{9}Cl], the fluorine signal of [PtL^{9}Cl$_3$] is broad due to a non-bonding orbital overlap with the methyl protons, and occurs at a higher chemical shift ($^-$86.5 ppm) than all other fluorinated Pt (IV) ^{19}F signals.

2.4.2.2 Mass Spectrometry

Electrospray positive ion mass spectrometry does not work for most of the complexes produced here. Unlike the ligands, most of the complexes do not contain any available sites for protonation. Different ionisation techniques were sought to characterise the complexes. Electron ionisation (EI) mass spectrometry had been successfully used by previous group members to characterise related complexes. Unfortunately, the EI service used by the group was the Swansea-based EPSRC service, and only a limited number of samples could be sent per month.

Matrix assisted laser desorption ionisation (MALDI) mass spectrometry was investigated – most complexes were at least sparingly soluble in chloroform. Compared to EI, MALDI is a soft ionisation technique, and is often used to characterise polymers and biomolecules. In the MALDI experiment, the complexes were mixed with a UV-

absorbing compound, trans-2-[3,4-tert-butylphenyl]-2-methyl-2-propenylidene]malonitrile (dctb) and placed in a vacuum chamber. On applying a vacuum, all of the solvent evaporates, leaving behind the sample within a "matrix" of the UV-absorbing chromophore. The chromophore is excited with a laser, and passes some of the excess energy to the complex, forming charged species. Low resolution MALDI mass spectrometry gave mass peaks corresponding to the whole complex. Unfortunately, in the high resolution experiment, the mass that was detected corresponded to the complex minus the ancillary ligand, which hindered full characterisation of complexes resulting from ancillary ligand substitution. A low intensity peak at [2M-Cl] is also commonly observed, which corresponds to a chlorobridged dimer. It is unclear whether this species forms during the MALDI experiment, or whether such species form during complexation – perhaps this is an intermediate during cyclometallation.

A new technique, atmospheric solids analysis probe (ASAP) mass spectrometry has recently arrived in the department. ASAP uses an ambient ionization method, and can analyse a large array of substrates, including non-polar, high-melting point solids. This technique involves an atmospheric pressure ionization technique, where a hot desolvation gas is used to vaporise the sample, and the technique is ideally suited to analysis of the complexes. The complexes were input directly as solids, and the high resolution experiment returned peaks corresponding to the molecular ion and the molecular ion-minus-ancillary ligand. Sometimes however, the molecular ion peak is very weak, and the signal-to-noise ratio prevents accurate determination of this mass. When this was the case, the stronger peak corresponding to M – X (where X = ancillary ligand) has been reported. Furthermore, some of the masses reported correspond to the protonated molecule (e.g. $[M+H^+]$ was observed for $[PtL^{11}Cl]$). Such species often appear in ASAP experiments, and result from proton transfer from ionised water clusters present in the source.[72] Using ASAP mass spectrometry, it was possible to confirm and fully characterise the cyano-substituted and bromo-substituted complexes ($[PtL^2CN]$, $[PtL^{15}CN]$, $[PtL^{17}CN]$, and $[PtL^1Br]$).

ASAP mass spectrometry was employed to confirm the identity of $[PtL^{23}]$. Under standard operating conditions, the experiment always returned an isotopic envelope containing a mixture of peaks from the radical cation and the protonated molecule. In an attempt to see peaks corresponding to the molecular ion only, the ASAP experiment was carried out using a *dry* calibration source. Usually, a lock spray of methanol/water,

is employed. The spray contains a selection of molecules of known accurate mass, so that the experiment can be calibrated. In the dry experiment, heptacosa, $(C_4F_9)CN$, was used for calibration. This time, protonation did not occur, and a mass and isotope pattern that fit nicely with the theoretically predicted pattern for the radical cation was found. This further demonstrates that the ASAP experiment can be sensitive to moisture.[72]

The Pt(IV) complexes were characterised by ASAP mass spectrometry – peaks corresponding to the subsequent loss of chlorine could be observed in the spectrum. Whilst analysing these peaks, it was noticed that the isotope pattern did not always occur as expected. For example, for Pt(IV) complexes that contained a 3',5'-difluorinated aryl ring, peaks corresponding to [M-Cl] and [M-3Cl] did not give a good fit to the expected isotope patterns of the predicted radical cations – the observed envelope of peaks were one mass unit less than predicted. Instead, the experimental pattern gave a good fit to the expected radical minus a hydride ion (i.e. [(M-Cl)-H]. On the contrary, peaks corresponding to [M] and [M-2Cl] did give isotope patterns matching those predicted for the respective radical cation. The story gets more bizarre on considering the non-fluorinated Pt(IV) complex, $[PtL^7Cl_3]$ – this complex behaved completely differently during the mass spectrometry experiment. Here, the envelope patterns of peaks corresponding to [M] and [M-2Cl] fit well with the theoretical pattern for "$[M+H]^+$", whereas peaks corresponding to [M-Cl] and [M-3Cl] gave isotope patterns that fitted nicely with the theoretical patterns of the radical cations. As already mentioned, protonated species are often observed in the ASAP experiment, especially if the sample is slightly wet. However, here, the protonation was not consistent for all peaks observed in the same experiment. The ASAP experiment is still quite new, so the reason behind this odd behaviour cannot be explained at present. The mass spectrometry team at Durham who discovered this effect plan to undertake further investigations to understand why this occurs.

2.4.3 Crystal Structures

2.4.3.1 Crystal Structures of Pt (II) Complexes

Some of the complexes were successfully crystallised via slow evaporation of solvent – complex [PtL^2Cl] was obtained from a $CH_3CN/DCM/H_2O$ mix (1:1:1), [PtL^7Cl] was obtained from $CDCl_3$, [$PtL^{12}Cl$] was obtained from DMSO, [$PtL^{13}Cl$] was obtained from a DCM/EtOAc mix (1:1), and all other crystals of Pt (II) complexes were obtained from DCM. Important bond lengths/angles are given in Table 2 (note: complete crystal data are given in Appendix 1). X-ray diffraction studies confirm the expected N^C^N terdentate coordination, with binding of the anticipated ancillary ligand trans to the cyclometallating carbon. Crystal structures for complexes [PtL^9Cl], [$PtL^{10}Cl$], [PtL^1Br] and [PtL^1I] reveal that these molecules lie on a crystallographic 2-fold axis that passes through the metal ion, the chloride ligand and the cyclometallating carbon. The crystal structure of the substituted parent, [PtL^1Cl], which has been reported by Cárdenas et al. also displays this behaviour.[17] All other complexes involve a slight deviation from the ideal C_{2v} symmetry, as exemplified by the differing N-Pt-Cl and C-Pt-N bond angles within each complex. A similar observation was made on the structure of [PtL^7Cl] by Suzuki et al.[8]

In most cases, the metal centre, the three coordinating rings and the ancillary ligand are approximately co-planar, with C-Pt-ancillary bond angles approaching 180˚ {[$PtL^{12}Cl$] does not conform to this and will be discussed separately}. However, the N-Pt-N bond angles are distorted from linearity (but within the plane of the molecule), with angles approaching 160˚, and it is best to describe the Pt (II) centre as existing in a distorted square planar geometry. This distortion reflects the less-than-optimum bite angle imposed by the terdentate ligand. Similar distortions are also found in Pt (II) trpy complexes, which involve similar 5-membered chelations.[8,17,73,74] In the 1,3-dipyridylbenzene complexes, the Pt-C and Pt-N bond lengths are approximately 1.91 Å and 2.03 Å respectively. These bonds are much shorter than corresponding bonds in related 6-phenyl-2,2'-bipyridine complexes (where Pt-C and Pt-N are approximately 2.04 Å and 2.14 Å),[19] reflecting the greater degree of orbital overlap, which results in the enhanced ligand field induced by N^C^N coordination.

Table 2: Selected bond lengths (Å) and angles (deg) of the Pt (II) complexes (All structures were acquired at 120 K).

	[PtL^{2}Cl]	**[PtL^{9}Cl]**	**[PtL^{10}Cl]**	**[PtL^{11}Cl]**	**[PtL^{12}Cl]**
Pt-C$^{1'}$	1.917(4)	1.910(3)	1.909(9)	1.916(5)	1.910(5)
Pt-Cl	2.3908(12)	2.4116(8)	2.397(2)	2.3923(12)	2.4259(13)
Pt-N	2.029(4) and 2.030(4)	2.017(2)	2.027(5)	2.021(4) and 2.028(4)	2.064(4) and 2.067(4)
C$^{1'}$-Pt-Cl	178.08(13)	180.0	180.000(1)	179.61(15)	155.61(16)
N-Pt-N	162.00(15)	163.44(12)	161.9(3)	162.05(17)	160.78(17)
N-Pt-Cl	98.96(10) and 99.04(11)	98.28(6)	99.04(14)	98.72(12) and 99.23(12)	101.62(13) and 97.49(12)
C$^{1'}$-Pt-N	81.16(16) and 80.85(17)	81.72(6)	80.96(15)	80.92(19) and 81.14(19)	81.1(2) and 80.70(19)

	[PtL^{7}Cl]	**[PtL^{13}Cl]**	**[PtL^{22}Cl]**	**[PtL^{1}I]**	**[PtL^{1}Br]**
Pt-C$^{1'}$	1.911(7)	1.934(8)	1.895(7)	1.914(7)	1.893(6)
Pt-X	2.4171(15)	2.406(2)	2.3960(18)	2.7041(5)	2.5385(7)
Pt-N	2.034(5) and 2.051(5)	2.010(7) and 2.034(7)	2.023(6) and 2.022(6)	2.049(4)	2.034(4)
C$^{1'}$-Pt-X	177.2(2)	173.4(2)	177.6(2)	180.0	180.000(1)
N-Pt-N	162.2(2)	162.0(3)	161.4(2)	160.4(2)	161.5(2)
N-Pt-X	97.22(16) and 100.56(16)	98.2(2) and 99.76(19)	99.41(17) and 99.17(18)	99.81(12)	99.27(10)
C$^{1'}$-Pt-N	80.7(3) and 81.5(3)	81.0(3) and 81.1(3)	80.5(3) and 81.0(3)	80.19(12)	80.73(10)

In the [PtL^{1}X] series, the length of the Pt-X bond increases in the order:

$$I > Br > Cl$$

This simply reflects the increase in size of halogen upon descending group 17.

Complexes Displaying Significant Structural Deviations

[PtL^{12}Cl]

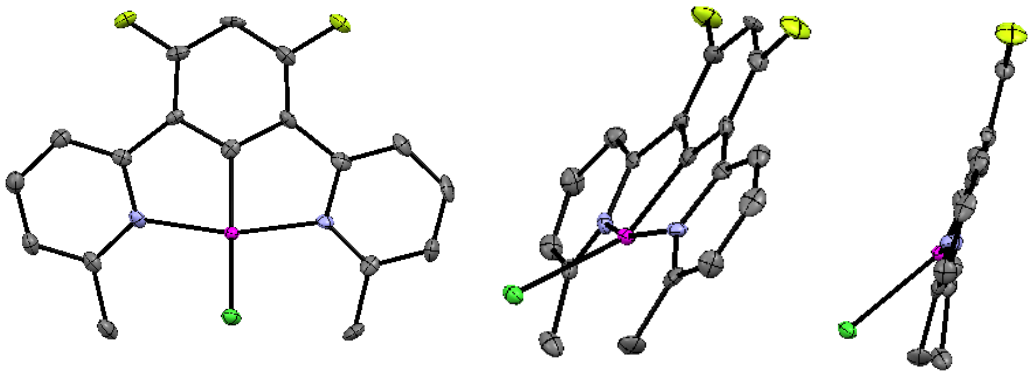

Figure 11: Molecular structure of [PtL^{12}Cl] viewed at various orientations, with displacement ellipsoids at the 50% level. Selected bond lengths (Å) and angles (deg): Pt-C 1.910(5), Pt-N 2.064(5) and 2.067(4), Pt-Cl 2.4259(13), N-Pt-N 160.61(16), C-Pt-Cl 155.61(16).

ORTEP diagrams for this complex at various orientations are shown in Figure 11 along with relevant bond lengths/angles. In [PtL^{1}Cl] and most of the Pt (II) complexes characterised by X-ray diffraction here, C-Pt-Cl bond angles are approximately 180˚, and the atoms lie within the plane of the molecule. In [PtL^{12}Cl], the Pt-N-Cl bond angle significantly deviates from linearity (155.61(16)˚), and the Pt-Cl bond protrudes from the plane encompassing the rest of the molecule. The deviation arises due to unfavourable steric interactions between the chloride and the methyl groups on the 6-pyridyl position. Other, more subtle deviations such as elongation of the Pt-N bonds and contraction of the N-Pt-N angle also result from the unfavourable sterics (see Table 2). The Pt-N bonds in this complex are 2.064(4) and 2.067(4) Å, whereas these bonds are typically 2.03 Å in less hindered systems such as [PtL^{1}Cl] and [PtL^{2}Cl].

Table 3: Distance (Å) of the halide, X, from the plane calculated through the two pyridyl nitrogens and the cyclometallating carbon.

	Distance of X from N^C^N Plane / Å
[PtL^{1}Cl]	0.036
[PtL^{1}Br]	0
[PtL^{1}I]	0
[PtL^{2}Cl]	0.114
[PtL^{7}Cl]	0.057
[PtL^{9}Cl]	0
[PtL^{10}Cl]	0
[PtL^{11}Cl]	0.001
[PtL^{12}Cl]	1.274
[PtL^{13}Cl]	0.366
[PtL^{22}Cl]	0.147

Another way of assessing this deviation is to consider the distance of the chloride atom from a plane calculated through the two pyridyl nitrogen atoms and the cyclometallating carbon (Table 3). For most of the complexes, the chloride lies approximately co-planar with this calculated plane. However, for [PtL^{12}Cl], the chloride lies 1.3 Å above the plane.

[PtL^{13}Cl]

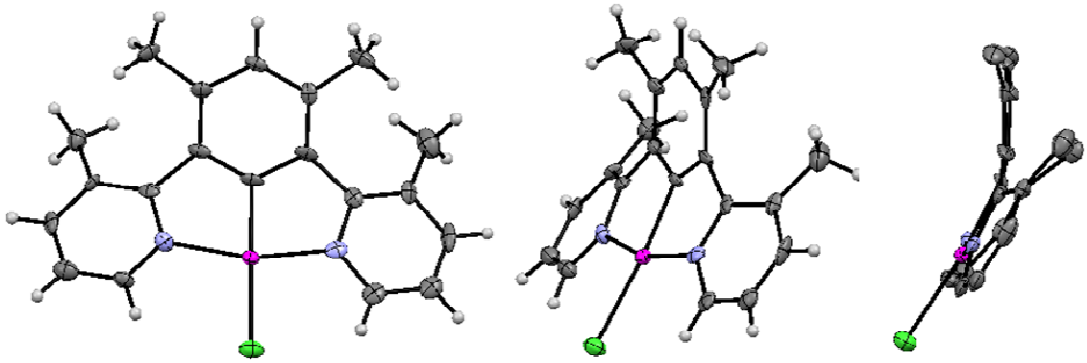

Figure 12: Molecular structure of [PtL^{13}Cl] viewed at various orientations, with displacement ellipsoids at the 50% level. Selected bond lengths (Å) and angles (deg): Pt-C 1.934(8), Pt-N 2.010(7) and 2.034(7), Pt-Cl 2.406(2), N-Pt-N 162.0(3), C-Pt-Cl 173.4(2).

ORTEP diagrams for this complex at various orientations are shown in Figure 12. Significant steric repulsions between neighbouring phenyl and pyridyl methyl-groups cause the terdentate ligand to adopt a non-planar configuration within this complex (note, however, that the platinum coordination plane is approximately planar). To quantify this effect, angles between planes of the phenyl and pyridyl rings were examined (Table 4). These values give an indication of the degree of distortion present in each complex – for a truly planar complex, angles between the planes of the aromatic rings should be zero, and a larger angle therefore indicates a greater deviation from planarity. Most of the complexes show only slight deviations from planarity (angles between planes ~ 0 – 5˚). However in [PtL^{13}Cl], large angles exist between the planes (~ 30˚), highlighting the severely distorted geometry.

Table 4: Calculated angles (deg) between planes formed by the aromatic rings.

	Phenyl-Pyridyl 1 (sd)	Phenyl-Pyridyl 2 (sd)	Pyridyl-Pyridyl (sd)
[PtL^{2}Cl]	1.9(0.3)	-0.4(0.3)	0.4(0.3)
[PtL^{9}Cl]	3.6(0.2)	-3.6(0.2)	0
[PtL^{10}Cl]	0.9(0)	-0.9(0)	0
[PtL^{11}Cl]	2.6(0.2)	-1.8(0.2)	1.3(0.2)
[PtL^{12}Cl]	5(0.3)	-0.9(0.3)	5.8(0.3)
[PtL^{13}Cl]	28.7(0.3)	33.9(0.3)	25.6(0.3)
[PtL^{22}Cl]	1.49(0.4)	-5.4(0.4)	4.4(0.4)
[PtL^{1}Br]	0.9(0.4)	-0.9(0.4)	0
[PtL^{1}I]	1.5(0.3)	-1.5(0.3)	0

Note: A difference in sign between the two phenyl-pyridyl interplane angles indicates that the nitrogen atoms of the two pyridyl rings lie on opposite sides of the plane created by the phenyl ring.

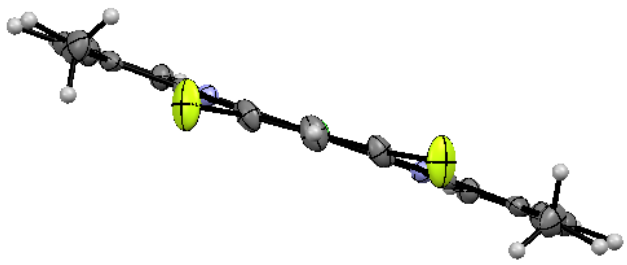

Figure 13: Molecular structure of [PtL^{9}Cl] viewed down the C2-axis.

The effect is much smaller in the related complex, [PtL^{9}Cl]. This complex contains methyl groups in the 3-pyridyl positions, and fluoro-substituents on the 3',5'-phenyl positions. Fluoro substituents are much smaller than methyl, and the calculated angles between the ring planes are much smaller than in [PtL^{13}Cl]. However, the steric interactions between neighbouring phenyl fluorine substituents and pyridyl methyl groups do cause a slight distortion from planarity within the terdentate ligand of [PtL^{9}Cl]. Considering the interplanar angles of the terpyridyl rings (Table 4), the plane

of the phenyl ring is twisted relative that of the co-planar pyridyl rings by 3.6˚. These distortions can be best visualised by looking at the molecule along the phenyl-Pt-Cl axis (Figure 13). One can see that the plane of the central phenyl group is twisted relative to the side pyridyl rings. This distortion occurs to reduce any unfavourable eclipsing of the methyl and fluoro groups.

Crystal Packing

For all complexes (except [PtL^{7}Cl]), the molecules arrange themselves in one-dimensional stacking columns, similar to those reported for [PtL^{1}Cl]. Within each stack, molecules adopt an antiparallel arrangement, effectively cancelling out the dipole moment of the nearest neighbour. The packing of [PtL^{13}Cl] displays a feature which is unique to this complex – it also adopts a columnar packing, but when viewed from above, *pairs* of molecules appear to be making the one-dimensional columns (Figure 14). The difference probably stems from the highly distorted geometry of this complex.

In the crystal packing of [PtL^{7}Cl], molecules form a two-dimensional sheet. This observation has also been made by Suzuki et al.,[8] who suggest that the formation of one-dimensional stacking columns is impeded by methyl groups at the 5-pyridyl positions. This explanation seems unlikely, especially as the difluorinated complex [PtL^{11}Cl], which also contains methyl groups attached to the 5-pyridyl positions, does form one-dimensional stacking columns.

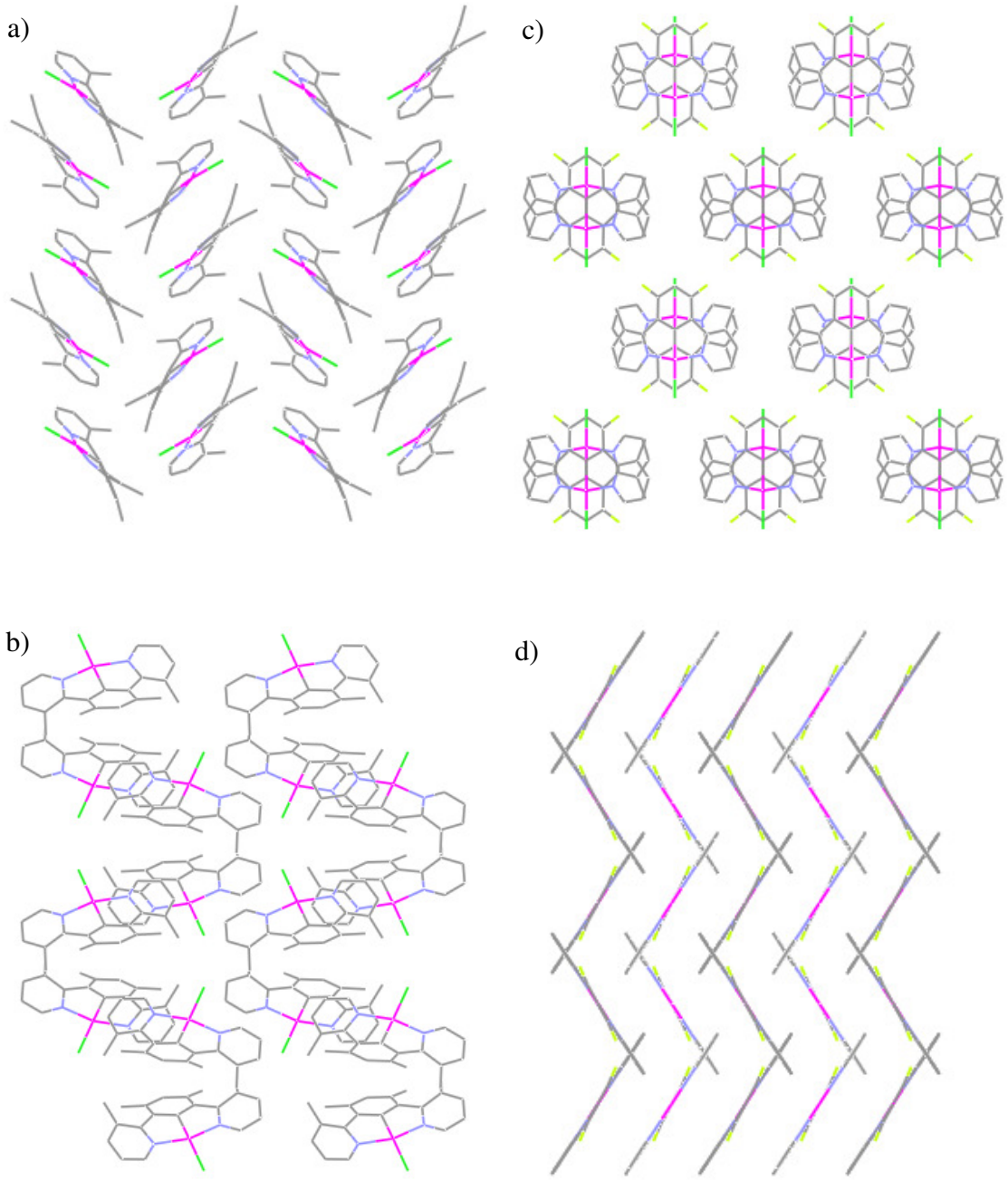

Figure 14: Packing of [PtL^{13}Cl] a) viewed along the a-axis, and b) viewed along the c-axis. Packing of [PtL^{9}Cl] c) viewed along the c-axis and d) viewed along the b-axis.

To estimate whether any significant π-π or Pt-Pt interactions exist in the crystal packing, centroid-to-centroid distances were analysed. Distances of less than 3.7 Å were taken to indicate the presence of such interactions. None of the complexes displayed significant Pt-Pt interactions in their packing, however some did exhibit π-π interactions (see Table 5). Within the chains, the molecules pack in a head-to-tail fashion – hence the phenyl rings in neighbouring molecules are far apart and phenyl-phenyl intermolecular interactions do not occur. Complexes which do not appear in the Table 5 do not contain any significant intermolecular interactions.

Table 5: Pt (II) complexes containing intermolecular π-π interactions, and the distance spanned by the interaction (Å).

	[PtL^{2}Cl] (sd)	[PtL^{7}Cl] (sd)	[PtL^{12}Cl] (sd)	[PtL^{13}Cl] (sd)	[PtL^{22}Cl] (sd)
Phenyl – Phenyl	------	------	------	------	------
Pyridyl – Pyridyl	------	3.570(3)	3.632(3) and 3.519(4)	3.466(7)	------
Phenyl - Pyridyl	3.598(2)	------	------	------	3.613(2)

2.4.3.2 Crystal Structures of Ligands

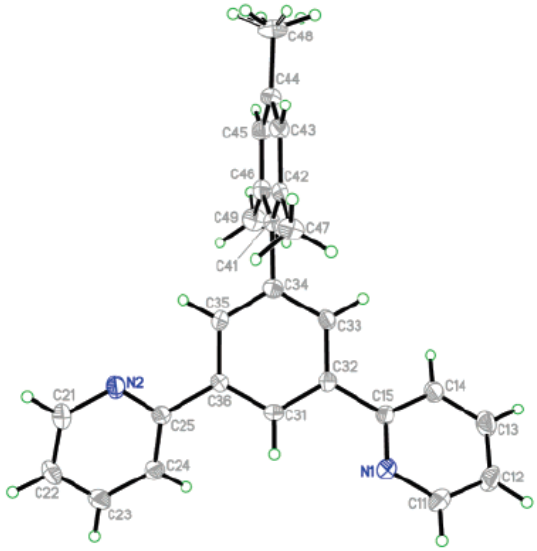

Figure 15: Molecular structure of 5-mesityl-1,3-di(2-pyridyl)benzene at 120 K, with displacement ellipsoids at the 50% level.[19] Note the head-to-tail disposition of the pyridyl rings.

Crystals of ligands HL^2, HL^{11} and HL^{22} have been isolated through slow evaporation of solvent (H_2O/acetone, $CDCl_3$ and $CDCl_3$ respectively). The structures confirm the expected connectivity. Williams et al. have published crystal structures of two related ligands, 1,3,5-tris(2-pyridyl)benzene and 5-mesityl-1,3-di(2-pyridyl)benzene: their structures show a head-to-tail disposition of the pyridyl rings (Figure 15).[19] This configuration may be adopted to reduce any electrostatic interaction between the nitrogen lone pairs. However none of the ligands isolated here adopt this arrangement.

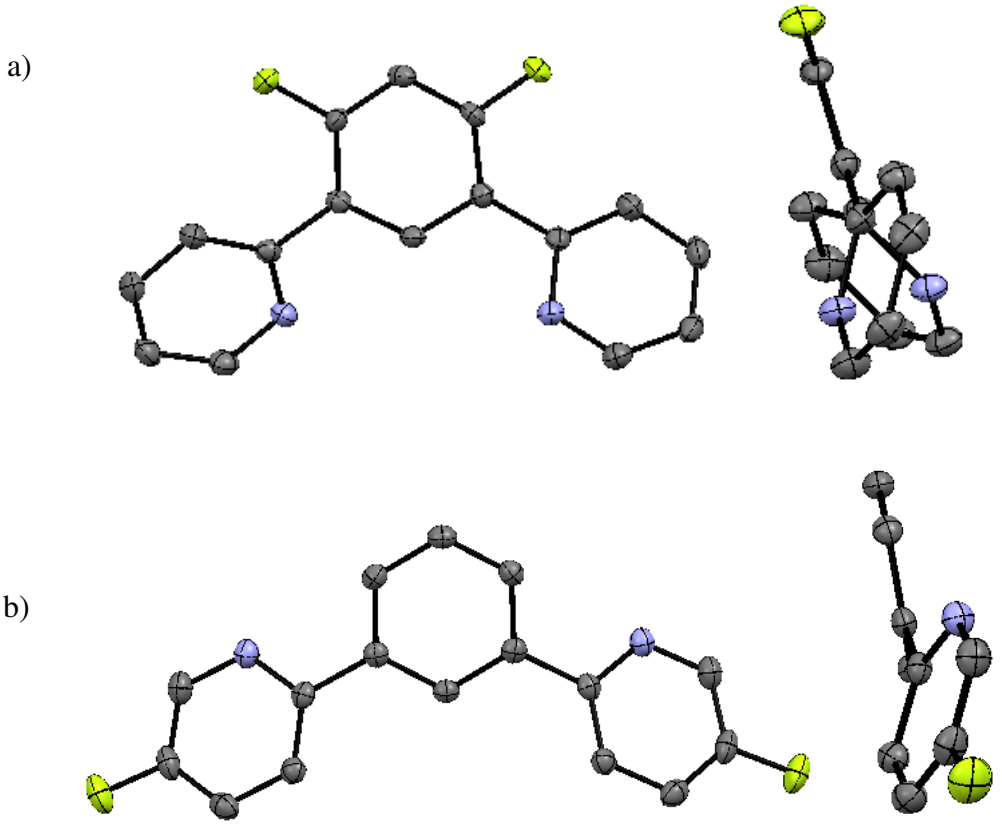

Figure 16: a) ORTEP diagrams of HL^2 viewed at two different orientations. Both pyridyl nitrogen atoms are below the phenyl ring, but the planes of the pyridyl rings are staggered about the plane of the phenyl ring to minimise electronic repulsions, and b) ORTEP diagrams of HL^{22} viewed at two different orientations. In this molecule, both pyridyl nitrogen atoms are facing the phenyl ring, and lie on the same side of the plane created by the phenyl ring.

In the molecular structures of HL^2 and HL^{11}, both nitrogen atoms face downwards, away from the phenyl ring (see Figure 16 a). The phenyl fluoro-substituents disfavour the head-to-tail arrangement: this conformation would result in an unfavourable electrostatic interaction between lone pairs of fluorine and the spatially close nitrogen atom. In these ligands, a more substantial twist occurs (w.r.t. the plane of the central phenyl ring), to minimise any unfavourable electrostatic interaction between the nitrogen lone pairs (Table 6). In the molecular structure of HL^{22}, both pyridyl rings are rotated so that the nitrogen atoms are facing the phenyl ring – there is no clear explanation as to why this ligand adopts this geometry over the head-to-tail arrangement. The arrangement adopted by HL^{22} resembles the *transoid* arrangement of pyridine units about the interannular bonds that is commonly found in the molecular structure of terpyridine ligands.[75,76,77,78,79,80]

Table 6: Angles (deg) between planes created by the aromatic rings

	Phenyl-Pyridyl 1	Phenyl-Pyridyl 2	Pyridyl-Pyridyl
HL^{2}	33.6	-32.7	53.8
HL^{11}	39.4	-32.4	60.0
HL^{22}	34.0	33.9	37.6

Note: A difference in sign between the two phenyl-pyridyl interplane angles indicates that the nitrogen atoms of the two pyridyl rings lie on opposite sides of the plane created by the phenyl ring

2.4.3.3 Pt (IV) Complexes

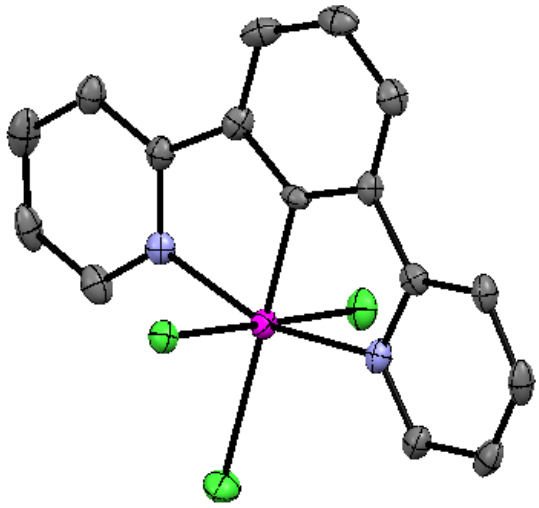

Figure 17: The molecular structure of [$PtL^{1}Cl_3$] at 120 K with displacement ellipsoids at the 50% level. Selected bond lengths (Å) and angles (deg): Pt-C 1.945(4), Pt-Cl 2.3189(10), 2.3195(10) and 2.4457(11), Pt-N 2.055(3) and 2.052(3), N-Pt-N 161.30(15), C-Pt-Cl 91.85(11), 87.99(11) and 176.69(11), N-Pt-Cl 90.30(10), 89.85(9) 90.70(9), 89.11(9), 97.72(11), 100.97(10), C-Pt-N 80.67(16) and 80.63(16)

The crystal structures of [$PtL^{1}Cl_3$], [$PtL^{12}Cl_3$] and [$PtL^{15}Cl_3$] were obtained via slow evaporation of chlorinated solutions of the respective Pt (II) complex (DCM, $CDCl_3$ and DCM respectively). Their formation indicates that the Pt (II) complexes are unstable to oxidation when dissolved in chlorinated solvents for prolonged periods. The complexes adopt an approximately octahedral geometry, and important bond lengths are given in

Table 7. The Pt-Cl bonds are non-equivalent – within each complex, the longest Pt-Cl bond always corresponds to that which is trans to the cyclometallating carbon. This is consistent with a greater trans influence of an anionic carbon ligand compared to chloride. Compared to structures of the Pt (II) complexes, the Pt (IV) complexes possess longer Pt-C bonds (approximately 1.91 and 1.95 Å respectively). This elongation probably occurs to reduce steric interactions with the additional chloride ligands. Similar metal-carbon bond lengths are found in related iridium (III) complexes – Ir (III) is isoelectronic with Pt (IV). For example, the complex, $Ir(N^C^N)(Cl)_2(DMSO)$ (where N^C^N = 1,3-di(2-pyridyl)-4,6-dimethylbenzene) possesses a Pt-C bond length of 1.976(4) Å.[81]

Table 7: Selected bond lengths (Å) and bond angles (deg) for the Pt (IV) complexes

	$[PtL^1Cl_3]$	**$[PtL^{12}Cl_3]$**	**$[PtL^{15}Cl_3]$**
Pt-$C^{1'}$	1.945(4)	1.950(4)	1.940(3)
Pt-Cl	2.3189(10), 2.3195(10), 2.4457(11)	2.3095(10), 2.3284(9), 2.4515(10)	2.3118(9), 2.3151(9), 2.4390(8)
Pt-N	2.055(3), 2.052(3)	2.096(3), 2.105(3)	2.042(3), 2.048(3)
$C^{1'}$-Pt-Cl	91.85(11), 87.99(11), 176.69(11)	94.13(11), 84.19(11), 169.53(11)	90.24(10), 88.48(10), 178.61(3)
N-Pt-N	161.30(15)	160.76(12)	162.33(10)
N-Pt-Cl	90.30(10), 89.85(9), 90.70(9),89.11(9), 97.72(11), 100.97(10)	89.28(9), 88.63(9), 91.22(9), 90.31(9), 96.63(9), 102.61(9)	88.19(8), 90.35(8), 91.08(8), 90.00(8), 99.64(8), 97.99(8)
$C^{1'}$-Pt-N	80.67(16), 80.63(16)	80.73(14), 80.35(14)	80.98(12), 81.42(12)

2.5 References

1. M. Beley, J-P. Collin and J-P Sauvage, *Inorg. Chem.*, 1993, **32**, 4539-4543
2. M. Beley, J-P. Collin, R. Louis, B. Metz and J-P. Sauvage, *J. Am. Chem. Soc.*, 1991, **113**, 8521 – 8522
3. A. M. W. Cargill Thompson, *Coord. Chem. Rev.*, 1997, **160**, 1-52
4. F. Kröhnke, *Synthesis*, 1967, 1-24
5. G. Albano, V. Balzani, E. C. Constable, M. Maestri and D. R. Smith, *Inorg. Chim. Acta*, 1998, **277**, 225-231
6. http://www.scripps.edu/chem/baran/images/grpmtgpdf/Omalley_Jun_04.pdf
7. B. Sorro, S. Stoccoro, G. Minghetti, A. Zucca, M. A. Cinellu, M. Manassero and S. Gladiali, *Inorg. Chim. Acta*, 2006, **359**, 1879
8. T. Abe, K. Shinozaki, N. Ikeda and T. Suzuik, *Acta Cryst. C*, 2007, C**63**, m456 – m458
9. G. R. Pabst and J. Sauer, *Tetrahedron Lett.*, 1998, **39**, 6687-6690
10. G. R. Pabst, K. Schmid and J. Sauer, *Tetrahedron Lett.*, 1998, **39**, 6691-6694
11. O.C. Pfüller and J. Sauer, *Tetrahedron Lett.*, 1998, **39**, 8821-8824
12. G. R. Pabst and J. Sauer, *Tetrahedron Lett.*, 1998, **39**, 8817-8820
13. V. N. Kozhevnikov, B. Donnio and D. W. Bruce, *Angew. Chem. Int. Ed.*, 2008, **47**, 1-5
14. Lecture notes of T. B. Marder, 4th Year Inorganic Chemistry, *Organometallics in Synthesis*, Durham University, 2005
15. N. Miyaura, *Advances in Metal-Organic Chemistry*, 1998, **6**, 187-243
16. M. Beley, S. Chodorowski, J-P. Collin and J-P Sauvage, *Tetrahedron Lett.*, 1993, **34**, 2933
17. D. J. Cárdenas and A. M. Echavarren, *Organometallics*, 1999, **18**, 3337-3341
18. J. A. G. Williams, A. Beeby, E. S. Davies, J. A. Weinstein and C. Wilson, *Inorg. Chem.*, 2003, **42**, 8609-8611
19. S. J. Farley, D. L. Rochester, A. L. Thompson, J. A. K. Howard and J. A. G. Williams, *Inorg. Chem.*, 2005, **44**, 9690 – 9703
20. D. Milstein and J. K. Stille, *J. Am. Chem. Soc.*,1978, **100(11)**, 3636 - 3638

21. J. K. Stille, *Angew. Chem. Int. Ed. Engl.*, 1986, **25**, 508 – 524

22. P.Espinet and A. M. Echavarren, *Angew. Chem. Int. Ed.*, 2004, **43**, 4704-4734

23. A. L. Casado and P. Espinet, *J. Am. Chem. Soc.*, 1998, **120**, 8978 - 8985

24. V. Farina, S. Kapadia, B. Krishnan, C. Wang and L. S. Liebeskind, *J. Org. Chem.*, 1994, **59**, 5905-5911

25. A. L. Casado and P. Espinet, *Organometallics*, 2003, **22**, 1305-1309

26. S. P. H. Mee, V. Lee and J. E. Baldwin, *Angew. Chem. Int. Ed.*, 2004, **43**, 1132-1136

27. A. M. Echavarren and D. J. Cárdenas, "Metal-Catalyzed Cross-Coupling Reactions" WILEY-VCH, Weinheim, 2004, 2nd Ed.

28. S. Kotha, K. Lahiri and D. Kashinath, *Tetrahedron*, 2002, **58 (48)**, 9633-9695

29. N. Miyaura, K. Yamada and A. Suzuki, *Tetrahedron Lett.*, 1979, **36**¸ 3437 – 3440

30. N. Miyaura and A. Suzuki, *Chem. Comm.*, 1979, 866 – 867

31. N. Miyaura and A. Suzuki, *Chem. Rev.*, 1995, **95**, 2457-2483

32. K. L. Billingsley and S. L. Buchwald, *Angew. Chem. Int. Ed.*, 2008, **47**, 4695-4698

33. Y. Yamamoto, M. Takizawa, X-Q. Yu and N. Miyaura, *Angew. Chem. Int. Ed.*, 2008, **47** 928-931

34. D. M. Knapp, E. P. Gillis and M. D. Burke, *J. Am. Chem. Soc.*, 2009, **131**, 6961-6963

35. J. Z. Deng, D. V. Paone, A. T. Ginnetti, H. Kurihara, S. D. Dreher, S. A. Weissman, S. R. Stauffer and C. S. Burgey, *Org. Lett.*, 2009, **11 (2)**, 345-347

36. A. Jouaiti, M. Geoffroy and J-P. Collin, *Inorg. Chim. Acta*, 1996, **245**, 69

37. M. Chavarot and Z. Pikramenou, *Tetrahedron Lett.*, 1999, **40**, 6865-6868

38. L-C. Campeau, S. Rousseaux and K. Fagnou, *J. Am. Chem. Soc.*, 2005, **127**, 18020-18021

39. D. Choi, T. Kim, S. Malla Reddy, J. Kang, *Inorg. Chem. Commun.*, 2009, **12**, 41

40. K. Onitsuka, M. Fujimoto, H. Kitajima, N. Ohshiro, F. Takei and S. Takahashi, *Chem. Eur. J.*, 2004, **10**, 6433-6446

41. B. A. Schweitzer and E. T. Kool, *J. Org. Chem.*, 1994, **59**, 7238-7242

42. http://highered.mcgraw-hill.com/sites/dl/free/0072424583/35353/carey_5e_ch22_summary.pdf

43. G. A. Kubiczak, F. Oesch, J. T. Borlakoglu, H. Kunz and L. W. Robertson, *J. Agric. Food Chem.*, 1989, **37**, 1160-1164

44. K. Tanabe, Y. Tachi, A. Okazaki and S-I. Nishimoto, *Chem. Lett.*, 2006, **35 (8)**, 938-939

45. U. S. Schubert, C. Eschbaumer and M. Heller, *Org. Lett.*, 2000, **2(21)**¸3373 – 3376

46. T. Kaminski, P. Gros and Y. Fort, *Eur. J. Org. Chem.*, 2003, 3855-3860

47. F. Effenberger, A. Krebs and P. Willrett, *Chem. Ber.*, 1992, **125**, 1131-1140

48. A. D'Aléo, S. Welter, E. Cecchetto and L. De Cola, *Pure Appl. Chem.*, 2005, **77(6)**, 1035 – 1050

49. J. Morgan and J. T. Pinhey, *J. Chem. Soc. Perkin. Trans. 1*, 1990, 715 – 720

50. L-E. Perret-Aebi, A. Von Zelewsky, C. Dietrich-Buchecker and J-P. Sauvage, *Angew. Chem. Int. Ed.*, 2004, **43**, 4482 – 4485

51. T. Ishyama, M. Murata and N. Miyaura, *J. Org. Chem.*, 1995, **60**, 7508 – 7510

52. M. H. Todd, S. Balasubramanian and C. Abell, *Tetrahedron Lett.*, 1997, **38(38)**, 6781 – 6784

53. P. A. McCusker, E. C. Ashby and H. S. Makowski, *J. Am. Chem. Soc.*, 1957, **79**, 5179 - 5181

54. H. C. Mattraw, C. E. Erickson and A. W. Laubengayer, *J. Am. Chem. Soc.*, **78**, 4901 - 4904

55. H. R. Snyder, J. A. Kuck and J. R. Johnson, *J. Am. Chem. Soc.*, 1938, **60**, 105 – 111

56. H. C. Brown and T. E. Cole, *Organometallics*, 1983, **2**, 1316 – 1319

57. P-E. Broutin, I. Čerňa, M. Campaniello, F. Leroux and F. Colobert, *Org. Lett.*, 2004, **6(24)**, 4419 – 4422

58. T. Ishiyama, K. Ishida and N. Miyaura, *Tetrahedron*, 2001, **57**, 9813 – 9816

59. T. Ishiyama, N. Miyaura, *J. Organometallic Chem.* , 2000, **611**, 392 – 402

60. C. J. Aspley and J. A. G. Williams, *New J. Chem.*, 2001, **25**, 1136 – 1147

61. V. L. Whittle and J. A. G. Williams, *Dalton Trans.*, 2009, 3929-3940

62. D. Cuperly, P. Gros and Y. Fort, *J. Org. Chem.*, 2002, **67 (1)**¸ 238-241

63. D. W. Slocum, R. Moon, J. Thompson, D. S. Coffey, J. D. Li and M. G. Slocum, *Tetrahedron Lett.*, 1994, **35 (3)**, 385-388

64. V. Snieckus, *Chem. Rev.*, 1990, **90**, 879-933

65. C. J. Woltermann and J. A. Schwindeman, *PharmaChem.*, 2002, 5-8

66. http://www.scripps.edu/chem/baran/images/grpmtgpdf/Krawczuk_March_08.pdf

67. C-C. Kwok, H. M. Y. Ngai, S-C. Chan, I. H. Sham, C-M. Che and N. Zhu

68. S. D. Kuduk, R. M. DiPardo and M. G. Bock, *Org. Lett.*, 2005, **7(4)**, 577-579

69. U. Belluco, "Organometallic and Coordination Chemistry of Platinum", Academic Press, London, 1974

70. W. R. Dolbier, "Guide to Fluorine NMR for Organic Chemists", Wiley and Sons, New Jersey, 2009

71. S. Berger, S. Braun and H-O. Kalinowski, NMR Spectroscopy of the Non-Metallic Elements", John Wiley and Sons Ltd. Chichester, 1997

72. A. D. Ray, J. Hammond and H. Major, *Eur. J. Mass Spectrom.*, 2010, **16**, 169-174

73. J. A. Bailey, M. G. Hill, R. E. Marsh, V. M. Miskowski, W. P. Schaefer and H. B. Gray, *Inorg. Chem.*, 1995, **34**, 4591-4599

74. S-W. Lai, M. C. W. Chan, K-K Cheung and C-M. Che, *Inorg. Chem.*, 1999, **38(19)**, 4262 – 4267

75. E. C. Constable, J. Lewis, M. C. Liptrot and P. R. Raithby, *Inorg. Chim. Acta*, 1990, **178**, 47-54

76. E. C. Constable, F. K. Khan, V. E. Marquez and P. R. Raithby, *Acta Cryst. Sect. C*, 1992, **48**, 932-934

77. W. Leslie, A. S. Batsanov, J. A. K. Howard and J. A. G. Williams, *Dalton Trans.*, 2004, 623-631

78. R-A. Fallahpour and A. Linden, *Acta Cryst. C*, 2008, **C64**, o283 – o285

79. A. Gulyani, R. S. Gopalan, G. U. Kulkarni and S. Bhattacharya, *J. Mol. Struct.*, 2002, **616**, 103 – 112

80. G. Kickelbick, R. Hoogenboom and U. S. Schubert, *Acta Cryst. E*, 2005, **E61**, o4322 – o4324

81. A. J. Wilkinson, H. Puschmann, J. A. K. Howard, C. E. Foster and J. A. G. Williams, *Inorg. Chem.*, 2006, **45**, 8685 – 8699

CHAPTER THREE:

Electronic Properties of the Complexes

3.1 Introduction

Platinum(II) complexes incorporating a 1,3-di(2-pyridyl)benzene ligand are generally highly luminescent, with lifetimes on the microsecond scale.[1,2,3] For example, the parent complex, [PtL^{1}Cl], exhibits a quantum yield (φ) of 0.60 in degassed DCM at room temperature, and a lifetime at infinite dilution (τ_0) of 7.2 μs. The absorption and emission spectra are typically highly structured (Figure 1). The absorption spectra typically consist of a series of very intense bands occurring below 300 nm (ε > 20,000 M^{-1} cm^{-1}), and a series of intense bands occurring between 320-430 nm (ε ~ 5,000 – 10,000 M^{-1} cm^{-1}). The former bands are due to ligand localised $^1\pi$-π^* transitions (similar bands occur in the absorbance spectra of the uncomplexed ligands), and the latter are due to transitions involving the metal or induced within the ligand by the cyclometallation process. These include charge transfer transitions. The lowest energy band in this region is considered as the S_1 peak, corresponding to the $S_0 \rightarrow S_1$ transition. Weak bands (ε ~ 200 M^{-1} cm^{-1}) are often observed at lower energy, which have been assigned to direct singlet-to-triplet ($S_0 \rightarrow T_1$) transitions. The highly structured emission spectra, the weak solvatochromic behaviour and small Stokes' shifts suggest that the emission emanates from a primarily $^3\pi$-π^* state, although recent theory implies that this state contains a significant ^{3}MLCT admixture.[3,4,5]

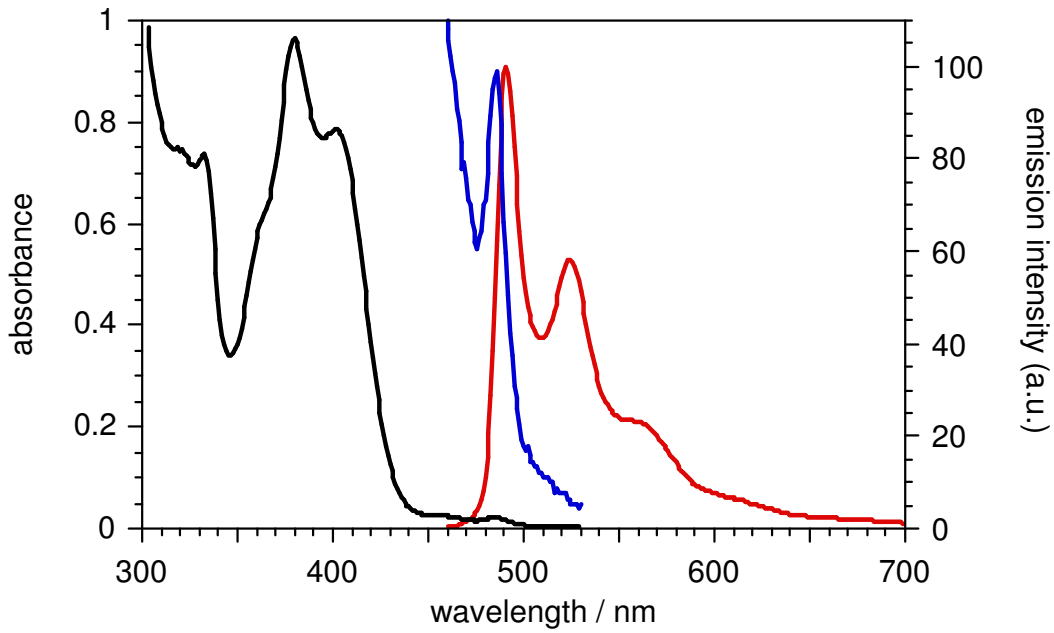

Figure 1: The absorption spectrum (black) and emission spectrum (red) of the unsubstituted parent complex, [PtL^{1}Cl] (DCM, 298 K). The absorption region between 450-530 nm has been expanded (blue) to highlight the weak $S_0 \rightarrow T_1$ band and to demonstrate the small Stokes' shift between this band and the highest energy emission maximum.

In emission, the highest intensity vibrational band is typically the one of highest energy, which corresponds to the electronic vibrational 0-0 origin of the $T_1 \rightarrow S_0$ transition (see Figure 1). The bands at lower energy (and intensity) correspond to transitions to higher vibrational levels of the ground state. The shape and highly structured nature of the spectrum indicates that little geometric rearrangement occurs between the ground and excited states – a testament to the rigidity of the system. The Franck-Condon principle is required to explain this. The principle states, "since electronic motions are much faster than nuclear motion, electronic transitions occur most favourably when the nuclear structure of the initial and final states are most similar".[6] This effectively means that the nuclear geometry is frozen during the electronic transition. In potential energy surface terms, the Franck-Condon-allowed electronic transitions are represented as vertical arrows between the ground and excited state (see Figure 2). When the equilibrium geometries of the excited and ground state are similar, the corresponding potential energy surfaces have minima at similar nuclear displacement, r_{xy}. In this case, the most probable transition back to the ground state is the 0-0 transition, the transition of highest energy. However, if the equilibrium geometries of the excited and ground states are different, say the excited state minimum lies at a higher nuclear displacement, then the most probable transition back to the ground state may not be the 0-0 transition, and the emission spectrum will look different.

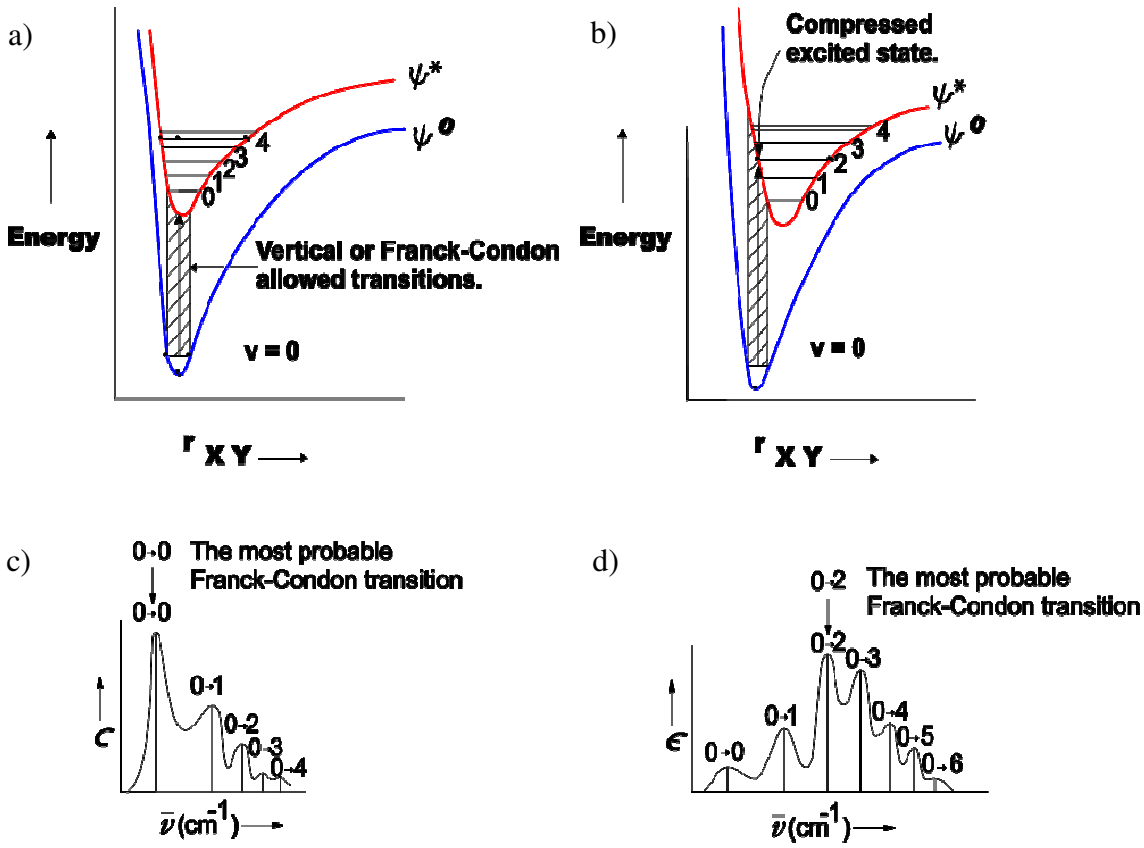

Figure 2: Potential energy curves for a) a molecule with similar ground and excited state equilibrium geometries, and b) a molecule with significantly different ground and excited state equilibrium geometries. c) and d) represent the resultant emission profiles, respectively (Images have been adapted and re-drawn from reference 6).

In solutions of elevated concentration, the complexes display significant self-quenching via excimer formation (see Chapter 1, Section 1.7.2 for a more detailed description). Excimers of these complexes are usually emissive. The broad, structureless excimer emission band grows in at lower energy, at the expense of the structured monomer emission (Figure 3).

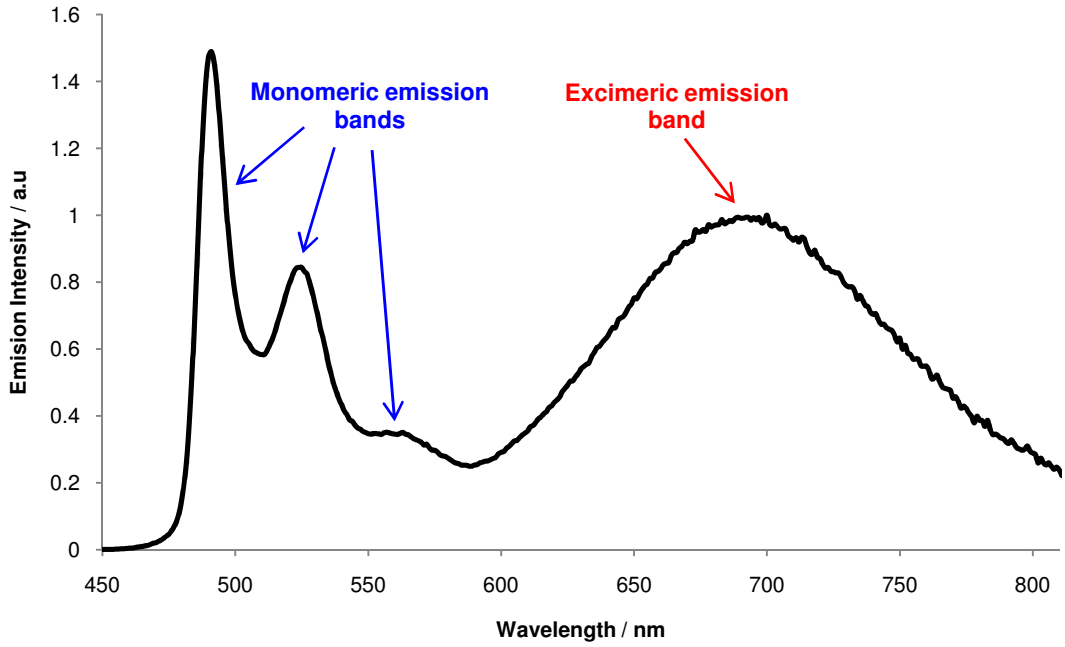

Figure 3: Chart showing both the highly structured monomeric and broad, structureless, excimeric emission of [PtL^{1}Cl] (10^{-4} M, DCM, 298 K)

As a consequence of self-quenching (i.e. conversion of the monomeric excited state to the excimer), the lifetime (τ_{obs}) is observed to decrease with increasing concentration. The lifetime (τ_{obs}) of the excited state of the monomer can be determined by monitoring the temporal decay of emission around the monomer emission maximum. Over the concentration range studied (typically 10^{-4} – 10^{-6} M) the emission decay remains monoexponential. The observed emission decay rate constant (k_{obs}) is related to τ_{obs} via

$$k_{obs} = \frac{1}{\tau_{obs}} \qquad Eqn.1$$

k_{obs} increases linearly with concentration and the results are well modelled by a Stern-Volmer expression[7,8] of the form

$$k_{obs} = k_0 + k_{sq}[Pt] \qquad Eqn.2$$

where k_0 is the emission decay rate constant at infinite dilution, and k_{sq} is the rate constant of self quenching. Hence, a plot of k_{obs} vs. concentration can be used to determine these two parameters (y-intercept and gradient respectively). $1/k_0$ is equal to the lifetime of the monomeric excited state at infinite dilution, τ_0, and k_{sq} gives a measure of how prone the complex is to excimer formation.

3.2 DFT Calculations on [PtL^{1}Cl]

Various research groups have performed theoretical analysis of the parent complex, [PtL^{1}Cl], and the individual atomic orbital contributions to the frontier molecular orbitals have been determined (Figure 4).[3,4,5] The electron density plots predicted by Rochester et al. do not exactly match those predicted by Sotoyama et al. and Shi et al.. However, although the results differ to some extent, all are in general agreement that electron density of the HOMO-based orbitals is mainly localised down the central axis of the molecule (on the phenyl ring, the metal centre and the ancillary chloride), whereas electron density of the LUMO-based orbitals mainly lies on the π^* orbitals of the terdentate ligand, (especially on the lateral pyridyl rings).

Additionally, Sotoyama et al. have performed DFT and TDDFT calculations on [PtL^{1}Cl] to determine which of the frontier molecular orbitals are involved in the electronic transitions responsible for absorption and emission.[4] Their results indicate that the $S_0 \rightarrow S_1$ transition (which corresponds to the S_1 peaks observed in the absorption spectrum) mainly involves transition between the b_1 and a_2^* states (i.e. HOMO $\rightarrow$ LUMO). On the other hand, the $T_1 \rightarrow S_0$ transition (observed in emission) involves transition between the b_1^* and b_1 states (i.e. LUMO+1 $\rightarrow$ HOMO). These theoretical results are in close agreement with the experimental. For example, the predicted and observed transition energies are similar. Also, the results predict a smaller difference in dipole moment between the S_0 ground state and T_1 ($\Delta\mu_z$ = -1.13) than between S_0 and S_1 ($\Delta\mu_z$ = -9.07), in agreement with the experimental observation that the absorption bands between 320 – 430 nm display significant negative solvatochromism, whereas the emission energy is scarcely affected by solvent.

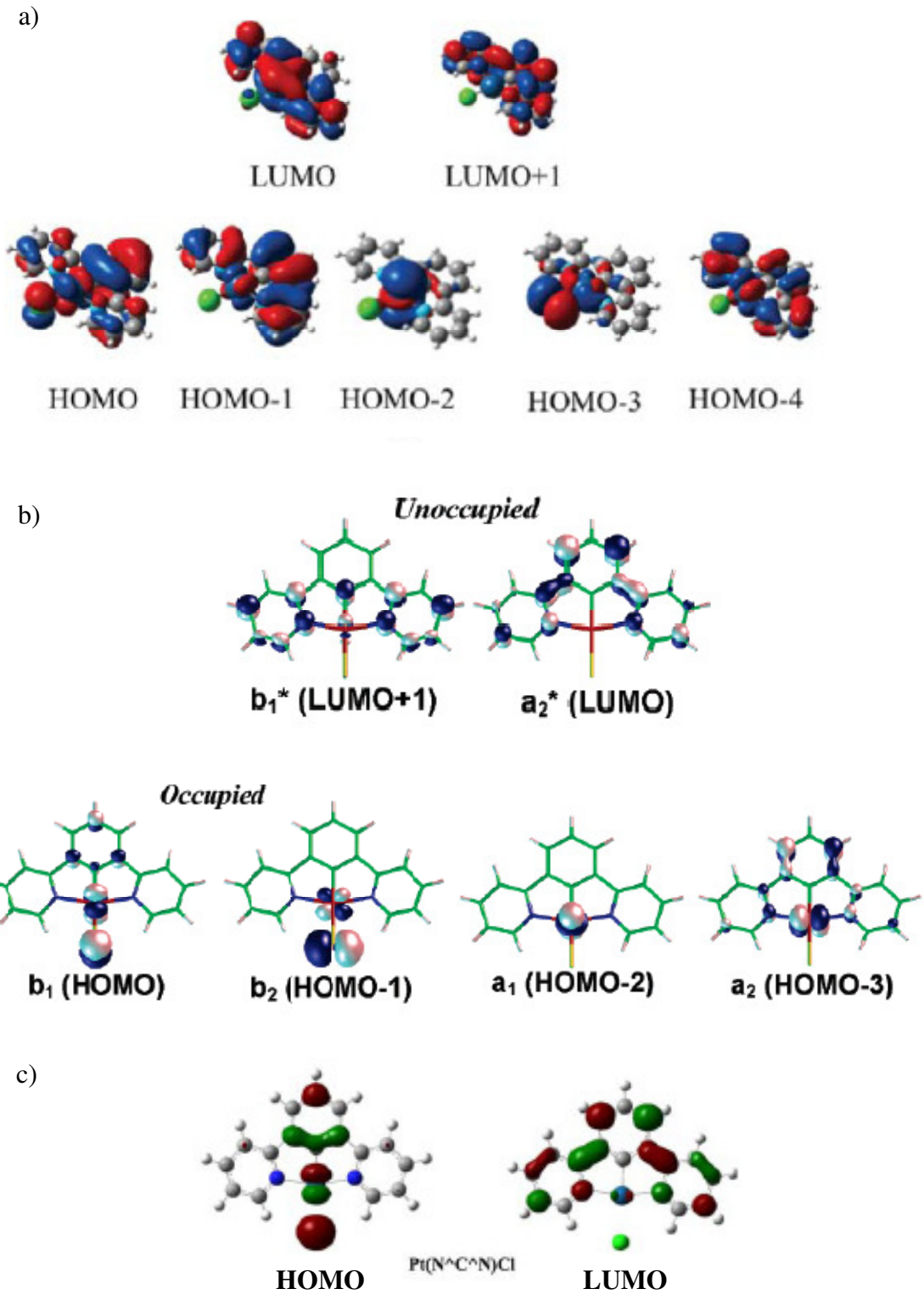

Figure 4: Contour plots of the frontier molecular orbitals of [PtL[1]Cl], as predicted by a) Rochester et al.,[3] b) Sotoyama et al.,[4] and c) Shi et al.[5]

By considering the contour plots of the molecular orbitals involved in the important transitions (i.e. absorption and emission), it should be possible to design complexes with tuned photophysical properties. For example, placing substituents of defined electronic character in certain positions on the terdentate ligand will confer differing degrees of

stabilisation/destabilisation on the HOMO-based and LUMO-based orbitals, affecting the transition energies. Williams et al. have shown that the emission energy of such complexes could be tuned by varying the electron donor/acceptor character of a 4-phenyl substituent.[2] Complexes containing substituents of greater electron donating character were found to emit at lower energies. This is consistent with the HOMO being largely localised on the central ring: electron donating substituents should destabilise the HOMO, increasing its energy and decreasing the transition energy gap, accounting for the observed red-shift. The opposite has been found for electron withdrawing substituents.[1]

What about pyridyl substituents? Since theory predicts that the pyridyl rings mainly contribute to the energy of the LUMO and LUMO+1, one could envisage that electron donating groups on the pyridyl rings would destabilise these orbitals leading to a blue shift (again, the opposite should be true for electron withdrawing groups).

Thirdly, the ancillary chloride ligand is largely involved in the HOMO-based orbitals, but less in the LUMO. It therefore seems reasonable to assume that ligand substitution with a more electron withdrawing ligand should have a greater stabilising effect on the HOMO and increase the energy of the electronic transitions.

With the theoretical atomic orbital calculations of the unsubstituted parent complex, [PtL^{1}Cl], in mind, 1,3-di(2-pyridyl)benzene Pt(II) complexes that exhibit blue-shifted emission have been targeted. Figure 5 sums up our initial thoughts of how functionalisation of the terdentate ligand was expected to lead to a blue shift. By applying the reverse of this reasoning, complexes exhibiting red-shifted emission were then targeted, to see if the effect was upholded. Finally, substitution of the ancillary chloride ligand was considered.

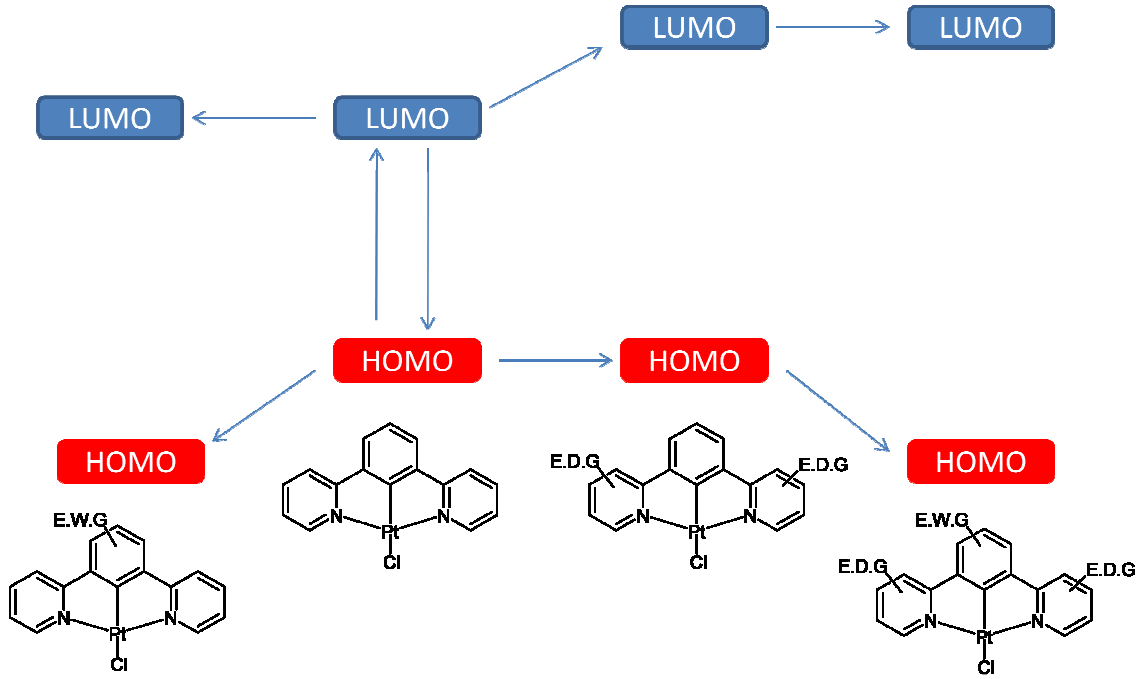

Figure 5: Crude schematic showing how functionalisation of the terdentate ligand was expected to affect the relative energies of the frontier molecular orbitals, leading to a blue-shift (note: "LUMO" here also represents the LUMO+1 state). E.W.G and E.D.G. represent an electron withdrawing group and electron donating group respectively.

3.3 Electrochemistry

Cyclic voltammetry was performed in DMSO, due to poor solubility of some of the complexes in the more usual solvents (e.g. DCM and acetonitrile). Tetrabutylammonium hexafluorophosphate (0.1 M) was used as a supporting electrolyte, and the solutions were purged with nitrogen before each run. All signals observed corresponded to irreversible processes – the peak potentials are reported for these irreversible waves (Table 1). The recorded values refer to a scan rate of 100 mV s^{-1}, and are reported relative to a Ferrocene/Ferrocinium (Fc/Fc^{+}) reference. Even in DMSO, the data were not of good quality – there was considerable scatter in potential between the different runs, so the data must be treated cautiously and as a guide only. For this reason, it is difficult to see any trends between related complexes.

Table 1: Electrochemical Data for the Pt(II) Complexes.

Complex	E_p^{ox} / V	E_p^{red} / V	Complex	E_p^{ox} / V	E_p^{red} / V
[PtL^{1}Cl]	0.31	-2.24, -2.49	**[PtL^{12}Cl]**	0.18	-2.15, -2.46
[PtL^{2}Cl]	0.31	-2.28, -2.61	**[PtL^{13}Cl]**	0.36	-2.33, -2.55
[PtL^{3}Cl]	0.31	-2.43, -2.71	**[PtL^{14}Cl]**	0.46	-2.18, -2.60
[PtL^{5}Cl]	0.36	-2.23, -2.60	**[PtL^{15}Cl]**	0.37	-2.23
[PtL^{6}Cl]	0.16	-2.42, -2.63	**[PtL^{16}Cl]**	0.35	-2.12, -2.50
[PtL^{7}Cl]	0.23	-2.32	**[PtL^{17}Cl]**	0.21	-2.21, -2.54
[PtL^{8}Cl]	0.14	-2.25, -2.53	**[PtL^{20}Cl]**	0.55	-2.15, -2.55
[PtL^{9}Cl]	0.30	-2.23, -2.50	**[PtL^{21}Cl]**	0.50	-2.15, -2.51
[PtL^{10}Cl]	0.30	-2.22, -2.52	**[PtL^{1}I]**	0.01 and 0.70	-2.19, -2.46
[PtL^{11}Cl]	0.15	-2.35, -2.62	**[PtL^{1}Br]**	0.25	-2.19

The values were determined from DMSO solutions at 298 K (≈ 10^{-4} M), in the presence of a 0.1 M tetrabutylammonium hexafluorphosphate supporting electrolyte. A scan rate of 100 mV s^{-1} was employed. All processes were chemically irreversible: E_p^{ox}/E_p^{red} represents the peak potential of the irreversible oxidation/reduction (in volts). All data are reported relative to Fc/Fc^+

In analogy with data reported for related complexes,[2] most of the complexes display one irreversible oxidation peak (see Figure 6 for an example). This has previously been assigned to a one-electron oxidation based on the Pt centre. The irreversibility of this peak makes it harder to determine the true value of the oxidation process. For a reversible process, one would record $E_{1/2,}$ which corresponds to the average of the forward and reverse waves, whereas for an irreversible process E_p^{ox} is taken as the maximum of the solitary forward wave. Natural variation of the peak maxima between runs for a reversible process will at most only cause small alteration in the experimentally observed value of $E_{1/2}$. For an irreversible process, natural variation of

the peak maximum makes it difficult to accurately determine E, as the value solely depends on the position of one peak.

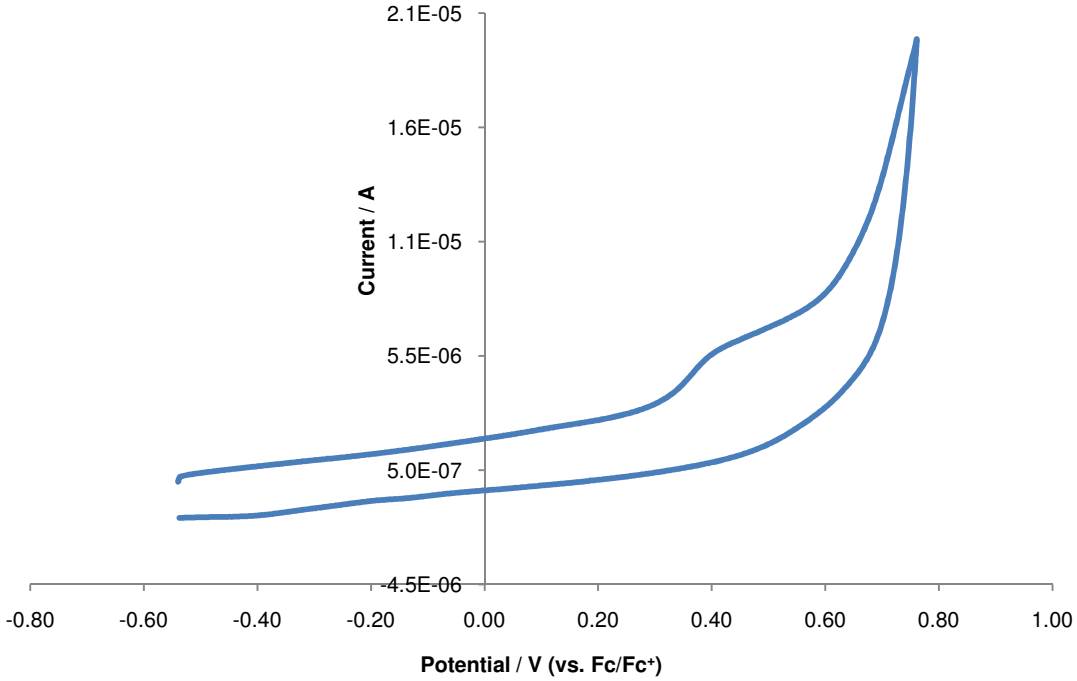

Figure 6: Cyclic voltammogram showing the irreversible oxidation peak observed for [PtL^{10}Cl]. The scan was performed in DMSO, in the presence of a 0.1 M tetrabutylammonium hexafluorophosphate background electrolyte, at a scan rate of 100 mV s^{-1}. The other complexes display similar profiles. The maximum is difficult to assign, due to the weakness of the signal and overlap of the band with the edge of the solvent window.

For each complex, two irreversible reduction waves were observed; the first at around -2.2 V and the second around -2.6 V. Reduction mainly occurs on the terdentate ligand.[2] These reductions occur very near to the edge of the solvent window – this sharp rise in current may have a distorting effect on the true value of E_p^{red}. Like oxidation these peaks are irreversible, which again does not aid the measurement of the value of E_p^{red}.

3.4 Photophysical Characterisation

3.4.1 Modification of the Chelating Ligand, and the Photophysical Implications

3.4.1.1 Substituents on the Phenyl Ring

DFT calculations predict that atoms of the central phenyl ring make a significant contribution to the HOMO, and a lesser contribution to the LUMO-based orbitals. Therefore, placing electron-withdrawing substituents around this ring can be expected to have a greater stabilising effect on the HOMO, and lead to a blue shift. Conversely, electron-releasing substituents may be expected to destabilise the HOMO, leading to a red shift.

2,6-Di(2-pyridyl)-3,5-difluorobenzene Platinum(II) Chloride, [PtL^{2}Cl]

Absorbance

[PtL^{2}Cl] was prepared, which possesses two inductively electron-withdrawing fluorine atoms at the 3' and 5' positions (see Chapter 2, Figure 7). The absorbance spectrum of the uncomplexed ligand was recorded and compared with that of [PtL^{2}Cl] (see Figure 7 and Table 2) – one can clearly see a similarity between the peaks occurring in the region 230 nm – 300 nm, indicating that bands occurring in this region of the complex absorption profile are due to ligand localised $^1\pi$-π^* transitions. Lower intensity bands in the range 310 – 380 nm are observed in the spectrum of complex [PtL^{2}Cl] but are absent in the ligand absorption, confirming that these bands arise upon ligand coordination to platinum. These bands are likely to include MLCT transitions and intraligand transitions, induced by the formal deprotonation of the central aryl ring that accompanies metallation, and combinations of such transitions.

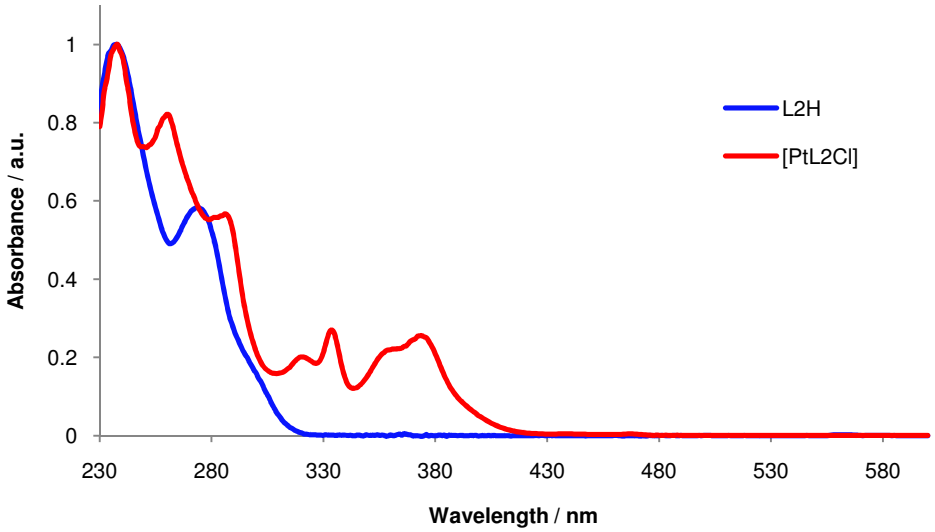

Figure 7: UV-vis absorption spectra of ligand L^2H (blue) and complex $[PtL^2Cl]$ (red) in DCM at 298 K. Spectra have been normalised at 238 nm to aid comparison.

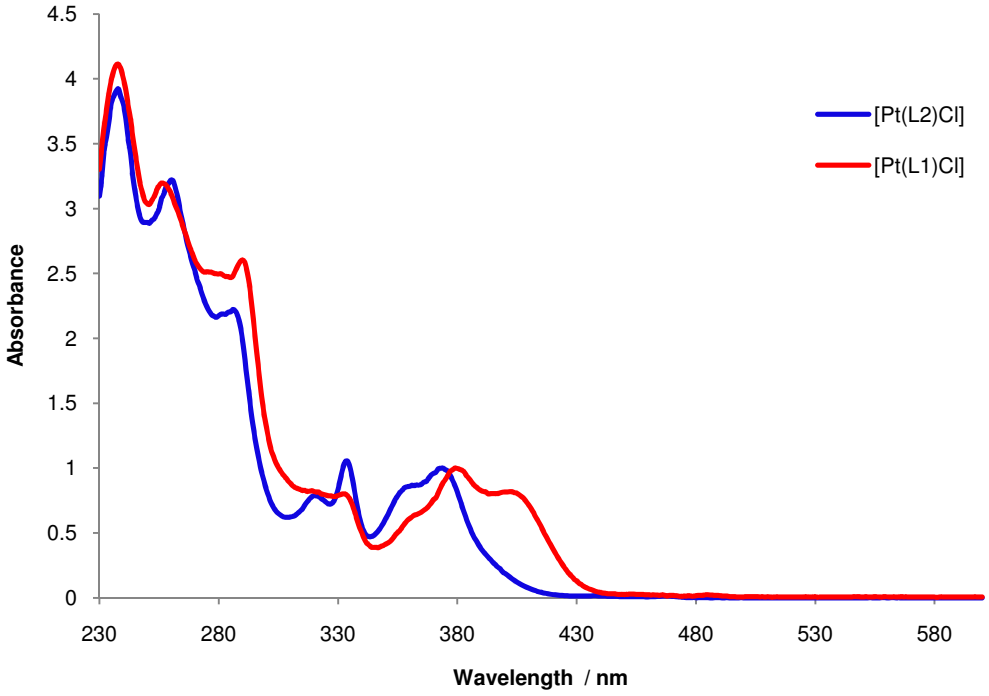

Figure 8: Normalised UV-vis absorption spectra of complexes $[PtL^1Cl]$ (red) and $[PtL^2Cl]$ (blue) in DCM at 298 K.

The latter set of bands were blue-shifted relative to those in $[PtL^1Cl]$ (Figure 8). Also, the lowest energy singlet absorption band occurring in the $[PtL^1Cl]$ spectrum appeared to be absent in the $[PtL^2Cl]$ spectrum. Perhaps this charge transfer band has blue-shifted so much that it has become hidden under the higher energy bands, although there is no

evidence from the extinction coefficient data to support this notion (Table 2). The ligand localised bands occurring below 300 nm were not affected by fluorine substitution. Weak bands were observed for [PtL^{2}Cl] at 437 nm and 467 nm (ε = 312 and 129 M^{-1} cm^{-1} respectively). In agreement with reference 2, these bands correspond to direct singlet-to-triplet excitations (S → T), which are formally spin-forbidden processes, accounting for the weakness of the bands.

Table 2: Solution-based photophysical properties of [PtL^{1}Cl] and [PtL^{2}Cl] (DCM, 298 K).

Complex	Absorbance λ_{max}/nm (ε / L $mol^{-1}cm^{-1}$)	Emission λ_{max}/nm	τ_0 degassed (aerated)/μs[a]	Φ_{lum} degassed (aerated)
[PtL^{1}Cl][b]	332 (6510), 380 (8690), 401 (7010), 454* (270), 485* (240)	491, 524, 562	7.2 (0.50)	0.60 (0.039)
[PtL^{2}Cl]	320 (6690), 334 (9180), 360 (7340), 374 (8500), 437* (140), 467* (140)	472, 502, 536sh	7.9 (0.67)	0.85 (0.087)

[a]Lifetime at infinite dilution, [b]Photophysical data from reference 1, *Forbidden S → T absorption bands, sh = shoulder. NOTE: comprehensive photophysical data for all complexes (in DCM at 298 K) is listed in Table 29, which can be found at the end of this chapter.

The absorption bands between 320 and 430 nm display negative solvatochromism – the peaks occur at lower energy in non-polar solvents such as CCl_4 and higher energy in polar solvents such as CH_3CN (see Figure 9 and Table 3). Solvatochromism indicates that a significant degree of charge transfer character is associated with these absorption bands. The relative destabilisation occurring in polar solvents indicates an excited state that is less polar than the ground state (lower dipole moment). Similar results were reported by Williams et al. for the parent complex, [PtL^{1}Cl], and 4-aryl substituted complexes.[1] The individual bands display different degrees of solvatochromism. The band around 380 nm exhibits an energy difference of 910 cm^{-1} between CH_3CN and CCl_4 solutions (λ_{max} = 371 and 384 nm respectively), whereas the peak around 335 nm only differs in energy by 540 cm^{-1} between these extremes of polarity (λ_{max} = 331 and 337 nm respectively). The relative peak intensities within this group of bands change as

a function of solvent polarity – the higher energy transitions increase in intensity with increasing polarity. The grow-in of a band at lower energy (around 400 nm) is observed with decreasing solvent polarity – perhaps this band is of the same origin as the lowest energy absorption band present in the [PtL^{1}Cl] absorption spectrum. With increasing solvent polarity, this band blue-shifts and overlaps with the higher energy absorptions. This may account for the increased relative intensity of these bands at higher polarity.

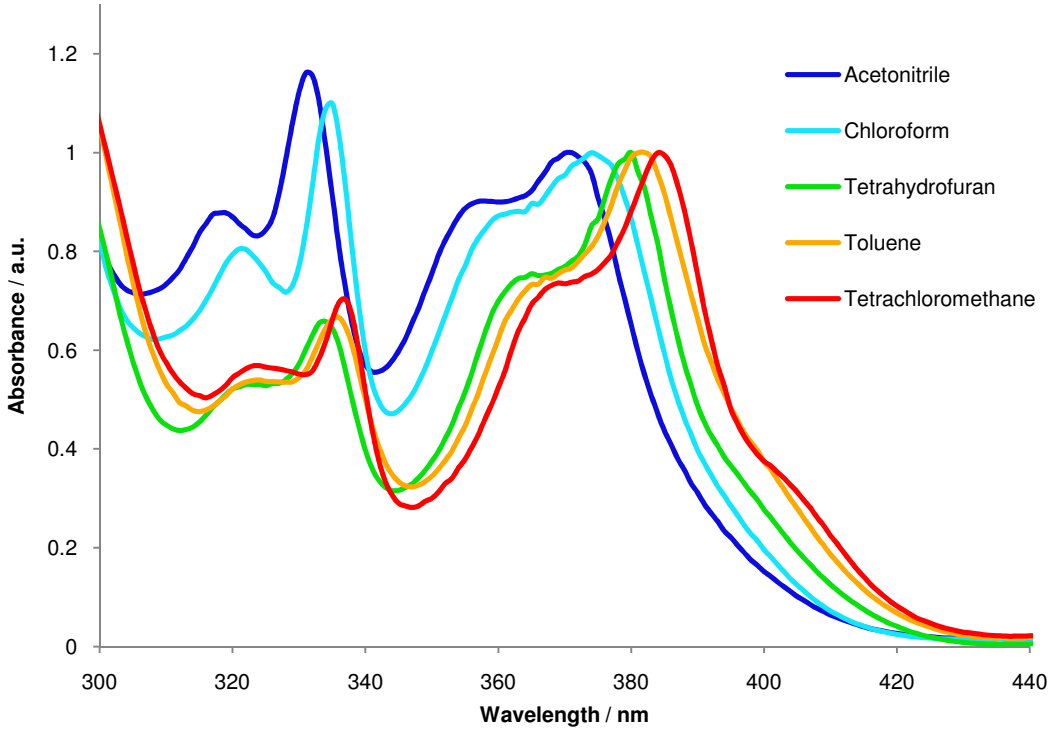

Figure 9: UV-vis absorption spectrum of [PtL^{2}Cl] recorded in various solvents at 298 K, demonstrating the solvatochromic behaviour.

Table 3: Absorbance band maxima (nm) occurring above 300 nm for [PtL^{2}Cl] in various solvents (298 K).

Solvent	**Absorbance λ_{max}/nm**
CCl_4	323, 337, 368sh, 384, 404sh
Toluene	323, 336, 366sh, 382, 398sh
THF	322, 334, 364sh, 380
$CHCl_3$	321, 335, 360sh, 374
CH_3CN	318, 331, 357sh, 371

Emission

Just like [PtL^{1}Cl], [PtL^{2}Cl] emits from DCM solution at room temperature (298 K), and the emission spectrum is highly structured, with the 0-0 transition having the greatest intensity (Figure 10). The emission maximum (λ_{max}) occurs at significantly shorter wavelength than [PtL^{1}Cl]; 472 nm (21200 cm^{-1}) and 491 nm (20400 cm^{-1}) respectively, (ΔE = 820 cm^{-1}), indicating that the introduction of fluorine atoms in the 3' and 5' positions is an efficient method for blue-shifting the emission. These results are consistent with the DFT orbital predictions, which estimate that orbitals of the phenyl ring make significant contribution to the HOMO but essentially none to the LUMO+1.

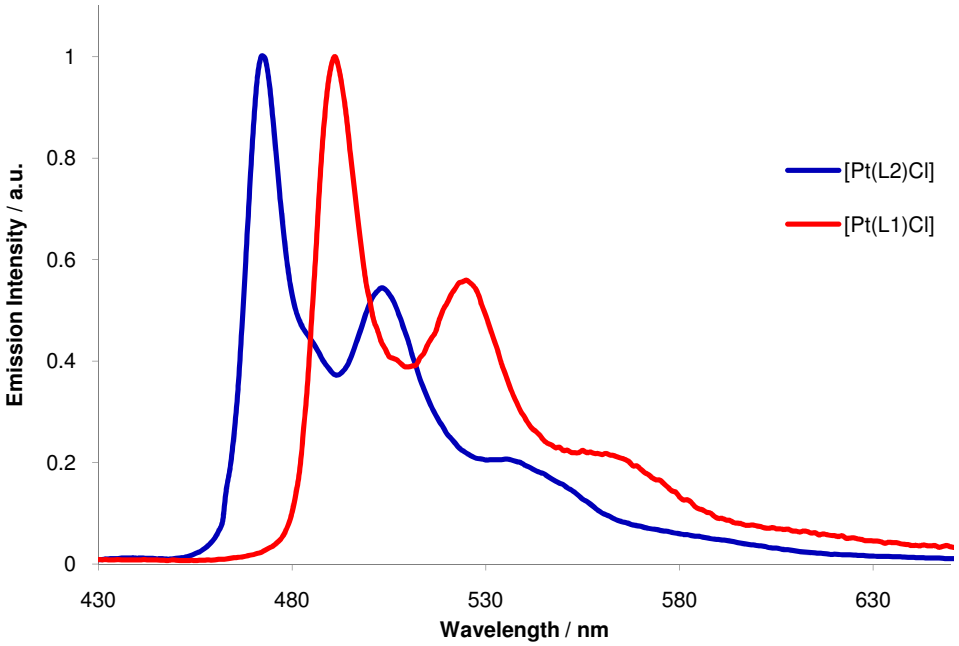

Figure 10: Emission spectra of [PtL^{1}Cl] (red) and [PtL^{2}Cl] (blue) in a dilute DCM solution (ca. 10^{-6} M) at 298 K (λ_{ex} = 401 nm and 374 nm respectively).

The emission of [PtL^{2}Cl] displayed only a slight negative solvatochromism (Figure 11) – a maximum energy difference of 180 cm^{-1} was found between solutions of complex in the solvent polarity extremes (CH_3CN and CCl_4). The emission energy is much less sensitive to solvent polarity than absorption energies. This indicates little redistribution of charge, or change in dipole moment, occurs in the triplet excited state.

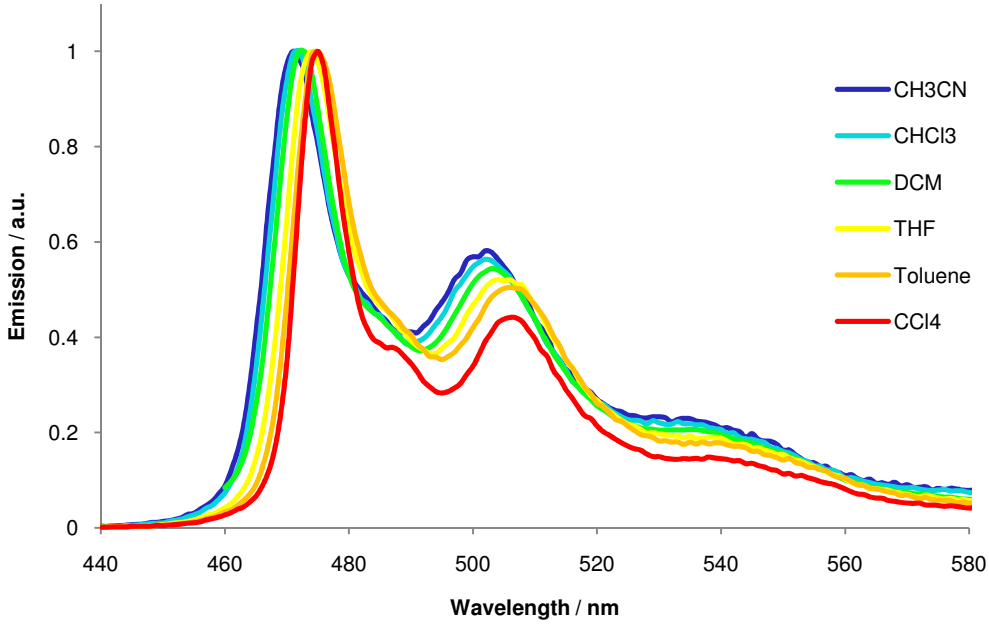

Figure 11: Emission spectra of a dilute sample of [PtL^{2}Cl] (ca. 10^{-5} M) in various solvents (298 K, λ_{ex} = 374 nm).

A quantum yield, φ, of 0.85 has been measured for [PtL^{2}Cl] – this value is exceptionally high for platinum based phosphors. The quantum yield is 42% higher than that of the parent complex, [PtL^{1}Cl] (0.60). However, the lifetime of the emissive state at infinite dilution, τ_0, is of a comparable magnitude to that of [PtL^{1}Cl] (7.8 μs and 7.2 μs). This tells us something about the origin of the relative efficiencies of the two complexes: φ and τ_0 are related to the radiative and non-radiative rate constants of the excited state:

$$k_r = \frac{\varphi}{\tau_0} \qquad Eqn.\,3$$

$$k_{nr} = \frac{1}{\tau_0} - k_r \qquad Eqn.\,4$$

Thus, the larger φ of [PtL^{2}Cl] but comparable τ_0 between the two complexes means that k_r is larger and k_{nr} is smaller for [PtL^{2}Cl], and this complex is a more efficient emitter (values for k_r and k_{nr} are given in Table 4).

Analogous heteroleptic bidentate complexes of a cyclometallating phenyl pyridine ligand have been prepared by Thompson et al. (see Figure 12).[9] The room temperature quantum yields of the *ppy* and *4,6-dfppy* complexes (0.15 and 0.02 respectively) are much lower than the quantum yields of [PtL^{1}Cl] and [PtL^{2}Cl] (φ = 0.60 and 0.85 respectively).

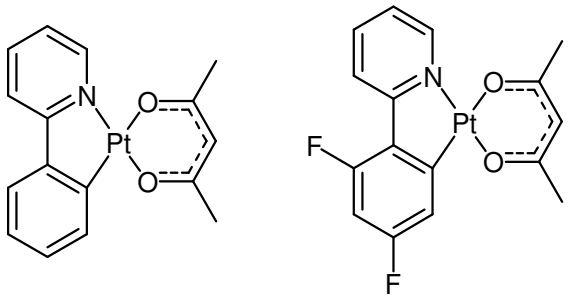

Figure 12: Chemical structures of bidentate N^C analogues, ppy and 4,6-dfppy.[9]

Table 4 gives a comparison of the radiative and non-radiative rate constants (k_r and k_{nr} respectively) for these four complexes. As can be seen, k_{nr} for the bidentate complexes is significantly higher indicating a greater degree of non-radiative decay of the emissive state for these bidentate analogues. This effect has been attributed to the differing rigidity between the complexes. Unlike the rigid terdentate systems, bidentate complexes are prone to D_{2d} distortions, which opens up another possible route to non-radiative decay (Chapter 1, Section 1.3).

Furthermore, the length of the Pt-C bond is much shorter in [PtL^{1}Cl] than in *ppy* – the crystals structure of [PtL^{1}Cl] revealed a Pt-C bond length of 1.91 Å,[10] whereas DFT calculations on *ppy* predict a Pt-C bond length of 1.98 Å[9] (note: a search of the CCSD revealed that complexes related to *ppy*, involving bidentate phenyl pyridine ligands possess Pt-C bonds of approximately 1.98 Å, indicating that the calculated bond length is probably quite reliable). The shorter Pt-C bond in the terdentate system will lead to a larger ligand field splitting. This means that the deactivating d-d* state will be at a lower energy in the bidentate systems compared with analogous terdentate complexes, and the probability of thermal promotion to this state will be greater for the bidentate complexes. Both of these factors account for the higher quantum yields of the terdentate complexes, relative to their bidentate analogues.

Table 4: Radiative and non-radiative rate constants of [PtL^{1}Cl] and [PtL^{2}Cl], and their bidentate analogues *ppy* and *4,6-dfppy* (DCM, 298 K).

	[PtL^{1}Cl]	***ppy*^{b}**	**[PtL^{2}Cl]**	***4,6-dfppy*^{b}**
k_r / s^{-1}	83000	58000	110000	100000
k_{nr} / s^{-1}	48000	327000	17000	4900000

[b]The quantum yields and lifetimes used to calculate the rate constants of *ppy* and *4,6-dfppy* were taken from reference 9 and reference 11 respectively. The estimated uncertainty on k_r and k_{nr} is ± 20 %.

Although the bidentate complexes possess slightly higher energy maxima than the terdentate versions, the emission spectra of the bidentate complexes appear broader, and contain a more significant green-yellow tail (Figure 13). The lower intensity of the green-yellow tail in the [PtLCl] systems is associated with the greater rigidity of the system, and as a consequence, under long-wave irradiation, dilute solutions of [PtL^{2}Cl] appear bluer than those of *4,6-dfppy*. Hence blue [PtLCl] emitters have greater colour purity than their bidentate analogues.

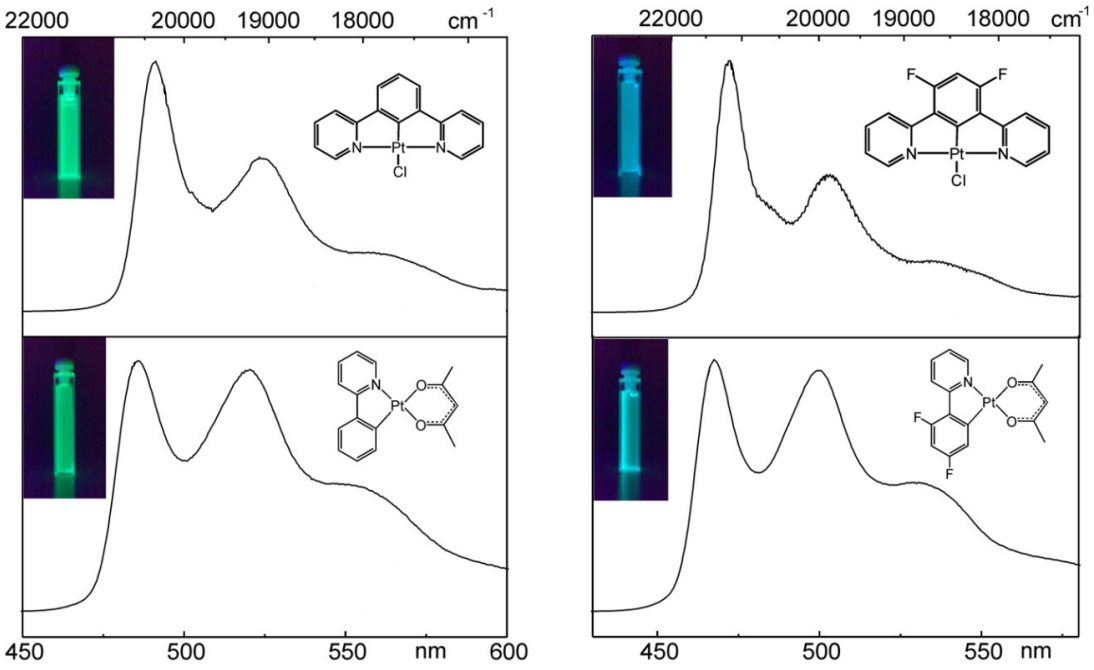

Figure 13: Emission spectra of dilute DCM solutions of [PtL^{1}Cl] (top, left), [PtL^{2}Cl] (top, right), *ppy* (bottom, left) and *4,6-dfppy* (bottom, right). Photographs of the solutions under long wavelength UV-irradiation are included as insets (this figure was taken from a talk given by A. Rausch, from the University of Regensburg).

To help put the emission properties of [PtL^{2}Cl] further into context, two related complexes prepared by other researchers will now be discussed (Figure 14). [PtL^{27}Cl], which was prepared by a former group member, exhibited red-shifted spectra relative to the parent complex. In this case, an electron-releasing methyl group has been incorporated at the 4'-position, and this has a greater destabilising effect on the HOMO, shifting the absorption and emission to lower energy (E = 19840 cm^{-1}, λ_{max} = 504 nm and φ = 68%, degassed DCM, 298 K).[1]

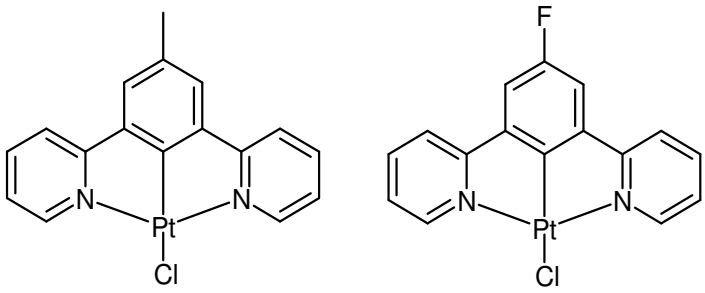

[PtL^{27}Cl] [PtL^{28}Cl]

Figure 14: Structures of complexes [PtL^{27}Cl] and [PtL^{28}Cl].

The complex containing a fluorine atom in the 4' position, [PtL^{28}Cl], has been prepared by the group of D. Roberto, Milan. The emission of this complex is red-shifted relative to [PtL^{1}Cl] (509 nm vs. 491 nm). At a first glance, this result seems counterintuitive. However, fluorine has strange properties in that it can act as a strong inductive electron acceptor or as a mesomerically electron releasing group (due to p-orbital overlap). When fluorine occupies the 4' position (para to the metal), the electron-donating resonance effect seemingly dominates (Figure 15), resulting in increased electron density on the phenyl ring and platinum. This destabilises the HOMO relative to [PtL^{1}Cl], accounting for the lower energy electronic transitions (Figure 16).

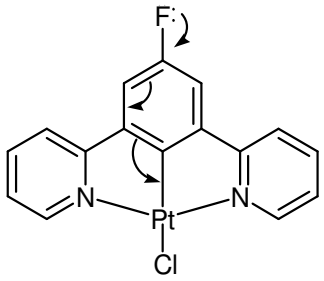

Figure 15: Representation of the electron-donating resonance effect of fluorine in [PtL^{28}Cl].

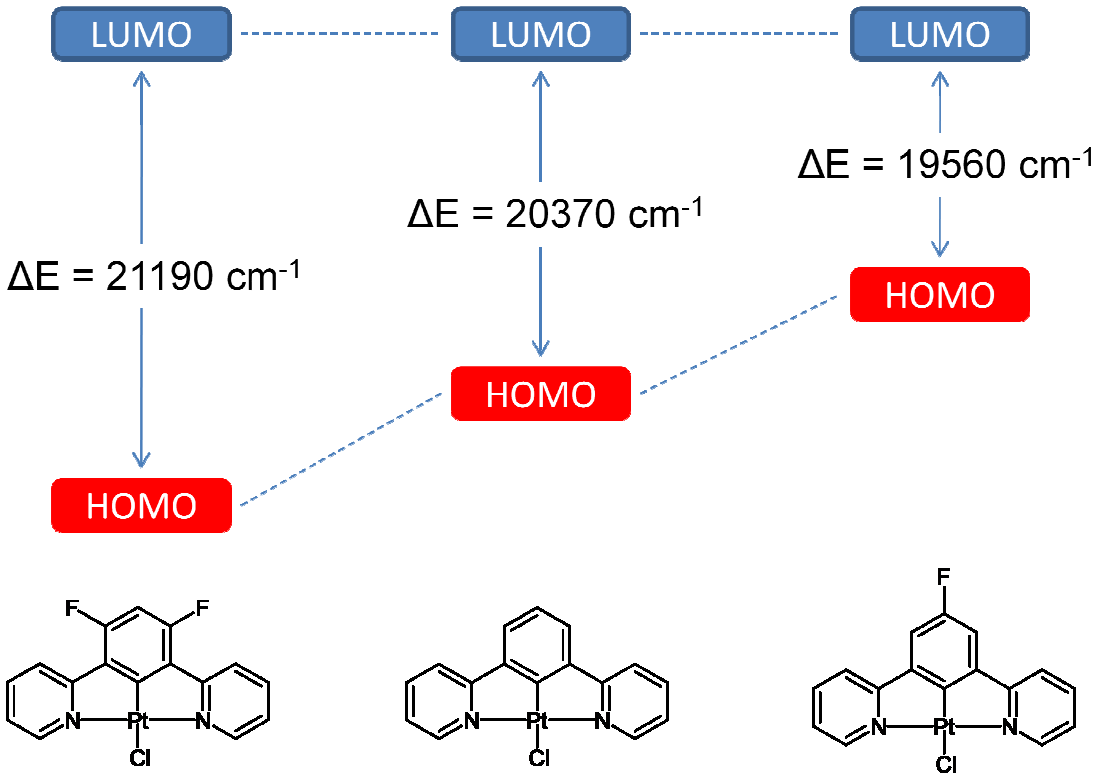

Figure 16: Schematic representation of the relative energies of the HOMO-based orbitals and LUMO-based orbitals of [PtL^{2}Cl] and [PtL^{28}Cl], relative to [PtL^{1}Cl].

2,6-di(2-pyridyl)-4-nitrobenzene Platinum(II) Chloride, [PtL^{3}Cl]

Absorbance

The complex containing an electron-withdrawing NO_2- group on the 4' position, [PtL^{3}Cl], was prepared. The absorption profile is similar to that of [PtL^{1}Cl], and contains absorption bands at similar energies (Table 5, Figure 17).

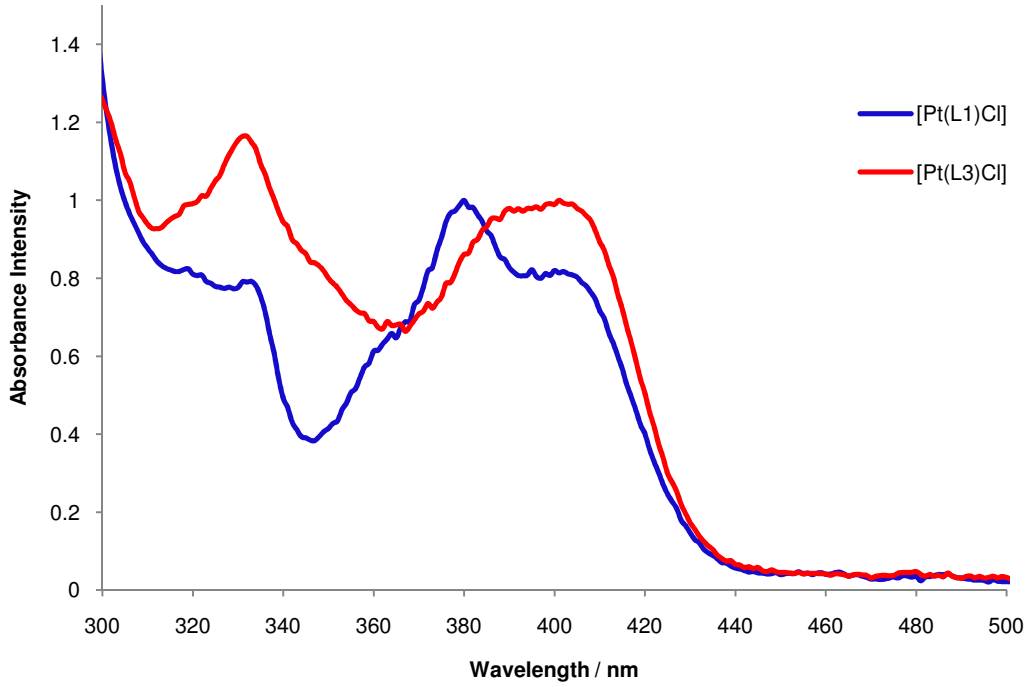

Figure 17: Normalised UV-vis absorption spectra of complexes [PtL^{3}Cl] (red) and [PtL^{1}Cl] (blue) in DCM at 298 K.

Table 5: Solution-based photophysical properties of [PtL^{1}Cl] and [PtL^{3}Cl] (DCM, 298 K).

Complex	Absorbance λ_{max}/nm (ε / L mol^{-1}cm^{-1})	Emission λ_{max}/nm	τ_0 degassed (aerated)/μs[a]	Φ_{lum} degassed (aerated)
[PtL^{1}Cl][b]	332 (6510), 380 (8690), 401 (7010), 454* (270), 485* (240)	491, 524, 562	7.2 (0.50)	0.60 (0.039)
[PtL^{3}Cl]	250, 285, 330, 388, 399, 480*	492, 515	0.78[c]	0.03 (0.02)

[a]Lifetime at infinite dilution, [b]Photophysical data from reference 1, [c]lifetime recorded for a dilute solution (absorbance < 0.05), *Forbidden S → T absorption bands, sh = shoulder. [PtL^{3}Cl] was too insoluble to perform accurate concentration-dependent analysis, and extinction coefficients could not be obtained.

Emission

The emission of [PtL^{3}Cl] occurs at similar energy to [PtL^{1}Cl], and the emission profile of the former complex is significantly less structured (Figure 18, Table 5). This result was unexpected; DFT orbital predictions for [PtL^{1}Cl] indicate that the HOMO is largely localised on the central phenyl ring, and a big orbital contribution is made at position 4'. Electron withdrawing groups at this position should have a greater stabilising effect on the HOMO, leading to a blue-shift. The results suggest that factors other than the electron-withdrawing nature of the nitro group are also involved in determining the electronic transition energy, but these factors remain unknown. The less structured spectrum may indicate significant geometry change between the ground and excited state, or that significant electronic perturbation occurs within the molecule upon excitation.

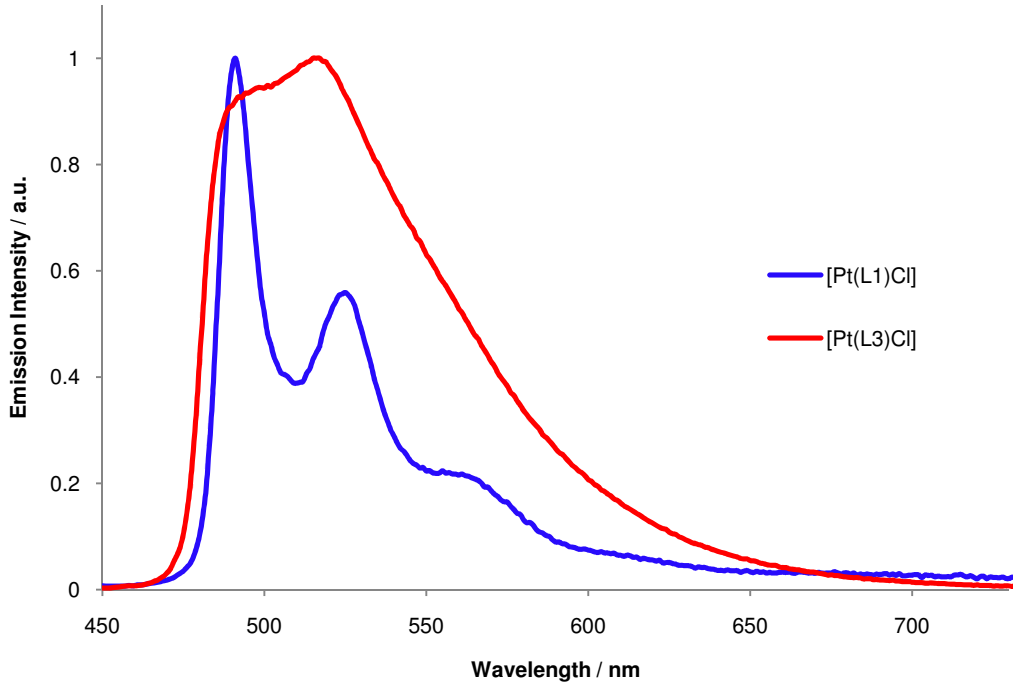

Figure 18: Normalised emission spectrum of dilute samples of [PtL^{3}Cl] (red) and [PtL^{1}Cl] (blue) in DCM at 298 K. Note the broader profile of [PtL^{3}Cl].

[PtL^{3}Cl] was only weakly luminescent in DCM at room temperature (φ = 0.03). The quenching of emission by the introduction of a nitro group to an aromatic organic fluorophore is well reported in the literature – the nitro group introduces a lower lying non-radiative n-π^* state.[12,13,14] It seems that the nitro group has had a similar effect on this complex. The complex was only sparingly soluble, which prevented determination

of the lifetime at infinite dilution. However, the lifetime of the dilute solution used to measure the quantum yield will be used as an approximation (τ_{obs} = 786 ns). This lifetime is very short for such complexes.

3.4.1.2 Exploring the Influence of the Substitution Position: Methyl Substituents on the Pyridyl Rings

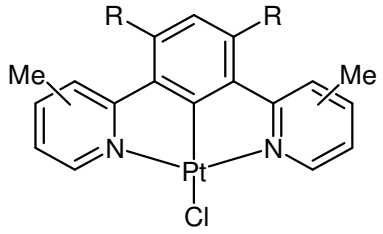

R = H or F

Figure 19: Representation of the two series of isomers under study. The series involving R = F will be referred to as the 3',5'-difluorinated series, and the series involving R = H will be referred to as the non-fluorinated series.

The pyridyl rings make a significant contribution to the LUMO-based orbitals, and little contribution to the HOMO. We expected that addition of electron donating substituents to the pyridyl rings would destabilise the LUMO-based orbitals and lead to a blue-shift. Two series of isomeric complexes, [PtL$^{5\text{-}8}$Cl] and [PtL$^{9\text{-}12}$Cl], containing methyl groups on each of the free pyridyl carbons were prepared. The first series incorporates an unsubstituted central phenyl ring and the second series incorporates the 3,5-difluorinated central ring (Figure 19). The latter were expected to show blue-shifted absorbance and emission relative to their non-fluorinated analogues, as established for the parent compounds, [PtL^{1}Cl] and [PtL^{2}Cl]. The absorbance and emission of the non-fluorinated and fluorinated complexes will be discussed relative to these reference parent complexes.

Absorbance

The absorption spectra of both series of isomers show a set of strong absorption bands below 305 nm, and lesser intense charge transfer bands between 305 and 430 nm, typical of such complexes. As for the parent compounds, all of the fluorinated complexes i) absorb at higher energy than their non-fluorinated analogues ii) display a sharpening of the band occurring around 330 nm, iii) appear to “lose” the lowest energy

singlet absorption band in this region. Direct S → T absorption bands were observed in the high concentration absorption spectrum of all the complexes (Table 6 and Table 7). These bands were very weak (ε ≈ 200 M^{-1} cm^{-1}) confirming the relative forbiddenness of these transitions.

Table 6: Solution-based photophysical properties of complexes containing methyl n-pyridyl substituents (DCM, 298 K).

Complex	Absorbance λ_{max}/nm (ε / L $mol^{-1}cm^{-1}$)	Emission λ_{max}/nm	τ_0 degassed (aerated)/μs[a]	Φ_{lum} degassed (aerated)
[PtL^{1}Cl][b]	332 (6510), 380 (8690), 401 (7010), 454* (270), 485* (240)	491, 524, 562	7.2 (0.50)	0.60 (0.039)
[PtL^{5}Cl]	322 (5180), 334 (5289), 363sh (4383), 382 (6333), 405sh (4299), 459*sh, 489*	497, 529, 565sh,	7.74 (0.34)	0.51 (0.024)
[PtL^{6}Cl][c]	326 (7820), 356 (6420), 374 (8930), 400 (7040), 479* (260)	487, 521, 560	10.0 (0.04)	0.73
[PtL^{7}Cl]	335 (12350), 360 (9150), 370 (11210), 399 (8464), 455*sh (280), 490* (130)	494, 528, 565sh,	11.1 (0.58)	0.13 (0.001)
[PtL^{8}Cl]	327 (6500), 339 sh (6030), 390 sh (6440), 413 (6730), 492* (310)	506, 529, 569sh	------[d]	0.03 (< 0.001)

[a]Lifetime at infinite dilution, [b]Photophysical data from reference 1, [c]Prepared by a former group member, [d]emission too weak to obtain lifetime, *forbidden S → T absorption bands, sh = shoulder.

Table 7: Solution-based photophysical properties of complexes containing a 3',5'-difluorinated aryl ring, and methyl n-pyridyl substituents (DCM, 298 K).

Complex	Absorbance λ_{max}/nm (ε / L mol^{-1}cm^{-1})	Emission λ_{max}/nm	τ_0 degassed (aerated)/μs[a]	Φ_{lum} degassed (aerated)
[PtL^{2}Cl]	320 (6690), 334 (9180), 360 (7340), 374 (8500), 437* (140), 467* (140)	472, 502, 537sh	7.9 (0.67)	0.85 (0.087)
[PtL^{9}Cl]	323 (6030), 336 (8010), 361 (6030), 375 (7110), 444*(110),474* (90)	487, 513, 555sh, 656 ex	7.3 (0.49)	0.39 (0.20)
[PtL^{10}Cl]	316 (8910), 329 sh (10790), 358 (9000), 372 (11320), 433* (180), 462* (150)	467, 498, 529sh	7.9 (0.70)	0.87 (0.088)
[PtL^{11}Cl]	322 (5820), 336 (8620), 358 (6330), 372 (6730), 442* (110), 473* (80)	478, 510, 543sh	10.5 (0.77)	0.67 (0.061)
[PtL^{12}Cl]	292 (13890), 329 (5550), 341 (5980), 382 (6480), 475* (120)	494, 530, 565 sh	------[b]	0.02 (0.0007)

[a]Lifetime at infinite dilution, [b]emission to weak to obtain lifetime, *forbidden S → T absorption bands, sh = shoulder.

On considering the absorption spectra of the fluorinated series, there is a degree of variation in energy with methyl position (Figure 20):

$$4\text{Me-} \approx 5\text{Me-} > \text{H-} > 3\text{Me-} > 6\text{-Me}$$

$$(\text{i.e. } [PtL^{10}Cl] \approx [PtL^{11}Cl] > [PtL^{2}Cl] > [PtL^{9}Cl] > [PtL^{12}Cl])$$

[PtL^{12}Cl] absorbs at lower energy than all other complexes and has the least structured spectrum. The lowest energy band only varies slightly between all other isomers and the [PtL^{2}Cl] reference. The maximum energy difference between the lowest energy peaks is 700 cm^{-1}.

The sharper peak around 330 nm varies in energy to a greater extent. The order of peak energy here is:

$$[PtL^{10}Cl] > [PtL^{2}Cl] > [PtL^{11}Cl] > [PtL^{9}Cl] > [PtL^{12}Cl]$$

with a maximum energy difference of 1070 cm^{-1}. The intensity of this peak (and the band around 355 nm) relative to the lowest energy band also seems to vary with the position of the methyl group, and the peak is most pronounced in the spectrum of $[PtL^{11}Cl]$. Detailed theoretical investigations are required to determine the origin of this band.

For the non-fluorinated series, the energy ordering of the lowest energy band within this region is:

$$5Me- > 4Me- > H- > 3Me- > 6Me-$$

$$(\text{i.e. } [PtL^{7}Cl] > [PtL^{6}Cl] > [PtL^{1}Cl] > [PtL^{5}Cl] > [PtL^{8}Cl])$$

with an energy difference of 850 cm^{-1} between the extremes.

For both series, the absorption bands between 320 and 430 nm display negative solvatochromism. As for $[PtL^{2}Cl]$ and $[PtL^{1}Cl]$, the peaks occur at lower energy in non-polar solvents such as CCl_4 and higher energy in polar solvents such as CH_3CN. As found for $[PtL^{2}Cl]$, the difluorinated series experience a grow-in of a band at lower energy as solvent polarity is decreased. This can be seen in Figure 22 a), which compares the absorption profile of $[PtL^{11}Cl]$ in various solvents.

Interestingly, for the non-fluorinated series, the lowest energy absorption band exhibits the most significant increase in energy with increasing solvent polarity. Figure 22 b) shows the solvatochromic behaviour of $[PtL^{7}Cl]$. The lowest energy absorption shifts from 413 nm in CCl_4 to 391 nm in CH_3CN (ΔE = 1360 cm^{-1}), and changes appearance in the spectrum from a distinct band to a shoulder on the next lowest absorption peak. These results give more indication that the corresponding band in the difluorinated series is not absent in more polar solvents, but overlapping with higher energy transitions.

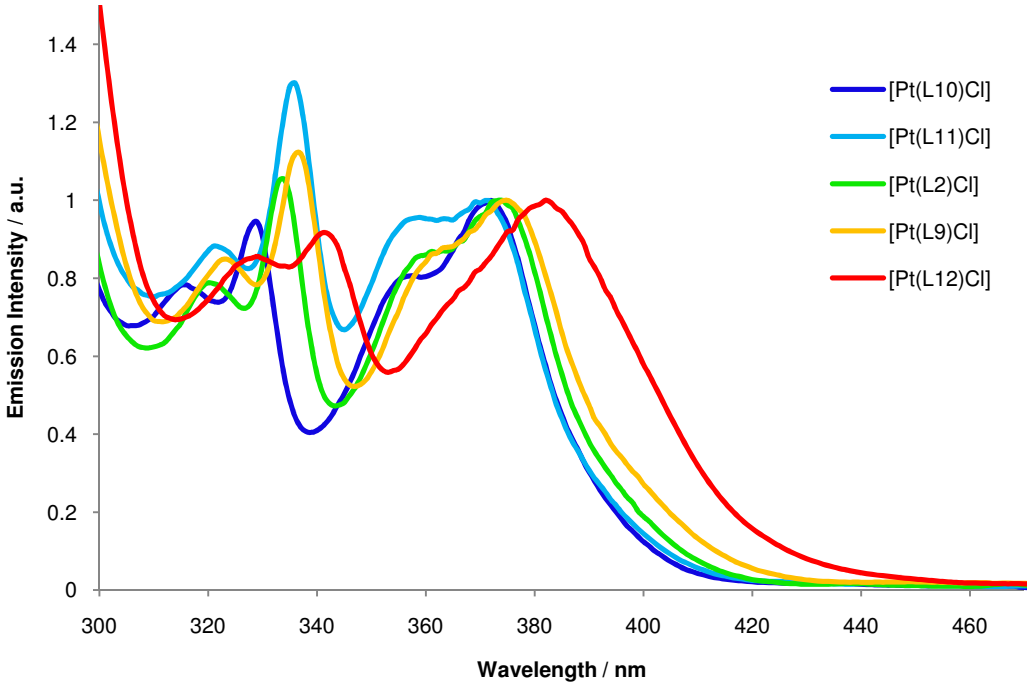

Figure 20: UV-vis absorption spectrum of the series of complexes containing n-methylated pyridyl rings and a difluorinated aryl ring, recorded in DCM 298 K.

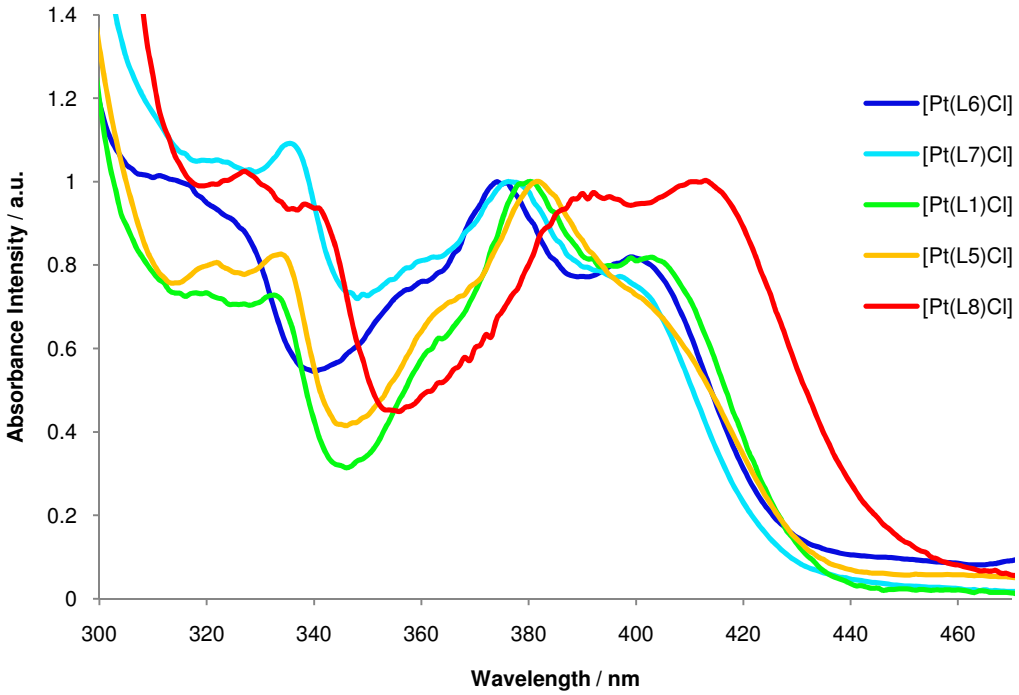

Figure 21: UV-vis absorption spectra of the complexes containing n-methylated pyridyl rings and a non-fluorinated aryl ring, recorded in DCM 298 K.

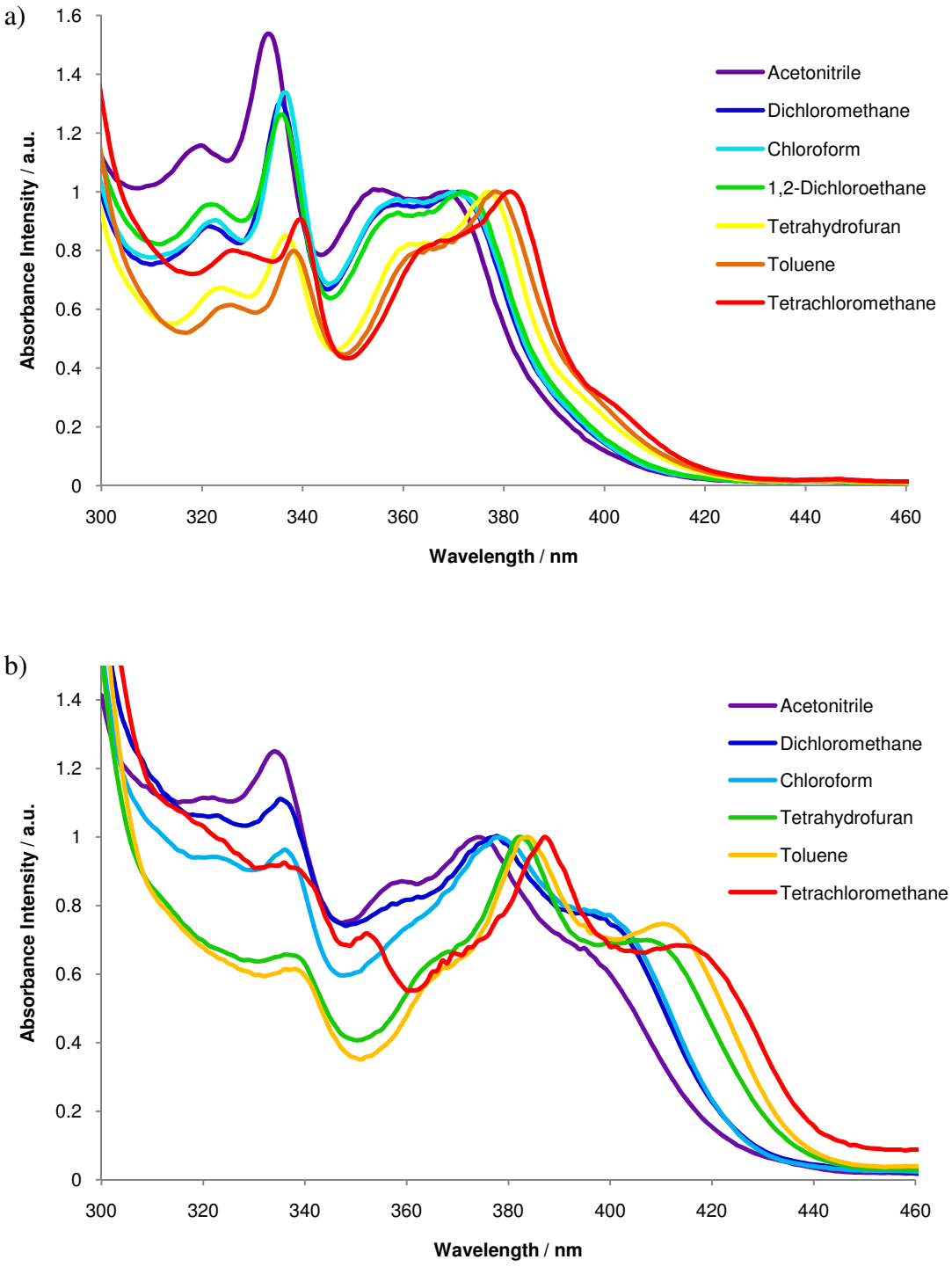

Figure 22: UV-vis absorption spectra of a) [PtL^{11}Cl] and b) [PtL^{7}Cl] recorded in various solvents at 298 K, demonstrating the solvatochromic behaviour.

Emission

All of the difluorinated complexes emit at higher energy than their non-fluorinated analogues (Figure 23, Table 6 and Table 7). As found for [PtL^{2}Cl], the emission spectra of these complexes are only weakly solvatochromic. For both series of isomers, the energy of emission was found to vary with methyl-group position in the following order:

$$4Me- > H- > 5Me- > 3Me- > 6Me-$$

In each series, the complex containing methyl groups on the 4-pyridyl positions, [PtL^{10}Cl] and [PtL^{6}Cl], emits at the highest energy (21400 cm^{-1} (467 nm) and 20500 cm^{-1} (487 nm) respectively). The other isomers all emit at lower energy than the respective reference compound (i.e. [PtL^{1}Cl] for the non-fluorinated series and [PtL^{2}Cl] for the fluorinated series). Placing the electron donating methyl group at the 4-pyridyl position therefore has the most destabilising effect on the LUMO+1. This is consistent with the theoretical orbital predictions, which show that the 4-position makes the largest contribution to the LUMO+1 energy, and zero contribution to the HOMO. Furthermore, the HOMO electron density plot predicted by Rochester et al. indicates that the other pyridyl positions make some contribution to the HOMO energy: if this is the case, any destabilisation of the LUMO may be outweighed by destabilisation of the HOMO.

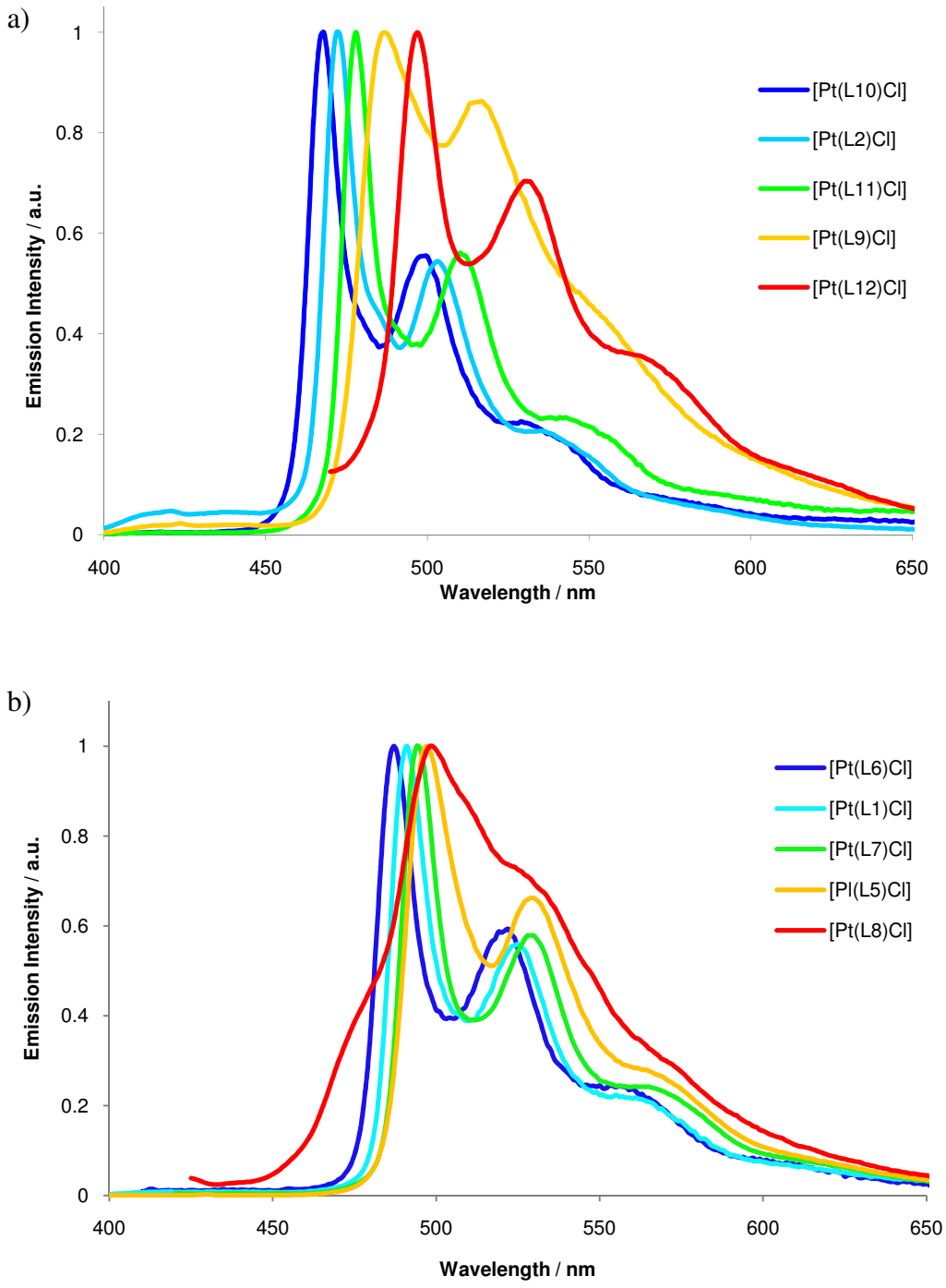

Figure 23: Normalised emission spectra of dilute samples of a) the difluorinated and b) the non-fluorinated methyl isomers, in DCM at 298 K.

The profiles of the [PtL^{8}Cl], [PtL^{9}Cl] and [PtL^{12}Cl] emission spectra notably differed from those of all the other complexes. The bands were less structured and the peak ratios of the subsequent vibronic bands relative to the highest energy 0-0 band were higher. These ratios are given in Table 8 and Table 9. As mentioned in Section 3.1, a 0-0 band of highest intensity indicates little geometry change between the ground and excited states. An increasing relative intensity of the 0-1 and 0-2 bands can therefore be

indicative of complexes that have a greater geometry difference between the ground and excited states. The crystal structure of [PtL^{12}Cl] shows that this complex involves a distortion from planarity (Chapter 2, Section 2.4.3.1): the Pt-Cl bond protrudes from the mean plane created by the rest of the molecule. The molecule also contains significant strain, as exemplified by longer Pt-N bonds than found for all other complexes. It is reasonable to assume that [PtL^{8}Cl], the non-fluorinated analogue of [PtL^{12}Cl], will contain similar distortions.

Table 8: Intensity of the 0-n vibronic bands relative to the intensity of the 0-0 vibronic band, for the difluorinated series of complexes

	Intensity of 0-0	**Intensity of 0-1**	**Intensity of 0-2**
[PtL^{2}Cl]	1	0.54	0.21
[PtL^{9}Cl]	1	0.86	0.43
[PtL^{10}Cl]	1	0.55	0.23
[PtL^{11}Cl]	1	0.56	0.23
[PtL^{12}Cl]	1	0.70	0.36

Table 9: Intensity of the 0-n vibronic bands relative to the intensity of the 0-0 vibronic band, for the non-fluorinated series of complexes

	Intensity of 0-0	**Intensity of 0-1**	**Intensity of 0-2**
[PtL^{1}Cl]	1	0.56	0.21
[PtL^{5}Cl]	1	0.66	0.27
[PtL^{6}Cl]	1	0.60	0.28
[PtL^{7}Cl]	1	0.58	0.24
[PtL^{8}Cl]	1	0.70	0.30

In the crystal structure of [PtL^{9}Cl], the plane of the phenyl ring is slightly twisted with respect to the plane created by the pyridyl rings (Chapter 2, Section 2.4.3.1). However, this distortion is relatively small, and is unlikely to account for the significantly broader spectral profile. The effect is more likely to result from the inherent electronic perturbation within this complex – during characterisation, we noticed that the ^{19}F NMR spectrum of this complex contained a broad multiplet that occurred at significantly higher chemical shift compared to all other isomers. The effect was due to a non-bonding orbital overlap between the fluorine and methyl protons, which are in close proximity (similar observations have been reported in molecules containing related arrangements of atoms).[15] This electronic perturbation will probably have an influence upon the photophysics. The emission profile of [PtL^{5}Cl], the non-fluorinated analogue of [PtL^{9}Cl], is not so significantly different from the other complexes in its series.

With the exception of the 6-diMe isomers, the quantum yields were high, in the range of 0.4 – 0.9 for the difluorinated series, and 0.1 – 0.7 for the non-fluorinated series. Lifetimes were on the microsecond scale, in the range of 7.3 – 10.5 μs and 7.2 – 11.1 μs respectively. The aerated quantum yields are also quite good (as high as 0.20), indicating that these complexes are not terribly susceptible to quenching by O_2 (see Table 29, p.216 - 220).

The quantum yields of [PtL^{8}Cl] and [PtL^{12}Cl] (φ = 0.03 and 0.02 respectively) were extremely poor compared to most other Pt(II) complexes incorporating 1,3-di(2-pyridyl)benzene ligands. Such poor luminescence could stem from a lower ligand field strength. Upon examination of the crystal structure of [PtL^{12}Cl], we noticed that the Pt-N bonds were longer in this molecule (2.064 and 2.067 Å) than in all of its isomers (crystal structures for complexes [PtL$^{9-11}$Cl] reveal Pt-N bond lengths in the range 2.017 – 2.028 Å). The greater Pt-N bond lengths in [PtL^{12}Cl] presumably occur to reduce unfavourable steric interactions between the 6-methyl groups and the ancillary chloride. The lengthened Pt-N bond implies a weakened interaction between the metal and the π-accepting pyridine groups, which would result in a lower ligand field around platinum. As a consequence, the deactivating d-d* state may exist at lower energy in [PtL^{12}Cl], so that thermal population of this state is viable. Similar arguments presumably account for the poor quantum yield of [PtL^{8}Cl], which also contains methyl groups on the 6-pyridyl position.

Also, as mentioned above, the crystal structure of [PtL[12]Cl] revealed significant distortion from planarity. The complex contains a C^Pt^Cl bond angle of 155.6 Å, which is far from the ideal of 180˚. In terms of potential energy surfaces, distortions between the ground and excited state can result in the excited state energy minima being significantly displaced relative to the ground state minima (Chapter 1, Section 1.3). If the potential energy surfaces cross near the energy minima of the excited state, then intersystem crossing, followed by non-radiative relaxation to the ground state will compete with radiative decay.

3.4.1.3 Photochemistry of a Sterically Demanding Complex

[PtL[13]Cl] contains methyl groups on the 3-pyridyl and 3,5-phenyl positions. It is reasonable to expect that this complex would suffer even more inhibition to attainment of a planar geometry than [PtL[9]Cl], since methyl groups are larger than fluorine atoms. The crystal structure for [PtL[13]Cl] has been collected, and confirms these expectations (Chapter 2, Section 2.4.3.1). Whilst the coordination plane around Pt is approximately planar, the terdentate ligand contains significant distortions from planarity.

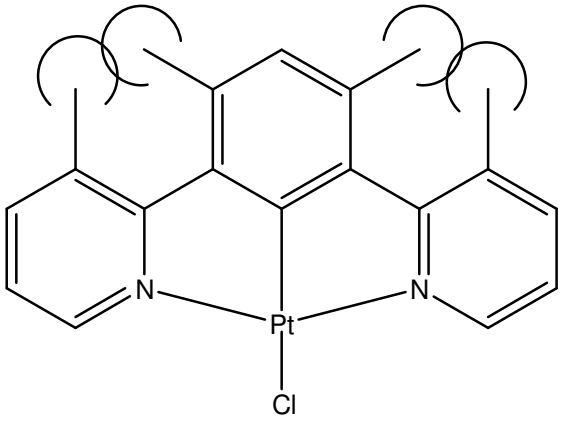

Figure 24: Representation of the unfavourable sterics that force [PtL[13]Cl] from planarity

Absorbance

The absorption spectrum of [PtL[13]Cl] contained the typical $^1\pi$-π^* bands of higher intensity between 230 and 300 nm and charge transfer bands between 320 and 420 nm. The spectrum was less structured than for [PtL[1]Cl]. An isomer of [PtL[13]Cl] was prepared for comparison ([PtL[14]Cl]). This complex contains methyl substituents on the

5-pyridyl positions. The absorbance spectrum of [PtL^{14}Cl] was more structured than [PtL^{13}Cl], but the lowest energy absorbance bands occurred at very similar wavelength (387 and 386 nm respectively). Interestingly, the lowest energy singlet absorption band present in the absorption spectrum of [PtL^{1}Cl] was absent in the absorption spectra of [PtL^{13}Cl] and [PtL^{14}Cl]. This band was also found to be absent in the absorption spectra of complexes containing 3',5'-fluoro substituents (Sections 3.4.1.1 and 3.4.1.2) – we initially thought that *fluorination* was causing this effect. However, the observations made here indicate that the effect is not due specifically to fluorine atoms, but to substitution in general at the 3,5-phenyl positions.

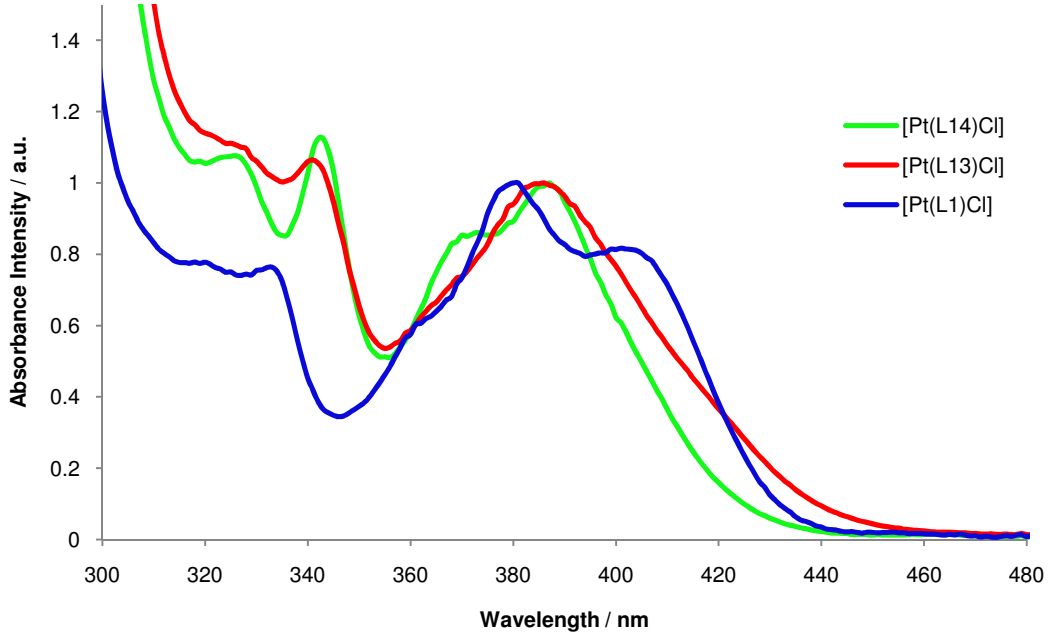

Figure 25: UV-vis absorption spectra of complexes [PtL^{13}Cl] (red) and [PtL^{14}Cl] (green) and reference complex [PtL^{1}Cl] (blue).

Emission

Despite the similarity in absorbance energy, the emission spectra were vastly different (Figure 26). [PtL^{14}Cl] gives a structured spectrum, typical of most other 1,3-dipyridylbenzene Pt(II) complexes. It emits at lower energy than [PtL^{1}Cl] (499 nm and 491 nm respectively, ΔE = 330 cm^{-1}), which is consistent with the DFT frontier orbital calculations, which predict a HOMO largely localised on the central phenyl ring. [PtL^{13}Cl] displays a broad, featureless emission spectrum, that occurs at significantly longer wavelength than [PtL^{14}Cl] (λ_{max} = 546 nm and 499 nm respectively, ΔE = 1,730

cm^{-1}). The broad, structureless emission is probably associated with the non-planar ground state of this molecule, and probably indicates that the excited state and ground state geometries are significantly different. Both of these complexes are highly luminescent, and have lifetimes of the order of several microseconds (Table 10). Surprisingly, [PtL^{13}Cl] has a higher quantum yield than both [PtL^{14}Cl] and [PtL^{1}Cl]. This seems counter-intuitive, as distortions tend to open up non-radiative decay pathways.

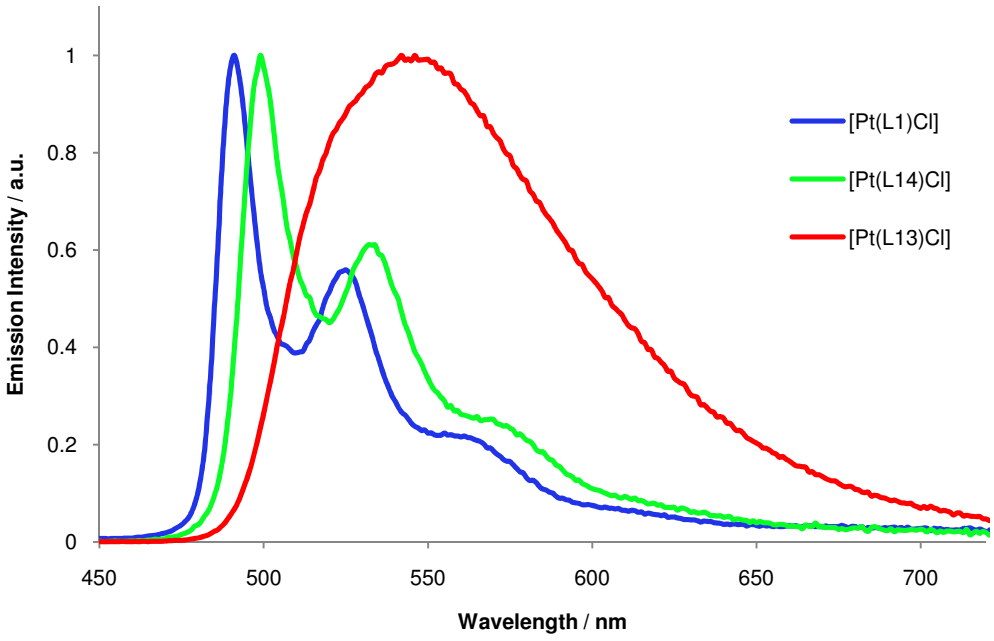

Figure 26: Normalised emission spectra of dilute samples of complexes [PtL^{13}Cl] (red), [PtL^{14}Cl] (green) and [PtL^{1}Cl] (blue), in DCM at 298 K.

Table 10: Photophysical data for complexes [PtL^{13}Cl] and [PtL^{14}Cl], with data for [PtL^{1}Cl] included for reference.

Complex	Absorbance λ_{max}/nm (ε / L mol^{-1} cm^{-1})	Emission λ_{max}/nm	τ_0 degassed (aerated) /μs[a]	Φ_{lum} degassed (aerated)
[PtL^{1}Cl][b]	332 (6510), 380 (8690), 401 (7010), 454* (270), 485* (240)	491, 524, 562	7.2 (0.50)	0.60 (0.039)
[PtL^{13}Cl]	327 sh (6300), 341 (6100), 367 sh (4010), 386 (5740), 488* sh (100)	546br	7.7 (0.34)	0.75 (0.046)
[PtL^{14}Cl]	325 (6450), 343 (6730), 374 sh (5190), 387 (6010), 461* (100), 493* (90)	499, 533, 573sh	11.9 (0.62)	0.55 (0.071)

[a]Lifetime at infinite dilution, [b]Photophysical data from reference 1, *forbidden S → T absorption bands, sh = shoulder, br = broad

3.4.1.4 Increasing the Electron-Donating Character of the 4-Pyridyl Substituent

Amongst the isomers incorporating methyl groups in the pyridyl rings, substitution at the 4-position was found to generate the largest blue shift of emission. In order to try to induce a further shift to the blue, complexes containing more strongly electron-donating groups (-OMe, -NMe_2) at this position were targeted. These groups should cause a greater destabilisation of the LUMO+1 than -Me. Previous results demonstrate that fluorinated complexes always emit at higher energy than their non-fluorinated analogues, so investigations here focused on complexes involving a 3,5-difluorinated phenyl ring.

Absorbance

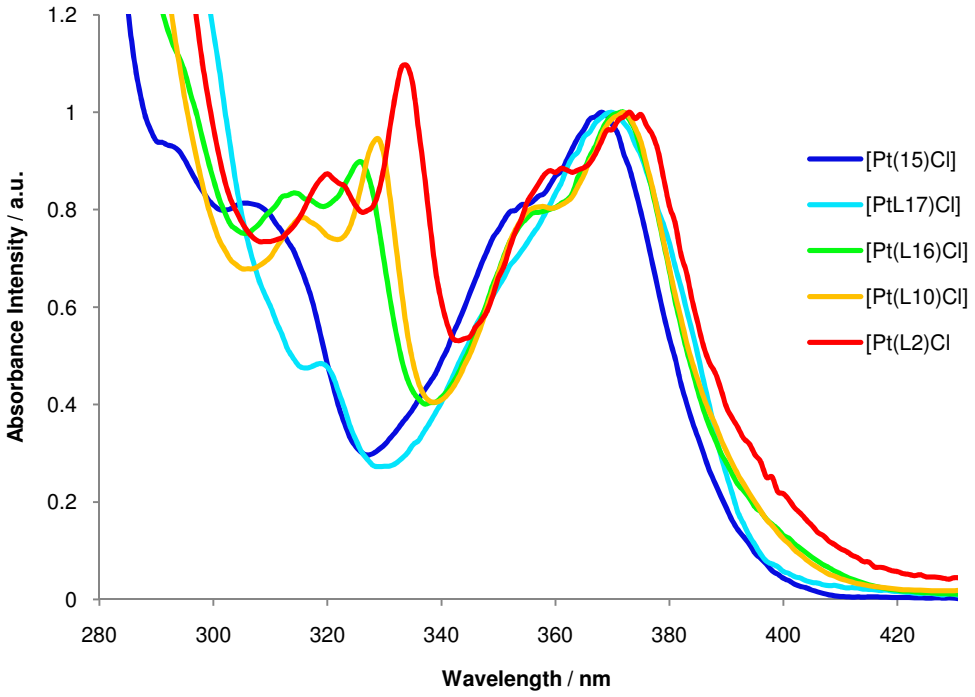

Figure 27: UV-vis absoption spectra of complexes containing a 3,5-difluorinated aryl ring and electron donating 4-pyridyl substituents (DCM, 298 K).

The resolved lowest energy singlet band observed in [PtL^{1}Cl] was absent from the absorption spectra of all of these complexes, consistent with 3',5'-substitution of the aryl ring being the cause of this effect. There was little variation in energy between the lowest two absorption bands within this series (ΔE_{max} = 440 cm^{-1}). However, both the energy and relative intensity of the sharp peak around 330 nm were dramatically affected by the nature of the 4-substituent (ΔE_{max} = 2740 cm^{-1}). The lowest energy absorption band varied with complex in the following order:

$$[PtL^{15}Cl] > [PtL^{17}Cl] > [PtL^{16}Cl] \approx [PtL^{10}Cl] > [PtL^{2}Cl], \qquad \Delta E_{max} = 440 \text{ cm}^{-1}$$

Contrary to what was expected, [PtL^{15}Cl] exhibited the highest energy absorption (Table 11). NMe_2- is a more powerful electron-donor than MeO-, so [PtL^{17}Cl] was expected to yield the largest blue-shift. Direct S → T absorptions were observed in higher concentration solutions of all complexes. The energy of this band did increase with increasing electron-donating character of the 4-substituent, and occurred at highest energy for [PtL^{17}Cl].

Table 11: Photophysical data for dilute solutions of complexes containing a 3,5-difluorinated aryl ring and electron donating 4-pyridyl substituents (DCM, 298 K)

	Absorbance λ_{max}/nm (ε / L mol^{-1}cm^{-1})	**Emission λ_{max}/nm**	**τ_0 degassed (aerated)/μs[a]**	**Φ_{lum} degassed (aerated)**
[PtL^{2}Cl]	320 (6690), 334 (9180), 360 (7340), 374 (8500), 467* (130)	472, 502, 537 sh	7.9 (0.67)	0.85 (0.087)
[PtL^{10}Cl]	316 (8910), 329 sh (10790), 358 (9000), 372 (11320), 462* (140)	467, 498, 529 sh	7.9 (0.70)	0.87 (0.088)
[PtL^{15}Cl]	294sh (6440), 306 (5680), 352sh (5560), 368 (6810), 427*sh (120), 445* (100), 455* (70)	461, 492, 519sh	7.60 (0.58)	0.71 (0.096)
[PtL^{16}Cl]	314 (6350), 326 (6790), 355sh (6010), 372 (7570), 436*sh (118), 464* (80)	470, 502, 532sh	6.02 (0.74)	0.75 (0.11)
[PtL^{17}Cl]	319 (6580), 352 sh (9310), 370 (13910), 443* (160)	455, 485, 512 sh	4.7 (0.13)	0.60 (0.033)

[a]Lifetime at infinite dilution, *Forbidden S → T absorption bands, sh = shoulder.

[PtL^{29}Cl], the non-fluorinated analogue of [PtL^{15}Cl] has been prepared by a previous group member, S. Develay. It was of interest to compare the photophysics of this complex with that of the other complexes containing 4-methyl substituents (prepared here). The absorption spectrum of this complex compared to [PtL^{6}Cl] and [PtL^{1}Cl] is shown in Figure 29. The absorption spectra of these three complexes possess a similar profile, and all of these complexes absorb at lower energy than their difluorinated analogue. The lowest energy singlet band occurs at similar energy for all three complexes, whereas higher energy singlet absorption bands show greater variation in energy between the complexes. These bands occur at highest energy for the [PtL^{29}Cl], which contains the most powerful electron donating 4-pyridyl substituent (-OMe), of

this mini-series of complex. Again, the direct S → T band was found to increase in energy with increasing electron donor ability of the 4-substituent.

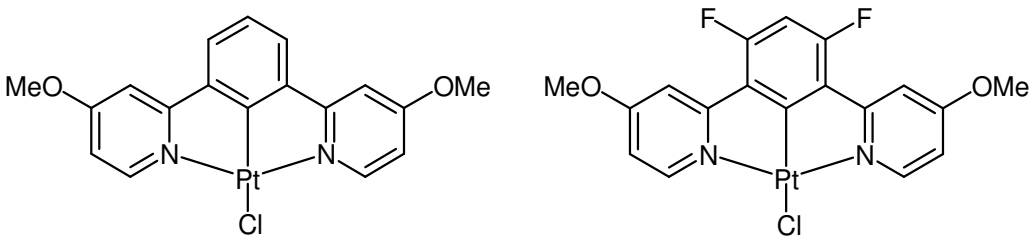

[PtL^{27}Cl] [PtL^{15}Cl]

Figure 28: Molecular structure of [PtL^{29}Cl], and its 3',5'-difluorinated analogue [PtL^{15}Cl].

Table 12: Solution-based photophysical data of complex [PtL^{29}Cl], with data for [PtL^{6}Cl] and [PtL^{1}Cl] included for comparison (DCM, 298 K).

	Absorbance λ_{max}/nm (ε / L mol^{-1} cm^{-1})	**Emission λ_{max}/nm**	**τ_0 degassed (aerated) /µs[a]**	**Φ_{lum} degassed (aerated)**
[PtL^{1}Cl][b]	332 (6510), 380 (8690), 401 (7010), 454* (270), 485* (240)	491, 524, 562	7.2 (0.50)	0.60 (0.039)
[PtL^{6}Cl][c]	326 (7820), 356 (6420), 374 (8930), 400 (7040), 479* (260)	487, 521, 560,	10.0 (0.34)	0.73 (0.04)
[PtL^{29}Cl][c]	310 (224010), 368 (24960), 401 (19200), 464* (330), 475* (310)	481, 515, 553	5.3 (0.37)	0.81 (0.05)

[a]Lifetime at infinite dilution, [b]Photophysical data from reference 1, [c]Complexes prepared by a former group member, *Forbidden S → T absorption bands, sh = shoulder

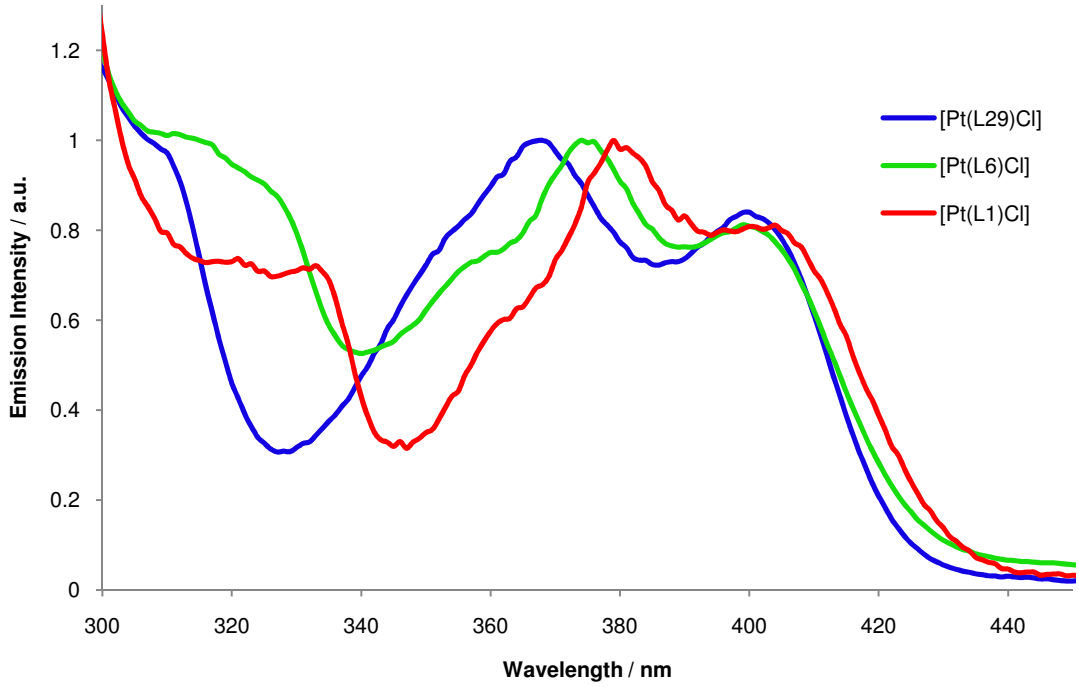

Figure 29: UV-vis absorption spectra of [PtL^{29}Cl] (blue), with [PtL^{1}Cl] (red) and [PtL^{6}Cl] (green) included for comparison (DCM, 298 K)

Emission

Increasing electron donor ability of substituent

NMe_2- > MeO- > Me- > H-

Increasing energy of emission

Figure 30: Schematic representation of the relationship between emission energy and electron donor ability of the 4-pyridyl substituent

The emission energy of the complexes discussed on pages 137 - 139 was found to increase with the electron donor ability of the 4-substituent, and [PtL^{17}Cl] was found to emit at the highest energy, in line with the expectations (see Figure 31). Again, difluorinated complexes were found to emit at higher energy than non-fluorinated analogues.

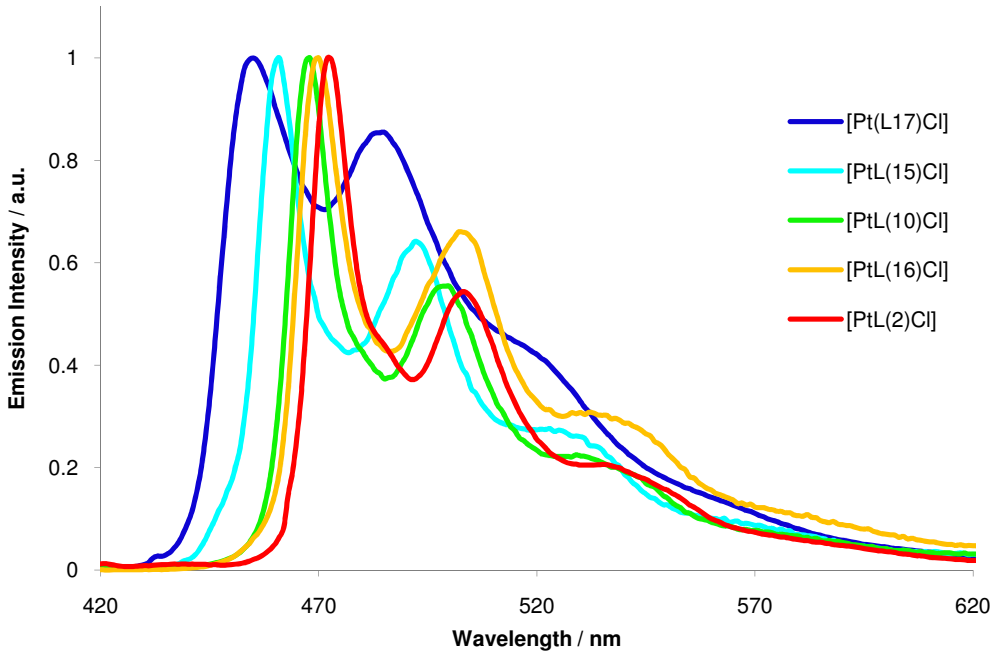

Figure 31: Normalised emission spectra of complexes containing a 3,5-difluorinated aryl ring and electron donating 4-pyridyl substituents (DCM, 298 K).

The high intensity of emission is retained in these new complexes incorporating the stronger electron donors, with φ in the range 0.60-0.87. There is, however, some evidence of a trend of a slight decrease in the quantum yield and lifetime with an increase in emission energy for the symmetrical complexes. This could be because the excited state is becoming closer in energy to a higher lying non-radiative state, such as the d-d* state, so that there is an increased probability of non-radiative decay via this state at 298 K.

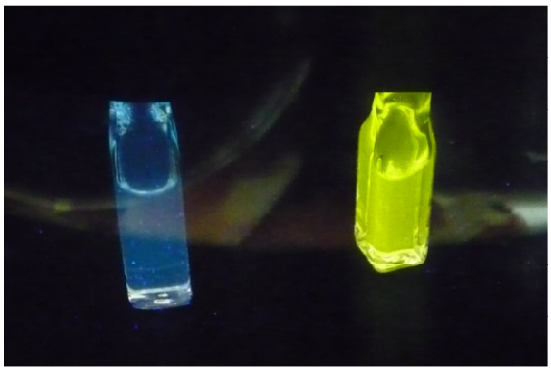

Figure 32: Photograph of a degassed dilute solution (~ 10^{-6} M) of [PtL^{17}Cl] (left) and [PtL^{13}Cl] (right) irradiated with long-wave UV light (DCM, 298 K). The picture demonstrates nicely how modification of the terdentate ligand allows the colour of emission to be tuned.

[PtL^{17}Cl] exhibits the bluest emission of all 1,3-dipyridylbenzene Pt(II) chloride complexes prepared to date, with an emission maximum occurring at 455 nm in DCM at ambient temperature. The spectrum is broader than the other 4-substituted complexes. Perhaps the strongly electron-donating nature of this substituent enforces a significant rearrangement of electron density between the ground and excited state. The emission of this complex is modulated by acid (Figure 33). Treatment with an excess of trifluoroacetic acid leads to a dramatic red-shift to 507 nm (ΔE = 2250 cm^{-1}). Protonation of the amine groups will attenuate their electron-donating ability, accounting for this effect.

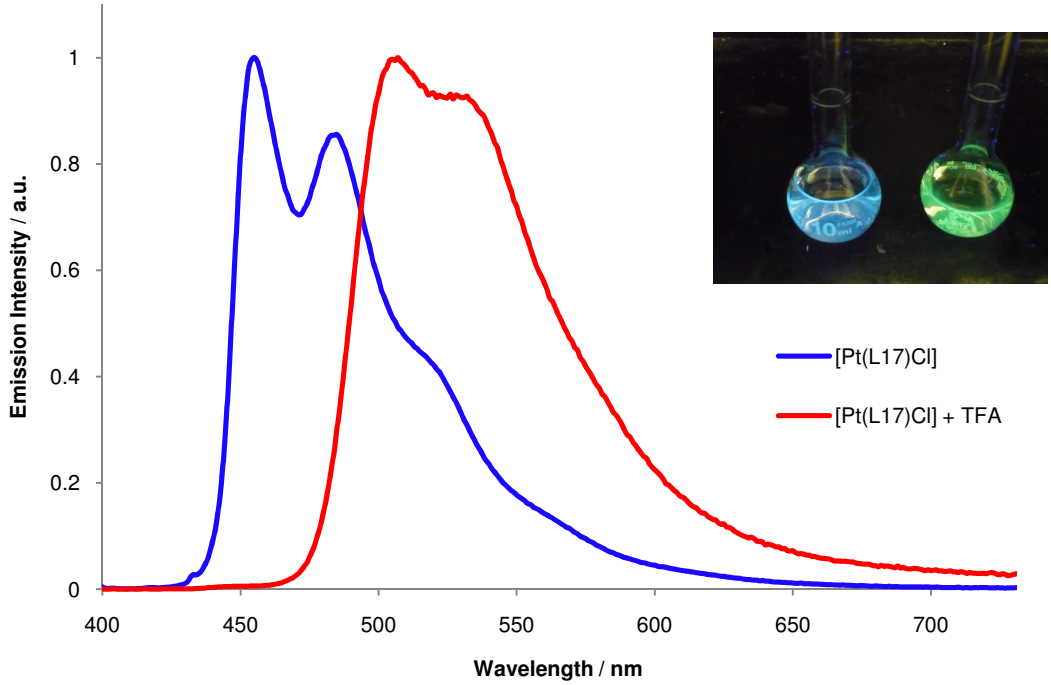

Figure 33: Normalised emission spectra of a dilute sample of [PtL^{17}Cl] in DCM at 298 K, in the absence (blue) and presence (red) of trifluoroacetic acid (TFA). Inset: photograph of a dilute solution of [PtL^{17}Cl] (~10^{-6} M), before (left) and after (right) addition of TFA.

Thompson et al., who investigated analogous bidentate N^C systems (first discussed in Chapter 1, Section 1.5), found a similar response of emission energy to electron donating substituents placed on the pyridyl ring. For example, incorporation of electron donating groups at the 4-pyridyl position gave complexes that exhibit high energy emission. Complexes *4,6-dfp-4meopy* and *4,6-dfp-4-dmapy* (Figure 34) were found to emit weakly at 456 and 447 nm respectively, from a 2-methyltetrahydrofuran solution at room temperature. Their terdentate analogues, [PtL^{15}Cl] and [PtL^{17}Cl] emit at 461 nm and 455 nm respectively from DCM at ambient temperature.

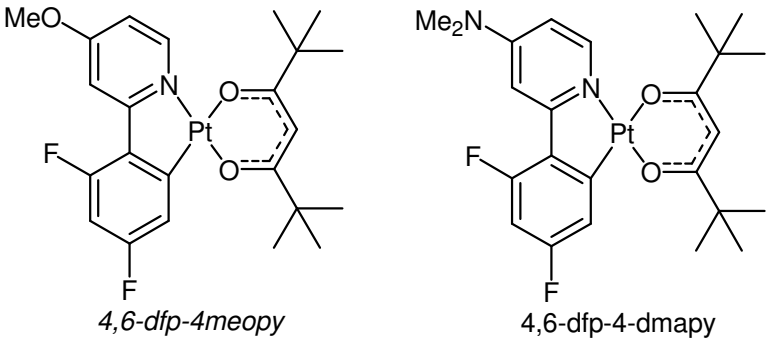

Figure 34: Structures of4,6-dfp-4meopy and 4,6-dfp-4-dmapy

It was noticed that all of the bidentate complexes prepared by Thompson et al. possess emission maxima at slightly higher energy than their terdentate analogues. Therefore, in terms of optimising the *energy* for blue emission, addition of a second pyridyl ring has no benefit. However, addition of the second pyridyl ring to the ligand framework leads to a dramatic improvement in quantum yield. For example, [PtL^{15}Cl] and [PtL^{17}Cl] are highly emissive, with quantum yields of 0.71 and 0.60 (DCM, 298 K) respectively, whereas the bidentate complexes *4,6-dfp-4meopy* and *4,6-dfp-4-dmapy* are almost non-emissive, with $\varphi < 0.01$ (2-methyltetrahydrofuran, 298 K). This affect can be attributed to the increased rigidity and increased ligand field splitting within the terdentate system. Furthermore, the green-yellow emission tails of the terdentate complexes are less intense than their bidentate analogues (as discussed in Section 3.4.1.1), leading to enhanced blue colour purity.

The unsymmetrical complex, [PtL^{16}Cl], containing one MeO- substituent emits at only a slightly shorter wavelength than the [PtL^{2}Cl] reference complex (470 nm, 21280 cm^{-1} and 472 nm, 21190 cm^{-1} respectively), whereas the symmetrical di-methoxy complex, [PtL^{15}Cl] emits at a significantly shorter wavelength (461 nm, 21690 cm^{-1}). A similar effect was observed by Williams et al. when investigating related N^C^N complexes involving pyrazoles (initially discussed in Chapter 1, Section 1.6.2).[16] Pyrazole is a poorer electron acceptor than pyridine. The unsymmetrical complex, complex **52** which contained one pyrazole and one pyridine ring (Figure 35) displayed emission at similar energy to [PtL^{1}Cl], whereas the symmetrical pyrazolate complex, complex **51** (i.e. two pyrazole rings) emitted at significantly higher energy.

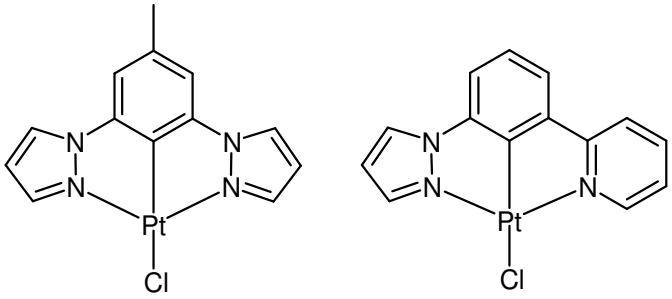

51 **52**

Figure 35: A reminder of the molecular structures of complexes 51 and 52.

DFT calculation results for the pyrazole-containing complexes indicated that the LUMO-based orbitals for the unsymmetrical complex were located on the lower energy pyridyl ring, and that the pyrazolate ring made essentially no contribution to these orbitals, accounting for the lower energy emission of the unsymmetrical complex relative to the symmetrical bis-pyrazole complex. Removal of the C_2-symmetry in [PtL^{16}Cl] probably alters the atomic contribution to the LUMO-based orbitals in a similar way. One can expect that the LUMO-based orbitals of the unsymmetrical complex will be mainly localised on the unsubstituted pyridyl ring, which is stabilised relative to the methoxy-substituted pyridyl. This would be consistent with the observation that the unsymmetrical complex emits at similar energy to [PtL^{2}Cl]. These results demonstrate the necessity to place electron donating substituents on both of the 4-pyridyl positions of the terdentate ligand, in order to bring about the maximal blue-shift.

3.4.1.5 Incorporation of Electron-withdrawing CF_3 Groups at the 4-Pyridyl Position

As placing electron-donating groups at the 4-pyridyl position led to complexes with blue-shifted emission, it was expected that electron-withdrawing substituents at the 4-pyridyl position should generate a red-shift. Synthesis of complex [PtL^{19}Cl], which contains fluorine atoms on the 4-pyridyl position, was attempted but unfortunately the ligand degraded during the complexation reaction.

Complexes [PtL^{20}Cl] and [PtL^{30}Cl] (this complex was prepared by a previous student, see Figure 36) contain electron-withdrawing CF_3- groups at the 4-pyridyl position. [PtL^{20}Cl] also contains the difluorinated phenyl ring. An unsymmetrical analogue of

[PtL^{20}Cl], in which one of the CF_3- substituents is replaced with an electron-donating MeO- substituent, has also been prepared ([PtL^{21}Cl]).

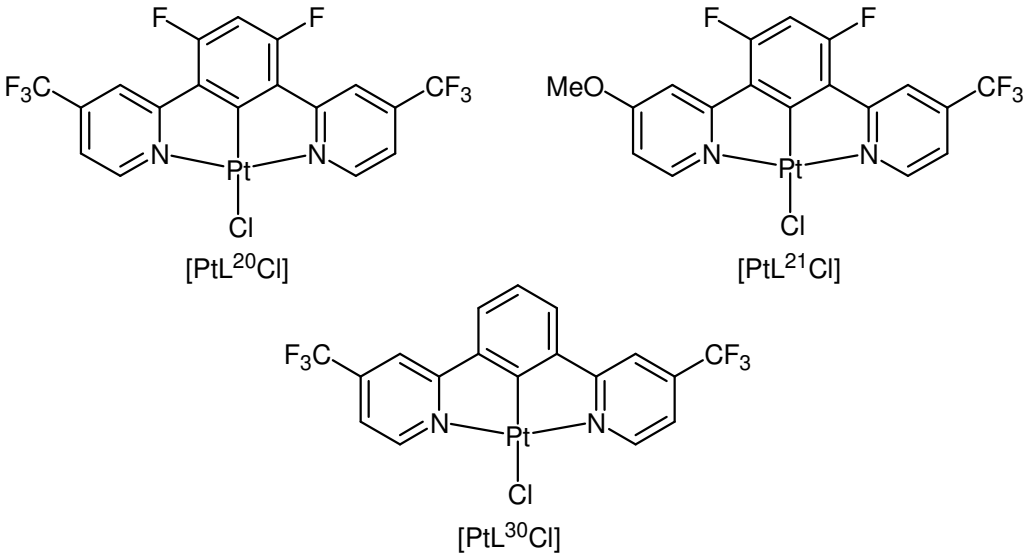

Figure 36: Molecular structures of the complexes containing CF_3 substituents on the 4-pyridyl positions.

DCM solutions of [PtL^{20}Cl] were found to exhibit thermochromism – on cooling to 77 K, the yellow solution turned into a deep blue glass (see Figure 37). A change in colour could indicate that intermolecular interactions between the molecules changes upon cooling, which could stem from a change in the ground state geometry. Reference 17 describes some bi-metallic N^C systems that exhibit thermochromism. At room temperature, intramolecular σ-interactions between the two Pt centres result in low energy, broad-featureless emission (from a ^{3}MMLCT state). On cooling, a blue-shift in absorbance and emission occurs (both on the solid and in solution), and the spectra become more structured: the emission is more typical of a ^{3}LC/^{3}MLCT excited state. This indicates that on cooling, the geometry must change leading to an increase in Pt-Pt distance. The solid form of [PtL^{20}Cl] does not change colour upon cooling, indicating that this is a solution-based effect. DCM solutions of the non-fluorinated analogue, [PtL^{30}Cl], also displays some thermochromic behaviour, but less dramatically. Upon cooling to 77 K, the yellow solution forms a deep orange glass.

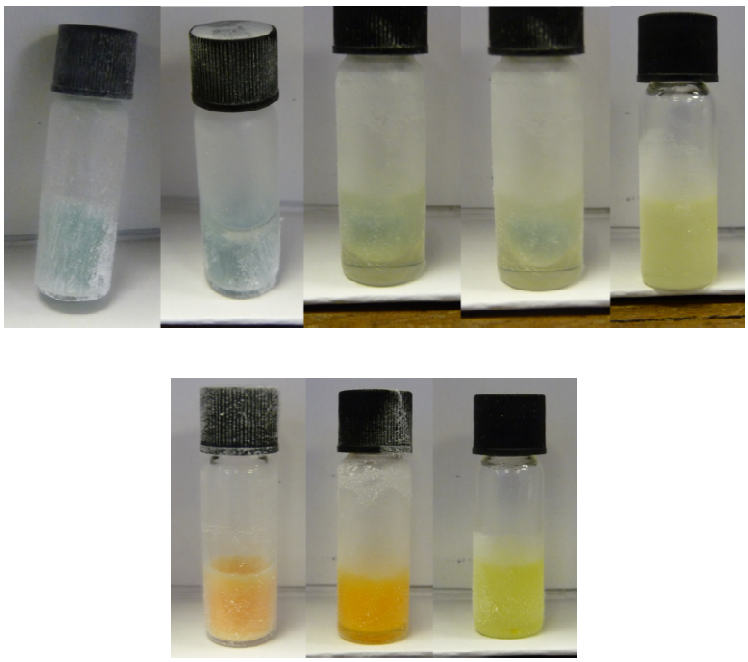

Figure 37: Thermochromism observed upon thawing from a 77 K DCM glass (left to right). Top: [PtL^{20}Cl], Bottom [PtL^{30}Cl].

Absorption

As expected, [PtL^{30}Cl] absorbs at longest wavelength. Its fluorinated analogue, [PtL^{20}Cl], absorbs at a similar wavelength to the second lowest energy maximum of [PtL^{1}Cl], indicating that the stabilisation conferred by CF_3 on the LUMO-based orbitals involved in the absorptive transition has been matched by the stabilisation conferred by the 3',5'-fluoro substituents on the HOMO. The unsymmetrical complex, [PtL^{21}Cl], has an unusual spectral profile – a weak shoulder is observed at 427 nm (ε = 800 L mol^{-1} cm^{-1}), along with a shoulder at 389 nm (ε = 3300 L mol^{-1} cm^{-1}) and a peak at 369 nm (ε = 4820 L mol^{-1} cm^{-1}). The different absorption profile of [PtL^{21}Cl] may reflect significantly different atomic orbital contributions to the frontier molecular orbitals (compared to C_{2v} symmetrical [PtLX] systems), brought about by the asymmetry of the terdentate ligand.[16]

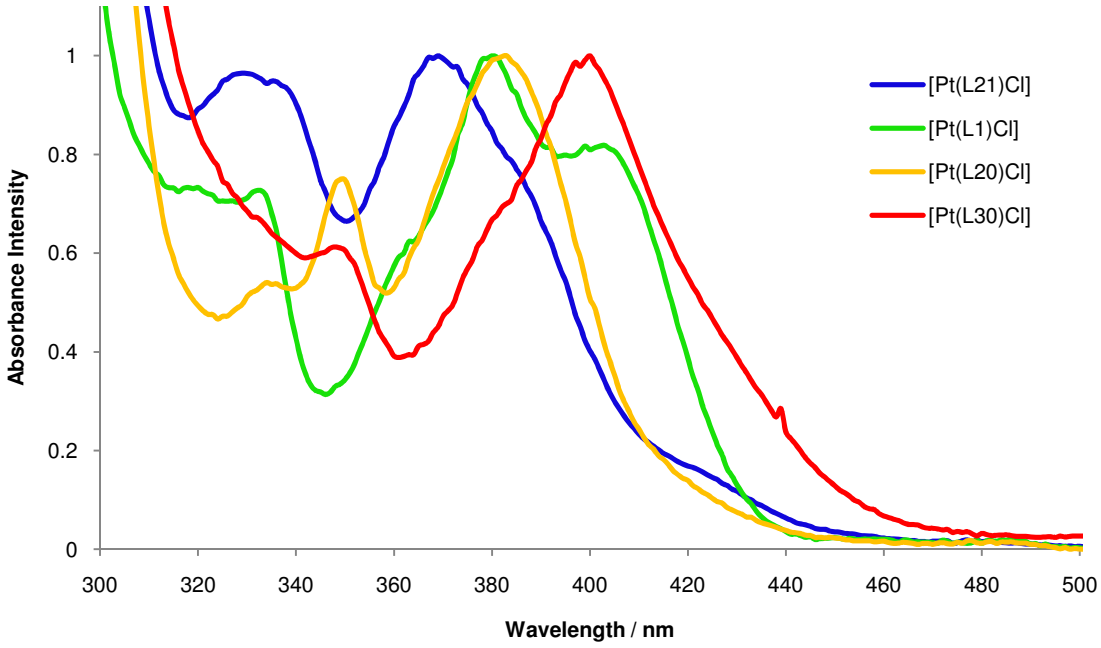

Figure 38: UV-vis absorption spectra of complexes containing 4-pyridyl CF_3 substituents, with the absorption spectrum of [PtL[1]Cl] included for reference (DCM, R.T.).

Table 13: Solution-based photophysical data of complexes containing CF_3 4-pyridyl substituents, with data for [PtL[1]Cl] included for comparison (DCM, 298 K).

	Absorbance λ_{max}/nm (ε/L mol^{-1} cm^{-1})	**Emission λ_{max}/nm**	**τ_0 degassed (aerated) /μs[a]**	**Φ_{lum} degassed (aerated)**
[PtL^{1}Cl][b]	332 (6510), 380 (8690), 401 (7010), 454* (270), 485* (240)	491, 524, 562	7.2 (0.50)	0.60 (0.039)
[PtL^{20}Cl]	334 sh (4470), 349 (6510), 383 (8190), 486 (170)*	497, 527, 575 sh	5.6 (1.7)	0.59 (0.21)
[PtL^{21}Cl]	329 sh (4580), 338 sh (4440), 369 (4820), 389 sh (3300), 427 sh (800), 480* (150)	495, 528, 573 sh	5.5 (0.67)	0.57 (0.038)
[PtL^{30}Cl][c]	284 (27900), 348 (4690), 400 (11400), 503* (200)	518, 548	4.1[d]	0.37 (0.087)

[a]Lifetime at infinite dilution, [b]Photophysical data from reference 1, [c]Prepared by a former group member, [d]Aerated lifetime not reported, *forbidden S → T absorption bands, sh = shoulder.

Emission

All complexes with 4-pyridyl CF_3 substituents emit at lower energy than [PtL^1Cl]. Amongst these four complexes, the emission of [$PtL^{30}Cl$] occurs at the lowest energy (518 nm, 19310 cm^{-1}). It is interesting to note that complex [$PtL^{20}Cl$] emits at lower energy than [PtL^1Cl], despite having fluorine atoms on the phenyl ring (497 nm/20120 cm^{-1} and 491 nm/20370 cm^{-1} respectively). This indicates that the 4-pyridyl CF_3-substituent has a greater stabilising effect on the LUMO-based orbital involved in the T → S transition, than phenyl 3',5'-difluoro substituents have on the HOMO. The unsymmetrical complex, [$PtL^{21}Cl$], emits at the same energy as [$PtL^{20}Cl$] – this gives further support to the theory that the LUMO-based orbitals are localised on the more stable pyridyl ring in unsymmetrical complexes.[16]

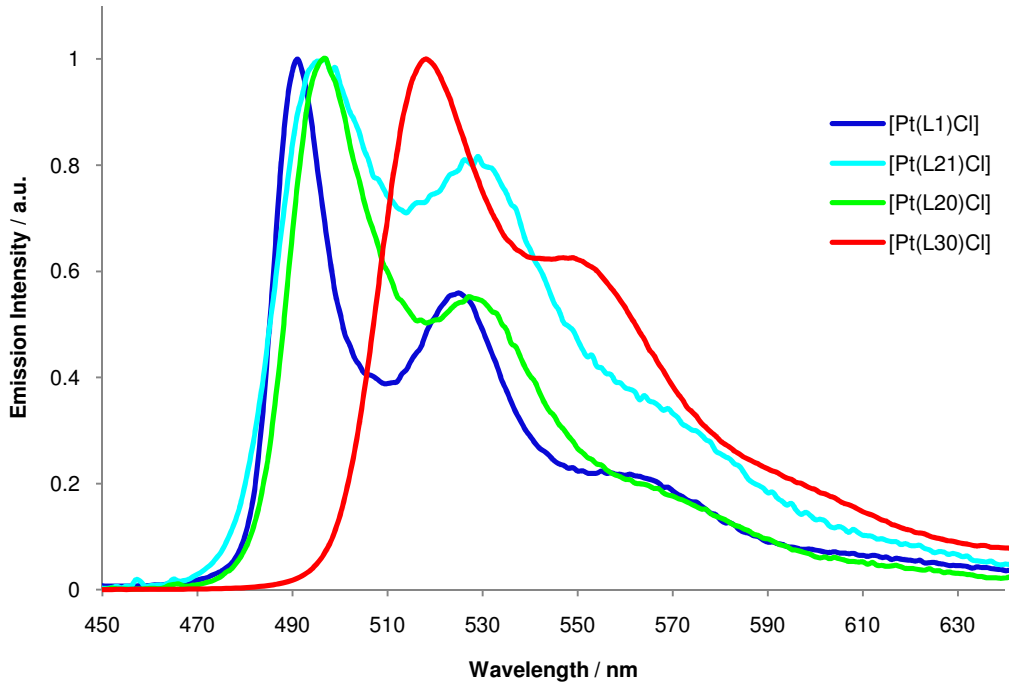

Figure 39: Normalised emission spectra of dilute solutions of complexes containing 4-pyridyl CF_3 substituents, with the emission spectrum of [PtL^1Cl] included for reference (DCM, 298 K).

These complexes are highly luminescent, with quantum yields in the range of 0.4 – 0.6 and the lifetimes are of the order of several microseconds. Of particular interest is the remarkably low sensitivity of [$PtL^{20}Cl$] to quenching by oxygen. The quantum yield and lifetime of this complex in an air-saturated DCM solution at R.T. are 0.21 and 1.7 µs respectively.

3.4.1.6 Fluoro-substituents at the 5-Pyridyl Position

Absorption

Complex [PtL^{22}Cl] contains electron-withdrawing fluorine atoms on the 5-pyridyl positions. The absorption profile of this complex contains the very intense bands between 230 and 300 nm that can be assigned to $^{1}\pi$-π^* transitions, and the less intense charge transfer bands between 330 – 430 nm. The energies of the absorption bands (see Table 14) are comparable to those of the unsubstituted parent, [PtL^{1}Cl]. The most significant difference between the absorption spectra of these two complexes is that the band around 400 nm appears only as a weak shoulder for [PtL^{22}Cl]. It was previously shown that this band does not appear in the DCM based absorption spectra of complexes containing a 3',5'-disubstituted phenyl ring. Rather than being absent entirely, solvatochromism studies suggested that this band had shifted to higher energy and had become mixed with the band of second lowest energy.

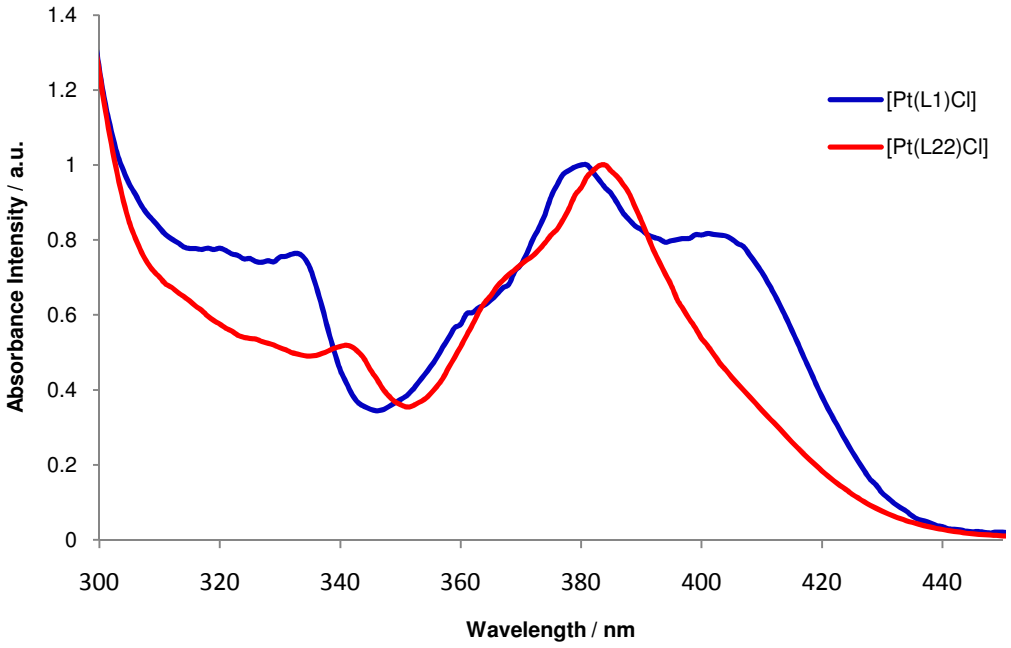

Figure 40: UV-vis absorption spectra of [PtL^{22}Cl] (red) and [PtL^{1}Cl] (blue), recorded in DCM at 298 K.

Table 14: Solution-based photophysical data of complex [PtL^{22}Cl], with data for [PtL^{1}Cl] included for comparison (DCM, 298 K).

	Absorbance λ_{max}/nm (ε/L mol^{-1} cm^{-1})	**Emission λ_{max}/nm**	**τ_0 degassed (aerated) /µs[a]**	**Φ_{lum} degassed (aerated)**
[PtL^{1}Cl][b]	332 (6510), 380 (8690), 401 (7010), 454* (270), 485* (240)	491, 524, 562	7.2 (0.50)	0.60 (0.039)
[PtL^{22}Cl]	341 (4590), 367sh (6110), 384 (8750), 460* (130), 492* (130)	499, 533, 571sh	9.62 (0.67)	0.61 (0.063)

[a]Lifetime at infinite dilution, [b]Photophysical data from reference 1, *forbidden S → T absorption bands, sh = shoulder.

Like [PtL^{20}Cl], cooling solutions of [PtL^{22}Cl] results in a dramatic colour change. The complex dissolves in DCM to give a yellow solution. On cooling to 77 K, the complex forms a deep red glass (Figure 41). During the thawing process, the sample exhibits another colour change, forming a deep blue intermediate, before thawing completely and returning the yellow solution. The colour change is likely to correspond to differing degrees of intermolecular interactions at the different temperatures – it would be of interest to follow the absorbance spectra of [PtL^{20}Cl] and [PtL^{22}Cl] as a function of temperature.

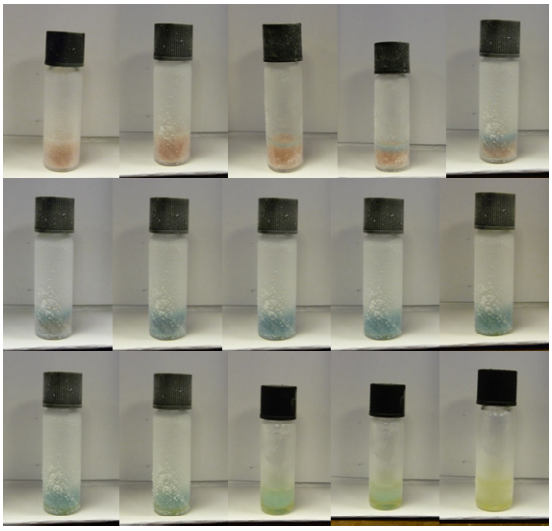

Figure 41: Photographs of [PtL^{22}Cl] in DCM, at various stages of thawing after being frozen with liquid nitrogen. The top left represents the sample after immediate removal from liquid nitrogen, and the bottom right represents a fully thawed solution.

Emission

The emission spectrum of [PtL^{22}Cl] is structured, with the 0-0 vibronic band holding the greatest intensity and occurring at 499 nm. The emission is red shifted relative to [PtL^{1}Cl] by 8 nm (ΔE = 330 cm^{-1}). This result is consistent with the DFT calculation results on [PtL^{1}Cl], which predict that the LUMO will be largely localised on the pyridyl rings. In this case, fluorine atoms on the 5-pyridyl positions must have a greater stabilising effect on the LUMO-based orbitals than on the HOMO, reducing the HOMO-LUMO energy gap.

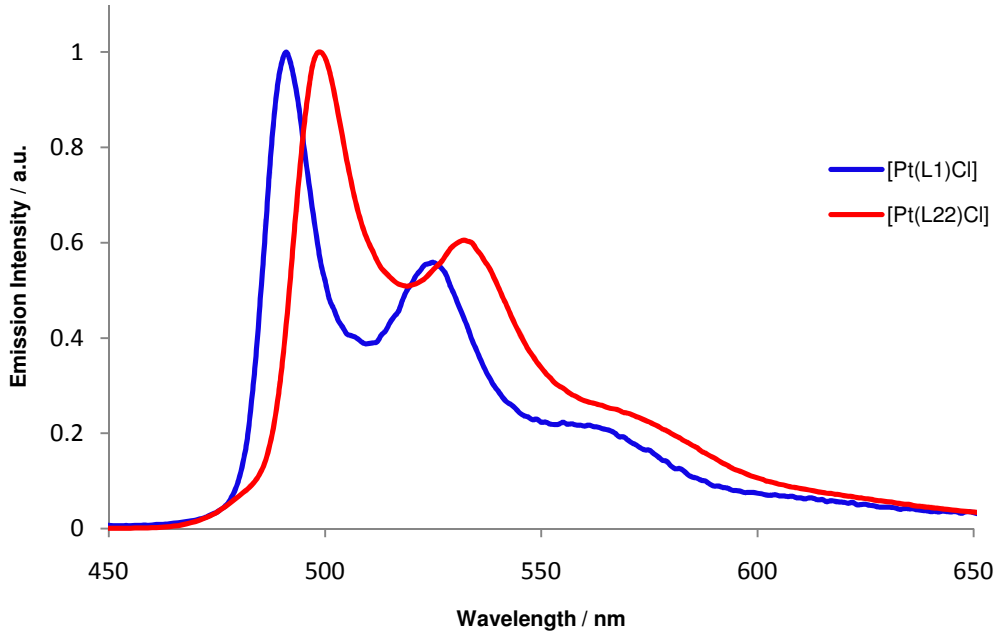

Figure 42: Normalised emission spectra of dilute solutions of [PtL^{22}Cl] (red) and [PtL^{1}Cl] (blue), in DCM at 298 K.

3.4.1.7 A Tetradentate Complex

Absorption

[PtL^{23}] was prepared primarily to be tested within living cells as a bio-imaging agent. The complex involves a tetradentate ligand only. The absorption profile of this complex is quite different to the terdentate complexes (Figure 43). There are a series of very intense absorptions between 250-350 nm, which are probably due to ligand centred

transitions ($^1\pi$-π^*), accompanied by a weak band around 390 nm, which probably represents a charge transfer band. Unfortunately, the complex was of low solubility in DCM, and it was not possible to determine accurate extinction coefficients.

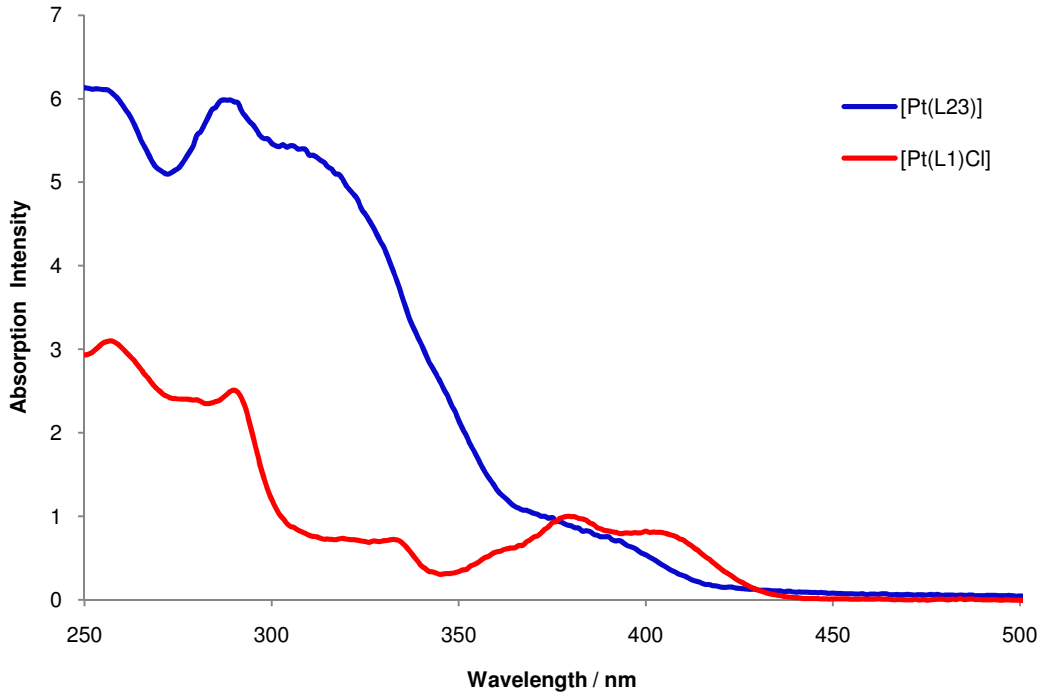

Figure 43: UV-vis absorption spectra of [PtL^{23}] (blue) and [PtL^{1}Cl] (red), recorded in DCM at 298 K.

Table 15: Solution-based photophysical data of complex [PtL^{23}], with data for [PtL^{1}Cl] included for comparison (DCM, 298 K).

	Absorbance λ_{max}/nm (ε / L mol^{-1} cm^{-1})	**Emission λ_{max}/nm**	**τ_0 degassed (aerated) /µs[a]**	**Φ_{lum} degassed (aerated)**
[PtL^{1}Cl][b]	332 (6510), 380 (8690), 401 (7010), 454* (270), 485* (240)	491, 524, 562	7.2, (0.5)	0.60 (0.039)
[PtL^{23}]	286, 308 sh, 373 sh, 390	494, 523, 560sh	23, (2.8)[c]	0.08 (0.01)

[a]Lifetime at infinite dilution, [b]Photophysical data from reference 1, [c]lifetime recorded for a dilute solution (absorbance < 0.05 at λ_{ex}), *Forbidden S → T absorption bands, sh = shoulder. [PtL^{23}] was too insoluble to perform accurate concentration-dependent analysis, and extinction coefficients could not be obtained.

Emission

[PtL^{23}] exhibited a relatively broad emission profile, with λ_{max} = 494 nm, which is slightly red-shifted compared to [PtL^{1}Cl]. This is surprising, as [PtL^{23}] absorbs at shorter wavelength than [PtL^{1}Cl].

Compared to the majority of terdentate complexes prepared here, the tetradentate complex is only weakly emissive in solution at room temperature (φ = 0.08). If the bite angles around the Pt centre are not optimum, significant strain could reside in this molecule, and this may account for the poor emissive properties. Alternatively, the trans-arrangement of the anionic oxygen and cyclometallating carbon could be unfavourable for luminescence. As explained in Chapter 1, Section 1.6.3, C^N^C type complexes are usually non-emissive at room temperature, mainly because of the trans-arrangement of the two strong-field cyclometallating carbon atoms. The lifetime of the dilute solution used to measure the quantum yield was recorded: τ_{obs} = 23 µs. The excited state of this complex is much longer lived than the terdentate complexes (τ_0 ~ 7 µs): this indicates that S → T transition has lower allowedness, and that the excited state of [PtL^{23}] contains a greater ^{3}LC contribution and smaller ^{3}MLCT contribution.[18]

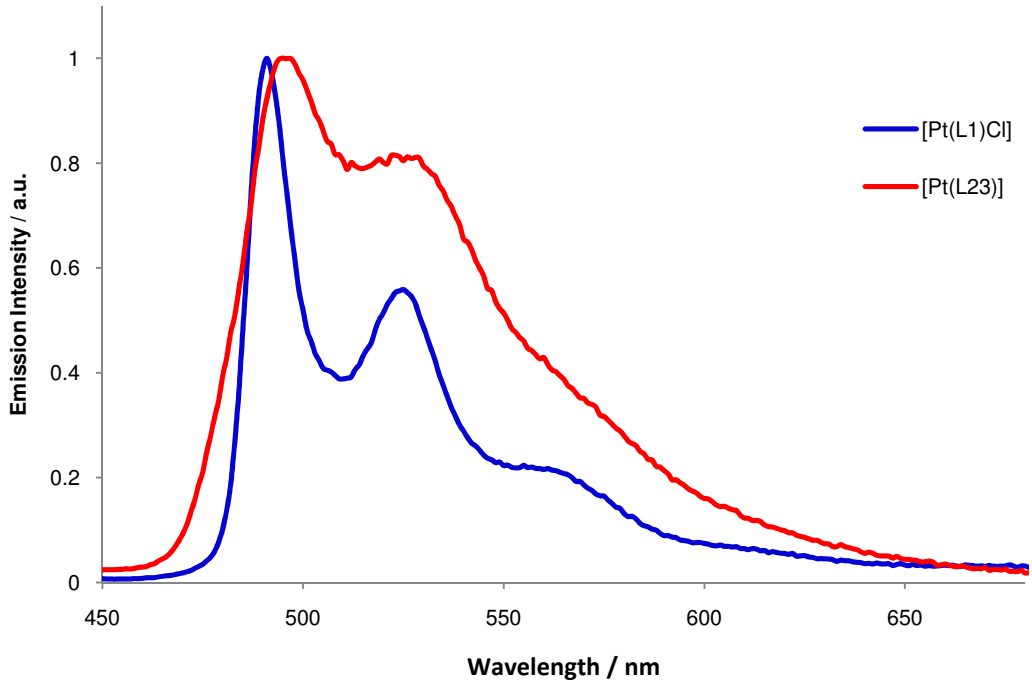

Figure 44: Normalised emission spectra of dilute samples of [PtL^{23}] (red) and [PtL^{1}Cl] (blue), in DCM at 298 K.

3.4.2 Ancillary Ligand Substitution

Much work has been done around substitution of the ancillary ligand(s) in related N^N^N, N^N^C and N^C complexes.[19,20,21,22,23,24,25,26,27] Replacement of chloride for stronger field ligands such as acetylides and cyanide often causes the d-d* state to shift to higher energy, decreasing its deactivating effect, which is observed as an increase in quantum yield. These substitutions are also commonly accompanied by an increase in emission energy, which also results from the increased ligand field splitting energy.

Very little research concerning ancillary ligand substitution in N^C^N complexes has been published to date.[28,29] Rochester, a previous group member produced a series of N^C^N complexes involving pyridine- or phosphine-based ancillary ligands.[28] These complexes had an overall charge of +1 and were unstable to decomposition in the presence of Lewis bases such as CH_3CN. The emission energies of phosphine-containing complexes are very similar to those of the analogous chloro-complexes, indicating that the ^{3}LC excited state energy is not significantly affected by these ancillary ligands. Unfortunately, photophysical data for the pyridine complexes was not reported.

3.4.2.1 Halide Exchange

The bromo- and iodo- forms of [PtL^{1}Cl] were prepared to study the effect of changing the ancillary halide. The emission was to be monitored at both room temperatures and cryogenic temperatures (Section 3.4.4.2) DFT calculations predict that the ancillary ligand makes a significant contribution to the HOMO, but minimal contribution to the LUMO-based orbitals. The electron withdrawing ability decreases on going down group 17, so one might expect the HOMO to increase in energy from chloride to iodide.

Absorption

The absorption profiles of [PtL^{1}Cl] and [PtL^{1}Br] are practically identical. [PtL^{1}I] absorption profile is similar in shape, but the charge transfer bands are red shifted by approximately 3 nm.

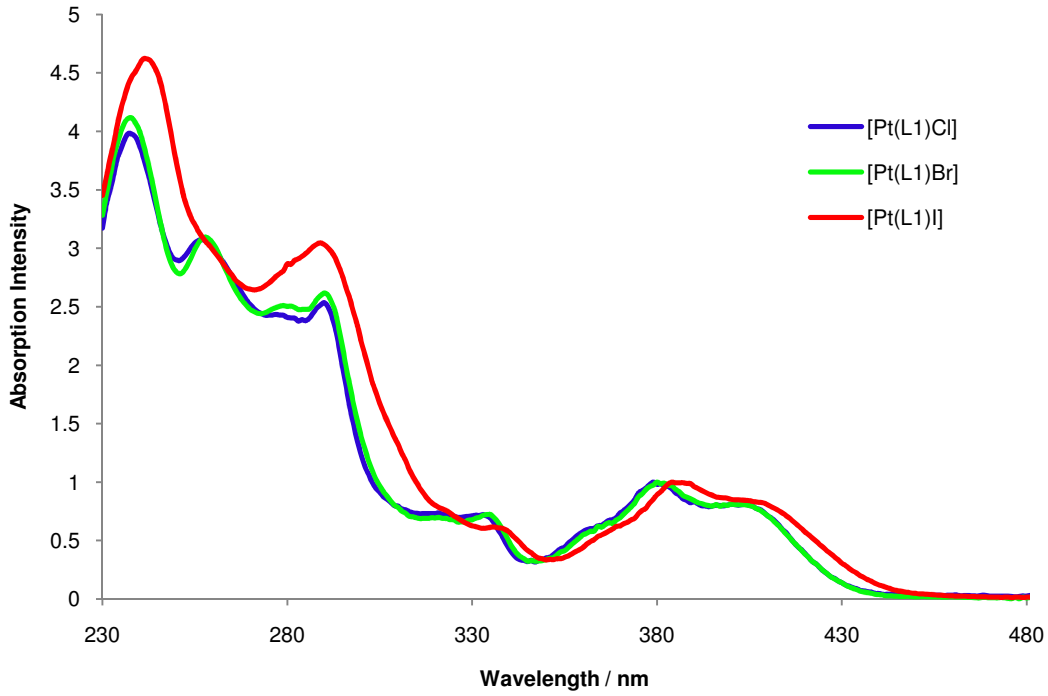

Figure 45: Normalised UV-vis absorption spectra of dilute solutions of [PtL[1]X], in DCM at 298 K.

Table 16: Solution-based photophysical data of complexes [PtL[1]X] (DCM, 298 K).

	Absorbance λ_{max}/nm (ε / L mol^{-1} cm^{-1})	**Emission λ_{max}/nm**	**τ_0 degassed (aerated) /µs[a]**	**Φ_{lum} degassed (aerated)**
[PtL[1]Cl][b]	332 (6510), 380 (8690), 401 (7010), 454* (270), 485* (240)	491, 524, 562	7.2 (0.50)	0.60 (0.039)
[PtL[1]Br]	334 (7180), 380 (9720), 401 (8120), 453* (210), 485* (180)	491, 524, 562	9.9 (0.67)	0.61, (0.072)
[PtL[1]I]	336 (4340), 385 (7130), 404 (6050), 487* (160)	491, 524, 562	8.4 (0.46)	0.57, (0.047)

[a]Lifetime at infinite dilution, [b]Photophysical data from reference 1, *Forbidden S → T absorption bands.

Emission

The normalised emission spectra (DCM, 298 K) of the three complexes are identical in energy. Similar observations were made by Tsuzuki et al., who used these complexes as

phosphorescent OLED dopants.[29] The relative band intensities (i.e. 0-0, 0-1, etc.) are the same for the [PtL^{1}X] complexes, regardless of the identity of the ancillary halogen. This implies that the equilibrium geometries of the ground and excited states are very similar in all three complexes, and are not affected by increasing the size of the ancillary ligand from chloride to iodide. The quantum yields and lifetimes are also quite similar. Substitution of the chloride with other halides is therefore not a useful strategy for tuning photophysical properties. From these results, it appears as if the halide ligand is merely a spectator ligand, contrary to the DFT predictions. However, it may just be that the halides are too similar in character to invoke a significant change. To further examine whether the halide ligand makes any contribution to the photophysics of the individual complexes, the emission was monitored at cryogenic temperatures (Section 3.4.4.2). At such low temperatures, the substates of the T_1 state can be studied in detail.

3.4.2.2 Substitution with Cyanide

Cyanide lies much higher up the spectrochemical series than the halides, so substitution with cyanide should augment the ligand field splitting. For the Pt N^C^N complexes, this effect should increase the HOMO-LUMO energy gap and lead to a blue-shift in the photophysical parameters. Furthermore, cyanide has electron withdrawing properties, so should have a stabilising effect on the HOMO, further augmenting a blue-shift.

Cyano-analogues of the two bluest complexes [PtL^{17}Cl] and [PtL^{15}Cl] were prepared, along with the cyano-analogue of [PtL^{2}Cl]. The solubility of the cyano-complexes was significantly reduced with respect to the chloro-analogues, so much so that complete photochemical analysis was only possible for [PtL^{15}CN] in DCM. [PtL^{17}CN] and [PtL^{2}CN] were soluble enough to obtain solution-based absorption and emission spectra (DCM, R.T.) and to determine some of the photophysical parameters.

Absorption

In absorption, the charge transfer bands of [PtL^{15}CN] and [PtL^{2}CN] were shifted to higher energy relative to their chloro analogues (see Table 17, Figure 46). This shift to higher energy was also observed for [PtL^{17}CN], but was accompanied by the

appearance of a new sharp band at shorter wavelength (381 nm). The weak direct S → T absorptions were observed for all cyano complexes.

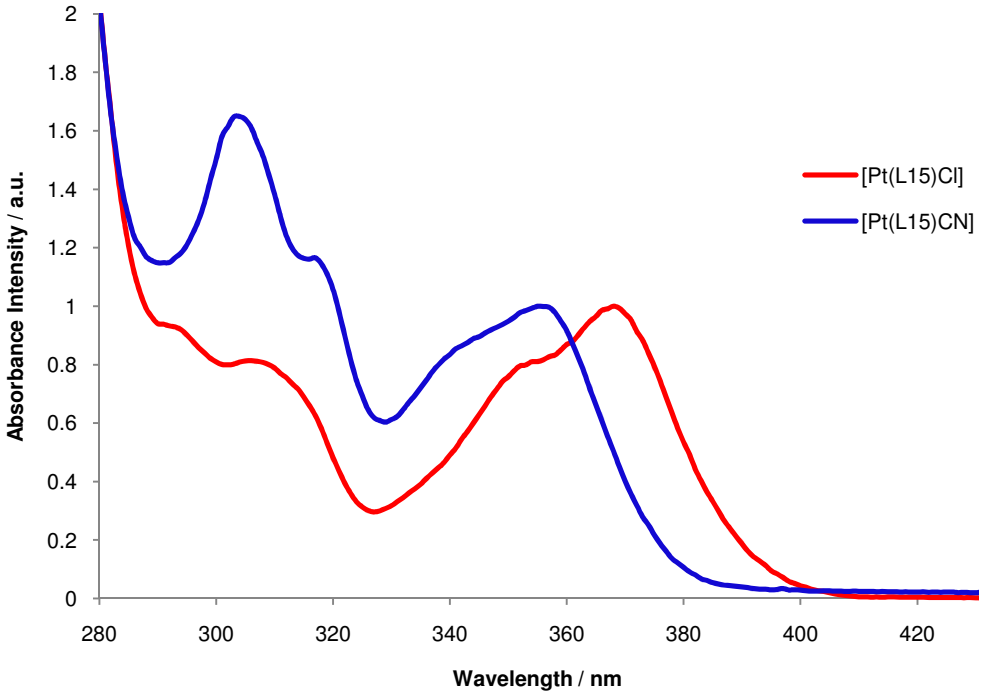

Figure 46: Normalised UV-vis absorption spectra of [PtL^{15}CN] (blue) and [PtL^{15}Cl] (red) (DCM, 298 K).

Table 17: Solution-based photophysical data of complexes containing an ancillary cyanide ligand (DCM, 298 K).

	Absorbance λ_{max}/nm (ε / L mol^{-1} cm^{-1})	**Emission λ_{max}/nm**	**τ_0 degassed (aerated) /µs[a]**	**Φ_{lum} degassed (aerated)**
[PtL^{2}CN]	259, 285, 310, 319, 334, 350, 433*, 463*	468, 499, 527	8.5 (1.52)[b]	0.66 (0.19)
[PtL^{15}CN]	263 (14300), 303 (5900), 315sh (4210), 338sh (2890), 355, (3700) 440* (70)	457, 488, 513	8.0 (0.58)	0.61 (0.17)
[PtL^{17}CN]	289, 319, 337sh, 355, 381, 440*	450, 477, 511	4.5 (0.167)[b]	0.41 (0.05)

[a]Lifetime at infinite dilution, [b]lifetime recorded for a dilute solution (absorbance < 0.05 at λ_{ex}), *forbidden S → T absorption bands, sh = shoulder. [PtL^{2}CN] and [PtL^{17}CN] were too insoluble to perform accurate concentration-dependent analysis, and extinction coefficients could not be obtained.

Emission

In all cases, a blue-shift of the emission maximum was observed relative to the chloro analogue (see Table 18). The largest increase in energy was found between the PtL^{17} cyano and chloro analogues ($\Delta E = 240\ cm^{-1}$). Compared to the chloro series, the cyano series have emission spectra with more significant green-yellow tails (i.e. the 0-1 and 0-2 vibronic peaks have a higher intensity relative to the 0-0 peak, see Table 19). A representative pair of spectra are shown in Figure 47.

Table 18: Comparison of highest energy emission maxima of cyano and chloro analogues.

	X = CN	**X = Cl**	
	λ_{max} / nm (Energy / cm^{-1})	**λ_{max} / nm (Energy / cm^{-1})**	**ΔE / cm^{-1}**
$[PtL^2X]$	468 (21370)	472 (21190)	180
$[PtL^{15}X]$	457 (21880)	461 (21690)	190
$[PtL^{17}X]$	450 (22220)	455 (21980)	240

Table 19: Table showing the intensity of the 0-n vibronic bands relative to the intensity of the 0-0 vibronic band, for the cyano and chloro analogues

	Intensity 0-0	**Intensity 0-1**	**Intensity 0-2**
$[PtL^2CN]$	1	0.66	0.31
$[PtL^2Cl]$	1	0.54	0.21
$[PtL^{15}CN]$	1	0.78	0.39
$[PtL^{15}Cl]$	1	0.64	0.27
$[PtL^{17}CN]$	1	0.99	0.55
$[PtL^{17}Cl]$	1	0.86	0.46

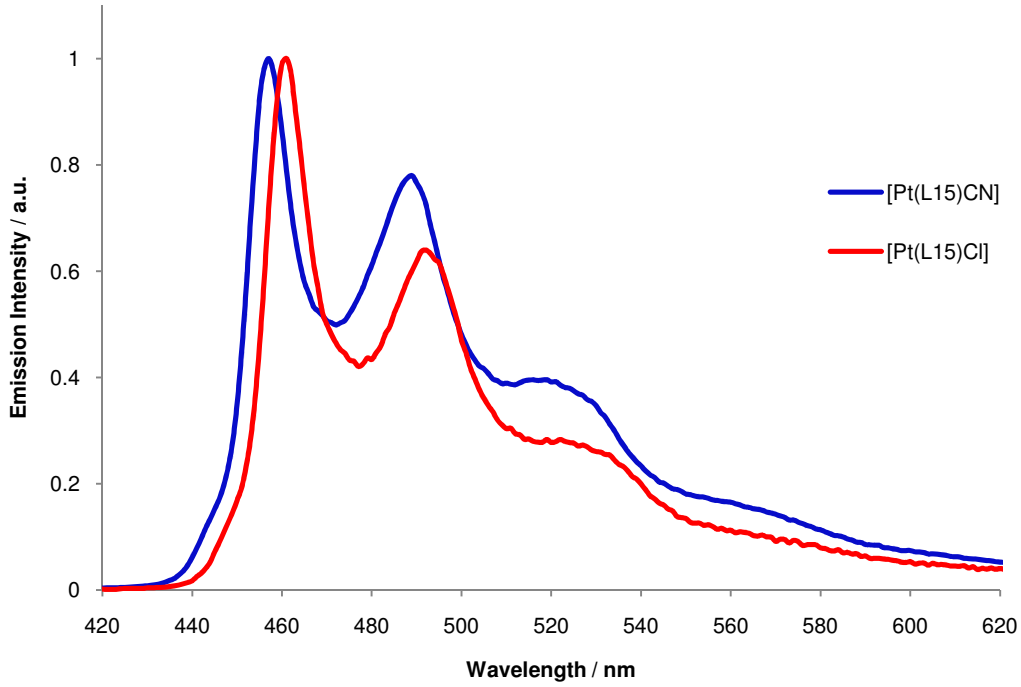

Figure 47: Normalised emission spectra of [PtL^{15}CN] (blue) and [PtL^{15}Cl] (red, DCM, 298 K).

The quantum yields of the cyano-complexes were all reduced relative to the chloro-analogues (see Table 17), but the complexes are still highly luminescent (φ above 0.41). As for the chloro analogues, quantum yield was found to decrease with an increase of emission energy of the complex. Within the experimental error, the lifetime of [PtL^{15}CN] was the same as that of the analogous chloro complex (τ_0 = 7.1 and 7.6 µs respectively). This indicates a greater k_{nr} for the cyano-complex, which suggests that the higher lying excited state has become closer in energy to the deactivating d-d* state, and [PtL^{15}CN] therefore has a higher probability of decay via this state at 298 K. Because of insolubility issues, it was not possible to determine τ_0 for [PtL^{2}CN] and [PtL^{17}CN]. Nevertheless, a value (τ_{obs}) was recorded for the very dilute solutions used to measure the quantum yield, and these values were of a similar magnitude to the τ_0 values determined for the chloro analogues.

[PtL^{17}CN] is the bluest-emitting Pt(II) N^C^N complex reported to date (λ_{max} = 450 nm, energy = 22200 cm^{-1}). Its emission occurs at even higher energy than the bispyrazolyl complex, complex **51**, reported by Williams et al.[16] (λ_{max} = 455 nm, energy = 22000 cm^{-1}). Another advantageous feature of this series of blue emitters is that they are much more luminescent than the bispyrazolyl complex (φ > 0. 41 and φ = 0.02 respectively).

3.4.3 Excimers and aggregates

3.4.3.1 Self-Quenching

As discussed in Section 3.1, the rate of emission decay of 1,3-dipyridyl benzene Pt(II) complexes decreases with increasing concentration. This is indicative of self-quenching or reaction of the excited state with ground state molecules.[7] The emission decay as a function of concentration can be fitted to a Stern-Volmer equation, of the form shown in *Eqn.* 2 (see p. 117). From this, it is possible to determine the self-quenching rate constant, k_{sq} – this value gives a measure of the affinity of the complex to form excimers (Table 20).

For most of the complexes prepared here, k_{sq} values are in the range of $2 – 6 \times 10^9$ M^{-1} s^{-1}. These are of a similar magnitude to k_{sq} values reported by Williams et al. for related complexes.[2] However, for [$PtL^{13}Cl$], the k_{sq} value is 0.50×10^9 M^{-1} s^{-1} – this is significantly smaller than values obtained for the other complexes, indicating a lower propensity to self-quench. As previously discussed, the pyridyl and phenyl methyl-groups are in close proximity in [$PtL^{13}Cl$], resulting in a non-planar geometry (Section 3.4.1.3). The non-planar geometry may hinder close approach of two molecules, accounting for a lower tendency to self-quench. Other groups have also noticed that sterics can influence self-quenching[30,31,32] The relative size of a molecule will also influence k_{sq}. For example, heavier molecules will diffuse through a solution more slowly, meaning excimers may take longer to form. Also, it seems that increasing both the electron donor or acceptor character of the 4-pyridyl substituent decreases the susceptibility of a complex to form excimers ([PtL^6Cl] is an exception).

Table 20: Self-quenching constants of the 1,3-dipyridylbenzene Pt(II) complexes (the estimated uncertainty in each k_{sq} value is ± 10 %).

	k_{sq} / 10^9 M^{-1} s^{-1}		k_{sq} / 10^9 M^{-1} s^{-1}
[PtL^{1}Cl]	5.3	**[PtL^{13}Cl]**	0.5
[PtL^{1}Br]	6.9	**[PtL^{14}Cl]**	2.9
[PtL^{1}I]	6.1	**[PtL^{15}Cl]**	2.9
[PtL^{2}Cl]	6.0	**[PtL^{15}CN]**	2.3
[PtL^{2}CN]	-----[a]	**[PtL^{16}Cl]**	3.2
[PtL^{3}Cl]	-----[a]	**[PtL^{17}Cl]**	2.1
[PtL^{5}Cl]	3.0	**[PtL^{17}CN]**	-----[a]
[PtL^{6}Cl]	8.3	**[PtL^{20}Cl]**	2.6
[PtL^{7}Cl]	3.9	**[PtL^{21}Cl]**	2.0
[PtL^{8}Cl]	-----[a]	**[PtL^{22}Cl]**	5.6
[PtL^{9}Cl]	3.9	**[PtL^{23}]**	-----[a]
[PtL^{10}Cl]	5.1	**[PtL^{29}Cl]**	3.2
[PtL^{11}Cl]	3.7	**[PtL^{30}Cl]**	3.0
[PtL^{12}Cl]	-----[a]		

[a]It was not possible to determine a k_{sq} value for [PtL^{8}Cl] or [PtL^{12}Cl] complexes, due to the weakness of their emission, and a difficulty in detecting their emission decay. Nor was it possible to determine a k_{sq} value for [PtL^{3}Cl], [PtL^{2}CN] [PtL^{17}CN] or [PtL^{23}] due to their low solubility.

3.4.3.2 Excimeric Emission

Excimers of 1,3-dipyridyl benzene Pt(II) systems tend to be emissive, and excimeric emission occurs at lower energy than emission resulting from the isolated molecules (monomeric emission). This effect can be seen in Figure 48 for [PtL^{15}Cl]; here the emission profile of a dilute sample (DCM at 298 K) is compared to emission profiles of solutions of increasing concentration. Note that this figure has been normalised with

respect to the monomeric emission (λ_{max} = 461 nm). In reality, as concentration is increased, the excimeric emission grows in at the expense of the monomeric emission. The overall colour of light observed depends on the ratio of the monomeric-to-excimeric emission, hence colour can be controlled simply by controlling concentration. This effect is being increasingly exploited in OLED design.

For increased clarity, charts in this section comparing excimeric emissions will show only the range of emission associated with the excimer – in all cases, in the range of concentrations studied (10^{-4} – 10^{-6} M) monomeric emission was always present.

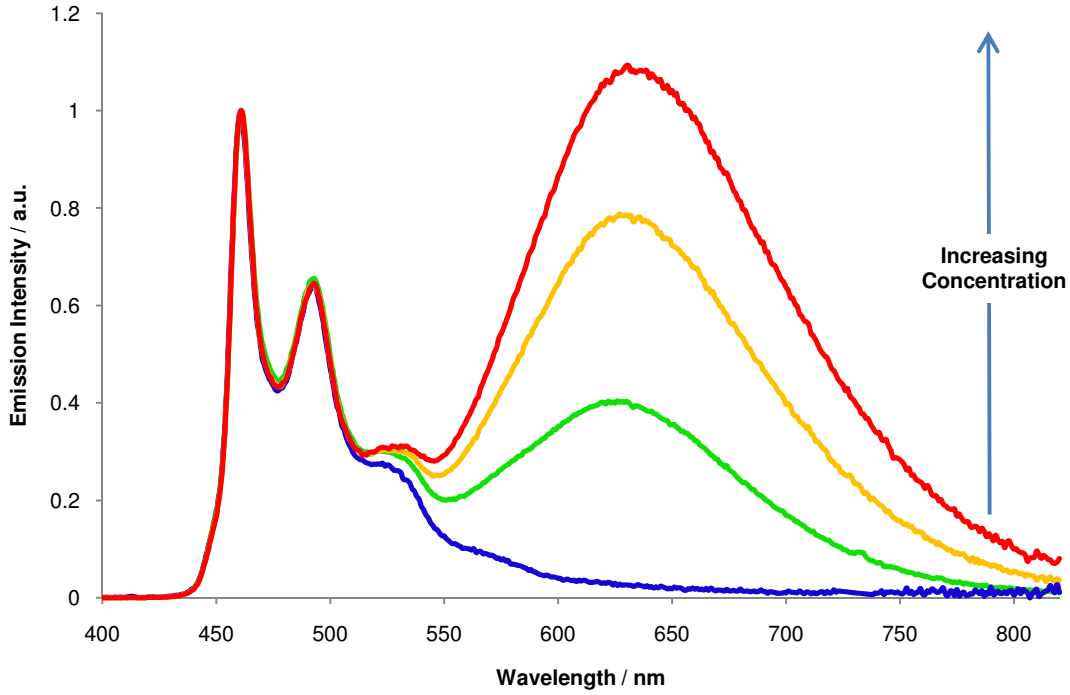

Figure 48: Emission spectra of various concentrations of [PtL^{15}Cl] (normalised at 461 nm) in DCM at 298 K. Note the increasing contribution from excimer emission with increasing concentration (10^{-6} – 10^{-4} M).

Lifetime decay plots measured at monomeric and excimeric emission maxima tend to have the form shown in Figure 49. The decay measured at the monomeric emission maximum occurs "instantaneously" after excitation (i.e. within the instrument response time of about 1 ns). When monitored at the excimer emission maximum, the plot shows an initial grow-in followed by the decay. This initial grow-in corresponds to the timescale of formation of the excimer, which can only occur after excitation.[33,34]

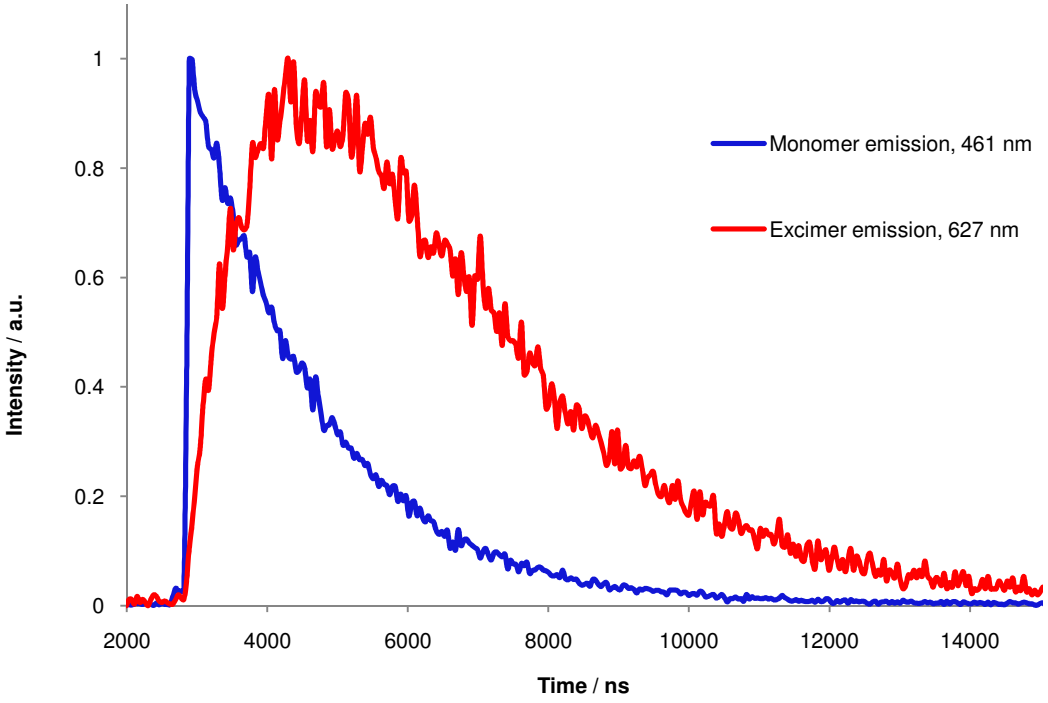

Figure 49: Excited state decay curves of 1.7 x 10^{-4} M [$PtL^{15}Cl$] in DCM at 298 K, emission monitored at 461 nm (blue) and 627 nm (red).

3.4.3.3 Variation of the Energy of the Excimeric Band 1: Modification of the N^C^N Chelating Ligand

Modification of the Phenyl Ring

Figure 50 shows the excimeric emission bands of [PtL^1Cl] and [PtL^2Cl]. As with the monomeric emission, the [PtL^2Cl] excimer emits at higher energy than [PtL^1Cl] (λ_{max} = 677 and 691 nm respectively, ΔE = 300 cm^{-1}). This energy shift is about 2.5 times less than found with the monomeric emission, indicating that fluorination in the 3,5-phenyl positions has a smaller impact on excimer energy. A saturated solution of [PtL^3Cl] did not display excimeric emission. Either this complex does not form excimers readily, the solubility is too low, or like monomer emission, the excimer emission is very weak.

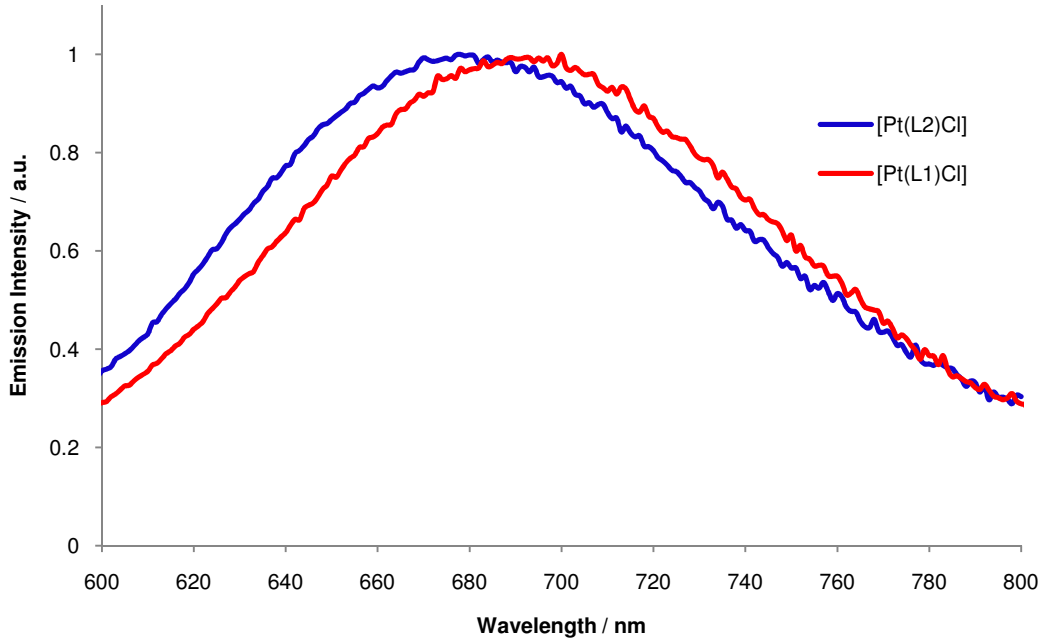

Figure 50: Normalised excimeric emission of [PtL^{2}Cl] (blue) and [PtL^{1}Cl] (red) from DCM solution at 298 K.

We attempted to see if the excimer band was solvatochromic (see Figure 51 and Table 21). To observe excimer emission, the solution must be sufficiently concentrated – unfortunately, [PtL^{2}Cl] was not sufficiently soluble in some of the solvents used to study monomeric solvatochromism. The complex was sufficiently soluble in DCM, toluene and CH_3CN, so these solvents were investigated. As found for monomeric emission, the excimeric emission occurred at highest energy in the most polar solvent (CH_3CN), and at lowest energy in the least polar solvent (toluene). The energy difference between the solvent extremes is 570 cm^{-1}. For monomeric emission, the energy difference between CH_3CN and toluene is only 190 cm^{-1}, indicating that the energy of the excimer is more influenced by solvent than monomeric emission. This seems reasonable, as excimers involve intermolecular interactions that could easily be perturbed by solvent.

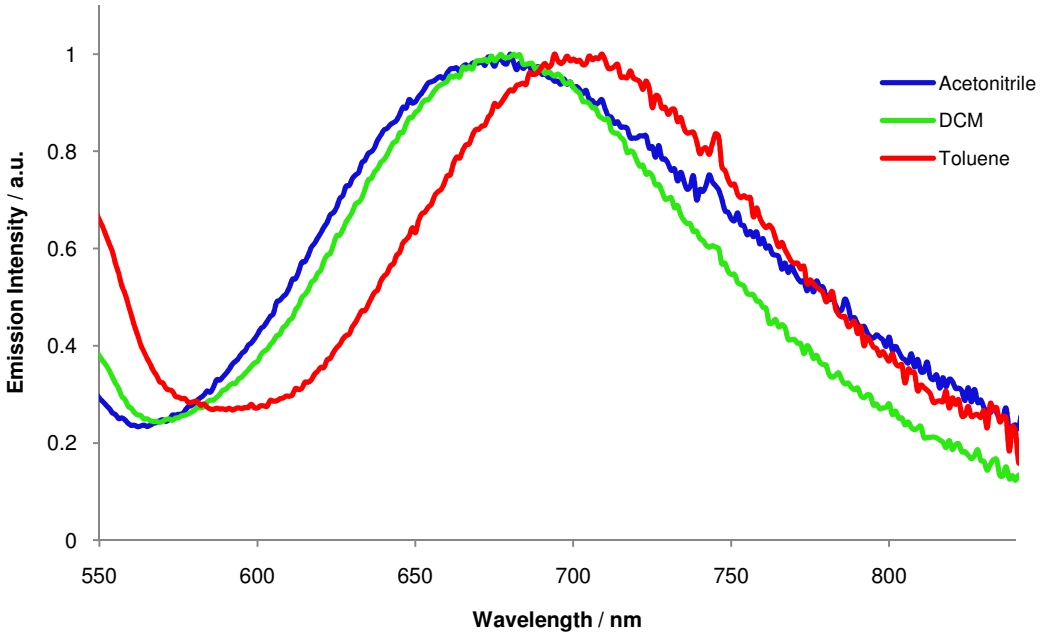

Figure 51: Normalised excimeric emission of [PtL^{2}Cl] from various solvents at 298 K.

Table 21: The position (and energy) of the excimeric emission maximum of [PtL^{2}Cl] in various solvents.

	λ_{max} / nm (Energy / cm^{-1})
Toluene	700 (14290)
DCM	677 (14770)
Acetonitrile	673 (14860)

Methyl Substituents on the Pyridyl Rings

With the exception of [PtL^{12}Cl], the 3',5'-difluorinated isomers containing methyl groups on the pyridines ([PtL^{9}Cl], [PtL^{10}Cl] and [PtL^{11}Cl]) all showed excimeric emission (see Figure 52a and Table 22). Like the monomeric emission, the energy of the excimer band varies with methyl position. The emission energy varied with substituent position in the following order:

4Me- > 5Me- > H- > 3Me-

The excimeric band of [PtL^{9}Cl] occurs at lower energy than the [PtL^{2}Cl] reference, which was also the case for the monomeric emission. However, unlike the monomeric emission, the excimer of [PtL^{11}Cl] emits at higher energy than [PtL^{2}Cl]. The maximum energy difference, between [PtL^{10}Cl] and [PtL^{9}Cl] is 470 cm^{-1}. This is a little less than the energy difference between their monomeric emission peaks (610 cm^{-1}).

Excimeric emission was not observed for [PtL^{12}Cl] within the concentration range studied (10^{-4} – 10^{-6} M). Perhaps [PtL^{12}Cl] does not form excimers because of its non-planar ground state geometry (discussed in Chapter 2, Section 2.4.3.1), or maybe excimeric emission from this complex is just very weak (as with the monomeric emission). Unfortunately, k_{sq} could not be determined for this complex, because the emission was too weak to be analysed by the same procedure as the other complexes (i.e. similar concentration ranges and excitation power per pulse).

Table 22: Wavelengths (and energies) corresponding to the excimeric emission maxima of the two series of isomers containing n-methyl-pyridyl substituents (DCM, 298 K).

	Excimeric Emission λ_{max}/nm (Energy / cm^{-1})		**Excimeric Emission λ_{max}/nm (Energy / cm^{-1})**
[PtL^{1}Cl]	691 (14470)	**[PtL^{2}Cl]**	677 (14770)
[PtL^{5}Cl]	692 (14450)	**[PtL^{9}Cl]**	681 (14680)
[PtL^{6}Cl]	674 (14840)	**[PtL^{10}Cl]**	660 (15150)
[PtL^{7}Cl]	688 (14530)	**[PtL^{11}Cl]**	673 (14860)
[PtL^{8}Cl]	-----[a]	**[PtL^{12}Cl]**	-----[b]

[a]Could not assign an accurate value due to weakness of excimer emission, combined with overlap with monomer emission tail, [b]Excimer emission was not observed for the concentration range studied (10^{-6} – 10^{-4} M).

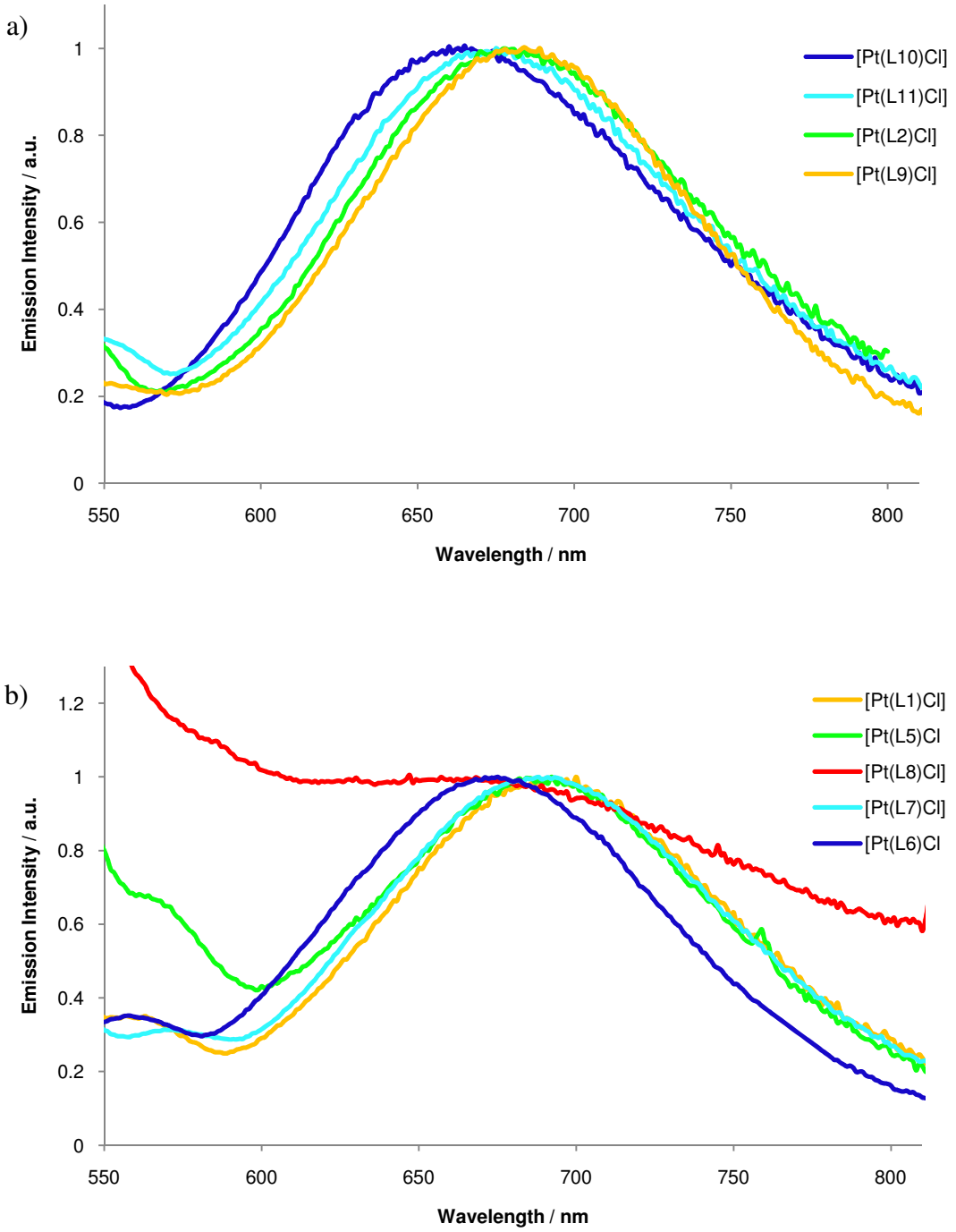

Figure 52: Normalised excimeric emission of a) 3',5'-difluorinated complexes containing methyl substituents and b) their non-fluorinated analogues (DCM, 298 K).

The excimeric emission of the non-fluorinated complexes ([PtL$^{5\text{-}7}$Cl]) occur at slightly lower energy than their difluorinated analogue (approximately 300 cm^{-1}). Of this series, [PtL^{6}Cl] exhibits highest energy excimer emission, followed by [PtL^{7}Cl], [PtL^{1}Cl] and [PtL^{5}Cl] (note that the excimer band maxima of the latter three complexes all occur within 4 nm of each other, so their excimeric emission occurs at the same energy within the experimental error).

In contrast to all other isomers, which displayed obvious excimeric emission at higher concentration, higher concentration solutions of [PtL^{8}Cl] showed only a very weak band at lower energy. This band was assigned as excimeric emission, however it is superimposed on the monomeric emission tail, and its signal is distorted so that a true value of λ_{max} cannot be ascertained. Like [PtL^{12}Cl], [PtL^{8}Cl] contains methyl groups on the 6-pyridyl position, so it is reasonable to think that similar steric repulsions will exist and the complex will adopt a non-planar ground state. Unfortunately, k_{sq} could not be determined for this complex, because the emission was too weak to be analysed by the same procedure as the other complexes (i.e. similar concentration ranges and excitation power per pulse).

[PtL^{13}Cl] and [PtL^{14}Cl]

As mentioned in Section 3.4.3.1, [PtL^{13}Cl] has a very low k_{sq} value. In line with this, excimeric emission was not observed over the concentration range studied (10^{-6} – 10^{-4} M). This further suggests that the significant distortions within the molecule prevent close approach of other complex molecules and sufficient overlap of orbitals. Its isomer, [PtL^{14}Cl], does exhibit excimer emission, and intriguingly, whereas the monomeric emission was red shifted relative to [PtL^{1}Cl], the excimeric emission is blue shifted (λ_{max} = 678 nm) and occurs at similar wavelength to the [PtL^{2}Cl] excimer (λ_{max} = 677 nm). This clearly demonstrates that substituents can affect monomer and excimer emission in different ways, and perhaps suggests that excimer emission energy is more receptive to the electronic nature of the pyridyl substituent.

For all complexes (for which a suitable crystal was isolated), the molecular structures reveal a head-to-tail arrangement of neighbouring molecules (Chapter 2, Section 2.4.3.1). It is possible that the excimer also involves a head-to-tail arrangement of the excited state and ground state molecule (Figure 53 gives a postulated arrangement of molecules in an excimer). In fact, the photophysical results may indicate that this is so. As previously mentioned, pyridyl substituents seem to have a greater influence on excimeric energy than phenyl substituents – in a head-to-tail arrangement, the pyridyl rings are likely to be involved in the intermolecular interaction (i.e. π-π), whereas the phenyl rings are too displaced to interact much with one another. Furthermore, the series of 1,3-dipyridylbezene complexes prepared by Williams et al., which contain differing substituents at the 4'-position (and no pyridyl substituents), all gave excimers

with energies comparable to [PtL[1]Cl] (between 690 – 700 nm), despite showing greater variation between their monomeric emission energies.[2]

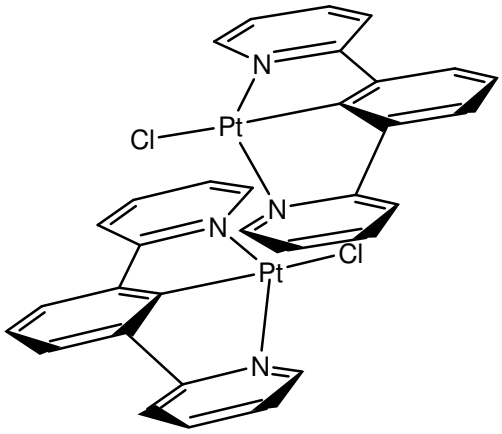

Figure 53: Postulated arrangement of molecules in an excimeric interaction.

4-Pyridyl Substituted Complexes: Electron Donating Substituents

Excimer energy was found to increase significantly with increasing electron donating ability of the 4-pyridyl substituent (see Figure 54 a) and b), and Table 23). The energy separations between the excimeric emission maximum of each complex are summed up in Figure 55.

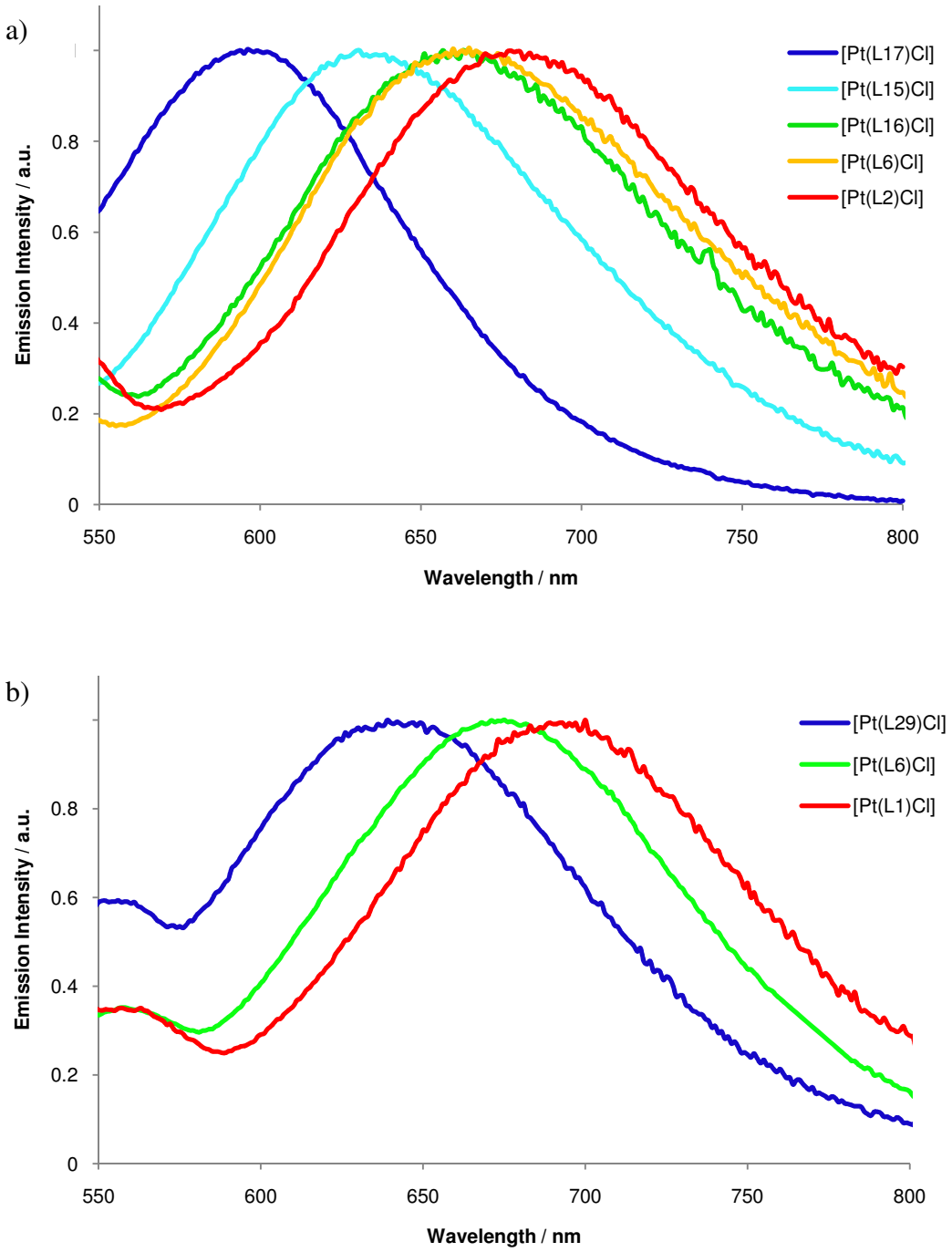

Figure 54: Normalised excimeric emission of a) 3',5'-difluorinated complexes containing electron donating 4-pyridyl substituents and b) their non-fluorinated analogues (DCM, 298 K).

Table 23: Wavelengths (and energies) corresponding to the excimeric emission maxima of the complexes containing electron donating 4-pyridyl substituents (DCM, 298 K).

	Excimeric Emission λ_{max}/nm (Energy / cm^{-1})		**Excimeric Emission λ_{max}/nm (Energy / cm^{-1})**
[PtL^{1}Cl]	691 (14470)	**[PtL^{2}Cl]**	677 (14770)
[PtL^{6}Cl]	674 (14840)	**[PtL^{10}Cl]**	660 (15150)
[PtL^{29}Cl]	639 (15650)	**[PtL^{15}Cl]**	630 (15870)
		[PtL^{16}Cl]	660 (15150)
		[PtL^{17}Cl]	596 (16780)

[PtL^{17}Cl], which was found to have the highest energy monomeric emission, also has the highest energy excimeric emission (λ_{max} = 596 nm, 16780 cm^{-1}). The excimers of [PtL^{17}Cl], [PtL^{15}Cl], and [PtL^{29}Cl] all emit at higher energy than the excimer of the unsymmetrical pyrazole/pyridine complex reported by Williams et al. (λ_{max} = 650 nm, 15400 cm^{-1}), which to our knowledge is the highest energy excimer reported in the literature for N^C^N Pt(II) complexes.[16]

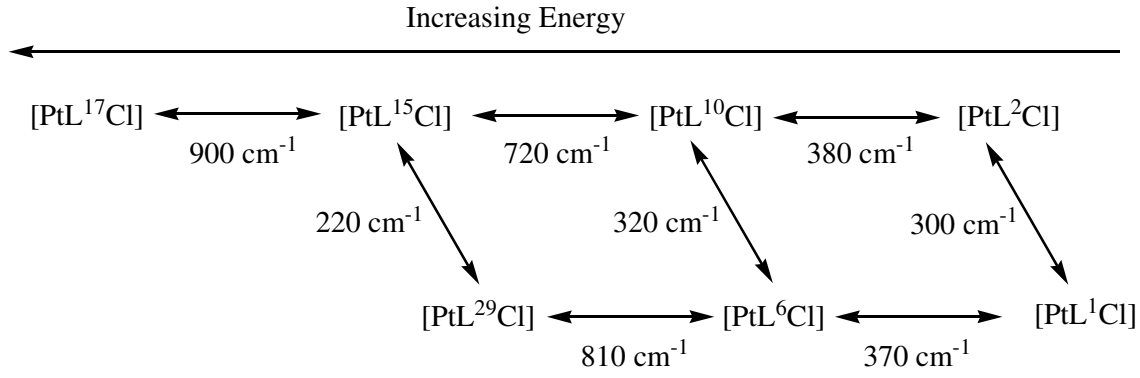

Figure 55: Energy separations between the excimeric maxima of complexes containing an electron donating 4-pyridyl substituent

To re-The monomeric emission of the unsymmetrical complex [PtL^{16}Cl] occurred at similar energy to [PtL^{2}Cl] (see Section 3.4.1.4). However, the excimeric emission significantly differs between these two complexes: the excimeric emission of [PtL^{16}Cl]

occurs at higher energy (15150 cm^{-1} and 14770 cm^{-1} respectively). The presence of the more electron rich 4-MeO-pyridyl ring in [$PtL^{16}Cl$] appears to destabilise the excimer, despite having no effect on the monomer emission. Excimer formation involves an electron donor-acceptor interaction between an excited state and ground state molecule.[35] The increased electron density in the substituted 4-MeO pyridyl ring of [$PtL^{16}Cl$] may make the ground state a poorer π-acceptor, weakening the interaction with an excited state molecule. This would account for the higher energy excimer emission relative to [$PtL^{2}Cl$], which does not contain any pyridyl substituents. A similar observation was made by Williams et al., when comparing the excimeric emission of the unsymmetrical N^C^N pyrazole complex, complex **52**, with that of [$PtL^{1}Cl$] (Chapter 1, Section 1.7.3).

4-Pyridyl Substituted Complexes: Electron Withdrawing Substituents

Placing electron withdrawing CF_3 groups at the 4-pyridyl position leads to a red shift in excimer emission relative to [$PtL^{1}Cl$], regardless of whether or not fluorine substituents are present on the aryl ring (see Figure 56, Table 24). A similar observation was made for monomeric emission. Of this set of complexes, [$PtL^{30}Cl$] displayed the lowest energy excimeric emission (λ_{max} = 756 nm, 13230 cm^{-1}). The excimeric emission of [$PtL^{20}Cl$], the 3',5'-difluorinated analogue of [$PtL^{30}Cl$], occurred at slightly higher energy (λ_{max} = 733 nm, 13640 cm^{-1}). Substitution of one CF_3 group for an electron donating MeO- group in [$PtL^{21}Cl$] slightly blue-shifted the excimeric band (λ_{max} = 710 nm, 14100 cm^{-1}) relative to that of [$PtL^{20}Cl$], indicating that the electron donating nature of MeO- had slightly offset the electron withdrawing effect of CF_3. In contrast, monomeric emission of these two complexes occurred at the same energy. This observation gives further support to the theory that the electronic nature of the 4-pyridyl substituent has a greater influence on excimeric emission than monomeric.

Table 24: Wavelengths (and energies) corresponding to the excimeric emission maxima of the complexes containing 4-trifluoromethyl-substituted pyridines (DCM, 298 K).

	Excimeric Emission λ_{max}**/nm (Energy / cm^{-1})**
[PtL^{1}Cl]	691 (14470)
[PtL^{20}Cl]	733 (13640)
[PtL^{21}Cl]	710 (14080)
[PtL^{30}Cl]	756 (13230)

The excimeric emission of complexes [PtL^{20}Cl], [PtL^{21}Cl] and [PtL^{30}Cl] remained weak, even from solutions of the highest concentration. The k_{sq} values of these complexes are between 2 and 3 x 10^{9} M^{-1} s^{-1}, which are quite low when compared to most complexes investigated here. This indicates that such complexes have a lower propensity to form excimers. However, other complexes such as [PtL^{15}Cl] and [PtL^{17}Cl] have similar k_{sq} values, yet display more intense excimeric emission bands. This could be because the excimers of [PtL^{15}Cl] and [PtL^{17}Cl] are more emissive than for the complexes involving CF_3 pyridyl substituents. An experiment was designed to determine the relative brightness of the excimers, and is discussed in Section 3.4.3.5.

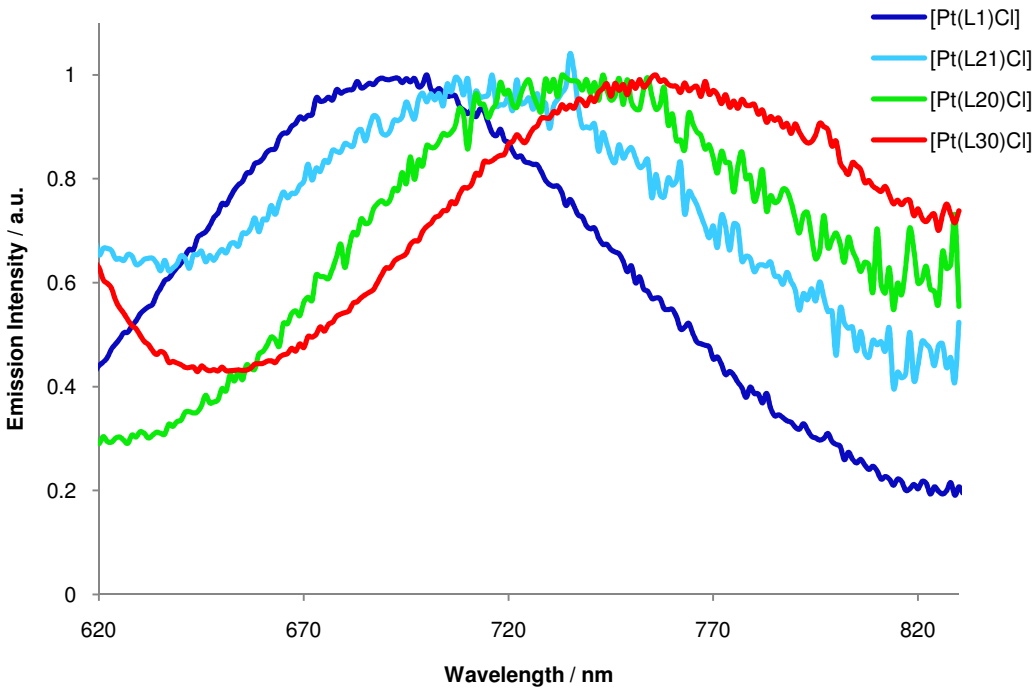

Figure 56: Normalised excimeric emission of complexes containing electron withdrawing CF_3 substituents at the 4-pyridyl position (DCM, 298 K)

[PtL^{22}Cl]

As was found for the respective monomeric emission, the excimeric emission of [PtL^{22}Cl] occurred at lower energy than [PtL^{1}Cl] (707 nm and 691 nm respectively, ΔE = 330 cm^{-1}). Despite having an intermediate self-quenching constant (5.6 x 10^{9} M^{-1} s^{-1}), the intensity of this band remained weak at higher concentration. This implies that the complex readily forms excimers, but the luminescent efficiency of excimeric emission is low.

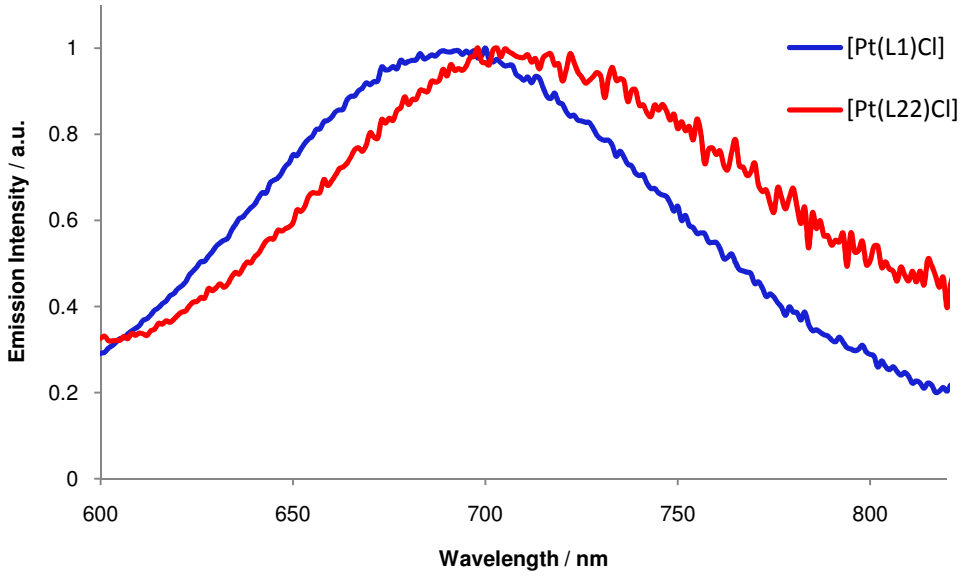

Figure 57: Normalised excimeric emission of [PtL^{22}Cl] (red), with that of [PtL^{1}Cl] (blue) included for reference (DCM, 298 K).

3.4.3.4 Variation of the Energy of the Excimeric Band 2: Variation of the Ancillary Ligand

Halide Exchange

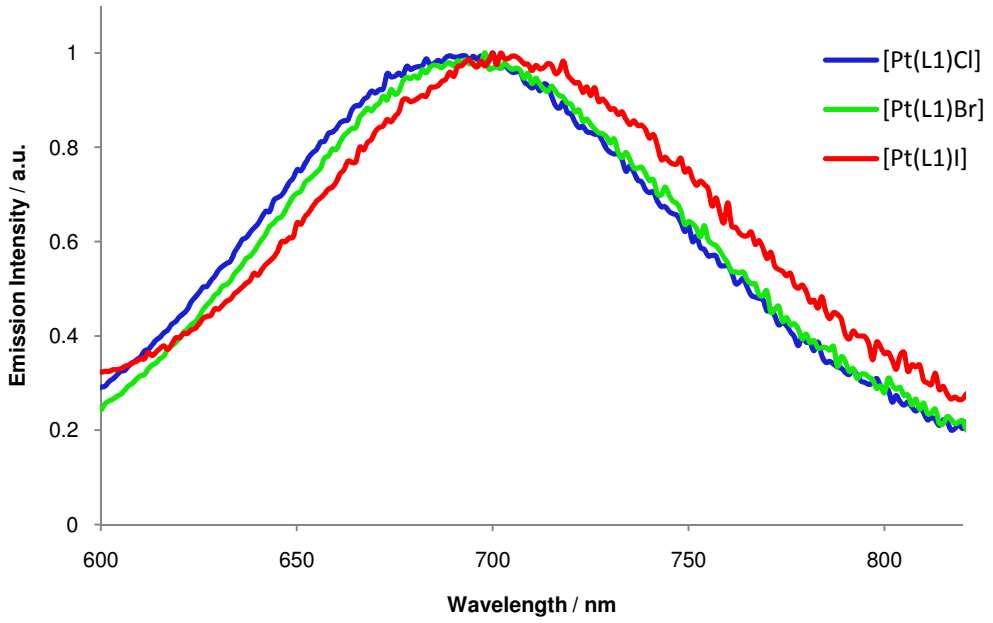

Figure 58: Normalised excimeric emission of the [PtL^{1}X] series (DCM, 298 K).

Excimeric emission occurred around 691 nm for both [PtL^{1}Cl] and [PtL^{1}Br], and at the slightly lower energy of 702 nm for [PtL^{1}I], giving a maximum energy difference of only 230 cm^{-1}. A similar situation was found when comparing the monomeric emission – substitution of the ancillary chloride of [PtL^{1}Cl] with bromide or iodide hardly affected the energy.

Substitution of Chloride for Cyanide

Introduction of a cyanide ancillary ligand was found to significantly increase the energy of excimeric emission relative to the analogous chloride complex (by approximately 800 cm^{-1}, see Figure 59 and Table 25). This is significantly larger than the corresponding effect on monomer emission (~ 200 cm^{-1}). Perhaps substitution with cyanide destabilises the donor-acceptor interaction necessary to form an excimer.

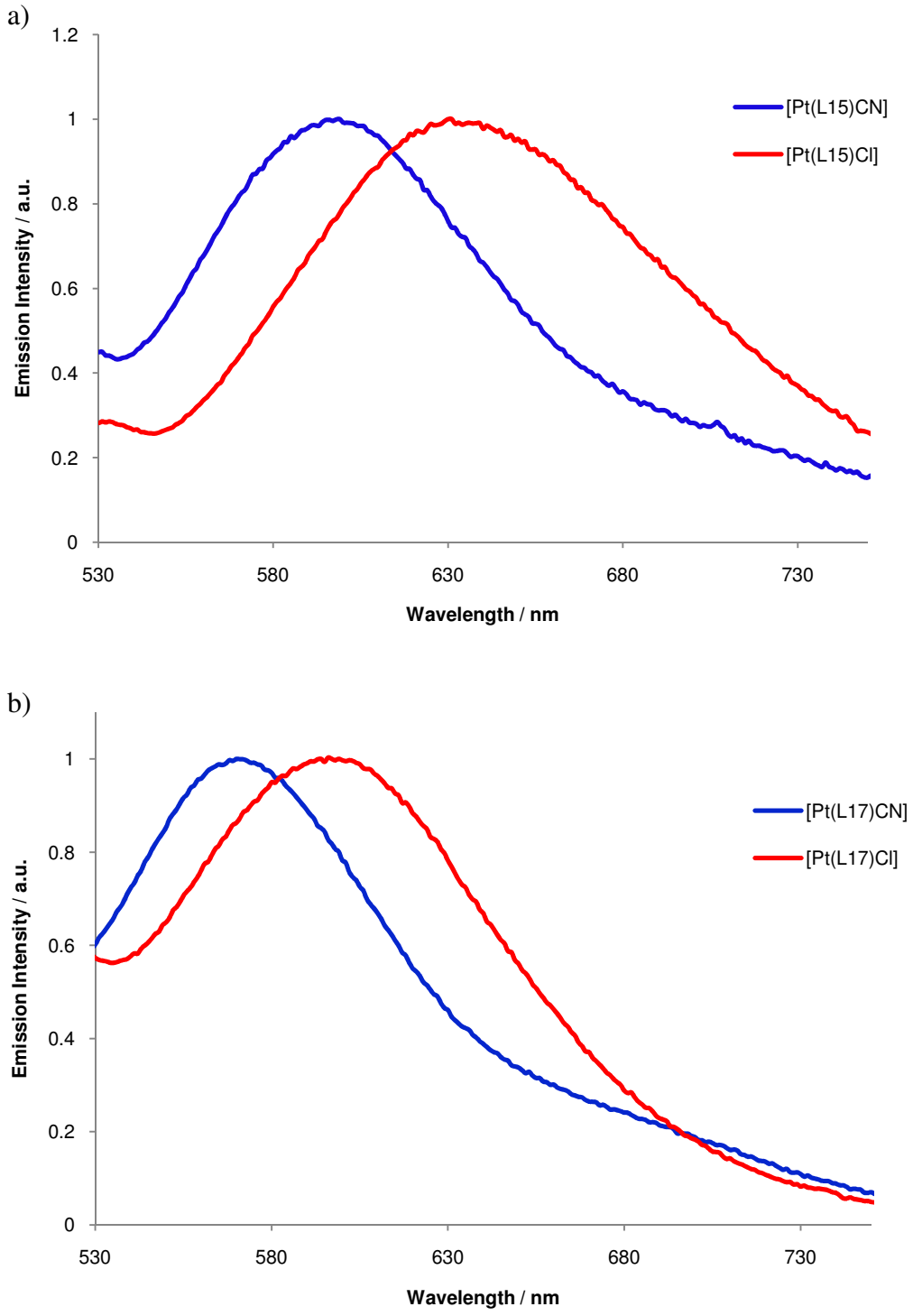

Figure 59: Normalised excimeric emission of a) [PtL^{15}CN] (blue) and [PtL^{15}Cl] (red) and b) [PtL^{17}CN] (blue) and [PtL^{17}Cl] (red) (DCM, 298 K).

Table 25: Comparison of the excimeric emission maxima of chloro and cyano analogues

		[PtL^{17}X]	**[PtL^{15}X]**	**[PtL^{2}X]**
λ_{max} / nm (Energy / cm^{-1})	X = Cl	596 (16780)	630 (15870)	677 (14770)
	X = CN	569 (17570)	599 (16690)	643 (15550)
ΔE (CN – Cl) / cm^{-1}		800	820	780

3.4.3.5 Excimer Brightness

The apparent intensity of excimeric emission varies between the complexes. To determine which complexes were the best excimeric emitters, the emission spectrum was recorded for a solution of each complex at a constant concentration (1.7 x 10^{-4} M, DCM, 298 K), and the intensities of emission were then compared (see Figure 60). Such knowledge could be useful in selecting suitable phosphorescent dopants for OLEDs. As can be seen from Figure 60, there is no apparent relationship between the energy of excimeric emission and the observed intensity of excimer emission, and complex [PtL^{9}Cl], for which excimeric emission occurs at intermediate energy (compared to other Pt(II) complexes), has the most intense excimeric emission.

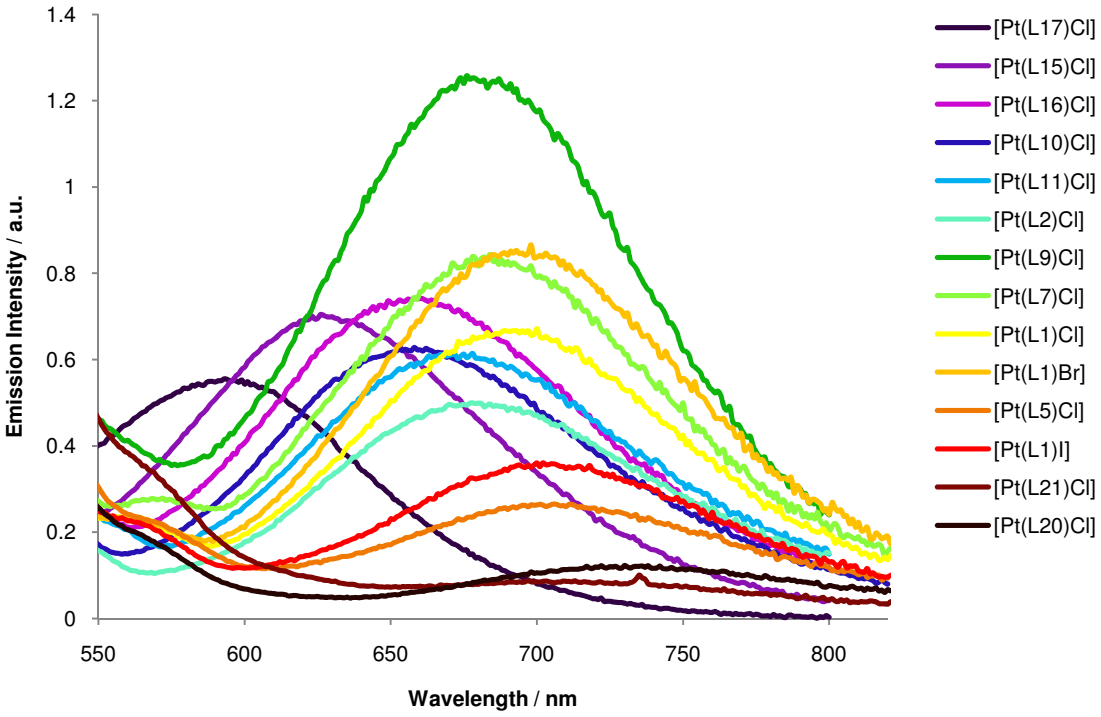

Figure 60: Excimeric emission of 1.7 x 10^{-4} M DCM solutions of the Pt complexes (298 K). This figure was used to compare the apparent intensity of excimeric emission between complexes.

The apparent excimer intensity depends upon both the rate of excimer formation and the excimeric quantum yield. For example, some complexes exhibit bright excimeric luminescence, whilst having small k_{sq} values (e.g. [PtL^{17}Cl]). We can write an expression for the observed excimeric intensity:

$$I_{obs} = \left(\frac{k_{sq}[M]}{k_{sq}[M] + k_r^{mon} + k_{nr}^{mon}}\right) \times \eta_{em}$$

$$I_{obs} = k_{sq}[M] \times \tau_{obs} \times \eta_{em}$$

where I_{obs} is the observed intensity of emission, k_{sq} is the self-quenching rate constant, [M] corresponds to the concentration of complex, k_r^{mon} and k_{nr}^{mon} correspond to the radiative and non-radiative decay rates of the excited monomer, τ_{obs} corresponds to the lifetime of the monomer at that concentration, and η_{em} corresponds to the "brightness" of the excimer (takes into account the excimeric quantum yield).

By dividing all of the emission spectra by $k_{sq}.\tau_{obs}$ ([M] is constant here), it should be possible to gain a crude approximation of the relative radiative *efficiencies* of excimeric emission. The emission spectra shown in Figure 61 are those from Figure 60 divided by $k_{sq}.\tau_{obs}$. There appears to be a general trend by which the brightness of excimeric

emission decreases with decreasing excimeric emission energy. This trend appears to be following the energy gap law, which predicts that non-radiative decay will be more significant for systems with smaller T_1-S_0 gaps.

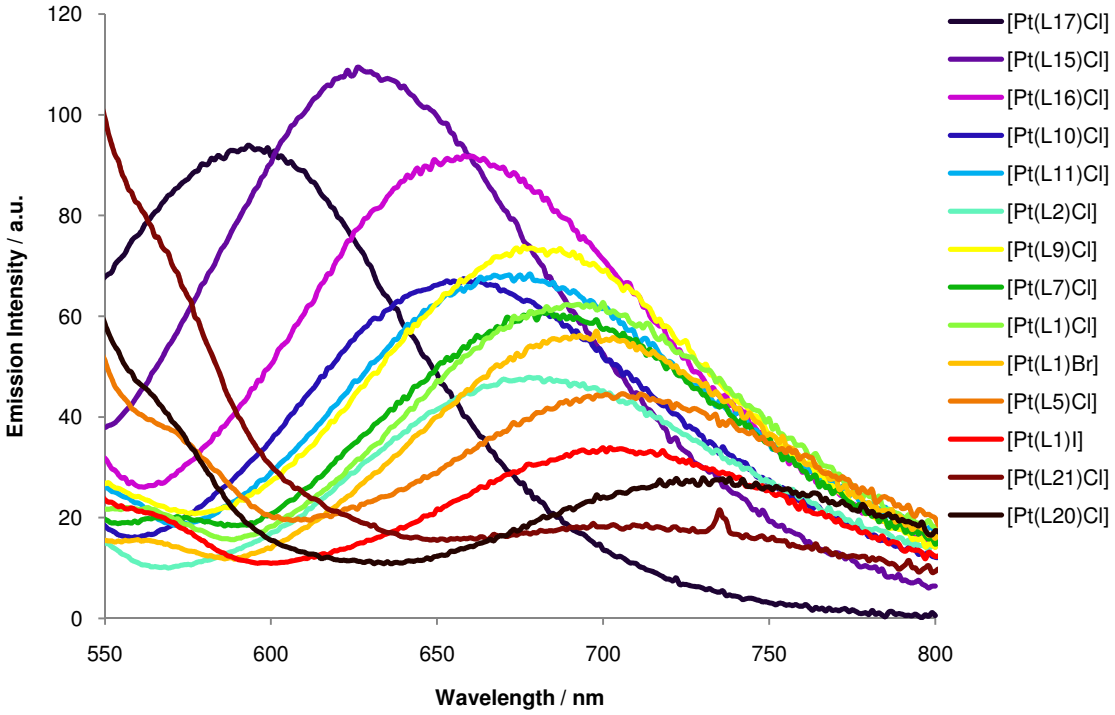

Figure 61: This figure represents the emission spectra represented in Figure 60 divided by $k_{sq}\tau_{obs}$ for the individual Pt complexes. It gives a representation of the relative efficiencies of excimer emission.

3.4.3.6 Mixed Excimer Effect

It was of interest to consider what would happen to the excimeric emission if two complexes were mixed. In solutions of higher concentration, the excimeric emission of complexes [$PtL^{15}Cl$] and [$PtL^{5}Cl$] occur at significantly different wavelength (630 nm and 706 nm respectively, ΔE = 1700 cm^{-1}), making them suitable for such a study. Solutions containing a known ratio of these two complexes were prepared, and the emission spectra were recorded. To make the solutions, stock solutions of 2.4 x 10^{-4} M were prepared, and then mixed to the required ratios. An excitation wavelength of 376 nm was selected, at which value the two complexes have equal excitation coefficients. Similar to solutions containing a single complex, the solutions of the mixed complexes displayed only one excimeric band. However, the energy maximum of the band was found to depend on the relative amount of the two complexes present (see Figure 62a). Hence, tuning of the excimeric band maximum between the extremes of the pure

complexes is possible – this effect could be utilised in white OLED design. A comparable effect was observed with other combinations of complexes, for example, Figure 62b shows the mixed excimer effect for [PtL^{17}Cl] and [PtL^{1}Cl] (λ_{max} = 596 nm and 691 nm respectively, $\Delta E = 2310\ cm^{-1}$).

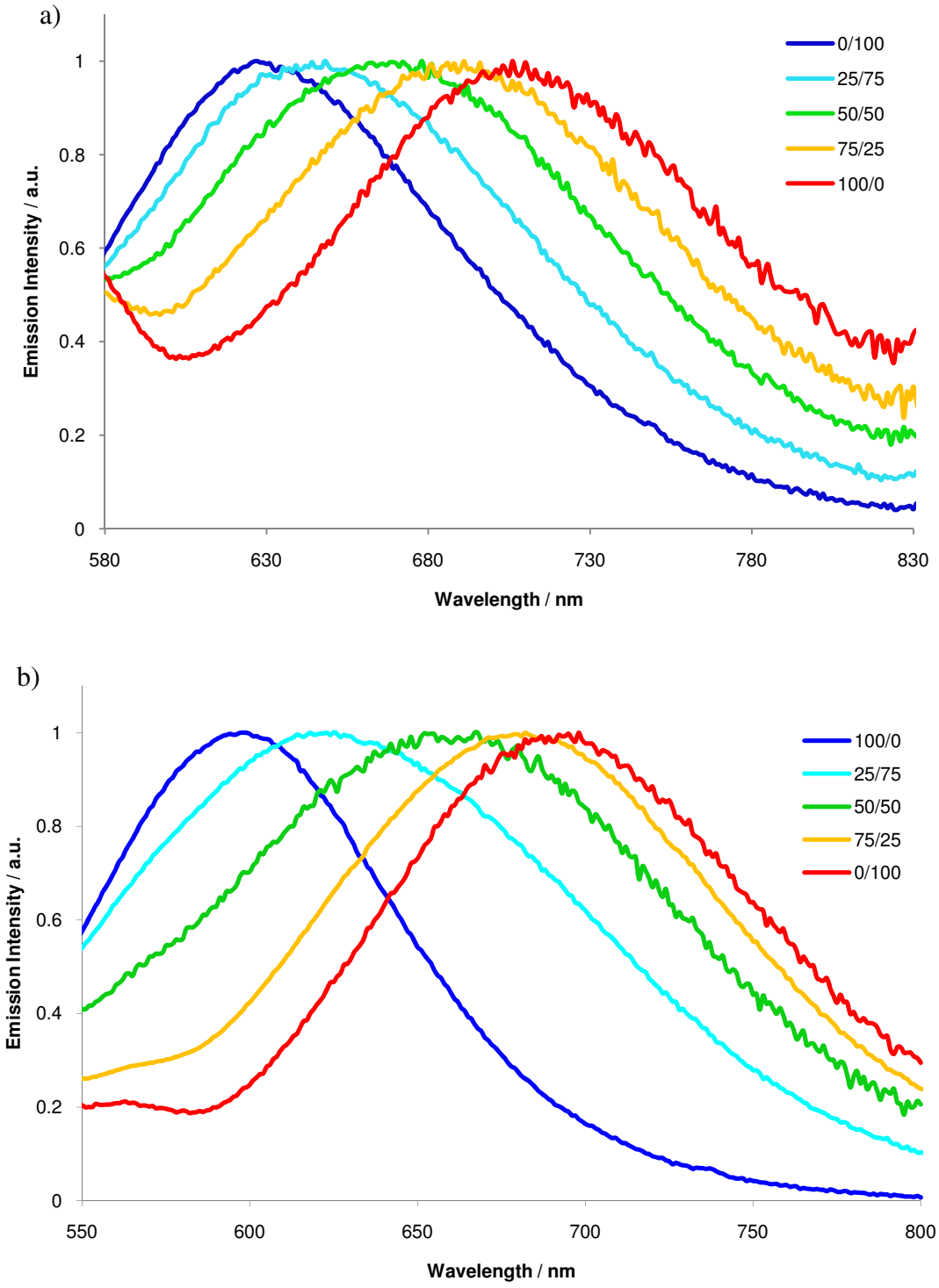

Figure 62: Normalised excimeric emission of DCM solutions containing a) different ratios of [PtL^{5}Cl]/[PtL^{15}Cl] and b) different ratios of [PtL^{17}Cl]/[PtL^{1}Cl] (298 K).

It is not easy to tell whether the excimer bands from mixed solutions are due to a mixed excimer species, a sum of emission from the 'pure' excimers (formed between molecules of the same complex), or both. In an attempt to discover the origin of the excimer, the emission spectra of the two pure solutions were summed and normalised (w.r.t. excimer maximum), then superimposed with the spectrum obtained for the 50:50 mixture (see Figure 63). The excimer bands have the same maximum energy, suggesting that the emission in mixed solutions could be a sum of the 'pure' excimers. However, the emission band of the 50:50 solution is narrower. In terms of white OLED fabrication, the identity of excimer configuration isn't really important, just the energy of the excimer band.

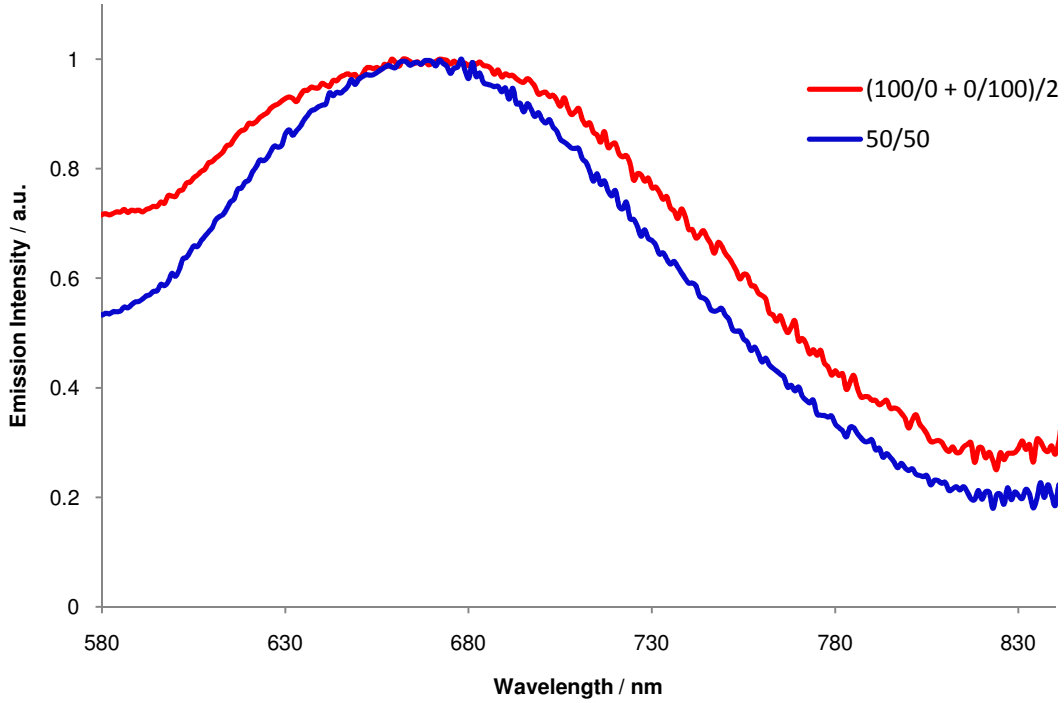

Figure 63: Comparison of the excimeric emission of a solution containing a 50/50 ratio of [PtL^{15}Cl]/[PtL^{5}Cl] (blue), with a spectrum created by taking the average of two spectra containing pure samples of [PtL^{15}Cl] and [PtL^{5}Cl] (red) (DCM, 298 K).

3.4.3.7 Aggregation Phenomena

Behaviour in CH_3CN/Water Mixtures

As discussed in the introduction, the square planar geometry of platinum complexes lends itself to the formation of excimers *and* aggregates, and these bimolecular species are distinctly different. So far, we have only discussed excimers for these Pt(II) complexes, but aggregates also form under certain conditions.

It was noticed that solutions of [PtLCl] complexes dissolved in CH_3CN appear yellow, whereas CH_3CN/H_2O solutions containing a high water content appear pink. The absorption spectrum of solutions containing higher water content show a new band at lower energy, confirming that an additional species is absorbing, and that this species exists in the ground state. These observations may be rationalised in terms of aggregate formation - the intrinsic hydrophobicity and charge neutrality of these Pt(II) complexes lend themselves to the formation of aggregates when in contact with water.

Figure 64: A 10 µM solution of [PtL^2Cl] in CH_3CN/ H_2O (2:8), irradiated with long-wave UV light.

The emission of the aggregate looks red under long-wave UV irradiation, as opposed to the blue/green emission of the monomer (Figure 64). If the concentration of complex is sufficiently high, the aggregate will precipitate out of solution and form a pink suspension.

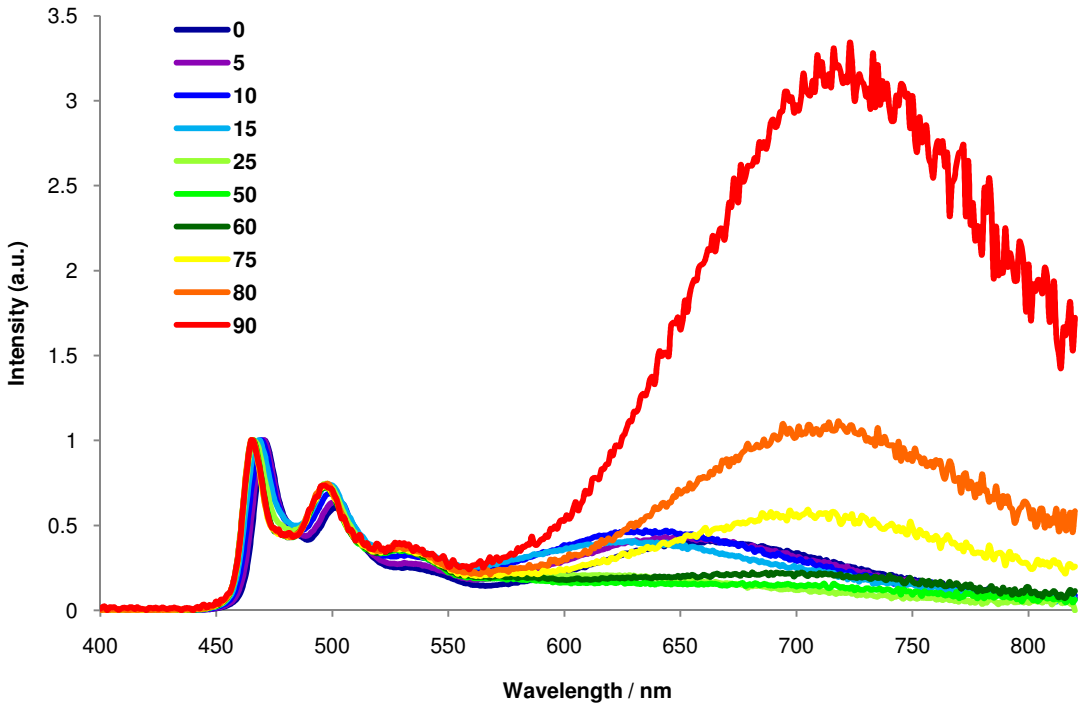

Figure 65: Emission of [PtL^{2}Cl] from acetonitrile solutions containing different water content. The legend refers to the percentage water content relative to acetonitrile, and the spectra have been normalised at the monomeric emission maximum (298 K).

An experiment was designed to confirm the distinction between excimer and aggregate. In this experiment, we aimed to modulate the emission origin by slowly increasing the water content. A constant concentration of [PtL^{2}Cl] was used throughout this experiment (4.4 x 10^{-5} M). This concentration is sufficient to give both monomeric and excimeric emission in 100% CH_3CN solution. Solutions containing higher CH_3CN compositions (100-85%) showed both monomeric and excimeric emission (around 470 nm and 660 nm respectively), both of which shifted to higher energy as the amount of water increased (see Figure 65). This observation is consistent with the results of the solvatochromic studies described earlier (Sections 3.4.1.1 and 3.4.3.3), which implied that both the monomeric excited state and the excimer are destabilised in more polar media.

Solutions containing between 25 and 50% H_2O showed only monomeric emission – under such conditions, the excimer is probably too unstable (high energy) to form. Above 50% H_2O content, a broad, featureless aggregate band grows in at lower energy than the initial excimer emission occurred in solutions of lower water content ($\lambda_{max} \approx$ 725 nm). The intensity of this band relative to monomeric emission increases as the water content is increased, and the band can be tentatively assigned to an aggregate

rather than excimer. In this experiment, solutions of higher water content also showed a pink colouration, which has previously been ascribed to aggregate formation.

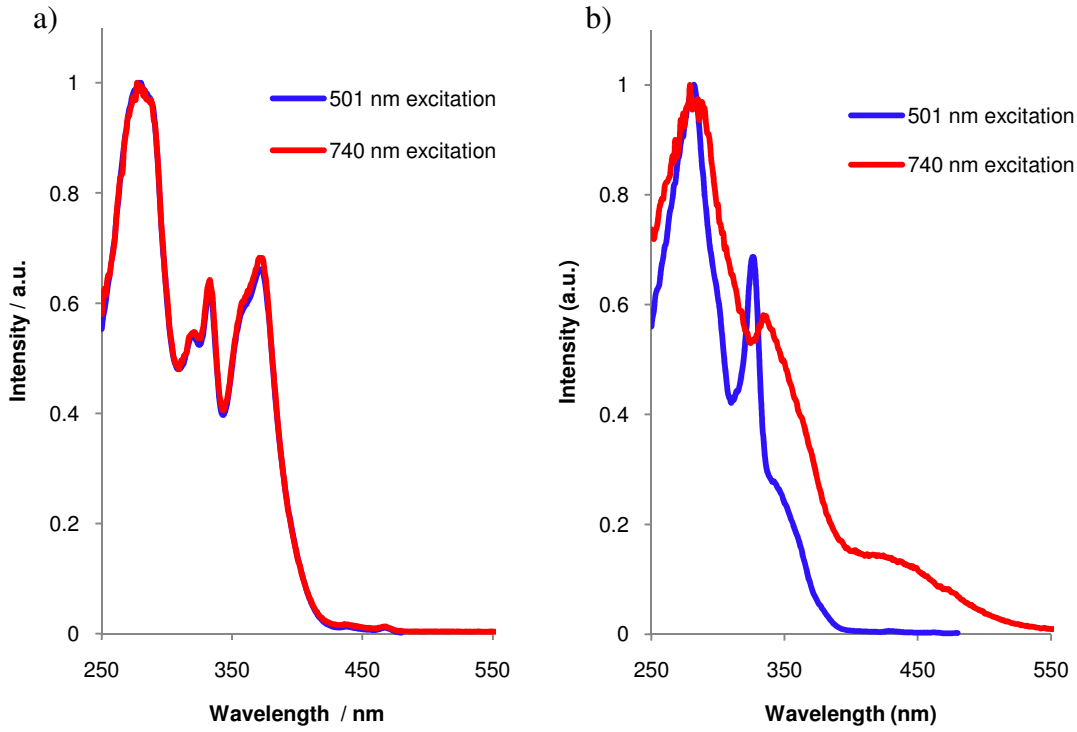

Figure 66: Excitation spectra of [PtL^{2}Cl] in a) pure CH_3CN and b) a 1:9 CH_3CN/water mixture, recorded at λ_{em} 501 nm (blue) and 740 nm (red).

The excitation spectra recorded for solutions containing 100% CH_3CN and 1:9 CH_3CN/H_2O, registered at higher (501 nm) and lower (740 nm) emission energy provide further support for the distinction between the origin of the two lower energy bands observed under the different conditions.[36] In 100% CH_3CN the excitation spectra at the two λ_{em} are identical – confirming that the band occurring around 660 nm is excimeric. In 100% water, the excitation spectra at the two emission wavelengths are significantly different, indicating that they arise from the excitation of different ground state species. Such behaviour supports the notion that the band emitting around 725 nm is due to an aggregate. Similar results were observed for the [PtL^{15}Cl] complex.

Yam et al. have prepared similar studies on cationic terpyridyl Pt(II) systems involving acetylide ancillary ligands.[37] Here, solutions of varying acetonitrile/diethyl ether content were prepared. As the proportion of ether was increased, solvent-induced aggregation was observed, and the new lower energy bands were assigned to a MMLCT state which resulted from increased Pt-Pt and π-π intermolecular interactions. Interestingly, the counter-ion was found to have a large impact on the extent of these intermolecular

interactions and hence aggregation. The counter-ion dramatically affected the colour of the solution – such systems show promise as colorimetric anion probes.

Solid State Emission

The solid state emission profiles were recorded for powder samples of the complexes (except for [PtL^{3}Cl], [PtL^{8}Cl], [PtL^{12}Cl] and [PtL^{23}], which were too weak). The solid-state emission of many Pt(II) complexes depends upon the extent of intermolecular interactions, which are often sensitive to their environment. For example, intermolecular interactions can be perturbed by solvent or solvent vapour. For comparative purpose, all solids were obtained from the same solvent - the powders were obtained by dissolving each complex in DCM, then evaporating to dryness under a high vacuum. [38,39,40]

The solid state spectra were generally less structured, and there was no obvious trend between complex structure and emission energy/profile. Some of the complexes emitted at similar energy to the solution-based monomeric emission (e.g. [PtL^{1}Cl], [PtL$^{5-7}$Cl], [PtL$^{9-11}$Cl], [PtL^{14}Cl] and [PtL^{21}Cl]) – these bands retained a degree of structure. Some of the complexes emitted at much lower energy than solution based monomeric emission (e.g. [PtL^{2}Cl], [PtL^{17}Cl], [PtL^{2}CN], [PtL^{15}CN] and [PtL^{17}CN]) – these bands were typically broad and unstructured, and resembled aggregate/excimer emission. The remaining complexes displayed degrees of both types of emission in their profiles (see Figure 67 and Figure 68 for examples of solid state emission spectra).

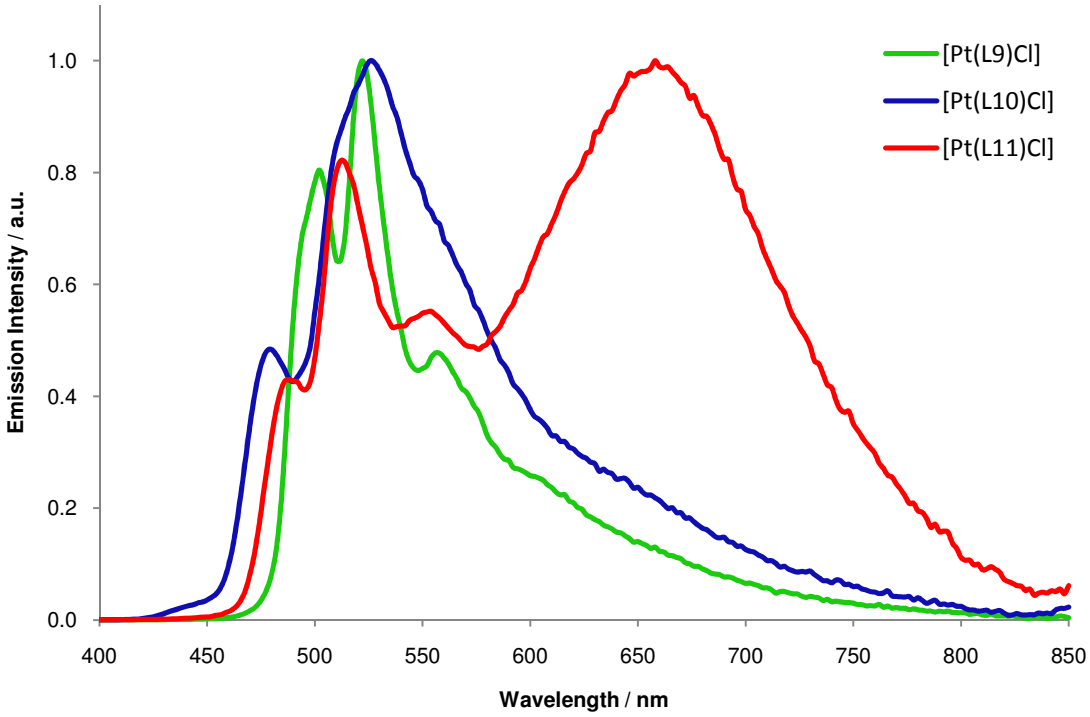

Figure 67: Solid-state emission of the 3´,5´-difluorinated n-methylpyridyl isomers, [PtL$^{9\text{-}11}$Cl]. [PtL^{12}Cl] is not included because its emission was too weak to detect.

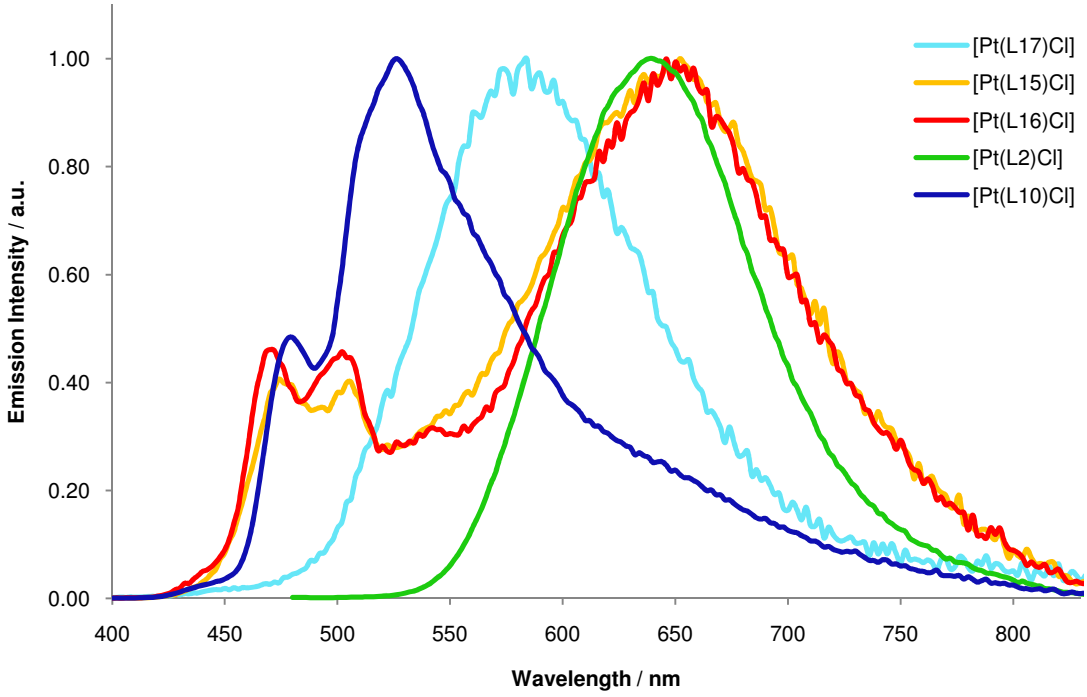

Figure 68: Solid state emission of 3',5'-difluorinated complexes containing an electron donating 4-pyridyl substituent.

The broad, unstructured emission at lower energy that was observed for some complexes is likely to arise from intermolecular interactions. In the powder, many

complex molecules will be sufficiently close to interact. It is not possible to say for certain what type of interactions exist in the powders, but the interactions may involve π-π interactions, Pt-Pt interactions, or a combination of both. From crystallographic data, we know that π-π intermolecular interactions occur in the crystal structure of some of the complexes (Chapter 2, Section 2.4.3.1). The Pt centres are always sufficiently displaced, and Pt-Pt interactions never occur. However, the powder is a more disordered phase than the crystal, so such interactions should not be ruled out, and the low energy emission may emanate from a ^{3}MMLCT state.

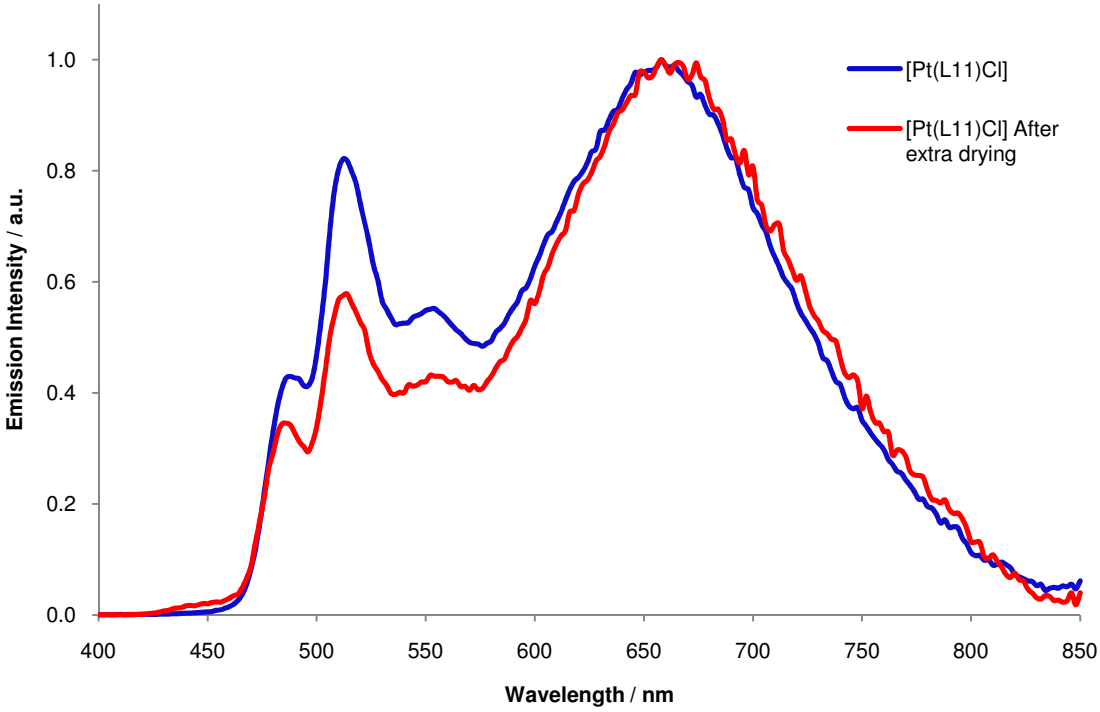

Figure 69: Solid state emission of [PtL^{11}Cl] before (blue) and after (red) drying the complex under vacuum for an extra 2 h.

[PtL^{11}Cl] was one of the complexes which exhibited both structured and unstructured emission. After recording the initial powder spectrum, the sample was dried for an additional 2 h on the vacuum line. The powder spectrum was re-measured – the intensity ratio of the structured and unstructured emission had changed (the unstructured emission had gained intensity – see Figure 69). This further indicates that the solid state emission is very sensitive to its surroundings, and that the emission profile may differ between different samples of the same species. So, although we cannot say that the spectra recorded here represent the absolute solid state emission of each of the complexes, the spectra do show that emissive multimolecular interactions can occur in the solid state.

Solvent Effect on [PtL^{2}Cl]

The solid complex of [PtL^{2}Cl] is sensitive to the presence of DCM. On evaporation from a DCM solution, the complex is initially obtained as a bright yellow solid. Further drying results in a marked colour change, giving a deep orange solid. The effect can be explained in terms of packing of the [PtL^{2}Cl] molecules, which is evidenced in the respective powder emission spectra (Figure 70).

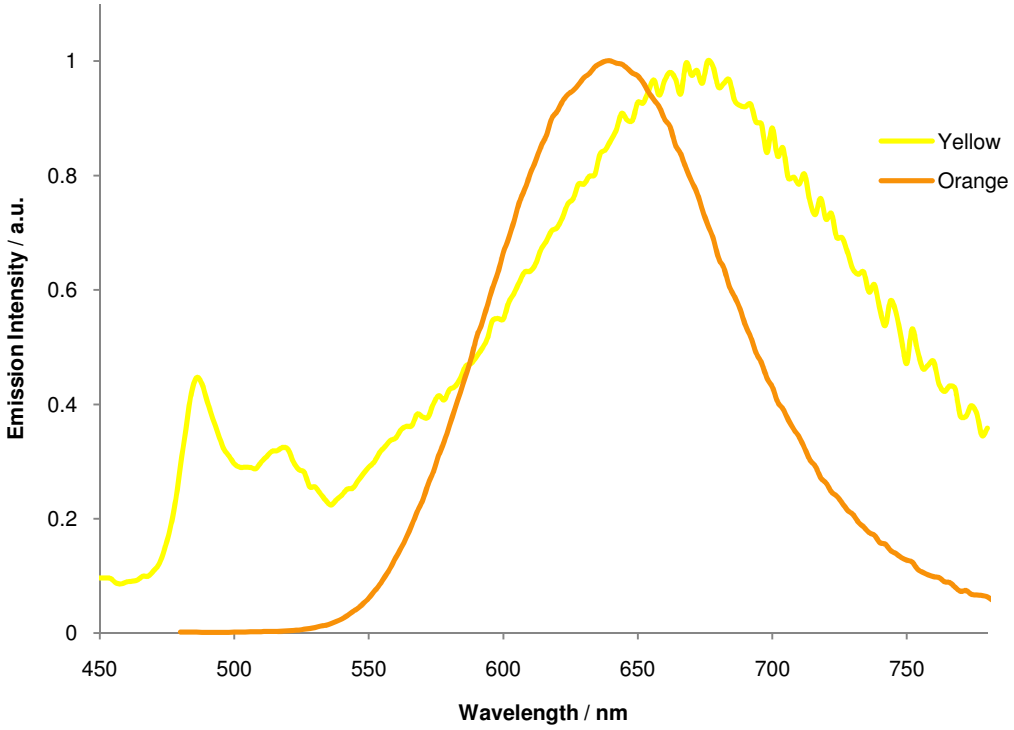

Figure 70: Emission spectra of the yellow and orange solid forms of [PtL^{2}Cl]

The orange form shows only a broad structureless emission band, which occurs at lower energy than the solution based emission. In the powder, we can expect molecules to be sufficiently close to form intermolecular interactions, which probably accounts for this aggregate-like emission. The yellow form contains both structured emission at an energy comparable to the solution based monomeric emission, and a broad emission band at lower energy (surprisingly, the low energy component occurs at a different energy to the emission from the orange form). In the yellow form, DCM molecules may be interacting with the complex molecules, disrupting some of the intermolecular interactions. The relative intensity of the lower energy structureless band grew as the yellow sample was left over time. This was accompanied by a colour change back to orange, and probably represents the slower evaporation of the DCM molecules that were involved in weak interactions with the complex molecules.

3.4.4 Low Temperature Spectroscopy

3.4.4.1 Emission at 77 K

To obtain the emission spectra at 77 K, a small amount of complex was dissolved in a 2:2:1 solvent mix of ether/isopentane/ethanol, and cooled with liquid nitrogen. This solvent mixture is chosen because it forms an inert transparent glass at 77 K. All complexes emitted at 77 K (see Table 26). The 77 K emission spectra of the complexes were more sharply structured than obtained at room temperature. The emission spectra of [PtL^{2}Cl] at 77 K and 298 K are shown in Figure 71 as an example. For most complexes, the emission spectra at 77 K were slightly blue-shifted compared to room temperature, by approximately 200 cm^{-1}. More significant blue-shifts were observed for [PtL^{8}Cl], [PtL^{9}Cl], [PtL^{12}Cl] and [PtL^{13}Cl] (520, 430, 420 and 530 cm^{1} respectively). All of these complexes have ground states that are distorted from planarity. The larger blue-shift observed on cooling is consistent with a requirement for a change in the conformation for maximal conjugation to be attained.[2]

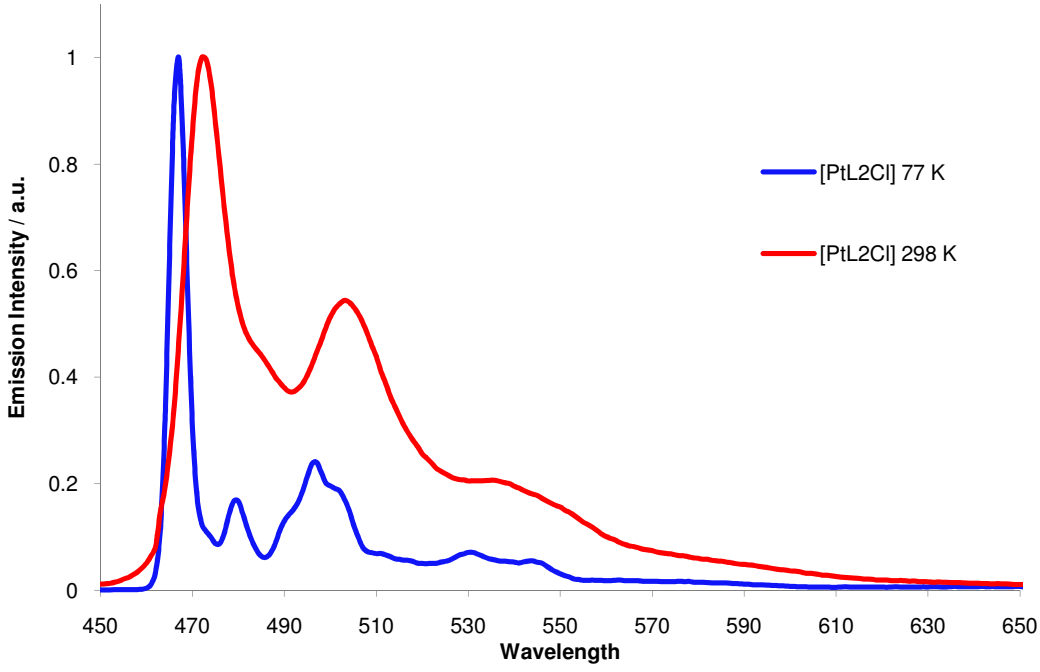

Figure 71: Emission spectrum of [PtL^{2}Cl] recorded at 77 K in an EPA glass (blue), and at 298 K from a DCM solution (red).

[PtL^{15}Cl] exhibits a surprisingly large blue shift upon cooling to 77 K (780 cm^{-1}). It is likely that the large shift stems from an intrinsic electronic effect within this molecule.

The analogous cyano complex, [PtL^{15}CN], also exhibits a larger blue-shift than all other complexes (540 cm^{1}), further indicating that the methoxy-substituents are intimately linked to the increase in energy observed at 77 K. The mono-methoxy functionalised complex, [PtL^{16}Cl], does not display such a dramatic blue shift on cooling, indicating that the large shift is dependent upon the symmetrical substitution pattern in [PtL^{15}Cl] and [PtL^{15}CN], and is consistent with the theory that the LUMO-based orbitals of [PtL^{16}Cl] will be localised on the unsubstituted pyridyl ring.

For most complexes, the 0-0 transition remains the band possessing the greatest intensity at 77 K. Interestingly though, in the 77 K emission spectrum of [PtL^{20}Cl], the 0-1 vibrational peak intensity is greater than the 0-0 peak. At 77 K molecular motion is essentially frozen out – perhaps CF_3-substituents enforce some significant distortion during the cooling process. This could tie in with the observation that concentrated DCM solutions of such complexes exhibit dramatic colour changes upon cooling (Section 3.4.1.5).

Table 26: The photophysical parameters of the complexes at 77 K, compared to 298 K.

Complex	Emission λ_{max} at 77 K /nm	Emission λ_{max} at 298 K /nm	Δ E / cm^{-1}	τ_0 at 77 K /µs
[PtL^{1}Cl]	486, 516, 548 sh	491, 524, 562 sh	210	6.4
[PtL^{1}Br]	486, 518, 550	491, 524, 562 sh	210	6.3
[PtL^{1}I]	486, 519, 553 sh	491, 524, 562 sh	210	3.9
[PtL^{2}Cl]	467, 478, 496, 526	472, 502, 536 sh	230	5.8
[PtL^{2}CN]	462, 474, 490 517	468, 498, 526 sh	280	12.6
[PtL^{3}Cl]	484	492, 515	340	0.6
[PtL^{5}Cl]	493, 527, 560sh	497, 529, 565 sh	160	6.0
[PtL^{6}Cl]	482, 516, 540sh	487, 521, 560 sh	210	6.3
[PtL^{7}Cl]	491, 526, 553	494, 528, 565 sh	120	7.1
[PtL^{8}Cl]	493, 519, 538	506, 529, 569 sh	520	6.3
[PtL^{9}Cl]	477, 508, 541sh	487, 513, 555 sh	430	5.6
[PtL^{10}Cl]	463, 482, 494, 520	467, 498, 529 sh	180	5.6
[PtL^{11}Cl]	473, 505, 530	478, 510, 543 sh	220	7.5
[PtL^{12}Cl]	484, 514	494, 530, 565 sh	420	0.7
[PtL^{13}Cl]	531 br	546 br	520	6.8
[PtL^{14}Cl]	493, 525, 563	499, 533, 573 sh	240	7.2
[PtL^{15}Cl]	445, 456, 472	461, 492, 519 sh	780	4.6
[PtL^{15}CN]	446, 477, 504	457, 488, 513 sh	540	7.9
[PtL^{16}Cl]	464, 499, 512	470, 502, 532 sh	280	6.3
[PtL^{17}Cl]	449, 478, 516, 539sh	455, 485, 512 sh	290	3.9
[PtL^{17}CN]	446, 477, 499sh, 540sh	450, 477, 503sh	200	7.9
[PtL^{20}Cl]	488, 522*, 558	497, 527, 575 sh	370	4.8
[PtL^{21}Cl]	496, 534, 553 sh	496, 528, 573 sh	0	3.8
[PtL^{22}Cl]	492, 528, 560sh	499, 533, 571 sh	290	6.2

3.4.4.2 Spectroscopy at Cryogenic Temperatures

The high resolution excitation and emission spectra of [PtL^{1}Cl] were measured at cryogenic temperatures (1.2 – 4.2 K), in the presence and absence of external magnetic fields, to gain further insight into the nature of the emitting state.[41]

Based on experimental observations at room temperature (highly structured spectra, small Stokes' shift, weakly solvatochromic emission, etc.), Williams et al. assigned the emission of [PtL^{1}Cl] and related complexes to a primarily ^{3}LC state.[1] However, the lifetime of the T_1 state is relatively short (7 μs) implying that there must be a significant contribution from the metal orbitals to the excited state to induce the necessary SOC. This idea is backed by theory. DFT calculations performed by Sotoyama et al. predict that the T_1 and S_1 states of such complexes contain significant ^{3}MLCT admixture.[4] They modelled [PtL^{1}Cl] in the gas phase and found that the T_1 and S_1 states possess 25% and 32% dπ* character respectively.

Another way to assess the extent of metal contribution to the excited state is to determine the zero field splitting (ZFS) of the T_1 state.[42] Larger ZFS imply a greater SOC contribution and hence greater metal participation. Yersin et al. have created a scale that links the ZFS to the extent of MLCT character of the triplet state. The intrinsic properties of the T_1 state cannot be measured at room temperature or 77 K, because of inhomogeneous broadening.

To study the T_1 state in detail, a low concentration of [PtL^{1}Cl] was dissolved in n-octane and cryogenically cooled to liquid helium temperatures. On cooling, the n-octane forms a polycrystalline host matrix, in which the platinum complex 'guest' molecules will lie in well defined positions (Shpol'skii matrix technique[43]). Applying this Shpol'skii technique results in highly resolved spectra, with line widths of a few cm^{-1} (due to residual inhomogeneity). This is in contrast to the overlapping and relatively broad bands with half widths of approximately 500 cm^{-1} observed in the spectra measured in solution at room temperature.

Sometimes the guest molecules can occupy several different orientations (sites) within the matrix. As a consequence, spectra obtained from Shpol'skii matrices often contain superpositions of spectra stemming from these different sites. It is possible to study one particular site in isolation (usually the most dominant site) by selective excitation with a dye-laser. Fortunately, all [PtL^{1}Cl] molecules appear to occupy the same orientation

within the matrix, so site-selective excitation was not necessary here. The emission spectrum of [PtL^{1}Cl] at 4.2 K is shown in Figure 72 (left), with the spectra recorded at 300 K and 77 K overlaid for comparison. The distinct emission band occurring at 20254 cm^{-1} corresponds to the electronic 0-0 transition from one specific substate of T_1, the II substate. This was assigned based on the behaviour of the excitation and emission spectra at different cryogenic temperatures (Figure 72).

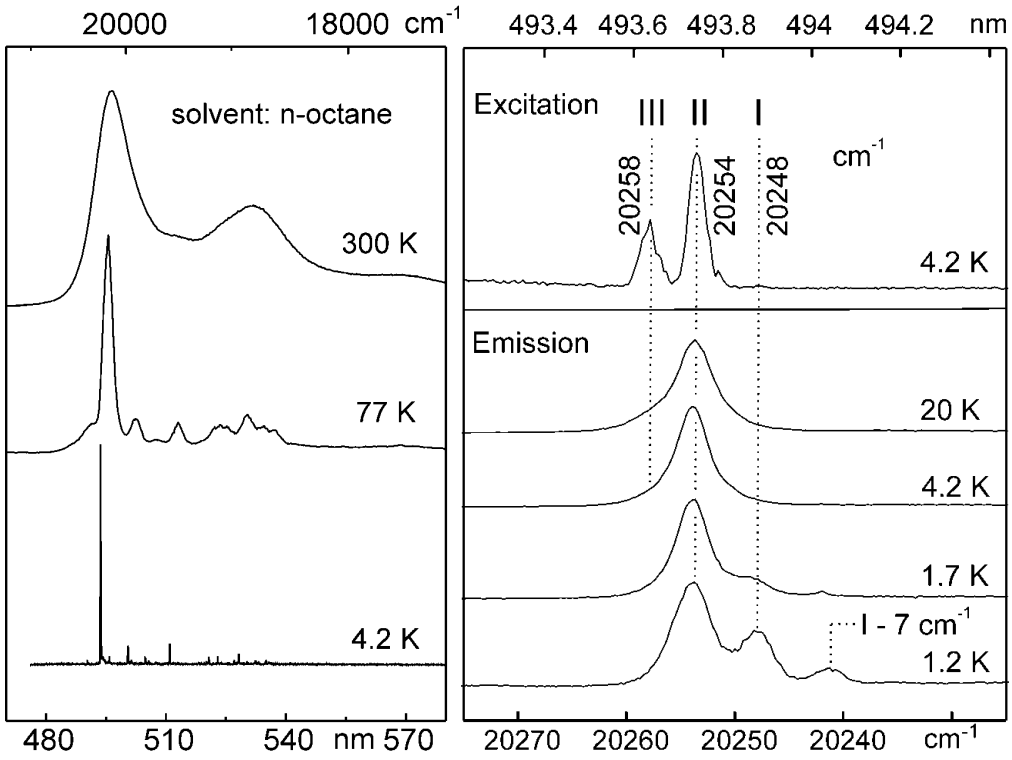

Figure 72: Left: the emission spectrum of [PtL^{1}Cl] in n-octane, recorded at different temperatures, and Right: the excitation spectrum and emission spectra of [PtL^{1}Cl] recorded at cryogenic temperatures.

The excitation spectrum at 4.2 K shows bands due to substates II and III. Substate I does not appear in the spectrum – its weakness indicates that substate I is largely forbidden, and therefore must contain less singlet admixture than II and III. The excitation and emission bands of substates II and III occur at the same energy indicating that these are purely electronic transitions. The relative intensity of the excitation peaks of substates II and III is 2.3. This represents the oscillator strengths of the transitions and indicates that II is a more allowed substate (i.e. contains a greater singlet admixture). This is borne out in the behaviour of the emission spectra at various temperatures – at higher temperatures, emission from substate II continues to dominate. Emission from substate I is observed at the lowest temperatures, 1.2 K and 1.7 K (and is accompanied by a lower energy phonon band), where thermal population of substate II

from substate I is not possible. The ZFS parameters of the emitting T_1 state were determined from these electronic spectra:

$$\Delta E_{II-I} = 5.7 \text{ cm}^{-1}$$

$$\Delta E_{III-I} = 9.9 \text{ cm}^{-1}$$

The overall ZFS is 9.9 cm^{-1}. The scale put together by Yersin et al. indicates that a ZFS of this magnitude is consistent with a mixed ^{3}LC – ^{3}MLCT state, containing a larger ^{3}LC contribution.[42,44]

The emission spectrum of [PtL^1Cl] at 14 K was recorded under several different magnetic field strengths (B = 0 – 12 T). As the field was increased the relative intensity of substate I also increased. Application of an external magnetic field induces mixing of the wavefunctions of the T_1 substates (Zeeman effect), and the extent of mixing is proportional to the magnetic field strength. The greater degree of mixing of substate I with higher lying singlet states increases the allowedness of substate I, so that its emission dominates at higher field strength. The increased interaction at higher field also results in an increase in the splitting of the substates. At B = 0 T, the ZFS is 9.9 cm^{-1}, whereas at B = 12 T the ZFS is 23 cm^{-1}.

Under normal conditions (B = 0 T), the relative intensity of the substate bands in the excitation spectrum indicate that substate II is most allowed, followed by substate III then substate I which is almost forbidden. The allowedness (oscillator strength) can also be approximated by measuring the individual decay times (lifetimes) of the substates. The shorter the lifetime, the more allowed the transition. A decay curve measured at 1.2 K is shown in Figure 73. The decay is bi-exponential, and consists of a short component (300 ns) and long component (49.4 μs). The short component represents spin-lattice relaxation of II → I. The long component corresponds to the thermalised emission decay from all substates. At this temperature, emission from substate I will dominate.

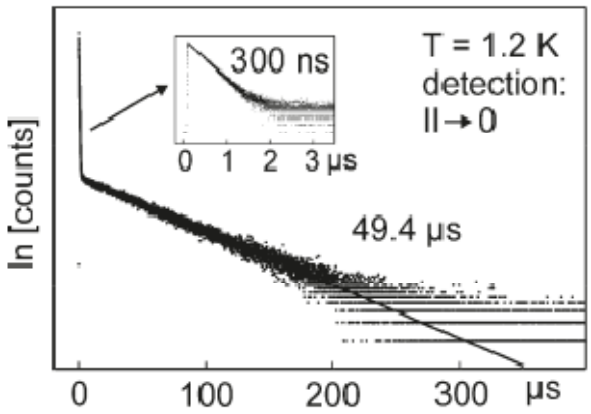

Figure 73: Emission decay curve of [PtL[1]Cl] in n-octane at 1.2 K, after UV excitation at 355 nm. The emission was detected at the electronic 0-0 transition II → 0 (20254 cm^{-1}).

To determine the individual emission decay of the substates, the temperature dependence of the thermalised emission decay was monitored (see Figure 74 a)). Along with the experimentally determined ZFS parameters, these data were fitted to *Eqn.* 5 to determine the lifetimes of the individual substates (values are given in Figure 74 a) inset).

$$\tau_{therm}(T) = \frac{1 + exp\left(\frac{-\Delta E_{II/I}}{k_B T}\right) + exp\left(\frac{-\Delta E_{III/I}}{k_B T}\right)}{\frac{1}{\tau_I} + \frac{1}{\tau_{II}}.exp\left(\frac{-\Delta E_{II/I}}{k_B T}\right) + \frac{1}{\tau_{III}}.exp\left(\frac{-\Delta E_{III/i}}{k_B T}\right)} \qquad Eqn.5$$

The lifetime of substate I is significantly longer than that of substate II and III, again demonstrating the forbiddenness of this state. The ratio, k_{II}/k_{III} is 2.4, and is in good agreement with the band intensity ratio (2.3) determined from the 4.2 K excitation spectrum. This indicates that substates II and III have comparable radiative and non-radiative decay mechanisms.

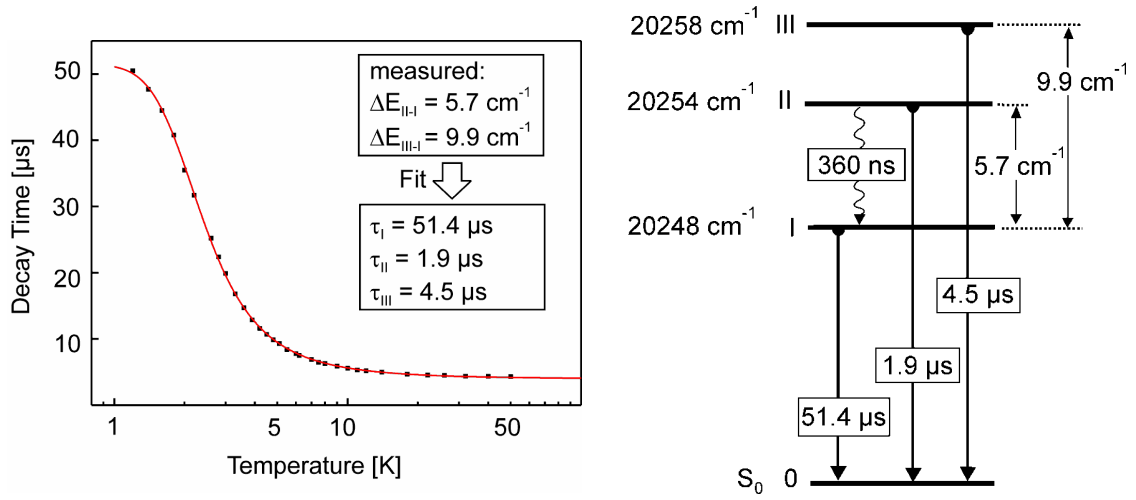

Figure 74: Left: Thermalised emission decay of [PtL^{1}Cl] in n-octane versus temperature after pulsed UV excitation at 355 nm. The emission was detected at the electronic 0-0 transition II → 0 (20254 cm^{-1}). The solid line represents a fit of *Eqn.* 5 to the experimental data. Right: the energy level diagram of [PtL^{1}Cl], showing the individual properties of the T_1 substates.

A similar investigation was performed on [PtL^{2}Cl]. This complex was dissolved in a n-decane matrix, because the 1.2 K emission spectrum of [PtL^{2}Cl] in n-octane was not highly resolved (indicates that the molecule doesn't "fit" into the lattice sites of an n-octane matrix). The total ZFS of T_1 state in [PtL^{2}Cl] was found to be 11.3 cm^{-1}, which is slightly higher than that for [PtL^{1}Cl], and indicates a greater MLCT contribution to the T_1 state. The 1.2 K excitation spectrum of [PtL^{2}Cl] revealed peaks corresponding to all three substates (see Figure 75), whereas the 1.2 K excitation spectrum of [PtL^{1}Cl] only revealed peaks corresponding to substates II and III.

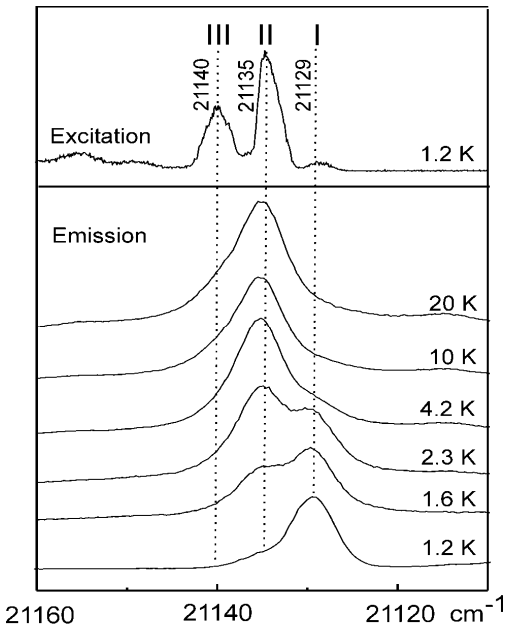

Figure 75: The excitation spectrum and emission spectra of [PtL^{2}Cl] recorded at cryogenic temperatures (in n-decane).

This observation indicates that substate I of [PtL^{2}Cl] carries a higher allowedness than substate I of [PtL^{1}Cl]. This was further confirmed upon analysis of the lifetimes of the individual substates: substate I of [PtL^{2}Cl] has a much shorter lifetime than substate I of [PtL^{1}Cl] (28 and 51 µs respectively).

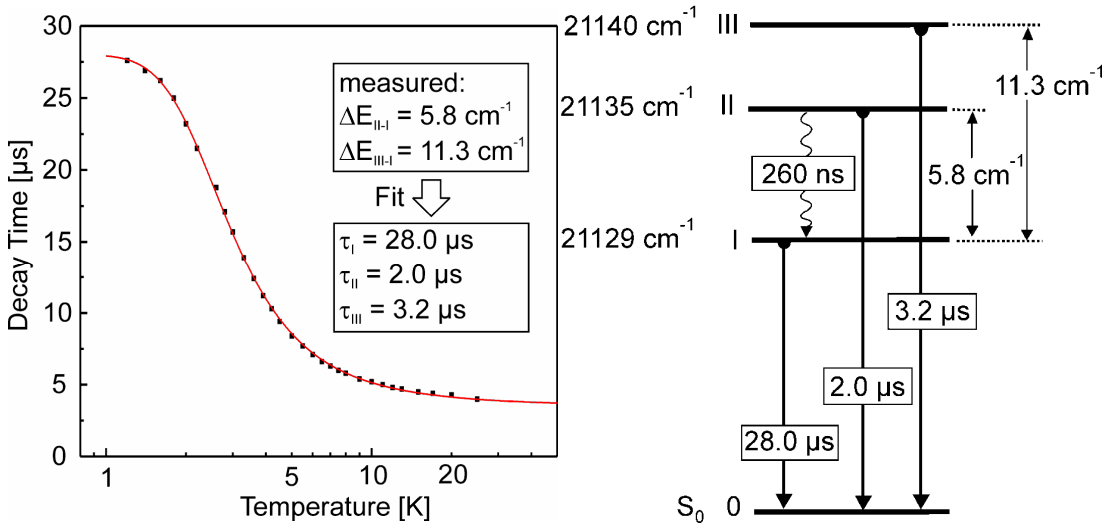

Figure 76: Left: Thermalised emission decay of [PtL^{2}Cl] in n-decane versus temperature after pulsed UV excitation at 355 nm. The emission was detected at the electronic 0-0 transition II → 0 (21135 cm^{-1}). Right: the energy level diagram of [PtL^{2}Cl], showing the individual properties of the T_1 substates

Halide Complexes

The complexes, [PtL^{1}Cl], [PtL^{1}Br] and [PtL^{1}I] were prepared to investigate the influence of the chloride ligand upon the photophysics. All complexes were found to emit at very similar energies (Section 3.4.2.1) with similar decay times, both at R.T. and 77 K, indicating that the halide ligands were acting as spectator ligands (rather than chromophoric ligands). However, all theoretical studies on [PtL^{1}Cl] predict that the the HOMO-based orbitals are partly located at the chloride ligand, whereas the LUMO-based orbitals are not. This means that during the electronic transition, charge should be re-distributed from the chloride ligand, and the T_1 state should be partly located at the chloride. We expected that detailed study of the T_1 states would allow us to determine whether the halide ligand was truly ancillary, or whether the halide ligand was chromophoric (but resulting in subtle differences between complexes).

At cryogenic temperatures, the highly resolved spectra of the [PtL^{1}Cl] and [PtL^{1}Br] are very similar, however, [PtL^{1}I] shows a larger splitting between substates I and II. From comparison of the energy level diagrams of the three complexes, we can see that the total ZFS increases slightly on going from Cl to Br to I. Hence, [PtL^{1}I] contains the greatest ^{3}MLCT character in its T_1 state. This could be related to the fact that iodine is a heavier atom than bromine and chlorine, and has a greater spin-orbit coupling constant.

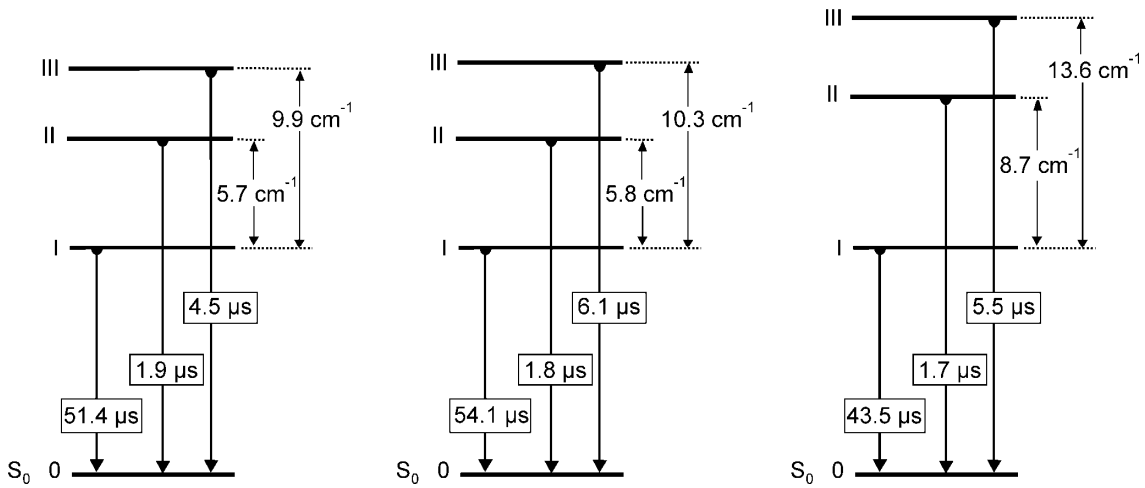

Figure 77: Energy level diagrams of the series [PtL^{1}X], showing how the ZFS increases with increasing size/mass of the halide (left: [PtL^{1}Cl], middle: [PtL^{1}Br] and right: [PtL^{1}I]).

These results indicate that replacement of the chloride ligand with bromide and iodide does have a small influence on the photophysical properties, despite the very similar behaviour observed at higher temperatures.

3.5 Pt(IV) Complexes

While the photochemistry of cyclometallated Pt(II) complexes has been heavily investigated over the last few decades, much less research has been reported regarding the photophysics of cyclometallated Pt(IV) complexes. This may be because, in contrast to the respective Pt(II) complexes, the first platinum(IV) complexes prepared involving cyclometallated ligands were non-emissive at room temperature.[45,46,47]

The first luminescent Pt(IV) complexes involving polypyridyl-type ligands were reported by Balzani et al.[48] These complexes involve two cyclometallating ligands (2-phenylpyridine or 2-(2-thienyl)pyridine), which introduce a sufficient ligand field to remove deactivating d-d* states to sufficiently high energy. Hence, creation of a stronger ligand field around Pt(IV) than Pt(II) is essential to observe luminescence. As a second example, $[Pt(bipy)(CH_3)_3I]$ is emissive at room temperature, whereas $[Pt(bipy)_2Cl_2]^{2+}$ emits only at 77 K. CH_3^- is a strong field ligand.[49]

Platinum(IV) complexes of the form $[PtLCl_3]$ were prepared for several complexes, by passing chlorine gas through a chloroform solution containing the respective Pt(II) complex.[50] These Pt(IV) complexes were found to absorb at higher energy than the respective Pt(II) complex (see Figure 78 for a representative example).

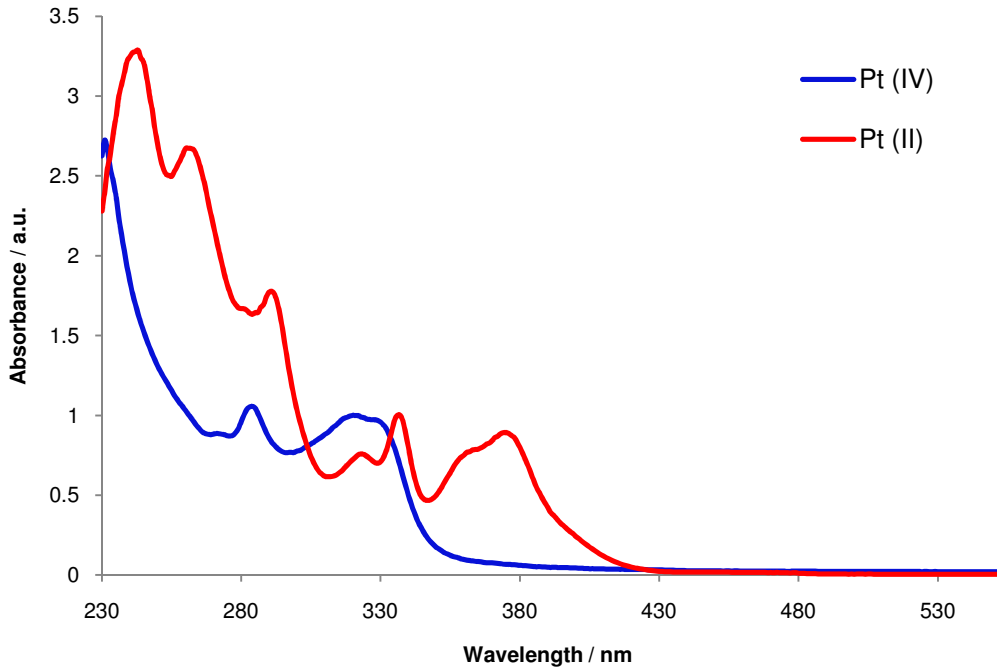

Figure 78: Normalised UV-vis absorption spectra of $[PtL^9Cl_3]$ (blue) and $[PtL^9Cl]$ (red). Measurements were performed in DCM at 298 K

These Pt(IV) complexes were only emissive at 77 K. Chloride is a weak field ligand, and the combination of three chlorides and one terdentate ligand does not create a sufficient ligand field splitting to allow emission at room temperature. The 77 K emission of the Pt(IV) complexes occurred at higher energy than the analogous Pt(II) complex (see Table 27, and Figure 79 for a representative example). Unfortunately, although NMR indicated that the oxidation had gone to completion, emission from the Pt(II) precursor was always detected in the emission spectra of the Pt(IV) complexes. This was confirmed by comparing the 77 K and R.T. emission spectra, where emission from the Pt(II) species only was observed in the latter. The Pt(II) complexes are so emissive that trace amounts are sufficient to contaminate the Pt(IV) spectra.

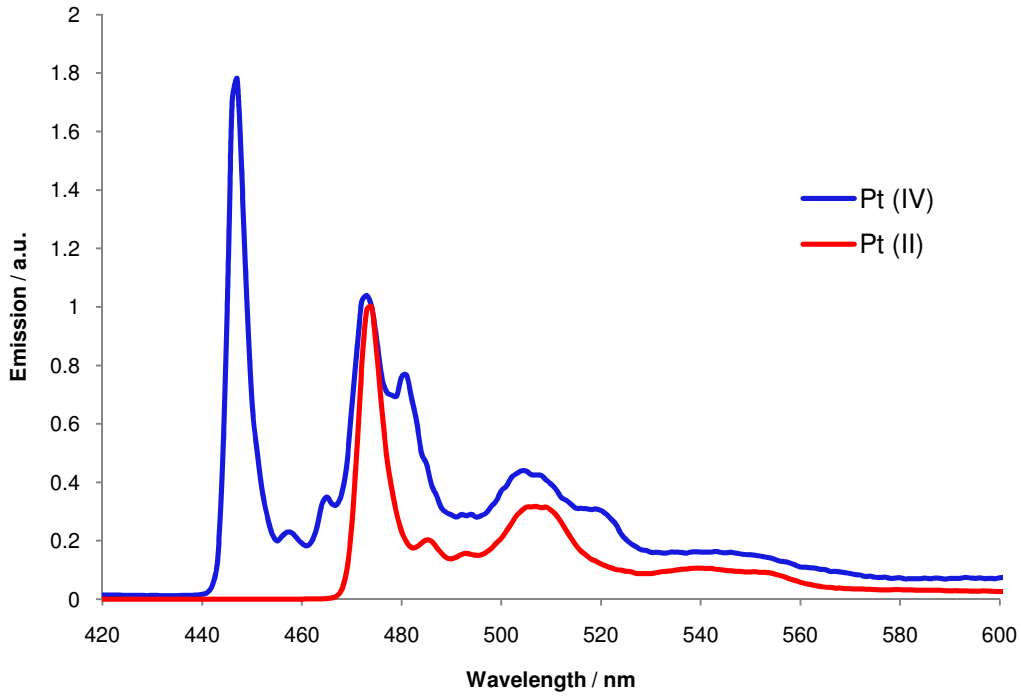

Figure 79: 77 K emission spectra of impure [$PtL^{11}Cl_3$] (blue) and [$PtL^{11}Cl$] (red) from an EPA glass (spectra have been normalised at 474 nm).

The Pt(IV) complexes had lifetimes in the range 1 – 2 s. The lifetimes are greater than those of the Pt(II) complexes by a factor of 10^5, which indicates a lesser contribution of the metal to the triplet state. In the higher oxidation state, the metal centred orbitals will be more contracted and will interact less with the ligand orbitals.

Table 27: 77 K emission and lifetimes of the Pt (IV) complexes (EPA)

Complex	Emission λ_{max} at 77 K / nm (Energy / cm^{-1})	τ_0 at 77 K / s
$[PtL^2Cl_3]$	440 (22730)	1.3
$[PtL^7Cl_3]$	462 (21650)	1.2
$[PtL^9Cl_3]$	443 (22570)	1.0
$[PtL^{10}Cl_3]$	439 (22780)	1.6
$[PtL^{11}Cl_3]$	447 (22370)	1.3

3.6 Application in OLEDs

The complexes presented herein possess many properties that make them good candidates for OLED dopants. For example, the complexes are phosphorescent emitters, have high quantum yields, are charge-neutral and possess good thermal stability. Related complexes prepared by a previous group member were successfully incorporated into OLEDs, through collaboration with Drs V. Fattori and M. Cocchi from the Institute of Organic Photosynthesis and Photoreactivity, Bologna, Italy, giving devices with extremely high quantum efficiency and good performances.[51] The colour of the device was tuned simply by varying the dopant concentration (i.e. excimer:monomer ratio).

Some of the complexes reported here have been successfully incorporated into OLEDs as phosphorescent dopants ($[PtL^2Cl]$, $[PtL^6Cl]$, $[PtL^{10}Cl]$,[52] and $[PtL^{15}Cl]$[53]) – the properties of these devices are given in Table 28. Device architecture can play an important role in determining device efficiency – for example, the redox properties of the layers must be matched to the phosphorescent dopant, to achieve maximum emission (for more detailed descriptions, see reference 54). Here, the device architecture has been optimised to match the electronic properties of the [PtLCl] dopants: the typical device structure is shown in Figure 80. These devices consists of an indium-tin oxide

anode (ITO), N,N'-bis(m-tolyl)-1,1'-biphenyl-4,4'-diamine:bisphenol-A-polycarbonate (TPD:PC) and 4,4,4''-tris(*N*-carbazolyl-triphenylamine) (TCTA) hole transporting layers, an emissive layer consisting of the phosphorescent complex doped into a TCTA host matrix, a 3-phenyl-4-(1'-naphthyl)-5-phenyl-1,2,4-triazole (TAZ) electron transporting layer, and a LiF/Al cathode. The device is prepared by initially spin-coating the TPD:PC layer onto the ITO anode, followed by subsequent vacuum deposition of all other layers. TCTA acts as an exciton blocking layer, preventing quenching by the non-radiative triplet of TPD, whereas TAZ acts as both an exciton and hole blocking layer, and the combined effect restricts the electron-hole recombination process within the emissive layer. Most devices prepared here display external quantum efficiencies in the range of 5 – 18.3% ph/e, power efficiencies of 0.47 – 11.8 lm/W and luminous efficiencies of 1.6 – 44.8 cd/A. The upper limits of these efficiencies are extremely high for such devices.

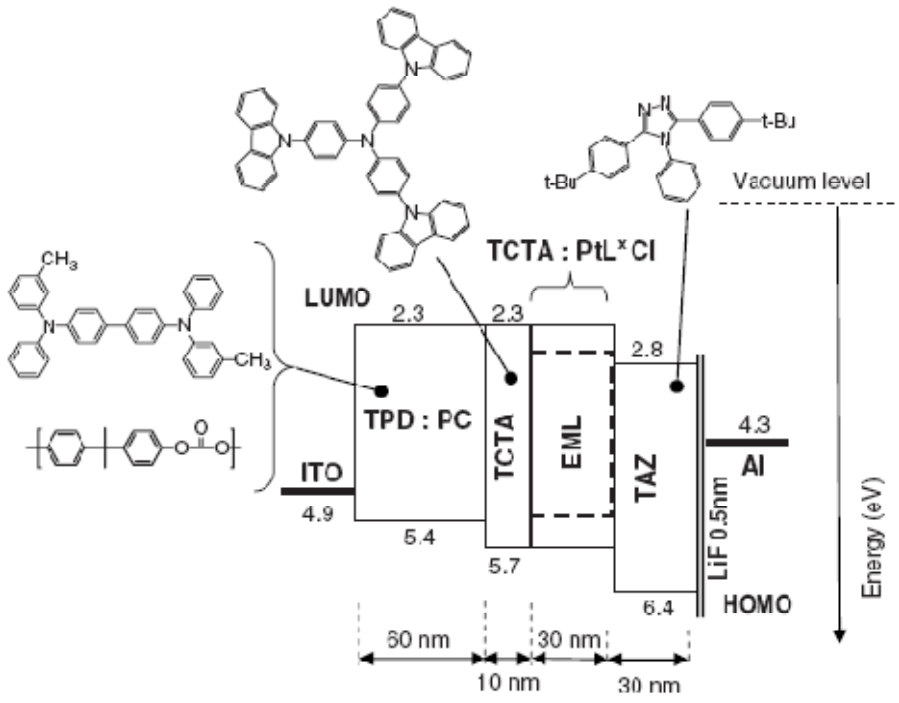

Figure 80: The architecture of the LEDs, and the molecular structures of materials used. An energy level diagram is also shown, to help understand the exciton and electronic traffic within the devices. The HOMO values presented for each material correspond to their respective ionisation potentials, and the LUMO values correspond to the molecular electron affinity. The Fermi level positions for ITO and Al electrode contacts are added for completeness. The numbers correspond to electron volts and are relative to the vacuum level at zero energy.

Table 28: Performances of OLEDs prepared with [PtLCl] complexes. Each device is listed by concentration of the Pt complex in the emitting layer (at ~ 500 cd/m^2).

Complex	Amount (%)	Bias (V)	j (mA/cm^2)	QE (%ph/e)	PE (lm/W)	LE (cd/A)	CIE (x,y)	CRI
[PtL^{2}Cl]	5	8.4	3.1	7.8	6.9	15.9	0.19,0.42	__
	100	10.6	31.3	5.3	0.47	1.6	0.63,0.35	__
[PtL^{6}Cl]	5	8.6	1.2	15.5	16.4	44.8	0.24,0.57	__
	100[a]	19.0	9.6	0.1	0.02	0.1	0.57,0.40	__
[PtL^{10}Cl]	5	8.8	1.5	13.0	9.3	26.0	0.18,0.35	__
	10	8.7	1.7	18.3	11.8	32.7	0.27,0.37	63
	15	7.7	1.9	18.1	11.8	29.1	0.33,0.38	65
	20	7.6	2.6	14.9	8.3	20.2	0.45,0.38	68
	25	8.2	2.6	16.8	8.0	21.0	0.53,0.38	80
	100	8.7	3.7	14.7	5.0	13.9	0.61,0.38	__
[PtL^{15}Cl]	5	11.8	4.7	6.1	2.8	10.7	0.18,0.27	__
	10	11.4	3.6	7.6	3.8	13.7	0.23,0.30	__
	15	11.6	2.5	10.9	5.4	20.0	0.28,0.32	70
	20	9.8	2.5	11.5	6.8	21.3	0.34,0.35	74
	25	10	2.1	13.6	7.9	25.0	0.39,0.37	78
	30	9.8	1.7	16.6	9.6	29.5	0.42,0.38	81
	35	10.8	1.7	17.0	8.7	30.0	0.47,0.39	80
	100	10	1.8	16.0	8.1	27.7	0.58,0.41	__

[a]At ~ 10 cd/m^2

The complexes under study all display blue/turquoise monomeric emission and red/orange excimeric emission, and the relative intensities are dependent upon concentration. Consequently, the colour of a device can be controlled by varying the dopant concentration. Figure 81 shows how the CIE coordinates of a device varied with dopant concentration for complex [PtL^{10}Cl], from blue-biased emission at low concentration, through approximate white light emission at intermediate concentration, to emission occurring in the red region from the neat films.

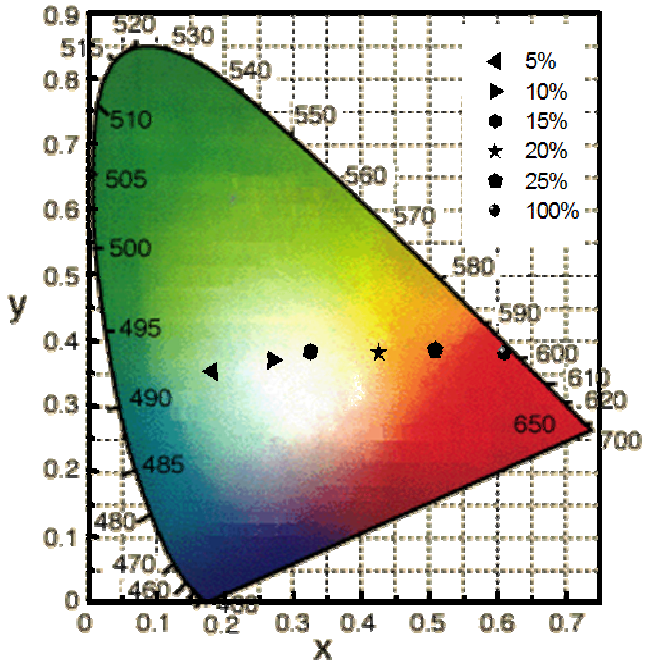

Figure 81: CIE chromaticity coordinates of OLEDs prepared with various concentrations of [PtL^{10}Cl]

These complexes, which display blue-biased monomeric emission compared to previously investigated 1,3-dipyridylbenzene Pt(II) systems,[51] are better candidates for white OLEDs, as they offer a greater coverage of the visible spectrum. Some of the devices prepared with these new complexes, using intermediate dopant concentrations, performed well as white light emitting devices (see Table 28). For example, a device consisting of 20% [PtL^{15}Cl] dopant gave CIE coordinates of (0.34, 0.35), which are very close to the equal energy point (0.33, 0.33) representing pure white light (see Figure 82). This device had a high CRI index of 74, and an external QE of 9.8%.

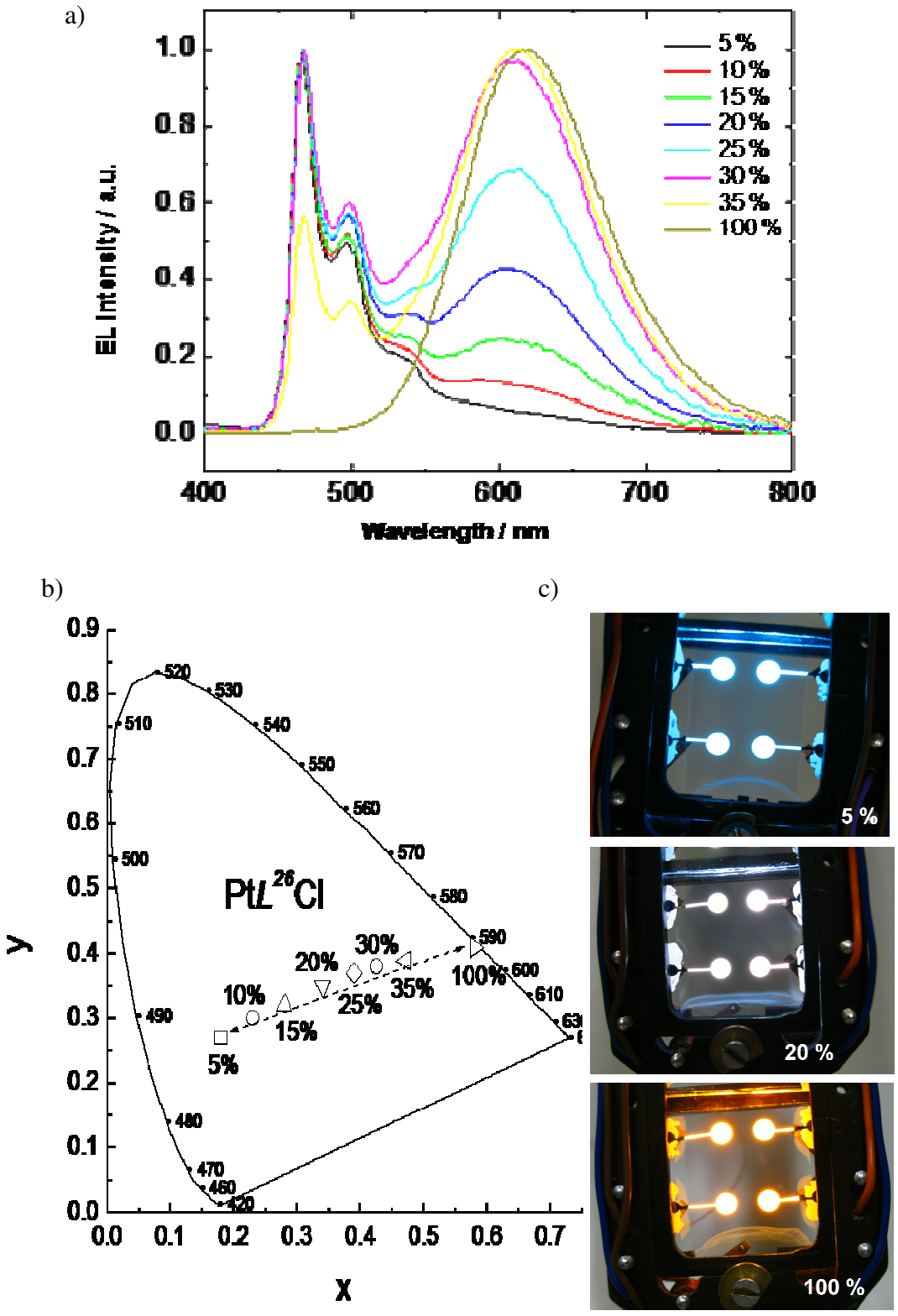

Figure 82: a) The electroluminescence spectra of OLEDs containing various concentrations of [PtL^{15}Cl], b) the CIE chromaticity coordinates of these devices and c) photographs of actual devices containing [PtL^{15}Cl] (dopant concentration is given at bottom of each image).

During the testing of [PtL^{2}Cl] as a phosphorescent dopant in OLEDs, Jabbour et al. reported the use of [PtL^{2}Cl] in another OLED device. The device composition differed to ours (see reference 55). Jabbour also reported on the colour variation with dopant

concentration – for example, a blue device (CIE coordinates = 0.18, 0.32) incorporating 2% [PtL^2Cl] was prepared, with external QE of 8.6%, and a device consisting of 8% of this complex gave approximately white emission (CIE = 0.33, 0.36), with an external quantum efficiency of 9.3%.

Our collaborators in Bologna realised that OLEDs displaying dual monomer/excimer emission may have application as horticultural lighting sources.[56] They noted that plants tend to absorb in the blue and red regions of the visible spectrum, so under typical lighting, a large amount of energy is wasted. In contrast, the blue-biased monomeric emission and red excimeric emission observed from OLEDs involving our complexes can be tuned to give a good fit with the photosynthetic action spectrum of plants, resulting in minimal energy wastage. For example, a typical photosynthetic action spectrum shows an extremely good fit to the electroluminescence spectrum of an OLED containing 20% [$PtL^{10}Cl$] (see Figure 83). Furthermore, a plant's behaviour varies between seasons (morphogenesis). This behaviour is related to the position of the sun, i.e. the relative contributions of blue and red light. For example, provision of excess blue light stimulates greening and stem growth and enriches chlorophyll production whereas a greater red light contribution stimulates flowering, fruiting and seeding (the plants "think" winter is coming). By varying the OLED dopant concentration, it may therefore be possible to re-create the seasons, allowing control over plant morphogenesis.

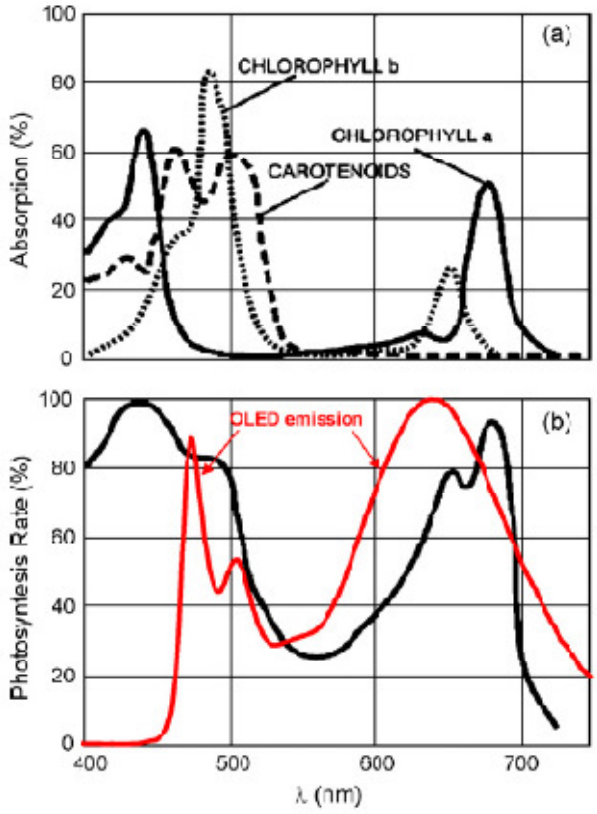

Figure 83: a) Absorption spectra of chloroplast chlorophyll-a and -b, and carotenoids, and b) an action spectrum of photosynthesis (black) compared with the emission spectrum the OLED incorporating 20% [PtL^{10}Cl] (red). Note the remarkable correspondence between the OLED spectrum and the action spectrum.

3.7 Concluding Remarks

A few groups have performed DFT calculations on the unsubstituted parent complex, [PtL^{1}Cl] (Section 3.2). The calculations predict that the HOMO-based orbitals are localised along the central axis of the molecule (including the phenyl ring, the platinum centre and the ancillary ligand), and the LUMO-based orbitals are mainly localised on the lateral pyridyl rings. Using this as a starting point, rational structure modification has been employed to prepare complexes with tuneable emission.

On considering the terdentate ligand, we realised that functionalisation of the phenyl ring should alter the energy of the HOMO-based orbitals more significantly than the LUMO-based orbitals. In most cases, experimental results agreed with theory. For example, placing fluorine at the 3,5-phenyl positions resulted in a blue shift – in these positions, fluorine is behaving as an electron withdrawing group, which causes greater stabilisation of the HOMO-based orbitals relative to the LUMO.

Placing electron donating groups on the lateral pyridyl rings was expected to have a greater destabilising effect on the LUMO-based orbitals, leading to a further blue shift. The validity of this assumption was assessed, by preparing two series of complexes containing methyl-substituents in each of the available pyridyl positions ([PtL$^{5\text{-}8}$Cl] and [PtL$^{9\text{-}12}$Cl]). Placing methyl-substituents at only one position, the 4-pyridyl position, led to a blue shift. Closer examination of the DFT results revealed two points, 1) the contour plots predicted by Williams et al. suggest that the other pyridyl positions also make a contribution to the HOMO-based orbitals, and 2) the 3-pyridyl position isn't really involved in the LUMO-based orbitals. This may partly account for why placing methyl groups at the other positions did not lead to a blue-shift.

To prepare complexes displaying increasingly blue-shifted emission, the 4-pyridyl position was functionalised with groups of greater electron donating character (-OMe and -NMe_2). This led to complexes exhibiting the highest energy emission ever recorded for 1,3-dipyridylbenzene Pt(II) chloride systems (e.g. [PtL^{17}Cl] and [PtL^{15}Cl]). In further agreement with theory, incorporation of an electron withdrawing CF_3-substituent at the 4-pyridyl position led to a red-shift in emission (e.g. [PtL$^{20\text{-}21}$Cl] and [PtL^{30}Cl]).

Substituting the ancillary chloride for cyanide led to a further blue-shift in emission – to our knowledge, [PtL^{17}CN] and [PtL^{15}CN] display the highest energy emission of any Pt(II) complex containing a terdentate ligand. Cyanide lies much higher up the spectrochemical series than chloride, and causes greater ligand field splitting. Furthermore, DFT predicts that the ancillary position makes a significant contribution to the HOMO, and cyanide is a more electron withdrawing group than chloride. On the contrary, substitution of chloride with other halides (Br^- and I^-) had virtually no effect on the room temperature emission – perhaps these ligands are too similar in character.

Most of the Pt(II) complexes were found to be highly emissive from DCM solution at 298 K, with quantum yields reaching as high as 0.87. The quantum yields of these complexes were found to be significantly higher than complexes involving analogous bidentate ligands, highlighting the importance of the extra rigidity conferred by the terdentate system. Unsymmetrical complexes ([PtL^{16}Cl] and [PtL^{21}Cl]) incorporating pyridyl rings which contain different substituents, show monomeric emission at similar energy to symmetrical complexes containing the most stable pyridyl ring (i.e. [PtL^{1}Cl] and [PtL^{20}Cl] respectively). This implies that the LUMO-based orbitals are localised on

the most stable pyridyl ring, which is consistent with the work of Williams et al. reported in reference 16.

The emission profiles of complexes containing significant distortion from planarity ([PtL^{8}Cl], [PtL^{12}Cl] and [PtL^{13}Cl]) are much less structured, and the 0-1 and 0-2 vibronic bands have higher intensity relative to the 0-0 band. These factors indicate that considerable differences in geometry exist between the ground and excited states. Furthermore, the quantum yields of [PtL^{8}Cl] and [PtL^{12}Cl] are very poor compared to most other complexes reported here (φ = 0.03 and 0.02 respectively), in line with the idea that distortions disfavour radiative decay. However, the quantum yield of [PtL^{13}Cl] is quite high (φ = 0.75). The emission profiles of [PtL^{9}Cl] and [PtL^{17}Cl] are also broader with less structure. However, the crystal data for [PtL^{9}Cl] indicates only slight deviations from planarity. Also, it seems reasonable to assume that [PtL^{17}Cl] will be approximately planar (there are no unfavourable sterics). ^{19}F NMR data for [PtL^{9}Cl] indicate significant electronic perturbations exist in this molecule, through non-bonding overlap of the fluorine and methyl hydrogen atom orbitals (see Chapter 2, Section 2.4.2.1). It is suggested that this electronic perturbation is responsible for the broader emission profile. Similarly, the NMe_2 group is a very strong electron donor, and significant electronic reorganisation between the ground and the excited state may account for the broader profile of [PtL^{17}Cl].

The Pt(II) complexes exhibited self-quenching via excimer formation in solution at elevated concentration. Self-quenching rate constants, k_{sq}, were generally of the order of 2-6 x 10^{9} M^{-1} s^{-1}, except for [PtL^{13}Cl], which had a much lower k_{sq} of 0.50 x 10^{9} M^{-1} s^{-1}. This complex contains significant steric interactions and distortions from planarity, which probably reduces the tendency to self-quench. The excimers of most complexes were found to be emissive, and the energy of this broad, structureless band was found to depend upon a) the nature of substituents present on the terdentate ligand and b) the identity of the ancillary ligand. However, the substituents altered the monomeric and excimeric emission to differing degrees. It seems that the nature of substituents on the pyridyl rings has more influence on excimeric emission energy than substituents on the phenyl ring – this may be related to the orientation adopted by the molecules forming the excimer.

Excimeric emission was not observed for complexes [PtL^{8}Cl], [PtL^{12}Cl] and [PtL^{13}Cl] under the concentration range studied (10^{-6} – 10^{-4} M). The extremely low k_{sq} value

found for [PtL^{13}Cl] indicates that this complex has a low propensity to form excimers. Unfortunately, k_{sq} values for [PtL^{8}Cl], [PtL^{12}Cl] could not be determined due to the weakness of their emission. Therefore it is not possible to say whether these complexes have a low propensity to form excimers, or whether these complexes form excimers which only emit weakly (as found for monomeric emission).The Pt(II) complexes form aggregates in more polar solutions, which emit at lower energy than the monomer, but are distinctly different from excimers.

The emission of the complexes has been examined at lower temperatures. Upon lowering the temperature, spectral resolution increases as the contribution from inhomogeneous broadening is reduced. At cryogenic temperatures (1.2 – 4.2 K), the spectra appear as individual bands with line-widths of a few cm^{-1} (residual inhomogeneity). Such high resolution allows the study of the individual substates of the T_1 state. From this work, the zero-field splitting (ZFS) parameter could be determined – this value is useful in assessing the relative contribution of the metal to the excited state. ZFS parameters have been determined for [PtL^{1}Cl] and [PtL^{2}Cl] (9.9 cm^{-1} and 11.3 cm^{-1} respectively). With reference to the scale devised by Yersin,[44] the magnitude of these values indicates that the complexes emit from a state containing a ^{3}LC/^{3}MLCT admixture, but with a larger ^{3}LC contribution. The ZFS parameters were determined for the [PtL^{1}X] series of complex. The ZFS increases from 9.9 cm^{-1} for [PtL^{1}Cl], to 13.1 cm^{-1} for [PtL^{1}I] – this indicates that [PtL^{1}I] contains the greatest MLCT contribution to its T_1 state. This could be related to the fact that iodine is much heavier, and has a greater spin-orbit coupling constant. These results indicate that the halogen atom does have a small influence on the photophysical properties, which would have been missed if only the room temperature and 77 K studies were considered.

Some of these Pt(II) complexes have been incorporated into OLEDs as phosphorescent dopants (e.g. [PtL^{2}Cl], [PtL^{6}Cl], [PtL^{10}Cl] and [PtL^{15}Cl]). Devices ranging from blue emission to orange/red emission have been prepared for each complex investigated, simply by varying the concentration of complex (i.e. variation of the monomer:excimer ratio). Of particular note, devices displaying white emission have been prepared at intermediate concentrations – some of these WOLEDs have very similar CIE coordinates to pure white light (0.33, 0.33). For example, a device incorporating 20% [PtL^{15}Cl] has CIE coordinates of 0.34, 0.35, and a CRI of 74. The OLEDs typically have external quantum efficiencies in the range of 5 – 18.3%, and devices at the top of this range are some of the most efficient OLEDs reported to date.

3.8 References

1. J. A. G. Williams, A. Beeby, E. S. Davies, J. A. Weinstein and C. Wilson, *Inorg. Chem.*, 2003, **42**, 8609-8611

2. S. J. Farley, D. L. Rochester, A. L. Thompson, J. A. K. Howard and J. A. G. Williams, *Inorg. Chem.*, 2005, **44**, 9690 – 9703

3. D. L. Rochester, S. Develay, S. Záliš and J. A. G. Williams, *Dalton Trans.*, 2009, 1728-1741

4. W. Sotoyama, T. Satoh, H. Sato, A. Matsuura and N. Sawatari, *J. Phys. Chem. A*, 2005, **109**, 9760-9766

5. L. L. Shi, T. Li, S. S. Zhao and H. Li, *Theor. Chem. Acc.*, 2009, **124**, 29-36

6. N. J. Turro, "Modern Molecular Photochemistry", The Benjamin/Cummings Publishing Co., Inc., California, 1978

7. W. B. Connick, D. Geiger and R. Eisenberg, *Inorg. Chem.*, 1999, **38**, 3264-3265

8. D. M. Roundhill, "Photochemistry and Photophysics of Metal Complexes", Plenum Press, New York, 1994

9. J. Brooks, Y. Babayan, S. Lamansky, P. I. Djurovich, I. Tsyba, R. Bau and M. E. Thompson, *Inorg. Chem.*, 2002, **41**, 3055-3066

10. D. J. Cárdenas and A. M. Echavarren, *Organometallics*, 1999, **18**, 3337-3341

11. A. F. Rausch, H. H. H. Homeier and H. Yersin, *Top. Organometal. Chem.*, 2009, **29/2010**, 193 - 235

12. G. Verdasco, M. A. Martín, B. del Castillo, P. López-Alvarado and J. C. Menéndez, *Anal. Chim. Acta*, 1995, **303**, 73-78

13. V. Tsaryuk, V. Zolin and J. Legendziewicz, *J. Luminescence*, 2003, **102-103**, 744 – 750

14. A. O. Doroshenko, O. A. Ponomarev, V. G. Mitina and V. V. Ivanov, *Theoretical and Experimental Chem.*, 1989, **24(5)**, 581 - 586

15. S. Berger, S. Braun and H-O. Kalinowski, NMR Spectroscopy of the Non-Metallic Elements", John Wiley and Sons Ltd. Chichester, 1997.

16. S. Develay and J. A. G. Williams, *Dalton Trans.*, 2008, 4562-4564

17. A. A. Rachford and F. N. Castellano, *Inorg. Chem.*, 2009, 48, 10865-10867

18. H. Yersin, W. Humbs and J. Strasser, *Coord. Chem. Rev.*, 1997, **159**, 325-359

19. M. Hissler, W. B. Connick, D. K. Geiger, J. E. McGarrah, D. Lipa, R. J. Lachicotte and R. Eisenberg, *Inorg. Chem.*, 2000, **39**, 447-457

20. M. H. Wilson, L. P. Ledwaba, J. S. Field and D. R. McMillin, *Dalton Trans.*, 2005, 2754-2759

21. V. W-W. Yam, R. P-L. Tang, K. M-C. Wong and K-K. Cheung, *Organometallics*, 2001, **20**¸4476 - 4482

22. Q-Z. Yang, L-Z. Wu, Z-X. Wu, L-P. Zhang and C-H. Tung, *Inorg. Chem.*, 2002, **41**, 5653-5655

23. S-W. Lai, M. C. W. Chan, K-K. Cheung and C-M. Che, *Inorg. Chem.*, 1999, **38(19)**, 4262-4267

24. C. Deuschel-Cornioley, T. Ward and A. Von Zelewsky, *Helv. Chim. Acta*, 1988, **71**, 130

25. J. H. K. Yip, Suwarno and J. J. Vittal, *Inorg. Chem.*, 2000, **39**, 3537-3543

26. P-I. Kvam, M. V. Puzyk, K. P. Balashev and J. Songstad, *Acta. Chem. Scand.*, 1995, **49**¸ 335-343

27. F. N. Castellano, I. E. Pomestchenko, E. Shikhova, F. Hua, M. L. Muro and N. Rajapakse, *Coord. Chem. Rev.*, 2006, **250**, 1819-1828

28. D. L. Rochester, "Cyclometallated Platinum and Palladium Complexes with N^C^N-Coordinating Terdentate Ligands: Synthesis, Luminescence and Catalytic Properties", Ph.D Thesis, Durham University, 2007

29. T. Tsuzuki and S. Tokito, *Proc. Int. Symp. Super-Functionality Organic Devices*, IPAP Conf. Series 6, 99 - 103

30. M. M. Mdleleni, J. S. Bridgewater, R. J. Watts and P. C. Ford, *Inorg. Chem.*, 1995, **34**, 2334-2342

31. V. W. W. Yam, K. M. C. Wong and N. Zhu, *J. Am. Chem. Soc.*, 2002, **124**, 6506-6507

32. A. S. Ionkin, W. J. Marshall and Y. Wang, *Organometallics*, 2005, **24**, 619-627

33. B. Ma, P. I. Djurovich and M. E. Thompson, *Coord. Chem. Rev.*, 2005, **249**, 1501-1510

34. J. B. Birks, "Photophysics of Aromatic Moloecules", Wiley Interscience, London, 1970

35. N. J. Turro, V. Ramamurthy and J. C. Scaiano, “Modern Molecular Photophysics of Organic Molecules”, University Science Books, California, 2010

36. K-T. Wan, C-M. Che and K-C Cho, *Dalton Trans.*, 1991, 1077 – 1080

37. V. W-W. Yam, K. H-Y. Chan, K. M-C. Wong and N. Zhu, *Chem. Eur. J.*, 2005, **11**, 4535-4543

38. L. J. Grove, J. M. Rennekamp, H. Jude and W. B. Connick, *J. Am. Chem. Soc.*, 2004, **126**, 1594-1595

39. P. Du, J. Schneider, W. W. Brennessel and R. Eisenberg, *Inorg. Chem.*, 2008, **47(1)**, 69-77

40. M. Kato, *Bull. Chem. Soc. Jpn.*, 2007, **80(2)**, 287-294

41. A. F. Rausch, L. Murphy, J. A. G. Williams and H. Yersin, *Inorg. Chem.*, 2009, **48**, 11407-11414

42. H. Yersin, *Top. Curr. Chem.*, 2004, **241**, 1 - 26

43. E. V. Shpol’skii, *Sov. Phys. Usp. (Engl. Transl.)*, 1960, **3**, 372

44. H. Yersin, W. J. Finkenzeller, “Highly Efficient OLEDs with Phosphorescent Materials”, Wiley-VCH, Weinheim, 2008

45. R. H. Hill and R. J. Puddephatt, *J. Am. Chem. Soc.*, 1985, **107**, 1218 – 1225

46. A. Vogler and H. Kunkely, *Inorg. Chem.*, 1982, **21** 1172 – 1175

47. D. M. Roundhill, *J. Am. Chem. Soc.*, 1985, **107**, 4354 – 4356

48. L. Chassot, A. Von Zelewsky, D. Sandrini, M. Maestri and V. Balzani, *J. Am. Chem. Soc.*, 1986, **108**, 6084 – 6085

49. H. Kunkely and A. Vogler, *Coord. Chem. Rev.*, 1991, **111**, 15 – 25

50. U. Belluco, “Organometallic and Coordination Chemistry of Platinum”, Academic Press, London, 1974

51. M. Cocchi, J. Kalinowski, D. Virgili, V. Fattori, S. Develay and J. A. G. Williams, *Appl. Phys. Lett.*, 2007, **90**, 163508

52. M. Cocchi, J. Kalinowski, V. Fattori, J.A.G. Williams and L. Murphy, *Applied Physics Letters*, 2009, **94(7)**, 073309

53. M. Cocchi, J. Kalinowski, L. Murphy, J.A.G. Williams and V. Fattori, *Organic Electronics*, 2010, **11**, 388-396

54. L. S. Hung and C. H. Chen, *Materials Science and Engineering R*, 2002, **39**, 143 - 222

55. X. Yang, Z. Wang, S. Madakuni, J. Li and G. E. Jabbour, *Adv. Mater.*, 2008, **20**, 2405-2409

56. V. Fattori, J.A.G. Williams, L. Murphy, M. Cocchi and J. Kalinowski, *Photonics and Nanostructures – Fundamentals and Applications*, 2008, **6(3-4)**, 225-230

3.9 Comprehensive Photophysical Data

Table 29: Photophysical data for the Pt(II) complexes, in DCM at 295 K

Complex	Absorbance λ_{max}/nm (ε / L mol^{-1} cm^{-1})	Emission λ_{max}/nm	τ_0 degassed (aerated) /μs[a]	k_{SQ}(self-quenching)/10^9 M^{-1} s^{-1}	Φ_{lum} degassed (aerated)	k_Q(O_2 quenching)/10^8 M^{-1} s^{-1}
[PtL^{1}Cl][b]	332 (6510), 380 (8690), 401 (7010), 454* (270), 485* (240)	491, 524, 562, 691ex	7.2 (0.50)	5.3	0.60 (0.039)	10.4
[PtL^{2}Cl]	320 (6687), 334 (9183), 360 (7341), 374 (8498), 437* (143), 467* (139)	472, 502, 536sh, 677ex	7.9 (0.67)	6.0	0.85 (0.087)	6.2
[PtL^{3}Cl]	250, 285, 330, 388, 399, 480*	492, 515	0.78[d] (------)	------[f]	0.03 (0.02)	-----[f]
[PtL^{5}Cl]	322 (5180), 334 (5289), 363sh (4383), 382 (6333), 405sh (4299), 459*sh, 489*	497, 529, 565sh, 706ex	7.7 (0.34)	3.0	0.51 (0.024)	12.8

[PtL^{6}Cl][c]	326 (7820), 356 (6420), 374 (8930), 400 (7040), 479* (260)	487, 521, 560, 674ex	10.0 (0.34)	8.3	0.73 (0.04)	12.6
[PtL^{7}Cl]	335 (12348), 360 (9145), 370 (11206), 399 (8464), 455*sh (284), 490* (130)	494, 528, 565sh, 688ex	11.1 (0.58)	3.9	0.13 (0.001)	7.4
[PtL^{8}Cl]	327 (6503), 339 sh (6030), 390 sh (6439), 413 (6733), 492* (311)	506, 529, 569sh	------[g]	-----[g]	0.03 (> 0.001)	------[g]
[PtL^{9}Cl]	323 (6030), 336 (8012), 361 (6028), 375 (7105), 444*(108),474* (85)	487, 513, 555sh, 681ex	7.3 (0.49)	3.9	0.39 (0.20)	8.7
[PtL^{10}Cl]	316 (8905), 329 sh (10789), 358 (8997), 372 (11323), 433* (179), 462* (150)	467, 498, 529sh, 660ex	7.9 (0.70)	5.1	0.87 (0.088)	5.8
[PtL^{11}Cl]	322 (5823), 336 (8618), 358 (6331), 372 (6729), 442* (106), 473* (80)	478, 510, 543sh, 673ex	10.5 (0.77)	3.7	0.67 (0.061)	5.3

[PtL^{12}Cl]	292 (13885), 329 (5553), 341 (5975), 382 (6475), 475* (124)	494, 530, 565sh	------[g]	------[g]	0.02 (0.0007)	-----[g]
[PtL^{13}Cl]	327 sh (6302), 341 (6100), 367 sh (4013), 386 (5735), 488* sh (95)	546br	7.7 (0.34)	0.5	0.75 (0.035)	12.8
[PtL^{14}Cl]	325 (6446), 343 (6725), 374 sh (5191), 387 (6013), 461* (100), 493* (85)	499, 533, 573sh, 678ex	11.9 (0.62)	2.9	0.55 (0.039)	6.9
[PtL^{15}Cl]	294sh (6441), 306 (5683), 352sh (5558), 368 (6809), 427*sh, 445*, 455*	461, 492, 519sh, 630ex	7.6 (0.58)	2.9	0.71 (0.068)	7.2
[PtL^{16}Cl]	314 (6348), 326 (6786), 355sh (6013), 372 (7568), 436*sh, 464*	470, 502, 532sh 660ex	6.0 (0.74)	3.2	0.75 (0.079)	5.4
[PtL^{17}Cl]	319 (6580), 352 sh (9313), 370 (13905), 418*sh (312), 443* (161)	455, 485, 512sh, 596ex	4.7 (0.13)	2.1	0.60 (0.020)	34.0

[PtL^{20}Cl]	334 sh (4470), 349 (6508), 383 (8186), 453*sh (221), 486 (171)*	497, 527, 575sh, 733ex	5.6 (1.7)	2.6	0.59 (0.21)	2.6
[PtL^{21}Cl]	329 sh (4579),338 sh (4437), 369 (4820), 389 sh (3303), 427 sh (801), 480* (145)	495, 528, 573sh, 710ex	5.5 (0.67)	2.0	0.57 (0.067) (0.038)	2.0
[PtL^{22}Cl]	341 (4586), 367sh (6105), 384 (8746), 460* (133), 492* (126)	499, 533, 571sh, 707ex	9.6 (0.67)	5.6	0.61 (0.10) (0.063)	6.3
[PtL^{23}]	286, 308 sh, 373 sh, 390	494, 523, 560sh	23.0 (2.8)[d]	------[f]	0.08 (0.01)	1.4[e]
[PtL^{25}Cl]	375 (3328), 413sh, (3497), 433sh (3506)	554, 579sh	31.5 (0.15)	0.22	0.073 (0.011)	30.2
[PtL^{26}Cl]	320 (13490), 378 (3540), 413 sh (3430), 436 (3730), 504* (70)	548, 580	24.1 (0.40)	0.28	0.31 (0.006)	11.2
[PtL^{29}Cl][c]	310 (224010), 368 (24960), 401 (19200), 464* (330), 475* (310)	481, 515, 553, 639ex	5.3 (0.37)	3.2	0.81 (0.05)	10.4

[PtL^{30}Cl][c]	284 (27900), 348 (4690), 400 (11400), 503* (200)	518, 548, 756ex	4.1	3.0	0.37 (0.087)	
[PtL^{1}Br]	334 (7180), 380 (9720), 401 (8120), 453* (210), 485* (180)	491, 524, 562, 691ex	9.9 (0.67)	6.9	0.61 (0.072)	6.3
[PtL^{1}I]	336 (4340), 385 (7130), 404 (6050), 487* (160)	491, 524, 562, 702ex	8.4 (0.46)	6.1	0.57 (0.047)	9.3
[PtL^{2}CN]	259, 285, 310, 319, 334, 350, 433*, 463*	468, 499, 527, 643ex	8.5 (1.5)[d]	------[f]	0.66 (0.19)	2.5[e]
[PtL^{15}CN]	263 (14300), 303 (5900), 315sh (4210), 338sh (2890), 355, (3700) 440* (70)	457, 488, 513, 599ex	8.0 (0.58)	2.3	0.61 (0.17)	7.3
[PtL^{17}CN]	289, 319, 337sh, 355, 381, 440*	450, 477, 511, 569ex	4.5 (0.17)[d]	------[f]	0.41 (0.05)	25.8[e]

[a]Lifetime at infinite dilution, [b]Photophysical data taken from reference 1, [c]Complexes prepared by previous group members, but data included for comparison, [d]lifetime recorded for a dilute solution (absorbance < 0.05), [e]$k_Q(O_2)$ values calculated using lifetimes measured for dilute solution (rather than τ_0), [f]low solubility of the complex prevented determination of these values, [g]These values could not be determined as the complexes were only weakly emissive, and their emission decay could not be detected, *Forbidden S → T absorption bands, sh = shoulder, ex = excimer, and br = broad.

CHAPTER FOUR:

Cation Sensor Complexes

4.1 Introduction

The excited state energies of luminescent Pt complexes are often sensitive to local environment. Various groups have tried to take advantage of this sensitivity, by linking a luminescent complex to a group that is susceptible to binding a particular analyte. For example, luminescent Pt(II) complexes have been appended with crown ether and azacrown groups, which selectively bind certain cations.[1,2,3] Binding of a cation perturbs the electronic environment within the molecule, affecting the environment around the Pt(II) centre and causing a change in the absorption and/or emission. The crown ether units themselves are non-emissive, and it is therefore difficult to detect cation binding without linkage to a spectroscopically active group (here, the Pt(II) complex).

The group of J-L. Fillaut and V. Guerchais, Rennes, have been studying the ion selectivity of 3-hydroxyl/ethynyl flavone-appended metal complexes. Cornard et al. had previously demonstrated that free hydroxyflavones selectively bind to cations (in particular, Pb^{2+}), and this binding could be followed by monitoring the absorption spectrum.[4,5] Fillaut et al. initially thought that, by incorporating a 3-hydroxyflavone into the ligand structure of a luminescent metal complex, the absorbance and emission would shift into the visible region of the spectrum (and out of the UV-region where many organic species absorb and emit), aiding the sensitivity of detection.

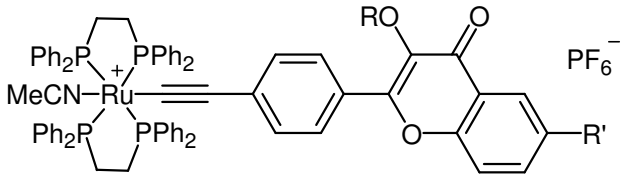

	R	R'
1a	H	H
1b	H	OH
1c	CH_3	H

Figure 1: Molecular structures of flavanol-based Ru complexes, **1a** – **1c**.

In 2008, the group reported a series of flavanol-based alkynyl ruthenium complexes (Figure 1).[6] The anion binding properties reported focus on complex **1a**. Acetonitrile solutions of this complex absorb and emit in the visible region (λ_{em} = 565 nm), and the emissive state has a lifetime of 2.1 ns, under both degassed and aerated conditions. This very short lifetime suggests that the emission is fluorescence, which emanates from a flavanol-based singlet state. This is despite the presence of the heavy metal – many

ruthenium coordination complexes emit via phosphorescence. This implies that in the excited state, the flavanol unit is effectively decoupled from the metal centre. The ion binding capability of this complex was tested with a selection of metal perchlorate salts (Li^+, Na^+, Ba^{2+}, Ca^{2+}, Cd^{2+}, Mg^{2+}, Co^{2+}, Cr^{2+}, Ni^{2+}, Zn^{2+} and Pb^{2+}) in acetonitrile. Absorbance and emission titrations were performed with each cation – addition of Na^+, Ba^{2+}, Ca^{2+}, Mg^{2+}, Co^{2+} and Cr^{2+} did not cause any significant changes in the photophysical spectra. In contrast, addition of Pb^{2+} resulted in a large red-shift in both absorbance and emission (Figure 2), which was accompanied by a decrease in quantum yield.

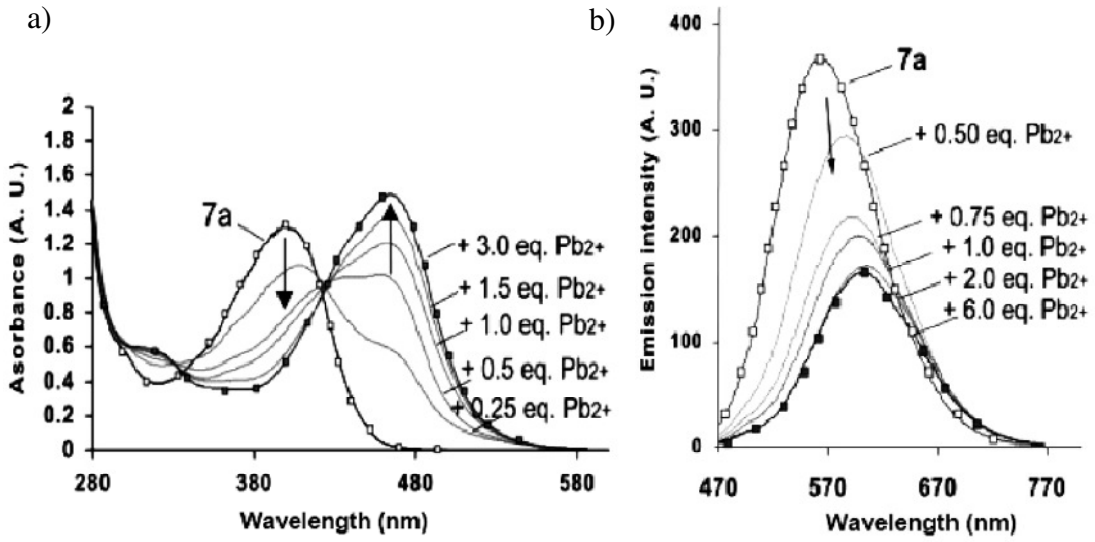

Figure 2: Changes in a) the absorption and b) the fluorescence spectra of **1a** (5 x 10^{-5} M), in air-equilibrated CH_3CN upon addition of Pb^{2+} cations in the form of their perchlorate salt (1 x 10^{-2} M). Taken from reference 6.

These ion-binding studies led to the conclusion that this sensor bound to Pb^{2+} with a 1:1 stoichiometry. The studies revealed that Ni^{2+} and Zn^{2+} cations also affected the fluorescence of the sensor, indicating a binding interaction. However, the fluorescence response was different to that observed upon binding to Pb^{2+}. Addition of Ni^{2+} quenched the emission without causing any shift. Addition of a small amount of Zn^{2+} caused an initial decrease in intensity, but as the amount of Zn^{2+} was increased, an additional shoulder appeared at higher energy. The effects that these two cations have on emission are not as pronounced as the effect caused by Pb^{2+}, and higher concentrations are required. Based on these results and previous studies by Roshall et al.,[7,8] it was concluded that binding of Pb^{2+}, Ni^{2+} and Zn^{2+} to the sensor involved formation of a chelating complex, in which the carbonyl and 3-hydroxy oxygen atoms participate.

In the same year,[9] the group published results for other flavanol-based cation sensors. These sensors involved a luminescent Pt(II) complex bound to a flavone unit via an ethynyl linker (see Figure 3 for structures). The sensors were charge-neutral, and contained bulky tert-butyl groups, which sterically inhibit undesirable intermolecular interactions. All complexes were highly emissive (λ_{max} 565-570 nm, CH_3CN, 298 K), and the emissive states were found to have relatively long lifetimes (12 – 20 μs) compared to related Pt C^N^N complexes that do not contain flavanoid substituents (e.g. for [Pt(^{t}Bu$_2$-phbpy)(-C≡C-Ph)], τ = 0.8 μs[10]). The emission was assigned to a ^{3}IL state, associated with the appended flavones perturbed by the Pt centre.

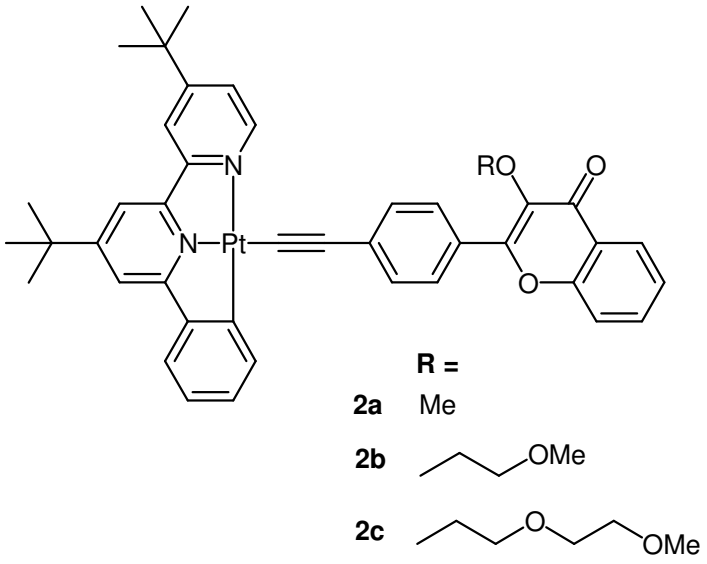

Figure 3: Molecular structures of Pt complexes **2a**-**2c**, which contain a flavones-based alkyne ligand

Complex **2b** was found to have a high selectivity for Pb^{2+} binding. The photophysical properties of this complex were highly perturbed upon addition of Pb^{2+}, but remained practically unaltered in the presence of all other cations tested (Figure 4). For example, with increasing Pb^{2+} concentration, the emission band at 565 nm decreased in intensity, and a new band at around 450 nm grew in intensity.

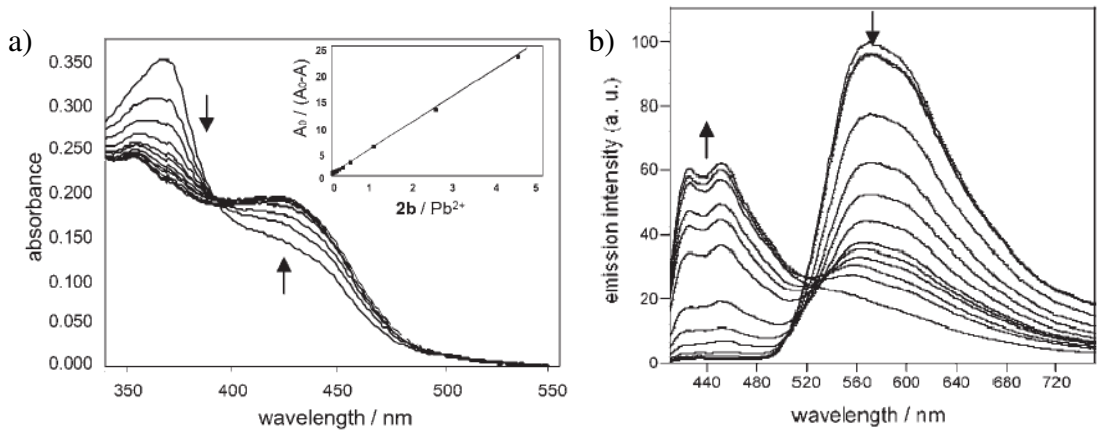

Figure 4: a) Changes in the absorption spectra of **2b** (10^{-5} M), in CH_3CN upon addition of $Pb(ClO_4)_2$. The inset shows the plot of $A_0/(A_0 - A)$ against [2b]/[Pb^{2+}]. b) The emission spectra of 2b (10^{-5} M), in CH_3CN upon addition of $Pb(ClO_4)_2$ (λ_{ex} = 393 nm). Images taken from reference 9.

From the dramatic changes observed in the photophysics, it could be concluded that binding of Pb^{2+} causes a profound alteration in the excited state properties of the molecule. Further evidence as to how Pb^{2+} affected the excited state came from a closer examination of the distinct emission bands. It was found that the profile of the higher energy band, and the lifetime associated with it (1.7 ns, λ_{em} = 450 nm) were similar to those of the free flavone acetylide unit. Also, upon addition of Pb^{2+}, the lifetime monitored at λ_{em} = 570 nm is much shorter (~ 700 ns) than in the absence of Pb^{2+}, and is of a similar magnitude to related N^N^C Pt(II) complexes that do not contain a flavone substituent. These effects have been rationalised as follows: upon binding to Pb^{2+}, the highest occupied flavone-localised orbitals decrease in energy, breaking the partial conjugation with the Pt(II) centre that was initially responsible for the formation of the flavone triplet excited state. Effectively, interaction between the flavone-unit and Pt(C^N^N)(-C≡C) unit is lost, and the new band around 450 nm corresponds to fluorescence from the ^{1}IL state of the flavone. Furthermore, the origin of the band around 570 nm switches from a ^{3}IL state associated with the appended flavone perturbed by the Pt centre, to a ^{3}MLCT state associated with Pt unit, as the flavone orbitals become decoupled from those of the Pt(C^N^N)(-C≡C) moiety upon the addition of Pb^{2+}.

It was speculated that sensor **2b** binds to Pb^{2+} in the manner shown in Figure 5. The binding interaction involves the ketone oxygen and the terminal oxygen. The oxygen in the 3-position of the flavones is not involved in binding (complex **2a** displayed no affinity for any of the cations tested, providing further evidence for this). Furthermore, increasing the length of the polyether arm led to a loss of selectivity: complex **2c** was found to bind to a greater selection of cations.

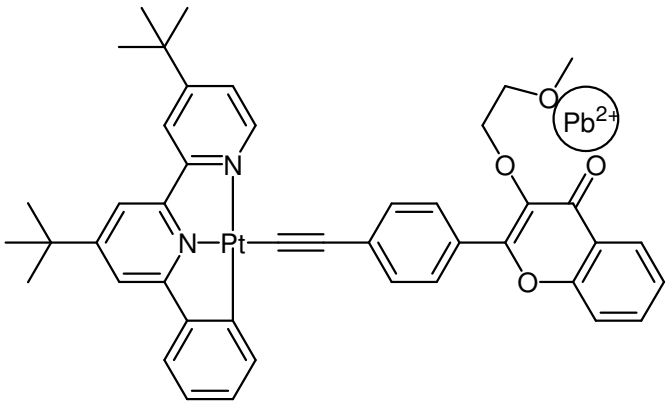

Figure 5: Postulated binding mode of complex **2b** with Pb^{2+}.

The interaction between the complex and lead binding domain is quite remote – it was believed that the sensory properties could be improved if the two regions were directly linked (i.e. if the flavone was directly attached to the terdentate ligand). Based on this rationale, two new complexes have been prepared in collaboration with the group of Fillaut and Guerchais (structures shown in Figure 6). Our group specialises in the preparation of luminescent Pt(II) complexes involving N^C^N ligands. Such complexes often have superior photophysical properties compared to related N^N^C systems, as discussed in Chapter 1.

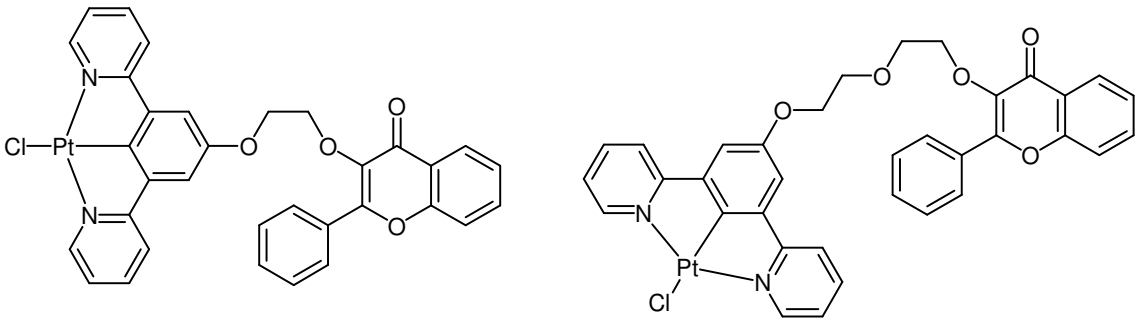

[$PtL^{25}Cl$] [$PtL^{26}Cl$]

Figure 6: The two new complexes prepared to be tested as cation sensors.

4.2 Synthesis

4.2.1 Synthesis of Ligands HL^{24} – HL^{26}

The synthesis of these ligands could be envisaged by O-alkylation of 3,5-dipyridylphenol (HL^{24}). However, the yield of this compound from the Stille reaction of 3,5-dibromophenol with 2-tri-n-butylstannylpyridine was only 15%. We therefore adopted the alternative strategy of O-alkylation prior to Stille coupling (see Scheme 1). 3,5-Dibromophenol was alkylated with 1,2-dibromoethane using Williamson ether synthesis conditions (note, a 15-fold excess of 1,2-dibromoethane was used to minimise di-alkylation). In such alkylations, the presence of a carbonate base promotes generation of a highly reactive alkoxide ion in situ. The alkoxide attacks the alkylating group (usually a primary haloalkane) via an S_N2 process. This reaction is disfavoured in protic and apolar solvents (such solvents lower the availability of free nucleophile), so acetonitrile and DMF are commonly used. Both solvents were tested here – acetonitrile is the preferred solvent, as it is much easier to isolate products from it. The second step, connecting the flavanoid group, is also a Williamson ether synthesis – these reactions proceeded well and were generally high yielding.

Table 1: The synthesis of ligands HL^{24} – HL^{26}: the reactive precursors and the conditions employed.

Ligand	Precursors	Synthetic Procedure	Solvent	Catalyst System	Yield / %
HL^{24} 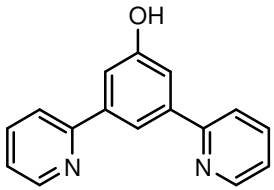	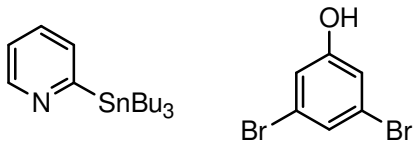	Stille	Toluene	$Pd(PPh_3)_2Cl_2$	15
HL^{25} 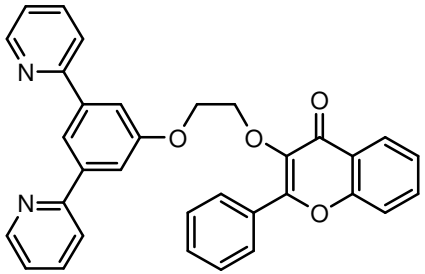	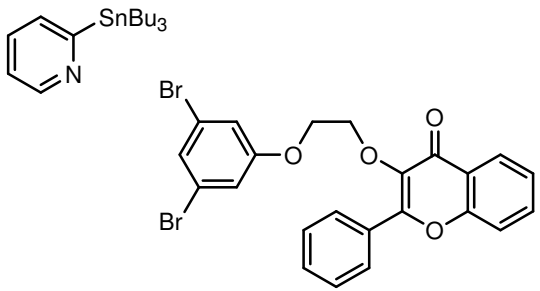	Stille	Toluene	$Pd(PPh_3)_2Cl_2$	29
HL^{2} 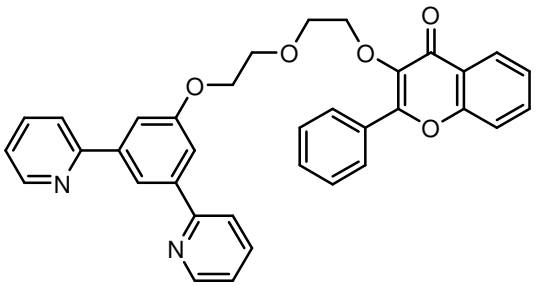	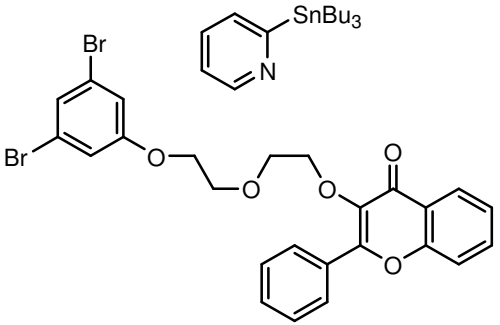	Stille	Toluene	$Pd(PPh_3)_2Cl_2$	29
		Stille	Xylene	$Pd(PPh_3)_2Cl_2 + PPh_3$	47

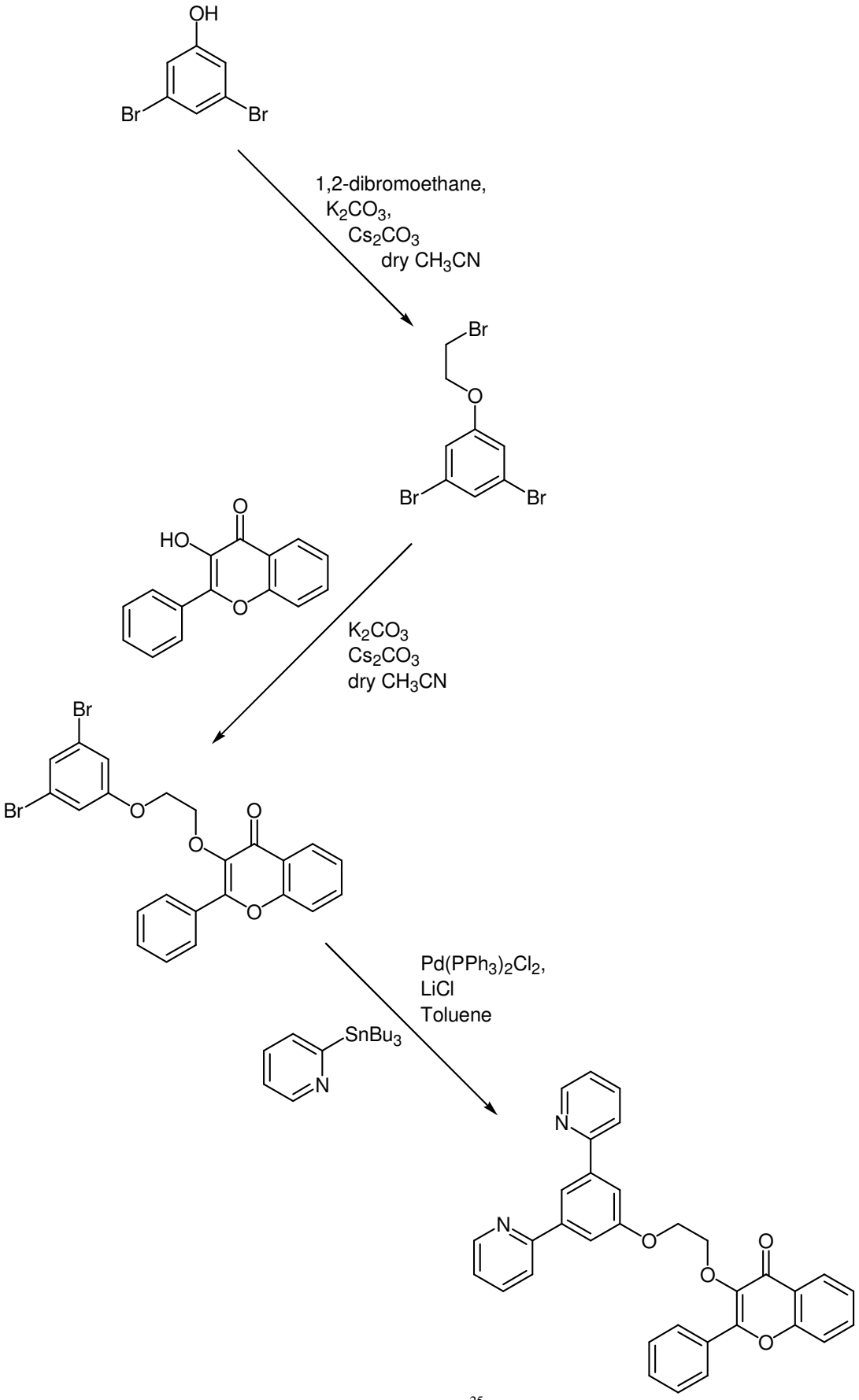

Scheme 1: Synthesis of flavanoid appended ligand, HL[25] (note: the same synthetic steps were taken to prepare HL[26], but step 1 was performed in Rennes by P-H. Lanoë).

4.2.2 Synthesis of complexes [PtL^{25}Cl] and [PtL^{26}Cl]

Complexation with Pt(II) was achieved by refluxing in acetic acid for 3 days. The respective complexes, [PtL^{25}Cl] and [PtL^{26}Cl] were obtained in moderate yield (35% and 53% respectively). Characterisation using ^{1}H NMR and MS (ASAP) confirmed that the complexation reactions had been successful (see Chapter 2, Section 2.4.2). Slow evaporation of solvent (MeOH/DCM 1:1) gave crystals of [PtL^{25}Cl] suitable for X-ray diffraction. The molecular structure confirms the expected connectivity – an ORTEP diagram is shown in Figure 7.

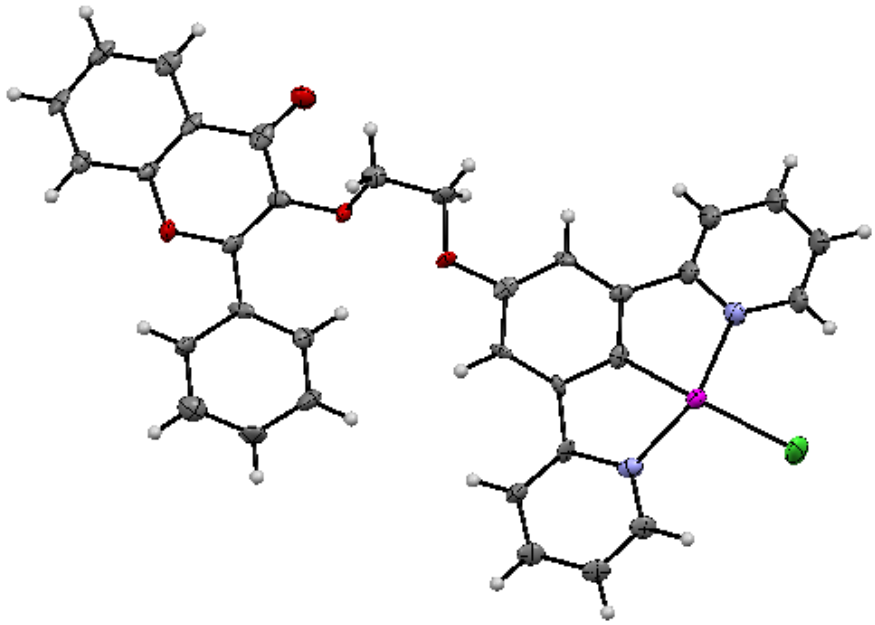

Figure 7: Molecular structure of [PtL^{25}Cl], with displacement ellipsoids set at the 50% level. Selected bond lengths (Å) and angles (deg): Pt-C 1.882(9), Pt-N 2.025(8) and 2.039(8), Pt-Cl 2.417(3), N-Pt-N 161.0(3), C-Pt-Cl 178.1(3).

As found for most of the [PtLCl] complexes (Chapter 2, Section 2.4.3.1), the [PtL^{25}Cl] molecules pack in one-dimensional chains, in which neighbouring molecules are aligned in a head-to-tail fashion. The mean plane of the flavone unit is approximately parallel to the plane of the Pt N^C^N unit.

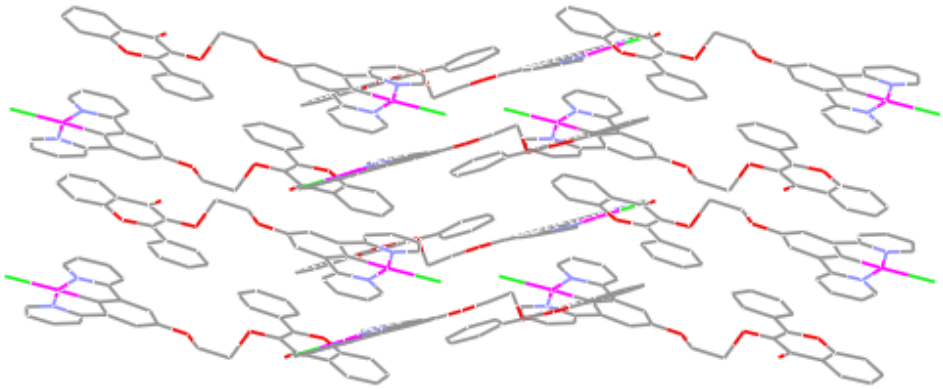

Figure 8: Packing of [PtL^{25}Cl], as viewed along the b-axis.

4.3 Photophysics

4.3.1 Absorbance

The absorption spectra of DCM solutions of these complexes contain very intense absorption bands between 230 and 320 nm, which can be assigned to ligand-based $^{1}\pi$-π^* transitions, and intense bands occurring between 350 – 450 nm that can be assigned to charge transfer transitions (see Figure 9 and Table 2). The lowest energy absorption maxima occur at lower energy than most other complexes prepared during the project, possibly due to transitions with significant intraligand charge-transfer character.[11]

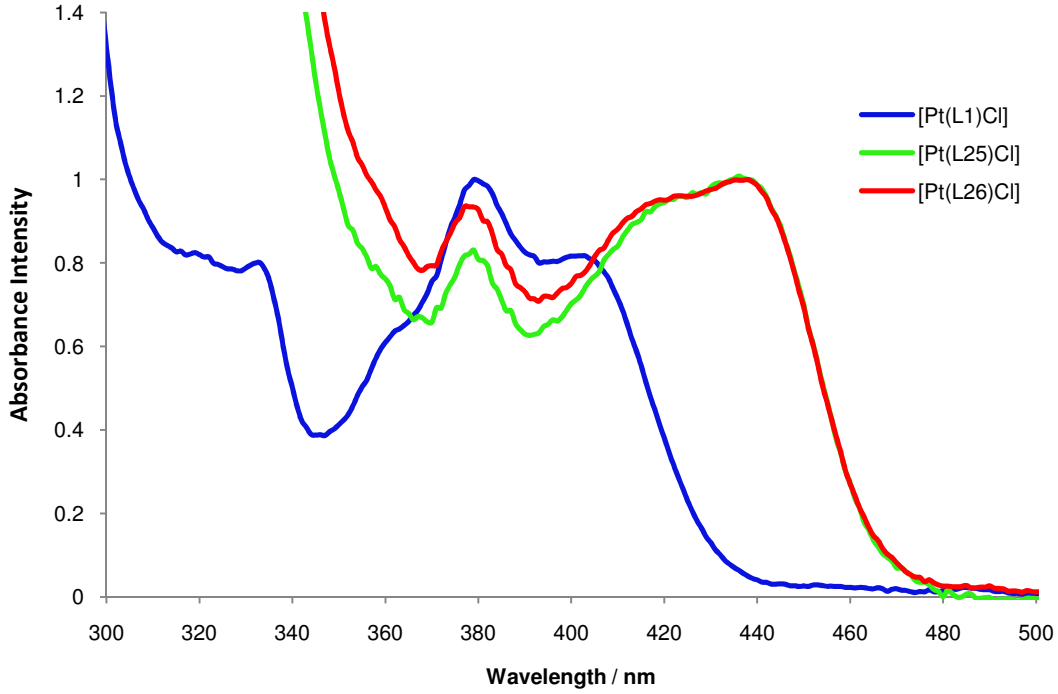

Figure 9: Normalised UV-vis absorption spectra of [PtL^{25}Cl] (green) and [PtL^{26}Cl] (red), with that of [PtL^{1}Cl] (blue) included for comparison (DCM, 298 K).

Table 2: Solution-based photophysical properties of [PtL^{25}Cl] and [PtL^{26}Cl] (DCM, 298 K), with that of [PtL^{1}Cl] included for comparison.

Complex	Absorbance λ_{max}/nm (ε / L mol^{-1}cm^{-1})	Emission λ_{max}/nm	τ_0 degassed (aerated)/μs[a]	Φ_{lum} degassed (aerated)
[PtL^{1}Cl][b]	332 (6510), 380 (8690), 401 (7010), 454* (270), 485* (240)	491, 524, 562	7.2	0.60 (0.039)
[PtL^{25}Cl]	375 (3328), 413sh, (3497), 433sh (3506)	554, 579sh	31.5 (0.15)	0.07 (0.01)
[PtL^{26}Cl]	320 (13490), 378 (3540), 413 sh (3430), 436 (3730), 504* (70)	548, 580	24.1 (0.40)	0.31 (0.006)

[a]Lifetime at infinite dilution, [b]Photophysical data taken from reference 12, *Forbidden S → T absorption bands

4.3.2 Emission

[PtL^{25}Cl] and [PtL^{26}Cl] emit at significantly lower energy than the majority of Pt(II) complexes prepared during the project {18050 cm^{-1} (554 nm) and 18250 cm^{-1} (548 nm) respectively}. Also, the emission profiles are broad and less structured (see Figure 10). The quantum yields are relatively low for Pt(II) complexes involving a 1,3-dipyridylbenzene ligand, and the lifetimes are extremely long. The longer lifetimes indicate a smaller metal contribution to the excited state. The emission behaviour is comparable to complex **2b**, prepared by the Rennes group, in the absence of cation. Perhaps the emission of [PtL^{25}Cl] and [PtL^{26}Cl] also emanates from a ^{3}IL state localised on the flavanol unit, that has been perturbed by the presence of the heavy platinum.

The complexes did not show excimeric emission under the concentration range studied (10^{-6} – 10^{-4} M). Their k_{sq} values are very low compared to most Pt(II) complexes prepared here, indicating that the lack of excimer emission probably stems from a lower tendency to undergo intermolecular interactions than from the excimers being particularly weak emitters here. The large flavanoid substituents probably hinder close contact of two molecules, which is necessary for excimer formation.

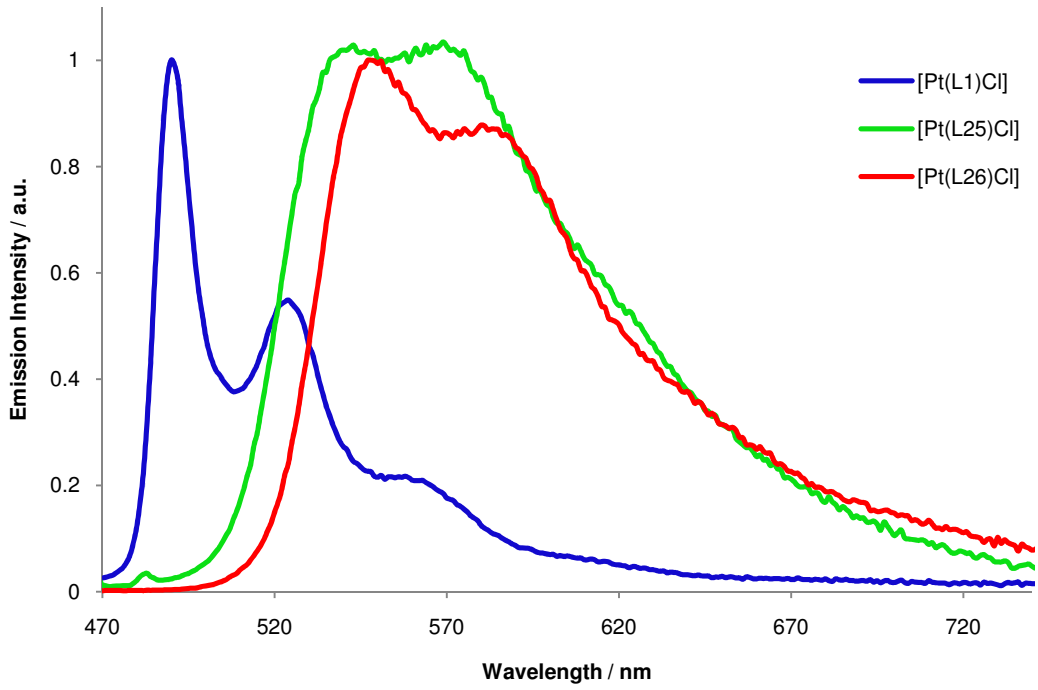

Figure 10: Normalised emission spectra of dilute samples of complexes [PtL^{25}Cl] (green), [PtL^{26}Cl] (red) with emission spectrum of [PtL^{1}Cl] (blue) included for reference (DCM at 298 K).

4.4 Preliminary Cation Binding Studies

The absorption and emission spectra of both complexes were monitored in the presence and absence of an excess of an array of cations. These experiments were performed in degassed acetonitrile, as both the complex and the metal salts were soluble in this solvent.

For both [PtL^{25}Cl] and [PtL^{26}Cl], the lowest energy absorbance band was found to blue-shift in the presence of cation (which was also visually apparent, as a "bleaching" of the yellow colour), but this effect was unselective to which cation was added. For a representative example, see Figure 11.

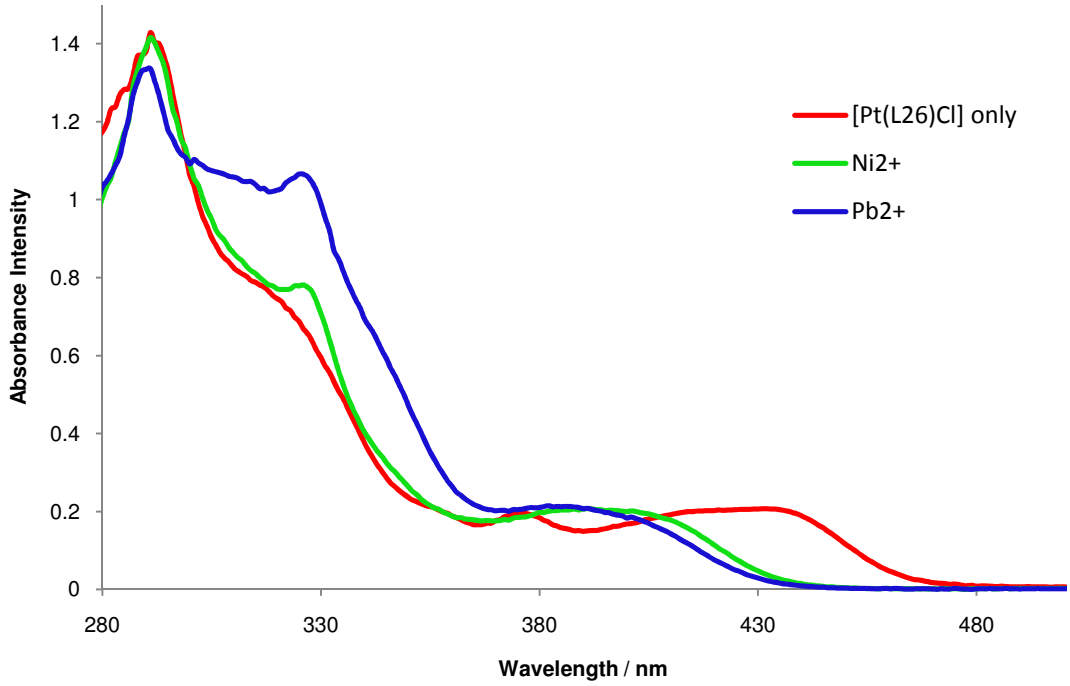

Figure 11: UV-vis absorption spectra of [PtL^{26}Cl] in the absence (red) and presence of certain cations {Ni^{2+} (green) and Pb^{2+} (blue)}. The spectra were recorded in CH_3CN at 298 K.

The emission of complex [PtL^{25}Cl] was affected by all cations tested (see Figure 12). All cations had a quenching effect, but this effect varied between cation. For example, the quenching caused by addition of Ba^{2+} and Mg^{2+} was accompanied by the appearance of a new band at lower energy (~ 610 nm), whereas Pb^{2+}, Zn^{2+} and Ca^{2+} just appeared to cause a similar reduction in intensity. The complicated emission responses observed with all cations tested therefore renders [PtL^{25}Cl] unsuitable as a sensor for specific cations.

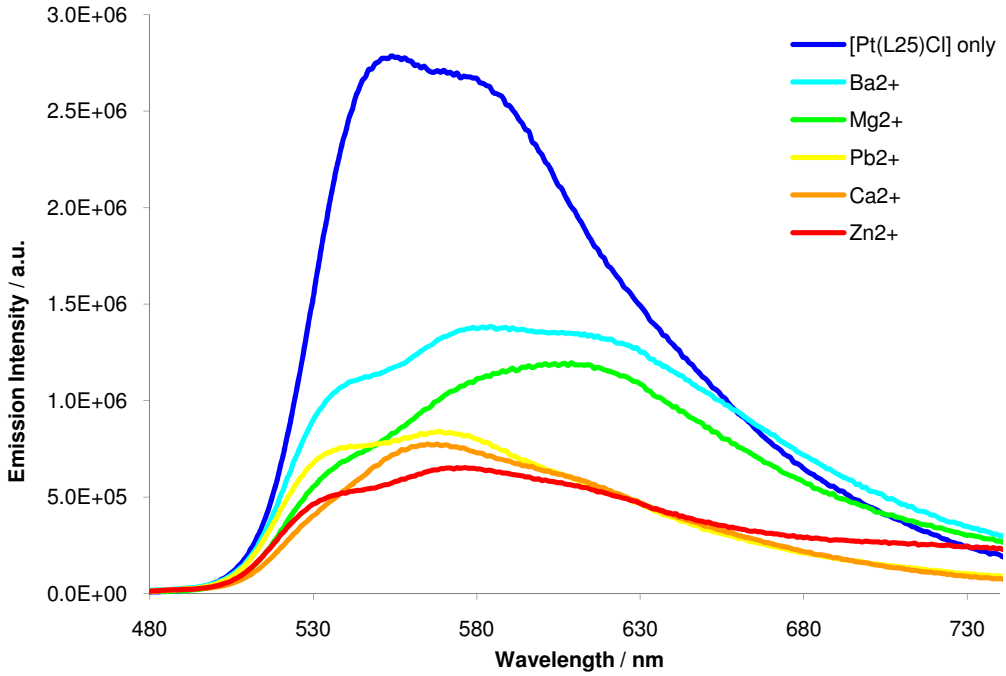

Figure 12: The emission spectra of [PtL^{25}Cl] (2 x 10^{-5} M) in CH_3CN, in the absence (dark blue) and presence of excess cations (see legend). The cations were added as their perchlorate salts. (λ_{ex} = 400 nm, 298 K).

The emission intensity of [PtL^{26}Cl] was also found to decrease in the presence of cation, and was accompanied by a switch of maximum peak intensity from the 0-0 vibrational band to the 0-1 vibrational band. This time however, the complex was more sensitive to Pb^{2+} cations – the emission was almost completely quenched in the presence of excess lead (see Figure 13).

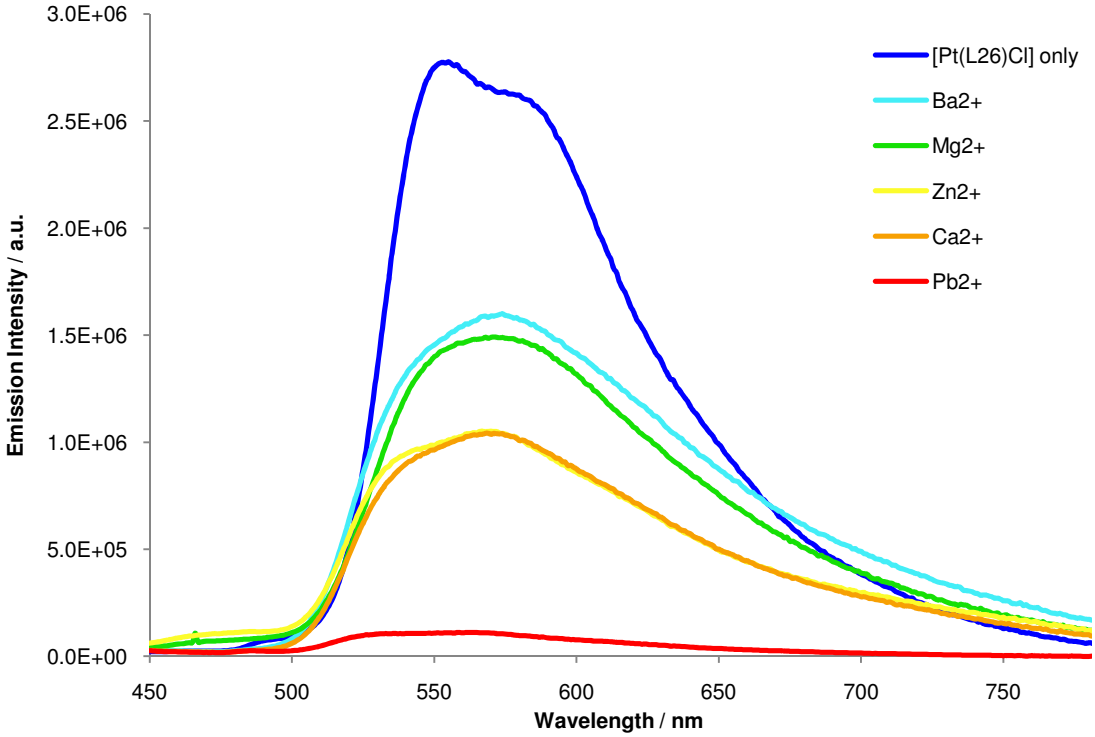

Figure 13: The emission spectra of [PtL^{26}Cl] (2 x 10^{-5} M) in CH_3CN, in the absence (dark blue) and presence of excess cation (see legend). The cations were added as their perchlorate salts. (λ_{ex} = 398 nm, 298 K).

4.5 Concluding Remarks

In summary, the photophysical properties of complex [PtL^{25}Cl] are perturbed by all cations, and selectivity is low. The poor selectivity of [PtL^{25}Cl] may be due to steric constraints present within the complex, preventing a binding site of suitable size from being created. [PtL^{26}Cl] contains an extra CH_2CH_2O unit in the diethyl ether bridging arm, so should contain fewer steric constraints. The absorbance spectrum of complex [PtL^{26}Cl] shows an unselective hypsochromic shift upon addition of all cations. Again, addition of all cations causes a decrease in intensity of emission, but with this complex, the effect seems most pronounced with Pb^{2+}, which almost quenches the emission entirely. [PtL^{26}Cl] therefore may have some application as a sensor for Pb^{2+} cations (perhaps at lower concentrations), but further work must be done (e.g. determination of binding constants) to say for sure. Regardless, [PtL^{26}Cl] will never be as effective as a Pb^{2+} sensor as complex **2b** previously prepared by the Rennes group, in which the absorbance and emission appear to respond solely to this cation.

4.6 References

1. Q-Z. Yang, L.Z. Wu, H. Zhang, B. Chen, Z-X Wu, L-P. Zhang and C-H. Tung, *Inorg. Chem.*, 2004, **43**, 5195-5197

2. V. W-W. Yam, R. P-L. Tang, K. M-C. Wong and K-K. Cheung, *Organometallics*, 2001, **20**¸4476 - 4482

3. P-H. Lanoë, H. Le Bozec, J. A. G. Williams, J-L. Fillaut and V. Guerchais, *Dalton Trans.*, 2010, **39**, 707-710

4. L. Dangleterre and J-P Cornard, *Polyhedron*, 2005, **24**, 1593 – 1598

5. J. P. Cornard and J. C. Merlin, *J. Molec. Struct.*, 2003, **651-653**, 381 – 387

6. J-L. Fillaut, J. Andriès, R. D. Marwaha, P-H. Lanoë, O. Lohio, L. Toupet and J. A. G. Williams, *J. Organometallic Chem.*, 2008, **693**¸228 – 234

7. A. D. Roshal, A. V. Grigorovich, A. O. Doroshenko, V. G. Pivovarenko and A. P. Demchenko, *J. Photochem. Photobiol. A: Chem.*, 1999, **127**, 89

8. A. D. Roshal, A. V. Grigorovich, A. O. Doroshenko, V. G. Pivovarenko and A. P. Demchenko, *J. Phys. Chem. A*, 1998, **102**, 5907

9. P-H. Lanoë, J-L. Fillaut, L. Toupet, J. A. G. Williams, H. Le Bozec and V. Guerchais, *Chem. Commun.*, 2008, 4333 – 4335

10. W. Lu, B-X. Mi, M. C. W. Chan, Z. Hui, C-M. Che, N. Zhu and S-T. Lee, *J. Am. Chem. Soc.*, 2004, **126**, 4958

11. D. L. Rochester, S. Develay, S. Záliš and J. A. G. Williams, *Dalton Trans.*, 2009, 1728-1741

12. J. A. G. Williams, A. Beeby, E. S. Davies, J. A. Weinstein and C. Wilson, *Inorg. Chem.*, 2003, **42**, 8609-8611

CHAPTER FIVE:

Application of Luminescent Organometallics as Bio-imaging Agents

5.1 Introduction

The living cell, often referred to as the building block of life, consists of a complex array of "machinery" (organelles), which carry out specific functions that are essential for life.[1,2] For example, the mitochondria are associated with respiration and providing the cell with energy in the form of ATP, and the nucleus, which contains most of the genetic material and a large selection of proteins, controls the activities of the cell by regulating gene expression. A basic representation of a eukaryotic cell is given in Figure 1.

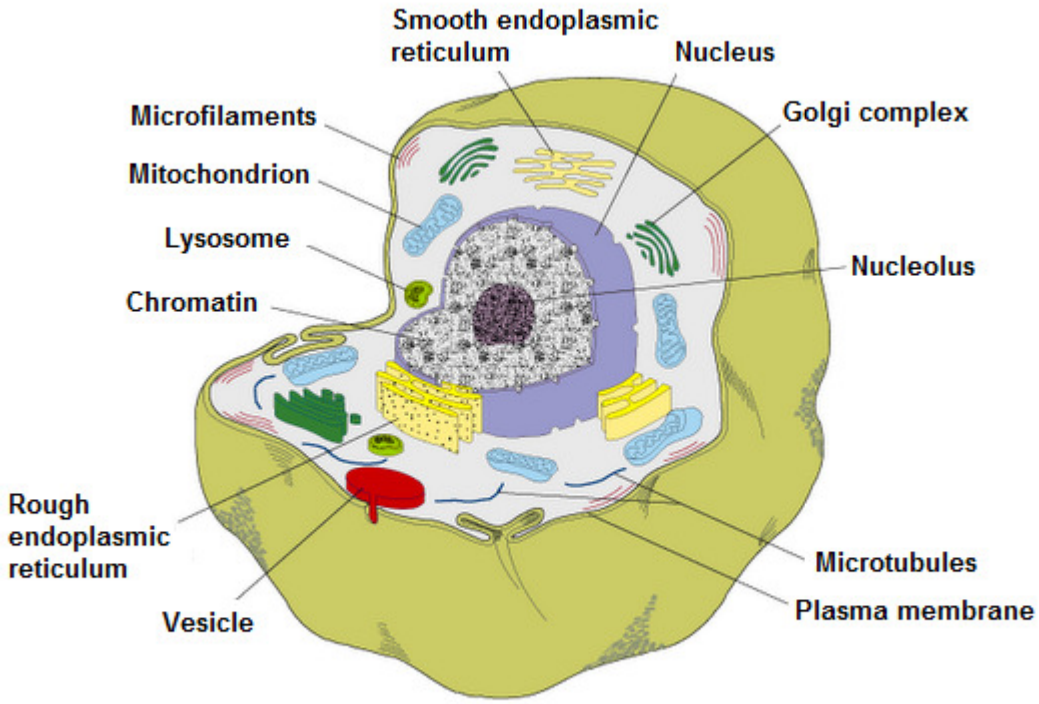

Figure 1: Diagram of a mammalian eukaryotic cell, taken from reference 3.

Through cellular imaging, it is possible to study biological function, via the study of cellular dynamics. Diseases often target certain organelles, causing changes in morphology for example. By following such changes it may be possible to get a deeper understanding of how such a disease functions, potentially leading to the development of a suitable treatment. Drugs often work by binding to target biomolecules. Following these binding events will lead to a greater understanding of the drug's action, allowing more effective drugs to be developed.

5.1.1 Fluorescence Microscopy

Microscopy is commonly used to observe the intracellular environment. The technique is direct and non-invasive, allowing cells to be observed in their natural state, without disruption of normal cellular function. A sub-set of this, fluorescence microscopy, is very popular with biochemists, as the technique is highly sensitive and can be used to observe specific sub-cellular components. The cells must normally be dosed with a luminescent stain prior to imaging; this stain should be of low toxicity.

Fluorescence microscopes typically consist of a light source, an excitation filter, a dichroic mirror, an emission filter and a detector – a schematic diagram is shown in Figure 2 for an inverted fluorescence microscope. The inverted part simply refers to the fact that emission is detected below the sample. The excitation filter, dichroic mirror and emission filter are chosen to match the photophysical properties of the luminescent stain. The dichroic mirror acts to separate the excitation and emission beams – each dichroic mirror has an associated transition wavelength value, and wavelengths below this value (i.e. the excitation beam) will be reflected, but wavelengths longer than this value (i.e. emission) will be transmitted. The filter sets help to tune the excitation and emission wavelengths – the emission filter acts as a second barrier to any high energy light that may have traversed the mirror, helping to improve the signal-to-noise ratio.

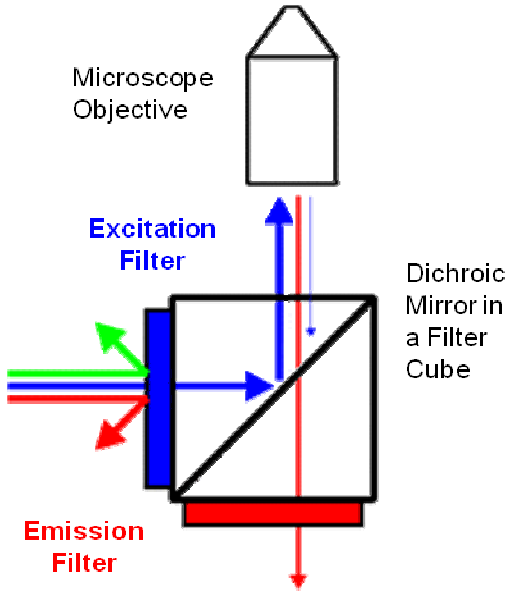

Figure 2: Schematic diagram of an inverted fluorescence microscope, showing how the filters and dichroic mirror function to allow only emitted light from the sample to reach the detector.[4]

With conventional wide-field fluorescence microscopy, the entire sample is illuminated at once. As a consequence, the whole sample is excited simultaneously (even lumophores outside the focal plane), and the detected fluorescence often includes a large unfocused background contribution. In comparison, confocal fluorescence microscopy offers greater resolution and the ability to create three-dimensional images.[5] This method utilises point-illumination, so that only a small section of the sample is illuminated at one time. To obtain the full image, the emission must be scanned over a regular raster, and the technique is often combined with scanning discs or moving mirrors. Because the technique focuses on a thin slice of the sample, confocal microscopy can be used to create 3D images.

5.1.2 Luminescent Labelling Agents

As discussed earlier, to apply fluorescence microscopy to imaging of the intracellular environment, cells must first be "marked" with a luminescent stain. Most commercially developed organelle stains are based on organic fluorophores, a selection of which are shown in Figure 3.[6,7,8,9,10] The majority incorporate structures of extended conjugation, which absorb UV-light and emit in the visible region. Cells are dosed with the bio-marker for a specified time length, during which, uptake (typically via diffusion) and site-specific localisation occurs.

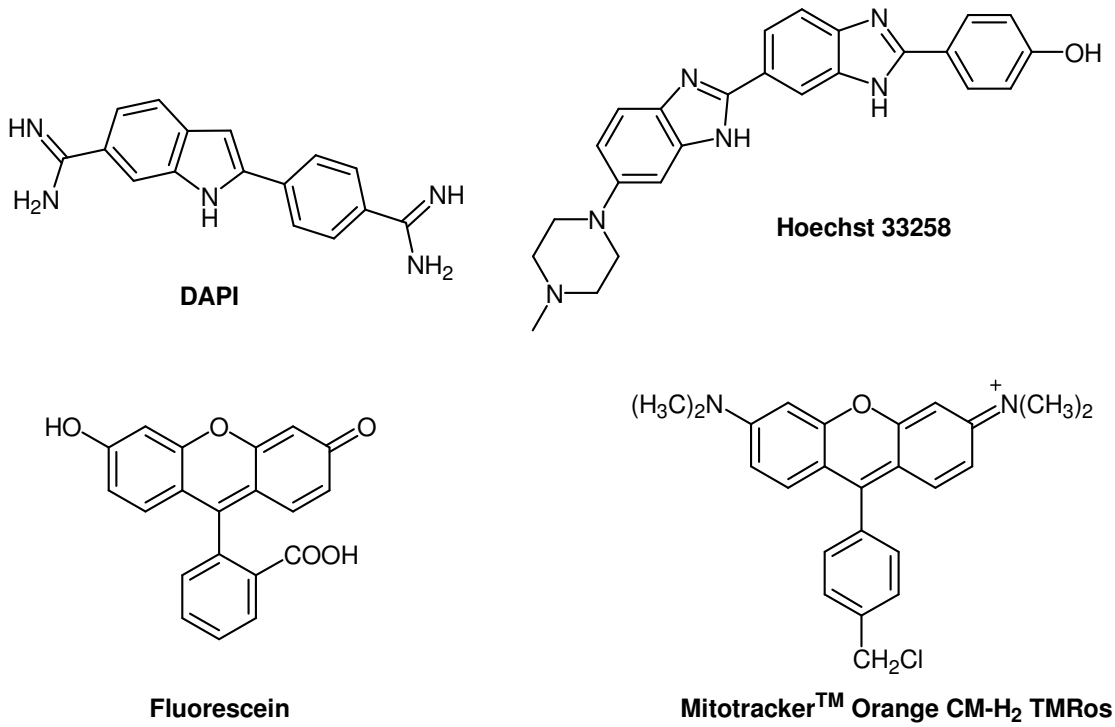

Figure 3: A selection of commercial fluorophores.

Such molecules can involve complicated syntheses and as a consequence can be expensive. Other downsides include photo bleaching with time and small Stokes' shifts: overlap of the excitation and emission bands can lead to difficulties in finding appropriately matched filter sets. It is therefore desirable to target new lumophores with more optimal characteristics.

Characteristics that should be considered during development of new lumophores include:

- Low cytotoxicity – it is no good if the lumophore causes cell death, or induces morphological changes within the cell
- Uptake – the lumophore should enter the cell without need for any chemical stimulated permeabilisation of the membrane, as this again may alter the natural behaviour. Low molecular weight, hydrophobic molecules are generally favoured.
- Localisation – the lumophore should target a specific intracellular location, or involve a structure that can be readily appended with a non-luminescent targeting group

- Stability – the lumophore should be stable in the imaging environment, and should display good photostability (i.e. should not degrade upon excitation with light).

Quantum dots (Qdots) have been employed in live cell fluorescence imaging.[11] These are emissive nanoparticles of semiconducting material, which behave differently from the bulk or individual molecules. For example, the emission energy of Qdots is easily tuned by variation of the particle size, morphology or its constituents. Typically, the smaller the particle size, the higher the emission energy - it is therefore easy to tailor the photophysical parameters to the desired application. Qdots typically possess high quantum yields, large Stokes' shifts, and narrow emission bands, and are inert to photobleaching.

Figure 4: Solutions of monodisperse CdSe nanocrystals with increasing diameter (2 to 7 nm) from left to right. (Image taken from reference 12).

Unfortunately, the inorganic components of Qdots (e.g. cadmium selenide) are highly toxic, so for live cell imaging purpose, the nanoparticles must first be coated with an inert shell. As a consequence Qdots suitable for bio-imaging can be expensive to produce. Also, in some cases, degradation of the protective coating has been observed, and the long term *in vivo* behaviour needs further study.[13] Qdots are unresponsive to their local environment, so must also be appended with biorecognition molecules that are capable of targeting desired biomolecules.[14]

Various lanthanide complexes have been developed as intracellular imaging agents.[15,16,17,18] A large amount of this work has been undertaken by the Parker group, who are also based in Durham. These complexes display several advantages over

standard organic fluorophores: 1) larger Stokes' shifts and narrow emission bands, 2) insensitivity to dissolved oxygen, 3) long emissive lifetimes (allowing time resolved spectral or microscopic acquisition) and 4) a good chemical stability profile.[15] Unfortunately, lanthanide ions are rather toxic, so sophisticated ligand systems are required, which completely encapsulate the ion. Secondly, direct excitation of the Ln^{3+} ion involves a parity (Laporte) forbidden transition, and is very inefficient ($\varepsilon \leq 1$ M^{-1} cm^{-1}).[16] Hence all lanthanide complexes require the incorporation of an antennae chromophore, further complicating the ligand architecture. The position and connectivity of this sensitizer group does allow the intracellular behaviour of the Ln^{3+} complexes to be varied.

Organometallic systems incorporating heavy metal ions and polypyridyl ligands and/or their cyclometallated analogues are often luminescent, and as exemplified in Chapter 1, such complexes are often exploited in OLEDs and luminescent sensors. Recently, a few groups have started to look at the applicability of these organometallic complexes in luminescence-based live-cell imaging, and the initial reports look very promising.[19,20,21,22,23,24] Such complexes often possess high quantum yields, large Stokes' shifts, and a stability towards photobleaching: all of which are desirable properties of potential bio-markers. Unlike traditional fluorophores, functionalisation of the polypyridyl ligand structure is relatively easy, allowing facile incorporation of groups that target specific intracellular locations/biomolecules. Modification of the structure of the polypyridyl backbone also allows greater control over the photophysical properties of a complex. Additionally, the organometallic complexes involving 2nd and 3rd row metals emit light via phosphorescence, a relatively long-lived process. Such complexes are thus suitable candidates for time-resolved emission imaging (Section 5.1.5). One possible flaw is that phosphorescent organometallic complexes are quenched by oxygen, which results in the formation of oxygen in its singlet state. Singlet oxygen is much more reactive than triplet oxygen, and is toxic to living cells.

During this project, the intracellular behaviour of Pt(II) complexes and some related Ir(III) complexes have been studied, hence literature examples of related complexes will take up the rest of this introduction. It should be appreciated, however, that other phosphorescent organometallic systems (e.g. ruthenium[23,25,26] and rhenium[24,27,28,29]) are also being investigated as probes for fluorescence cell imaging.

5.1.3 [Pt(trpy)R]$^{(+)}$ Complexes and their Interaction with Biomolecules

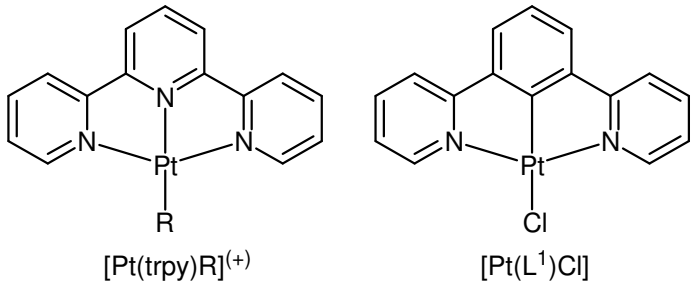

Figure 5: Structures of $[Pt(trpy)R]^{+}$ and $[PtL^{1}Cl]$.

There are many examples of $[Pt(trpy)R]^{(+)}$ complexes interacting with biomolecules in the literature.[30,31,32] Aside from the difference in charge, the structure of these complexes is very similar to the 1,3-dipyridyl benzene Pt(II) complexes prepared during the project, and it might be expected that the [Pt(dpyb)X] complexes may interact similarly with biomolecules. In particular, if X is displaced by, for example, a water molecule, then the charge increases to +1, resembling even more closely the trpy systems. It is therefore important to consider the literature reporting these interactions. Furthermore, knowledge of the results of such *in vitro* studies may be useful in interpreting the results obtained from intracellular studies.

Terpyridyl based Pt(II) complexes are well established as DNA intercalators.[30,32,33,34,35] The planar, extended aromatic structure of the trpy ligand inserts between the base pairs of DNA, and forms non-covalent intermolecular binding interactions with the DNA strand. These Pt complexes exhibit a preference for binding between G-C base pairs – the positively charged Pt(II) centre is stabilised via interaction with two guanine O6 atoms.[36] Intercalation results in modification of the physical properties of DNA (length, melt temperature, viscosity, etc.), and alters the UV-vis spectra of the complexes. Binding of the complexes to DNA also leads to induced circular dichroism.

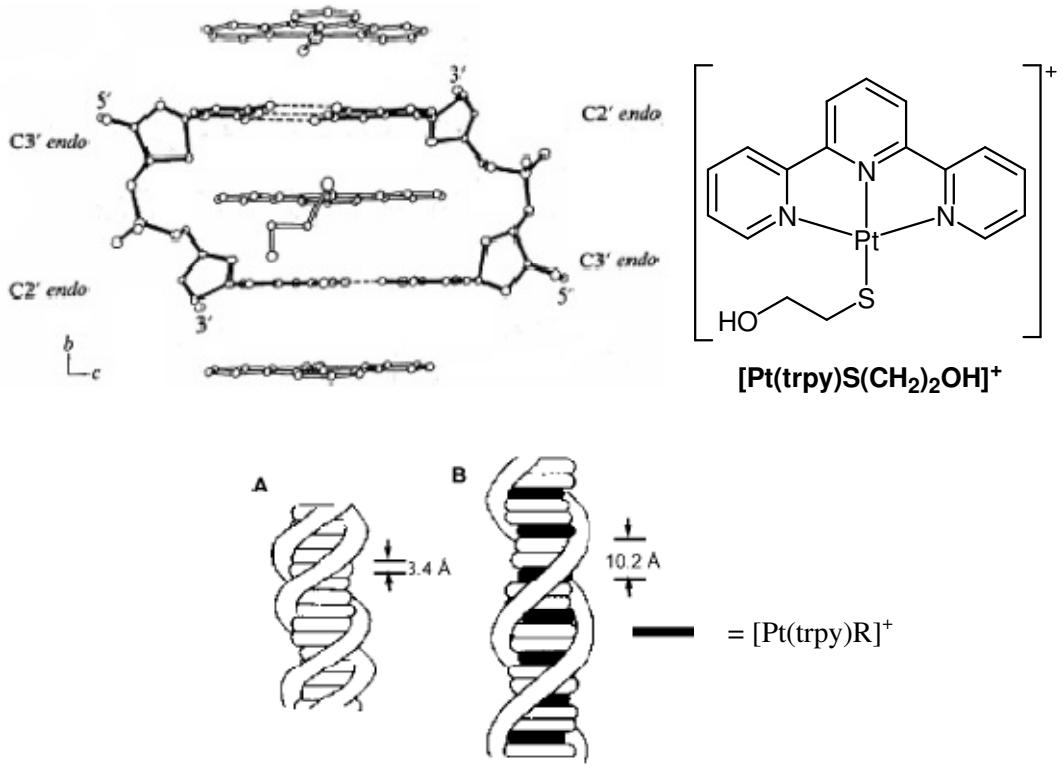

Figure 6: Top: X-ray crystal structure of deoxycytidinyl-(3′,5′)-deoxyguanosine:$[Pt(trpy)S(CH_2)_2OH]^+$ (2:2) looking down the a-axis, and Bottom: Schematic representation of a normal helix (left) and the neighbour exclusion binding (right) of an intercalator (shaded area) to a double stranded polynucleotide (demonstrating distortions to the DNA structure upon intercalation). Images sourced from reference 36.

In addition to intercalation, covalent binding to DNA has been observed for $[Pt(trpy)R]^+$ complexes containing labile Pt-ancillary bonds (i.e. Pt-Cl, Pt-O and Pt-N type bonds).[30,37] For example, $[Pt(trpy)Cl]^+$ and $[Pt(trpy)OH]^+$ bind to DNA via both intercalation and covalent binding. Modelling studies involving DNA-base adducts have revealed that covalent binding of complex with DNA (platination) occurs at the N^7 position of guanine.

$[Pt(trpy)R]^+$ complexes can also bind to other biomolecules, such as proteins.[38,39] Kostic et al. have screened the binding of $[Pt(trpy)Cl]^+$ with amino acids, and have found that it binds only to three chemical moieties present in certain amino acids.[38] These are the thiol of cysteine, the imidazole in histidine and the guanidine unit of arginine. Binding of complex to amino acids containing these groups was evident from the appearance of new bands in the UV-vis spectrum, the ^1H and ^{195}Pt NMR, and in the mass spectrum.

$[Pt(trpy)Cl]^+$ also binds to other sulphur-containing molecules, such as glutathione.[32] Glutathione is a tripeptide with antioxidant behaviour, that helps protect cells from reactive oxygen species such as free radicals and peroxides.[40,41] In some cases, it plays a role in detoxification of foreign species that may enter the cell, via direct conjugation

with the toxin.[42] Kinetic studies indicate that binding to thiol-containing biomolecules occurs approximately 300 times faster than binding to imidazole-containing molecules, suggesting a stronger interaction occurs between Pt(II) and sulphur than between Pt(II) and nitrogen.[38] This observation is easily rationalised – platinum(II) is a relatively soft centre and sulphur is a soft donor, whereas nitrogen is a hard donor.

5.1.4 Platinum in Cells

Since the discovery of the anti-cancer behaviour of cis-platin in 1965,[43] a vast amount of research has been conducted around the development of platinum-based drugs.[44,45,46,47,48] As a consequence, most cell-based studies involving Pt(II) complexes have focused around the anticancer activity of such species, and the development of phosphorescent platinum complexes as imaging agents is a relatively new area. Some groups have developed intracellular oxygen sensors based on luminescent platinum-porphyrin systems,[49,50] but so far, only two groups (ours and Lam et al.) have studied the applicability of luminescent Pt(II) complexes as bio-markers for intracellular components.

Platinum(II) complexes of the form [Pt(N^C^N)Cl], where N^C^N is a 1,3-di(2-pyridyl) benzene ligand, have recently been explored as intracellular imaging agents by our group.[19] These complexes rapidly enter the cell (within 5 minutes) and retain their emission. The cytotoxicity of the complexes in the three cell lines studied (human dermal fibroblast (HDF), melanoma C8161 and Chinese hamster ovary (CHO)) was relatively low, despite the complex being a moderately good sensitizer of singlet oxygen in aqueous media. This was accounted for by shielding of the complex by large hydrophobic biomolecules within the cell. Despite a structural similarity to anticancer drugs such as cis-platin (i.e. a labile Pt-Cl bond), the complex did not appear to be more toxic to the cancerous melanoma cells.

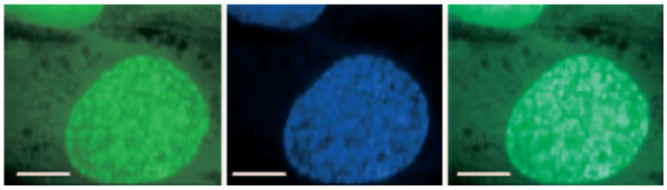

Figure 7: Determination of the intracellular localisation of [PtL^{1}Cl] by co-staining experiments.[19] CHO-K1 cells were incubated with [PtL^{1}Cl] (100 µM) and DAPI (300 nM) for 5 min, then fixed using 4% (wt/vol) paraformaldehyde. Samples were mounted for epifluorescence microscopy and visualised by using a magnification x 100 oil-immersion objective lense. Left: [PtL^{1}Cl] localisation was identified by using the FITC channel (λ_{ex} = 485 nm; λ_{em} = 520 nm), Middle: DAPI was used to identify nuclei (λ_{ex} = 400 nm; λ_{em} = 460 nm) and Right: Superimposed [PtL^{1}Cl] and DAPI images (Scale bar: 5 µm).

Confocal fluorescence microscopy and co-staining studies with DAPI indicate localisation of the platinum complexes in the nucleus, and optimum emission is observed from nucleoli. These platinum complexes were found to display readily detectable emission upon two-photon excitation in the near-infrared region. The application of two-photon excitation to bio-imaging has several advantages. Prolonged exposure to high energy UV radiation can damage cells (phototoxicity), or lead to photobleaching of the label, so the ability to excite the luminescent label with lower energy radiation is much preferred. Secondly, the relatively inert infra-red radiation can penetrate deeper into biological material than UV-radiation, meaning two-photon emission microscopy can be used to image tissues as well as isolated cells.

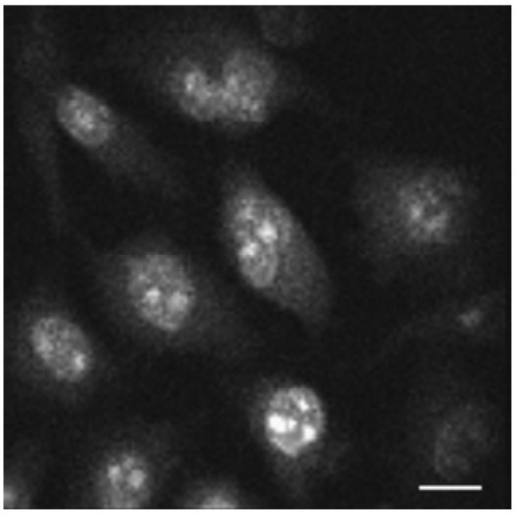

Figure 8: A two-photon excitation high-resolution emission image of live CHO cells incubated with [PtL^{1}Cl] obtained under 758 nm, 180 fs excitation (Scale bar: 10 µM). Image taken from reference 19.

The group of Lam et al. have recently published several reports involving [Pt(N^N^C)Cl] systems (N^N^C = a derivatised 2-phenyl-6-(pyrazol-3-yl)pyridine unit) as bio-imaging agents (see Figure 9).[20,51,52] Like the related N^C^N systems just discussed, these complexes possess two-photon induced luminescence properties, and images can be obtained after only a 5 minute incubation of the cells with complex. The unsubstituted parent complex, complex **A**, which contains a proton bound to the 1-pyrazolyl position, emits from within cells but does not appear to localise in any specific organelle.[20] On the contrary, **B**, which contains a triphenylphosphonium group linked via the 1-pyrazolyl position targeted the nucleus, and in particular the cell nucleoli.[51] Cytotoxicity studies revealed that this complex is a potent inhibitor of RNA synthesis. Isolation of nuclear components indicated that this complex did not bind to DNA or RNA, but bound to proteins, implying that the localisation in the nucleus is mediated by binding with nuclear proteins.

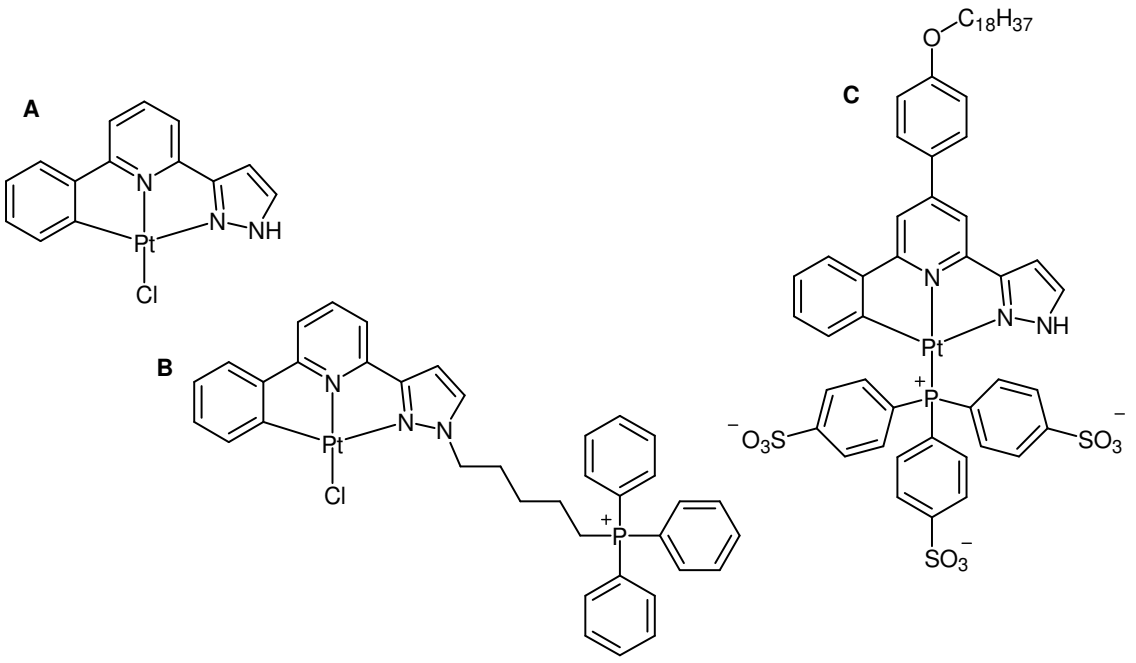

Figure 9: A selection of Pt(II) N^N^C complexes prepared by Lam et al., and investigated as intracellular imaging agents.

Rational structure modification of complex **A** gave complex **C**.[52] The incorporation of a hydrophobic C18 chain replacement of the ancillary chloride with a para-trisulfonated triphenylphosphine resulted in a water soluble complex with amphiphilic properties. This complex was rapidly taken up by cells and two-photon microscopy revealed that the complex targeted the cell membrane (Figure 10). Although the toxicity analysis indicated that this complex is not toxic at the dose and incubation length used to generate Figure 10, the cells look rather unhealthy (note the rather balled up appearance

of the cells, especially in Figure 10 d)). Perhaps the long chain present on the complex is having a destabilising effect on the membrane.

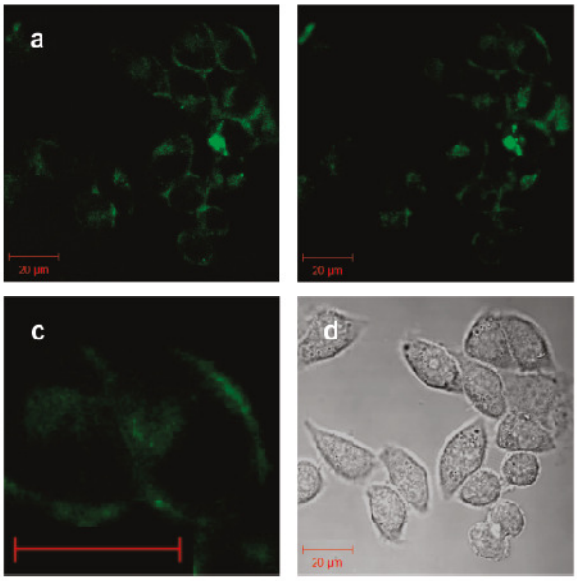

Figure 10: a) Linear confocal microscopy image (λ_{ex} = 400 nm) of HeLa cells after 30 min of exposure to complex **C** from Figure 9 (1 µg/mL in the culture medium). b) Two-photon (λ_{ex} = 720 nm, filter band-pass for λ_{em} = 500 – 550 nm) confocal microscopy image after 30 min of exposure to complex **C**. c) A 3.5x magnified duplicate of b. d) Bright field image of a and b (Scale bar: 20 µM). Images taken from reference 52.

5.1.5 Time-resolved emission imaging

The three fundamental emission parameters are wavelength, intensity and lifetime.[19] To date, most luminescent imaging has made use of spatial variation of emission intensity, or differences in wavelength. Intensity is often influenced by uptake efficiency and the local environment, and intensity based imaging generates mainly qualitative results. Secondly, many biomolecules are naturally fluorescent, and spontaneous emission can interfere with the images obtained. Additional factors such as scattering, reflection and natural fluorescence of the microscope objective and immersion oil can all add to this interference, further reducing the contrast of the image.[53] Recently, advances have been made into luminescent lifetime-based imaging. Unlike intensity, the lifetime of a luminophore is often independent of concentration, and can be calibrated absolutely. Temporal imaging therefore offers a more quantitative analysis, which is fully complementary to the more traditional luminescence microscopy techniques.

Most commercial bio-imaging agents are fluorescent, and therefore have lifetimes of the order of a few nanoseconds (0.5-20 ns). Fluorescence lifetime based imaging (FLIM) allows images to be created based on the lifetime of the bio-marker(s) – for example, intracellular areas can be discriminated if biomarkers with different fluorescent lifetimes are incorporated.[54] This is particularly useful if the spectral properties of the bio-markers are similar. In some cases, the lifetime of the marker is affected by the environment (i.e. changes in pH, oxygen concentration, etc.),[55,56,57] and FLIM can be used to probe the surroundings of the fluorophore. As FLIM is used to study such small changes in lifetime, subnanosecond light sources and fast detectors are required, which can prove quite costly and involve complicated set-up. Another disadvantage is that the inherent autofluorescence of naturally occurring biomolecules also occurs on the nanosecond timescale, and so can still cause interference in the image.

Time-resolved emission imaging microscopy (TREM), which makes use of longer lifetimes (hundreds of nanoseconds to milliseconds), potentially offers solutions to the problems faced by FLIM.[53] The technique does not need such fast excitation or detection methods (can be performed with nanosecond lasers and slower gated detectors), and autofluorescence can easily be removed from the images by application of a time gate (time-gated emission imaging).

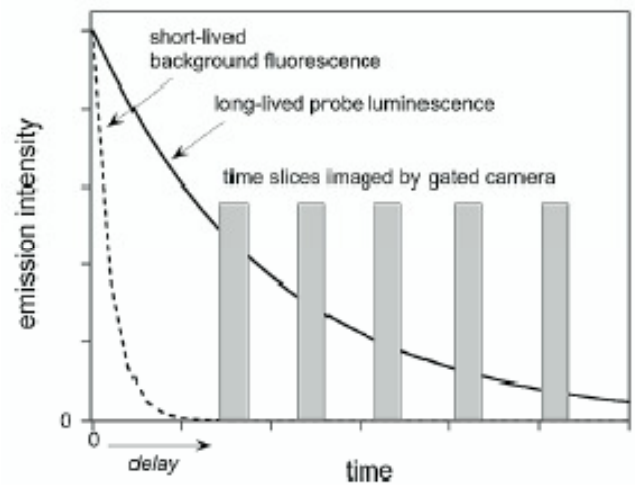

Figure 11: Diagrammatic illustration of the concept of time gating to eliminate short-lived background fluorescence, and of time slicing to monitor the temporal decay of emission and obtain quantitative data (image taken from reference 19).

A time-gated image simply requires a delay to be set between excitation and acquisition of the image. If the delay is long compared to the lifetime of autofluorescence (a few ns) but short compared to the lifetime of the lumophore (e.g. ~ of the order of 1 μs for

organometallic phosphors) then the gated image will be devoid of interference from autofluorescence. In the situation so described, a delay of 50 – 100 ns is ideal. The technique can be taken a step further if a series of delays are used with a finite gate time in each case (e.g. ~ 100 ns in the above example), during which the intensity is measured (see Figure 11). In this case, a plot of the emission for each time slice versus the delay time will yield the kinetics of decay of the luminophore. This can become powerful if the luminescence lifetime of the bio-marker is highly sensitive to the local environment or to binding with other species.

Development of TREM has been hindered by a lack of suitable phosphorescent luminophores, which are both cell permeable and of low toxicity.[19] Luminescent organometallic bio-markers may be ideally suited to TREM and time-gated imaging (e.g. long phosphorescent lifetime, high quantum yields, etc.). However, few have been investigated to date. Of these few cases, Haas et al. have used a time-resolved module to monitor the phosphorescence of Pt(II) porphyrin-based complexes from within strongly autofluorescent tissues and cells.[58,59] These Pt(II) complexes were linked to antibodies which target specific biomolecules. Application of a delay between removal of the excitation pulse and acquisition of the luminescent image allowed the phosphorescence of the bio-marker to be detected in the absence of autofluorescence, improving image contrast. Unfortunately, the Pt(II) porphyrin complexes are quite cytotoxic – they have long phosphorescent lifetimes (τ ~ 100 μs), which encourage sensitisation of singlet oxygen within the cell.

One can envisage that complexes displaying shorter phosphorescent lifetimes should display lower toxicity via O_2 sensitisation, and be more suitable as TREM agents. Pt(II) complexes of the form [Pt(L)Cl], where L = a 1,3-dipyridylbenzene system, typically exhibit lifetimes on the low microsecond timescale (τ ~ 5 μs). Such complexes have recently been investigated as TREM imaging agents by our group.[19] The quantitative kinetics of the emissive decay could easily be monitored in different cells and even within different regions within the same cell. From these studies, the lifetime of [PtL^1Cl] in the nucleus was determined (760 ± 100 ns).

The analytical power of time-gated imaging was demonstrated by using the technique to study cells that were co-labelled with fluorescein and [PtL^1Cl]. Fluorescein, with its emissive lifetime of 3.6 ns, labels living cells unanimously and provides a good model for autofluorescence. Images recorded immediately after the laser pulse were dominated

by fluorescein emission, and it was not possible to discriminate any intracellular regions. Images recorded after a 10 ns delay showed emission emanating from only [PtL^{1}Cl], which localises in the cell nuclei. The majority of the fluorescein emission had decayed during the delay.

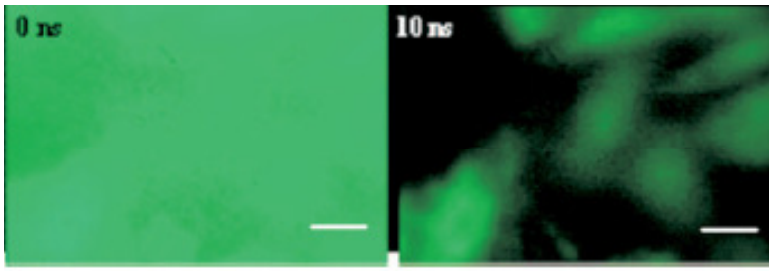

Figure 12: Time-gated cellular imaging: live CHO cells pre-incubated with [PtL^{1}Cl], imaged in the presence of a basic solution of fluorescein. The images were taken at 0 ns (Left) and at 10 ns (Right) delays after the 355 nm laser pulse (Scale bar: 10 μm, images taken from reference 19).

5.1.6 Iridium Complexes as Bio-imaging Agents

Iridium(III) complexes involving polypyridyl ligands or cyclometallated analogues are often highly luminescent. They typically possess large Stokes' shifts and phosphorescent lifetimes of the order of a few microseconds. Very recently, reports involving such complexes as bio-imaging agents for live cells have started to appear amongst the literature.[21,22,60,61,62] The first of these reports appeared in 2008, and involved two structurally related Ir(III) complexes, containing two 4,6-difluorophenyl pyridine ligands and a N^N ligand (Complexes **1** and **2**, see Figure 13).[22] In an aerated DMSO/PBS (pH 7, 49:1) solution at ambient temperature, complex **1** was found to emit at 530 nm, whereas complex **2** was found to emit at 643 nm (λ_{ex} 360 nm), and both complexes had quantum yields exceeding 3%. The lower emission energy of complex **2** was attributed to the higher level of conjugation in the N^N ligand. Cellular uptake of these complexes was found to be rapid – intense images were obtained after only 10 min incubation with a 20 μM solution. Emission was observed from the cytoplasmic region of the cells. Spectrum scan experiments revealed intracellular emission maxima of 512 nm and 617 nm for cells dosed with complexes **1** and **2** respectively, confirming that the emission corresponded to the Ir(III) complexes. Cytotoxicity studies indicated that the complexes were relatively non-toxic ($IC_{50} \leq 100$ μM), and photostability studies revealed that the complexes were significantly more stable to photobleaching than DAPI, a commercially available stain for cell nuclei.

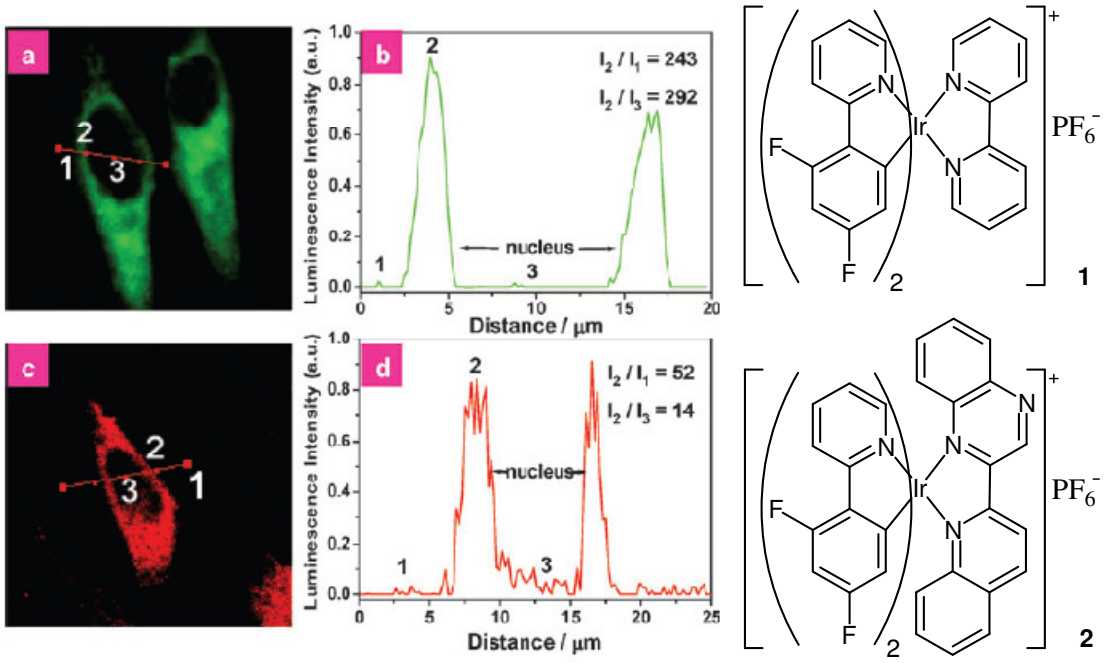

Figure 13: Confocal luminescence images (left) and luminescence intensity profile (right, recorded across the lines shown in a) and c)) of HeLa cells incubated with 20 µM of complex 1 (top) or 2 (bottom) in DMSO/PBS (pH 7, 1:49 v/v) for 10 min at 25 °C. The signal-to-noise ratios (I_2/I_1) and cytoplasm-to-nucleus ratios are also shown (λ_{ex} = 405 nm). Images and charts were taken from reference 22.

Related complexes, incorporating long alkyl chains on the N^N ligand were prepared by Lo et al. – these complexes were also found to localise in the cytoplasm.[62] Lo et al. believe that the complexes are interacting with hydrophobic organelles such as the endoplasmic reticulum, mitochondria and Golgi apparatus, however no co-staining studies were reported. Lengthening of the alkyl chain led to an increase in lipophilicity of the complex. The increase in lipophilicity was expected to correlate with increasing uptake and hence cytotoxicity, however this was not found to be the case. For example, the complex which contains the longest alkyl chain displayed the lowest cytotoxicity, despite being the most hydrophobic, and therefore most likely to cross the cell membrane. One possible suggestion for this was that the complex was so hydrophobic, that aggregation in the dosing solution reduced the tendency to enter cells. Internalisation was not observed for any complex when cells were dosed at 4 °C: at this temperature, energy-dependent processes are suppressed, and lack of uptake therefore indicates an activated uptake route.[63]

In 2009, Lo et al. investigated intracellular uptake of Ir(III) complexes containing biotin groups attached to the polypyridyl ligands.[60] These complexes were found to possess low cytotoxicity (IC_{50} > 400 µM), whereas the un-biotinylated analogue prepared for comparison was found to be much more potent (3.2 ± 0.4 µM). In this case, the lower

cytotoxicity of biotinylated complexes did correlate with a lower lipophilicity and lower uptake rate (biotin is a relatively polar group). Like all previous examples, these Ir(III) complexes were all found to localise in the cytoplasmic region of the cell. The biotinylated complexes gave a punctate emission pattern from discrete vesicles within the cytoplasm, whereas for the non-biotinylated complex, emission from these discrete vesicles was accompanied by a more diffuse emission from throughout the cytoplasm. Uptake studies indicate that these complexes enter the cell via two distinct mechanisms – an energy-independent diffusion-based uptake, and an energy-dependent endocytosis pathway.

5. 2 Aims

The unsubstituted parent complex, [PtL^1Cl], and related complexes containing 4'-phenyl substituents enter living cells and retain their emission. Through use of fluorescence and confocal microscopy, the complexes are found to localise in the cell nucleus, in particular the nucleoli. This localisation was confirmed by counterstaining experiments with a known nuclear-targeting fluorophore (DAPI). The rate of uptake was fast, as demonstrated by the very short dosage times required for imaging. Additionally, the long phosphorescent lifetimes emanating from the triplet emission of these platinum complexes makes them ideal candidates for time-gated and time-resolved imaging, relatively underexplored areas.

The aim of this section of the project was to study the new complexes prepared in living cells, and to explore whether different substituents in the ligands would influence the intracellular localisations etc. Other complexes prepared by previous group members were also screened, as were a selection of iridium complexes. Aside from luminescence microscopy, the uptake of complex was also examined via other techniques including flow cytometry, and time-resolved imaging was used to determine intracellular lifetime.

5.3. Pt(II) Complexes as Bio-Imaging Agents

5.3.1 Intracellular Localisation

Two cell lines were studied – Chinese hamster ovary (CHO) and mouse skin fibroblast (NIH 3T3). Both are adherent cell lines, meaning the cells grow attached to the surface of the culture dish. For imaging purposes, cells were grown in twelve-well plates, each well containing a cover-slip, which the cells attached to. The cells require certain nutrients and growth factors to survive, so are cultured in water-based solutions containing these supplements (growth medium). CHO cells were maintained in F-12 (Ham) medium, and NIH 3T3 cells were maintained in DMEM. In each case, the medium was supplemented with 10% (v/v) foetal bovine serum (FBS) and 1% penicillin and streptomycin.

Stock solutions of complex were made up in the media appropriate for the cell line being studied. Unfortunately, these Pt(II) complexes are insoluble in a purely aqueous environment, so were first dissolved in the minimum amount of DMSO, prior to dilution. At high exposure, DMSO is toxic to cells, but cells can tolerate a small amount. After full dilution, the total DMSO content never exceeded 6%. Cytotoxicity studies (Section 5.3.7) with water/DMSO controls indicated that DMSO was non-toxic at this level, for the duration of the experiments. Cells were dosed with several concentrations of complex (0-100 μM) for a selection of dosage times (5 min – 24 h), then studied via fluorescence microscopy using a G365 excitation filter and either a FITCex (450-500 nm) or FITCem (515-565 nm) emission filter. For each complex, the emission filter chosen was that which gave best overlap with the position of the 0-0 vibronic band, previously determined from solution-based emission experiments.

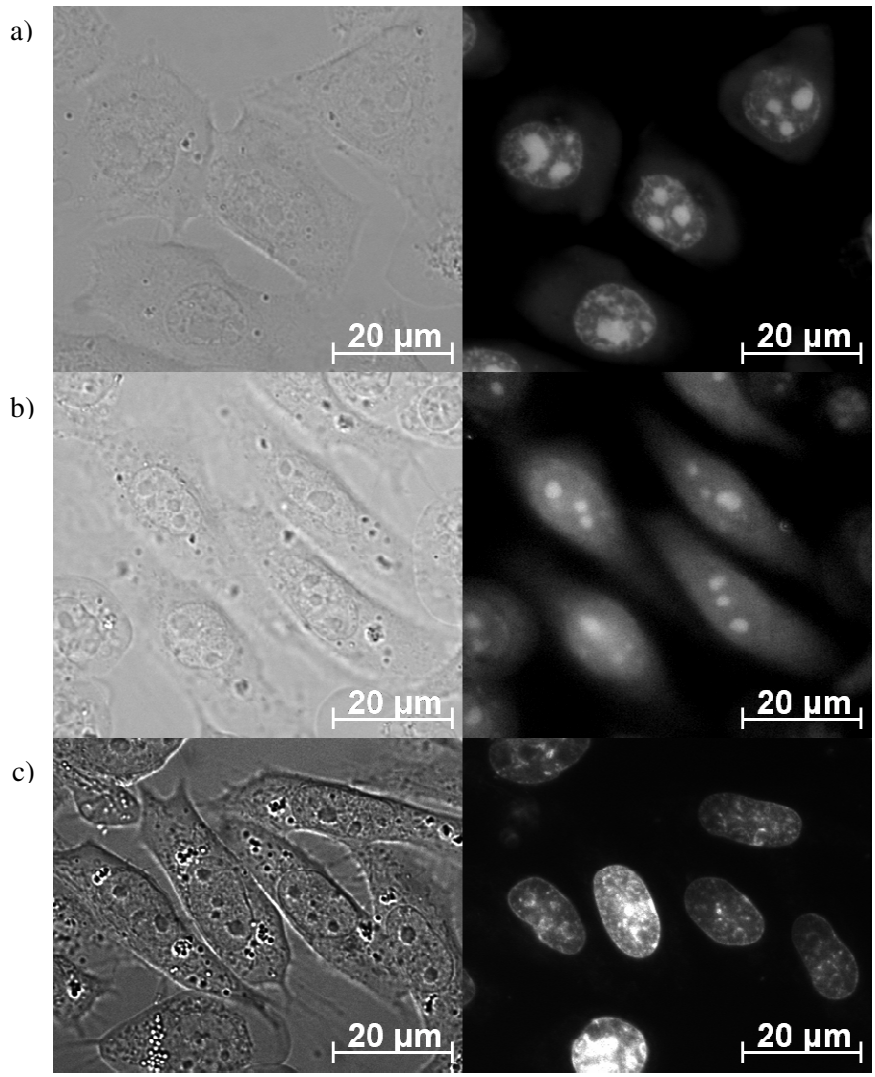

Figure 14: Bright field (left) and fluorescence microscopy images (right) of cells dosed with various species: a) NIH 3T3 cells dosed with [$PtL^{11}Cl$] (50µM, 5min, G365/FITCex), b) CHO cells dosed with [$PtL^{2}Cl$] (50 µM, 5 min, G365/FITCem), and c) CHO cells dosed with DAPI, a commercial nuclear stain (300 nM, 5 min, G365/TRICem).

After dosing with most complexes (Table 1), the cells appeared to glow under UV-irradiation. Fluorescence microscopy revealed that emission was occurring from distinct sub-cellular components, indicating that the complexes were localising in certain organelles. The localisation patterns of all of the emissive complexes were similar. Co-staining studies indicated that the complexes were localising in the nucleus of the cell (Figure 14). The most intense emission was observed from distinct spots within the nucleus, which correspond to the nucleoli. Williams et al. recently reported similar findings for intracellular studies on the unsubstituted parent complex, [$PtL^{1}Cl$], which also appears to localise in the nucleoli.

Table 1: List of complexes screened for intracellular emission, the most appropriate filter sets and whether or not emission was observed from the nucleus.

Complex	Filter Set (Ex^{n}/Em^{n})	Is Emission Observed from the Nucleus Upon Dosing with the Complex?	Complex	Filter Set (Ex^{n}/Em^{n})	Is Emission Observed from the Nucleus Upon Dosing with the Complex?
[PtL^{1}Cl]	G365/FITCem	Yes	**[PtL^{14}Cl]**	G365/FITCem	Yes
[PtL^{1}Br]	G365/FITCem	Yes	**[PtL^{15}Cl]**	G365/FITCex	Yes
[PtL^{1}I]	G365/FITCem	Yes	**[PtL^{16}Cl]**	G365/FITCex	Yes
[PtL^{1}py]$^{+}$	G365/FITCex	Yes	**[PtL^{22}Cl]**	G365/FITCem	Yes
[PtL^{2}Cl]	G365/FITCex	Yes	**[PtL^{23}]**	G365/FITCem	No
[PtL^{5}Cl]	G365/FITCem	Yes	**[PtL^{25}Cl]**	G365/FITCem	No
[PtL^{6}Cl]	G365/FITCem	Yes	**[PtL^{30}Cl]**	G365/FITCem	No
[PtL^{7}Cl]	G365/FITCem	Yes	**[PtL^{31}Cl]**	G365/FITCem	No
[PtL^{8}Cl]	G365/FITCem	Yes	**[PtL^{32}Cl]**	G365/FITCem	Yes[a]
[PtL^{9}Cl]	G365/FITCex	No	**[PtL^{33}Cl]**	G365/FITCem	Yes[a]
[PtL^{10}Cl]	G365/FITCex	Yes	**[PtL^{34}Cl]**	G365/TRICem	Yes[a]
[PtL^{11}Cl]	G365/FITCex	Yes	**[PtL^{35}Cl]**	G365/FITCem	Yes[a]
[PtL^{12}Cl]	G365/FITCem	Yes	**[PtL^{36}Cl]**	G365/FITCem	No
[PtL^{13}Cl]	G365/FITCem	No	**[PtL^{37}Cl]**	G365/FITCem	Yes[b]

[a]Weak/very weak emission observed, for all dosage concentrations (10 – 100 μM) and incubation lengths (5 min – 24 h) studied, [b]only certain cells labelled (Section 5.3.5).

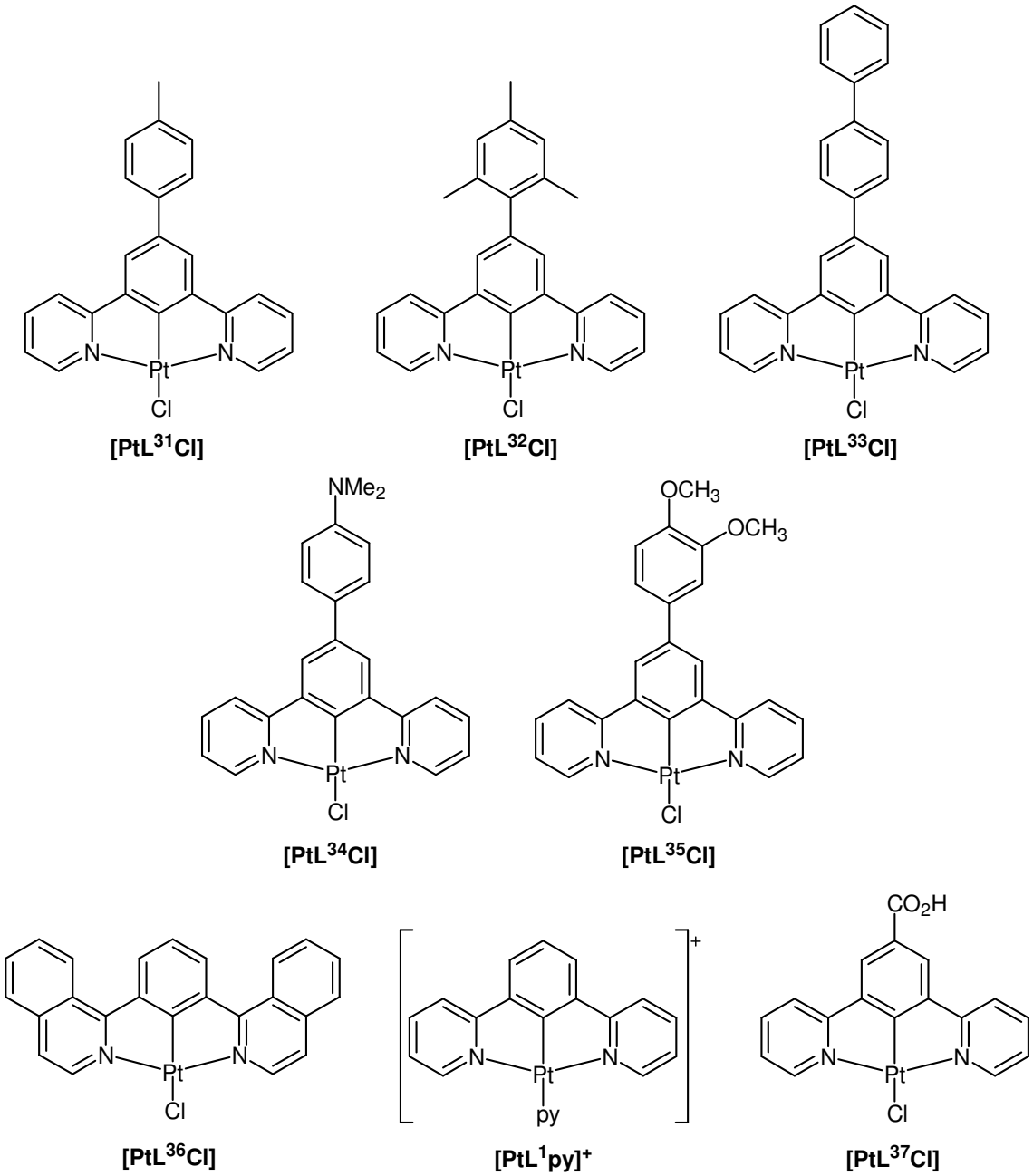

Figure 15: Structures of Pt(II) complexes not already discussed elsewhere.

It appears that the size of the terdentate ligand is maybe affecting the ability of a complex to enter the nucleus. Complexes containing terdentate ligands with extended aromatic structure either do not show emission from the nuclei ([PtL^{25}Cl], [PtL^{31}Cl] and [PtL^{36}Cl]), or are at best only weakly emissive ([PtL$^{32\text{-}35}$Cl]), implying that cell entry is inhibited by the extended structures of these complexes. Most of the complexes containing smaller substituents do exhibit nuclear emission ([PtL^{9}Cl] and [PtL^{13}Cl] are exceptions, see Section 5.3.4).

Dosing solutions of complex were made up in the respective cell media: these solutions were only weakly emissive, and glowed red under long wavelength UV-irradiation. The complexes are hydrophobic, and the red emission probably emanates from an aggregate species which forms in the aqueous environment (see Chapter 3, Section 3.4.3.7). Phosphorescent emission is quenched by oxygen, which accounts for the weakness of emission of the aerated solution. The switch-on of blue-green emission upon entering the nucleus suggests that the complex has become sufficiently shielded from oxygen. It is likely that the complex molecules undergo binding interactions with one (or several) of the biomolecules present in the nucleus – perhaps the biomolecule surrounds the complex, effectively shielding it from oxygen. Also, the blue-green emission is characteristic of monomer emission, suggesting that the molecules of complex do not interact with each other within the nucleus. The nucleus is an environment rich in DNA, RNA and protein. DNA binding studies on structurally related Pt(II) trpy complexes have revealed that such complexes can both intercalate DNA and covalently bind with DNA via N^7 of guanine. Other studies found that trpy complexes involving labile Pt-ancillary bonds (e.g. ancillary = Cl) can also covalently bind to other biomolecules such as proteins, via basic amino acid substituents such as thiol and imidazole groups. It is expected that [Pt(dpyb)Cl] complexes would exhibit similar binding, but it is not possible to say at this stage whether localisation in the nucleoli involves binding with DNA, RNA, protein, combinations of all three or other.

The brightness (intensity) of intracellular emission of the Pt(II) complex was found to depend on the dosage concentration, and to a lesser extent on the incubation time. Assuming that uptake is related to intracellular brightness, uptake of complex is extremely rapid; luminescent images could be obtained after only a 5 min incubation period (note: a more quantitative measure of uptake would involve the determination of platinum concentration per cell. This could be achieved by cell sorting/counting using Flow Cytometry, followed by ICP-MS, and should be considered for future studies). For 5 min incubation, 50 μM dosage tended to give the best luminescent images. Lower concentrations suffered greater interference from autofluorescence of biomolecules, whereas cells dosed with higher concentrations looked less healthy. The luminescent images of cells dosed with lower concentrations (> 20 μM) did improve slightly with increased incubation length (up to 24 h), however dosing with 50 μM for longer than 1 h typically led to some cell death. Cytotoxicity studies (Section 5.3.7) are in agreement with these observations.

The intensity of emission was also dependent upon the identity of the complex. Complexes $[PtL^1X]$ (where X = Cl, Br or I), $[PtL^2Cl]$, $[PtL^{11}Cl]$ and $[PtL^{16}Cl]$ gave images with the best contrast. Another complex, $[PtL^1py]^+$ (py = pyridine), also gave good images (Figure 16). We initially thought that uptake of charged molecules might be hindered, due to the need to cross the lipophilic membrane. Li et al. observed that monocationic Ir(III) complexes also enter cells.[22] Coogan et al. believes that the low positive charge possessed by such complexes actually facilitates entry into cells.[21] The interior of a cell is at a relatively negative potential compared to the exterior: this leads to a potential-driven preferential uptake of cationic species, and therefore accumulation of such species within the cells. A higher positive charge may disfavour uptake, due to a decreasing membrane permeability.

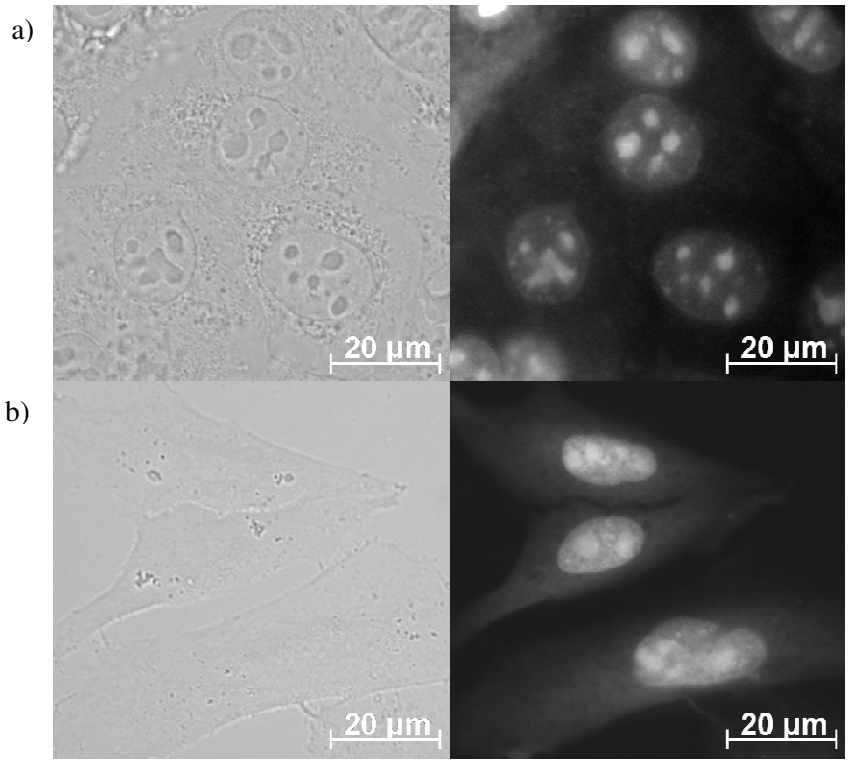

Figure 16: Bright field images (right) and fluorescence microscopy images (left) of a) NIH 3T3 cells and b) CHO cells, dosed with $[PtL^1py]^+$ (50 µM, 5 min, G365/FITCex).

5.3.2 Flow Cytometry as a Means to Quantify Uptake

Flow cytometry is a technique used to count and analyse microscopic particles such as cells.[23,25,64,65] It offers high-throughput quantification of light scatter and fluorescence parameters, and multiple parameters may be simultaneously measured from the same sample. The technique uses hydrodynamic focusing to align the cells into single file so

that they pass through the laser beam one at a time. The laser light (from up to 3 lasers) is focused onto the single file stream of cells, and various detectors are arranged to record the scattered and luminescent light from the cells. This gives useful information about the individual particle. The information from each particle can be combined with that from all other particles to give an averaged picture, representational of the whole population.

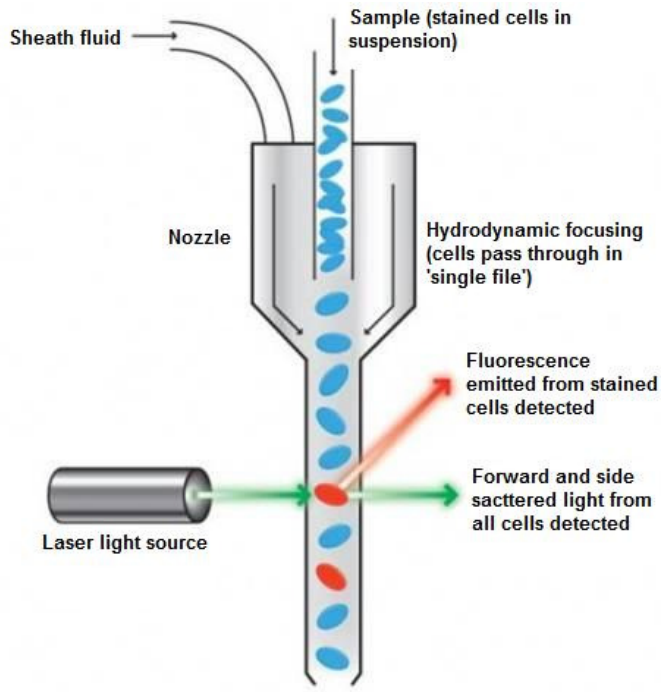

Figure 17: Schematic representation of a jet-in-air flow cytometer

The basic set-up of detectors is described here: a detector is placed beyond the sample stream, approximately opposite the probe beam – this records the 'forward' scatter of light and gives information on the cell size. Other detectors are placed perpendicular to the beam – some detect the 'side' scatter, which gives information about the cells granularity, whereas other detectors include fluorescence detectors – very useful for cells containing a fluorescent tag (such as our complexes). The fluorescence intensity of each cell can be measured, and the data can be compiled in either a logarithmic or linear mode. A few other groups have used mean fluorescence intensity values to quantify cellular uptake of luminescent organometallic complexes.[25,61] Some groups have used the technique to measure cytotoxicity of a dopant, by co-staining with live (e.g. calcein, fluorescein) and dead (e.g. PI) fluorescent stains. In one case, Jiménez-Hernández et al. have used flow cytometry to prove that a luminescent ruthenium complex could itself act as a viability stain.[23]

Initial studies with flow cytometry and [PtL^{2}Cl] have demonstrated that the technique can be useful in measuring cellular uptake of the 1,3-dipyridylbenzene Pt(II) complexes – the mean luminescence intensity (450/40 nm) of the cell population gives a relative measure of this. Figure 18 demonstrates how uptake of complex increases with both concentration and incubation time (for the concentration range investigated, 20 – 100 µM). For a fixed dosage time, at a certain concentration one can expect the cells to become saturated with complex, so that further increases would have no added effect, and the mean fluorescence intensity vs. dose plots (Figure 19) should plateau. However, it is possible that higher concentrations combined with higher dosage times were resulting in cell death (e.g. 100 µM for 1h) – there were far fewer cells present in these samples. This observation is in agreement with cytotoxicity studies (Section 5.3.7).

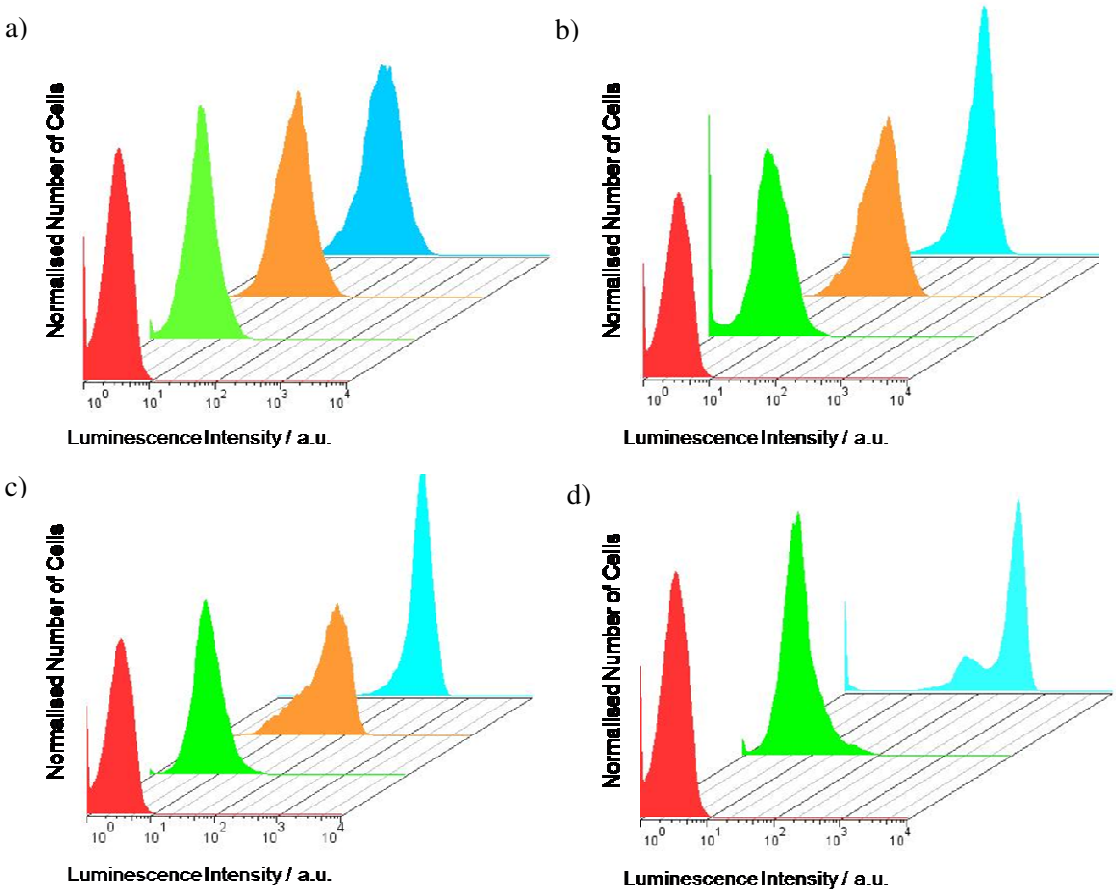

Figure 18: Histograms showing number of cells vs. log luminescence intensity (λ_{em} = 450/40) for various dosage concentrations of [PtL^{2}Cl] and a set dosage time: a) 5 min, b) 30 min, c) 1 h and d) 3 h dosage. The colours of the histograms correspond to the dosage concentration as follows: red = undosed cells, green = 20 µM, orange = 50 µM and blue = 100 µM.

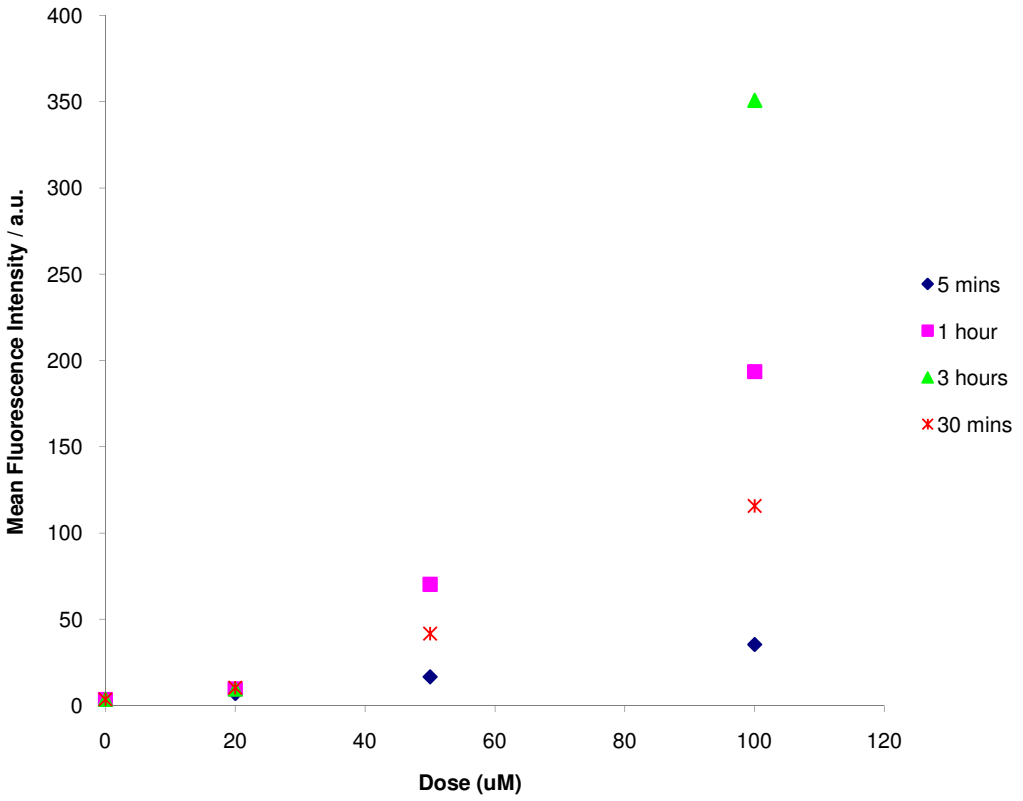

Figure 19: Plot of mean luminescence intensity (λ_{em} = 450/40 nm) vs. dosage concentration of [PtL^{2}Cl] at a set dosage time (see legend).

5.3.3 Uptake Mechanisms

Williams et al. report that [PtL^{1}Cl] probably enters the cell via passive diffusion, a non-activated process.[19] Experiments were performed to see if complexes prepared here also enter the cell via passive diffusion. The first experiment involves monitoring uptake at 4˚C. At this temperature, active uptake processes such as endocytosis are inhibited. Therefore, a decrease in image intensity compared to 37˚C would indicate an active uptake process. Cells were incubated in the fridge for varying time-lengths (15 min, 30 min and 1h) before dosing with the complex. The dosing solution of complex was also placed in the fridge during this time. After a quick dosing with complex, cells were returned to the fridge and incubated for a further 5 min. Upon removal from the fridge, the coverslip was quickly rinsed with ice cold PBS, attached to the microscope slide and imaged. The rapidity of this process was essential, as warming to room temperature could re-instigate active processes. The intensity of emission did not decrease significantly upon 4˚C incubation, suggesting a passive uptake.

To further check this, cells were dosed with a selection of drugs that inhibit or activate certain endocytotic uptake routes (Table 2). After 30 min incubation with each drug, cells were dosed with complex and incubated for a further 5 min. The intensity of the images obtained were compared – if complex was entering the cell via one of the activated routes, then inhibition of this route would result in a decrease in intensity. All images were of a similar brightness to the control sample, which contained cells dosed with complex only (5 min dosage). This further suggests that uptake is via a passive route.

Table 2: Perturbation of endocytosis and intracellular trafficking

Treatment	**Dosage**	**Effect**	**Mechanism**
Low temperature (4˚C)	-	General inhibitor of activated processes, including endocytosis	Energy depletion
Chloropromazine	50 µM	Specific inhibitor of clathrin mediated endocytosis (CME)	Dissociation of clathrin lattice
Filipin	1mg/mL	Specific inhibitor of caveolae	Cholesterol binding
Amiloride	3 mM	Specific inhibitor of macropinocytosis	Inhibits the Na^+/H^+ exchange protein
Wortmanin	300 nM	Inhibitor of macropinocytosis	Phosphatidyl inositol-3-phosphate inhibitor
Monensin	2 µM	Inhibitor of endosome maturation	Prevents endosome acidification
Chloroquine	10 µM	Disrupting endosomes and lysosomes	Prevents endosome acidification and causes swelling to endosomes and lysosomes
Poly-L-lysine		Disrupts interactions with cell membrane	Non-specifically binds to cell membrane
Sucrose	50 mM	Inhibitor of clathrin mediated endocytosis	Unselective inhibition of clathrin-coated pit

Note: table adapted from reference 66.

Propidium iodide (PI) is a well-known DNA intercalating agent. Upon binding to DNA, its emission intensity is enhanced 20-30 fold. However, PI is membrane impermeant, and can only enter cells with compromised membranes. Consequently, it is often used to

label dead cells. To test whether the membrane was becoming compromised upon uptake of the Pt(II) complexes, cells were cross-dosed with PI (Figure 20). Propidium iodide is excited and emits at longer wavelength than the Pt(II) complexes, so its emission could be monitored selectively by changing the filter set (a 510/50 excitation and 620-625 emission filter combination). The results indicated that compromisation of the membrane is not a requirement for complex uptake (i.e. cells showed emission due to Pt(II) complex without PI emission). The studies also gave qualitative information on the toxicity of the Pt complexes. For example, cells incubated with higher concentrations (50 – 100 µM) remain viable if the incubation time is kept short (less than 1 h), but start to die if exposed to such concentrations for extended dosing times. Cells dosed with lower concentrations (< 20 µM) remain viable for much longer dosings. More quantitative cytotoxicity studies were found to agree with these results (see Section 5.3.7).

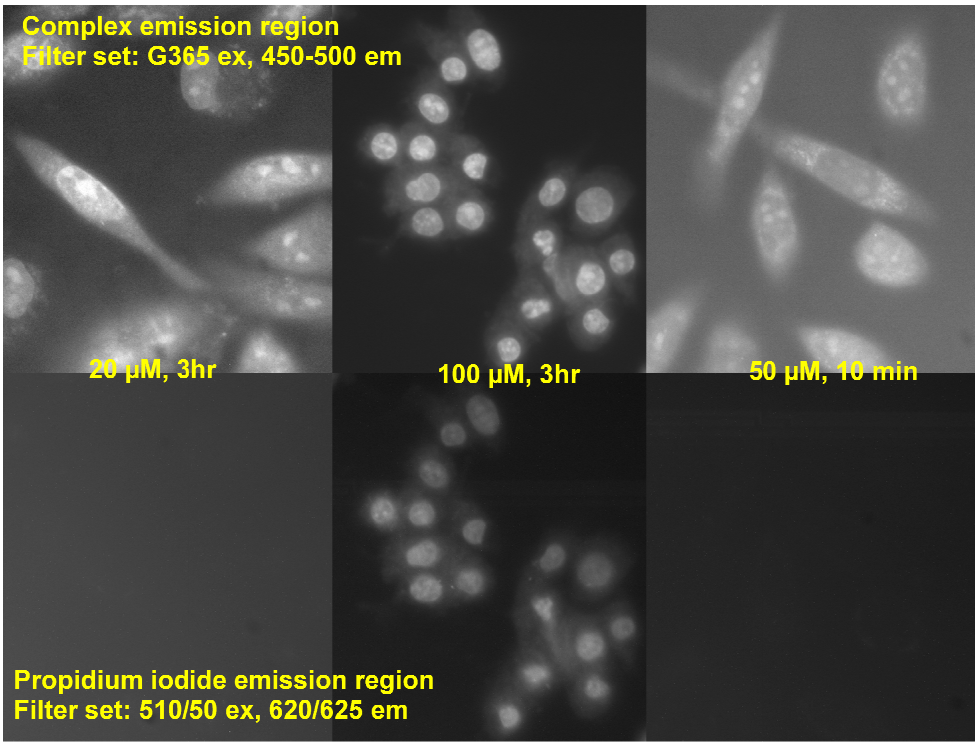

Figure 20: Fluorescence microscopy images of cells co-dosed with PI (1.8 nM, 5 min) and [PtL^{2}Cl] under various conditions: 20 µM, 3h (left), 100 µM, 3h (middle) and 50 µM, 10 min (right). Top: images obtained using a G365/FITCex filter set (allows visualisation of [PtL^{2}Cl] emission) and bottom: images obtained using a 510/50/620-625 filter set (allows visualisation of PI emission).

5.3.4 Complexes Not Exhibiting Nuclear Luminescence

Dosing cells with certain complexes (Table 1) did not result in nuclear emission, but the fluorescence images obtained did show weak emission emanating from the peri-nuclear region. However, similar images were obtained with un-dosed cells (control). Certain biomolecules are themselves fluorescent, and the images obtained from the control demonstrate that the autofluorescence can be observed using the filter sets employed (Figure 21). Indeed, this is one of the driving forces for development of TREM, as described in the introduction of this chapter. This overlap makes it difficult to say whether or not the complexes were emitting from platinum-dosed cells. Since the intensities were comparable to autofluorescence, it is suspected that that these complexes do not emit significantly from inside cells.

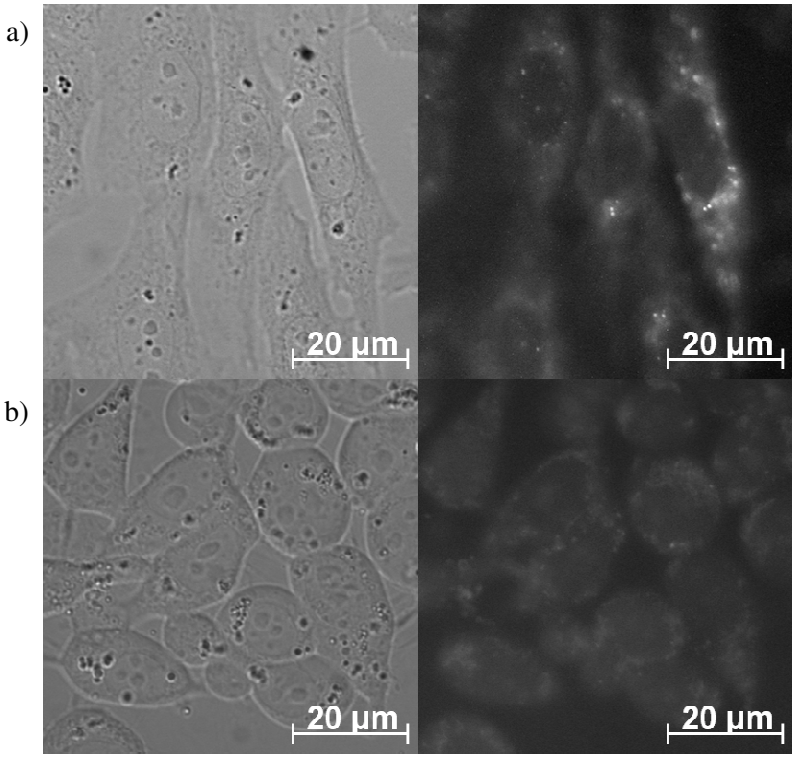

Figure 21: Left: bright field images and right: fluorescence microscopy images of a) undosed cells and b) cells dosed with [PtL^{9}Cl] (50µM, 5 min). Luminescent images were acquired using a G365/FITCex filter set.

As mentioned in Section 5.3.1, most of the complexes that did not display nuclear emission contain terdentate ligands with extended structures, or structures distorted from planarity. However, incubation of cells with [PtL^{9}Cl] also did not result in nuclear emission – this is unusual, this complex only contains small substituents (fluorine and methyl), and dosing with all other isomers ([PtL^{10}Cl], [PtL^{11}Cl] and [PtL^{12}Cl]), and the non-fluorinated analogue ([PtL^{5}Cl]), led to nuclear emission. The lack of nuclear

emission cannot be attributed to a low solution-based quantum yield; for example, [PtL^{12}Cl] has a much lower quantum yield in solution (φ = 0.02 in degassed DCM, 298 K), yet displays obvious emission from within the nucleus.

As already mentioned, complexes which localise in the nucleus may be binding to biomolecules covalently through displacement of the ancillary chloride ligand, or may be binding to DNA/RNA via intercalation. The complex, [PtL^{23}], was prepared to assist the study of these possibilities – this complex contains a tetradentate ligand, and does not contain a labile chloride ligand. The terdentate framework should act as a cage, preventing covalent binding with biomolecules. On the other hand, if nuclear emission were to be observed from cells dosed with this complex, it would indicate that intercalation played a prominent role in the intracellular interactions of the complexes.

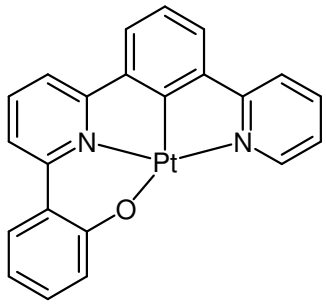

Figure 22: Structure of [PtL^{23}].

Nuclear emission was not observed for cells dosed with this complex, suggesting that the intracellular interactions of complex involve covalent bonds. However, the crystal structure of this complex could not be obtained, so these results must be treated with caution – if the bite angles around platinum are far from optimum, significant strain may exist within the molecule, which may result in a deviation from planarity. Moreover, the compound is found to be only a weak emitter in solution (φ = 0.08), and thus may emit poorly in the cell too.

5.3.5 Complex Displaying Selective Labelling of Cells

Upon dosage, most of the Pt(II) complexes were found to label all of the cells unselectively. However, the uptake of [PtL^{37}Cl] which contains a carboxylic acid substituent at the 4'-position, appears to be more selective (Figure 23b) – this complex is only entering a few of the cells. This selective response was found for all concentrations (10, 20 and 50 μM) and dosing times investigated (5 min – 3 h).

a)

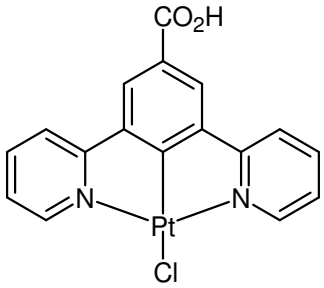

b)

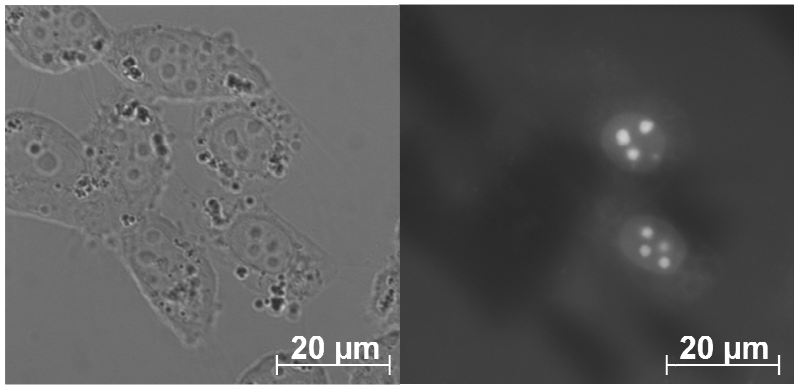

Figure 23: a) Structure of [PtL^{37}Cl], and b) Bright field (left) and fluorescence microscopy (right) images of CHO cells labled with this complex (dosing: 50 μM, 5 min). The fluorescence microscopy image was acquired using a G365/FITCem filter set. Note that emission is only occuring from certain cells.

Although the labelled cells appeared healthy in the bright field image, one possible explanation is that the complex was entering only those cells with a compromised membrane (i.e. dead cells). If this were the case, the complex would have applicability as a stain for dead cells.[23] To test this, cells were cross-incubated with complex and PI. The images obtained revealed that the luminescent species were labelling different cells, indicating that the complex was not specifically labelling dead cells, refuting this hypothesis.

To test whether incorporation of the complex and PI was mutually exclusive within the cell, cells were incubated with various combinations of saponin, complex and PI. Saponin is a surfactant that permeabilises cell membranes, allowing molecules to enter

and leave the cell more freely. Cells incubated with just saponin and complex showed nuclear emission from all cells, which was detected with filter set 1 (G365/FITCem). Similarly, upon incubation with saponin and PI, PI labelled the nuclei of all cells – this emission was detected using filter set 2 (510/50/620-625), but could not be observed using filter set 1. When cells were incubated with saponin, complex and PI, nuclear emission from all cells was detected with both filter set 1 and 2. This observation confirms that the labels are not mutually exclusive. Perhaps the complex is only taken up by the cell at a certain point during the cell cycle (Figure 24). To test this, the cell cycle would have to be synchronised, and cells would have to be incubated with complex at certain points during the cycle.[67]

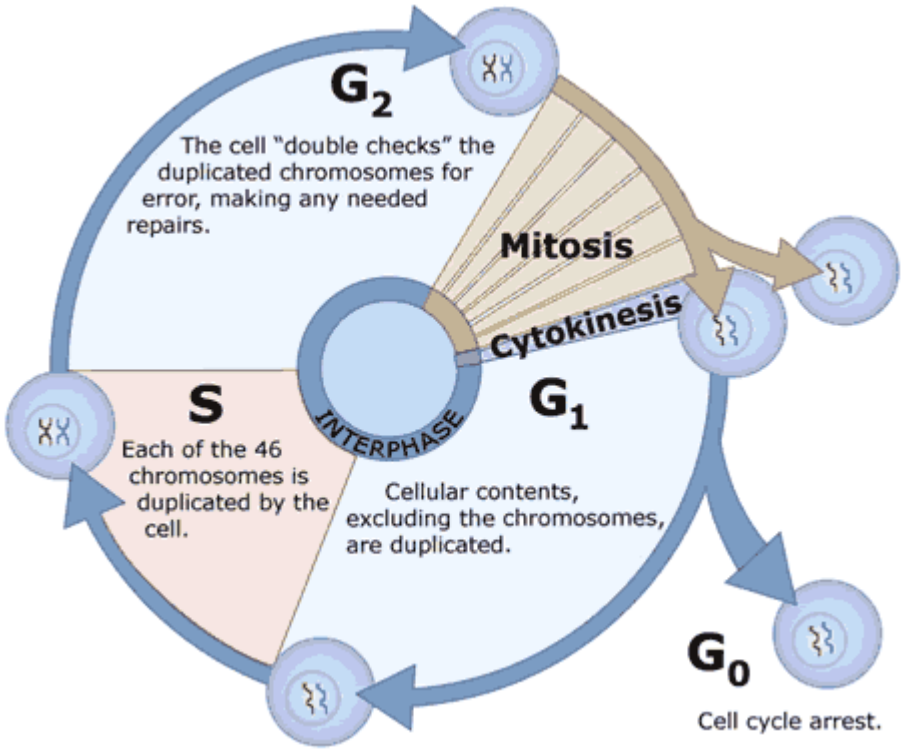

Figure 24: Different phases of the cell cycle. During the first phase (G_1), the cell grows. Once the cell reaches a certain size, it enters the second phase (S-phase) during which the chromosomes are duplicated. Once replication is complete, the cell then prepares itself for division (G_2). Mitosis (M) then follows; during this phase, the cell divides into two daughter cells, which each get one copy of all duplicated chromosomes. After division is complete, the cells enter G_1. They then may enter a resting phase (G_0), or start the process over again (image taken from reference 67).

5.3.6 Observation-Wavelength-Dependent Localisation Profile

As discussed previously, most complexes involving smaller ligands show localisation in the nucleus, when emission is monitored around 500 nm. When the emission was monitored using a longer-wavelength emission filter (660-710 nm; excitation filter unchanged) a distinctly different localisation pattern was observed (Figure 25). Now, emission is mainly observed within the cytoplasmic region (though with some nuclear emission still apparent). The emission intensity is not homogeneous throughout the cytoplasm - emission emanates from discrete areas, indicating localisation within a cytoplasm-based organelle. Many organelles exist in the cytoplasm, including the endoplasmic reticulum, golgi apparatus, mitochondria and lysosomes.

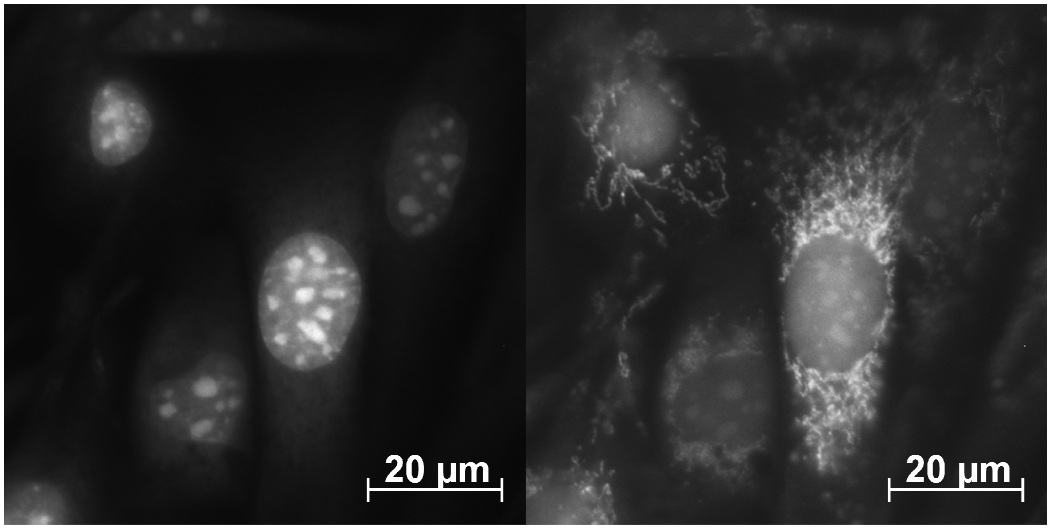

Figure 25: Fluorescence microscopy images of NIH 3T3 cells dosed with [PtL^{1}Cl] (50 µM, 5 min). Left: image acquired using a G365ex/FITCem em filter set, and Right: image acquired using a G365ex/660-710em filter set.

Co-staining studies were performed to determine the localisation of this low-energy emission. Lysosomal localisation was checked by co-staining cells with Pt(II) complex and LysoTracker red^{TM} (LTR). The complex and LTR were localising in distinctly different areas of the cytoplasm - the lysosomes appear as bright spots, whereas the complex appears to be localising in a more "stringy" organelle. Co-staining with MitoTracker red^{TM} (MTR) strongly suggests that the lower energy emission emanates from the mitochondria (Figure 26).

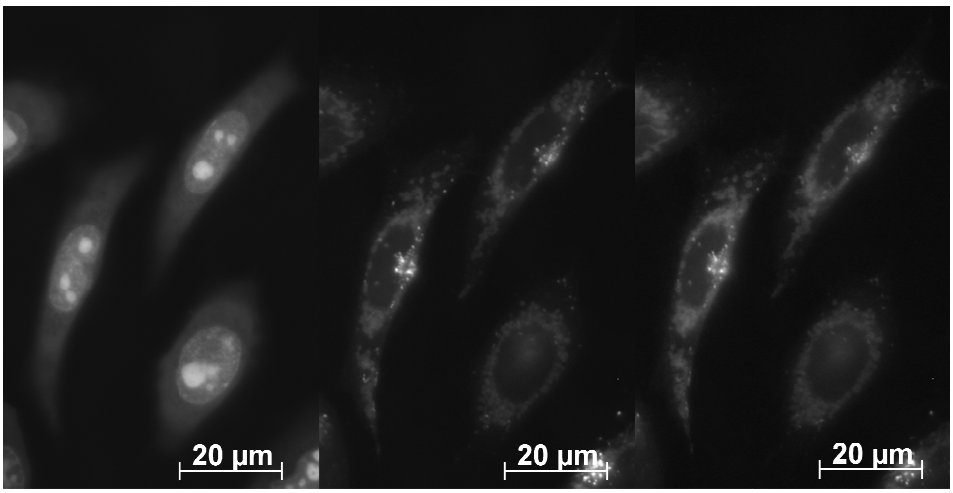

Figure 26: Fluorescence microscopy images of CHO cells co-stained with [PtL^{1}Cl] (50 µM, 5 min) and MitoTracker red^{TM} (300 nM, 30 min). Left: image acquired using a G365ex/FITCem filter set, Middle: image acquired using a G365ex/660-710em filter set, and Right: image acquired using a Conan 546ex/long-pass 590em filter set (this set allows visualisation of the MTR co-stain). Image contrast has been altered.

The mitochondria contain an abundance of thiols.[68] In fact, these thiols are expected to be the target of the commercial MitoTracker probes. Platinum(II) is a "soft" centre, and related complexes have previously demonstrated an affinity for sulphur binding[19,31] Furthermore, the emission of these sulphur adducts was significantly red-shifted compared to the chloro-analogues. It is therefore likely that the mitochondrial emission results from platinum-linked thiols, where the ancillary chloride has been replaced. Another possibility is that the complex accumulates in the mitochondria in high concentration, and the red emission is due to an aggregate or an excimer. To help determine the origin more conclusively, recording the intracellular emission spectrum should help – a technique allowing such measurements will be available in the department in the near future.

5.3.7 Cytotoxicity

As discussed in the introduction, intracellular probes should be of low toxicity to the biological system under study – it is therefore important to determine the cytotoxicity of these Pt(II) complexes. The toxicity of some of the complexes was investigated by monitoring the metabolic activity of the cells after incubation with complex for 24 h. An MTT assay was used to measure the metabolic activity {MTT = 3-(4,5-dimethythiazol-2-yl)-2,5-diphenyltetrazolium bromide}. Such assays are commonly used to determine cytotoxicities of Pt-based anticancer drugs.[69,70,71,72,73] Yellow MTT gets reduced by

living cells to formazan, a purple dye, by mitochondrial reductase enzyme, which is only active in viable cells. The absorption intensity of formazan (here measured at 541 nm) is proportional to the number of living cells present. By comparing the intensity of formazan absorption from cells which were previously incubated with complex with those that have not been incubated with complex (i.e. a control), the percentage of living cells can be determined.

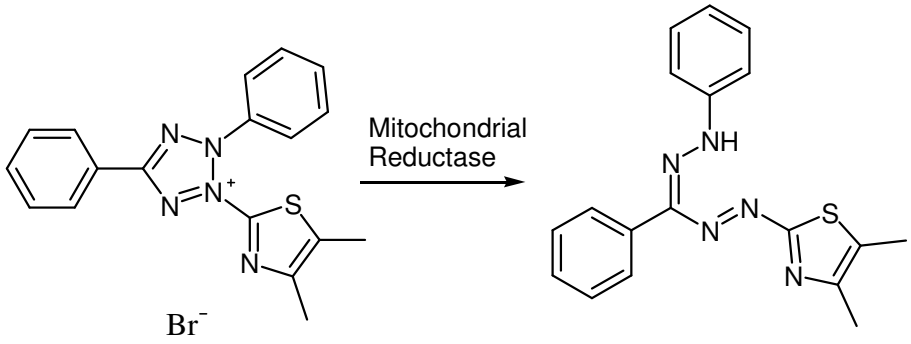

Scheme 1: The reduction of yellow MTT to purple formazan.

100 μL aliquots containing an approximately equal number of cells (1 x 10^4) were transferred to a 96-well plate and incubated overnight, during which, the cells attached to the surface of the microplate. The following morning, cells were dosed with varying concentrations of complex and incubated at 37˚C for a further 24 h. After this time, the media was removed, the cells were washed with PBS and fresh media was added, followed by MTT. The cells were incubated for a further 4 h. The medium and MTT were then removed, followed by addition of DMSO (DMSO is added to solubilise the formazan dye). Measurements for each complex were repeated at least three times. The IC_{50} value (the concentration required to kill half the population of cells in the specified dosage time) was determined from a plot of the percentage of live cells against log[complex]. The average values of IC_{50} are given in Table 3.

Table 3: Cytotoxicity values of Pt(II) complexes, determined for a 24 h dose. The estimated uncertainty in each IC_{50} value is ± 25 %.

Complex	IC_{50} / µM
[PtL^{1}Cl]	45
PtL^{2}Cl]	28
[PtL^{7}Cl]	42
[PtL^{8}Cl]	7
[PtL^{9}Cl]	32
[PtL^{10}Cl]	10
[PtL^{11}Cl]	29
[PtL^{12}Cl]	14
[PtL^{16}Cl]	25
[PtL^{35}Cl]	45

The IC_{50} values for the Pt complexes at 24 h dosing range from 7 to 45 µM. However, good quality images can be obtained after much shorter dosing periods. It was anticipated that cells would be able to tolerate higher concentrations of complex over shorter dosing periods. To test this, the cytotoxicity of [PtL^{1}Cl] to cells was investigated after just a 1 h dose with complex. An alternate method to MTT assay was investigated here. This method involved staining cells with trypan blue – this diazo dye accumulates inside cells with compromised membranes (i.e. dead cells) but is excluded by living cells. The live and dead cells were counted using a haemocytometer, and this was repeated 4 times. Using this method, the IC_{50} value for a 1 h dose was found to be 68 µM. This value is higher than the IC_{50} determined for a 24 h dose (45 µM) and indicates that cells can tolerate a higher dose of complex when incubated for shorter periods.

Assessing the cytotoxicity using the trypan blue method is not as efficient as the MTT assay. It takes much longer to acquire data using the trypan blue method, as each sample must be prepared and counted individually. The MTT assay method is much more suited to screening a vast number of samples/parameters, as a large amount of data can be accumulated rapidly.

5.3.8 Time-Resolved Emission Microscopy (TREM)

As discussed in Section 5.1.5, time resolved emission microscopy (TREM), is a complementary process to steady-state fluorescence microscopy. The technique can be used to discriminate luminescent species with similar spectral properties (i.e. excitation and emission wavelengths), as long as the lifetimes differ. This could prove invaluable in co-staining, where the excitation and emission parameters of commercial co-stains often overlaps. The inherent autofluorescence of biomolecules and residual background scatter of the lens etc. can often interfere with cellular images obtained via steady-state luminescence imaging. In theory, TREM can be used to generate images of greater contrast, by the removal of this autofluorescence and background scatter (provided that the bio-probe is sufficiently long lived).

Development of TREM for use in biological systems has been hindered by a lack of suitable bio-imaging agents. The Pt(II) complexes prepared here seemed ideal candidates for TREM (i.e. exhibit intracellular emission and have solution-based lifetimes of the order of several microseconds), and cells dosed with some of the complexes have been imaged using the technique. The samples were excited with a Q-switched Nd:YAG laser (355 nm), and emission was detected with either a long-pass 420 nm or long-pass 475 nm emission filter. The resolution of this camera was not as good quality as for the fluorescence microscope used for live-cell imaging. This microscope was not built for such imaging purposes initially, hence images obtained using this microscope are of a poorer quality. Nevertheless, the data are more than adequate to demonstrate the power and potential of the technique using the Pt complexes as luminophores. The expected nuclear emission was observed, and the luminescent image was monitored at various delays after removal of the excitation pulse, for a constant acquisition (gate) time. The intensity of emission decreased with increasing delay. In most cases, emission was still observed after a delay of 2 μs (though the emission intensity was by then obviously much weaker than that of the un-gated image).

The intracellular lifetimes of the complexes were determined by selecting an area of the image corresponding to a cell nucleus, and monitoring the luminescent intensity of this area as a function of time. The data were fitted to an equation modelling the exponential decay of photoluminescence,

$$I(t) = I_0 e^{-\frac{t}{\tau}} \qquad \textit{Eqn.}\ 1$$

where I_0 is the amplitude, and τ is the lifetime of photoluminescence. In each case, the decay was found to be mono-exponential, and the data generally gave a good fit to equation *Eqn.* 1 (Figure 27), from which the lifetime of the emission could be determined. Lifetimes were of the order of 2 µs (Table 4) which confirms that the observed intracellular emission was phosphorescence rather than fluorescence, and therefore must be due to the Pt(II) complex.

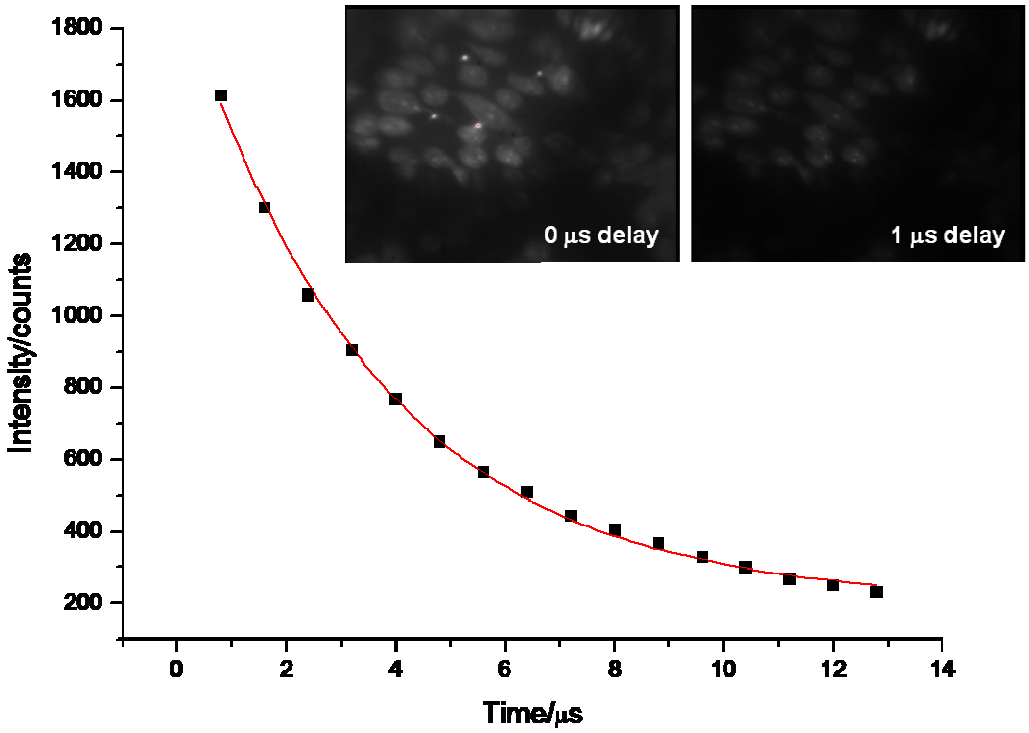

Figure 27: Emission kinetic trace obtained from the nuclei of live CHO cells incubated for 5 min with a 50 µM solution of [PtL^{10}Cl]. Solid line represents monoexponential fit to the data. Inset: luminescence images of the cells taken with a zero delay (left) and 1 µs delay (right). The images were recorded after 355 nm laser excitation, using a 475 nm long-pass emission filter. The time gate used was 200 ns. Image contrast and brightness have not been altered.

Table 4: Intracellular emission lifetimes of a selection of the Pt(II) complexes

	Intracellular lifetime (τ) / μs
[PtL^{1}Cl]	2.1
[PtL^{2}Cl]	2.1
[PtL^{5}Cl]	1.7
[PtL^{7}Cl]	1.6
[PtL^{9}Cl]	-----[a]
[PtL^{10}Cl]	3.5
[PtL^{11}Cl]	1.3
[PtL^{12}Cl]	1.9
[PtL^{16}Cl]	3.3
[PtL^{35}Cl]	1.6

[a]Emission could not be detected

The TREM technique was used to try to clarify whether perinuclear emission observed from cells dosed with [PtL^{9}Cl] (see Section 5.3.4) was due to the complex or whether it was due to autofluorescence of the cells. However, no emission could be observed (even from the un-gated image). This emission was always relatively weak when observed with the fluorescence microscope, and perhaps the lower signal-to-noise ratio of this microscope/camera means that the emission cannot be distinguished from the background.

5.3.9 Preliminary *in vitro* Investigations to Probe Interactions with Biomolecules

We wanted to see if the platinum complexes would bind to certain biomolecules *in vitro* – such studies may be able to shed some light on the intracellular binding interactions. As discussed in the introduction to this chapter, related [Pt(trpy)R]$^{+}$ complexes bind to nucleic acids, and in some cases to other biomolecules such as proteins. Recently, structurally related cyclometallated complexes have been shown to bind to proteins.[51,74] For example, detailed investigations on one of the N^N^C

complexes prepared by Lam et al., which also targets the cell nucleoli, revealed a strong binding interaction with protein and negligible interaction with DNA or RNA, suggesting that the complex interacts with nuclear proteins within the cell rather than with nucleic acids.[51]

To probe interactions of our complexes with biomolecules, 10 μM solutions of complex in phosphate buffered saline (PBS) were prepared, and the emission was monitored before and after addition of the desired biomolecule. A small amount of DMSO (less than 1% of the final volume) was required for initial solubilisation. Three of the complexes, [PtL^1Cl], [PtL^2Cl] and [PtL^9Cl] were investigated for binding. When cells are dosed with complexes [PtL^1Cl] and [PtL^2Cl], these complexes localise in the nuclei and emit brightly. On the contrary, complex [PtL^9Cl] does not emit from the nucleus – it was therefore of interest to see how this complex would interact with biomolecules *in vitro*.

5.3.9.1 Protein

The protein investigated was bovine serum albumin (BSA) - BSA or immunoglubulin G (IgG) are used as standards in most protein detection methods.[74] The emission of the PBS solution containing the complex (10 μM, 2.5 mL) was recorded before adding any BSA. The monomeric emission of these solutions was very weak, and accompanied by a more intense structureless band at lower energy (Figure 28). This band probably corresponds to an aggregate – we previously demonstrated that these complexes form such species in aqueous environments (Chapter 3, Section 3.4.3.7). This also accounts for the red-glow of the stock solutions made up in cell media (Section 5.3.1).

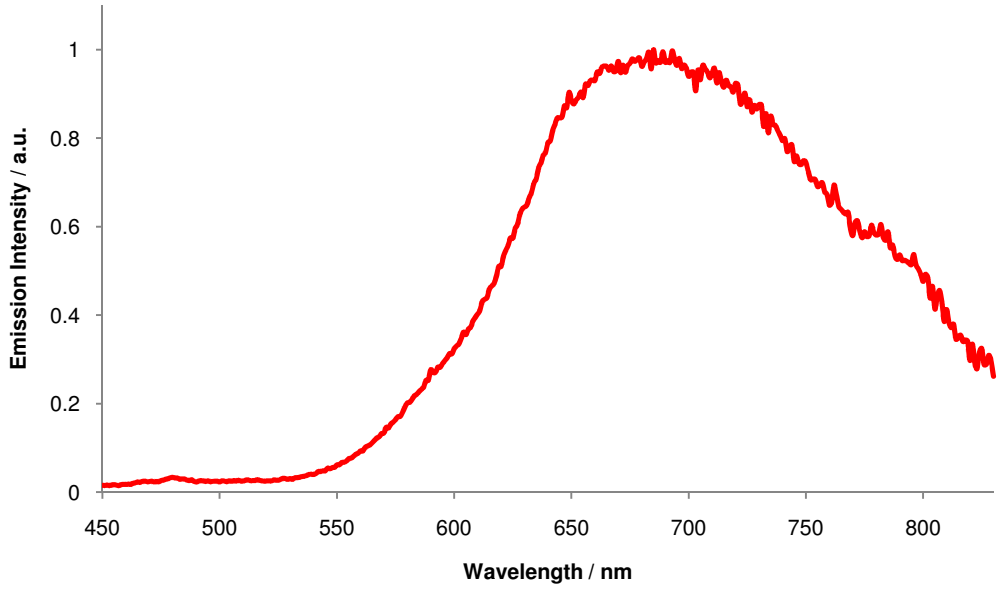

Figure 28: Normalised emission spectrum of a 10 µM solution of [PtL^{2}Cl] in PBS (λ_{ex} = 372 nm, 298 K).

Initially, titration experiments were performed, where 3 µL aliquots of 0.8 mM BSA were added to the solution of complex (10 µM, 2.5 mL), which was held in a quartz cuvette. For all complexes, the intensity of monomeric emission appeared to increase dramatically with BSA concentration (Figure 29 a)). Similar results were found by Che et al. who were studying protein binding of carboxylic acid-appended [Pt(N^N^C)Cl] complexes.[74] However, we later realised that the intensity also increased as a function of time, for a fixed BSA concentration. Figure 29 b) and Figure 29 c) show emission profiles of [PtL^{1}Cl] (10 µM), initially mixed with 2 µM and 22 µM of BSA respectively, and monitored over 5 hours. One can see that in both cases, the monomeric intensity continues to increase throughout the experiment. This observation may imply a slow binding process between complex and BSA. Alternatively, the time-dependent intensity change may be due to slow solubilisation of the aggregate formed in the aqueous medium. The intensity of complex mixed with a lower concentration of BSA is practically double that of complex mixed with an excess of BSA at the end of the experiment. Perhaps too much BSA alters the refractive index of the solution significantly. It is therefore not straightforward to perform titrations based on concentration alone.

Regardless of the kinetics/mechanism, these complexes clearly do bind to the protein. Addition of BSA appears to activate monomeric emission (and deactivate aggregate emission) – the complex may bind within a hydrophobic environment of the protein, which prevents intermolecular interactions between complex molecules. After "switch-

on" of the monomeric emission by protein addition, the lifetimes were recorded – in each case, the lifetime was very long (> 15 μs), and was found to be constant with increasing time or BSA concentration. These lifetimes are even longer than those predicted for the complexes at infinite dilution (see Chapter 3, Table 29). The protein must be very effective at shielding the complex from oxygen, and maybe disfavouring non-radiative decay pathways that involve coupling of the excited state to molecular motions.

Perhaps within the cell, complexes [PtL^{1}Cl] and [PtL^{2}Cl] are binding to nuclear proteins, accounting for the blue/green emission observed when cells are dosed with such complexes. If this is the case, it implies that complex [PtL^{9}Cl] is for some reason excluded from the cell nucleus, as aerated aqueous samples of this complex also demonstrated a switch-on of luminescence upon addition of BSA.

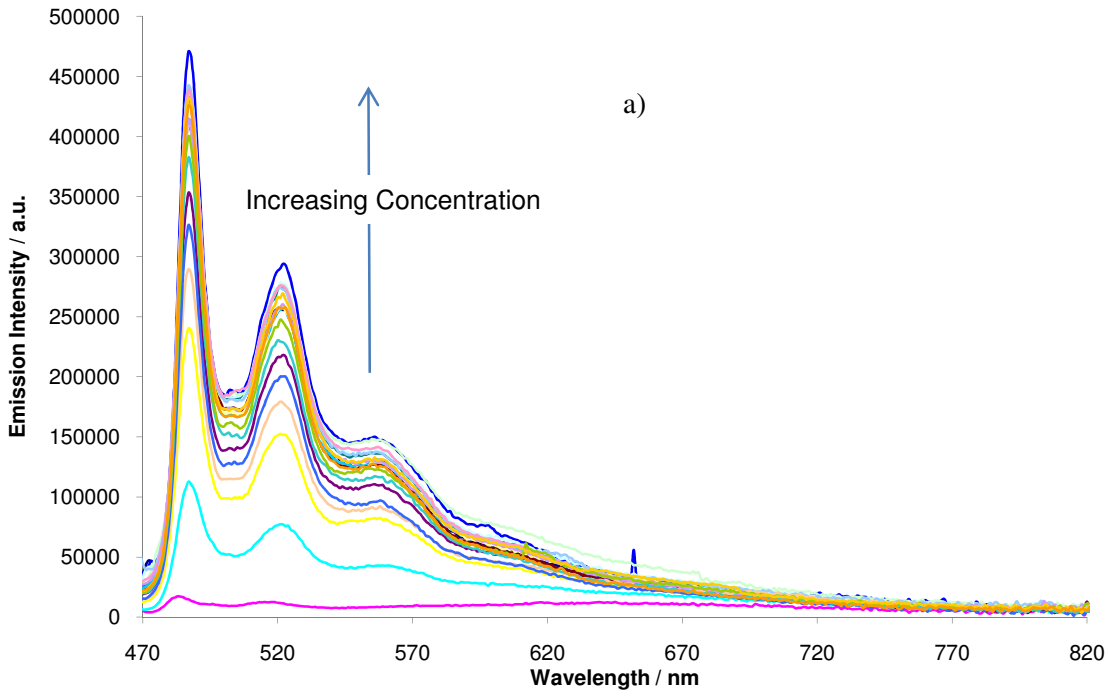

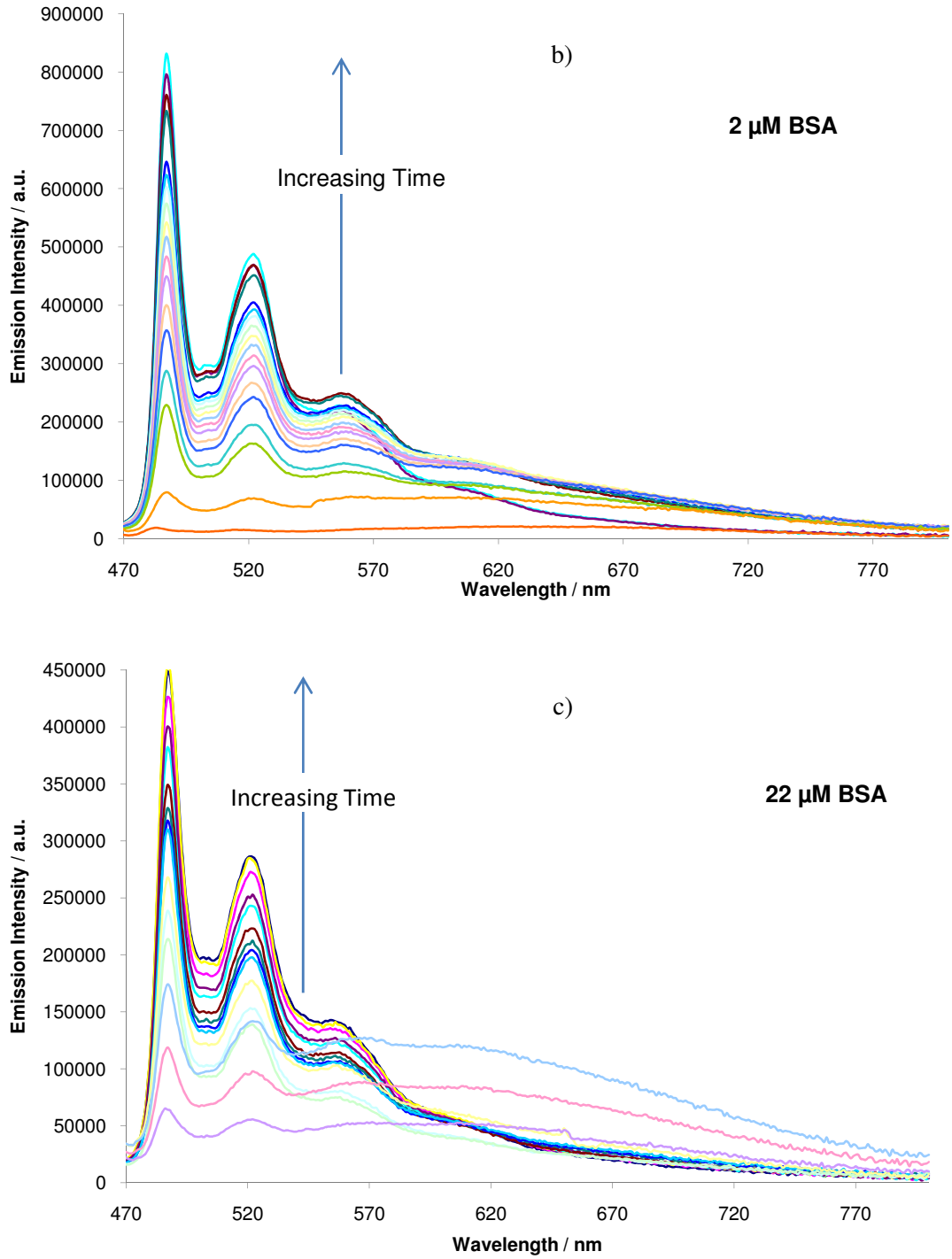

Figure 29: a) Chart showing increasing monomeric emission intensity of a 10 µM [PtL^{1}Cl] solution in PBS, with an increasing BSA concentration (λ_{ex} = 401 nm, 298 K). b) and c), Charts showing increasing monomeric emission intensity of [PtL^{1}Cl] (10 µM solution in PBS), with time, after an initial addition of BSA (2 µM and 22 µM respectively). The emission was monitored over 5 h (λ_{ex} = 401 nm, 298 K).

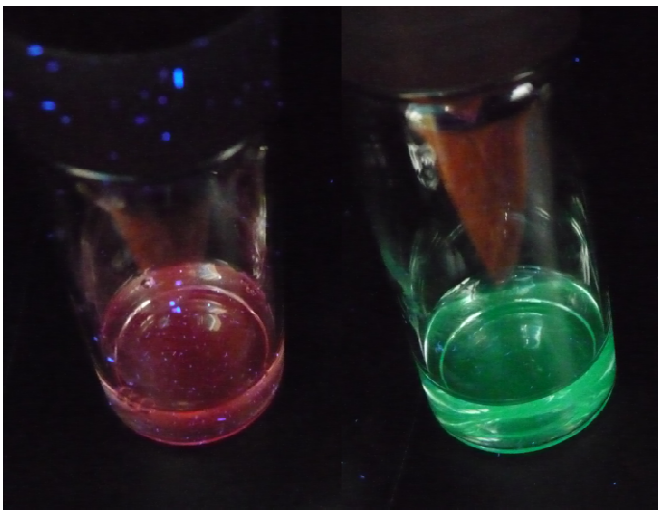

Figure 30: Solutions of [PtL^{1}Cl] in PBS (10^{-5} M), in the absence (left) and presence (right) of BSA (1 x 10^{-6} M), under long wavelength UV-irradiation.

5.3.9.2 DNA

The interaction of these three platinum complexes with DNA (calf-thymus DNA, A_{260}, Aldrich) in a PBS solution was monitored by emission spectroscopy. The emission profile of 10 μM solutions of [PtL^{1}Cl], [PtL^{2}Cl] and [PtL^{9}Cl] was monitored over 2 h in the absence and presence of excess DNA. Addition of DNA to solutions of complexes [PtL^{1}Cl] and [PtL^{2}Cl] also caused a "turn-on" of the monomeric emission, but the response was much slower than with protein (the monomeric intensity did not increase as significantly, and aggregate emission remained quite prominent, e.g. Figure 31). For [PtL^{9}Cl], although a slight increase in intensity was observed upon DNA addition, the monomeric emission remained very weak after 2h. These results therefore suggest that [PtL^{9}Cl] only interacts weakly with DNA.

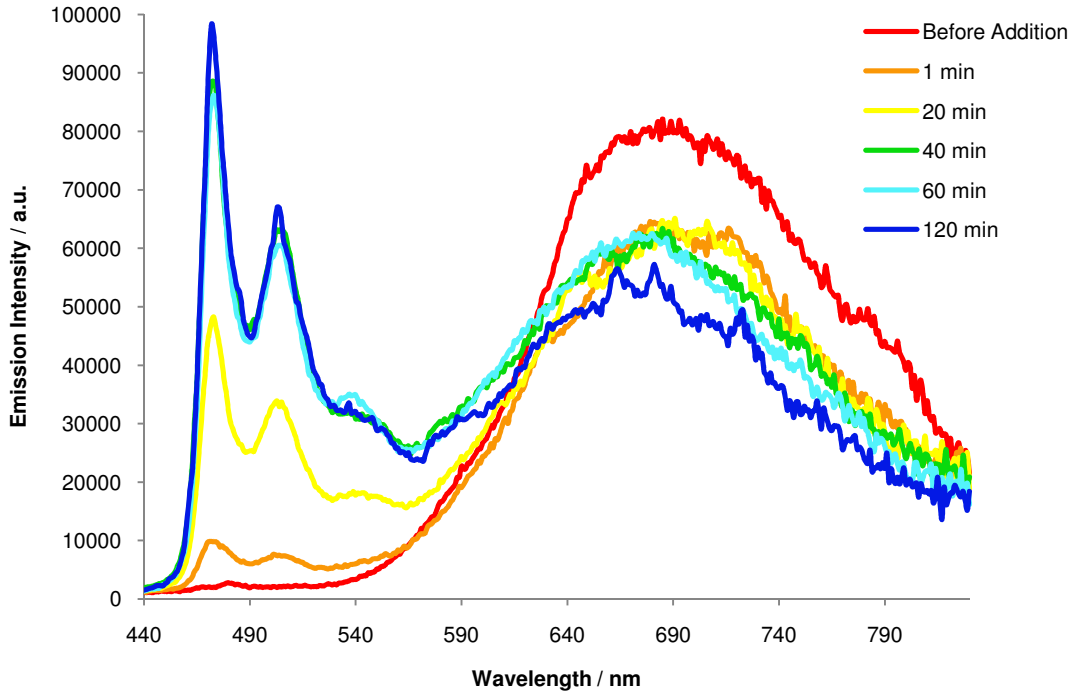

Figure 31: The emission of a solution of [PtL^{2}Cl] (10 μM in PBS), containing excess DNA (calf-thymus, Aldrich), monitored over 2 h (λ_{ex} = 372 nm, 298 K).

Unfortunately, these experiments were hindered by precipitation of small particles that glowed green under long wavelength UV-irradiation. It is believed that these particles correspond to complex-bound-DNA (the particles would have glowed red if they were merely aggregates of complex)

From these preliminary investigations, it is clear that such complexes can form interactions with biomolecules such as protein and DNA. However, the extent of such interactions is related to the structure of the complex, and subtle changes can have a large impact. Multiple variables, such as time and concentration of added biomolecule, affect the emission intensity and performing titrations is not straightforward and needs further investigation. To further probe interactions with DNA, other techniques such as circular dichroism, monitoring the viscosity of the DNA solution and monitoring the melt temperature of DNA, which are some of the many techniques used to probe interactions of [Pt(trpy)X]$^+$ systems with DNA,[32,35,75,76] should be considered.

5.4 Iridium(III) Complexes as Bio-Imaging Agents

As well as the Pt(II) complexes, luminescent iridium(III) complexes involving polypyridyl ligands are prepared within our research group. Other groups have recently reported that complexes of the form $[Ir(ppy)_2(bpy)]^+$ and derivatives are amenable to fluorescence microscopy in cells.[22,60,62] We were interested to see if a series of pyridyl benzimidazole-based cyclometallated complexes of iridium would also enter cells and localise in specific organelles. The structures of the iridium complexes investigated here are given in Figure 32. The complexes are comprised of bidentate or terdentate cyclometallating ligands, the latter being very similar to those described in this thesis with Pt, and include both cationic and charge-neutral compounds with essentially identical masses.

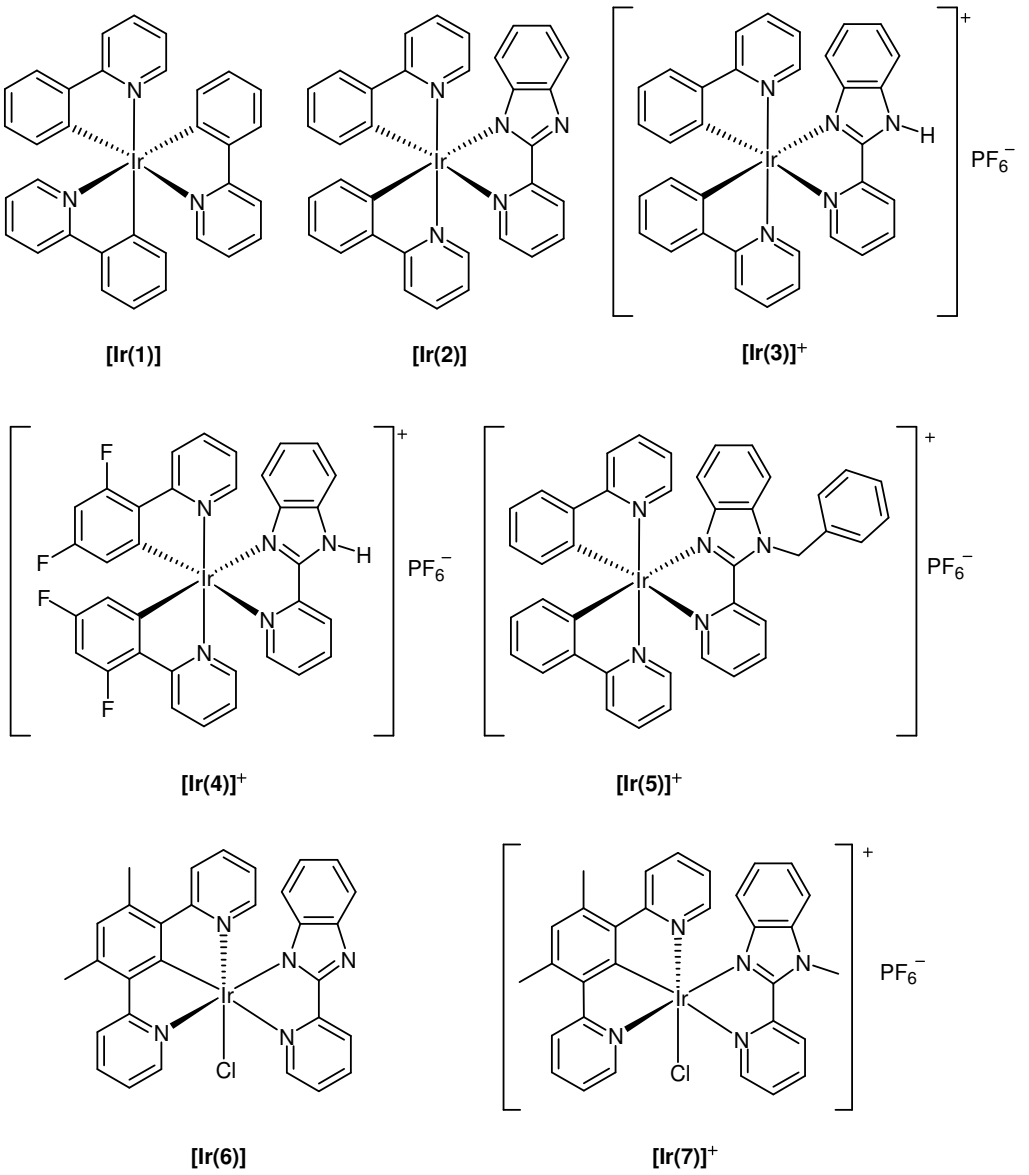

Figure 32: The series of iridium(III) complexes that were investigated as bio-markers for living cells

5.4.1 Localisation

These complexes absorb at similar wavelengths to the Pt(II) complexes, and emit between 500 nm and 600 nm. Therefore, a G365 excitation and FITCem (515-565 nm) emission filter were selected to monitor their intracellular luminescence. In contrast to the Pt(II) species, the iridium complexes did not emit from the cell nuclei. On the other hand, bright emission was observed from distinct areas within the cytoplasm, which differed between complexes containing exclusively bidentate ligands ([Ir(1)] – $[Ir(5)]^+$) and those containing a terdentate ligand ([Ir(6)] – $[Ir(7)]^+$).

Complexes [Ir(1)] – $[Ir(5)]^+$ appeared to localise in discrete vesicles dotted throughout the cytoplasm (Figure 33). The images were compared with fluorescent images of cells dosed with LTR. Unfortunately, *co-loading* the cell with an iridium complex and this co-stain could not be used to confirm co-localisation – emission due to the complexes also appeared in the detectable range of the co-stain. Nevertheless, the dotty localisation of complexes 1-5 throughout the cytoplasm looks very similar to the localisation profile of LTR, suggesting that these complexes are localising in the cell lysosomes. A similar punctate emission was observed recently in cells dosed with biotin-linked Ir(III) complexes – Lo et al. believe that these complexes are localising in endosomes.[60]

As a further note, the images obtained with the LTR co-stain were always quite poor (even when a fresh solution of co-stain had been prepared from stock, immediately prior to imaging), suggesting room for improvement on the commercial co-stain front.

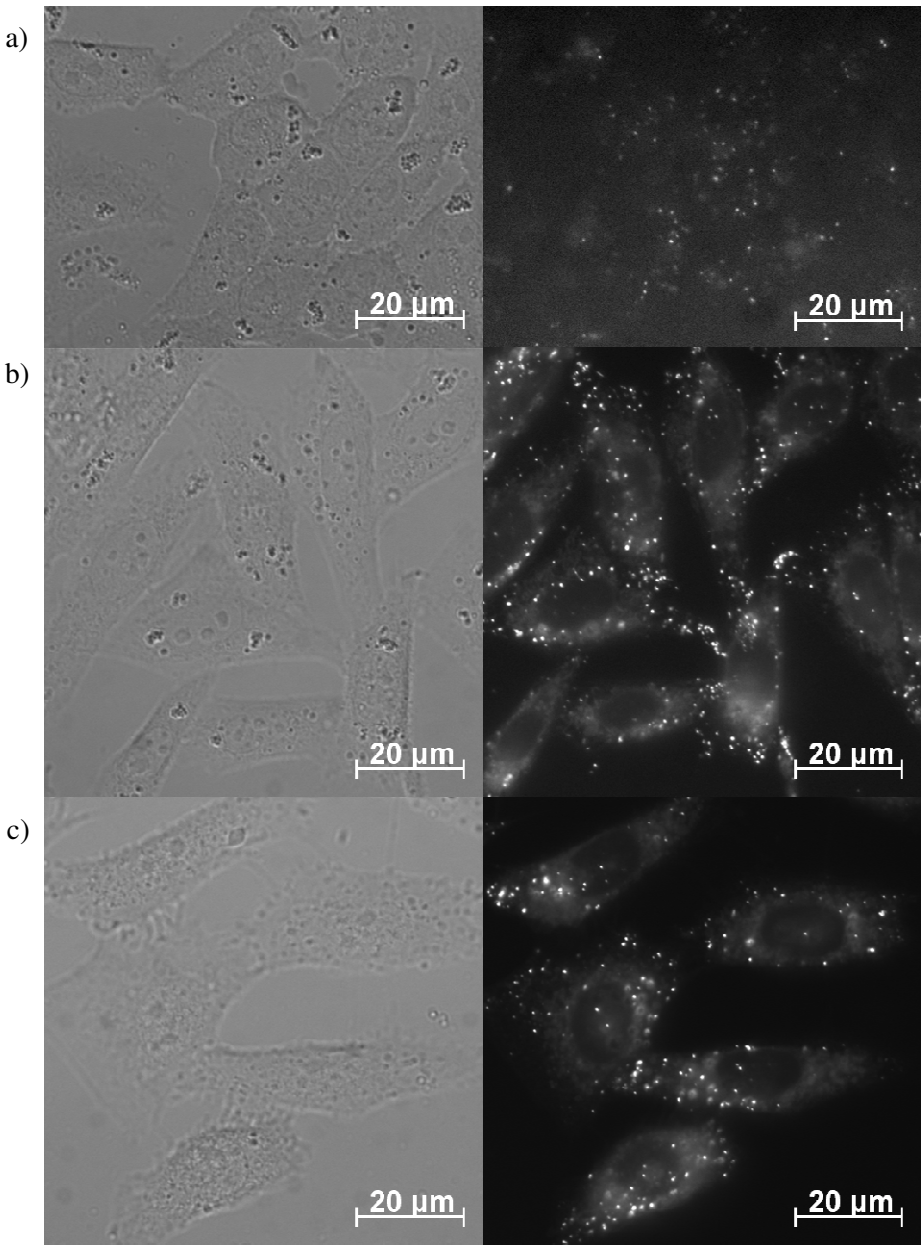

Figure 33: Bright field (left) and fluorescence microscopy images (right) of CHO cells dosed with various species: a) cells dosed with LTR (80 nM, 30 min), b) cells dosed with [Ir(2)] (10 µM, 5 min, G365/FITCem), and c) cells dosed with $[Ir(4)]^+$ (10 µM, 1 h, G365/FITCem).

Complexes [Ir(6)] and $[Ir(7)]^+$, which involve a terdentate N^C^N ligand, also localise within the cytoplasmic region, but the emission pattern differs from that observed with complexes [Ir(1)] – $[Ir(5)]^+$ (Figure 34). At first sight, the more "stringy" localisation of these complexes was thought to resemble the lower-energy emission of the Pt(II) complexes, which had been assigned to mitochondrial localisation.

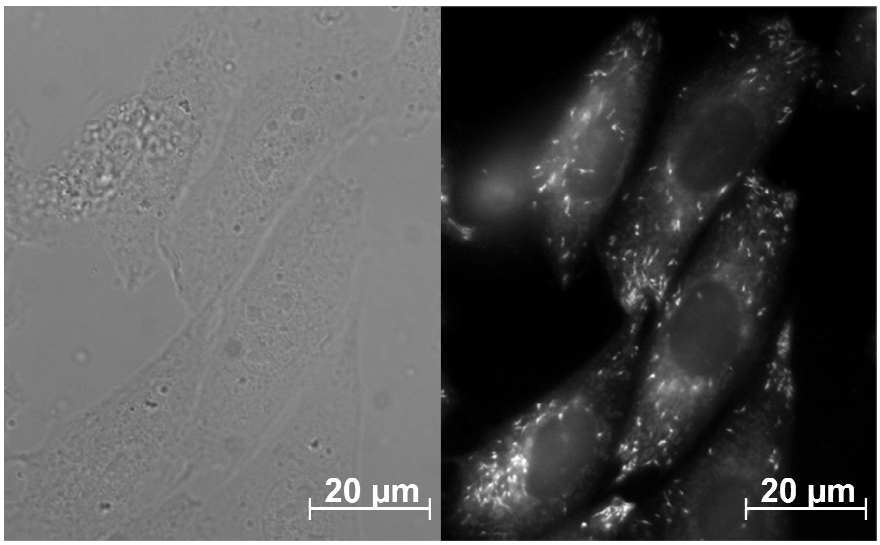

Figure 34: Bright field (left) and fluorescence microscopy images (right) of CHO cells dosed with [Ir(6)] (10 µM, 1 h, G365/FITCem).

Cells were dosed with both complex and a MTR co-stain. The images obtained with [Ir(6)] are shown in Figure 35 (similar observations were made with $[Ir(7)]^+$, although the intracellular emission intensity was significantly weaker). Although some overlap is observed, the images are not identical, indicating that these complexes are localising in a different cytoplasm based organelle. Perhaps these complexes are binding to cytoskeletal filaments such as actin or tublin.[1,2,77] However, further studies must be performed to verify the exact intracellular localisation of these complexes.

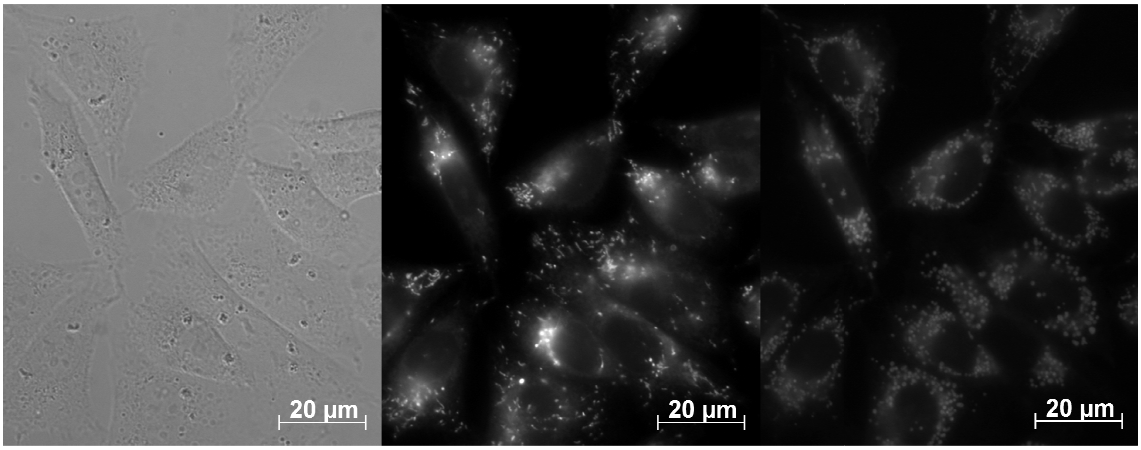

Figure 35: Images of CHO cells co-stained with [Ir(6)] (10 µM, 1 h) and MitoTracker red™ (250 nM, 30 min). Left: bright field image, Middle: image acquired using a G365/FITCem filter set (this filter set allows visualisation of [Ir(6)] emission), and Right: image acquired using a Conan 546ex/long-pass 590em filter set (this filter set allows visualisation of the MTR co-stain).

5.4.2 Uptake

All iridium complexes were found to enter the cell rapidly (within 5 min). For complexes containing bidentate ligands, a 5 min incubation involving dosing concentrations as low as 10 µM could be used to obtain images of good contrast. Increasing the concentration at this incubation time did not improve the quality of the image. In fact, longer incubation times and/or higher dosing concentrations proved detrimental to image quality – high intensity emission was observed from certain bright spots, assumed to correspond to a higher local concentration of complex, and these bright spots swamped the emission from the rest of the sample (Figure 36). The intracellular emission of complexes containing terdentate ligands ([Ir(6)] and $[Ir(7)]^+$) was inherently weaker, but could be improved by increasing the dosing time. For these complexes, the best images were obtained when 10 µM solutions were incubated with the cells for 1 h.

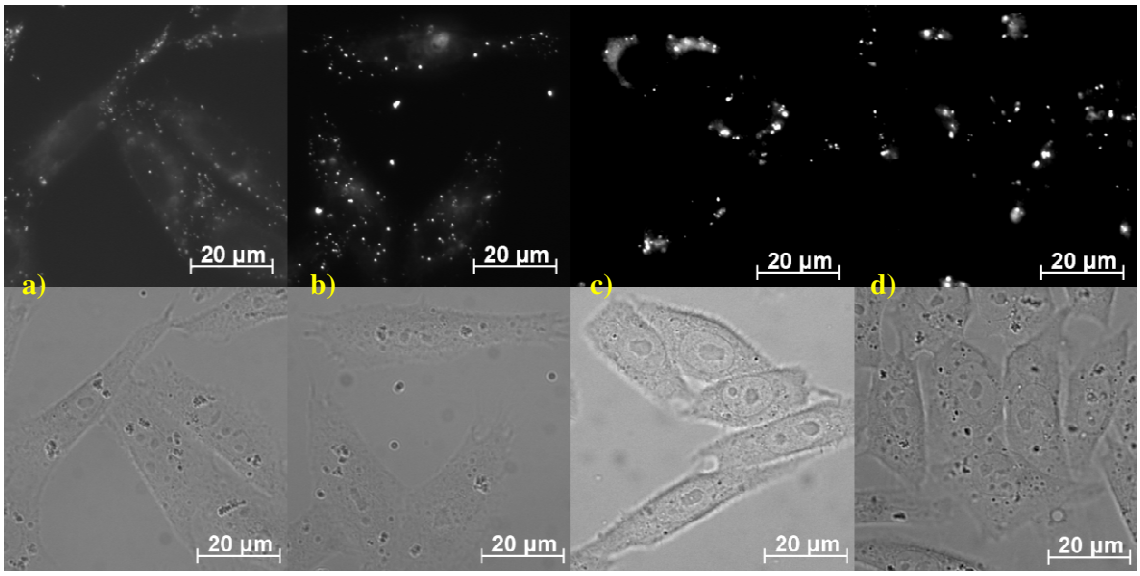

Figure 36: Comparative images of CHO cells dosed with [Ir(2)] (10 µM), for varying incubation lengths: a) 5 min, b) 1 h, c) 4 h, d) 24 h. Image contrast and brightness have not been adjusted. The fluorescence microscopy images (top) were acquired using a G365/FITCem filter set.

The uptake of iridium complexes at 4˚ C was monitored, and the emission was compared to that obtained at 37˚ C. At 4˚ C, the cells were still highly luminescent, implying that the iridium complexes can enter the cells via a non-activated pathway. However, image intensity was often slightly lower when dosed at 4˚ C. Lo et al., who have investigated biotin-linked phenylpyridine complexes, made similar observations with their complexes, where additional uptake inhibition studies indicated that these complexes were also taken up by the cell via an active route.[60] Uptake via both an

energy-independent route and an energy-activated route may also occur for our complexes (experiments with uptake inhibitor/activator drugs should be performed to check this).

As for the Pt(II) complexes, uptake could be monitored using flow cytometry. Figure 37 shows histograms representing the luminescence intensity of a population of cells, which have been incubated with a certain concentration of the stated complex for a set incubation time. The average luminescence intensity of the population increases with both dosage concentration and incubation length. From the results, complex [Ir(1)] has a much lower intracellular luminescence intensity than the other two complexes investigated ([Ir(2)] and $[Ir(3)]^{+}$). This result is consistent with the imaging experiments – longer acquisition times were required to capture images of cells dosed with [Ir(1)]. For the longer incubation period (4 h), cells dosed with the two highest concentrations (100 μM and 1000 μM) have a similar mean luminescence intensity. This implies that saturation has almost been reached, and that further increases in concentration for this incubation length will have little effect.

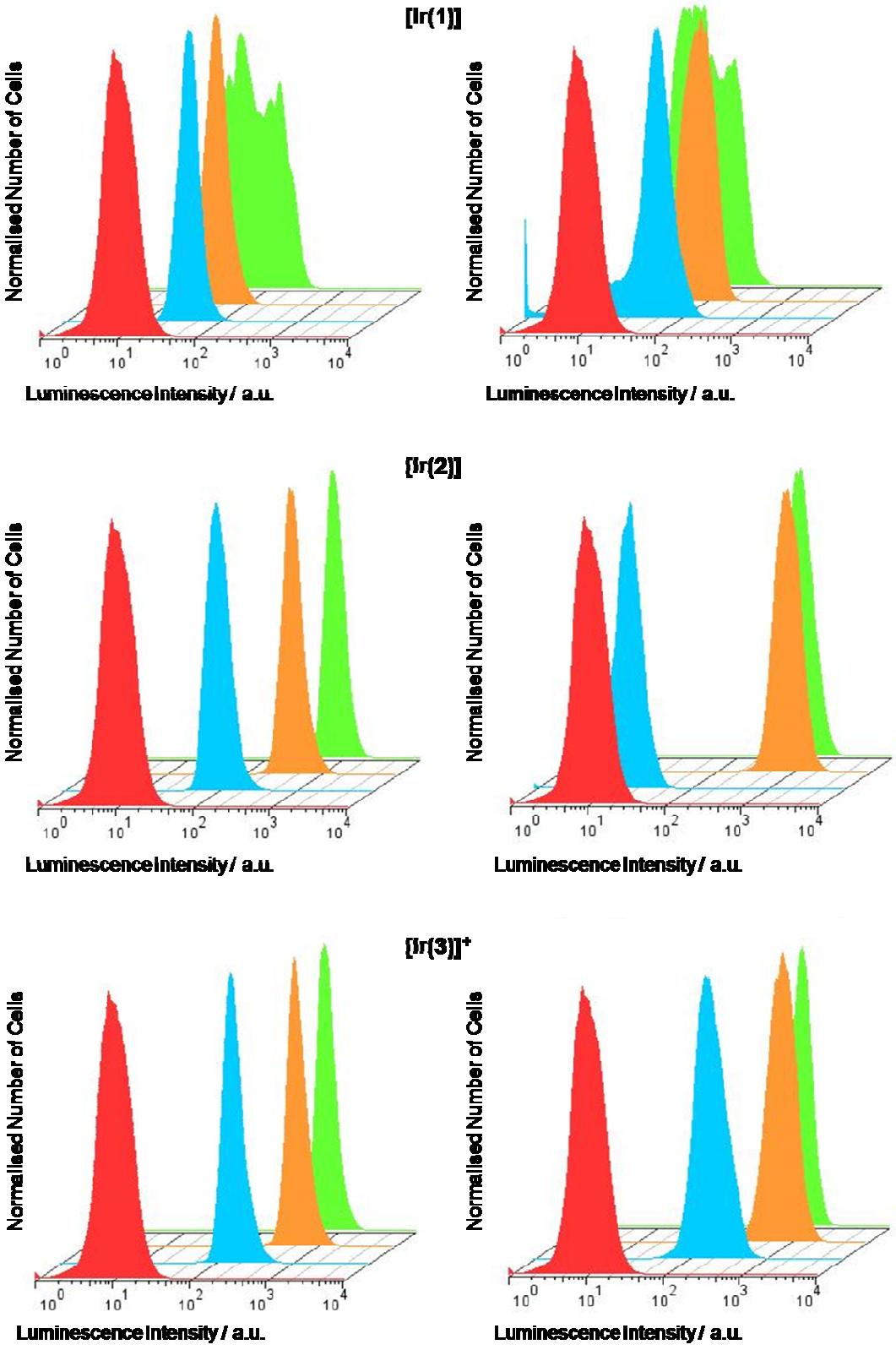

Figure 37: Histograms showing number of cells vs. log luminescence intensity (λ_{em} = 530/40) for various dosage concentrations of [Ir(X)], and a set dosage time of 1 h (left) and 4 h (right). The top plots correspond to CHO cells dosed with [Ir(1)], the middle plots correspond to CHO cells dosed with [Ir(2)], and the bottom plots correspond to CHO cells dosed with $[Ir(3)]^+$. The colours of the histograms correspond to the dosage concentration as follows: red = undosed cells, blue = 10 μM, orange = 100 μM and green = 1000 μM.

5.4.3 Cytotoxicity

The cytotoxicity of complexes [Ir(1)] – $[Ir(3)]^+$ and [Ir(6)] – $[Ir(7)]^+$ was determined via MTT assay (Table 5). Cells were dosed with various concentrations of each complex for 24 h. Complexes [Ir(2)] and [Ir(3)] demonstrated relatively low cytotoxicity – the IC_{50} for these complexes occurs outside the concentration range studied (0 – 200 μM). The other three complexes had IC_{50} values similar to those of the Pt(II) complexes. It seems that the cytotoxicity is related to the intrinsic structure of the ligands – a similar observation was made by Lo et al.[62] Additionally, the higher toxicities of [Ir(6)] and $[Ir(7)]^+$ compared to [Ir(2)] and $[Ir(3)]^+$ may be associated with their differential intracellular localisation.

Table 5: Cytotoxicity values determined for the Ir(III) complexes, over a 24 h incubation. The estimated uncertainty in each IC_{50} value is ± 25 %.

Complex	**IC_{50} / μM**
[Ir(1)]	35
[Ir(2)]	> 200
$[Ir(3)]^+$	> 200
[Ir(6)]	10
$[Ir(7)]^+$	39

5.4.4 Time-Resolved Emission Microscopy

The intracellular emission lifetimes of the iridium complexes are given in Table 6. All lifetimes are around 1 μs, confirming phosphorescence. As found for the Pt(II) complexes, the emission intensity followed a monoexponential decay, and the decay data gave a good fit to *Eqn.* 1 (see p. 285).

Table 6: Intracellular emission lifetimes of the Ir(III) complexes

	Intracellular lifetime (τ) / µs
[Ir(1)]	0.91
[Ir(2)]	1.20
[Ir(3)]$^+$	1.07
[Ir(5)]$^+$	1.13
[Ir(6)]	0.88
[Ir(7)]$^+$	1.18

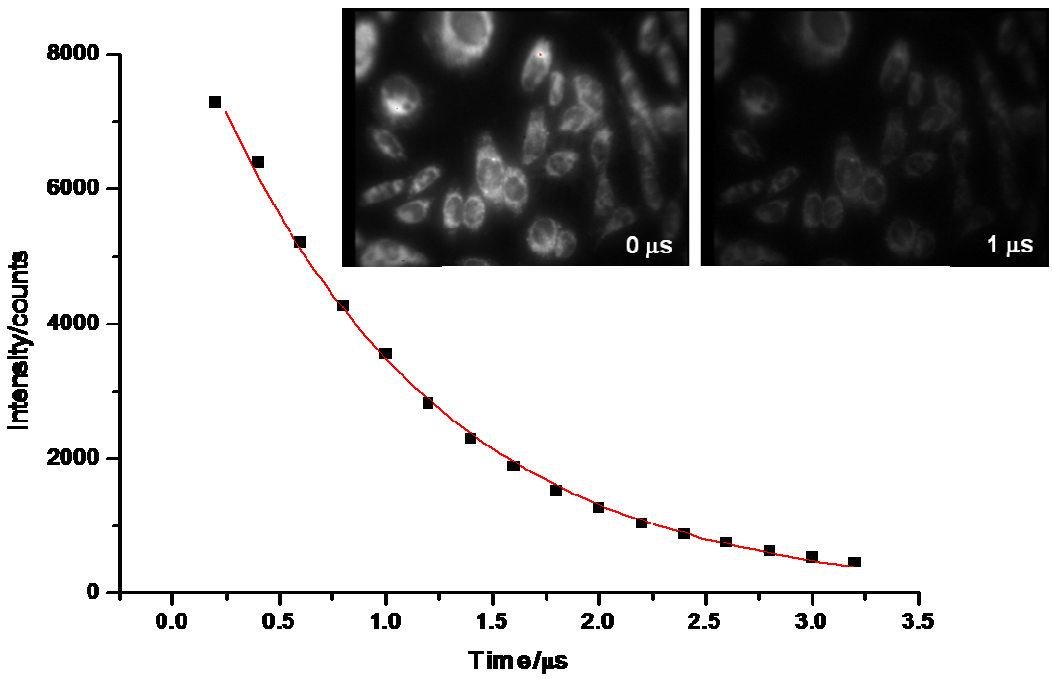

Figure 38: Emission kinetic trace obtained from the perinuclear region of live CHO cells incubated for 1 h with a 10 µM solution of [Ir(3)]$^+$. Solid line represents monoexponential fit to the data. Inset: luminescence images of the cells taken with a zero delay (left) and 1 µs delay (right). The images were recorded after 355 nm laser excitation, using a 475 nm long-pass emission filter. The time gate used was 200 ns. Image contrast and brightness have not been altered.

As mentioned in Section 5.3.8, TREM should be able to distinguish between emitters with similar excitation and emission wavelengths, on the basis of time, if the lifetimes differ. To test this, cells were co-loaded with an iridium complex, and either Hoechst or DAPI, which are commercial nuclear stains. These stains possess similar excitation and emission wavelengths to the iridium (and platinum) complexes, and it was not possible to discriminate emission from each luminophore from steady state images. However, these nuclear stains emit light via fluorescence, hence have much shorter lifetimes. (note, Williams et al. did manage to selectively image cells co-stained with [PtL^1Cl] and DAPI using steady-state microscopy, by exciting the Pt(II) complex at the weak $S_0 \rightarrow T_1$ absorption band. Unfortunately, attempts to re-create this failed, possibly because excitation around this forbidden band resulted in an emission intensity that was too weak to detect using the apparatus in Durham).[19]

Cells were dosed with an iridium complex (10 μM and 50 μM) for 1 h, and Hoechst (350 nM) was added for the last 5 min. The cells were then studied using TREM (Figure 39). In the –1 μs delay image (i.e. the image was acquired over the excitation pulse), extremely bright emission is observed from within the nucleus. This emission was accompanied by a much weaker punctate emission from the cytoplasm, which was of slightly higher relative intensity for cells dosed with 50 μM Ir complex. However, in the 0 μs delay image, the nuclear emission is not observed, and only bright emission from the cytoplasmic region is seen. Though the intensity of this emission does decrease with increasing delay, emission from the cytoplasm can still be observed after a delay of 1 μs.

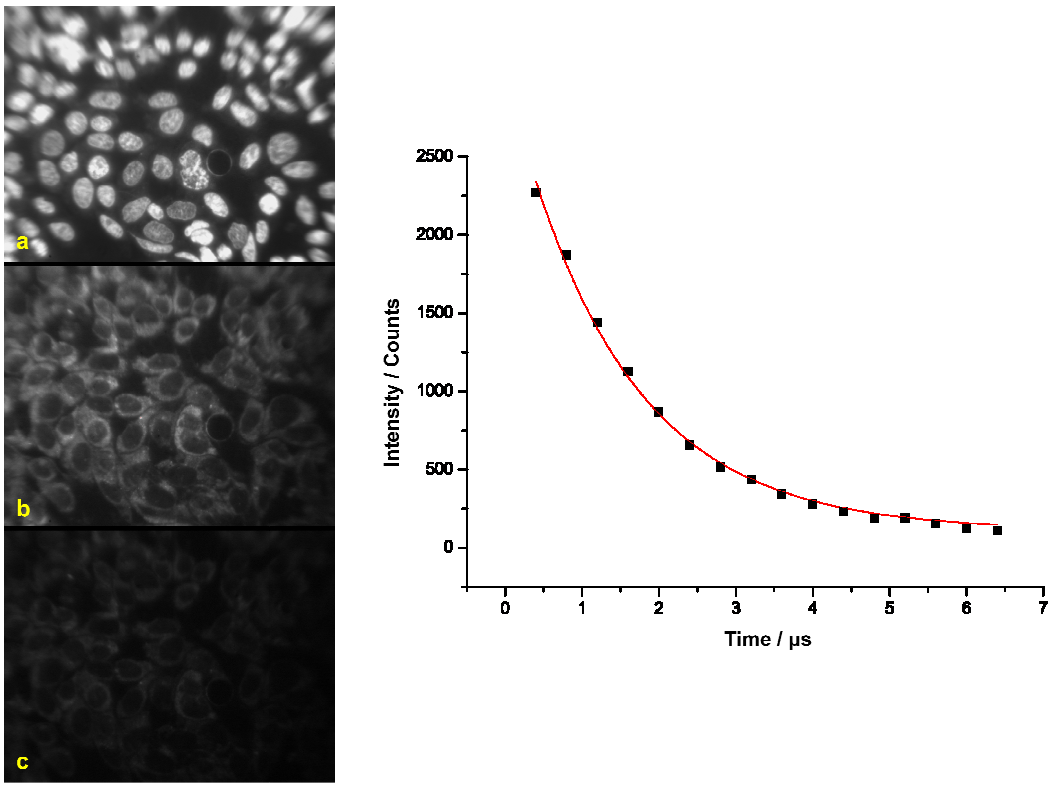

Figure 39: Left: fluorescence microscopy images of live CHO cells co-stained with [Ir(2)] (10 µM, 1 h) and Hoechst (350 nM, 5 min), taken at various time delays after excitation (λ_{ex} = 355 nm): a) -1 µs delay, b) 0 µs delay, and c) 1 µs delay. The time gate used was 200 ns. Right: Emission kinetic trace obtained from monitoring emission from a perinuclear region of the cells. Solid line represents monoexponential fit to the data. The lifetime determined from the decay was the same as that determined for cells dosed with [Ir(2)] only. Similar images were taken for cells dosed with other Ir(III) complexes and Hoechst.

These observations are easily rationalised. In the –ve delay image, emission is observed primarily from the fluorescent Hoechst: this must have a higher intracellular quantum yield than the Ir complexes. The term "0 µs delay image", is not quite true – the camera actually waits for ~ 5 ns after removal of the excitation pulse, before recording the image. The lifetime of Hoechst has been determined to be 3.6 ns, so during this brief waiting period, most of the emission from Hoechst will have decayed and hence its intensity will have diminished. The iridium complexes have intracellular lifetimes of the order of 1 µs, hence their emission dominates in the 0 µs delay image. Such novel experiments further demonstrate the power of the TREM technique – it is possible to selectively observe different subcellular compartments of the same sample, simply by setting a time delay between excitation and acquisition of the image.

5.5 Concluding Remarks

The majority of Pt(II) complexes that have been screened here were found to enter cells and retain their luminescence (of the few complexes which did not appear to enter cells, most contained larger, more bulky ligands, which probably hindered their entry). Uptake of complex was found to be rapid, and good quality luminescent images could be obtained after only a 5 min dosage. The complexes appear to localise in the nucleus of the cells, and in the mitochondria – it is possible to selectively image each organelle separately, by choosing the appropriate filter set. G365/FITCex and/or G365/FITCem filter sets were best for observing the blue/green emission of Pt(II) complex from the nucleus, and a G365/660-710 filter set was found to be best for observing the red emission of Pt(II) complex from the mitochondria. Cytotoxicity studies indicate that the complexes are of low toxicity, and remain non-toxic for the duration of the imaging experiments.

A selection of cyclometallated complexes of Ir(III) containing a pyridyl benzimidazole-based ligand were also examined for suitability as bio-markers in living cells. These complexes also entered the cells rapidly (within 5 min). However, the intracellular localisation was very different from the Pt(II) complexes – the Ir(III) complexes did not enter the nucleus, but instead appeared to localise in organelles based in the cytoplasm. Complexes containing only bidentate ligands gave a punctate staining pattern, similar to that observed when cells are stained with LysoTracker Red^{TM}. Complexes [Ir(6)] and $[Ir(7)]^{+}$, which also contain a terdentate ligand, appear to localise in a different cytoplasm-based organelle, with a more filamentous structure, but the identity of this organelle remains uncertain, and requires further investigation. Again, cytotoxicity studies indicate that the complexes are of low toxicity, and remain non-toxic for the duration of the imaging experiments.

Flow cytometry was used to measure cellular uptake of the luminescent complexes, by monitoring the mean luminescence intensity of a population of cells. The results show that uptake of complex increases with both dosage concentration and incubation time. The intracellular emission lifetimes have been determined using TREM. The lifetimes are approximately 1-2 μs, which confirms that the emission is due to phosphorescence and hence emanates from the organometallic complex. The suitability of the organometallic complexes for TREM has been demonstrated by monitoring the emission from cells co-dosed with an organometallic complex and a commercial

fluorophore (e.g. Hoechst). The two luminophores have similar excitation and emission parameters, but vastly different lifetimes. We have shown that it is possible to selectively image different areas of the cell based on lifetime. When an image was recorded without incorporation of a time delay, emission from the brighter organic fluorophore dominated. However, when a suitable time-delay was incorporated between removal of the excitation pulse and acquiring the image, only emission from the phosphorescent organometallic complex was observed.

The field of using organometallic complexes as bio-imaging agents is still in its infancy, and much work is required to fully understand why certain complexes target certain organelles (e.g. more detailed binding studies, further investigation into uptake mechanisms, etc.), and what overall effect such complexes have on the cell. Through such studies, it should become possible to design specific complexes to target certain areas/biomolecules, and it may be possible to design complexes of lower cytotoxicity. The results presented here give some indication of the possibilities offered by luminescent organometallic species, and it is anticipated that this area of research will grow rapidly over the next few years.

5.6 References

1. G. M. Cooper and R. E. Hausman, "The Cell a Molecular Approach", ASM Press, Washington DC, 2004, 3rd Ed.

2. R. A. Reid and R. M. Leech, "Cell Organelles", Blackie and Son Ltd., Glasgow, 1980

3. http://scienceblogs.com/clock/upload/2006/11/a2%2520animal%2520cell.png&imgrefurl=http://scienceblogs.com/clock/2006/11/cell_structure.php&usg=__kaQVgRvoF2p_Bg4s-uYopuSSGBc=&h=331&w=400&sz=137&hl=en&start=3&um=1&itbs=1&tbnid=rIEwZDw7ry8O8M:&tbnh=103&tbnw=124&prev=/images%3Fq%3Dthe%2Beukaryotic%2Bcell%26um%3D1%26hl%3Den%26sa%3DX%26tbs%3Disch:1

4. http://www.fluorescence.com/images/tutorial/dichro2.gif&imgrefurl=http://www.fluorescence.com/tutorial/fm-optic.htm&usg=__SDnkftrHuUyKb8nzGDbWYR3vy1o=&h=314&w=268&sz=8&hl=en&start=6&um=1&itbs=1&tbnid=8IoOnnxRCQqKTM:&tbnh=117&tbnw=100&prev=/images%3Fq%3Dfluorescence%2Bmicroscope%26um%3D1%26hl%3Den%26tbs%3Disch:1

5. http://www.physics.emory.edu/~weeks/confocal/flu-microscope3.gif&imgrefurl=http://www.physics.emory.edu/~weeks/confocal/&usg=__D3h43WL2S1irDIle13W5QtaxXRw=&h=356&w=448&sz=11&hl=en&start=6&um=1&itbs=1&tbnid=JaaAqSUHhO0F5M:&tbnh=101&tbnw=127&prev=/images%3Fq%3Dconfocal%2Bfluorescence%2Bmicroscope%26um%3D1%26hl%3Den%26tbs%3Disch:1

6. S. Hamada and S. Fujita, *Histochemistry*, 1983, **79**, 219 – 226

7. W. D. Wilson, F. A. Tanious, H. J. Barton, R. L. Jones, K. Fox, R. L. Wydra and L. Strekowski, *Biochem.*, 1990, 8452 – 8461

8. W. Pendergrass, N. Wolf and M. Poot, *Cytometry A*, 2004, **61A**, 162 – 169

9. M. Poot, Y-Z. Zhang, J. A. Krämer, K. S. Wells, L. L. Jones, D. K. Hanzel, A. G. Lugade, V. L. Singer and R. P. Haughland, *J. Hist. Cyt.*, 1996, **44(12)**, 1363 – 1372

10. R. G. W. Anderson and L. Orci, *J. Cell. Biol.*, 1988, **106**, 539 – 543

11. X. Michalet, F. F. Pinaud, L. A. Bentolila, J. M. Tsay, S. Doose, J. J. Li, G. Sundaresan, A. M. Wu, S. S. Gambhir and S. Weiss, *Science*, 2005, **307(5709)**, 538-544

12. http://www.bk.tudelft.nl/live/pagina.jsp?id=5550e07d-ec54-4f77-bcf0-5736863ef4b8&lang=en

13. X. Gao, L. Yang, J. A. Petros, F. F. Marshall, J. W. Simons and S. Nie, *Current Opinion in Biotechnology*, 2005, **16**, 63-72

14. X. Gao, Y. Cui, R. M. Levenson, L. W. K. Chung and S. Nie, *Nature Biotechnology*, 2004, **22(8)**, 969-976

15. R. A. Poole, C. P. Montgomery, E. J. New, A. Congreve, D. Parker and M. Botta, *Org. Biomol. Chem.*, 2007, **5**, 2055 – 2062

16. S. Pandya, J. Yu and D. Parker, *Dalton Trans.*, 2006, 2757 – 2766

17. C. P. Montgomery, D. Parker and L. Lamarque, *Chem. Commun.*, 2007, 3841 – 3843

18. C. P. Montgomery, B. S. Murray, E. J. New, R. Pal and D. Parker, *Acc. Chem. Res.*, 2009, **42**, 925

19. S. W. Botchway, M. Charnley, J. W. Haycock, A. W. Parker, D. L. Rochester, J. A. Weinstein and J. A. G. Williams, *PNAS*, 2008, **105(42)**, 16071-16076

20. C-K. Koo, K-L. Wong, C. W-Y. Man, Y-W. Lam, L. K-Y. So, H-L. Tam, S-W. Tsao, K-W. Cheah, K-C. Lau, Y-Y. Yang, J-C. Chen and M. H-W. Lam, *Inorg. Chem.*, 2009, **48**, 872-878

21. V. Fernández-Moreira, F. L. Thorp-Greenwood and M. P. Coogan, *Chem. Commun.*, 2010, **46**, 186 - 202

22. M. Yu, Q. Zhao, L. Shi, F. Li, Z. Zhou, H. Yang, T. Yi and C. Huang, *Chem.Commun.*, 2008, 2115-2117

23. M. E. Jiménez-Hernández, G. Orellana, F. Montero and M. T. Portolés, *Photochem. And Photobiol.*, 2000, **72(1)**, 28-34

24. K. K.-W. Lo, M.-W. Louie, K.-S. Sze and J. S.-Y. Lau, *Inorg. Chem.*, 2008, **47**, 602

25. C. A. Puckett and J. K. Barton, *J. Am. Chem. Soc*, 2007, **129**, 46

26. K. K.-W. Lo, T. K.-M. Lee, J. S.-Y. Lau, W.-L. Poon and S.-H. Cheng, *Inorg. Chem.*, 2008, **47**, 200

27. K. A. Stephenson, S. R. Banerjee, T. Besenger, O. O. Sogbein, M. K. Levadala, N. McFarlane, J. A. Lemon, D. R. Boreham, K. P. Maresca, J. D. Brennan, J. W. Babich, J. Zubieta and J. F. Valliant, *J. Am. Chem. Soc.*, 2004, **126**, 8598

28. H. D. Soule, J. Vazquez, A. Long, S. Albert and M. Brennan, *J. Natl. Cancer Inst.*, 1973, **51**, 1409

29. A. J. Amroso, M. P. Coogan, J. E. Dunne, V. Fernández-Moreira, J. B. Hess, A. J. Hayes, D. Lloyd, C. Millet, S. J. A. Pope and C. Williams, *Chem. Commun.*, 2007, 3066 - 3068

30. K. W. Jennette, S. J. Lippard, G. A. Vassiliades and W. R. Bauer, *Proc. Nat. Acad. Sci. USA*, 1974, **71(10)**, 3839-3843

31. K. G. Strothkamp and S. J. Lippard, *Proc. Natl. Acad. Sci. USA*, 1976, **73(8)**, 2536-2540

32. I. Eryazici, C. N., C. N. Moorefield, G. R. Newkome, *Chem. Rev.*, 2008, **108**, 1834 – 1895

33. K. W. Jennette, J. T. Gill, J. A. Sadownick and S. J. Lippard, *J. Am. Chem. Soc.*, 1976, **98(20)**, 6159-6168

34. W. D. McFadyen, L. P. G. Wakelin, I. A. G. Roos and B. L. Hillcoat, *Biochem. J.*, 1987, **242**, 177-183

35. M. Cusumano, M. L. Di Pietro and A. Giannetto, *Inorg. Chem.*, 1999, **38**, 1754-1758

36. A. H. Wang, J. Nathans, M. G. van der, J. H. Van Boom and A. Rich, *Nature*, 1978, **276**, 471

37. M. Howe-Grant, K. C. Wu, W. R. Bauer and S. J. Lippard, *Biochemistry*, 1976, **15(19)**¸ 4339-4346

38. H. M. Brothers II and N. M. Kostić, *Inorg. Chem.*, 1988, **27(10)**, 1761-1767

39. E. M. A. Ratilla, B. K. Scott, M. S. Moxness and N. M. Kostić, *Inorg. Chem.*, 1990, **29**, 918-926

40. A. Pompella, A. Visvikis, A. Paolicchi, V. De Tata and A. F. Casini, *Biochem. Pharmacol.*, 2003, **66(8)**, 1499 – 1503

41. http://www.drugs.com/pdr/immunocal-powder-sachets.html

42. A. Muscella, N. Calabriso, S. A. De Pascali, L. Urso, A. Ciccarese, F. P. Fanizzi, D. Migoni and S. Marsigliante, *Biochem.Pharmacol.*, 2007, **74**, 28-40

43. B. Rosenberg, L. Vancamp and T. Krigas, Nature, 1965, **205**, 698-699

44. C. Molenaar, J-M. Teuben, R. J. Heetebrij, H. J. Tanke and J. Reedijik, *J. Biol. Inorg. Chem.*, 2000, **5**, 655-665

45. G. V. Kalayda, G. Zhang, T. Abraham, H. J. Tanke and J. Reedjik, *J. Med. Chem.*, 2005, **48**¸5191-5202

46. M. Lu, J. C. Chang and B. L. Bergquist, *J. Inorg. Biochem.*, 1991, **42**, 231-235

47. I. H. L. Hamelers, E. Van Loenen, R. W. H. M. Staffhorst, B. De Kruijff and A. I. P. M. De Kroon, *Mol. Cancer Ther.*, 2006, **5(8)**, 2007-2012

48. M. Akaboshi, K. Kawai, Y. Tanaka, J. Takada and T. Sumino, *J.Radioanal. Nuc. Chem.*, 1999, **2**, 405-409

49. C. Wu, B. Bull, K. Christensen and J. McNeill, *Angew. Chem.*, 2009, **48**, 2741 – 2745

50. C. O'Donovan, J. Hynes, D. Yashunski and D. B. Papkovsky, *J. Mater. Chem.*, 2005, **15**, 2946 - 2951

51. C-K. Koo, L. K-Y. So, K-L. Wong, Y-W. Lam, M. H. W. Lam, K-W. Cheah, C. C-W. Cheng and W-M. Kwok, *Chem. Eur. J.*, 2010, **16(13)**, 3942-3950

52. C-K. Koo, K-L. Wong, C. W-Y. Man, H-L. Tam ,S-W. Tsao, K-W. Cheah and M. H-W. Lam, *Inorg. Chem.*, 2009, **48**, 7501-7503

53. A. Beeby, S. W. Botchway, I. M. Clarkson, S. Faulkner, A. W. Parker, D. Parker and J. A. G. Williams, *J. Photochem. Photobiol. B*, 2000, **57**, 83-89

54. K. Suhling, P. M. W. French and D. Phillips, *Photochem. Photobiol. Sci.*, 2005, **4**, 13-22

55. H. C. Gerritsen, R. Sanders, A. Draaijer, C. Ince and Y. K. Levine, *J. Fluoresc.*, 1997, **7(1)**, 11-16

56. R. Sanders, A. Draailer, H. C. Gerritsen, P. M. Houpt and Y. K. Levine, *Anal. Biochem.*,1995, **227**, 302-308

57. H-J. Lin, P. Herman and J. R. Lakowicz, *Cytometry*, 2003, **52A**, 77-89

58. R. R. De Haas, R. P. M. van Gijlswijk, E. B. van der Tol, H. J. M. A. A. Zijlmans, T. Bakker-Schut, J. Bonnet, N. P. Verwoerd and H. J. Tanke, *J. Histochem. Cytochem.*, 1997, **45(9)**, 1279-1292

59. R. R. De Haas, R. P. M. van Gijlswijk, E. B. van der Tol, J. Veuskens, H. E. van Gijssel, R. B. Tijdens, J. Bonnet, N. P. Verwoerd and H. J. Tanke, *J. Histochem. Cytochem.*, 1999, **47(2)**, 183-196

60. K. Y. Zhang and K. K-W. Lo, *Inorg. Chem.*, 2009, **48**, 6011-6025

61. J. S-Y. Lau, P-K. Lee, K. H-K. Tsang, C. H-C. Ng, Y-W. Lam, S-H. Cheng and

K. K-W. Lo, *Inorg. Chem.*, 2009, **48**, 708-718

62. K. K-W. Lo, P-K. Lee and J. S-Y. Lau, *Organometallics*, 2008, **27**, 2998-3006

63. S. Kessner, A. Krause, U. Rothe and G. Bendas, *Biochimica et Biophysica Acta*, 2001, **1514**, 177-190

64. X-J. Liang, D-W. Shen, K. G. Chen, S. M. Wincovitch, S. H. Garfield and M. M. Gottesman, *J. Cell. Physiology*, 2005, **202**, 635-641

65. A. L. Givan, "Flow Cytometry First Principles", Wiley-Liss, New York, 1992

66. I. A. Khalil, K. Kogure, H. Akita and H. Harashima, *Pharm. Rev.*, 2006, **58(1)**, 32-45

67. http://www.cbu.edu/~seisen/CellCycle_files/image001.gif

68. K. L. Haas and K. J. Franz, *Chem. Rev.*, 2009, **109**, 4921-4960

69. A. Muscella, N. Calabriso, S. A. De Pascali, L. Urso, A. Ciccarese, F. P. Fanizzi, D. Migoni and S. Marsigliante, *Biochem.Pharmacol.*, 2007, **74**, 28-40

70. S. A. De Pascali, D. Migoni, P. Papadia, A. Muscella, S. Marsigliante, A. Ciccarese and F. P. Fanizzi, *Dalton Trans.*, 2006, 5077-5087

71. T. Mosmann, *J. Immunol. Methods*, 1983, **65**, 55-63

72. J. Carmichael, W. G. DeGraff, A. F. Gazdar, J. D. Minna and J. B. Mitchell, *Cancer Res.*, 1987, **47(4)**¸ 936-942

73. M. D. Hall, S. Amjadi, M. Zhang, P. J. Beale and T. W. Hambley, *J. Inorg. Biochem.*, 2004, **98**, 1614-1624

74. P. Wu, E. L-M. Wong, D-L. Ma, G. S-M. Tong, K-M. Ng and C-M. Che, *Chem. Eur. J.*, 2009, **15**, 3652 – 3656

75. W. D. McFadyen, L. P. G. Wakelin, I. A. G. Roos and B. L. Hillcoat, *Biochem. J.*, 1986, **238**, 757-763

76. L. P. G. Wakelin, W. D. McFayden, A. Walpole and I. A. G. Roos, *Biochem. J.*, 1984, **222**, 203-215

77. www.microscopyu.com/.../fluorescence/cells.html

CHAPTER SIX:

Experimental Methods

6.1 Materials and Equipment

6.1.1 General Experimental

The following solvents: DCM, MeOH, DMSO, EtOAc and EtOH, were obtained as analytical reagent grade, and were used as supplied. Acetonitrile was obtained as HPLC grade. Dry DMSO was obtained from Aldrich and stored under nitrogen. Other dry, air-free solvents (THF, hexane, toluene and ether) were obtained by passing the HPLC-grade solvent through a Pure Solv 400 solvent purification system. All other solvents were laboratory grade, and were used as supplied. Water was purified using the "Purite$_{STILL}$ Plus" system and had a conductivity of 0.04 S cm^{-1}. All reagents were used as supplied by commercial sources unless otherwise stated in the methods section. Reactions requiring an inert atmosphere were carried out using Schlenk-line techniques under an atmosphere of dry nitrogen.

Thin layer chromatography was carried out using neutral aluminium oxide plates (Merck Art 5550) or silica plates (Merck Art 5554), both of which are fluorescent under short-range UV irradiation (254 nm). Column chromatography was performed using neutral alumina (Merck Aluminium Oxide 90, activity I, 70-230 mesh) or silica (Merck Silica Gel 60, 230-400 mesh)

6.1.2 Characterisation Techniques

^{1}H NMR spectra were recorded in the appropriate solvents on Mercury-400, Varian-200, Varian-500 or Huple-VNMRS-700 MHz instruments. ^{13}C spectra were recorded at 126 MHz on the Varian Inova-500 or at 176 MHz on the Huple-VNMRS-700 MHz. ^{19}F NMR spectra were recorded at 376 MHz on the Mercury-400, at 470 MHz on the Varian-500, or at 188 MHz on the Varian-200. Chemical shifts are quoted relative to the appropriate protio-solvent resonance. All J values are given in Hz, and are quoted to the nearest 0.5 Hz.

Low-resolution electrospray mass spectra (ES) were recorded using a Thermo Finnigan LTQ FT mass spectrometer, with methanol as the carrier solvent. Low resolution ASAP mass spectra were recorded on a Xevo QToF mass spectrometer (Waters, Ltd, UK) and MALDI on an Autoflex II ToF/ToF MS (Bruker Daltonik, GmbH), using trans-2-[3,4-

tert-butyl phenyl]-2-methyl-2-propenylidene]malonitrile (dctb) as the matrix element. Accurate ES mass spectra were obtained using either a LCT Premier XE mass spectrometer (Waters Ltd, UK) or a LTQ FT mass spectrometer (Thermo-Finnigan Corporation). Accurate MALDI mass spectra were obtained using a LTQ FT mass spectrometer (Thermo-Finnigan Corporation), and accurate ASAP spectra were recorded with a Xevo QToF mass spectrometer (Waters, Ltd, UK). High resolution electron impact (EI) mass spectrometry was performed at the EPSRC National Mass Spectrometry Centre, Swansea.

Elemental analysis was performed using an Exeter Analytical E-440 elemental analyser. Melting points were determined on a Gallenkamp 889339 capillary melting point apparatus.

Crystallographic data for all reported structures were collected at 120 K. X-ray diffraction data for [PtL^1Cl_3] and [$PtL^{13}Cl$] were collected on an Oxford Diffraction Gemini S Ultra diffractometer using graphite monochromated Mo *Kα* radiation (λ = 0.71073 Å). The data were collected and integrated using Oxford Diffraction CrysAlis software.[1] X-ray diffraction data for [$PtL^{11}Cl$] was collected at 120 K on a Nonius Kappa CCD diffractometer using graphite monochromated Mo *Kα* radiation (λ = 0.71073 Å); data were collected using the strategy calculated by the *COLLECT* software (Nonius, 1999)[2] and integrated using *HKL Scalepack*.[3] The remaining X-ray diffraction data were collected at 120 K on a Bruker APEX CCD diffractometer. These data were collected using the SMART software, with subsequent data processing carried out in SAINT.[4] All of the structures were solved by direct methods in SHELXS-97 and refined by full matrix least squares on F^2 in SHELXL-97.[5]

6.1.3 Photophysical Characterisation

UV/Vis absorption spectra were measured using a Biotek Instruments UVIKON XS spectrometer operating with LabPower software. The sample was held in a quartz cuvette of 1 cm path length, and spectra were recorded against a reference of pure solvent held in a matched cuvette. Extinction coefficients were determined using a dilution method, and graphical application of the Beer-Lambert law:

$$A(\lambda) = \varepsilon(\lambda)cl \qquad Eqn.1$$

where A(λ) is the absorbance at a specified wavelength, c is the concentration of the absorbing species (mol dm^{-3}) , l is the path length (cm) and ε is the extinction coefficient (mol^{-1} dm^3 cm^{-1}).

Solution-based emission and excitation spectra were acquired on a Jobin Yvon-Spex Fluoromax-2 spectrometer. All samples were contained within quartz cuvettes of 1 cm path length. Samples that were to be measured in the absence of air were placed in quartz cuvettes that were modified with appropriate glassware to allow connection to a high vacuum line. To remove air prior to the measurement, the sample was degassed within the cuvette by three freeze-pump-thaw cycles. Emission was recorded at 90˚ to the excitation source, and appropriate filters were used when required to remove second order peaks. All emission spectra were corrected after acquisition for dark count and for the spectral response of the detector. Excitation spectra were automatically corrected upon measurement for lamp output, through use of a beam splitter which directs 8% of the excitation light to a reference photodiode.

The quantum yields were determined relative to a reference solution containing 2,6-di(2-pyridyl)benzene-1-platinum(II) chloride ([PtL^1Cl]). The quantum yield of this complex is well established as 0.60 in degassed DCM.[6] To measure the quantum yield, a sample of complex in DCM was prepared so that the absorbance at the chosen excitation wavelength was below 0.1, to minimise inner filter effects. A solution containing [PtL^1Cl] with similar absorbance intensity was prepared, and the emission spectra of the complex and reference were measured under identical conditions (i.e. same excitation wavelength, same slit size). The quantum yield was determined from the absorbance and emission data by use of equation 2:

$$\Phi = \Phi_{ST}\left(\frac{Int}{Int_{ST}}\right)\left(\frac{A_{ST}}{A}\right)\left(\frac{n^2}{n^2{}_{ST}}\right) \qquad Eqn.\,2$$

where Φ is the quantum yield of the sample, Φ_{ST} is the quantum yield of the standard, Int and Int_{ST} are the overall intensities of the sample and standard respectively (obtained from integration of the respective emission spectrum), A and A_{ST} are the absorbance of the sample and standard at the chosen excitation wavelength, and n^2 and $n^2{}_{ST}$ are the refractive indices of the solvents (so not required here). The estimated uncertainty in the reported quantum yields is ± 20 %.

Lifetimes were determined using an Edinburgh Instruments OB 920 fluorimeter. Luminescence lifetimes of the complexes up to approximately 10 μs were measured by time-correlated single-photon counting method, using an EPL-375 pulsed-diode laser as excitation source (374 nm excitation, pulse length of 60 ps). The laser repetition rate was selected so that the pulse period was at least 5-10 times longer than the complex lifetime. The emission was detected at 90˚to the excitation source, after passage through a monochromator using a Peltier-cooled R928. Lifetimes in excess of 10 μs were measured by multichannel scaling, and a xenon flash lamp was used as the excitation source (excitation wavelength matched to that of complex, pulse length of 2 μs).

The lifetimes were obtained by least-squares fitting to a monoexponential decay of the form

$$I_t = I_0 \exp\left(-t/\tau\right)$$

and goodness of fit was assessed from the residuals.

Low temperature (77 K) experiments were performed using a glass vacuum cold finger apparatus built in house. A small amount of sample was dissolved in a 2:2:1 solvent mix of ether/isopentane/ethanol (EPA), and placed into a glass tube. The cold finger was filled with liquid nitrogen and the tube containing the sample was inserted. EPA forms an amorphous glass upon freezing, which has a very low propensity for cracking.

For investigations at cryogenic temperatures, complexes [PtL^{1}Cl], [PtL^{1}Br] and [PtL^{1}I] were dissolved in n-octane, and [PtL^{2}Cl] was dissolved in n-decane, at concentrations of ≈ 10^{-5} M. The measurements were carried out on a He cryostat (Cryovac Konti Cryostat IT) in which the He gas flow, He pressure, and heating were controlled. For magnetic field experiments, an Oxford Instruments MD10 cryostat equipped with a 12 T magnet was used. A pulsed Nd:YAG laser (IB Laser Inc., DiNY pQ 02) with a pulse width of about 7 ns was used as the excitation source for emission spectra and lifetime measurements, using the third harmonic at 355 nm (28170 cm^{-1}). For measurements of excitation spectra, a pulsed dye laser (Lambdaphysik Scanmate 2C) with Coumarin 102 was operated. The spectra were recorded with an intensified CCD camera (Princeton PIMAX) or a cooled photomultiplier (RCA C7164R) attached to a triple spectrograph (S&I Trivista TR 555). Time-resolved emission spectra were recorded with a gated photon counter (Stanford Research Systems, Model SR 400). Decay times were

registered using a FAST Comtec multichannel scaler PCI card with a time resolution of 250 ps.[7]

Solid state emission was recorded using the Edinburgh Instruments OB 920 fluorimeter, and data was corrected by an in-built calibration curve.

Cyclic voltammetry was carried out using a μAutolab Type III potentiostat with computer control, using GPES Manager software. A three electrode set-up was employed, consisting of a glassy carbon working electrode (GCE), a platinum flag counter electrode, and a platinum wire pseudo-reference electrode. The complex (~ 1 x 10^{-3} M) was dissolved in a solution of DMSO containing a tetrabutylammonium hexafluorophosphate (0.1 M) background electrolyte. The solution was stirred and purged with nitrogen prior to the measurement. All measurements reported are reported relative to a Fc/Fc^{+} reference.

6.1.4 Cellular Studies

Two cell lines were chosen for cellular studies: Chinese hamster ovary (CHO) and mouse skin fibroblast (NIH 3T3). Both are adherent cell lines, and were maintained in exponential growth as monolayers in appropriate medium: F-12 (Ham) and Dulbecco's Modified Eagle Medium (DMEM) respectively. For each cell line, the medium was supplemented with 10% foetal bovine serum (FBS) and 1% penicillin and streptomycin. To prevent overcrowding and build up of toxins (both of which could cause uncharacteristic behaviour of the cells) the cells were sub-cultured every three-to-four days.

Sub-culturing was performed as follows: Sterile solutions of trypsin, PBS and fresh medium were warmed in a water bath to 37˚C over 30 min. The culture flask containing the cells was removed from the incubator, and the old medium was removed. Cells were rinsed with sterile phosphate-buffered saline (PBS, pH 7.5) (6 mL), then incubated with trypsin (1.5 mL) for 3 min. During this time, the cells became detached from the surface of the flask. After gentle tapping of the flask, the trypsin suspension was transferred to a centrifuge tube, along with a washing with fresh medium (7 mL). The sample was spun at 1500 rpm for 3 min, during which the cells settled to the bottom of the tube. The trypsin/medium solution was poured off, and cells were re-suspended in fresh medium

(stock solution, 4 mL). Some of these cells (500-600 µL) were transferred to a fresh culture flask containing fresh medium (10 mL), and replaced in the incubator. If experiments were to be performed, cells were also transferred to the appropriate microplates at this stage. For cytotoxicity experiments, which require a known number of cells, cell counting was performed using a haemocytometer.

6.1.4.1 Microscopy

Cells were seeded in twelve-well plates containing glass coverslips, and allowed to grow to 60-80% confluence in an incubator set at 37˚C and 5% CO_2. At this stage, the old medium was removed and replaced with fresh medium containing the appropriate dosages of complex etc. Following incubation, the coverslips were removed and washed with sterile PBS, then mounted on a microscope slide and held in place with clear nail varnish. The cells were imaged straight away. Epifluorescence images were taken using a Zeiss Axiovert 200M epifluorescence microscope with a digital camera, and were processed using the Zeiss Axiovision software. A x 40 oil-immersion objective lense was used to visualize the image. The filter sets and dichroic mirrors were chosen to match the solution based photophysics of the complexes. G365 filters (Zeiss) were employed for excitation of all complexes. For the Pt(II) complexes, FITCex (450-500 nm) or FITCem (515-565 nm) filters were used to monitor blue-green emission and a 660-710 (Comar) filter was used to monitor the lower energy emission component. For Ir(III) complexes, the FITCem filter was used to monitor emission.

6.1.4.2 Cytotoxicity

MTT Method

A suspension containing approximately 1 x 10^6 NIH-3T3 cells in DMEM media (10 mL) was prepared from the 4 mL stock solution (prepared during sub-culturing). This was transferred to a 96-well microplate in 100 µL aliquots (i.e. approximate number of cells per well = 1 x 10^4), and the cells were incubated at 37˚C and 5% CO_2 overnight, during which time adhesion occurred. The following morning, cells were dosed (in

triplicate) with a selection of concentrations of the complex under study, and incubated for a further 24 h. The dosing media was then removed, cells were rinsed with sterile PBS (pH 7.5, 100 µL), and fresh medium was added (100 µL). 3-(4,5-dimethylthiazol-2-yl)-2,5-diphenyltetrazolium bromide (MTT, 1.0 mM)[8] was added to each well, and the cells were incubated for another 4 h. After this time, the culture medium was removed, and DMSO (150 µL) was added to each well. The 96-well plate was then shaken for 20 s, and the absorbance of each well at 541 nm was measured against a "blank" (a microplate containing only 150 µL DMSO per well) that had been recorded prior to the measurement (absorbance was measured using an Analytic Jena FLASHScan 530, using WinFLASH version 1.5 software). To get the percentage of live cells per concentration, the average absorbance for a given concentration was divided by the average absorbance of wells containing un-dosed cells.

Trypan-blue Method

Approximately 5 x 10^4 NIH-3T3 cells in DMEM (500 µL) were seeded into each well of two 12-well microplates. The cells were incubated at 37˚C and 5% CO_2 overnight, during which time adhesion to the base of the microplate occurred. The following day, cells were dosed (in duplicate) with a selection of concentrations of the complex under study, and incubated for a further 1 h. The media was removed, the cells were rinsed with PBS (500 µL), then incubated with trypsin (100 µl) for 3 min. The cells were transferred to a centrifuge tube. Media (500 µl) was used to rinse the well, and this washing was also transferred to the centrifuge tube. The sample was spun at 1500 r.p.m. for 3 min, during which the cells settled to the bottom of the tube. The solution was decanted, and sterile PBS (100 µL) was added. Trypan blue was then added (100 µL), and the mixture was left for 3-5 min. The number of dead and live cells was then counted using a haemocytometer (dead cells = blue, live cells = colourless). This was repeated four times.

6.1.4.3 Flow Cytometry

Flow cytometric analysis was conducted with a DakoCytomation Inc. MoFlo multi-laser flow cytometer (Fort Collins, CO, USA) operating at 60 Psi with a 70 µM nozzle.

Samples were interrogated with a 100 mW 488 nm solid state laser and a UV-laser operating at 50 mW. Luminescence signals were detected through interference filters: for Pt complexes, a 450/65 bandpass interference filter was selected, and for Ir complexes a 530/40 bandpass filter was used. Fluorescence signals were collected in the logarithmic mode. The data was analysed using Summit v4.3 (Beckman Coulter) software.

For flow cytometric analysis, cells were seeded in twelve-well plates and grown to 70-80% confluence. The old medium was then replaced with fresh media containing the desired complex dosage, and cells were incubated for set time lengths. After incubation, cells were detached from the plate by incubation with trypsin (200 μL) for 3 min at 37˚ C. This cell suspension was placed in a centrifuge tube. The well was washed with media (1 mL), this washing was added to the centrifuge tube, and the sample was spun at 1500 rpm for 3 min. The supernatant was removed from the cell pellet, which was re-suspended in sterile PBS (2 ml) and placed on ice. The cells were analysed by flow cytometry as soon as possible. Immediately prior to the analysis, the cell suspension was filtered through a 40 μM filter to remove any cell clumps.

6.1.4.4 Time Resolved Emission Imaging

Time-resolved microscopy was performed based upon time-gated detection as follows. The excitation source was a Q-switched Nd:YAG laser (UV FQ, Elforlight LtD) and its output is optical pulses at 355 nm through internal third harmonic generation with a temporal width of ~5 ns (FWHM). The microscope was a Leica 135 axiovert epifluorescence microscope. The laser excitation pulses were fed into the microscope through a beam expander and focused onto the sample using long working distances objective lenses (Zeiss LD plan neofluar, 10X, 40X or 63X). The photoluminescence was detected using a combination of dichroic mirrors and band pass or long pass filters. The photoluminescence signal was collected using a time-gated CCD camera (752 by 582 pixels), (Imagex nanoCCD, Photonics Research Systems). In the excitation-detection sequence, the CCD camera control unit triggered the laser with TTL pulse and the photoluminescence signals were acquired with a suitable delay and time gate combination.

The CCD camera system has 16 different time banks. Time-resolved photoluminescence microscopy decays can therefore be recorded using a constant gate with 16 different delays. These decays were subsequently analysed and fitted to model of exponential decay of the photoluminescence,

$$I(t) = I_o e^{-\frac{t}{\tau}}$$

where I_0 is the amplitude and the τ is the photoluminescence lifetime.

6.2 Synthesis of Ligands and Ligand Precursors

The following compounds were prepared by literature procedures: 1,3-di(2-pyridyl)benzene (HL^1) and 2,6-di(2-pyridyl)benzene platinum(II) chloride ([Pt(L^1)Cl]),[9] 2-tri-n-butylstannyl pyridine,[10] 1,3-Dibromo-4,6-difluorobenzene,[11,12] 1,3-dibromo-5-nitrobenzene,[13] 4-methyl-2-tri-n-butylstannylpyridine,[14] 2-bromo-4-dimethylaminopyridine,[15] 2-bromopyridine-N-oxide, 2-bromo-4-nitropyridine-N-oxide, 2-bromo-4-nitrropyridine and 2-bromo-4-methoxypyridine.[16] Synthetic details of all other ligands, ligand precursors and complexes are given in the following sections.

6.2.1 General Procedures

Some standard procedures were used frequently in the synthesis of ligands and ligand precursors. The general details of such reactions will be given here to avoid repetition throughout the chapter.

6.2.1.1 General Suzuki-Miyaura Procedure

Benzene-1,3-diboronic acid (or a substituted benzene 1,3-diboronic ester derivative) and an n-substituted-2-bromopyridine were placed in a Schlenk tube and dissolved in dimethoxyethane (DME). A solution of aqueous 1M Na_2CO_3 was then added, a condenser was inserted and the mixture was degassed by five freeze-pump-thaw cycles. The solution was then subjected to a very high flow of nitrogen. The catalyst,

tetrakis(triphenylphosphine) palladium, $Pd(PPh_3)_4$, was added quickly as a solid. The mixture was heated at 80 °C for two days under nitrogen. After cooling to room temperature, the crude Suzuki product was washed with water (2 x 15 mL) and extracted into DCM (3 x 25 mL). The DCM solution was dried with $MgSO_4$, filtered and the solvent was removed *in vacuo*. The product was purified with column chromatography.

6.2.1.2 General Stille Procedure

A 2-tri-n-butylstannyl pyridine derivative, a 1,3-dibromobenzene derivative, bis(triphenylphosphine) palladium dichloride $\{Pd(PPh_3)_2Cl_2\}$, and LiCl were placed into a Schlenk tube. Toluene was added and a condenser was fitted. The mixture was degassed by five freeze-pump-thaw cycles, then placed under nitrogen and heated at 120˚C for three days. On cooling to room temperature, a saturated aqueous solution of KF (10 mL) was added, and the mixture was stirred for 30 min. The precipitated solid was removed by filtration and washed with water (2 x 15 mL) and toluene (3 x 30 mL). Aqueous $NaHCO_3$ (10%, 50 mL) was added to the filtrate, which was then extracted into DCM (2 x 50 mL). The DCM portion was dried with $MgSO_4$, filtered and the solvent was removed *in vacuo*. The crude product was purified with column chromatography.

6.2.1.3 Stannylation of 2-bromopyridines via lithium-halogen exchange

The appropriate 2-bromopyridine was placed in a 200 mL two-necked round-bottomed flask fitted with a condenser and suba seal. Dry THF (25 mL) was added to this under nitrogen and the reaction was cooled to -78 °C. nBuLi (1.1 equiv) was added slowly (over 20 min) and the reaction was stirred at -78 °C for a further 90 min. Tributyltin chloride (Bu_3SnCl, 1.2 equiv) was then added under nitrogen, and the mixture was stirred at -78 °C for a further 2 h, then allowed to warm gradually to room temperature. Water (15 mL) was added to hydrolyse any remaining n-BuLi – this was stirred for 10 min. The mixture was extracted into diethyl ether (3 x 30 mL), dried over $MgSO_4$, then the solvent was removed *in vacuo*. ^1H NMR was used to assess the purity of the stannane, and the crude product was used directly in Stille reactions.

6.2.1.4 Stannylation of 4-R-pyridines via ortho-directed lithiation

A two-necked round bottomed flask (250 mL) was fitted with a suba seal and a condenser. The flask was attached to a nitrogen line via the condenser and purged with nitrogen. A solution of 2-(dimethylamino)ethanol was added to the flask under nitrogen. Dry hexane (25mL) was also added under nitrogen. The mixture was cooled to 0 °C, and n-BuLi was added dropwise over 20 min. The mixture was left stirring at 0 °C for a further 15 min. The 4-substituted pyridine in hexane (5 mL) was added under nitrogen. The mixture was stirred at 0°C for 1 h. The mixture was then cooled to -78 °C and treated with a solution of Bu_3SnCl in THF (5 mL) under nitrogen. After stirring at -78 °C for 1h, the mixture was warmed to room temperature, then cooled to 0 °C and water (15 mL) was added. The organic layer was then extracted three times with diethyl ether (3 x 20 mL) and dried with $MgSO_4$. After filtration of the solution, the solvent was removed *in vacuo*. ^1H NMR was used to estimate the purity of the stannane, and the crude product was used directly in Stille reactions.

6.2.1.5 Double Borylation of functionalised 1,3-dibromobenzenes

Dry DMSO (5 mL) was degassed in a 2-necked round bottom flask (left open to vacuum for 30 min) then placed under nitrogen. The appropriate 1,3-dibromobenzene, bispinacolatodiboron (B_2pin_2), $Pd(dppf)Cl_2$ and KOAc were placed in a Schlenk tube, degassed (open to vacuum then back-filled with nitrogen x 3) and put under nitrogen. The dry DMSO was transferred across under nitrogen, and the mixture was heated at 85˚C for 18 h. On cooling to room temperature, the crude was washed with a mixture of 50:50 EtOAc and water (50 mL), and the organic phase was collected. This was washed with water (2 x 30 mL) and brine (2 x 50 mL), dried with $MgSO_4$, and the solvent was removed *in vacuo*. The crude product was purified by column chromatography (an iodine tank was used to visualise the TLC plate).

6.2.1.6 Williamson Ether Synthesis

Dry K_2CO_3 and Cs_2CO_3 were placed in a Schlenk with stirrer bar and dissolved in CH_3CN. The bromo-electrophile and oxygen-based nucleophile were added, and the

reaction was placed under nitrogen. The mixture was heated at 80˚C for four days. The reaction was allowed to cool to room temperature, then the mixture was washed with brine (2 x 20 mL) and extracted into DCM (3 x 30 mL). After drying with $MgSO_4$ and filtering, the solvent was removed *in vacuo*. The crude product was purified by column chromatography.

6.2.2 Synthetic Details and Characterisation

HL^2: 1,3-di(2-pyridyl)-4,6-difluorobenzene

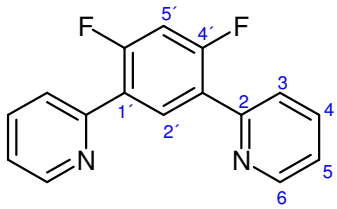

The ligand was prepared via the Stille methodology. Reagents: 2-Tri-n-butylstannylpyridine (4.17 g, assumed 85% pure, 9.6 x 10^{-3} mol), 1,3-dibromo-4,6-difluorobenzene (1.09 g, 4.0 x 10^{-3} mol), $Pd(PPh_3)_2Cl_2$ (0.10 g, 1.5 x 10^{-4} mol) and LiCl (1.24 g, 2.93 x 10^{-2} mol). Solvent: toluene (6 mL). Purification: column chromatography (silica, hexane/ether gradient elution from 100/0 to 25/75). The desired product was obtained as a pale yellow solid (0.57 g, 53%), mp = 156-158 °C, R_f 0.54 (silica, hexane/ether 25/75). ^{1}H NMR (500 MHz, $CDCl_3$) δ_H = 7.05 (1H, t, $^3J(^{19}F)$ = 11.0, $H_{5'}$), 7.28 (2H, m, H_5), 7.77 (4H, m, H_3 and H_4), 8.63 (1H, t, $^4J(^{19}F)$ = 9.5, $H_{2'}$), 8.74 (2H, dt, $J(^1H)$ = 5.0 and 1.0, H_6), ^{13}C {^{1}H} NMR (126 MHz, $CDCl_3$). δ_C = 105.0 (t, $J(^{19}F)$ = 28.0, $C_{5'}$), 123.0 (s, C_5), 124.5 (t, $J(^{19}F)$ = 5.0, C_3), 125.0 (dd, $J(^{19}F)$ = 11.0 and 5.0, $C_{1'}$), 134.0 (t, $J(^{19}F)$ = 5.0, $C_{2'}$), 136.5 (s, C_4), 150.0 (s, C_6), 153.0 (t, $J(^{19}F)$ = 1.5, C_2), 161.0 (dd, $J(^{19}F)$ = 254.5 and 12.5, $C_{4'}$). ^{19}F NMR (376 MHz, $CDCl_3$) δ_F = -113.4 (2F, t, $J(^1H)$ = 9.5). HRMS (ES^+): *m/z* 291.0707 [11%, $M+Na^+$], 269.0886 [100, $M+H^+$]; calcd for [$C_{16}H_{11}F_2N_2$], 269.0885, calcd for [$C_{16}H_{10}F_2N_2{}^{23}Na$], 291.0710. Anal. $C_{16}H_{10}F_2N_2$ (268.25): calcd C, 71.63; H, 3.76; N, 10.44; found C, 71.52; H, 3.81; N, 10.43.

HL^3: 1,3-di(2-pyridyl)-5-nitrobenzene

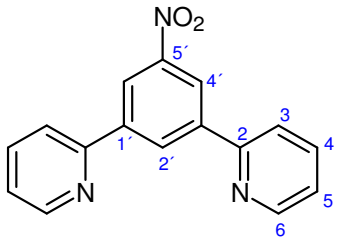

Ligand HL^3 was prepared via the Stille method. Reagents: 2-Tri-n-butylstannylpyridine (3.33 g, assumed 85% pure, 7.7 x 10^{-3} mol), 1,3-dibromo-5-nitrobenzene (0.90 g, 3.2 x 10^{-3} mol), $Pd(PPh_3)_2Cl_2$ (0.084 g, 1.2 x 10^{-4} mol) and LiCl (0.992 g, 2.34 x 10^{-2} mol). Solvent: toluene (5 mL). Purification: column chromatography (silica, hexane/ether gradient elution from 100/0 to 40/60). The desired product was obtained as a pale yellow solid (0.49 g, 55%), mp = 98 – 100 °C, $R_f = 0.16$ (silica, hexane/ether 50/50). ^{1}H NMR (500 MHz, $CDCl_3$) δ_H = 7.36 (2H, ddd, J(^{1}H) = 8.0, 5.0 and 1.0, H_5), 7.87 (2H, td, J(^{1}H) = 8.0 and 2.0, H_4), 7.93 (2H, dt, J(^{1}H) = 8.0 and 1.0, H_3), 8.78 (2H, ddd, J(^{1}H) = 5.0, 2.0 and 1.0, H_6), 8.93 (2H, d, J(^{1}H) = 2.0, $H_{4'}$), 9.07 (1H, t, J(^{1}H) = 2.0, $H_{2'}$), ^{13}C {^{1}H} NMR (126 MHz, $CDCl_3$) δ_C = 121.0 (C, s, C_3), 122. 1 (C, s, $C_{2'}$), 123.6 (C, s, C_5), 131.1 (C, s, $C_{4'}$), 137.4 (C, s, C_4), 141.7 (C, s, $C_{1'}$), 149.7 (C, s,$C_{5'}$), 150.3 (C, s, C_6), 155.0 (C, s, C_2). HRMS (ES^+): *m/z* 278.0923 [100%, $M+H^+$]; calcd for [$C_{16}H_{12}N_3O_2$], 278.0924. Anal. $C_{16}H_{11}N_3O_2$ (277.27): calcd C, 69.30; H, 4.00; N, 15.16; found C, 66.65; H, 4.58; N, 13.27.

3,5-Dibromoaniline

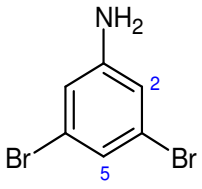

1,3-Dibromo-5-nitrobenzene (0.50 g, 1.8 x 10^{-3} mol) and Sn powder (1.50 g, 1.3 x 10^{-3} mol) were placed in a round bottomed flask (100 mL) with stirrer bar and fitted with a condenser. 5 M HCl was added (10 mL). EtOH was added in 5 mL portions until 3,5-dibromo-1-nitrobenzene dissolved (35 mL total). The mixture was heated to reflux. Once at reflux, a further 20 mL of the 5 M HCl was added. The mixture was heated at reflux overnight. On cooling to room temperature, the solvent was removed *in vacuo*

leaving a pale yellow solid (protonated amine). Excess NaOH solution was added to basify the solution, which was then extracted into DCM (30 mL). The DCM portion was washed with a Na_2CO_3 solution (10%, 2 x 20 mL). The DCM phase was dried with $MgSO_4$, filtered, and the solvent was removed *in vacuo*. The product was obtained as a brown oil (0.20 g, 45%). ^{1}H NMR (300 MHz, $CDCl_3$) δ_H = 3.75 (2H, s, NH_2), 6.73 (2H, d, J(^{1}H) = 2.0, H_2), 7.01 (1H, t, J(^{1}H) = 2.0, H_5)

HL^4: 1,3-di(2-pyridyl)-5-aminobenzene

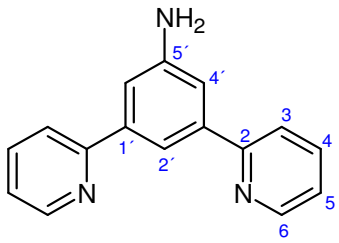

This ligand, HL^4, was prepared via the Stille method. Reagents: 2-Tri-n-butylstannylpyridine (0.74 g, assumed 85% pure, 1.68 x 10^{-3} mol), 3,5-dibromo aniline (0.18 g, 7.2 x 10^{-4} mol), $Pd(PPh_3)_2Cl_2$ (0.020 g, 3 x 10^{-5} mol) and LiCl (0.22 g, 5.24 x 10^{-3} mol). Solvent: toluene (6 mL). Purification: column chromatography (silica, hexane/ether gradient elution from 100/0 to 0/100, then DCM/MeOH gradient elution from 100/0 to 95/5). The desired product was obtained as a yellow oil (0.055 g, 31%), R_f = 0.15 (silica, hexane/ether 25/75). ^{1}H NMR (500 MHz, $CDCl_3$) δ_H = 3.5-4.1 (2H, br, m, NH_2), 7.23 (2H, ddd, J(^{1}H) = 7.5, 5.0 and 1.0, H_5), 7.44 (2H, s, $H_{4'}$), 7.74 (2H, td, J(^{1}H) = 7.5 and 1.0, H_4), 7.80 (2H, d, J(^{1}H) = 7.5, H_3), 7.93 (1H, s, $H_{2'}$), 8.69 (2H, d, J(^{1}H) = 5.0, H_6), ^{13}C{^{1}H} NMR (126 MHz, $CDCl_3$) δ_C = 114.5 (s, $C_{4'}$), 116.0 (s, $C_{2'}$), 121.0 (s, C_3), 122.5 (s, C_5), 128.5 (d, J = 12.2, $C_{5'}$), 137.0 (s, C_4), 141.0 (s, $C_{3'}$), 149.7 (s, C_6), 157.5 (s, C_2). HRMS (ES$^+$): *m/z* 248.1184 [100%, M+H$^+$]; calcd for [$C_{16}H_{14}N_3$], 248.1182.

3-Methyl-2-tri-n-butylstannylpyridine

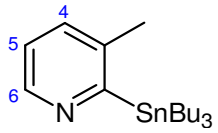

This stannane was prepared via the lithium-halogen exchange/stannylation route, using 2-bromo-3-methylpyridine (1.50g, 8.72 x 10^{-3} mol), nBuLi (3.84 mL, 2.5M in hexanes, 9.59 x 10^{-3} mol) and Bu_3SnCl (2.84 mL, 1.05 x 10^{-2} mol). The desired product was obtained as an orange liquid (4.23 g, assumed 50% pure by mass, therefore 2.11 g, 63%). ^1H NMR (400 MHz, $CDCl_3$), δ_H = 0.7-1.7 (27H, m, $3Bu_3$), 2.35 (3H, s, CH_3), 6.99 (1H, dd, J(^1H) = 8.0 and 5.0, H_5), 7.30 (1H, ddd, J(^1H) = 8.0, 2.0 and 1.0, H_4), 8.52 (1H, ddd, J(^1H) = 5.0, 2.0 and 1.0, H_6)

HL^5: 1,3-di(3-methyl-2-pyridyl)benzene

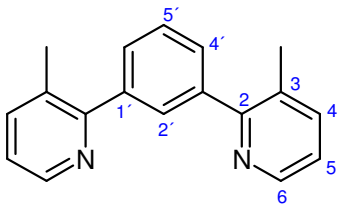

Ligand HL^5 was prepared via Stille methodology. Reagents: 3-Methyl-2-tri-n-butylstannyl pyridine (1.74 g, 4.54 x 10^{-3} mol), 1,3-dibromobenzene (0.487 g, 2.06 x 10^{-3} mol), $Pd(PPh_3)_2Cl_2$ (0.054 g, 8 x 10^{-5} mol) and LiCl (0.63 g, 1.49 x 10^{-2} mol). Solvent: toluene (6 mL). Purification: column chromatography (silica, hexane:EtOAc, 100:0 → 0:100). The desired product was obtained as an orange oil (0.230 g, 8.9 x 10^{-4} mol, 43%) R_f = 0.24 (100% EtOAc). ^1H NMR (500 MHz, $CDCl_3$) δ_H = 2.39 (6H, s, CH_3), 7.18 (2H, dd, J(^1H) = 7.5 and 5.0, H_5), 7.57 (5H, m, H_4, $H_{4'}$ and $H_{5'}$), 7.70 (1H, td, J(^1H) = 1.5 and 0.5, $H_{2'}$), 8.53 (2H, dd, J(^1H) = 5.0 and 2.0, H_6). ^{13}C {^1H} NMR (126 MHz, $CDCl_3$) δ_C = 20.0 (s, CH_3), 122.4 (s, C_5), 128.2 (s, $C_{1'}$), 128.8 (s, $C_{4'}$), 130.0 (s, $C_{2'}$), 131.2 (s, C_3), 138.7 (s, C_4), 140.8 (s, $C_{5'}$), 147.2 (s, C_6), 158.7 (s, C_2). HRMS (ES^+): *m/z* 283.1207 [32%, M+Na^+], 261.1387 [36, M+H^+]; calcd for [$C_{18}H_{17}N_2$], 261.1386.

HL[7]: 1,3-di(5-methyl-2-pyridyl)benzene

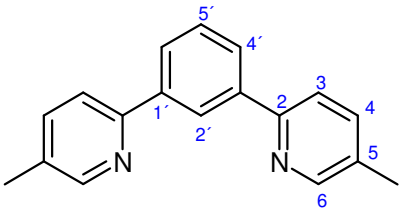

HL^7 was prepared via Suzuki-Miyaura methodology. Reagents: Benzene-1,3-diboronic acid (0.11 g, 6.6 x 10^{-4} mol) 2-bromo-5-methyl pyridine (0.260 g, 1.5 x 10^{-3} mol), Na_2CO_3 (1M, 5 mL), $Pd(PPh_3)_4$ (0.091 g, 8 x 10^{-5} mol). Solvents: DME (5 mL), water (5 mL). Purification: Column chromatography (silica, hexane/EtOAc, 100:0 → 50:50). The desired product came off around 35% EtOAc and was isolated as a yellow oil (0.123 g, 72%). R_f = 0.57 (silica, 100% EtOAc). ^1H NMR (400 MHz, $CDCl_3$), δ_H = 2.35 (6H, s, $2CH_3$), 7.52-7.57 (3H, m, $H_{5'}$ and H_4), 7.71 (2H, d, J(^1H) = 8.5, H_3), 8.01 (2H, dd, J(^1H) = 8.0 and 1.5, $H_{4'}$), 8.53 (2H, dd, J(^1H) = 1.5 and 0.5, H_6), 8.57 (1H, t, J(^1H) = 1.5, $H_{2'}$), $^{13}C\{^1H\}$ NMR (126 MHz, $CDCl_3$) δ_C = 18.5 (C, s, $2CH_3$), 120.5 (C, s, C_3), 125.5 (C, s, $C_{2'}$), 127.0 (C, s, $C_{4'}$), 129.5 (C, s, $C_{5'}$), 132.0 (C, s, C_5), 137.5 (C, s, C_4), 140.0 (C, s, $C_{1'}$), 150.0 (C, s, C_6), 155.0 (2C, s, C_2). HRMS (ES^+): *m/z* 283.1210 [10%, $M+Na^+$], 261.1385 [100, $M+H^+$]; calcd for [$C_{18}H_{17}N_2$], 261.1386.

HL[8]: 1,3-di(6-methyl-2-pyridyl)benzene

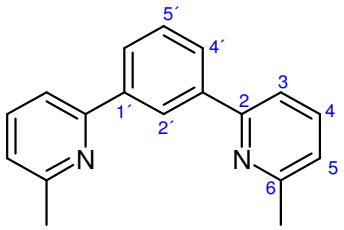

Ligand HL^8 was prepared via Suzuki-Miyaura methodology. Reagents: Benzene-1,3-diboronic acid (0.52 g, 3.2 x 10^{-3} mol), 2-bromo-6-methyl pyridine (1.26 g, 7.28 x 10^{-3} mol), Na_2CO_3 (1M, 5 mL) and $Pd(PPh_3)_4$ (0.44 g, 3.8 x 10^{-4} mol). Solvents: DME (5 mL) and water (5 mL). Purification: Column chromatography (silica, DCM/MeOH, 100/0 → 92/8), giving the desired product as a pale yellow oily solid (0.22 g, 27%), R_f = 0.56 (silica, DCM/MeOH 99:1). ^1H NMR (500 MHz, $CDCl_3$), δ_H = 2.65 (6H, s, $2CH_3$), 7.12 (2H, dd, J(^1H) = 7.5 and 0.5, H_5), 7.57 (1H, t, J(^1H) = 8.0, $H_{5'}$), 7.62 (2H, d, J(^1H) = 7.5, H_3), 7.67 (2H, t, J(^1H) = 7.5, H_4), 8.04 (2H, dd, J(^1H) = 8.0 and

1.5, $H_{4'}$), 8.57 (1H, t, J(^{1}H) = 1.5, $H_{2'}$), $^{13}C\{^1H\}$ NMR (126 MHz, $CDCl_3$) δ_C = 25.0 (s, $2CH_3$), 118.0 (s, C_3), 122.0 (s, C_5), 125.5 (s, $C_{2'}$), 127.5 (s, $C_{4'}$), 129.5 (s, $C_{5'}$), 137.5 (s, C_4), 140.5 (s, $C_{1'}$), 157.0 (s, C_2). HRMS (ES^+): *m/z* 261.1385 [100%, $M+H^+$]; calcd for [$C_{18}H_{17}N_2$], 261.1386.

HL^9: 1,3-di(3-methyl-2-pyridyl)-4,6-difluorobenzene

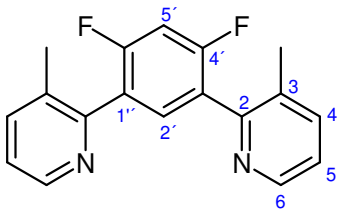

Ligand HL^9 was prepared via Stille methodology. Reagents: 3-Methyl-2-tri-n-butylstannyl pyridine (1.03 g, 2.7 x 10^{-3} mol), 1,3-dibromo-4,6-difluorobenzene (0.37 g, 1.4 x 10^{-3} mol), bis-(triphenylphosphine) palladium (II) dichloride (0.38 g, 5 x 10^{-5} mol) and LiCl (0.42 g, 9.9 x 10^{-3} mol). Solvent: Toluene (8 mL). Purification: Column chromatography (silica, hexane/EtOAc gradient elution from 100/0 to 80/20). The pure product was obtained as a pale yellow oil (0.11 g, 27%). R_f = 0.26 (silica, 100% EtOAc), ^{1}H NMR (400 MHz, $CDCl_3$) δ_H = 2.29 (6H, s, $2CH_3$), 6.99 (1H, t, J(^{19}F) = 10.0, $H_{5'}$), 7.21 (2H, dd, J(^{1}H) = 8.0 and 4.5, H_5), 7.58 (3H, m, $H_{2'}$ and H_4), 8.50 (2H, dd, J(^{1}H) = 4.5 and 1.0, H_6), $^{13}C\{^1H\}$ NMR (126 MHz, $CDCl_3$) δ_C = 20.5 (s, $2CH_3$), 104.0 (t, J(^{19}F) = 27.5, $C_{5'}$), 123.2 (s, C_5), 125.3 (dd, J(^{19}F) = 15.0 and 6.0, $C_{1'}$), 133.1 (s, C_3), 134.3 (t, J(^{19}F) = 5.5, $C_{2'}$), 138.3 (s, C_4), 147.3 (s, C_6), 153.1 (s, C_2), 159.8 (dd, J(^{19}F) = 253.0 and 12.5, $C_{4'}$). ^{19}F NMR (376 MHz, $CDCl_3$) δ_F = -111.4 (2F, t, J(^{1}H) = 9.0). HRMS (ES^+): *m/z* 319.10179 [4%, $M+Na^+$], 297.1198 [100, $M+H^+$]; calcd for [$C_{18}H_{14}N_2F_2{}^{23}Na$], 319.1017, calcd for [$C_{18}H_{15}N_2F_2$], 297.1198.

HL[10]: 1,3-di(4-methyl-2-pyridyl)-4,6-difluorobenzene

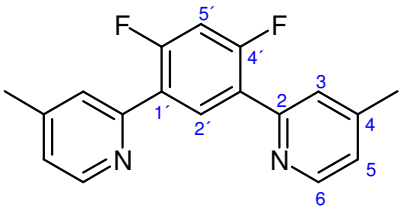

The ligand, HL^{10}, was prepared via the Stille methodology. Reagents: 4-Methyl-2-tri-n-butylstannyl pyridine (0.23 g, 6.1 x 10^{-4} mol), 1,3-dibromo-4,6-difluorobenzene (0.075 g, 2.8 x 10^{-4} mol), $Pd(PPh_3)_2Cl_2$ (0.010 g, 1.4 x 10^{-5} mol) and triphenylphosphine (0.007 g, 3 x 10^{-5} mol). Solvent: Xylene (7 mL). The mixture was heated under reflux at 160 °C under a nitrogen atmosphere for 20 h. Purification: Column chromatography (silica, hexane/diethyl ether gradient elution from 0/100 to 100/0). The product was obtained as a pale brown solid (0.072 g, 88%), mp = 90 – 95 °C, R_f = 0.26 (silica, hexane/ether 50/50). ^{1}H NMR (300 MHz, $CDCl_3$) δ_H = 2.42 (6H, s, CH_3), 7.02 (1H, t, J(^{19}F) = 10.5, $H_{5'}$), 7.09 (2H, ddd, J(^{1}H) = 5.0 and 1.0, H_5), 7.58 (2H, s, H_3), 8.52 (1H, t, J(^{19}F) = 8.5, $H_{2'}$), 8.56 (2H, d, J(^{1}H) = 5.0, H_6), ^{13}C{^{1}H} NMR (126 MHz, $CDCl_3$) δ_C = 21.5 (s, C_7), 105.0 (t, J(^{19}F) = 27.0, $C_{5'}$), 124.0 (s, C_5), 125.0 (s, $C_{1'}$), 125.5 (t, J(^{19}F) = 4.0, C_3), 134.0 (s, $C_{2'}$), 148.0 (s, C_4), 150.0 (s, C_6), 153.0 (s, C_2), 161.0 (d, J(^{19}F) = 242.0, $C_{4'}$). ^{19}F NMR (376 MHz, $CDCl_3$) δ_F = -113.5 (2F, t, J(^{1}H) = 9.8). HRMS (ES^+): *m/z* 297.1201 [100%, $M+H^+$]; calcd for [$C_{18}H_{15}N_2F_2$], 297.1198. Anal. $C_{18}H_{14}F_2N_2$ (296.31): calcd C, 72.96; H, 4.76; N, 9.46; found C, 72.56; H, 4.81; N, 9.30.

5-Methyl-2-tri-n-butylstannylpyridine

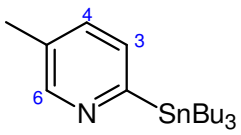

This stannane was prepared via the lithium-halogen exchange/stannylation route. Reagents: 2-Bromo-5-methyl pyridine (1.00 g, 5.81 x 10^{-3} mol), nBuLi (2.42 mL, 2.5M in hexanes, 6.06 x 10^{-3} mol), Bu_3SnCl (1.89 mL, 6.96 x 10^{-3} mol) The product, 5-methyl-2-tri-n-butylstannyl pyridine, was obtained as a yellow liquid (2.80 g, assumed 70% pure by mass, therefore 1.96 g, 88%). ^{1}H NMR (200 MHz, $CDCl_3$), δ_H = 0.83-1.70 (27H, m, $3Bu_3$), 2.72 (3H, s, CH_3), 7.29 (2H, m, H_3 and H_4), 8.58 (1H, s, H_6).

HL[11]: 1,3-di(5-methyl-2-pyridyl)-4,6-difluorobenzene

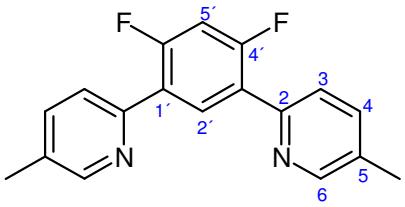

The ligand HL[11] was prepared via Stille cross-coupling methodology. Reagents: 1,3-Dibromo-4,6-difluorobenzene (0.30 g, 1.10 x 10^{-3} mol), 5-methyl-2-tri-n-butylstannyl pyridine (0.99 g, 2.59 x 10^{-3} mol), $Pd(PPh_3)_2Cl_2$ (0.029 g, 4.1 x 10^{-5} mol) and LiCl (0.33 g, 7.9 x 10^{-3} mol). Solvent: Toluene (10 mL). Purification: Column chromatography (silica, hexane/EtOAc, 100:0 → 0:100). The product, 1,3-di(5-methyl-2-pyridyl)-4,6-difluorobenzene, was obtained as a white powder (0.13 g, 39%), mp = 140-142 °C, R_f = 0.64 (silica, 100% EtOAc). ^{1}H NMR (500 MHz, $CDCl_3$), δ_H = 2.40 (6H, s, $2CH_3$), 7.01 (1H, t, J(^{19}F) = 10.5, $H_{5'}$), 7.58 (2H, dd, J(^{1}H) = 8.0, and 2.0, H_4), 7.67 (2H, d, J(^{1}H) = 8.0, H_3), 8.50-8.60 (3H, m, $H_{2'}$ and H_6). ^{13}C{^{1}H} NMR (126 MHz, $CDCl_3$) δ_C = 18.7 (s, CH_3), 105.0 (t, J(^{19}F) = 27.0, $C_{5'}$), 123.9 (t, J(^{19}F) = 4.5, C_3), 124.7 (dd, J(^{19}F) = 11.0 and 5.5, $C_{1'}$), 132.3 (s, C_5), 133.4 (t, J(^{19}F) = 4.5, $C_{2'}$), 137.2 (s, C_4), 150.1 (t, J(^{19}F) = 2.0, C_2), 150.5 (s, C_6), 160.3 (dd, J(^{19}F) = 255.5 and 12.5, $C_{4'}$). ^{19}F NMR (376 MHz, $CDCl_3$) δ_F = -114.0 (2F, t, J(^{1}H) = 10.0). HRMS (ES^+): *m/z* 319.1018 [9%, $M+Na^+$], 297.1197 [100, $M+H^+$]; calcd for [$C_{18}H_{14}N_2F_2{}^{23}Na$], 319.1017, calcd for [$C_{18}H_{15}N_2F_2$], 297.1198. Anal. $C_{18}H_{14}F_2N_2$ (296.31): calcd C, 72.96; H, 4.76; N, 9.46; found C, 70.53; H, 4.92; N, 8.93

6-Methyl-2-tri-n-butylstannylpyridine

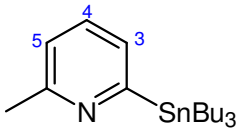

This stannane was prepared via the lithium-halogen exchange/stannylation route. Reagents: 2-Bromo-6-methyl pyridine (0.86 g, 5.0 x 10^{-3} mol), nBuLi (2.2 mL, 2.5M in hexanes, 5.5 x 10^{-3} mol), Bu_3SnCl (1.63 mL, 6.01 x 10^{-3} mol) The product was obtained as a yellow liquid (2.75 g, assumed 50% pure by mass, therefore 1.37 g, 72%). ^{1}H NMR (400 MHz, $CDCl_3$), δ_H = 0.8-1.8 (27H, m, $3Bu_3$), 2.53 (3H, s, CH_3), 6.94 (1H, dd, J(^{1}H)

= 7.0 and 1.0, H_5), 7.17 (1H, d, $J(^1H)$ = 7.0, $^4J(^{117/118}Sn)$ = 16.0, H_3), 7.35 (1H, t, $J(^1H)$ = 7.0, H_4).

HL^{12}: 1,3-di(6-methyl-2-pyridyl)-4,6-difluorobenzene

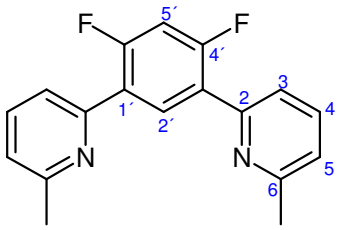

The ligand, HL^{12}, was prepared via Stille cross-coupling methodology. Reagents: 6-Methyl-2-tri-n-butylstannyl pyridine (1.37 g, 3.6 x 10^{-3} mol), 1,3-dibromo-4,6-difluorobenzene (0.49 g, 1.8 x 10^{-3} mol), $Pd(PPh_3)_2Cl_2$ (0.051 g, 7 x 10^{-5} mol) and LiCl (0.53 g, 1.3 x 10^{-2} mol). Solvent: toluene (8 mL). Purification: column chromatography (silica, hexane/EtOAc gradient elution from 100/0 to 65/35). The pure product was obtained as a white powder (0.31 g, 58%), mp = 93 – 96˚C. R_f = 0.72 (silica, 100% EtOAc), ^1H NMR (700 MHz, $CDCl_3$) δ_H = 2.61 (6H, s, $2CH_3$), 6.98 (1H, t, $J(^{19}F)$ = 10.5, $H_{5'}$), 7.10 (2H, d, $J(^1H)$ = 8.0, H_5), 7.51 (2H, d, $J(^1H)$ = 8.0, H_3), 7.62 (2H, t, $J(^1H)$ = 8.0, H_4), 8.49 (1H, t, $J(^{19}F)$ = 8.5, $H_{2'}$). $^{13}C\{^1H\}$ NMR (176 MHz, $CDCl_3$) δ_C = 25.2 (s, CH_3), 105.0 (t, $J(^{19}F)$ = 27.5, $C_{5'}$), 121.5 (t, $J(^{19}F)$ = 4.5, C_3), 122.2 (s, C_5), 125.1 (dd, $J(^{19}F)$ = 11.5 and 5.0, $C_{1'}$), 133.9 (t, $J(^{19}F)$ = 4.5, $C_{2'}$), 136.8 (s, C_4), 152.2 (s, C_2), 158.8 (s, C_6), 160.6 (dd, $J(^{19}F)$ = 254.5 and 13.0, $C_{4'}$), ^{19}F NMR (376 MHz, $CDCl_3$) δ_F = -111.4 (2F, t, $J(^1H)$ = 9.0). HRMS (ES^+): *m/z* 297.1196 [100%, $M+H^+$]; calcd for [$C_{18}H_{15}N_2F_2$], 297.1198. Anal. $C_{18}H_{14}F_2N_2$ (296.31): calcd C, 72.96; H, 4.76; N, 9.46; found C, 72.66; H, 4.80; N, 9.50.

1,3-Dimethyl-4,6-(4,4,5,5-tetramethyl-1,3,2-dioxaborolan-2-yl)benzene

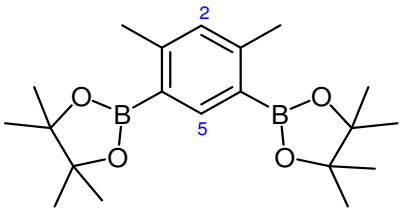

This diboronate ester was prepared via the double borylation method. Reagents: 1,3-dibromo-4,6-dimethyl benzene (0.253 g, 9.59 x 10^{-4} mol), bispinacolatodiboron (B_2pin_2, 0.53 g, 2.11 x 10^{-3} mol), $Pd(dppf)Cl_2$ (0.047 g, 5.75 x 10^{-5} mol) and KOAc (0.471 g, 4.80 x 10^{-3} mol). Solvent: Dry DMSO. Purification: Column chromatography (silica, hexane/EtOAc 100:0 → 90:10). The product, 1,3-dimethyl-4,6-(4,4,5,5-tetramethyl-1,3,2-dioxaborolan-2-yl)benzene, was obtained as a white crystalline solid (0.24 g, 6.59 x 10^{-4} mol, 69%) R_f = 0.65 (silica, hexane/EtOAc 70:30). ^1H NMR (500 MHz, $CDCl_3$) δ_H = 1.36 (24H, s, CH_3), 2.53 (6H, s, CH_3-ph) 7.00 (1H, s, H_2), 8.15 (1H, s, H_5), ^{13}C {^1H} NMR (126 MHz, $CDCl_3$) δ_C = 22.6 (s, CH_3-Ph), 25.1 (s, CH_3), 83.5 (s, C-O(CH_3)$_2$), 131.8 (s, C_2), 143.9 (s, C_5), 148.0 (s, C_1). HRMS (ASAP): *m/z* 357.2638 [20%, M+H^+]; calcd for [$C_{20}H_{33}O_4{}^{10}B_2$], 357.2638.

HL^{13}: 1,3-di(3-methyl-2-pyridyl)-4,6-dimethylbenzene

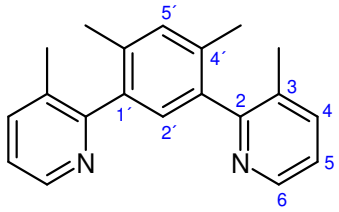

Synthesis of ligand HL^{13} was performed twice, via two different routes – Stille cross-coupling and Suzuki-Miyaura cross-coupling (methods A and B respectively)

Method A:

Reagents: 1,3-dibromo-4,6-difluorobenzene (0.26 g, 9.9 x 10^{-4} mol), 2-tri-n-butylstannyl-3-methylpyridine (0.83 g, 2.2 x 10^{-3} mol), $Pd(PPh_3)_2Cl_2$ (0.026 g, 4 x 10^{-5} mol), LiCl (0.29 g, 6.90 x 10^{-3} mol). Solvent: toluene (4 mL). Purification: The product was purified by column chromatography (alumina, hexane/EtOAc 100:0 →50:50). The product was obtained as a pale yellow oil (0.024 g, 8 x 10^{-5} mol, 8.4%).

Method B:

Reagents: 1,3-Dimethyl-4,6-(4,4,5,5-tetramethyl-1,3,2-dioxaborolan-2-yl)benzene (0.07 g, 2.0 x 10^{-4} mol), 2-bromo-3-methylpyridine (0.074 g, 4.3 x 10^{-4} mol), Na_2CO_3 (1M, 5 mL) and $Pd(PPh_3)_4$ (0.023 g, 2 x 10^{-5} mol). Solvents: DME (5 mL) and water (5 mL). Purification: Column chromatography (alumina, hexane/EtOAc 100:0 →50:50). The product was obtained as a pale yellow oil (0.024 g, 8 x 10^{-5} mol, 42%). R_f = 0.65 (alumina, 100% EtOAc). ^1H NMR (700 MHz, $CDCl_3$) δ_H = 2.11 (6H, s, CH_3), 2.15 (6H, s, CH_3), 7.00 (1H, s, $H_{5'}$), 7.17 (2H, dd, J(^1H) = 8.0 and 4.5, H_5), 7.20 (1H, s, $H_{2'}$), 7.56 (2H, d, J(^1H) = 8.0, H_4), 8.49 (2H, d, J(^1H) = 4.5, H_6), ^{13}C {^1H} NMR (176 MHz, $CDCl_3$) δ_C = 19.1 (s, CH_3), 19.2 (s, CH_3), 122.3 (s, C_5), 129.0 (s, $C_{5'}$), 132.1 (s, C_3), 132.3 (s, $C_{2'}$), 135.4 (s, $C_{1'}$), 137.7 (s, $C_{4'}$), 138.0 (s, C_4), 146.7 (s, C_6), 159.5 (s, C_2). HRMS (ES^+): *m/z* 289.1711 [100%, M+H^+]; calcd for [$C_{20}H_{21}N_2$], 289.1699.

HL^{14}: 1,3-di(5-methyl-2-pyridyl)-4,6-dimethylbenzene

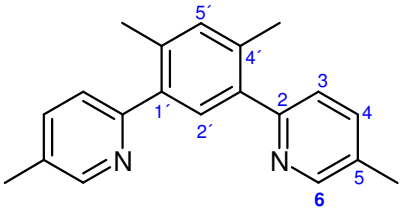

Ligand HL^{14} was prepared via the Suzuki-Miyaura method. Reagents: 1,3-Dimethyl-4,6-(4,4,5,5-tetramethyl-1,3,2-dioxaborolan-2-yl)benzene (0.065 g, 1.8 x 10^{-4} mol), 2-bromo-5-methyl pyridine (0.069 g, 4.0 x 10^{-4} mol), $Pd(PPh_3)_4$ (0.021 g, 2 x 10^{-5} mol) and Na_2CO_3 (1M, 5 mL). Solvents: DME (5 mL), water (5 mL). Purification: Column chromatography (silica, hexane/EtOAc 100:0 → 60:40). The product was obtained as a white powder (0.050 g, 1.7 x 10^{-4} mol, 95%). R_f = 0.45 (silica, EtOAc 100%). ^1H NMR (500 MHz, $CDCl_3$), δ_H = 2.19 (6H, s, C_5-CH_3), 2.40 (6H, s, $C_{4'}$-CH_3), 7.18 (1H, s, $H_{5'}$), 7.33 (2H, d, J(^1H) = 8.0, H_3), 7.43 (1H, s, $H_{2'}$), 7.53 (2H, dd, J(^1H) = 8.0 and 1., H_4), 8.51 (2H, d, J(^1H) = 1.5, H_6), ^{13}C {^1H} NMR (176 MHz, $CDCl_3$) δ_C = 20.0 (s, $C_{4'}$-$\underline{C}H_3$), 30.1 (s, C_5-$\underline{C}H_3$), 123.9 (s, C_3), 131.1 (s, $C_{2'}$), 131.2 (s, C_5), 133.5 (s, $C_{5'}$), 135.8 (s, $C_{4'}$), 137.0 (s, C_4), 138.1 (s, $C_{1'}$), 149.7 (s, C_6), 157.1 (s, C_2). HRMS (ES^+): *m/z* 289.1719 [100%, M+H^+]; calcd for [$C_{20}H_{21}N_2$], 289.1705.

4-Methoxy-2-n-tributylstannylpyridine

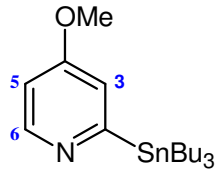

This stannane was prepared via the lithium-halogen exchange/stannylation route. Reagents: 2-Bromo-4-methoxy pyridine (1.12 g, 6.0 x 10^{-3} mol), n-BuLi (3.6 mL, 8.8 x 10^{-3} mol) and $SnBu_3Cl$ (3.0 mL, 9.4 x 10^{-3} mol). The product was obtained as a brown oil (5.4 g, assumed 40% pure by ^1H NMR, therefore 2.16 g, 5.4 x 10^{-3} mol, 91%) and used without further purification. ^1H NMR (200 MHz, $CDCl_3$) δ_H = 6.65 (1H, m, H_5), 6.96 (1H, dd, J(^1H) = 3.0 and 0.5, $^4J(^{117/118}Sn)$ = 22, H_3), 8.53 (1H, dd, J(^1H) = 6.0 and 0.5, H_6).

HL^{15}: 1,3-di(4-methoxy-2-pyridyl)-4,6-difluorobenzene

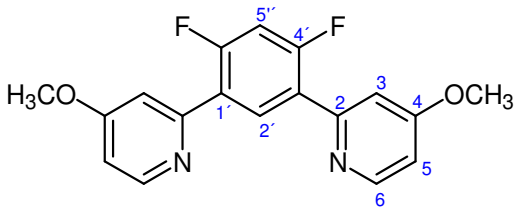

HL^{15} was prepared via the Stille methodology. Reagents: 4-Methoxy-2-tri-n-butylstannylpyridine (4.57 g, assumed 40% pure by NMR, therefore 1.83 g, 4.6 x 10^{-3} mol), 1,3-dibromo-4,6-difluorobenzene (0.57 g, 2.1 x 10^{-3} mol), $Pd(PPh_3)_2Cl_2$ (0.054 g, 8 x 10^{-5} mol) and LiCl (0.62 g, 1.46 x 10^{-2} mol). Solvent: Toluene (6 mL). Purification: Column chromatography (alumina, hexane/EtOAc, 100:0 → 0:100, then MeOH/DCM 100:0 → 98:2. The desired product came off at 40% EtOAc, and a useful side product, 1-bromo-2,4-difluoro-5-((4-methoxy)-2-pyridyl)benzene, came off at 10% EtOAc). The desired product had a slight impurity – to purify further, the solid was washed with hexane, filtered, and the residue was dissolved in DCM. The desired product was obtained as an off-white solid (0.21 g, 6.5 x 10^{-4} mol, 31%). mp = 113-114 °C, R_f = 0.35 (alumina, hexane/EtOAc 60:40). ^1H NMR (500 MHz, $CDCl_3$) δ_H = 3.90 (6H, s, OCH_3), 6.80 (2H, dd, J(^1H) = 6.0 and 2.0, H_5), 7.01 (1H,t, J(^{19}F) = 11.0, $H_{5'}$), 7.90 (2H, d, J(^1H) = 2.0, H_3), 8.53 (1H, d, J(^{19}F) = 6.0, $H_{2'}$), 8.56 (2H, t, J(^1H) = 6.0, H_6). ^{13}C {^1H} NMR (126 MHz, $CDCl_3$). δ_C = 31.2 (s, OCH_3), 105.2 (t, J(^{19}F) = 27.5, $C_{5'}$), 108.9 (s,

C_5), 110.7 (t, J(^{19}F) = 4.5, C_3), 124.6 (q, J(^{19}F) = 5.5, $C_{1'}$), 133.9 (t, J(^{19}F) = 4.5, $C_{2'}$), 151.1 (s, C_6), 154.2 (t, J(^{19}F) = 1.5, C_2), 160.6 (dd, J(^{19}F) = 255.0 and 12.5, $C_{4'}$), 166.2 (s, C_4). ^{19}F NMR (376 MHz, $CDCl_3$) δ_F = -113.0 (2F, t, J(^{1}H) = 10.0). HRMS (ES$^+$): *m/z* 329.1098 [100%, M+H$^+$]; calcd for [$C_{18}H_{15}F_2N_2O_2$], 329.1096. Anal. $C_{18}H_{14}F_2N_2O_2$ (328.31): calcd C, 65.85; H, 4.30; N, 8.53; found C, 64.98; H 4.10; N 7.95.

1-Bromo-2,4-difluoro-5-(4-methoxy-2-pyridyl)benzene

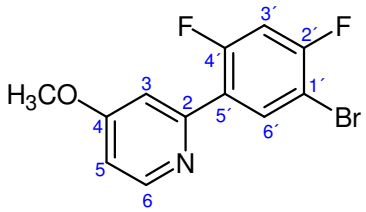

1-Bromo-2,4-difluoro-5-(4-methoxy-2-pyridyl)-benzene was obtained as a side product from the synthesis of HL[15]. Purification: Column chromatography (alumina, hexane/EtOAc, 100:0 → 90:10). The product still contained a slight impurity – this was successfully removed by washing the solid with hexane. The product was obtained as a white semi-crystalline solid (0.20 g, 6.7 x 10^{-4} mol, 32%). R_f = 0.48 (alumina, hexane/EtOAc 90:10). ^{1}H NMR (700 MHz, $CDCl_3$) δ_H = 3.90 (3H, s, CH_3), 6.81 (1H, dd, J(^{1}H) = 6.0 and 2.0, H_5), 6.98 (1H, dd, J(^{19}F) = 11.0 and 8.0, $H_{3'}$), 7.27 (1H, d, J(^{1}H) = 2.0, H_3), 8.25 (1H, t, J(^{19}F) = 8.0, $H_{6'}$), 8.49 (1H, d, J(^{1}H) = 6.0, H_6). ^{13}C {^{1}H} NMR (176 MHz, $CDCl_3$) δ_C = 55.5 (s, OCH_3) 104.6 (dd, J(^{19}F) = 21.0 and 4.0, $C_{5'}$), 105.7 (dd, J(^{19}F) = 29.0 and 26.0, $C_{3'}$), 109.09 (s, C_5), 110.9 (d, J(^{19}F) = 10.0, C_3), 125.3 (dd, J(^{19}F) = 12.5 and 4.0, $C_{1'}$), 135.3 (s, $C_{6'}$), 151.1 (s, C_6), 152.8 (s, C_2), 158.8 (dd, J(^{19}F) = 60.0 and 10.5, $C_{4'}$), 160.2 (dd, J(^{19}F) = 60.0 and 10.5, $C_{2'}$), 166.3 (s, C_4). ^{19}F NMR (376 MHz, $CDCl_3$) δ_F = -113.9 (1F, q, J(^{1}H) = 9.0), -103.1 (1F, q, J(^{1}H) = 8.0). HRMS (ES$^+$): *m/z* 299.9833 [91%, ^{79}Br, M+H$^+$], 300.9867 [100, ^{81}Br, M+H$^+$]; calcd for [$C_{12}H_9{}^{79}BrF_2NO$], 299.9830.

HL[16]: 1-(4-methoxy-2-pyridyl)-3-(2-pyridyl)-4,6-difluorobenzene

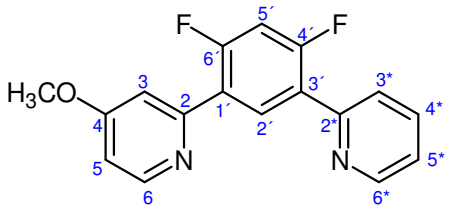

Ligand HL[16] was prepared via the Stille methodology. Reagents: 1-bromo-2,4-difluoro-5-(4-methoxy-2-pyridyl)-benzene (0.11 g, 3.7 x 10^{-4} mol), 2-tri-n-butylstannyl pyridine (0.19 g, assumed 85% pure, 4.4 x 10^{-4} mol), $Pd(PPh_3)_2Cl_2$ (0.011 g, 2 x 10^{-5} mol) and LiCl (0.12 g, 2.7 x 10^{-3} mol). Solvent: Toluene (5 mL). Purification: Column chromatography (silica, hexane/EtOAc, 100:0 → 50:50, the product came off at 45% EtOAc). The product was obtained as a white solid (0.040 g, 1.4 x 10^{-4} mol, 38%). R_f = 0.42 (silica, EtOAc 100%). ^1H NMR (500 MHz, $CDCl_3$) δ_H = 3.90 (3H, s, OCH_3), 6.80 (1H, dd, J(^1H) = 6.0 and 2.5, H_5), 7.02 (1H, t, J(^{19}F) = 11.0, $H_{5'}$), 7.27 (1H, m, H_{5*}), 7.29 (1H, t, J(^1H) = 2.0, H_3), 7.75 (2H, m, H_{3*} and H_{4*}), 8.53 (1H, d, J(^1H) = 6.0, H_6), 8.60 (1H, t, J(^{19}F) = 9.0, $H_{2'}$), 8.72 (1H, dt, J(^1H) = 5.0 and 1.0, H_{6*}). ^{13}C {^1H} NMR (126 MHz, $CDCl_3$) δ_C = 55.5 (s, OCH_3), 105.0 (t, J(^{19}F) = 27.5, $C_{5'}$), 108.9 (s, C_5), 110.7 (d, J(^{19}F) = 8.5, C_3), 122.7 (s, C_{5*}), 124.5 (d, J(^{19}F) = 8.0, C_{3*}), 124.7 (m, $C_{1'}$ and $C_{3'}$), 133.9 (t, J(^{19}F) = 4.5, $C_{2'}$), 136.7 (s, C_{4*}), 150.0 (s, C_{6*}), 151.1 (s, C_6), 152.7 (d, J(^{19}F) = 2.5, C_{2*}), 154.2 (d, J(^{19}F) = 2.5, C_2), 159.7 (dd, J(^{19}F) = 13.0 and 6.5, $C_{4'}$), 161.7 (dd, J(^{19}F) = 12.0 and 5.0, $C_{6'}$), 166.2 (s, C_4). ^{19}F NMR (188 MHz, $CDCl_3$) δ_F = -113.3 (1F, q, J(^1H) = 10.0), -113.0 (1F, q, J(^1H) = 10.0). HRMS (ES^+) = *m/z* 299.0988 [100%, $M+H^+$]; calcd for [$C_{17}H_{13}F_2N_2O$], 299.0991.

1,3-Difluoro-4,6-(4,4,5,5-tetramethyl-1,3,2-dioxaborolan-2-yl)benzene

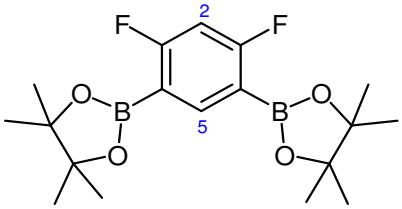

This diboronate ester was prepared via the double borylation method. Reagents: 1,3-dibromo-4,6-difluorobenzene (0.30 g, 1.1 x 10^{-3} mol), B_2pin_2 (0.620 g, 2.4 x 10^{-3} mol), $Pd(dppf)Cl_2$ (0.054 g, 7 x 10^{-5} mol) and KOAc (0.545 g, 5.6 x 10^{-3} mol). Solvent: Dry

DMSO (5 mL). Purification: Column chromatography (silica, hexane/EtOAc 100:0 → 80:20). The product was obtained as a white crystalline solid (0.33 g, 9.6 x 10^{-4} mol, 86%) R_f = 0.75 (silica, hexane/EtOAc 50:50). ^{1}H NMR (500 MHz, $CDCl_3$) δ_H = 1.33 (24H, s, CH_3), 6.71 (1H, t, J(^{19}F) = 10.0, H_2), 8.11 (1H, t, J(^{19}F) = 7.5, H_5), ^{13}C {^{1}H} NMR (126 MHz, $CDCl_3$) δ_C = 25.0 (s, CH_3), 84.2 (s, O<u>C</u>$(CH_3)_2$), 103.6 (t, J(^{19}F) = 28.0, C_2), 146.1 (t, J(^{19}F) = 10.0, C_5), 170.4 (dd, J(^{19}F) = 259.0 and 14.0, C_1), 207.5 (m, C_4), ^{19}F NMR (376 MHz, $CDCl_3$) δ_F = -94.6 (2F, t, J(^{1}H) = 8.5). HRMS (ASAP): *m/z* 366.2076 [62%, ^{11}B, M], calcd for [$C_{18}H_{26}{}^{11}B_2F_2O_4$], 366.1985.

HL[17]: 1,3-di(4-dimethylamino-2-pyridyl)-4,6-difluorobenzene

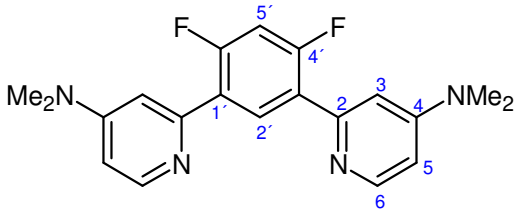

Ligand HL[17] was prepared via the Suzuki-Miyaura method. Reagents: 1,3-Difluoro-4,6-(4,4,5,5-tetramethyl-1,3,2-dioxaborolan-2-yl)benzene (0.100 g, 2.7 x 10^{-4} mol), 2-bromo-4-dimethylaminopyridine (0.121 g, 6.0 x 10^{-4} mol), $Pd(PPh_3)_4$ (0.032 g, 3 x 10^{-5} mol), Na_2CO_3 (1M in 3 mL water). Solvents: DME (3 mL), water (3 mL). Purification: The product was purified by column chromatography (alumina, hexane/EtOAc, 100:0 → 0:100, then DCM/MeOH 100:0 → 90:10) and was obtained as a white oily solid (0.050 g, 1.4 x 10^{-4} mol, 51%), R_f = 0.43 (alumina, 100% EtOAc). ^{1}H NMR (700 MHz, $CDCl_3$) δ_H = 3.04 (12H, s, CH_3), 6.45 (2H, dd, J(^{1}H) = 6.0 and 2.5, H_5), 6.90 (2H, d, J(^{1}H) = 2.0, H_3), 6.94 (1H, t, J(^{19}F) = 10.5, $H_{5'}$), 8.29 (2H, d, J(^{1}H) = 6.0, H_6), 8.35 (1H, t, J(^{19}F) = 9.0, $H_{2'}$). ^{13}C {^{1}H} NMR (176 MHz, $CDCl_3$) δ_C = 39.2 (s, CH_3), 104.8 (t, J(^{19}F) = 27. 0, $C_{5'}$), 105.7 (s, C_5), 107.4 (t, J(^{19}F) = 3.5, C_3), 125.5 (dd, J(^{19}F) = 11.5 and 5.0, $C_{1'}$), 133.9 (t, J(^{19}F) = 4.5, $C_{2'}$), 149.7 (s, C_6), 153.1 (s, C_2), 154.9 (s, C_4), 160.2 (dd, J(^{19}F) = 254.0 and 12.5, $C_{4'}$), ^{19}F NMR (376 MHz, $CDCl_3$) δ_F = -112.8 (2F, br m). HRMS (ES^+): *m/z* 377.1546 [22%, M+Na^+], 355.1726 [100, M+H^+]; calcd for [$C_{20}H_{21}F_2N_4$], 355.1729, calcd for [$C_{20}H_{20}F_2N_4{}^{23}Na$], 377.1548.

HL[18]: 1,3-di(4-nitro-2-pyridyl)benzene

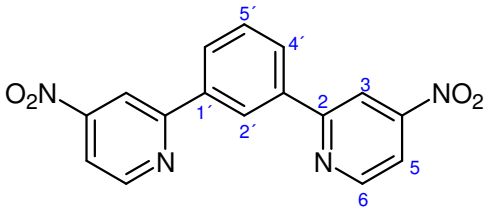

Ligand HL[18] was prepared via the Suzuki-Miyaura method. Reagents: Benzene-1,3-diboronic acid (0.37 g, 2.2 x 10^{-3} mol), 2-bromo-4-nitropyridine (1.0 g, 4.9 x 10^{-4} mol), Na_2CO_3 (5 mL of a 1M solution in water), $Pd(PPh_3)_4$ (0.32 g, 2.7 x 10^{-4} mol). Solvents: DME (5 mL), water (5 mL). Purification: Column chromatography (silica, hexane/EtOAc 100:0 → 40:60). The product was obtained as a creamy white solid (0.273 g, 38%), R_f 0.41 (silica, hexane/EtOAc 70:30). ^1H NMR (700 MHz, $CDCl_3$) δ_H = 7.71 (1H, t, J(^1H) = 8.0, $H_{5'}$), 8.00 (2H, dd, J(^1H) = 5.0 and 2.0, H_5), 8.21 (2H, dd, J(^1H) = 8.0 and 2.0, $H_{4'}$), 8.56 (2H, d, J(^1H) = 2.0, H_3), 8.86 (1H, t, J(^1H) = 2.0, $H_{2'}$), 9.03 (2H, d, J(^1H) = 5.0, H_6), ^{13}C {^1H} NMR (176 MHz, $CDCl_3$) δ_C = 113.3 (s, C_3), 115.1 (s, C_5), 126.3 (s, $C_{2'}$), 129.1 (s, $C_{4'}$), 130.2 (s, $C_{5'}$), 138.5 (s, $C_{1'}$), 152.5 (s, C_6), 155.4 (s, C_4), 160.1 (s, C_2). MS (ES^+): *m/z* 323.5 [M+H^+]; calcd for [$C_{16}H_{11}N_4O_4$], 323.

HL[19]: 1,3-di(4-fluoro-2-pyridyl)benzene

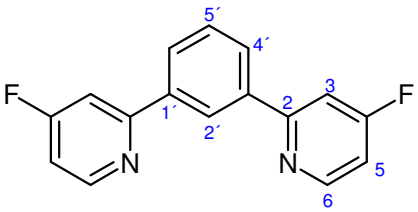

This ligand was prepared via fluorodenitration of HL[18], and two solvent systems were investigated. The procedures reported here are adaptations of the fluorodenitration of 2-bromo-4-nitropyridine, reported in reference 17.

Method A:

1,3-di(4-nitro-2-pyridyl)benzene (0.072 g, 2.2 x 10^{-4} mol) was dissolved in DMF (3 mL). A solution of tetrabutylamonnium fluoride (TBAF) in THF (1M, 0.25 mL, 8.9 x 10^{-4} mol) was added, and the reaction was stirred at room temperature for 30 min. The mixture was poured into a 1:1 mixture of EtOAc:water (50 mL) and the organic layer

was extracted. The organic layer was washed with water (2 x 30 mL) and brine (2 x 30 mL), then dried over Na_2SO_4 and filtered. The solvent was removed *in vacuo*. Proton NMR of the crude product indicated incomplete conversion. The reaction was repeated with the crude mixture. This time a larger excess of TBAF (0.5 mL, 1.8 x 10^{-5} mol) was added, and the reaction was stirred for 1 h. TLC indicated complete conversion at this point. The crude product was purified via column chromatography (silica, hexane/EtOAc, 100:0 → 50:50). The product obtained as a white powder (0.043 g, 1.6 x 10^{-4} mol, 72%).

Method B:

1,3-di(4-nitro-2-pyridyl)benzene (0.025 g, 7.8 x 10^{-5} mol) was dissolved in DCM (5 mL). A solution of tetrabutylamonnium fluoride (TBAF) in THF (1M, 0.1 mL, 3.1 x 10^{-4} mol) was added, and the reaction was stirred at 70˚C for 30 min. TLC was used to check the reaction, and indicated incomplete conversion. More TBAF (0.6 mL, 2.0 x 10^{-3} mol) was added, and the reaction was stirred at 70˚C for an additional 1 h. The mixture was poured into a 1:1 mixture of EtOAc:water (50 mL) and the organic layer was extracted. The organic layer was washed with water (2 x 30 mL) and brine (2 x 30 mL), then dried over Na_2SO_4 and filtered. The solvent was removed *in vacuo* and the crude product was purified via column chromatography (silica, hexane/EtOAc, 100:0 → 50:50). The product was obtained as a white powder (0.020 g, 7.5 x 10^{-5} mol, 96%). R_f = 0.70 (silica, 100% EtOAc). ^1H NMR (500 MHz, $CDCl_3$) δ_H = 7.03 (2H, ddd, J(^{19}F) = 8.3, J(^1H) = 5.5 and 2.5, H_5), 7.57 (2H, dd, J(^{19}F) = 10.5 and J(^1H) = 2.5, H_3), 7.63 (1H, t, J(^1H) = 8.0, $H_{5'}$), 8.09 (2H, dd, J(^1H) = 8.0 and 2.0, $H_{4'}$), 8.64 (1H, t, J(^1H) = 2.0, $H_{2'}$), 8.70 (2H, dd, J(^{19}F) = 9.0 and J(^1H) = 5.5, H_6), ^{13}C {^1H} NMR (126 MHz, $CDCl_3$) δ_C = 108.7 (d, J(^{19}F) = 17.0, C_3), 110.5 (d, J(^{19}F) = 17.0, C_5), 125.9 (s, $C_{2'}$), 128.3 (s, $C_{4'}$), 129.7 (s, $C_{5'}$), 139.2 (d, J(^{19}F) = 3.5, $C_{1'}$), 152.2 (d, J(^{19}F) = 7.0 C_6), 160.4 (d, J(^{19}F) = 7.0, C_2), 169.7 (d, J(^{19}F) = 260.5, C_4). ^{19}F NMR (376 MHz, $CDCl_3$) δ_F = -102.7 (2F, q, J(^1H) = 9.0). HRMS (ES^+): *m/z* 269.0889 [100%, M+H^+]; calcd for [$C_{16}H_{11}F_2N_2$], 269.0885.

HL^{20}: 1,3-di(4-trifluoromethyl-2-pyridyl)-4,6-difluorobenzene

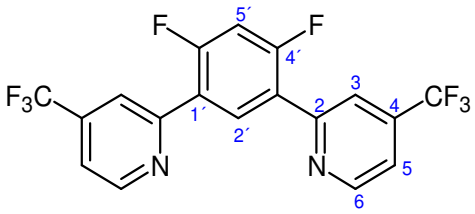

Ligand HL^{20} was prepared via the Suzuki-Miyaura method. Reagents: 1,3-Difluoro-4,6-(4,4,5,5-tetramethyl-1,3,2-dioxaborolan-2-yl)benzene (0.045 g, 1.2 x 10^{-4} mol), 2-chloro-4-trifluoromethylpyridine (0.049 g, 2.7 x 10^{-4} mol), Na_2CO_3 (1M, in 2 mL water), $Pd(PPh_3)_4$ (0.017 g, 2 x 10^{-5} mol). Solvents: DME (2 mL), water (2 mL). Purification: The product was purified by column chromatography (silica, hexane/EtOAc 100:0 → 80:20), and was obtained as a white oily solid (0.040 g, 1.09 x 10^{-4} mol, 89%), R_f = 0.42 (silica, hexane/EtOAc 80:20). ^{1}H NMR (700 MHz, $CDCl_3$) δ_H = 7.12 (1H, t, J(^{19}F) = 11.0, $H_{5'}$), 7.51 (2H, dd, J(^{1}H) = 5.0 and 0.5, H_5), 8.04 (2H, s, H_3), 8.83 (1H, t, J(^{19}F) = 9.0, $H_{2'}$), 9.21 (2H, d, J(^{1}H) = 5.0, H_6), ^{13}C {^{1}H} NMR (176 MHz, $CDCl_3$) δ_C = 105.7 (t, J(^{19}F) = 27.5, $C_{5'}$), 118.5 (q, J(^{19}F) = 3.5, C_5), 119.9 (m, C_3), 123.1 (q, J(^{19}F) = 270.0, CF_3), 123.6 (dd, J(^{19}F) = 10.5 and 5.0, $C_{1'}$), 134.0 (t, J(^{19}F) = 4.0, $C_{2'}$), 139.3 (q, J(^{19}F) = 34.0, C_4), 150.9 (s, C_6), 153.6 (t, J(^{19}F) = 1.5, C_2), 161.4 (dd, J(^{19}F) = 257.0 and 13.0, $C_{4'}$). ^{19}F NMR (376 MHz, $CDCl_3$) δ_F = -111.1 (2F, t, J = 10.0), -65.2 (6F, s). HRMS (ES^+): *m/z* 405.0636 [15%, $M+H^+$]; calcd for [$C_{18}H_9F_8N_2$], 405.0633.

2-Tri-n-butylstannyl-4-trifluoromethylpyridine

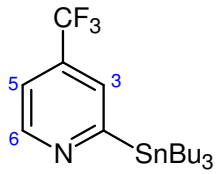

This stannane was prepared via the ortho-directed lithiation/stannylation route. Reagents: 2-(Dimethylamino)ethanol (0.8 mL, 8 x 10^{-3} mol), n-BuLi (6.4 mL, 2.5 M in hexanes, 1.6 x 10^{-2} mol), 4-trifluoromethylpyridine (0.50 g, 3.4 x 10^{-3} mol) $SnBu_3Cl$ (1.22 g, 1.02 mL, 3.7 x 10^{-3} mol). The product was obtained as a dark brown liquid (2.09 g, assumed 40% pure from NMR, therefore 0.84 g product, 57%). ^{1}H NMR (400

MHz, $CDCl_3$) δ_H = 0.5-2 (27H, m, $SnBu_3$ H), 7.29 (1H, m, H_5), 7.56 (1H, quintet, $J(^1H)$ = 1.0, $^4J(^{117/118}Sn)$ = 16.0, H_3), 8.90 (1H, dt, $J(^1H)$ = 5.0 and 0.5, H_6).

HL^{21}: 1-(4-methoxy-2-pyridyl)-3-(4-trifluoromethyl-2-pyridyl)-4,6-difluorobenzene

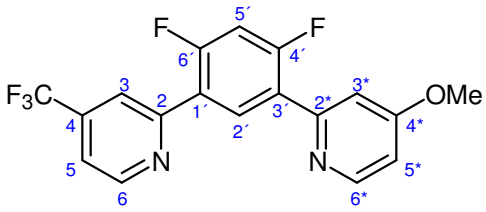

Ligand HL^{21} was prepared via the Stille methodology. Reagents: 1-Bromo-2,4-difluoro-5-(4-methoxy-2-pyridyl)benzene (0.060 g, 2.0 x 10^{-4} mol), 2-tri-n-butylstannyl-4-trifluoromethyl pyridine (0.11 g, 2.4 x 10^{-4} mol), $Pd(PPh_3)_2Cl_2$ (0.0052 g, 7 x 10^{-6} mol), LiCl (0.059 g, 1.4 x 10^{-3} mol). Solvent: toluene (3 mL). Purification: The product was purified by column chromatography (silica, hexane:EtOAc, 100:0 →30:70). The product was obtained as a yellow oil (0.040 g, 1.09 x 10^{-4} mol, 55%), R_f = 0.67 (silica, 100% EtOAc). ^1H NMR (700 MHz, $CDCl_3$) δ_H = 6.81 (1H, dd, $J(^1H)$ = 6.0 and 2.0, H_{5*}), 7.05 (1H, t, $J(^{19}F)$ = 10.0, $H_{5'}$), 7.30 (1H, t, $J(^1H)$ = 2.0, H_{3*}), 7.47 (1H, dd, $J(^1H)$ = 5.0 and 1.0, H_5), 7.99 (1H, s, H_3), 8.54 (1H, d, $J(^1H)$ = 6.0, H_{6*}), 8.68 (1H, t, $J(^{19}F)$ = 9.0, $H_{2'}$), 8.89 (1H, d, $J(^1H)$ = 5.0, H_6), ^{13}C {^1H} NMR (176 MHz, $CDCl_3$) δ_C = 56.5 (s, OCH_3), 105.4 (t, $J(^{19}F)$ = 27.5, $C_{5'}$), 109.0 (s, C_{5*}), 110.9 (d, $J(^{19}F)$ = 9.0, C_{3*}), 118.2 (q, $J(^{19}F)$ = 3.5, C_5), 119.8 (m, C_3), 123.1 (q, $J(^{19}F)$ = 270.0, CF_3), 123.3 (dd, $J(^{19}F)$ = 11.5 and 3.5, $C_{3'}$), 124.9 (dd, $J(^{19}F)$ = 11.5 and 3.5, $C_{1'}$), 134.0 (t, $J(^{19}F)$ = 4.0, $C_{2'}$), 139.1 (q, $J(^{19}F)$ = 34.5, C_4), 150.9 (s, C_6), 151.1 (s, C_{6*}), 153.8 (d, $J(^{19}F)$ = 2.5, C_{2*}), 154.0 (d, $J(^{19}F)$ = 2.5, C_2), 160.8 (dd, $J(^{19}F)$ = 256.0 and 12.0, $C_{6'}$), 161.0 (dd, $J(^{19}F)$ = 256.0 and 12.0, $C_{4'}$), 166.3 (s, C_{4*}). ^{19}F NMR (376 MHz, $CDCl_3$) δ_F = -107.8 (1F, sept, $J(^1H)$ = 13.0, F), -107.1 (1F, sept, $J(^1H)$ = 13.0, F), -65.3 (3F, s, CF_3). HRMS (ES^+): *m/z* 367.0867 [100%, $M+H^+$]; calcd for [$C_{18}H_{12}F_2N_2O$], 367.0864.

HL[22]: 1,3-di(5-fluoro-2-pyridyl)benzene

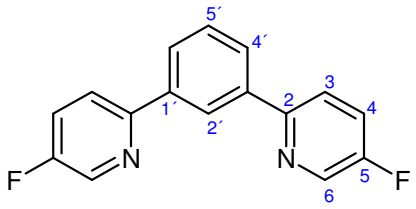

Ligand HL^{22} was prepared via the Suzuki-Miyaura method. Reagents: Benzene-1,3-diboronic acid (0.17 g, 1.0 x 10^{-3} mol) and 2-bromo-5-fluoro pyridine (0.40 g, 2.3 x 10^{-3} mol), Na_2CO_3 (1M in 5 mL) and $Pd(PPh_3)_4$ (0.14 g, 1.2 x 10^{-4} mol). Solvents: DME (5 mL) and water (5 mL). Purification: column chromatography (silica, hexane/EtOAc, 100:0 → 60:40). The product came off the column around 25% EtOAc, and was obtained as a white powder (0. 15 g, 5.6 x 10^{-4} mol, 54%). R_f = 0.76 (silica, 100% EtOAc). ^1H NMR (500 MHz, $CDCl_3$) δ_H = 7.50 (2H, dd, J(^{19}F) = 9.0, and J(^1H) = 3.5, H_4), 7.58 (1H, t, J(^1H) = 8.0, $H_{5'}$), 7.83 (2H, q, J(^1H) = 3.5, H_3), 8.00 (2H, dd, J(^1H) = 8.0 and 2.0, $H_{4'}$), 8.56 (1H, t, J(^1H) = 2.0, $H_{2'}$), 8.57 (2H, d, J(^{19}F) = 3.0, H_6). ^{13}C {^1H} NMR (126 MHz, $CDCl_3$) δ_C = 121.7 (d, J(^{19}F) = 4.0, C_3), 123.8 (d, J(^{19}F) = 19.0, C_4), 125.5 (s, $C_{2'}$), 127.4 (s, $C_{4'}$), 129.6 (s, $C_{5'}$), 138.1 (d, J = 23.5, C_6), 139.2 (s, $C_{1'}$), 153.6 (d, J(^{19}F) = 4.0, C_2), 159.2 (d, J(^{19}F) = 256.0, C_5). ^{19}F NMR (376 MHz, $CDCl_3$) δ_F = -129.8 (2F, q, J(^1H) = 4.0). HRMS (ES^+): *m/z* 291.0705 [14%, M+Na^+], 269.0883 [100, M+H^+]; calcd for [$C_{16}H_{11}F_2N_2$], 269.0885, calcd for [$C_{16}H_{10}F_2N_2{}^{23}Na$], 291.0704. Anal. $C_{16}H_{10}F_2N_2$ (268.25): calcd C, 71.63; H, 3.76; N, 10.44; found C, 71.13; H, 4.09; N, 9.32

2-(2-Methoxy-phenyl)-6-(3-pyridin-2-yl-phenyl)pyridine

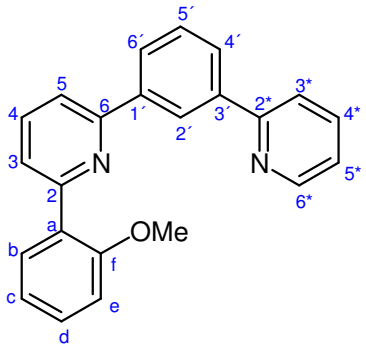

The synthesis of this ligand precursor, and HL^{23} was based on a method reported for the synthesis of 6-(2-hydroxyphenyl)-2,2'-bipyridine in reference 18.

Tetramethylethylenediamine (TMEDA) (0.26 mL, 1.7 x 10^{-3} mol) was transferred under nitrogen to a dry 100 mL two-necked round bottom flask. Dry ether (20 mL) was added under nitrogen, and the solution was cooled to 0˚C in an ice bath. n-BuLi (0.68 mL, 1.7 x 10^{-3} mol) was added dropwise (over 10 min), and the mixture was stirred for 15 min. Anisole (0.15 mL, 1.4 x 10^{-3} mol) was added at 0˚C, and the mixture was stirred for 30 min, before being allowed to warm to room temperature. The mixture was stirred for a further 2.5 h. The mixture was then transferred (over 20 min) under nitrogen to an ice-cold solution of 1,3-di(2-pyridyl)benzene (0.30 g, 1.3 x 10^{-3} mol) in ether (20 mL), and the mixture was allowed to warm to room temperature overnight. Water (15 mL) was added slowly and with vigorous stirring (10 min). The mixture was extracted with ether (3 x 30 mL), dried with $MgSO_4$, and the solvent was removed *in vacuo*. The crude product was dissolved in acetone and cooled in an ice bath. A saturated solution of $KMnO_4$ was prepared in cold acetone, and added dropwise until a purple tint remained. The MnO_2 by-product was removed by filtration through a celite plug. The filtrant was dried with $MgSO_4$ and solvent was removed *in vacuo*. The crude product was purified by column chromatography (silica, hexane/EtOAc, 100:0 → 65:35), and the desired product was obtained as a pale yellow oil (0.13 g, 3.8 x 10^{-4} mol, 30%). R_f 0.60 (silica, hexane/EtOAc 50:50). ^1H NMR (700 MHz, $CDCl_3$) δ_H = 3.86 (3H, s, CH_3), 7.00 (1H, d, J(^1H) = 8.0, H_e), 7.10 (1H, td, J(^1H) = 8.0 and 1.0, H_c), 7.24 (1H, ddd, J(^1H) = 7.5, 5.0 and 1.0, H_{5*}), 7.38 (1H, td, J(^1H) = 8.0 and 2.0, H_d), 7.58 (1H, t, J(^1H) = 8.0, $H_{5'}$), 7.75-7.88 (5H, m, H_3, H_4, H_5, H_{3*}, H_{4*}), 8.20-8.70 (2H, m, $H_{6'}$, H_b), 8.40 (1H, dt, J(^1H) = 8.0 and 1.5, $H_{4'}$), 8.68 (1H, t, J(^1H) = 1.5, $H_{2'}$), 8.72 (1H, ddd, J(^1H) = 5.0, 1.5 and 1.0, H_6), ^{13}C {^1H} NMR (176 MHz, $CDCl_3$) δ_C = 55.9 (s, CH_3), 111.7 (s, C_e), 118.8 (s, C_3), 121.1 (s, C_{3*}), 121.3 (s, C_c), 122.5 (s, C_{5*}), 124.0 (s, C_5), 125.7 (s, $C_{2'}$), 127.6 (s, $C_{6'}$), 127.9 (s, $C_{4'}$), 129.4 (s, $C_{5'}$), 129.5 (s, C_a), 130.2 (s, C_d), 131.8 (s, C_b), 136.6 (s, C_{4*}), 137.1 (s, C_4), 140.0 (s, $C_{1'}$), 140.5 (s, $C_{3'}$), 149.9 (s, C_{6*}), 155.7 (s, C_6), 156.8 (s, C_{2*}), 157.4 (s, C_2), 157.6 (s, C_f). HRMS (ES^+): *m/z* 339.1494 [100%, $M+H^+$]; calcd for [$C_{23}H_{19}N_2O$], 339.1492.

HL[23]: 2-(2-Hydroxy-phenyl)-6-(3-pyridin-2-yl-phenyl)pyridine

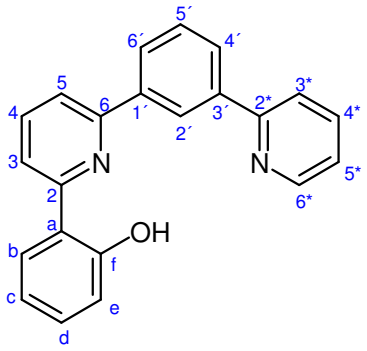

Pyridine (3.0 mL, 3.7 x 10^{-2} mol) and concentrated HCl (3.3 mL) were mixed in a 50 mL round bottom flask, and the mixture was distilled to remove water. The mixture was then heated to 220℃ for 5 min, giving pyridine hydrochloride (py.HCl). This was used directly in the next step without characterisation. The excess py.HCl was added hot to 2-(2-methoxy-phenyl)-6-(3-pyridin-2-yl-phenyl)-pyridine (0.13 g, 3.8 x 10^{-4} mol) and the mixture was heated at 230℃ overnight. The mixture was cooled and dissolved in dilute HCl. The solution was neutralised with NaOH, and the crude product was collected by filtration. This was dissolved in DCM, and further product was extracted from the aqueous phase with DCM. The DCM portions were combined, dried with $MgSO_4$, filtered and the solvent was removed *in vacuo*. The crude product was purified by column chromatography (silica, hexane/EtOAc, 100:0 → 60:40), and the desired product was obtained as a pale yellow oily solid (0.12 g, 3.7 x 10^{-4} mol, 96%). R_f = 0.67 (silica, EtOAc 100%), ^{1}H NMR (700 MHz, $CDCl_3$) δ_H = 6.94 (1H, ddd, J(^{1}H) = 9.0, 7.0 and 1.0, H_c), 7.06 (1H, dd, J(^{1}H) = 8.0 and 1.0, H_e), 7.27 (1H, ddd, J(^{1}H) = 7.5, 5.0 and 1.0, H_{5*}), 7.34 (1H, ddd, J(^{1}H) = 8.0, 7.5 and 1.0, H_d), 7.62 (1H, t, J = 8.0, $H_{5'}$), 7.75 (1H, d, J(^{1}H) = 7.5, H_5), 7.80 (1H, td, J(^{1}H) = 7.5 and 2.0, H_{4*}), 7.84 (1H, dt, J(^{1}H) = 8.0 and 1.0, H_{3*}), 7.85 (1H, dd, J(^{1}H) = 8.0 and 1.0, H_b), 7.87 (1H, d, J(^{1}H) = 8.0, H_3), 7.91 (1H, t, J(^{1}H) = 8.0, H_4), 8.01 (1H, ddd, J(^{1}H) = 8.0, 1.5 and 1.0, $H_{6'}$), 8.10 (1H, ddd, J(^{1}H) = 8.0, 1.5 and 0.5, $H_{4'}$), 8.54 (1H, t, J(^{1}H) = 1.5, $H_{2'}$), 8.73 (1H, d, J(^{1}H) = 5.0, H_{6*}). ^{13}C {^{1}H} NMR (176 MHz, $CDCl_3$) δ_C = 117.9 (s, C_3), 118.8 (s, C_e), 119.1 (s, C_c), 119.2 (s, C_a), 119.2 (s, C_5), 121.0 (s, C_{3*}), 122.7 (s, C_{5*}), 125.7 (s, $C_{2'}$), 126.6 (s, C_b), 127.6 (s, $C_{6'}$), 128.3 (s, $C_{4'}$), 129.8 (s, $C_{5'}$), 131.8 (s, C_d), 137.2 (s, C_{4*}), 138.8 (m, C_4 and $C_{1'}$), 140.5 (s, $C_{3'}$), 150.0 (s, C_{6*}), 154.9 (s, C_6), 157.1 (s, C_{2*}), 158.0 (s, C_2), 160.2 (s, C_f). HRMS (ES^+): *m/z* 325.1327 [100%, $M+H^+$]; calcd for [$C_{22}H_{17}N_2O$], 325.1335.

HL^{24}: 1,3-di(2-pyridyl)-5-hydroxybenzene

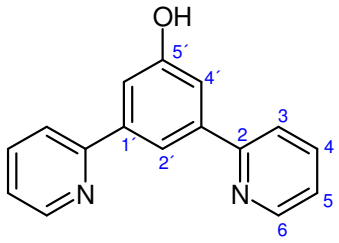

Ligand HL^{24} was prepared via the Stille methodology. Reagents: 2-Tri-n-butylstannylpyridine (1.89 g, assumed 85% pure, 4.4 x 10^{-3} mol), 3,5-dibromophenol (0.50 g, 2.0 x 10^{-3} mol), $Pd(PPh_3)_2Cl_2$ (0.051 g, 7 x 10^{-5} mol) and LiCl (0.59 g, 1.4 x 10^{-2} mol). Purification: The residue was purified with column chromatography (silica, hexane/ether gradient elution from 100/0 to 0/100) and the product was obtained as a white powder (0.073 g, 15%), R_f = 0.24 (silica, 100% ether). ^1H NMR (700 MHz, $CDCl_3$) δ_H =7.29 (2H, ddd, J(^1H) = 7.5, 5.0 and 1.0, H_5), 7.60 (2H, d, J(^1H) = 1.0, $H_{4'}$), 7.80 (2H, td, J(^1H) = 7.5 and 2.0, H_4), 7.83 (2H, dt, J(^1H) = 7.5 and 1.0, H_3), 8.11 (1H, t, J(^1H) = 1.0, $H_{2'}$), 8.69 (2H, ddd, J(^1H) = 5.0, 2.0 and 1.0, H_6), ^{13}C {^1H} NMR (176 MHz, $CDCl_3$) δ_C = 111.5 (s, $C_{4'}$), 118.3 (s, $C_{2'}$), 121.6 (s, C_3), 122.9 (s, C_5), 137.8 (s, C_4), 140.9 (s, $C_{5'}$), 149.2 (s, C_6), 156.8 (s, C_2), 151.5 (s, $C_{1'}$). HRMS (ES^+): *m/z* 249.1022 [100%, $M+H^+$]; calcd for [$C_{16}H_{13}N_2O$], 249.1022.

1,3-Dibromo-5-(2-bromoethoxy)benzene

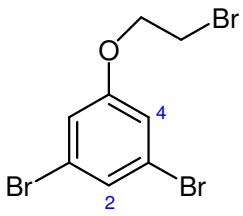

This was prepared via the Williamson ether synthesis route. Reagents: 3,5-Dibromophenol (0.20 g, 7.9 x 10^{-4} mol), 1,2-dibromoethane (2.24 g, 1.19 x 10^{-2} mol) K_2CO_3 (2.20 g, 1.59 x 10^{-2} mol) and Cs_2CO_3 (~10 mg). The solvent used was CH_3CN (20 mL). The product was obtained as a pale brown oil (0.26 g, 7.3 x 10^{-4} mol, 92%). This product did not need purifying. ^1H NMR (400 MHz, $CDCl_3$) δ_H = 3.60 (2H, t, J(^1H) = 6.0, CH_2(Br)), 4.23 (2H, t, J(^1H) = 6.0, CH_2(O)), 6.99 (2H, d, J(^1H) = 1.5, H_4), 7.27 (1H, t, J(^1H) = 1.5, H_2).

3-[2-(3,5-Dibromo-phenoxy)-ethoxy]-2-phenyl-chromen-4-one

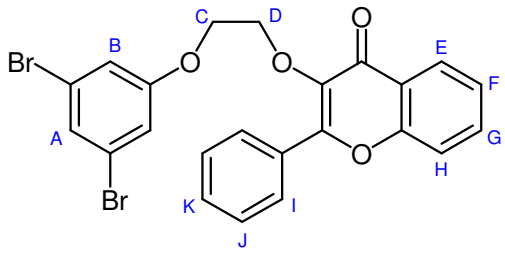

This compound was prepared via the Williamson-ether synthesis route. Reagents: 1,3-Dibromo-5-(2-bromo-ethoxy)-benzene (0.26 g, 7.3 x 10^{-4} mol), 3-hydroxy-2-phenyl-chromen-4-one (0.18 g, 7.3 x 10^{-4} mol), K_2CO_3 (2.03 g, 1.7 x 10^{-2} mol) and Cs_2CO_3 (5 mg). The solvent used was dry CH_3CN (40 mL). The product was obtained as a beige powder (0.28 g, 5.4 x 10^{-4} mol, 74%). ^1H NMR (400 MHz, $CDCl_3$) δ_H = 4.13 (2H, m, CH_2), 4.50 (2H, m, CH_2), 6.77 (2H, d, J(^1H) = 1.5, H_2), 7.21 (1H, t, J(^1H) = 1.5, H_1), 7.4-7.5 (4H, m, H_6, H_{10}, and H_{11}), 7.56 (1H, d, J(^1H) = 8.5, H_8), 7.71 (1H, ddd, J(^1H) = 8.5, 7.0 and 1.5, H_7), 8.09 (2H, m, H_9), 8.27 (1H, dd, J(^1H) = 8.0 and 1.5, H_5). MS (ES^+): *m/z* 541.1 [52%, ^{81}Br, M+Na^+,], 539.1 [58, ^{79}Br, ^{81}Br, M+Na^+], 537.1 [54, ^{79}Br, M+Na^+]; calcd for [$C_{23}H_{16}{}^{79}Br_2O_4{}^{23}Na$], 536.9. Anal. $C_{23}H_{16}Br_2O_4$ (516.16): calcd C, 53.52; H, 3.12; found C, 50.62; H, 3.41.

HL^{25}: 3-[2-(3,5-Di-pyridin-2-yl-phenoxy)-ethoxy]-2-phenyl-chromen-4-one

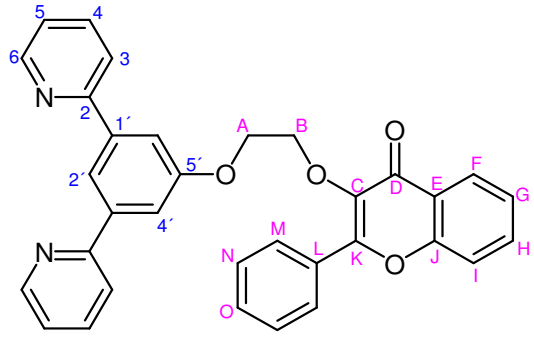

Ligand HL^{25} was prepared via the Stille method. Reagents: 3-[2-(3,5-Dibromo-phenoxy)-ethoxy]-2-phenyl-chromen-4-one (0.14 g, 2.7 x 10^{-4} mol), 2-tri-n-butylstannyl pyridine (0.26 g, assumed 85% pure, 6.1 x 10^{-4} mol), $Pd(PPh_3)_2Cl_2$ (0.007 g, 1 x 10^{-5} mol) and LiCl (0.082 g, 1.9 x 10^{-3} mol). The solvent used was toluene (10 mL). Purification of product was achieved via column chromatography (silica, hexane/EtOAc, 100:0 → 20:80). The product was obtained as a pale yellow solid (0.039

g, 29%). R_f (silica, 100% EtOAc) = 0.50. ^{1}H NMR (700 MHz, $CDCl_3$) δ_H = 4.35 (2H, t, J(^{1}H) = 4.5, CH_2), 4.60 (2H, t, J(^{1}H) = 4.5, CH_2), 7.25 (2H, m, H_5), 7.36 (1H, t, J(^{1}H) = 7.0, H_O), 7.41 (3H, m, H_N and H_G), 7.48 (2H, s, $H_{4'}$), 7.52 (1H, d, J(^{1}H) = 8.0, H_I), 7.66 (1H, ddd, J(^{1}H) = 9.0, 8.0 and 1.5, H_H), 7.76 (2H, td, J(^{1}H) = 7.0 and 1.5, H_4), 7.77 (2H, d, J(^{1}H) = 7.5, H_3), 8.16 (2H, d, J(^{1}H) = 7.5, H_M), 8.20 (1H, s, $H_{2'}$), 8.27 (1H, dd, J(^{1}H) = 8.0 and 1.0, H_F), 8.69 (2H, dt, J(^{1}H) = 4.5 and 0.5, H_6). ^{13}C {^{1}H} NMR (176 MHz, $CDCl_3$) δ_C = 67.2 (s, CH_2), 70.2 (s, CH_2), 113.9 (s, $C_{4'}$), 118.2 (s, C_I), 118.4 (s, $C_{2'}$), 121.0 (s, C_3), 122.6 (s, C_5), 124.4 (s, $C_{E\text{ or }L}$), 124.9 (s, C_G), 126.0 (s, C_F), 128.6 (s, C_N), 129.1 (s, C_M), 130.9 (s, C_O), 131.0 (s, $C_{E\text{ or }L}$), 133.7 (s, C_H), 137.0 (s, C_4), 140.4 (s, C_C), 141.2 (s, $C_{5'\text{ or }1'}$), 149.8 (2C, s, C_6), 155.5 (s, C_J), 156.1 (s, C_K), 157.1 (s, C_2), 159.6 (s, $C_{5'\text{ or }1'}$), 175.4 (s, C_D). HRMS (ES$^+$): *m/z* 513.1814 [100%, M+H$^+$]; calcd for [$C_{33}H_{25}N_2O_4$], 513.1814.

3-{2-[2-(3,5-Dibromo-phenoxy)-ethoxy]-ethoxy}-2-phenyl-chromen-4-one

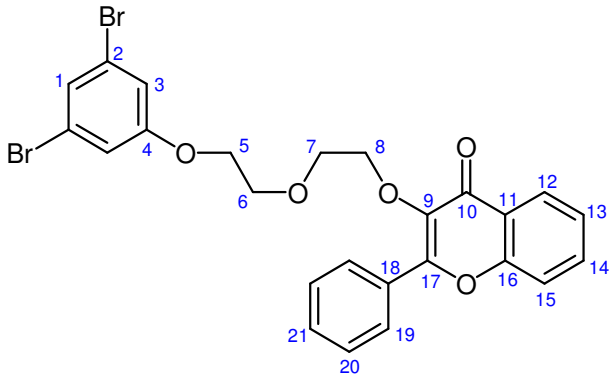

This was prepared via the Williamson ether synthesis route. Reagents: Dry K_2CO_3 (1.10 g, 8.0 x 10^{-3} mol), Cs_2CO_3 (~10 mg), 3,5-dibromophenol (0.12 g, 4.8 x 10^{-4} mol) and 3-[2-(2-bromo-ethoxy)-ethoxy]-2-phenyl-chromen-4-one (0.14 g, 3.5 x 10^{-4} mol). Solvent: CH_3CN (30 mL). Purification: The crude product was purified with column chromatography (silica, hexane/ether gradient elution, 100:0 → 60:40). The pure product was obtained as a yellow solid (0.090 g, 1.6 x 10^{-4} mol, 46%). R_f = 0.68 (silica, 100% ether). ^{1}H NMR (700 MHz, $CDCl_3$) δ_H = 3.68 (2H, t, J(^{1}H) = 5.0, H_7), 3.77 (2H, ddd, J(^{1}H) = 6.0, 3.0 and 1.5, H_6), 3.90 (2H, t, J(^{1}H) = 4.5, H_5), 4.32 (2H, ddd, J(^{1}H) = 6.0, 3.0 and 1.5, H_8), 6.93 (2H, d, J(^{1}H) = 1.0, H_3), 7.22 (1H, t, J(^{1}H) = 1.5, H_1), 7.34 (1H, t, J(^{1}H) = 7.5, H_{13}), 7.47 (3H, m, $H_{20/21}$), 7.53 (1H, d, J(^{1}H) = 8.0, H_{15}), 7.67 (1H, ddd, J(^{1}H) = 8.0, 6.5 and 1.5, H_{14}), 8.16 (2H, dd, J(^{1}H) = 7.0 and 4.0, H_{19}), 8.25 (1H, dd,

J(^{1}H) = 8.0 and 1.0, H_{12}). ^{13}C {^{1}H} NMR (176 MHz, $CDCl_3$) δ_C = 67.9 (1C, s, C_8), 69.0 (1C, s, C_7), 70.6 (1C, s, C_6), 71.4 (1C, s, C_5), 117.3 (2C, s, C_3), 118.2 (1C, s, C_{15}), 123.2 (2C, s, C_2), 124.3 (1C, s, C_{11}), 124.9 (1C, s, C_{13}), 126.0 (1C, s, C_{12}), 126.8 (1C, s, C_1), 128.6 (s, $C_{20\text{ or }21}$), 129.1 (2C, s, C_{19}), 130.9 (s, $C_{20\text{ or }21}$), 131.2 (1C, s, C_{18}), 133.7 (1C, s, C_{14}), 140.6 (1C, s, C_9), 155.5 (1C, s, C_{17}), 155.9 (1C, s, C_{16}), 160.1 (1C, s, C_4), 175.4 (1C, s, C_{10}). MS (ES^+): *m/z* 584.9 [30%, 2Br = 81, M+Na^+], 582.9 [100, 1Br = 79, 1Br = 81, M+Na^+], 580.9 [55, 2Br = 79, M+Na^+]; calcd for [$C_{25}H_{20}{}^{79}Br_2O_5$], 558.

HL^{26}: 3-{2-[2-(3,5-Di-pyridin-2-yl-phenoxy)-ethoxy]-ethoxy}-2-phenyl-chromen-4-one

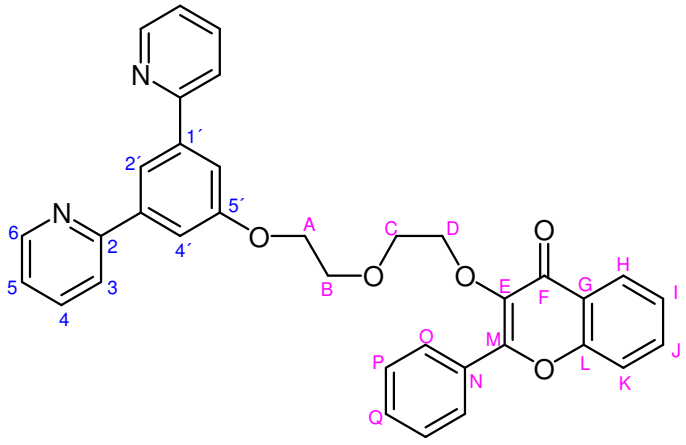

Two attempts at making HL^{26} were pursued (both Stille reactions, but different solvent systems, toluene and xylene, methods A and B respectively).

Method A:

Reagents: 3-{2-[2-(3,5-Dibromo-phenoxy)-ethoxy]-ethoxy}-2-phenyl-chromen-4-one (0.090 g, 1.6 x 10^{-4} mol), tri-n-butyl-2-stannyl pyridine (0.l4 g, assumed 85% pure, 3.3 x 10^{-4} mol), $Pd(PPh_3)_2Cl_2$ (0.004 g, 6 x 10^{-6} mol) and LiCl (0.050 g, 1.2 x 10^{-3} mol). Solvent: Toluene (12 mL). Purification: Column chromatography (silica, hexane/EtOAc, 100:0 → 0:80, the product came off around 75% EtOAc). The pure product was obtained as a yellow oily solid (0.026 g, 4.7 x 10^{-5} mol, 29%).

Method B:

Reagents: 3-{2-[2-(3,5-Dibromo-phenoxy)-ethoxy]-ethoxy}-2-phenyl-chromen-4-one (0.21 g, 3.8 x 10^{-4} mol), tri-n-butyl-2-stannyl pyridine (0.35 g, assumed 85% pure, 8.4 x

10^{-4} mol), $Pd(PPh_3)_2Cl_2$ (0.013 g, 2 x 10^{-5} mol), PPh_3 (0.010 g, 4 x 10^{-5} mol) and LiCl (0.12 g, 2.8 x 10^{-3} mol). Solvent: xylene (8 mL). Purification: column chromatography (silica, hexane/EtOAc, 100:0 → 0:80, the product came off around 75% EtOAc). The pure product was obtained as a yellow oily solid (0.10 g, 1.8 x 10^{-4} mol, 47%), R_f (silica, 100% EtOAc) = 0.47. ^{1}H NMR (700 MHz, $CDCl_3$) δ_H = 4.13 (2H, q, J(^{1}H) = 7.0, CH_2), 4.2-4.4 (6H, m, $3CH_2$), 6.72 (1H, dd, J(^{1}H) = 8.5 and 0.5, H_K), 6.73 (1H, td, J(^{1}H) = 7.5 and 1.0, H_I), 7.1-7.25 (6H, m, H_J, H_O, H_P and H_Q), 7.25 (2H, dd, J(^{1}H) = 7.5 and 1.5, H_5), 7. 66 (3H, m, H_4 and H_H), 7.78 (2H, ddd, J(^{1}H) = 8.5, 7.5 and 2.0, H_4), 7.84 (2H, dt, J(^{1}H) = 8.0 and 1.0, H_3), 8.26 (1H, t, J(^{1}H) = 1.5, $H_{2'}$), 8.72 (2H, dq, J(^{1}H) = 5.0 and 1.0, H_6). ^{13}C {^{1}H} NMR (176 MHz, $CDCl_3$) δ_C = 112.2 (s, C_K), 114.0 (s, $C_{4'}$), 118.7 (s, $C_{2'}$), 120.9 (s, C_I), 121.1 (s, C_3), 122.7 (s, C_5), 124.0 (s, C_G), 127.8 (s, C_J), 129.4 (s, C_H), 131.0 (s, C), 131.6 (s, C), 131.8 (s, C), 134.8 (s, C_E), 137.0 (s, C_4), 138.5 (s, C_L), 141.5 (s, $C_{1'}$). 143.9 (s, C_N), 149.8 (s, C_6), 156.0 (s, C_M), 157.1 (s, C_2), 159.9 (s, $C_{5'}$), 191.3 (s, C_F). HRMS (ES^+): *m/z* 557.2071 [100%, $M+H^+$], 579.1889 [93, $M+Na^+$]; calcd for [$C_{35}H_{29}N_2O_5$] 557.2077.

6.3 Synthesis of Platinum(II) Complexes

6.3.1 General Procedures

6.3.1.1 General Complexation Procedure #1

K_2PtCl_4, the appropriate terdentate ligand and concentrated glacial acetic acid were placed in a Schlenk tube. The mixture was degassed by five freeze-pump-thaw cycles, then heated under nitrogen at 130 °C for three days. After allowing to cool to room temperature, the mixture was centrifuged (5 min, 2000 rpm), then the acetic acid was removed with a pipette. The solid was washed with methanol, centrifuged (5 min, 2000 rpm) and the methanol was removed. The solid was also washed with water, ethanol and ether (same procedure as before). The solid was then extracted several times into DCM, until the extracts became colourless. The DCM extracts were then reduced *in vacuo*.

6.3.1.2 General Complexation Procedure #2

The appropriate terdentate ligand was placed in a Schlenk tube and dissolved in CH_3CN. A condenser was added, and the mixture was degassed by five freeze-pump-thaw cycles, then placed under nitrogen. K_2PtCl_4 and water were placed in a two-necked round bottom flask fitted with a suba-seal, and were also degassed and placed under nitrogen. The K_2PtCl_4/water solution was transferred to the Schlenk tube under nitrogen. The mixture was heated to 120 °C under nitrogen, and left for three days. After allowing to cool to room temperature, the mixture was centrifuged (5 min, 2000 rpm), the liquid was removed and the precipitate was washed with MeOH, water, EtOH and ether. It was then extracted several times into DCM, until the extracts remained colourless. The solvent was removed *in vacuo*.

6.3.1.3 Chloride Metathesis Reaction

The appropriate complex was suspended in acetone in a round-bottom flask. To this, silver triflate (AgOTf) was added, and the reaction was stirred for 1-1.5 h at room temperature, during which time, the complex dissolved and silver chloride precipitated. The solution was separated from the silver chloride via centrifugation. The potassium salt of the new ancillary ligand was added to the acetone solution, which was stirred at room temperature for 1-2 h. The complex precipitated from the reaction, and was isolated via centrifugation. The solid was washed with ethanol (10 mL), water (10 mL) and ether (10 mL) then dried under high vacuum.

6.3.1.4 Oxidation to Pt(IV)

The specified Pt(II) complex was suspended in chloroform (15 mL). The solution was stirred at room temperature and chlorine gas was bubbled through at a moderate rate for 30 min – 1 h. After removal of the Cl_2 gas supply, the solvent was removed *in vacuo*, yielding the desired Pt(IV) complex.

6.3.2 Synthetic Details and Characterisation

[PtL^{2}Cl]

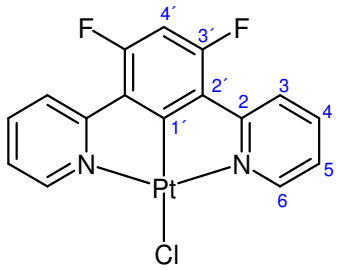

This complex was prepared by procedure #1. Reagents: 1,3-Di(2-pyridyl)-4,6-difluorobenzene (0.075 g, 2.8 x 10^{-4} mol), K_2PtCl_4 (0.12 g, 2.8 x 10^{-4} mol). Solvent: Concentrated glacial acetic acid (3 mL). The product, [PtL^{2}Cl], was initially obtained a bright yellow solid, but turned bright orange as the DCM fully evaporated (0.085 g, 1.71 x 10^{-4} mol, 61%). ^{1}H NMR (300 MHz, $CDCl_3$) δ_H = 6.72 (1H, t, J(^{19}F) = 11.0, $H_{4'}$), 7.32 (2H, ddd, J(^{1}H) = 5.0, 2.0 and 1.0, H_5), 7.92 (2H, d, J(^{1}H) = 7.0, H_3), 7.97 (2H, td, J(^{19}F) = 8.0 and 2.0, H_4), 9.35 (2H, dq, J(^{1}H) = 6.0 and 1.0, ^{3}J(^{195}Pt) = 42.0, H_6). ^{19}F NMR (376 MHz, $CDCl_3$) δ_F = -108.7 (2F, d, J(^{1}H) = 11.5, ^{4}J(^{195}Pt) = 54.0). HRMS (EI): *m/z* 497.0068 [M]; calcd for [$C_{16}H_9{}^{35}ClF_2N_2{}^{195}Pt$], 497.0065. Anal. $C_{16}H_9ClF_2N_2Pt$ (497.8): calcd C, 38.60; H, 1.82; N, 5.63; found C, 38.56; H, 1.79; N, 5.60.

[PtL^{3}Cl]

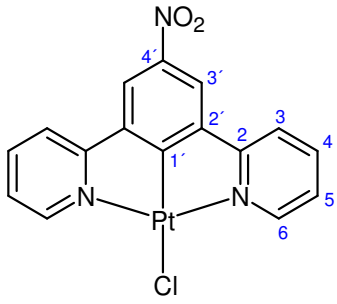

This complex was prepared by procedure #1. Reagents: 1,3-Dipyridyl-5-nitrobenzene (0.072 g, 2.6 x 10^{-4} mol), K_2PtCl_4 (0.11 g, 2.6 x 10^{-4} mol). Solvent: Concentrated glacial acetic acid (3 mL). The solid obtained after the washing sequence had very low solubility in DCM. The non-extracted solid was characterised (data given here), and

was found to be the desired product (0.072g, 55%). ^{1}H NMR (300MHz, DMSO) δ_H = 7.65 (2H, td, J(^{1}H) = 7.0 and 1.0, H_5), 8.28 (2H, td, J(^{1}H) = 8.0 and 1.0, H_4), 8.56 (2H, d, J(^{1}H) = 8.0, H_3), 8.69 (2H, s, $H_{3'}$), 9.15(2H, d, J(^{1}H) = 6.0, ^{3}J(^{195}Pt) = 40.0, H_6). HRMS (EI): *m/z* 506.0099 [M]; calcd for [$C_{16}H_{10}{}^{35}ClN_3O_2{}^{195}Pt$], 506.0109.

Attempted Synthesis of [PtL^{4}Cl]

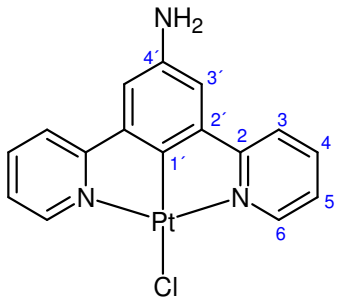

Complexation of this ligand was attempted via procedure #1. 1,3-Di(2-pyridyl)-5-aminobenzene (0.017 g, 7 x 10^{-6} mol), K_2PtCl_4 (0.029 g, 7 x 10^{-6} mol).Solvent: Concentrated glacial acetic acid (2 mL). A dull brown solid (0.015 g) was obtained. The material was only sparingly soluble in the DCM – an NMR was run on the remaining solid in DMSO, but was inconclusive as to whether the product, [PtL^{4}Cl], had formed (too noisy). The brown solid was washed with triethylamine to deprotonate the amine. Unfortunately the solid was still relatively insoluble, and attempts to get a decent NMR failed.

[PtL^{5}Cl]

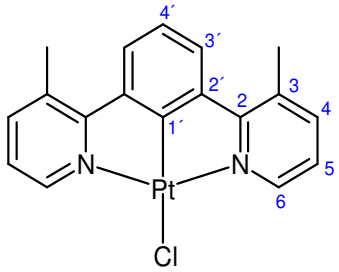

This complex was prepared via procedure #1. Reagents: 1,3-Di(3-methyl-2-pyridyl)benzene (0.060 g, 2.31 x 10^{-4} mol) and K_2PtCl_4 (0.096 g, 2.31 x 10^{-4} mol). Solvent: Concentrated glacial acetic acid (5 mL). The product was obtained as a yellow

solid (0.052 g, 46%). ^{1}H NMR (400 MHz, $CDCl_3$) δ_H = 2.78 (6H, s, CH_3), 7.23 (2H, m, H_5), 7.72-7.76 (5H, m, H_4, $H_{3'}$ and $H_{4'}$), 9.48 (2H, dd, J(^{1}H) = 6.0 and 1.5, ^{3}J(^{195}Pt) = 38.0, H_6). MS (MALDI): *m/z* 489.1 [100%, M], 943.6 [20, 2M-Cl], HRMS (MALDI): *m/z* 453.0846 [87%, M-Cl], HRMS (ASAP): *m/z* 453.0853 [85%, M-Cl] calcd for [$C_{18}H_{15}{}^{35}ClN_2{}^{194}Pt$], 489.0571, calcd for [$C_{18}H_{15}N_2{}^{194}Pt$], 453.0857.

[PtL^{7}Cl]

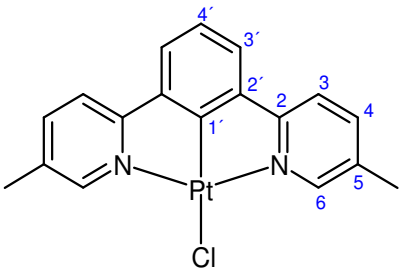

This complex was prepared via procedure #1. Reagents: K_2PtCl_4 (0.080 g, 1.9 x 10^{-4} mol) and 1,3-di(5-methyl-2-pyridyl)benzene (0.050g, 1.9 x 10^{-4} mol). Solvent: Concentrated glacial acetic acid (6mL). The product was obtained as a yellow solid (0.061 g, 65%). ^{1}H NMR (400 MHz, $CDCl_3$), δ_H = 2.38 (6H, s, $2CH_3$), 7.13 (1H, t, J(^{1}H) = 7.5, $H_{4'}$), 7.31 (2H, d, J = 7.5, $H_{3'}$), 7.51 (2H, d, J = 8.0, H_3), 7.68 (2H, dd, J = 8.0 and 1.0, H_4), 9.10 (2H s, ^{3}J(^{195}Pt) = 42.0, H_6). HRMS (ASAP): *m/z* 453.0843 [90%, M-Cl]; calcd for [$C_{18}H_{15}N_2{}^{194}Pt$], 453.0862.

[PtL^{8}Cl]

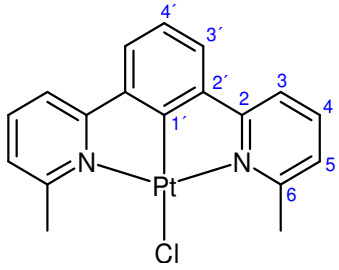

This complex was prepared via procedure #1. Reagents: K_2PtCl_4 (0.090 g, 2.2 x 10^{-4} mol) and 1,3-di(6-methyl-2-pyridyl) benzene (0.056 g, 2.2 x 10^{-4} mol). Solvent: Concentrated glacial acetic acid (6 mL). The product was obtained as a yellowy orange solid, [Pt(L^{8})Cl] (0.034 g, 32%). ^{1}H NMR (400 MHz, $CDCl_3$), δ_H = 3.28 (6H, s, $2CH_3$),

7.14-7.20 (3H, m, $H_{4'}$ and $H_{3'}$), 7.35 (2H, d, $J(^1H)$ = 8.0, H_5), 7.50 (2H, dd, $J(^1H)$ = 8.0, and 1.0, H_3), 7.73 (2H, t, $J(^1H)$ = 8.0 H_4). HRMS (FAB): *m/z* 489.0569 [$M+H^+$]; calcd for [$C_{18}H_{16}{}^{35}ClN_2{}^{194}Pt$], 489.0566.

[PtL^{9}Cl]

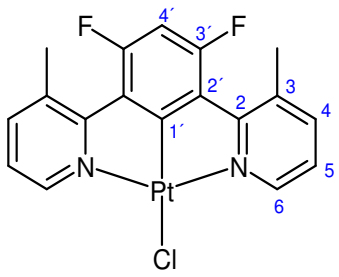

This complex was prepared via procedure #1. Reagents: 1,3-Di(3-Methyl-2-pyridyl)-4,6-difluorobenzene (0.055 g, 1.9 x 10^{-4} mol), and K_2PtCl_4 (0.077 g, 1.9 x 10^{-4} mol). Solvent: Concentrated glacial acetic acid (5 mL). 2,6-di(3-methyl-2-pyridyl)-3,5-difluorobenzene platinum(II) chloride, [Pt(L^9)Cl], was obtained as a bright yellow solid (0.056 g, 57%). ^1H NMR (400 MHz, $CDCl_3$), δ_H = 2.57 (6H, d, $J(^{19}F)$ = 10.0, $2CH_3$), 6.61 (1H, t, $J(^{19}F)$ = 12.0, $H_{4'}$), 7.17 (2H, dd, $J(^1H)$ = 8.0 and 5.5, H_5), 7.70 (2H, dd, $J(^1H)$ = 8.0, 1.5, H_4), 9.37 (2H, dd, J = 5.5 and 1.5, $^3J(^{195}Pt)$ = 40, H_6). ^{19}F NMR (376 MHz, $CDCl_3$) δ_F = -92.1 (2F, m), ^{19}F {^1H} NMR (470 MHz, $CDCl_3$) δ_F = -92.1 (2F, s, $^4J(^{195}Pt)$ = 24.0). HRMS (EI): *m/z* 524.0357 [M]; calcd for [$C_{18}H_{13}{}^{35}ClF_2N_2{}^{194}Pt$], 524.0356. Anal. $C_{18}H_{13}ClF_2N_2Pt$ (525.83): calcd. C, 41.11; H, 2.49; N, 5.33, found C, 40.78; H, 2.41; N, 5.05.

[PtL^{10}Cl]

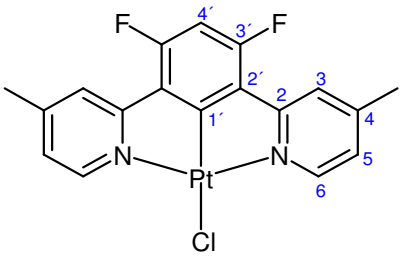

This complex was prepared via procedure #2. Reagents: 1,3-Di(4-methyl-2-pyridyl)-4,6-difluorobenzene (0.055 g, 1.9 x 10^{-4} mol) and K_2PtCl_4 (0.077g, 1.9 x 10^{-4} mol).

Solvents: CH_3CN (6 mL) and water (2 mL). The desired product was obtained as a bright yellow solid (0.081 g, 77%). (Note: subsequent complexation of this ligand was performed via procedure #1: these experiments gave comparable yields to that reported here.) δ_H = 2.49 (6H, s, $2CH_3$), 6.70 (1H, t, $J(^{19}F)$ = 11.5, $H_{4'}$), 7.11 (2H, dd, $J(^1H)$ = 6.0 and 1.5, H_5), 7.72 (2H, d, $J(^1H)$ = 1.5, H_3), 9.15 (2H, d, $J(^1H)$ = 6.0, $^3J(^{195}Pt)$ = 40, H_6). ^{19}F NMR (376 MHz, $CDCl_3$) δ_F = -109.3 (2F, d, $J(^1H)$ = 11.0, $^4J(^{195}Pt)$ = 55.0). HRMS (EI): *m/z* 525.0383 [M]; calcd for $[C_{18}H_{13}{}^{35}ClF_2N_2{}^{195}Pt]$, 525.0378. Anal. $C_{18}H_{13}ClF_2N_2Pt$ (525.83): calcd. C, 41.11; H, 2.49; N, 5.33, found C, 40.44; H, 2.46; N, 5.31.

[PtL^{11}Cl]

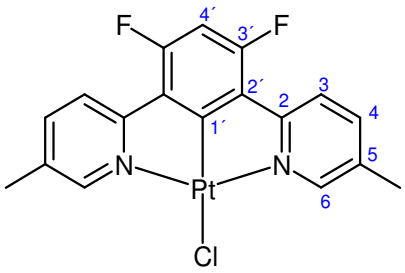

This complex was prepared via procedure #1. Reagents: K_2PtCl_4 (0.048 g, 1.2 x 10^{-4} mol) and 1,3-di(5-methyl-2-pyridyl) benzene (0.034 g, 1.2 x 10^{-4} mol). Solvent: Concentrated glacial acetic acid (6 mL). The product was obtained as a yellow solid, (0.049 g, 81%). ^1H NMR (400 MHz, $CDCl_3$), δ_H = 2.43 (6H, s, $2CH_3$), 6.53 (1H, t, $J(^{19}F)$ = 11.0, $H_{4'}$), 7.6-7.8 (4H, m, H_3 and H_4), 9.01 (2H, s, $^3J(^{195}Pt)$ = 41.0, H_6). ^{19}F NMR (376 MHz, $CDCl_3$) δ_F = -110.3 (2F, d, $J(^1H)$ = 11.5, $^4J(^{195}Pt)$ = 54.0). HRMS (ASAP): *m/z* 525.0460 [12%, $M+H^+$], 489.0641 [87, M-Cl]; calcd for $[C_{18}H_{13}{}^{35}ClF_2N_2{}^{194}Pt]$, 524.0362, $[C_{18}H_{14}ClF_2N_2{}^{194}Pt]$, 525.0440 $[C_{18}H_{13}F_2N_2{}^{194}Pt]$, 489.0674.

[PtL^{12}Cl]

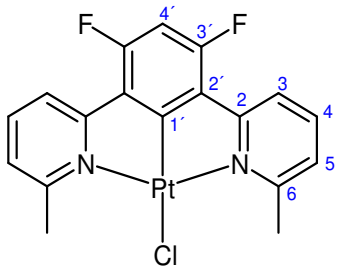

This complex was prepared via procedure #1. Reagents: 1,3-Di(6-Methyl-2-pyridyl)-4,6-difluorobenzene (0.059 g, 2.0 x 10^{-4} mol), K_2PtCl_4 (0.082 g, 2.0 x 10^{-4} mol). Solvent: Concentrated glacial acetic acid (5 mL). The product was not very soluble in DCM, so was obtained without extraction. The product was obtained as an orange solid, (0.046 g, 44%). ^{1}H NMR (400 MHz, DMSO), δ_H = 3.26 (6H, s, 2CH_3), 6.71 (1H, t, J(^{19}F) = 12.0, $H_{4'}$), 7.18 (2H, dd, J(^{1}H) = 6.5 and 3.0, H_5), 7.76 (4H, m, H_3 and H_4). ^{19}F NMR (376 MHz, DMSO) δ_F = -109.2 (2F, d, J(^{1}H) = 12.0, ^{4}J(^{195}Pt) = 57.0). HRMS (EI): *m/z* 489.0676 [85%, ^{194}Pt, M-Cl]; calcd for [$C_{18}H_{13}{}^{35}ClF_2N_2{}^{194}Pt$], 525.0362, calcd for [$C_{18}H_{13}F_2N_2{}^{194}Pt$], 489.0674.

[PtL^{13}Cl]

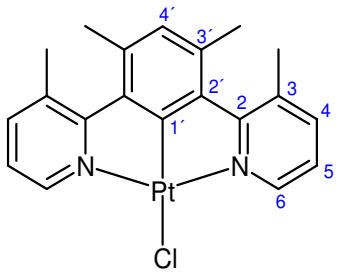

This complex was prepared via procedure #1. Reagents: 1,3-di(3-methyl-2-pyridyl-4,6-dimethylbenzene (0.024 g, 8.3 x 10^{-5} mol), K_2PtCl_4 (0.035 g, 8.3 x 10^{-5} mol). Solvent: acetic acid (3 mL). The product was obtained as a orangey yellow oily solid (0.017 g, 3.3 x 10^{-5} mol, 40%). ^{1}H NMR (400 MHz, $CDCl_3$) δ_H = 2.39 (6H, s, CH_3), 2.48 (6H, s, CH_3) 6.83 (1H, s, $H_{4'}$), 7.17 (2H, dd, J(^{1}H) = 8.0 and 5.5, H_5), 7.72 (2H, dd, J(^{1}H) = 8.0 and 1.0, H_3), 9.33 (2H, dd, J(^{1}H) = 5.5 and 1.0, ^{4}J(^{195}Pt) = 43.0, H_6). HRMS (ASAP): *m/z* 516.0884 [8%, M], 481.1174 [80, M-Cl]; calcd for [$C_{20}H_{19}{}^{35}ClN_2{}^{194}Pt$], 516.0882, calcd for [$C_{20}H_{19}N_2{}^{194}Pt$], 481.1175.

[PtL^{14}Cl]

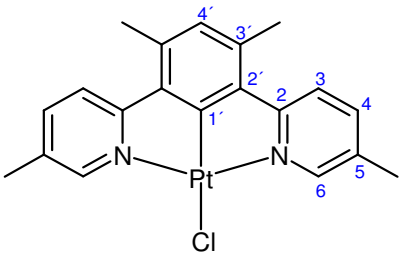

This complex was prepared via procedure #1. Reagents: 1,3-di(5-methyl-2-pyridyl)-4,6-dimethylbenzene (0.052 g, 1.8 x 10^{-4} mol), K_2PtCl_4 (0.076 g, 1.8 x 10^{-4} mol). Solvent: acetic acid (3 mL). The product was obtained as a yellow solid (0.065 g, 1.2 x 10^{-4} mol, 69%).^{1}H NMR (400 MHz, $CDCl_3$) δ_H = 2.40 (6H, s, CH_3-ph), 2.61 (6H, s, CH_3-py), 6.75 (1H, s, $H_{4'}$), 7.65-7.75 (4H, m, H_3 and H_4), 9.31 (2H, dd, J(^{1}H) = 1.5 and 1.0, ^{3}J(^{195}Pt) = 41.0, H_6). HRMS (ASAP): *m/z* 481.1153 [85%, M-Cl]; calcd for [$C_{20}H_{19}{}^{35}ClN_2{}^{194}Pt$], 516.0864, calcd for [$C_{20}H_{19}N_2{}^{194}Pt$], 481.1175. Anal. $C_{20}H_{19}CN_2Pt$ (517.90): calcd. C, 46.38; H, 3.70; N, 5.41, found C, 40.18; H, 4.16; N, 3.78.

[PtL^{15}Cl]

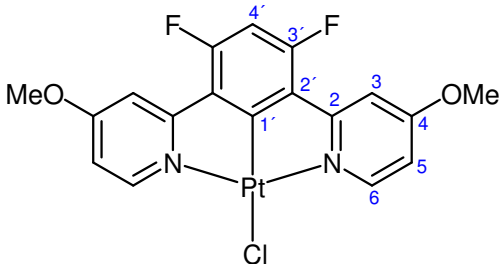

This complex was prepared via procedure #1. Reagents: 1,3-di(4-methoxy-2-pyridyl)-4,6-difluorobenzene (0.030 g, 9.1 x 10^{-5} mol), and K_2PtCl_4 (0.038 g, 9.1 x 10^{-5} mol). Solvent: Concentrated glacial acetic acid (2 mL). The product was obtained as a light yellow solid (0.031 g, 5.6 x 10^{-5} mol, 61%). ^{1}H NMR (500 MHz, $CDCl_3$) δ_H = 3.98 (6H, s, OCH_3), 6.68 (1H, t, J(^{19}F) = 11.0, $H_{4'}$), 6.78 (2H, dd, J(^{1}H) = 6.5 and 3.0, H_5), 7.39 (2H, d, J(^{1}H) = 3.0, H_3), 9.08 (2H, dd, J(^{1}H) = 6.5 and 0.5, ^{3}J(^{195}Pt) = 39.0, H_6) ^{19}F NMR (376 MHz, $CDCl_3$) δ_F = -109.2 (2F, d, J(^{1}H) = 11.0, ^{4}J(^{195}Pt) = 62.0). MS (MALDI): *m/z* 556.0 [M], 1077.0 [2M-Cl], HRMS (MALDI): *m/z* 521.05514 [85%, M-Cl]. HRMS (ASAP): *m/z* 521.0558 [80%, M-Cl]; calcd for [$C_{18}H_{13}{}^{35}ClF_2N_2O_2{}^{194}Pt$], 556.0260, calcd for [$C_{18}H_{13}F_2N_2O_2{}^{194}Pt$], 521.0572.

[PtL^{16}Cl]

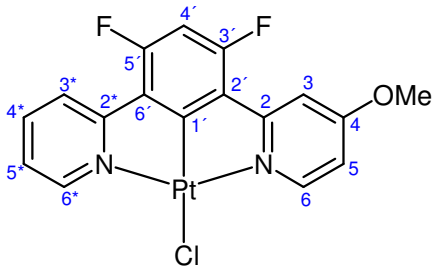

This complex was prepared via procedure #1. Reagents: 1-(4-Methoxy-2-pyridyl)-3-(2-pyridyl)-4,6-difluorobenzene (0.040 g, 1.4 x 10^{-4} mol) and K_2PtCl_4 (0.056 g, 1.4 x 10^{-4} mol). Solvent: Acetic acid (6 mL). The product was obtained as a yellow solid (0.035 g, 6.8 x 10^{-5} mol, 49%). ^{1}H NMR (400 MHz, $CDCl_3$) δ_H = 3.99 (3H, s, OCH_3), 6.69 (1H, t, J(^{19}F) = 11.0, $H_{4'}$), 6.79 (1H, dd, J(^{1}H) = 6.5 and 3.0, H_5), 7.30 (1H, dd, J(^{1}H) = 7.0 and 1.5, H_{5*}), 7.41 (1H, dd, J(^{1}H) = 3.0 and 1.0, H_3), 7.92 (2H, m, H_{3*} and H_{4*}), 9.08 (1H, d, J(^{1}H) = 6.5, ^{3}J(^{195}Pt) = 39, H_6), 9.35 (1H, dq, J(^{1}H) = 7.0 and 1.0, H_{6*}). ^{19}F NMR (188 MHz, $CDCl_3$) δ_F = -109.1 (1F, t, J(^{1}H) = 12.0), -108.8 (1F, t, J(^{1}H) = 12.0). MS (MALDI): *m/z* 527.1 [M], 1019.2 [2M-Cl]. HRMS (ASAP): *m/z* 526.0173 [8%, M], 491.0464 [78, M-Cl]; calcd for [$C_{17}H_{11}{}^{35}ClF_2N_2O^{194}Pt$], 526.0155, calcd for [$C_{17}H_{11}F_2N_2O^{194}Pt$], 491.0466. Anal. $C_{17}H_{11}ClF_2N_2OPt$ (527.80): calcd C, 38.68; H, 2.10; N, 5.31; found C, 37.56; H, 2.68; N, 4.43

[PtL^{17}Cl]

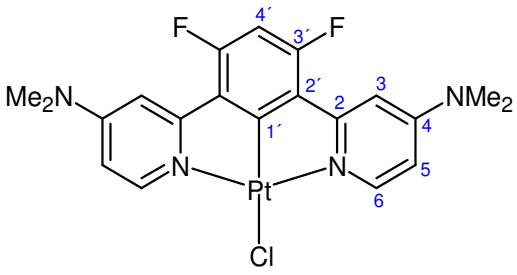

This complex was prepared via procedure #2. Reagents: 1,3-di(4-dimethylamino-2-pyridyl)-4,6-difluorobenzene (0.040 g, 1.1 x 10^{-4} mol), K_2PtCl_4 (0.047 g, 1.1 x 10^{-4} mol). Solvents: CH_3CN (3 mL), water (1 mL). Purification: This complex requires an additional washing with acetone. The product was obtained as a light green solid (0.044 g, 7.54 x 10^{-5} mol, 67%). ^{1}H NMR (400 MHz, $CDCl_3$) 3.13 (12H, s, CH_3), 6.38 (2H, dd, J(^{1}H) = 7.0 and 3.0, H_5), 6.63 (1H, t, J(^{19}F) = 11.5, $H_{4'}$), 7.08 (2H, d, J(^{1}H) = 3.0, H_3),

8.77 (2H, d, J(^{1}H) = 7.0, ^{3}J(^{195}Pt) = 37.0, H_6). ^{19}F NMR (376 MHz, $CDCl_3$) δ_F = -111.5 (2F, d, J(^{1}H) = 11.0, ^{4}J(^{195}Pt) = 59.0). MS (MALDI): *m/z* 584.1 [M], 1129.1 [2M-Cl] HRMS (MALDI): 547.1200 [100%, M-Cl]. HRMS (ASAP): *m/z* 547.1215 [80%, M-Cl]; calcd for [$C_{20}H_{19}{}^{35}F_2N_4{}^{195}Pt$], 547.1205. Anal. $C_{20}H_{19}ClF_2N_4Pt$ (583.91): calcd. C, 41.14; H, 3.28; N, 9.60, found C, 40.12; H, 2.81; N, 8.05.

[PtL^{20}Cl]

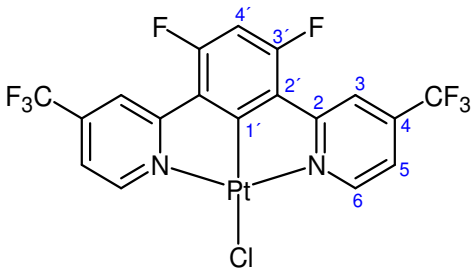

This complex was prepared via procedure #1. Reagents: 1,3-di(4-trifluoromethyl-2-pyridyl)-4,6-difluorobenzene (0.040 g, 9.9 x 10^{-5} mol), K_2PtCl_4 (0.041 g, 9.9 x 10^{-5} mol). Solvent: acetic acid (2 mL). The product was obtained as bright yellow solid (0.032 g, 5.1 x 10^{-5} mol, 51%). ^{1}H NMR (400 MHz, $CDCl_3$) δ_H = 6.84 (1H, t, J(^{19}F) = 11.0, $H_{4'}$), 7.55 (2H, dd, J(^{1}H) = 6.0 and 1.5, H_5), 8.09 (2H, s, H_3), 9.54 (2H, d, J(^{1}H) = 6.0, ^{3}J(^{195}Pt) = 41.0, H_6). ^{19}F NMR (376 MHz, $CDCl_3$) δ_F = -105.6 (2F, d, J(^{1}H) = 11.0, ^{4}J(^{195}Pt) = 49.0), -65.6 (6F, s, CF_3) MS (MALDI): *m/z* 633.0 [M], 1231.0 [2M-Cl], HRMS (ASAP): *m/z* 631.9783 [M]; calcd for [$C_{18}H_7ClF_8N_2{}^{194}Pt$], 631.9797. Anal. $C_{18}H_7ClF_8N_2Pt$ (633.78): calcd. C, 34.11; H, 1.11; N, 4.42, found C, 33.33; H, 1.93; N, 3.27.

[PtL^{21}Cl]

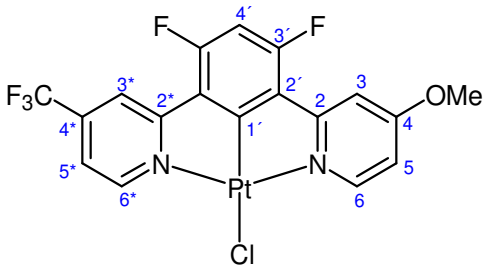

This complex was prepared via procedure #1. Reagents: 1-(4-methoxy-2-pyridyl)-3-(4-trifluoromethyl-2-pyridyl)-4,6-difluorobenzene (0.040 g, 1.1 x 10^{-4} mol), K_2PtCl_4 (0.045 g, 1.1 x 10^{-4} mol). Solvent: acetic acid (3 mL). The product was obtained as a greeny yellow solid (0.046 g, 7.7 x 10^{-5} mol, 71%), ^{1}H NMR (400 MHz, $CDCl_3$) δ_H = 3.99 (3H, s, CH_3), 6.74 (1H, t, J(^{19}F) = 11.0, $H_{4'}$), 6.81 (1H, dd, J(^{1}H) = 6.5 and 2.5, H_5), 7.41 (1H, d, J(^{1}H) = 2.5, H_3), 7.49 (1H, d, J(^{1}H) = 5.5, H_{5*}), 8.04 (1H, s, H_{3*}), 9.03 (1H, d, J(^{1}H) = 6.5, ^{3}J(^{195}Pt) = 40.0, H_6), 9.56 (1H, d, J(^{1}H) = 5.5, ^{3}J(^{195}Pt) = 39.0, H_{6*}). ^{19}F NMR (376 MHz, $CDCl_3$) δ_F = -107.9 (1F, t, J(^{1}H) = 13.5, ^{4}J(^{195}Pt) = 55.0), -107.1 (1F, t, J(^{1}H) = 13.5, ^{4}J(^{195}Pt) = 55.0), -65.52 (3F, s, CF_3). HRMS (ASAP): *m/z* 559.0325 [85%, M-Cl]; calcd for [$C_{18}H_{10}{}^{35}ClF_5N_2O^{194}Pt$], 594.0028, calcd for [$C_{18}H_{10}F_5N_2O^{194}Pt$], 559.0340.

[PtL^{22}Cl]

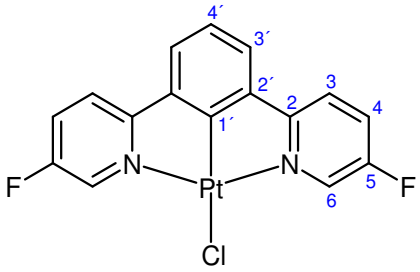

This complex was prepared via procedure #1. Reagent: 1,3-Di(5-fluoro-2-pyridyl) benzene (0.046 g, 1.7 x 10^{-4} mol), K_2PtCl_4 (0.071 g, 1.7 x 10^{-4} mol). Solvent: Concentrated glacial acetic acid (5 mL). The product was obtained as a bright yellow solid (0.042 g, 50%). ^{1}H NMR (200 MHz, $CDCl_3$) δ_H = 7.23 (1H, m, $H_{4'}$), 7.40 (2H m, H_3), 7.72 (4H, m, $H_{3'}$ and H_4), 9.30 (2H, td, J(^{1}H) = 3.0 and 1.0, ^{3}J(^{195}Pt) = 23.0, H_6). MS (MALDI): *m/z* 497.0 [M], 959.0 [2M-Cl]. HRMS (ASAP): 496.0069 [8%, M], 461.0343 [85, M-Cl]; calcd for [$C_{16}H_9{}^{35}ClF_2N_2{}^{194}Pt$], 496.0049, calcd for [$C_{16}H_9F_2N_2{}^{194}Pt$], 461.0361. Anal. $C_{16}H_{10}ClF_2N_2Pt$ (497.78): calcd C, 38.60; H, 1.82; N, 5.63; found C, 38.25; H, 1.76; N, 5.28.

[PtL^{23}]

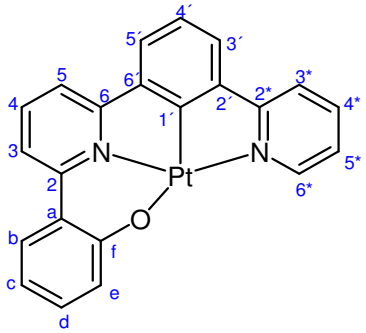

This complex was prepared via procedure #1. Reagents: 2-[6-(3-pyridin-2-yl-phenyl)-pyridin-2-yl]-phenol (0.040 g, 1.2 x 10^{-4} mol) and K_2PtCl_4 (0.051 g, 1.2 x 10^{-4} mol). Solvent: Acetic acid (4 mL). The product was obtained as a yellowy green solid (0.047 g, 8.5 x 10^{-5} mol, 69%). ^{1}H NMR (400 MHz, $CDCl_3$) δ_H = 7.96 (2H, d, m, H_c, and $H_{4'}$), 7.34 (1H, ddd, J(^{1}H) = 8.5, 7.0 and 1.5, H_{5*}), 7.59 (1H, ddd, J(^{1}H) = 8.0, 6.0 and 1.0, H_d), 7.75 (1H, dd, J(^{1}H) = 8.0 and 2.0, H_e), 8.1-8.3 (5H, m, H_3, H_4, H_5, H_{3*} and H_{4*}), 8.34-8.38 (2H, m, $H_{5'}$ and H_b), 8.43 (1H, d, J(^{1}H) = 8.5, $H_{3'}$), 9.51 (1H, ddd, J(^{1}H) = 6.0, 1.5 and 0.5, H_{6*}). HRMS (ASAP): *m/z* 517.0807 [85%, M+H$^+$]; HRMS (ASAP – *dry* calibration source): *m/z* 516.0728 [85%, M]; calcd for [$C_{22}H_{14}N_2OPt$], 516.0733, calcd for [$C_{22}H_{15}N_2OPt$], 517.0811

[PtL^{25}Cl]

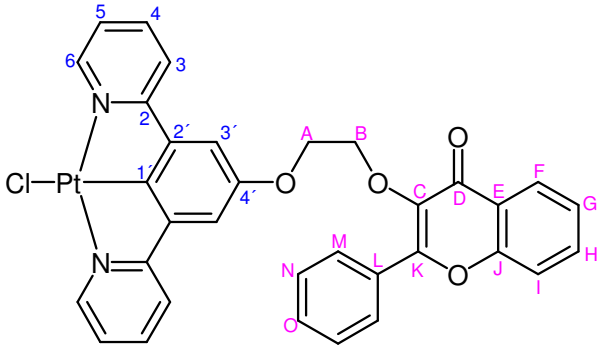

This complex was prepared via procedure #1. Reagents: 3-[2-(3,5-Di-pyridin-2-yl-phenoxy)-ethoxy]-2-phenyl-chromen-4-one (L^{23}) (0.039 g, 7.6 x 10^{-5} mol) and K_2PtCl_4 (0.047 g, 1.1 x 10^{-4} mol). The solvent used was acetic acid (6 mL). The product was obtained as an oily orangey yellow solid (0.029 g, 53%). ^{1}H NMR (700 MHz, $CDCl_3$) δ_H = 4.29 (2H, m, CH_2), 4.56 (2H, m, CH_2), 6.94 (2H, s, $H_{3'}$), 7.25 (2H, m, H_5), 7.4-7.5

(4H, m, H_G, H_N and H_O), 7.56 (3H, m, H_3 and H_I), 7.70 (1H, ddd, J(^{1}H) = 8.5, 7.0 and 1.5, H_H), 7.93 (2H, td, J(^{1}H) = 8.0 and1.5, H_4), 8.16 (2H, dd, J(^{1}H) = 8.0 and 1.5, H_M), 8.29 (1H, dd, J(^{1}H) = 8.0 and 1.5, H_F), 9.31 (2H, dd, J(^{1}H) = 5.5 and 1.0, H_6). MS (MALDI): *m/z* 742.3 [M], 1448.3 [2M-Cl]. HRMS (ASAP): *m/z* 740.0962 [M]; calcd for [$C_{33}H_{23}{}^{35}ClN_2O_4{}^{194}Pt$], 740.0973.

[PtL^{26}Cl]

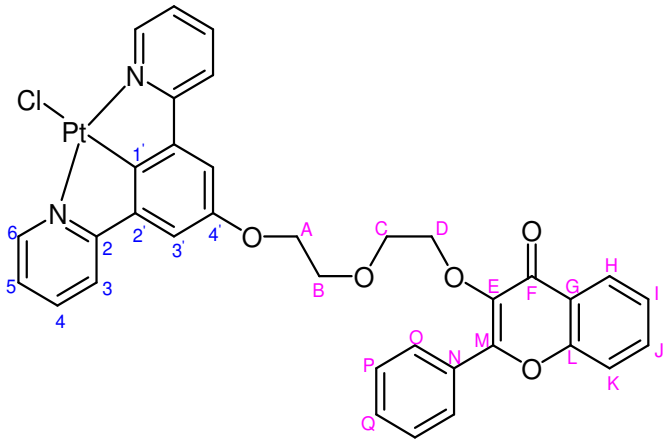

This complex was prepared via procedure #1. Reagents: 3-{2-[2-(3,5-Di-pyridin-2-yl-phenoxy)-ethoxy]-ethoxy}-2-phenyl-chromen-4-one (0.026 g, 4.7 x 10^{-5} mol) and K_2PtCl_4 (0.019 g, 4.7 x 10^{-5} mol). Solvent: Glacial acetic acid (5 mL). The product was obtained as a yellowy orange oily solid (0.013 g, 1.7 x 10^{-5} mol, 35%). ^{1}H NMR (400 MHz, $CDCl_3$) δ_H = 3.81 (2H, m, CH_2), 3.87 (2H, m, CH_2), 4.11 (2H, m, CH_2), 4.37 (2H, m, CH_2), 7.09 (2H, s, $H_{3'}$), 7.2-7.6 (8H, m, H_I, H_J, H_K, H_O, H_P and H_Q), 7.65 (2H, ddd, J(^{1}H) = 8.0, 6.5 and 2.0, H_5), 7.91 (2H, td, J(^{1}H) = 8.0 and 1.5, H_4), 8.17 (2H, dd, J(^{1}H) = 8.0 and 2.0, H_3), 8.23 (1H, ddd, J(^{1}H) = 8.0, 1.5 and 0.5, H_H), 9.32 (2H, ddd, J(^{1}H) = 5.5, 1.5 and 0.5, ^{4}J(^{195}Pt) = 39.0, H_6). HRMS (ASAP): *m/z* 784.1253 [55%, M]; calcd for [$C_{35}H_{27}{}^{35}ClN_2O_5{}^{194}Pt$], 784.1235.

[PtL^{2}CN]

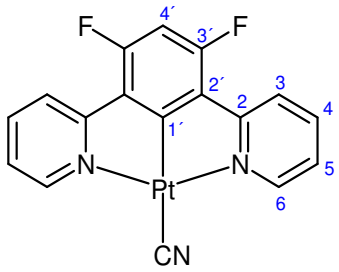

This complex was prepared via chloride metathesis reaction. Reagents: [PtL^{2}Cl] (0.025 g, 5.0 x 10^{-5} mol), AgOTf (0.016 g, 5.5 x 10^{-5} mol) and KCN (0.007 g, 1.1 x 10^{-4} mol). Solvent: Acetone (6 mL). Purification: The crude solid was washed with water (10 mL), EtOH (10 mL) and ether (10 mL), then dried *in vacuo*. The product, [PtL^{2}CN] was obtained as a bright yellow solid (0.020 g, 4.1 x 10^{-5} mol, 81%). ^{1}H NMR (400 MHz, $CDCl_3$) δ_H = 6.67 (1H, t, J(^{19}F) = 11.0, $H_{4'}$), 7.26 (2H, m, H_5), 7.93 (2H, d, J(^{1}H) = 8.0, H_3), 7.92 (2H, td, J(^{1}H) = 8.0, H_4), 9.22 (2H, ddd, J(^{1}H) = 6.0, 1.5 and 1.0, ^{3}J(^{195}Pt) = 47.0, H_6), ^{19}F NMR (376 MHz, $CDCl_3$) δ_F = -108.4 (2F, d, J(^{1}H) = 11.5, ^{4}J(^{195}Pt) = 33.0). HRMS (ASAP): *m/z* 488.0470 [45%, M]; calcd for [$C_{17}H_9F_2N_3{}^{195}Pt$], 487.7712.

[PtL^{15}CN]

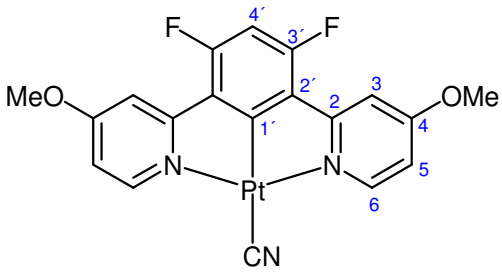

This complex was prepared via the chloride metathesis reaction. Reagents: [PtL^{15}Cl] (0.012 g, 2.2 x 10^{-5} mol) , AgOTf (0.007 g, 2.4 x 10^{-5} mol) and KCN (0.003 g, 4.6 x 10^{-5} mol). Solvent: Acetone (3 mL). Purification: The crude solid was washed with water (10 mL), EtOH (10 mL) and ether (10 mL), then dried *in vacuo*. The product, [PtL^{15}CN] was obtained as a bright yellow solid (0.010 g, 1.8 x 10^{-5} mol, 85%). ^{1}H NMR (400 MHz, $CDCl_3$) δ_H = 3.98 (6H, s, CH_3), 6.62 (1H, t, J(^{19}F) = 11.0, $H_{4'}$), 6.69 (2H, dd, J(^{1}H) = 7.0 and 3.0, H_5), 7.37 (2H, d, J(^{1}H) = 3.0, H_3), 8.96 (2H, d, J(^{1}H) = 7.0 ^{3}J(^{195}Pt) = 44, H_6), ^{19}F NMR (376 MHz, $CDCl_3$) δ_F = -109.0 (2F, d, J(^{1}H) = 11.0 ^{4}J(^{195}Pt) = 40.0). HRMS (ASAP): *m/z* 547.0609 [12%, M]; calcd for [$C_{19}H_{13}F_2N_3O_2Pt$], 547.0603.

[PtL^{17}CN]

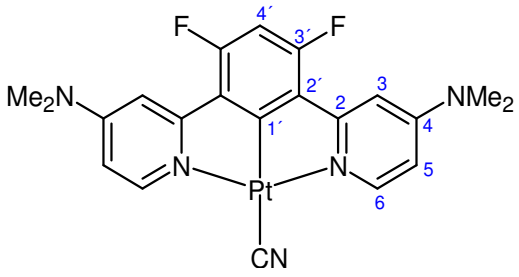

This complex was prepared via the chloride metathesis reaction. Reagents: [PtL^{17}Cl] (0.020 g, 3.4 x 10^{-5} mol), AgOTf (0.011 g, 3.8 x 10^{-5} mol) and KCN (0.005 g, 7.5 x 10^{-5} mol). Solvent: Acetone (5 mL). Purification: The crude solid was washed with water (10 mL), EtOH (10 mL) and ether (10 mL), then dried *in vacuo*. The product was obtained as an orangey yellow solid (0.014 g, 2.4 x 10^{-5} mol, 71%). ^{1}H NMR (400 MHz, $CDCl_3$) δ_H = 3.14 (6H, s, CH_3), 6.28 (2H, dd, J(^{1}H) = 7.0 and 3.0, H_5), 6.57 (1H, t, J(^{19}F) = 11.5, $H_{4'}$), 7.06 (2H, d, J(^{1}H) = 3.0, H_3), 8.66 (2H, d, J(^{1}H) = 7.0, ^{3}J(^{195}Pt) = 37.0, H_6), ^{19}F NMR (376 MHz, $CDCl_3$) δ_F = -111.3 (2F, d, J(^{1}H) = 12.0). HRMS (ASAP): *m/z* 573.1216 [15%, M]; calcd for [$C_{21}H_{19}F_2N_5{}^{195}$Pt], 573.1235.

[PtL^{1}Br]

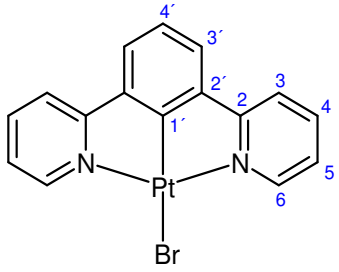

This complex was prepared via the chloride metathesis reaction. Reagents: [Pt L^{1}Cl] (0.027 g, 5.9 x 10^{-5} mol), AgOTf (0.019 g, 6.5 x 10^{-5} mol) and KBr (0.018 g, 1.5 x 10^{-4} mol). Solvent: Acetone (5 mL). The complex, [PtL^{1}Br], was obtained as a bright yellow solid (0.022 g, 4.4 x 10^{-5} mol, 74%). ^{1}H NMR (400 MHz, $CDCl_3$) δ_H = 7.24-7.28 (3H, m, H_5 and $H_{4'}$), 7.45 (2H, d, J(^{1}H) = 7.5, $H_{3'}$), 7.69 (2H, ddd, J = 8.0, 1.5 and 1.0, H_3), 7.92 (2H, ddd, J(^{1}H) = 8.5, 8.0 and 1.5, H_4), 9.56 (2H, ddd, J = 5.0, 1.5 and 1.0, ^{3}J(^{195}Pt) = 42, H_6). HRMS (ASAP): *m/z* 503.1086 [4%, M], 425.0544 [86, M-Br]; calcd for [$C_{16}H_{11}{}^{79}BrN_2{}^{194}$Pt], 503.9731, calcd for [$C_{16}H_{11}N_2{}^{194}$Pt], 425.0549.

[PtL^{1}I]

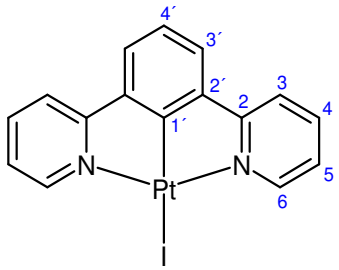

This complex was prepared via the chloride metathesis reaction. Reagents: [Pt L^{1}Cl] (0.020 g, 4.3 x 10^{-5} mol), AgOTf (0.014 g, 4.8 x 10^{-5} mol) and KI (0.014 g, 8.7 x 10^{-5} mol). Solvent: Acetone (5 mL). The product, [PtL^{1}I] was obtained as a bright yellow solid (0.018 g, 3.3 x 10^{-5} mol, 75%). ^{1}H NMR (400 MHz, $CDCl_3$) δ_H = 7.2-7.3 (3H, m, $H_{4'}$ and H_5), 7.45 (2H, d, J(^{1}H) = 7.5, $H_{3'}$), 7.69 (2H, ddd, J(^{1}H) = 8.0, 1.0 and 0.5, H_3), 7.92 (2H, td, J(^{1}H) = 8.0 and 1.5, H_4), 9.89 (2H, ddd, J(^{1}H) = 6.0, 1.5 and 0.5, ^{3}J(^{195}Pt) = 44.0, H_6). HRMS (ASAP): *m/z* 425.0545 [88%, M- I]; calcd for [$C_{16}H_{11}IN_2{}^{194}Pt$], 551.9593, calcd for [$C_{16}H_{11}N_2{}^{194}Pt$], 425.0549.

[PtL^{2}Cl$_3$]

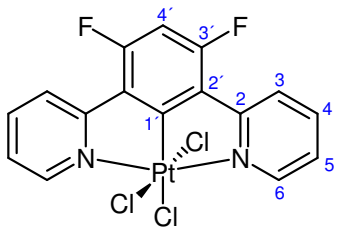

This complex was prepared by oxidation of [PtL^{2}Cl], using the oxidation to Pt(IV) method. Reagents: [PtL^{9}Cl] (0.010 g, 2.0 x 10^{-5} mol) and Cl_2 (excess). Solvent: Chloroform (15 mL). The product was obtained as a light yellow solid (0.009 g, 1.6 x 10^{-5} mol, 79%). ^{1}H NMR (400 MHz, $CDCl_3$) δ_H = 6.99 (1H, t, J(^{19}F) = 12.0, $H_{4'}$), 7.54 (2H, ddd, J(^{1}H) = 7.0, 6.0 and 1.5, H_5), 8.08 (2H, td, J(^{1}H) = 8.0 and 1.0, H_4). 8.16 (2H, d, J(^{1}H) = 8.0, H_3), 9.52 (2H, ddd, J(^{1}H) = 6.0, 1.5 and 0.5, ^{3}J(^{195}Pt) = 30.0, H_6), ^{19}F NMR (376 MHz, $CDCl_3$) δ_F = -103.0 (2F, d, J(^{1}H) = 11.0). HRMS (ASAP): *m/z* 564.9587 [M-H], 530.9720 [M-Cl]; calcd. for [$C_{16}H_8{}^{35}Cl_3F_2N_2{}^{194}Pt$] (M), 565.9425, calcd for [$C_{16}H_9{}^{35}Cl_2F_2N_2{}^{194}Pt$] (M-Cl), 530.9738.

[PtL^{7}Cl$_3$]

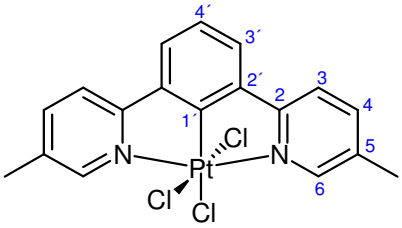

This complex was prepared by oxidation of [PtL^{7}Cl] using the oxidation to Pt(IV) method. Reagents: [PtL^{7}Cl] (0.011 g, 2.3 x 10^{-5} mol) and Cl_2 (excess). Solvent: Chloroform (15 mL). The product was obtained as a light yellow solid (0.008 g, 1.4 x 10^{-5} mol, 63%). ^{1}H NMR (400 MHz, $CDCl_3$) δ_H = 2.53 (6H, s, CH_3), 7.43 (1H, t, J(^{1}H) = 8.0, $H_{4'}$), 7.67 (2H, dd, J(^{1}H) = 8.0 and 1.5, H_4), 7.83 (4H, m, $H_{3'}$ and H_3), 9.34 (2H, s, ^{3}J(^{195}Pt) = 21.0, H_6). HRMS (ASAP): *m/z* 559.0027 [M+H$^+$], 523.0214 [M-Cl]; calcd for [$C_{18}H_{16}{}^{35}Cl_3N_2Pt$] ([M+H$^+$]), 559.0006, calcd for [$C_{18}H_{15}{}^{35}Cl_2N_2Pt$] ([M-Cl]) 523.0239.

[PtL^{9}Cl$_3$]

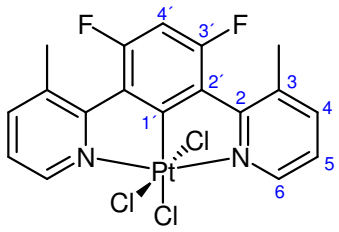

This complex was prepared by oxidation of [PtL^{9}Cl] using the oxidation to Pt (IV) method. Reagents: [PtL^{9}Cl] (0.010 g, 1.9 x 10^{-5} mol) and Cl_2 (excess). Solvent: Chloroform (15 mL). The product was obtained as a light yellow solid (0.009 g, 1.5 x 10^{-5} mol, 79%). ^{1}H NMR (400 MHz, $CDCl_3$) δ_H = 2.75 (6H, s, CH_3), 6.95 (1H, t, J(^{19}F) = 12.0, $H_{4'}$), 7.44 (2H, t, J(^{1}H) = 6.0, H_5), 7.89 (2H, d, J(^{1}H) = 8.0, H_4), 9.65 (2H, d, J(^{1}H) = 6.0, ^{3}J(^{195}Pt) = 25.0, H_6), ^{19}F NMR (376 MHz, $CDCl_3$) δ_F = -86.5 (2F, m). HRMS (ASAP): *m/z* 592.9774 [M-H], 559.0054 [M-Cl], 523.0370, [(M-2Cl)-H], 489.0689 [M-3Cl]; calcd for [$C_{18}H_{13}Cl_3F_2N_2Pt$] ([M]), 593.9738, calcd for [$C_{18}H_{13}Cl_2F_2N_2Pt$] ([M-Cl]), 559.0051, calcd for [$C_{18}H_{13}ClF_2N_2Pt$] ([M-2Cl]), 524.0362, calcd for [$C_{18}H_{13}F_2N_2Pt$] ([M-3Cl]), 489.0674.

[PtL^{10}Cl]

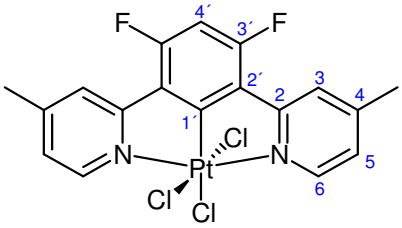

This complex was prepared by oxidation of [PtL^{10}Cl] using the oxidation to Pt (IV) method. Reagents: [PtL^{10}Cl] (0.008 g, 1.5 x 10^{-5} mol), Cl_2 (excess). Solvent: Chloroform (15 mL). The product was obtained as a pale yellow solid (0.009 g, 1.5 x 10^{-5} mol, 100%).^{1}H NMR (400 MHz, $CDCl_3$) δ_H = 2.68 (6H, s, CH_3), 6.96 (1H, t, J(^{19}F) = 11.0, $H_{4'}$), 7.33 (2H, d, J(^{1}H) = 5.5, H_5), 7.93 (2H, s, H_3), 9.30 (2H, d, J(^{1}H) = 5.5 ^{3}J(^{195}Pt) = 24.0, H_6), ^{19}F NMR (376 MHz, $CDCl_3$) δ_F = -103.7 (2F, d, J(^{1}H) = 11.5). HRMS (ASAP): *m/z* 592.9736 [M-H], 559.0032 [M-Cl], 523.0333 [(M-2Cl)-H], 489.0636 [M-3Cl]; calcd for [$C_{18}H_{13}Cl_3F_2N_2Pt$] ([M]), 593.9738, calcd for [$C_{18}H_{13}Cl_2F_2N_2Pt$] ([M-Cl]), 559.0051, calcd for [$C_{18}H_{13}ClF_2N_2Pt$] ([M-2Cl]), 524.0362, calcd for [$C_{18}H_{13}F_2N_2Pt$] ([M-3Cl]), 489.0674.

[PtL^{11}Cl$_3$]

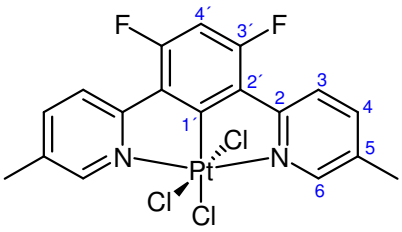

This complex was prepared by oxidation of [PtL^{11}Cl] using the oxidation to Pt (IV) method. Reagents: [PtL^{11}Cl] (0.010 g, 1.9 x 10^{-5} mol) and Cl_2 (excess). Solvent: Chloroform (15 mL). The product was obtained as a light yellow solid (0.008 g, 1.3 x 10^{-5} mol, 71%). ^{1}H NMR (400 MHz, $CDCl_3$) δ_H = 2.53 (6H, s, CH_3), 6.28 (2H, dd, J(^{1}H) = 7.0 and 3.0, H_5), 6.57 (1H, t, J(^{19}F) = 11.5, $H_{4'}$), 7.06 (2H, d, J(^{1}H) = 2.5, H_3), 8.66 (2H, d, J(^{1}H) = 7.0, ^{3}J(^{195}Pt) = 23.0, H_6), ^{19}F NMR (376 MHz, $CDCl_3$) δ_F = -104.7 (2F, d, J(^{1}H) = 11.0, ^{4}J(^{195}Pt) = 29.0). HRMS (ASAP): *m/z* 592.9825 [M-H], 559.0031 [M-Cl]; calcd for [$C_{18}H_{13}Cl_3F_2N_2Pt$] ([M]), 593.9738, calcd for [$C_{18}H_{13}Cl_2F_2N_2Pt$] ([M-Cl]), 559.0051.

6.4 References

1. Oxford Diffraction, (2009/2010) CrysAlis Pro Software, Oxford Diffraction, Yarnton, Oxford, UK

2. Nonius (1999). COLLECT, Nonius BV, Delft, The Netherlands

3. Z. Otwinowski and W. Minor, *Methods Enzymol.*, 1997, **276**, 307-326

4. Bruker (1998). SMART and SAINT, Bruker AXS Inc, Madison, Wisconsin, USA

5. G. M. Sheldrick, *Acta Cryst.*, 2008, **A64**, 112-122

6. J. A. G. Williams, A. Beeby, E. S. Davies, J. A. Weinstein and C. Wilson, *Inorg. Chem.*, 2003, **42**, 8609-8611

7. A. F. Rausch, L. Murphy, J. A. G. Williams and H. Yersin, *Inorg. Chem.*, 2009, **48**, 11407-11414

8. J. Carmichael, W. G. DeGraff, A. F. Gazdar, J. D. Minna and J. B. Mitchell, *Cancer Res.*, 1987, **47(4)**¸ 936-942

9. D. J. Cárdenas and A. M. Echavarren, *Organometallics*, 1999, **18**, 3337-3341

10. U. S. Schubert, C. Eschbaumer and M. Heller, *Org. Lett.*, 2000, **2(21)**, 3373-3376

11. N. Nazarpack-Kandlousy, M. I. Nelen, V. Goral and A. V. Eliseev, *J. Org. Chem.*, 2002, **67**, 59-65

12. B. A. Scweiter, E. T. Kool, *J. Org. Chem.*, 1994, **59**, 7238-7242

13. G. A. Kubiczak, F. Oesch, J. T. Borlakoglu, H. Kunz and L. W. Robertson, *J. Agric. Food Chem.*, 1989, **37**, 1160-1164

14. T. Kaminski, P. Gros and Y. Fort, *Eur. J. Org. Chem.*, 2003, 3855-3860

15. D. Cuperly, P. Gros and Y. Fort, *J. Org. Chem.*, 2002, **67 (1)**¸ 238-241

16. F. Effenberger, A. Krebs and P. Willrett, *Chem. Ber.*, 1992, **125**, 1131-1140

17. S. D. Kuduk, R. M. DiPardo and M. G. Bock, *Org. Lett.*, 2005, **7(4)**, 577-579

18. C-C. Kwok, H. M. Y. Ngai, S-C. Chan, I. H. Sham, C-M. Che and N. Zhu, *Inorg. Chem.*, 2005, **44(13)**, 4442-4444

APPENDIX

A.1 Crystallographic Data

Crystal data and structure refinement for **HL^2**		
Identification code	07srv131	
Empirical formula	C16 H10 F2 N2	
Formula weight	268.26	
Temperature	120(2) K	
Wavelength	0.71073 Å	
Crystal system	Monoclinic	
Space group	C 2/c	
Unit cell dimensions	a = 19.3935(18) Å	α= 90°.
	b = 7.1540(7) Å	β= 115.037(2)°.
	c = 19.2906(18) Å	γ = 90°.
Volume	2424.9(4) Å^3	
Z	8	
Density (calculated)	1.470 Mg/m^3	
Absorption coefficient	0.110 mm^{-1}	
F(000)	1104	
Crystal size	0.04 x 0.08 x 0.12 mm^3	
Theta range for data collection	2.32 to 26.37°.	
Index ranges	-20<=h<=24, -8<=k<=8, -24<=l<=20	
Reflections collected	6995	
Independent reflections	6995 [R(int) = 0.0000]	
Completeness to theta = 25.00°	100.0 %	
Absorption correction	None	
Max. and min. transmission	. and .	
Refinement method	Full-matrix least-squares on F^2	
Data / restraints / parameters	6995 / 0 / 182	
Goodness-of-fit on F^2	1.020	
Final R indices [I>2sigma(I)]	R1 = 0.0530, wR2 = 0.1212	
R indices (all data)	R1 = 0.0862, wR2 = 0.1387	
Largest diff. peak and hole	0.198 and -0.328 e.Å^{-3}	

Crystal data and structure refinement for **HL**[7]

Identification code	07srv405	
Empirical formula	C18 H14 F2 N2	
Formula weight	296.31	
Temperature	120(2) K	
Wavelength	0.71073 Å	
Crystal system	Monoclinic	
Space group	P 21/c	
Unit cell dimensions	a = 6.2629(3) Å	α= 90°.
	b = 11.8780(5) Å	β= 96.2500(10)°.
	c = 18.9531(7) Å	γ = 90°.
Volume	1401.55(10) $Å^3$	
Z	4	
Density (calculated)	1.404 Mg/m^3	
Absorption coefficient	0.102 mm^{-1}	
F(000)	616	
Crystal size	0.25 x 0.1 x 0.1 mm^3	
Theta range for data collection	2.03 to 26.37°.	
Index ranges	-7<=h<=6, -14<=k<=14, -23<=l<=23	
Reflections collected	9329	
Independent reflections	2858 [R(int) = 0.0442]	
Completeness to theta = 25.00°	100.0 %	
Absorption correction	None	
Max. and min. transmission	. and .	
Refinement method	Full-matrix least-squares on F^2	
Data / restraints / parameters	2858 / 0 / 201	
Goodness-of-fit on F^2	0.954	
Final R indices [I>2sigma(I)]	R1 = 0.0474, wR2 = 0.1238	
R indices (all data)	R1 = 0.0665, wR2 = 0.1354	
Largest diff. peak and hole	0.345 and -0.224 $e.Å^{-3}$	

Crystal data and structure refinement for **HL**[22]

Identification code	07srv404	
Empirical formula	C16 H10 F2 N2	
Formula weight	268.26	
Temperature	120(2) K	
Wavelength	0.71073 Å	
Crystal system	Orthorhombic	
Space group	P n m a	
Unit cell dimensions	a = 7.3752(3) Å	α= 90°.
	b = 25.8010(9) Å	β= 90°.
	c = 6.3567(2) Å	γ = 90°.
Volume	1209.60(8) $Å^3$	
Z	4	
Density (calculated)	1.473 Mg/m^3	
Absorption coefficient	0.110 mm^{-1}	
F(000)	552	
Crystal size	0.10 x 0.08 x 0.04 mm^3	
Theta range for data collection	1.58 to 26.36°.	
Index ranges	-7<=h<=9, -32<=k<=32, -7<=l<=7	
Reflections collected	7450	
Independent reflections	1260 [R(int) = 0.0476]	
Completeness to theta = 25.00°	100.0 %	
Absorption correction	None	
Max. and min. transmission	. and .	
Refinement method	Full-matrix least-squares on F^2	
Data / restraints / parameters	1260 / 0 / 94	
Goodness-of-fit on F^2	1.040	
Final R indices [I>2sigma(I)]	R1 = 0.0331, wR2 = 0.0853	
R indices (all data)	R1 = 0.0450, wR2 = 0.0905	
Largest diff. peak and hole	0.185 and -0.159 $e.Å^{-3}$	

Crystal data and structure refinement for **[PtL^{2}Cl]**

Identification code	07srv248	
Empirical formula	C16 H9 Cl F2 N2 Pt	
Formula weight	497.79	
Temperature	120(2) K	
Wavelength	0.71073 Å	
Crystal system	Monoclinic	
Space group	P 21/n	
Unit cell dimensions	a = 4.4712(13) Å	α= 90°.
	b = 13.743(3) Å	β= 94.705(7)°.
	c = 21.664(5) Å	γ = 90°.
Volume	1326.8(6) Å^3	
Z	4	
Density (calculated)	2.492 Mg/m^3	
Absorption coefficient	10.796 mm^{-1}	
F(000)	928	
Crystal size	0.08 x 0.03 x 0.03 mm^3	
Theta range for data collection	3.51 to 28.28°.	
Index ranges	-5<=h<=5, -18<=k<=18, -28<=l<=28	
Reflections collected	14466	
Independent reflections	3265 [R(int) = 0.0437]	
Completeness to theta = 25.00°	99.7 %	
Absorption correction	Semi-empirical from equivalents	
Max. and min. transmission	1.0000 and 0.6677	
Refinement method	Full-matrix least-squares on F^2	
Data / restraints / parameters	3265 / 0 / 199	
Goodness-of-fit on F^2	1.088	
Final R indices [I>2sigma(I)]	R1 = 0.0256, wR2 = 0.0459	
R indices (all data)	R1 = 0.0369, wR2 = 0.0482	
Largest diff. peak and hole	0.801 and -1.538 e.Å^{-3}	

Crystal data and structure refinement for **[PtL^{7}Cl]**

Identification code	07srv408	
Empirical formula	C18 H15 Cl N2 Pt	
Formula weight	489.86	
Temperature	120(2) K	
Wavelength	0.71073 Å	
Crystal system	Monoclinic	
Space group	P 21/n	
Unit cell dimensions	a = 9.6035(6) Å	α= 90°.
	b = 12.9196(8) Å	β= 107.5130(10)°.
	c = 12.9266(9) Å	γ = 90°.
Volume	1529.51(17) Å^3	
Z	4	
Density (calculated)	2.127 Mg/m^3	
Absorption coefficient	9.345 mm^{-1}	
F(000)	928	
Crystal size	0.12 x 0.05 x 0.05 mm^3	
Theta range for data collection	2.28 to 28.28°.	
Index ranges	-12<=h<=12, -17<=k<=15, -8<=l<=17	
Reflections collected	10349	
Independent reflections	3787 [R(int) = 0.0590]	
Completeness to theta = 25.00°	99.9 %	
Absorption correction	Semi-empirical from equivalents	
Max. and min. transmission	0.627 and 0.428	
Refinement method	Full-matrix least-squares on F^2	
Data / restraints / parameters	3787 / 0 / 201	
Goodness-of-fit on F^2	1.003	
Final R indices [I>2sigma(I)]	R1 = 0.0363, wR2 = 0.0704	
R indices (all data)	R1 = 0.0628, wR2 = 0.0779	
Largest diff. peak and hole	1.104 and -1.107 e.Å^{-3}	

Crystal data and structure refinement for **[PtL^{9}Cl]**

Identification code	08srv477	
Empirical formula	C18 H13 Cl F2 N2 Pt	
Formula weight	525.84	
Temperature	120(2) K	
Wavelength	0.71073 Å	
Crystal system	Orthorhombic	
Space group	P bcn	
Unit cell dimensions	a = 11.1153(4) Å	α= 90°.
	b = 16.4508(6) Å	β= 90°.
	c = 8.1531(3) Å	γ = 90°.
Volume	1490.84(9) Å^3	
Z	4	
Density (calculated)	2.343 Mg/m^3	
Absorption coefficient	9.615 mm^{-1}	
F(000)	992	
Crystal size	0.20 x 0.19 x 0.18 mm^3	
Theta range for data collection	2.21 to 26.37°.	
Index ranges	-13<=h<=13, -20<=k<=20, -10<=l<=10	
Reflections collected	16160	
Independent reflections	1528 [R(int) = 0.0218]	
Completeness to theta = 25.00°	100.0 %	
Absorption correction	Semi-empirical from equivalents	
Max. and min. transmission	0.177 and 0.119	
Refinement method	Full-matrix least-squares on F^2	
Data / restraints / parameters	1528 / 0 / 112	
Goodness-of-fit on F^2	1.091	
Final R indices [I>2sigma(I)]	R1 = 0.0123, wR2 = 0.0289	
R indices (all data)	R1 = 0.0169, wR2 = 0.0317	
Largest diff. peak and hole	1.299 and -0.602 e.Å^{-3}	

Crystal data and structure refinement for **[PtL^{10}Cl]**

Identification code	09srv092	
Empirical formula	C18 H13 Cl F2 N2 Pt	
Formula weight	525.84	
Temperature	120(2) K	
Wavelength	0.71073 Å	
Crystal system	Monoclinic	
Space group	C 2/c	
Unit cell dimensions	a = 15.3727(13) Å	α= 90°.
	b = 13.3686(11) Å	β= 108.552(2)°.
	c = 7.8281(6) Å	γ = 90°.
Volume	1525.2(2) Å^3	
Z	4	
Density (calculated)	2.290 Mg/m^3	
Absorption coefficient	9.398 mm^{-1}	
F(000)	992	
Crystal size	0.40 x 0.03 x 0.02 mm^3	
Theta range for data collection	2.07 to 26.37°.	
Index ranges	-19<=h<=11, -16<=k<=16, -9<=l<=9	
Reflections collected	3572	
Independent reflections	1553 [R(int) = 0.0436]	
Completeness to theta = 25.00°	99.6 %	
Absorption correction	Semi-empirical from equivalents	
Max. and min. transmission	0.829 and 0.504	
Refinement method	Full-matrix least-squares on F^2	
Data / restraints / parameters	1553 / 0 / 112	
Goodness-of-fit on F^2	1.028	
Final R indices [I>2sigma(I)]	R1 = 0.0323, wR2 = 0.0614	
R indices (all data)	R1 = 0.0438, wR2 = 0.0642	
Largest diff. peak and hole	1.106 and -0.984 e.Å^{-3}	

Crystal data and structure refinement for **[PtL^{11}Cl]**

Identification code	08srv479	
Empirical formula	C18 H13 Cl F2 N2 Pt	
Formula weight	525.84	
Temperature	120(2) K	
Wavelength	0.71073 Å	
Crystal system	Monoclinic	
Space group	P 21/c	
Unit cell dimensions	a = 7.6487(2) Å	α= 90°.
	b = 11.9204(4) Å	β= 99.0620(10)°.
	c = 17.4214(5) Å	γ = 90°.
Volume	1568.58(8) Å^3	
Z	4	
Density (calculated)	2.227 Mg/m^3	
Absorption coefficient	9.138 mm^{-1}	
F(000)	992	
Crystal size	0.40 x 0.04 x 0.02 mm^3	
Theta range for data collection	2.08 to 25.01°.	
Index ranges	-9<=h<=9, -14<=k<=13, -20<=l<=19	
Reflections collected	9039	
Independent reflections	2759 [R(int) = 0.0380]	
Completeness to theta = 25.00°	100.0 %	
Absorption correction	Semi-empirical from equivalents	
Max. and min. transmission	0.833 and 0.540	
Refinement method	Full-matrix least-squares on F^2	
Data / restraints / parameters	2759 / 0 / 219	
Goodness-of-fit on F^2	1.044	
Final R indices [I>2sigma(I)]	R1 = 0.0245, wR2 = 0.0600	
R indices (all data)	R1 = 0.0293, wR2 = 0.0633	
Largest diff. peak and hole	1.892 and -1.400 e.Å^{-3}	

Crystal data and structure refinement for **[PtL^{12}Cl]**

Identification code	07srv534	
Empirical formula	C18 H13 Cl F2 N2 Pt	
Formula weight	525.84	
Temperature	120(2) K	
Wavelength	0.71073 Å	
Crystal system	Monoclinic	
Space group	P 21/c	
Unit cell dimensions	a = 7.0679(4) Å	α= 90°.
	b = 11.8698(7) Å	β= 96.7990(10)°.
	c = 18.9947(10) Å	γ = 90°.
Volume	1582.35(15) Å^3	
Z	4	
Density (calculated)	2.207 Mg/m^3	
Absorption coefficient	9.059 mm^{-1}	
F(000)	992	
Crystal size	0.12 x 0.10 x 0.02 mm^3	
Theta range for data collection	2.03 to 26.37°.	
Index ranges	-8<=h<=8, -14<=k<=10, -23<=l<=23	
Reflections collected	9361	
Independent reflections	3233 [R(int) = 0.0460]	
Completeness to theta = 25.00°	100.0 %	
Absorption correction	Semi-empirical from equivalents	
Max. and min. transmission	0.834 and 0.482	
Refinement method	Full-matrix least-squares on F^2	
Data / restraints / parameters	3233 / 0 / 219	
Goodness-of-fit on F^2	1.022	
Final R indices [I>2sigma(I)]	R1 = 0.0289, wR2 = 0.0560	
R indices (all data)	R1 = 0.0390, wR2 = 0.0589	
Largest diff. peak and hole	0.812 and -0.918 e.Å^{-3}	

Crystal data and structure refinement for **[PtL^{13}Cl]**

Identification code	10srv021	
Empirical formula	C20 H19 Cl N2 Pt	
Formula weight	517.91	
Temperature	120(2) K	
Wavelength	0.71073 Å	
Crystal system	Monoclinic	
Space group	P 21/c	
Unit cell dimensions	a = 11.9563(3) Å	α= 90°.
	b = 13.5393(4) Å	β= 102.892(3)°.
	c = 10.8295(3) Å	γ = 90°.
Volume	1708.89(8) Å^3	
Z	4	
Density (calculated)	2.013 Mg/m^3	
Absorption coefficient	8.370 mm^{-1}	
F(000)	992	
Crystal size	0.170 x 0.115 x 0.024 mm^3	
Theta range for data collection	2.75 to 26.37°.	
Index ranges	-14<=h<=14, -16<=k<=16, -13<=l<=13	
Reflections collected	13159	
Independent reflections	3488 [R(int) = 0.0774]	
Completeness to theta = 25.00°	99.9 %	
Absorption correction	Semi-empirical from equivalents	
Max. and min. transmission	1.000 and 0.598	
Refinement method	Full-matrix least-squares on F^2	
Data / restraints / parameters	3488 / 24 / 221	
Goodness-of-fit on F^2	0.820	
Final R indices [I>2sigma(I)]	R1 = 0.0356, wR2 = 0.0641	
R indices (all data)	R1 = 0.0917, wR2 = 0.0718	
Largest diff. peak and hole	2.582 and -0.942 e.Å^{-3}	

Crystal data and structure refinement for **[PtL^{22}Cl]**

Identification code	09srv002	
Empirical formula	C16 H9 Cl F2 N2 Pt	
Formula weight	497.79	
Temperature	120(2) K	
Wavelength	0.71073 Å	
Crystal system	Monoclinic	
Space group	P 21/c	
Unit cell dimensions	a = 4.7014(3) Å	α= 90°.
	b = 18.1958(11) Å	β= 91.822(2)°.
	c = 15.9873(10) Å	γ = 90°.
Volume	1366.95(15) Å^3	
Z	4	
Density (calculated)	2.419 Mg/m^3	
Absorption coefficient	10.479 mm^{-1}	
F(000)	928	
Crystal size	0.40 x 0.02 x 0.02 mm^3	
Theta range for data collection	1.70 to 26.37°.	
Index ranges	-5<=h<=5, -22<=k<=21, -19<=l<=19	
Reflections collected	8689	
Independent reflections	2777 [R(int) = 0.0508]	
Completeness to theta = 25.00°	99.9 %	
Absorption correction	Semi-empirical from equivalents	
Max. and min. transmission	0.811 and 0.536	
Refinement method	Full-matrix least-squares on F^2	
Data / restraints / parameters	2777 / 0 / 199	
Goodness-of-fit on F^2	1.068	
Final R indices [I>2sigma(I)]	R1 = 0.0323, wR2 = 0.0741	
R indices (all data)	R1 = 0.0456, wR2 = 0.0817	
Largest diff. peak and hole	2.941 and -1.800 e.Å^{-3}	

Crystal data and structure refinement for **[PtL^{25}Cl]**

Identification code	08srv186	
Empirical formula	C33 H23 Cl N2 O4 Pt	
Formula weight	742.07	
Temperature	120(2) K	
Wavelength	0.71073 Å	
Crystal system	Triclinic	
Space group	P -1	
Unit cell dimensions	a = 7.3169(6) Å	α= 100.203(2)°.
	b = 18.7896(15) Å	β= 90.904(2)°.
	c = 21.8375(18) Å	γ = 94.254(2)°.
Volume	2945.4(4) Å^3	
Z	4	
Density (calculated)	1.673 Mg/m^3	
Absorption coefficient	4.895 mm^{-1}	
F(000)	1448	
Crystal size	0.40 x 0.03 x 0.02 mm^3	
Theta range for data collection	1.90 to 25.03°.	
Index ranges	-8<=h<=8, -17<=k<=22, -25<=l<=25	
Reflections collected	15782	
Independent reflections	10347 [R(int) = 0.0528]	
Completeness to theta = 25.00°	99.3 %	
Absorption correction	Semi-empirical from equivalents	
Max. and min. transmission	0.907 and 0.737	
Refinement method	Full-matrix least-squares on F^2	
Data / restraints / parameters	10347 / 210 / 739	
Goodness-of-fit on F^2	0.910	
Final R indices [I>2sigma(I)]	R1 = 0.0524, wR2 = 0.1036	
R indices (all data)	R1 = 0.1022, wR2 = 0.1141	
Largest diff. peak and hole	1.044 and -1.332 e.Å^{-3}	

Crystal data and structure refinement for **[PtL^{1}Br]**

Identification code	09srv360	
Empirical formula	C16 H11 Br N2 Pt	
Formula weight	506.27	
Temperature	120(2) K	
Wavelength	0.71073 Å	
Crystal system	Monoclinic	
Space group	C 2/c	
Unit cell dimensions	a = 10.5841(8) Å	α= 90°.
	b = 14.2348(10) Å	β= 99.5960(10)°.
	c = 9.0530(7) Å	γ = 90°.
Volume	1344.86(17) Å^3	
Z	4	
Density (calculated)	2.500 Mg/m^3	
Absorption coefficient	13.393 mm^{-1}	
F(000)	936	
Crystal size	0.40 x 0.14 x 0.08 mm^3	
Theta range for data collection	2.86 to 25.01°.	
Index ranges	-11<=h<=12, -12<=k<=16, -10<=l<=10	
Reflections collected	3385	
Independent reflections	1192 [R(int) = 0.0311]	
Completeness to theta = 25.00°	99.7 %	
Absorption correction	Semi-empirical from equivalents	
Max. and min. transmission	1.000 and 0.502	
Refinement method	Full-matrix least-squares on F^2	
Data / restraints / parameters	1192 / 0 / 93	
Goodness-of-fit on F^2	1.058	
Final R indices [I>2sigma(I)]	R1 = 0.0198, wR2 = 0.0480	
R indices (all data)	R1 = 0.0209, wR2 = 0.0485	
Largest diff. peak and hole	1.408 and -1.069 e.Å^{-3}	

Crystal data and structure refinement for **[PtL^{1}I]**

Identification code	10srv022	
Empirical formula	C16 H11 I N2 Pt	
Formula weight	553.26	
Temperature	120(2) K	
Wavelength	0.71073 Å	
Crystal system	Monoclinic	
Space group	C 2/c	
Unit cell dimensions	a = 10.6754(5) Å	α= 90°.
	b = 14.5303(7) Å	β= 100.8170(10)°.
	c = 9.1764(4) Å	γ = 90°.
Volume	1398.12(11) Å^3	
Z	4	
Density (calculated)	2.628 Mg/m^3	
Absorption coefficient	12.234 mm^{-1}	
F(000)	1008	
Crystal size	0.19 x 0.18 x 0.02 mm^3	
Theta range for data collection	2.40 to 25.02°.	
Index ranges	-12<=h<=12, -17<=k<=17, -10<=l<=10	
Reflections collected	7007	
Independent reflections	1236 [R(int) = 0.0397]	
Completeness to theta = 25.00°	100.0 %	
Absorption correction	Semi-empirical from equivalents	
Max. and min. transmission	1.000 and 0.597	
Refinement method	Full-matrix least-squares on F^2	
Data / restraints / parameters	1236 / 0 / 93	
Goodness-of-fit on F^2	1.065	
Final R indices [I>2sigma(I)]	R1 = 0.0203, wR2 = 0.0477	
R indices (all data)	R1 = 0.0225, wR2 = 0.0488	
Largest diff. peak and hole	0.916 and -1.188 e.Å^{-3}	

Crystal data and structure refinement for **[PtL^{1}Cl$_3$]**

Identification code	09srv361	
Empirical formula	C16 H11 Cl3 N2 Pt	
Formula weight	532.71	
Temperature	120(2) K	
Wavelength	0.71073 Å	
Crystal system	Monoclinic	
Space group	P 21/n	
Unit cell dimensions	a = 8.2638(2) Å	α= 90°.
	b = 14.2957(3) Å	β= 105.045(2)°.
	c = 13.6951(3) Å	γ = 90°.
Volume	1562.44(6) Å^3	
Z	4	
Density (calculated)	2.265 Mg/m^3	
Absorption coefficient	9.489 mm^{-1}	
F(000)	1000	
Crystal size	0.14 x 0.13 x 0.11 mm^3	
Theta range for data collection	2.62 to 26.37°.	
Index ranges	-10<=h<=10, -17<=k<=17, -17<=l<=17	
Reflections collected	12522	
Independent reflections	3196 [R(int) = 0.0393]	
Completeness to theta = 25.00°	100.0 %	
Absorption correction	Analytical	
Max. and min. transmission	0.741 and 0.297	
Refinement method	Full-matrix least-squares on F^2	
Data / restraints / parameters	3196 / 0 / 199	
Goodness-of-fit on F^2	0.898	
Final R indices [I>2sigma(I)]	R1 = 0.0219, wR2 = 0.0412	
R indices (all data)	R1 = 0.0350, wR2 = 0.0426	
Largest diff. peak and hole	1.210 and -0.510 e.Å^{-3}	

Crystal data and structure refinement for **[PtL^{12}Cl$_3$]**

Identification code	07srv249	
Empirical formula	C18 H13 Cl3 F2 N2 Pt	
Formula weight	596.74	
Temperature	120(2) K	
Wavelength	0.71073 Å	
Crystal system	Orthorhombic	
Space group	P 21 21 21	
Unit cell dimensions	a = 7.76220(10) Å	α= 90°.
	b = 14.4415(2) Å	β= 90°.
	c = 15.4510(2) Å	γ = 90°.
Volume	1732.02(4) Å^3	
Z	4	
Density (calculated)	2.288 Mg/m^3	
Absorption coefficient	8.589 mm^{-1}	
F(000)	1128	
Crystal size	0.20 x 0.10 x 0.05 mm^3	
Theta range for data collection	3.72 to 30.43°.	
Index ranges	-10<=h<=11, -19<=k<=20, -21<=l<=21	
Reflections collected	36530	
Independent reflections	4875 [R(int) = 0.0723]	
Completeness to theta = 25.00°	99.5 %	
Absorption correction	Semi-empirical from equivalents	
Max. and min. transmission	0.686 and 0.439	
Refinement method	Full-matrix least-squares on F^2	
Data / restraints / parameters	4875 / 0 / 237	
Goodness-of-fit on F^2	1.040	
Final R indices [I>2sigma(I)]	R1 = 0.0234, wR2 = 0.0508	
R indices (all data)	R1 = 0.0252, wR2 = 0.0514	
Absolute structure parameter	-0.015(5)	
Largest diff. peak and hole	1.268 and -1.791 e.Å^{-3}	

Crystal data and structure refinement for **[PtL^{15}Cl$_3$]**

Identification code	08srv328	
Empirical formula	C18 H13 Cl3 F2 N2 O2 Pt	
Formula weight	628.74	
Temperature	120(2) K	
Wavelength	0.71073 Å	
Crystal system	Monoclinic	
Space group	P 21/n	
Unit cell dimensions	a = 9.4001(10) Å	α= 90°.
	b = 10.7203(10) Å	β= 100.68(1)°.
	c = 19.1167(12) Å	γ = 90°.
Volume	1893.1(3) Å^3	
Z	4	
Density (calculated)	2.206 Mg/m^3	
Absorption coefficient	7.872 mm^{-1}	
F(000)	1192	
Crystal size	0.17 x 0.10 x 0.09 mm^3	
Theta range for data collection	2.17 to 26.37°.	
Index ranges	-11<=h<=11, 0<=k<=13, 0<=l<=23	
Reflections collected	4916	
Independent reflections	4917 [R(int) = 0.0000]	
Completeness to theta = 25.00°	99.9 %	
Absorption correction	Semi-empirical from equivalents	
Max. and min. transmission	0.492 and 0.346	
Refinement method	Full-matrix least-squares on F^2	
Data / restraints / parameters	4917 / 0 / 256	
Goodness-of-fit on F^2	0.978	
Final R indices [I>2sigma(I)]	R1 = 0.0226, wR2 = 0.0473	
R indices (all data)	R1 = 0.0300, wR2 = 0.0490	
Largest diff. peak and hole	1.351 and -0.669 e.Å^{-3}	

A.2 Relevant Publications

Aspects of the work presented in this thesis have been reported in the following publications:

1. J.A.G. Williams, S. Develay, D.L. Rochester and L. Murphy, "Optimising the Luminescence of Platinum (II) Complexes and their Application in Organic Light Emitting Devices (OLEDs)" *Coordination Chemistry Reviews*, 2008, **252**, 2596-2611

2. V. Fattori, J.A.G. Williams, L. Murphy, M. Cocchi and J. Kalinowski, "Organic Light Sources Look Forward to Optimise the Photosynthesis Process", *Photonics and Nanostructures – Fundamentals and Applications*, 2008, **6(3-4)**, 225-230

3. M. Cocchi, J. Kalinowski, V. Fattori, J.A.G. Williams and L. Murphy, "Colour-variable Highly Efficient Organic Electrophosphorescent Diodes Manipulating Molecular Exciton and Excimer Emissions", *Applied Physics Letters*, 2009, **94(7)**, 073309

4. A. Rausch, L. Murphy, J.A.G. Williams and H. Yersin, "Probing the Excited State Properties of Highly Phosphorescent Pt(dpyb)Cl Compound by High-Resolution Optical Spectroscopy", *Inorganic Chemistry*, 2009, **48**, 11407-11414

5. J. Kalinowski, M. Cocchi, V. Fattori, L. Murphy, and J.A.G. Williams, "Unified Approach to Electroluminescence Efficiency in Organic Light-Emitting Diodes, *Organic Electronics*, 2010, **11**, 724-730

6. M. Cocchi, J. Kalinowski, L. Murphy, J.A.G. Williams and V. Fattori, "Mixing of Molecular Exciton and Excimer Phosphorescence to Tune Colour and Efficiency of Organic LEDs", *Organic Electronics*, 2010, **11**, 388-396

7. L. Murphy and J. A. G. Williams, *Top. Organomet. Chem.*, 2010, **28**, 75-111

8. J. Kalinowski, M. Cocchi, L. Murphy, J. A. G. Williams and V. Fattori, *Func. Mater.*, 2010, in press